**Title**
A flexible framework for the damage-based modeling of frame elements with applications to steel structures



**Author**
Cohen, Jade

**Publication Date**
2022

Peer reviewed|Thesis/dissertation

# A flexible framework for the damage-based modeling of frame elements with applications to steel structures

by

Jade E. D. Cohen

A dissertation submitted in partial satisfaction of the

requirements for the degree of

Doctor of Philosophy

in

Engineering - Civil & Environmental Engineering

in the

Graduate Division

of the

University of California, Berkeley

Committee in charge:

Professor Filip C. Filippou, Chair
Professor Khalid M. Mosalam
Professor Panayiotis Papadopoulos

Fall 2022

A flexible framework for the damage-based modeling of frame elements with applications to steel structures

Abstract

A flexible framework for the damage-based modeling of
frame elements with applications to steel structures

by

Jade E. D. Cohen

Doctor of Philosophy in Engineering - Civil & Environmental Engineering

University of California, Berkeley

Professor Filip C. Filippou, Chair

The objective of this study is the development of analytical capabilities for the simulation of the inelastic response of structures under the strength and stiffness deterioration they experience when subjected to extreme events. The study addresses the development of such an analytical capability for steel frames. To this end, a family of 2d and 3d frame element models is proposed based on damage-plasticity. The strength and stiffness of these models degrade continuously as a function of one or more damage indices making them suitable for the damage assessment of steel frames up to incipient collapse.

The study extends an existing damage model to cover the damage evolution of the constitutive relation of the frame element under multiple, interacting stresses or stress resultants. The formulation uses several damage indices that evolve continuously with the weighted sum of the plastic energy dissipation of the stress resultants with the work-conjugate deformation variables. The damage evolution function accounts for low-cycle fatigue and the different rate of damage accumulation in primary and follower deformation cycles. The function also accounts for the fact that the behavior in one loading direction may be affected by the damage accumulated in the opposite direction.

The damage model operates as an independent wrapper of the effective force-deformation relation of the element, section or material and returns the true forces or stress resultants and the true tangent stiffness of the force-deformation relation under damage. With this modular formulation it is possible to use the damage wrapper with a material stress-strain relation, with a section force-deformation relation, or with the constitutive relation between the element basic forces and the work-conjugate deformations. Consequently, the study investigates the following three modeling alternatives for steel frame members without damage: a plasticity-based frame element with the basic forces and the work-conjugate deformations in the role of stress resultants and generalized strains, and a frame element that integrates the section force-deformation relation over the element length, with the section model based on plasticity theory for stress-resultants and generalized strains, or on the integration of the material stress-strain relation over the cross-section, a model commonly referred to as

fiber section model. With the introduction of the damage wrapper at the element, or at the section, or at the material level, six modeling alternatives for steel frame members under damage result.

Before embarking on the evaluation of the damage plasticity formulations, this study assesses the accuracy of the section model for stress-resultants by comparing its response with the response of the section model that integrates the material stress-strain relation over the cross section. To this end, an existing formulation is extended to accommodate the kinematic and isotropic hardening of the stress-resultants and the numerical implementation is enhanced with the scaling of the state determination variables to minimize the risk for an ill-conditioning of the Jacobian for the return-mapping algorithm of the section state determination.

The same process is repeated for two existing stress-resultant frame elements: a 2d beam element with linear elastic axial response, and a 3d beam-column element with axial force-biaxial flexure interaction and linear elastic torsional response. The former is suitable for steel girders experiencing small to negligible axial forces, while the latter is suitable for steel columns under any level of axial force, including variable axial forces due to the overturning effect of steel frames under lateral loads. The existing elements are extended to accommodate the kinematic and isotropic hardening of the stress-resultants and the numerical implementation is again enhanced with the scaling of the state determination variables to minimize the risk for an ill-conditioning of the Jacobian for the return-mapping algorithm of the element state determination. To account for the spread of inelasticity at the ends of steel beams and columns under strain hardening, both elements allow for the plastic hinges to be offset from the element ends. This feature requires the careful determination of the equivalent kinematic and isotropic hardening ratio for the element to match the moment-rotation relation of steel members under symmetric or anti-symmetric flexure. The study derives the necessary analytical expressions for this calibration, which are exact for beams and approximate for columns under axial force-flexure interaction. Correlation studies are conducted to assess the quality of the approximation for typical load-deformation scenarios of a steel member.

After completing the evaluation of the resultant plasticity formulations, the study compares the response of four alternatives for a frame element under damage against available experimental data from the hysteretic uniaxial and biaxial bending response of steel columns under constant and variable axial force. These comparisons lead to recommendations on a consistent set of damage parameter values for typical steel members.

The study concludes with the seismic response analysis of an irregular six-story steel frame under a strong ground acceleration in both principal directions at the base. The inelastic response history evaluates the effect of the damage evolution on the collapse risk of the frame and assesses the effect of nonlinear geometry and ground motion intensity on its global and local response.

# Contents

# List of Figures

# List of Tables

# Acknowledgments

I would like to express my deep gratitude to my advisor, Professor Filip C. Filippou, for giving me the opportunity to embark on this incredible journey by his side. His continuous guidance and support allowed me to overcome the many obstacles I encountered along the way, and his constant aim for perfection inspired me to always give my very best. I am equally thankful for the opportunity to serve as his Graduate Student Instructor in the Structural Analysis and Nonlinear Structural Analysis courses for several years in a row. Teaching under his mentorship has truly been a rewarding and inspirational experience.

I would also like to thank Professors Khalid M. Mosalam and Panayiotis Papadopoulos for agreeing to serve in my dissertation and qualifying examination committees; and would like to extend my thanks to the other members of my qualifying examination committee, Professors James M. Kelly and Per-Olof Persson. It is a real honor to have your names associated with my work and to have benefited from your valuable insights.

My gratitude extends to the Pacific Earthquake Engineering Research Center for their generous support and for granting me with my first graduate research opportunity.

I thank my dear friends in the group of SEMM, especially Dr. Tali Feinstein, Dr. Benjamin Worlsford and Paolo Martuscelli, whom I have been extremely lucky to meet through the program. Your patience, continuous encouragement, and sincere friendship have been invaluable to me. I thank Noa Dahan, who has been like a sister to me over the last four years, and always found the right words to cheer me up when I needed it the most. I am also incredibly grateful to my previous classmates at ENPC, who have become lifelong friends to me and have persistently encouraged me from overseas.

My deep gratitude goes to my parents and my sister who unfailingly supported me in this journey. A special thank to my nephew who brought an immense joy in my life since the day he was born. Finally, I am most in debt to my best friend and lifetime partner, Roy, for always supporting my ambitions and for giving me the strength to achieve my dreams, unconditionally. Thank you for being my family away from home.

# Chapter 1

# Introduction

## 1.1 Motivation

The probabilistic risk assessment and failure analysis of structures require the use of sophisticated numerical models for locating and quantifying the level of damage under a given excitation. The accuracy of these numerical models is important for assessing the performance of the structure in a way that agrees with experimental observations. Yet, in the context of large scale simulations under multiple loading scenarios, it is of equal importance that these numerical models are computationally robust and efficient.

Several sophisticated frame element models have been proposed in the literature to date for capturing the inelastic degrading behavior of slender structural members, such as beams, columns, and braces. However, the complexity of these models leads to a reduced computational efficiency, which can render their use prohibitively expensive for large scale simulations. Models with greater computational efficiency have also been proposed, but have accuracy limitations under complex loading conditions or involve ad hoc parameters that are difficult to calibrate. The suitability of each of these models depends on the final aim of the analysis. For large scale simulations under multiple loading scenarios, models with a high computational efficiency should be privileged. For the detailed analysis of a subpart of a structural model, more computationally involved elements can be employed.

The objective of this study is to propose an effective and flexible framework for the nonlinear analysis of degrading frame structures under uniaxial or biaxial excitations. To this end, the study aims to extend the available element library by developing a family of two-dimensional and three-dimensional frame elements based on damaged-plasticity with different degrees of accuracy and complexity. This dissertation focuses on the applicability of the proposed framework for the collapse simulation and earthquake-induced loss assessment of steel frame structures subjected to severe seismic excitations. However, the flexibility of the framework and of the proposed damage model is such that they can in theory be deployed for simulating the degrading behavior of other types of material, structural members or structural models.

## 1.2 Literature review

This section reviews the relevant literature in three parts: the first addresses the general formulation of inelastic frame elements, the second covers the formulation of cross section models, and the third covers the formulation of frame elements with explicit consideration of strength and stiffness deterioration.

### 1.2.1 Frame element models

Frame element models can be classified into three categories, based on the way they capture inelasticity:

1. Resultant/concentrated/lumped plasticity models: This type of element concentrates the inelastic deformations on discrete and predefined points, referred to as plastic hinges. The hinges are typically located at the element ends, while the rest of the element remains elastic. Because they concentrate the plasticity at few locations, these elements are numerically efficient.

2. Distributed plasticity models: These models monitor the element response at several integration points, also referred to as monitoring sections, distributed along the element length. The section state determination is performed at each integration point and the element response is obtained through numerical integration. The section response can either be determined from a stress-resultant section model or from a fiber section model, which is discussed in Section 1.2.2. This type of element considers that inelasticity can occur anywhere along the element and can spread within the cross section and along the element length, resulting in a model that is generally more computationally onerous.

3. Continuum mechanics models: These models discretize the member into several finite elements with prescribed stress-strain relation. This fundamental level of modeling offers the most versatility but renders their use forbiddingly expensive for the inelastic response simulation of large-scale structural models.

The following review covers resultant plasticity and distributed plasticity frame elements, which are suitable for the nonlinear analysis of large structural models.

#### 1.2.1.1 Resultant plasticity frame elements

Resultant plasticity models are widely used for the response simulation of steel structural members [58], [61], reinforced-concrete members [85], [29], or concrete-filled steel tubes [33].

The resultant plasticity element originated with the two-component model of Clough, Benuska and Wilson [20]. It consists of two components in parallel: one linear elastic-perfectly plastic and the other linear elastic. To overcome some of the limitations of the two-component model, Giberson [32] introduced two years later the one-component model, which consists of a linear elastic beam element in series with two rigid-hardening springs at its

ends. Both the two-component and the one-component model assume that the axial response is linear elastic and uncoupled from the flexural response, but the one-component model has been successfully extended to include the consideration of the axial-flexure interaction [34], [67]. One advantage of the one-component model over the two-component model is its ability to accommodate additional springs in series to capture complex deformation mechanisms, such as the pull-out of reinforcing bars in reinforced concrete structural members [29], or its ability to account for interaction between axial and flexural forces. Another advantage is that that any kind of uniaxial hysteretic law can be assigned to the nonlinear springs.

One of the challenges associated with concentrated-plasticity models is the difficulty to calibrate the plastic hinge parameters, which not only depend on the material parameters but also on the element geometry, inelastic zone length, and the boundary conditions. Yet, the calibration of these plastic hinge properties is of crucial importance to the accuracy of the numerical model [52], [2]. A second shortcoming is that most concentrated-plasticity models fail to explicitly account for the spread of inelastic deformations into the element under hardening conditions. To address this, Soleimani et. al. [77] proposed a model in which the zone of inelastic deformations gradually spreads from the beam-column interface into the member as a function of loading history. This idea was also pursued by Meyer et al. [56]. Another proposal to account for spread-of-plasticity effects is the quasi-plastic-hinge model by Attalla et al. [3]. A third challenge associated with concentrated plasticity formulations is the use of a very large elastic stiffness to artificially represent the rigid-plastic behavior of the plastic hinges, as these models are more prone to numerical issues under dynamic loading [16]. A fourth and last limitation is that, many resultant plasticity models in current commercial software like Perform3d [65] or OpenSees [60], make use of zero-length spring elements to model the plastic hinges. This results in additional degrees of freedom at the interface between the hinges and the elastic beam element that either increase the computational effort or else need to be condensed out and may give rise to numerical issues [16].

To overcome some of the above-mentioned limitations, Do [24] proposed a two-dimensional concentrated-plasticity beam model for describing the inelastic uniaxial bending response of steel frames. The model consists of a linear elastic element in series with two rigid-plastic springs. The formulation accounts for the axial-flexure interaction through the consideration of a polynomial yield envelope which evolves with kinematic and isotropic hardening. The plastic hinges can be offset from the element ends to account for the spread of inelasticity under hardening response and the size of the damage zone under softening response. Because the element specifies the plastic hinges implicitly in the element state determination rather than as separate zero-length elements, the element requires fewer degrees of freedom and achieves both a good computational efficiency and numerical robustness. However, the proposed formulation yields a hardening behavior of the element that is dependent on the plastic hinge offsets, which can lead to difficulties in the calibration of these hinge offset and hardening parameters.

#### 1.2.1.2 Distributed plasticity frame elements

The second category of frame elements for describing the inelastic behavior of beam and column structural members are distributed plasticity models. These elements use either a displacement-formulation [9], [93] [92], or a force- or mixed-formulation [17], [80], [81], [82], [57], [66], [79], [35], [88], [59]. The displacement formulation relies on the use of displacement interpolation functions to describe the kinematic relation between section and element deformations, whereas the force- or mixed-formulations rely on force interpolation functions to relate the section forces to the element forces.

Taylor et al. [88] and Lee [49] performed comparative studies and highlighted the superiority of the force-formulation over the displacement-based distributed plasticity element. Two particular advantages of the force-formulation are that the section forces are exact under linear geometry and that most structural members can be modeled with a single element. On the other hand, the displacement-formulation requires the use of multiple elements to model a single structural member.

Both types of distributed plasticity are associated with a pathological mesh sensitivity known to cause localization problems under strain-softening behavior, unless an additional parameter, the plastic hinge length, is prescribed [22]. In particular, the extension of the zone where curvatures and damage localize is not objectively determined, but depends on the dimension of the element for the displacement-based formulation, or else on the location of the integration points for the force-formulation [1]. To remedy this, Scott and Fenves [70], proposed the formulation of an efficient and objective beam element with a fixed inelastic zone length for softening response. Scott and Hamutçuoglu [71] later improved the formulation to accommodate the spread of plasticity under strain-hardening behavior. Addessi and Ciampi [1] also proposed another regularization technique to avoid localization issues in the presence of softening. Lee [50], [49] later proposed a new numerical integration of the inelastic response of frame elements that uses a variable inelastic zone length under strain hardening conditions, and a fixed damage zone length under softening conditions, at each end of the element. More recently, Yadav [91] proposed a new integration scheme with minimal number of integration points along the element in which the end points are assigned a variable integration weight to capture the spread of plasticity under hardening conditions. In addition to resolving the lack of mesh objectivity associated with distributed plasticity elements, these integration techniques allow for a reduced number of monitoring sections along the element length, which greatly improves their numerical efficiency.

### 1.2.2 Section models

Distributed plasticity elements require the use of section models for describing the section response at each integration point. The section response can either be described by a resultant plasticity model that is based on the relation between section stress-resultants and corresponding deformations [87], [39], or else through a fiber section model. The latter approach discretizes the cross section into several integration points, also referred to as

fibers, and determines the section stress-resultants by integration of the stress-strain material constitutive relation assigned to the fibers [86], [81], [82].

A benefit of the fiber section model is its ability to accurately represent complex nonlinear section responses through the use of sophisticated material models (e.g. the Giuffrè-Menegotto-Pinto model [55], [30] for the Bauschinger effect in metals). A second benefit lies in its adaptability, as each fiber can be assigned its own material constitutive relation, which is particularly suitable for modeling heterogeneous sections such as those for reinforced concrete. A third advantage is that it inherently accounts for the coupling between the axial force and the flexural forces. Furthermore, fiber section models have been successfully extended to include different degrees of interaction between internal forces [7], [48]. However, due to the large number of fibers required to discretize the cross section, and the same number of material state determination to be performed at each fiber, the distributed plasticity element with fiber section is computationally expensive.

On the other hand, section models based on resultant plasticity tend to be more economical but few formulations are available in the literature. Jin and El Tawil [39] proposed a resultant section model with a loading and bounding surface in stress-resultant space to describe the spread of plasticity along the length of the element and within the cross section. The model accounts for the axial-flexure interaction and for kinematic hardening but fails to consider isotropic hardening.

### 1.2.3 Frame element models with degrading response

There are four ways to model the strength and stiffness deterioration of the inelastic response of frame elements:

1. Account for damage at the material level through a degrading stress-strain relation. This can be achieved with a distributed plasticity frame element with fiber section discretization, or with a continuum mechanics finite element model.

2. Account for damage at the section level through a degrading relation between section forces and section deformations (e.g moment-curvature). This can be achieved with a distributed plasticity element with either a fiber section or a stress-resultant section.

3. Account for damage at the component level, e.g. by degrading the hysteretic moment-rotation relation of a concentrated plastic hinge. This can be achieved with a resultant plasticity frame element.

4. Account for damage at the element level by degrading the relation between the element forces and the corresponding deformations. This can be achieved with any type of inelastic frame element.

One way to describe the degradation at the material level is with 3d constitutive models that are based on continuum damage mechanics (CDM). These models rigorously describe the evolution of the material strength and stiffness deterioration as the result of the initiation,

growth and coalescence of microcracks or microvoids. Examples of models based on CDM are those by Lemaitre and Chaboche [51], Simo and Ju [74], and Huang [36] for ductile materials, and those by Mazars and Pijaudier-Cabot [53] and Wu and Faria [90] for concrete. A more recent example is the one by Azadi Kakavand and Taciroglu [4]. These models use one or more damage parameters to characterize the deterioration of the material response. While they are suitable for the simulation of the local response of structural members, their computational costs renders them prohibitively expensive for large structural models.

Strength and stiffness deterioration can also be accounted for with generic hysteretic models that describe the degrading response between any pair of work-conjugate variables. These models are often used to capture the damage at the material level (1d stress-strain relation), section level (moment-curvature relation), or component level (inelastic spring moment-rotation relation). They can be grouped into two categories: the polygonal hysteretic models (PHMs) and the smooth hysteretic models (SHMs). PHMs use a piecewise linear behavior to describe the response between the pair of variables, whereas SHMs refer to models with a continuous change of stiffness. Both types of model use similar sets of rules to prescribe the strength and stiffness deterioration, with criteria typically based on measures of maximum deformation and/or of hysteretic dissipated energy.

Examples of PHMs include the peak-oriented model of Clough [21] with refinements by Takeda et al. [84], the three-parameter model with pivot rule by Park et al. [63], the model by Song and Pincheira [78], and the model with four deterioration modes by Ibarra et al. [37]. Sivaselvan and Reinhorn [76] presented a detailed description of a general framework for PHMs. A recent approach that uses PHMs to describe the strength and stiffness deterioration in column members is the fiber hinge element by Kasai et al. [42]. The inelastic behavior is localized at the column base and modeled by the zero-length fiber hinge element, with each fiber assigned a phenomenological degrading stress-strain relation. Because of their multilinear formulation, PHMs accommodate the degradation at discrete instants of load or deformation reversal rather than on a continuous basis. Examples of SHMs include the model originally proposed by Bouc [10] and later extended by Wen [89]; Baber and Wen [6], Baber and Noori [5]; Casciati [12]; Reinhorn et al. [69]. Because of their smooth formulation, SMHs are able to account for strength and stiffness deterioration on a continuous basis. While they tend to be more computationally involved than PHMs, they are also more consistent and numerically robust. However, a limitation that remains with both PHMs and SHMs is that they only describe a 1d degrading relation between a force and the work-conjugate deformation.

For describing the degradation of two or more interacting work-conjugate variables (e.g. the element end forces and corresponding element deformations, or the section stress-resultants and the corresponding section deformations), researchers have applied concepts of CDM. Some of the earliest efforts to combine resultant plasticity models with the theory of CDM include the work by Cipolina et al. [18], Florez-Lopez [31], and Inglesis et al. [38]. The models adopt a bilinear force-deformation with kinematic hardening for the base response and propose different damage evolution laws for steel and reinforced concrete components. However, these damage formulations do not take into account the effect of cumulative plastic

deformations under cyclic loading. Kaewkulchai et al. [41] and Faleiro et al. [28] addressed this limitation. The model of Kaewkulchai et al. [41] employs a multi-linear lumped plasticity model in which inelasticity is assumed concentrated at the element ends. The model accounts for the interaction of the axial force and the bending moment, as well as for the strength and stiffness deterioration through a damage-variable that depends linearly on the maximum deformation and the cumulative plastic energy. Faleiro et al. [28] proposed a plastic-damage frame element model based on an energy variable with the plasticity and damage uncoupled and concentrated at the ends of the member. Lastly, Jin and El-Tawil [39] proposed a model for simulating the inelastic cyclic behavior of steel braces. The model uses stress-resultant plasticity concepts for modeling the section behavior. The degradation of the axial stiffness due to local buckling is accounted for through a damage model that is based on the cumulative axial and flexural plastic energy.

These damage models rely on the use of one or more damage indices with values between 0 (no damage) and 1 (failure). Examples of damage index models include those by Park and Ang [62], Kratzig et al. [46] and Rao et al. [68] for concrete members, and those by Krawinkler and Zohrei [47] and Ballio and Castiglioni [8] for steel members. The Park and Ang [62] damage index is based on the linear combination of the normalized maximum deformation and the normalized hysteretic energy. The damage index of Kratzig et al. [46] uses the normalized hysteretic energy of each load cycle to establish the damage index of the component. The model makes use of the concept by Konig and Ötes [44] of primary and follower half-cycles. Accordingly, a primary half-cycle (PHC) indicates any half cycle with maximum deformation amplitude; whereas a follower half-cycle (FHC) is one with smaller deformation amplitude. The energy contribution of a FHC is assumed to result in a slower rate of damage accumulation than that of a PHC. Mehanny and Deierlein [54] adopted the concept of PHCs and FHCs but based the damage index on the maximum plastic deformations rather than on the hysteretic energy. Finally, Bozorgnia and Bertero [11] modified the Park-Ang damage index to neglect the damage in the elastic range and introduced a weight coefficient for the contribution of the normalized maximum deformation.

One limitation of the existing damage models is related to the criteria for detecting the onset of damage and the description of the damage evolution. Damage evolution laws based on measures of elastic energy fail to capture the low-cycle fatigue behavior due to repeated cycles between the same range of deformation values. On the other hand, models based on the cumulative plastic deformations do not distinguish between the reduced damage accumulation for FHCs relative to PHCs. While a couple of models differentiate the damage evolution under positive and negative forces to distinguish between tensile and compressive response, very few account for the influence of positive damage on the negative response and vice versa. Furthermore, models that account for the simultaneous deterioration in different coupled mechanisms (e.g. in the axial response and flexural response of a frame element) fail to consider the effects of the damage in one mechanism on the damage in the remaining mechanisms. In particular, many models fail to capture the effect of a variable axial force on the strength deterioration in flexure, which is critical in tall structures where columns are subjected to large variations of axial force under overturning effects.

To overcome some of these limitations, Do [24], [25], [26] proposed a 1d damage model based on CDM that is able to degrade any hysteretic constitutive relation between a pair of work-conjugate variables. The strength and stiffness deterioration is described by a positive and a negative damage variables which continuously grow with the hysteretic dissipated energy and with the extreme deformation values. The damage evolution function accounts for the effect of positive damage on the negative response and vice-versa, as well as for the effect of PHC/FHC. The proposed model was validated against experimental data for different structural components and was able to describe vastly different hysteretic behaviors with a relatively consistent set of parameters. While Do [24] extended his damage model to the formulation of a resultant plasticity frame element with the damage concentrated in the plastic hinges, his proposal does not account for the damage evolution in the presence of interaction between multiple stress-resultants and the corresponding deformations.

## 1.3 Objectives and scope

The objective of this study is to extend the available element library by developing a family of computationally efficient, accurate and numerically robust damage-plasticity frame elements for the nonlinear analysis of degrading steel frames under uniaxial or biaxial excitations.

The more economical elements are based on resultant plasticity theory with a multivariate damage model inspired by continuum damage mechanics that is wrapped around the element response. They constitute an effective solution for the damage identification and collapse simulation of large scale structural models under multiple loading scenarios as they allow to capture the strength and stiffness deterioration at the global structural level and the local element level while requiring a relatively low computational effort.

The higher order elements are based on distributed plasticity formulations with a damage model that can be wrapped either at the material, or at the section, or at the element level depending on the accuracy requirements of the analysis. These elements tend to be more computationally involved but can be deployed either in small structural models or alternatively, to gradually refine specific elements of a large model at targeted locations of interest where the plasticity and damage are expected to localize.

The dissertation is organized in eight chapters, with the following contents and objectives:

1. To develop a 2d/3d resultant plasticity section model that is suitable for the non-degrading uniaxial/biaxial bending response of homogeneous cross sections. The model accounts for the interaction between the axial and the flexural responses. To compare and calibrate the section model against the existing fiber section. This is presented in Chapter 2.

2. To improve the kinematic and isotropic hardening formulation of an existing resultant plasticity beam element with plastic hinge offsets and to develop a consistent calibration

procedure for the associated hardening and hinge offset parameters. This is presented in Chapter 3.

3. To propose a 2d/3d resultant plasticity column element with plastic hinge offsets suitable for the non-degrading uniaxial/biaxial bending response of homogeneous frame elements. The proposed formulation accounts for the interaction between axial and flexural forces under the kinematic and isotropic hardening behavior that is characteristic of steel members. To compare and calibrate the element model against the existing force-based distributed plasticity element with fiber section discretization. This is presented in Chapter 4.

4. To propose a generalized damage model for the representation of strength and stiffness deterioration in the cyclic response of structural components. The model takes an existing constitutive relation between any two sets of work-conjugate variables, and computes a corresponding degraded multivariate response with consistent tangent stiffness. The damage formulation captures the low cycle fatigue behavior and accounts for the different rate of damage evolution in primary and follower half cycles, as well as the interaction between the multiple dissipating mechanisms. The model formulation is kept general so that it can be used in combination with any existing frame element, cross section, and material models. This is presented in Chapter 5.

5. To combine the multidimensional damage model with the library of proposed resultant plasticity elements as well as with existing distributed plasticity beam-column elements. The resulting element family allows the representation of the strength and stiffness deterioration of the material response, section response, or overall element response. To calibrate and validate the proposed family against experimental data under a set of complex loading scenarios with uniaxial and biaxial bending under constant or variable axial force of multiple levels. This is presented in Chapter 6.

6. To deploy the proposed resultant plasticity element with damage for the nonlinear dynamic analysis of an irregular multistory steel frame under an extreme biaxial earthquake excitation. To assess the effect of modeling assumptions on the global and local response of the frame and its damage assessment. This is presented in Chapter 7.

The dissertation concludes with Chapter 8, which summarizes the key findings of the study and offers conclusions and recommendations for further development.

# Chapter 2

# Stress resultant section with axial-flexure interaction

## 2.1 Overview

This chapter presents a section model based on plasticity theory for stress resultants that is suitable for the non-degrading uniaxial and biaxial flexural response of homogeneous cross sections under axial force. The proposed formulation accounts for the axial-flexure interaction through a polynomial yield envelope which evolves with kinematic and isotropic hardening. The section state determination is based on the return-mapping algorithm, ensuring numerical robustness with quadratic convergence of the residual for the governing equations. Following the presentation of the model, correlation studies evaluate its suitability for the moment-curvature analysis of wide-flange sections under biaxial flexure with constant or variable axial force.

## 2.2 Preliminaries

### 2.2.1 Local coordinate system for section analysis

Under Euler-Bernoulli's theory of plane sections remaining plane under the state of axial-flexural deformation, the behavior of a cross section can be described by three kinematic variables or section deformations, and three work-conjugate section forces or stress resultants. These variables are defined with reference to the local coordinate system x-y-z in Figure 2.1. The y- and z-axes correspond to the weak and strong bending axes of the section, respectively. For a right handed Cartesian coordinate system x-y-z, the x-axis is normal to the plane of the section and points toward the viewer.

The three kinematic variables are collected into the section deformation vector $\boldsymbol{e}$:

$$\boldsymbol{e} = \begin{bmatrix} \varepsilon_a & \kappa_z & \kappa_y \end{bmatrix}^T \tag{2.1}$$

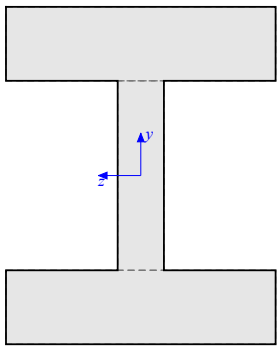


Figure 2.1: Local coordinate system for section analysis

where $\varepsilon_a$ is the normal strain at the origin of the local y-z coordinate system, also called the reference axial strain, $\kappa_z$ is the curvature about the z-axis or strong axis, and $\kappa_y$ is the curvature about the y-axis or weak axis. The curvatures are rotations per unit of length with their sign defined by the right hand screw rule.

The three section forces or stress resultants are collected into the section force vector $\boldsymbol{s}$:

$$\boldsymbol{s} = \begin{bmatrix} N & M_z & M_y \end{bmatrix}^T \tag{2.2}$$

where $N$ is the axial force, $M_z$ the bending moment about the z-axis or strong axis, and $M_y$ the bending moment about the y-axis or weak axis.

For the description of the uniaxial flexural behavior about the strong axis of the section, when $\kappa_y = 0$ and $M_y = 0$, the section deformation and section force vector reduce to:

$$\tilde{\boldsymbol{e}} = \begin{bmatrix} \varepsilon_a & \kappa_z \end{bmatrix}^T \tag{2.3}$$

$$\tilde{\boldsymbol{s}} = \begin{bmatrix} N & M_z \end{bmatrix}^T \tag{2.4}$$

In the context of nonlinear analysis, a section model needs to relate the section deformations to the section forces through a constitutive relation. Specifically, a key feature of an analytical section model is the state determination, which describes the process of determining the section forces $\boldsymbol{s}$ and the corresponding section stiffness for given section deformations $\boldsymbol{e}$.

### 2.2.2 Fiber section model

A commonly used section model is the fiber section model [86], [81], [82]. This model determines the section forces and the corresponding section stiffness by integration of the material stress-strain relation at several integration points or fibers. A common method for the evaluation of the section integrals is the midpoint integration rule. It consists of subdividing each rectangular component of the cross section into a uniform fiber mesh and

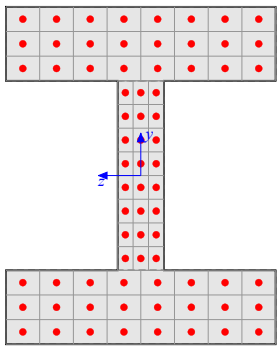

Figure 2.2: Fiber discretization of cross section

uses the fiber area as the integration and the fiber center of gravity as the monitoring point for the stress-strain relation, as Figure 2.2 shows.

The section state determination of the fiber model consists of the following steps:

1. For given section deformations $\boldsymbol{e} = \begin{bmatrix}\varepsilon_a & \kappa_z & \kappa_y\end{bmatrix}^T$, the normal strain $\varepsilon$ at each fiber monitoring point with coordinates $(y, z)$ is $\varepsilon(y, z) = \varepsilon_a - y\kappa_z + z\kappa_y$ according to the planar normal strain distribution of the Euler-Bernoulli assumption;

2. The normal stress and material modulus at each fiber monitoring point results from the material constitutive relation, which gives the stress $\sigma$ and tangent material modulus $E_t$ for a given strain $\varepsilon$;

3. The numerical integration with the midpoint rule sums up the stresses $\sigma$ and the material moduli $E_t$ over all integration points after multiplication by the corresponding integration weights to give the stress resultants $\boldsymbol{s}$ and the section stiffness $\mathbf{k}_s$.

## 2.3 Section model for stress resultants and generalized strains

An alterative section model that is computationally more economical uses plasticity theory for stress resultants to directly establish the relation between the section forces and the corresponding deformations for a homogeneous steel section. The model accounts for the interaction between the axial force and the uniaxial or biaxial bending moments with a smooth polynomial yield surface that approximates the $N$-$M_z$-$M_y$ interaction surface of the cross section. The model includes kinematic and isotropic strain hardening using concepts of plasticity theory for stress resultants.

The following presentation covers first the 2d section model for uniaxial flexure with axial force and then the 3d section model for biaxial flexure with axial force.

While the section model that directly derives the stress resultants in terms of section deformations does not provide information about the stress distribution inside the section, it offers an excellent alternative to the fiber section model for metallic structures because of its reduced computational cost.

### 2.3.1 Stress resultant model for section under uniaxial bending

This section presents the stress resultant model for a homogeneous metallic section under uniaxial bending. Even though it is not significant for the following derivations about which principal axis the flexure takes place, the presentation is based on flexure about the strong z-axis. For uniaxial bending about the weak y-axis, the subscript $z$ of the section variables should be replaced by the subscript $y$ in the following derivations.

The 2d stress resultant model has two section deformations $\boldsymbol{e}$ and two work-conjugate section forces $\boldsymbol{s}$, as follows

$$\boldsymbol{e} = \begin{bmatrix} \varepsilon_a & \kappa_z \end{bmatrix}^T \tag{2.5}$$

$$\boldsymbol{s} = \begin{bmatrix} N & M_z \end{bmatrix}^T \tag{2.6}$$

where $\varepsilon_a$ is the reference axial strain, $\kappa_z$ is the curvature about the z-axis, $N$ is the axial force, and $M_z$ the bending moment about the z-axis.

#### 2.3.1.1 Series model of section deformations

Plasticity theory is based on the concept of additive decomposition of the total strain into the strain of an elastic spring and the plastic strain of friction-slip device [73]. The same concept for section deformations decomposes the total section deformation vector $\boldsymbol{e}$ into the deformation vector $\boldsymbol{e}_e$ of the elastic component and the deformation vector $\boldsymbol{e}_p$ of the plastic component:

$$\boldsymbol{e} = \boldsymbol{e}_e + \boldsymbol{e}_p \tag{2.7}$$

with

$$\boldsymbol{e}_e = \begin{bmatrix} \varepsilon_{a,e} & \kappa_{z,e} \end{bmatrix}^T \tag{2.8}$$

$$\boldsymbol{e}_p = \begin{bmatrix} \varepsilon_{a,p} & \kappa_{z,p} \end{bmatrix}^T \tag{2.9}$$

Consistent with the series model assumption of plasticity theory, the forces of the two components are equal at all times:

$$\boldsymbol{s} = \boldsymbol{s}_e = \boldsymbol{s}_p \tag{2.10}$$

$\boldsymbol{s}_e$ denotes the section forces of the elastic component and $\boldsymbol{s}_p$ the forces of the plastic component.

#### 2.3.1.2 Constitutive relation

The section forces of the elastic component follow Hooke's law and are proportional to the corresponding deformations according to

$$\boldsymbol{s} = \mathbf{k}_{se}\boldsymbol{e}_e = \mathbf{k}_{se}\left(\boldsymbol{e} - \boldsymbol{e}_p\right) \tag{2.11}$$

where $\mathbf{k}_{se}$ is the elastic section stiffness under uniaxial bending, given by

$$\mathbf{k}_{se} = \begin{bmatrix} EA & 0 \\ 0 & EI_z \end{bmatrix} \tag{2.12}$$

for the case that the reference axis coincides with the center of gravity of the cross section. $E$ is the Young modulus of the material, $A$ the cross-sectional area of the section, and $I_z$ its moment of inertia about the z-axis.

#### 2.3.1.3 Yield function

In the absence of hardening, the absolute value of the axial force $N$ and the bending moment $M_z$ cannot exceed the respective plastic capacities $N_p$ and $M_{pz}$, which depend on the material properties and the section geometry and can be easily computed for a given cross section. Consequently, the axial force $N$ and the bending moment $M_z$ are constrained to lie within the closed intervals $[-N_p, N_p]$ and $[-M_{pz}, M_{pz}]$, respectively, in the absence of interaction. To account for the interaction between the axial force and the bending moment, the values of $N$ and $M_z$ are constrained to lie in a domain enclosed by the function $f : \mathbb{R}^2 \to \mathbb{R}$

$$f\left(\boldsymbol{s}\right) = M_{pz}\left(\phi\left(\boldsymbol{s}\right) - 1\right) \tag{2.13}$$

where $\phi : \mathbb{R}^2 \to \mathbb{R}$ is a smooth polynomial of the normalized section forces $\boldsymbol{s}$ that approximates the interaction surface of the cross section. The polynomial is defined by:

$$\phi\left(\boldsymbol{s}\right) = \sum_m a_m \left|\frac{N}{N_p}\right|^{b_m} \left|\frac{M_z}{M_{pz}}\right|^{c_m} \tag{2.14}$$

where $a_m$, $b_m$, and $c_m$ are user defined coefficients. The set of admissible section forces for a section without hardening is then defined by

$$\mathbb{E}_{\boldsymbol{s}} = \{\boldsymbol{s} \in \mathbb{R}^2 \mid f(\boldsymbol{s}) \leq 0\} \tag{2.15}$$

or equivalently

$$\mathbb{E}_{\boldsymbol{s}} = \{\boldsymbol{s} \in \mathbb{R}^2 \mid \phi(\boldsymbol{s}) \leq 1\} \tag{2.16}$$

The interior of $\mathbb{E}_{\boldsymbol{s}}$, defined by

$$\mathrm{int}(\mathbb{E}_{\boldsymbol{s}}) = \{\boldsymbol{s} \in \mathbb{R}^2 \mid f(\boldsymbol{s}) < 0\} \tag{2.17}$$

is referred to as the *elastic range*; whereas the boundary, defined as:

$$\partial \mathbb{E}_{\boldsymbol{s}} = \{\boldsymbol{s} \in \mathbb{R}^2 \mid f(\boldsymbol{s}) = 0\} \tag{2.18}$$

is called the *yield surface*.

The coefficients $a_m$, $b_m$, and $c_m$ are selected to match the interaction diagram of the given cross section. Following the calibration study by Do [24] that was also confirmed by Singh [75], the following polynomial approximates the interaction diagram of most U.S. standard wide-flange steel sections:

$$\phi(\boldsymbol{s}) = 1.2\left|\frac{N}{N_p}\right|^2 + 1.0\left|\frac{M_z}{M_{pz}}\right|^2 + 3.5\left|\frac{N}{N_p}\right|^2\left|\frac{M_z}{M_{pz}}\right|^2 \tag{2.19}$$

Figure 2.3 shows the smooth polynomial representation of the yield surface for the 2d stress resultant section model according to Equation (2.19). The yield surface according to Equation (2.19) was used throughout this study unless mentioned otherwise.

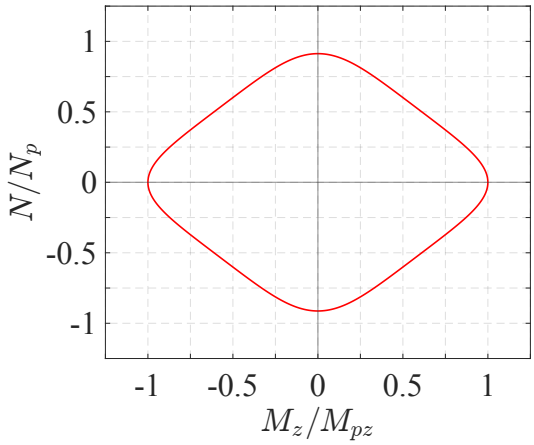


Figure 2.3: Typical initial yield envelope for 2d resultant section model

To describe the hardening behavior that metals exhibit, additional variables are necessary and the yield function needs to be modified accordingly. First, the internal variables $\boldsymbol{s}_{bk}$ representing the *section back forces* are introduced. This 2x1 vector has two components which describe the location of the yield surface center in the stress resultant space:

$$\boldsymbol{s}_{bk} = \begin{bmatrix} N_{bk} & M_{bk,z} \end{bmatrix}^T \tag{2.20}$$

Following the shift of this center during loading agrees with the experimental observation that the yield surface of many metals shifts in the direction of plastic flow. This effect is known as *kinematic hardening*.

Second, the positive *internal hardening variable* $\alpha \in \mathbb{R}^+$ is introduced. This variable describes the expansion of the elastic range $\text{int}(\mathbb{E}_{\boldsymbol{s}})$ with increasing plastic flow, without

affecting the position of the yield surface center. Because $\alpha$ expands the elastic range in all directions, it is referred to as *isotropic hardening variable*.

With the introduction of the two hardening variables the yield criterion changes to $f : \mathbb{R}^2 \times \mathbb{R}^2 \times \mathbb{R}^+ \to \mathbb{R}$ where

$$f\left(\boldsymbol{s}, \boldsymbol{s}_{bk}, \alpha\right) = M_{pz}\left[\phi\left(\boldsymbol{s} - \boldsymbol{s}_{bk}\right) - \left(1 + 2\alpha\frac{H_i}{M_{pz}}\right)\right] \tag{2.21}$$

$\phi$ is given by Equation (2.14) and $H_i \in \mathbb{R}$ is the *isotropic hardening modulus*. The set of admissible section forces becomes:

$$\mathbb{E}_{\boldsymbol{s}} = \{(\boldsymbol{s}, \boldsymbol{s}_{bk}, \alpha) \in \mathbb{R}^2 \times \mathbb{R}^2 \times \mathbb{R}^+ \mid f(\boldsymbol{s}, \boldsymbol{s}_{bk}, \alpha) \leq 0\} \tag{2.22}$$

Accordingly, the elastic domain takes the form:

$$\text{int}(\mathbb{E}_{\boldsymbol{s}}) = \{(\boldsymbol{s}, \boldsymbol{s}_{bk}, \alpha) \in \mathbb{R}^2 \times \mathbb{R}^2 \times \mathbb{R}^+ \mid f(\boldsymbol{s}, \boldsymbol{s}_{bk}, \alpha) < 0\} \tag{2.23}$$

whereas the yield surface is defined as:

$$\partial\mathbb{E}_{\boldsymbol{s}} = \{(\boldsymbol{s}, \boldsymbol{s}_{bk}, \alpha) \in \mathbb{R}^2 \times \mathbb{R}^2 \times \mathbb{R}^+ \mid f(\boldsymbol{s}, \boldsymbol{s}_{bk}, \alpha) = 0\} \tag{2.24}$$

Note that states $(\boldsymbol{s}, \boldsymbol{s}_{bk}, \alpha)$ outside $\mathbb{E}_{\boldsymbol{s}}$ are not admissible, as required by classical plasticity theory.

#### 2.3.1.4 Evolutionary equations

The flow rule describes the evolution of the plastic section deformations $\boldsymbol{e}_p$ with the irreversibility of plastic flow. The following evolution is prescribed:

$$\dot{\boldsymbol{e}}_p = \frac{\partial f}{\partial \boldsymbol{s}}\gamma = \boldsymbol{n}\gamma \tag{2.25}$$

where $\boldsymbol{n}$ is the normal to the yield surface in the stress resultant space defined as:

$$\boldsymbol{n} = \frac{\partial f}{\partial \boldsymbol{s}} = \begin{bmatrix}\dfrac{\partial f}{\partial N} & \dfrac{\partial f}{\partial M_z}\end{bmatrix}^T \tag{2.26}$$

and the parameter $\gamma \in \mathbb{R}^+$ is a nonnegative function, called the *consistency parameter*, which obeys the following Kuhn-Tucker complementarity conditions:

$$\begin{cases}\gamma \geq 0\ ,\ f(\boldsymbol{s}, \boldsymbol{s}_{bk}, \alpha) \leq 0, \\ \text{and} \\ \gamma f(\boldsymbol{s}, \boldsymbol{s}_{bk}, \alpha) = 0\end{cases} \tag{2.27}$$

In addition to the conditions of Equation (2.27), the parameter $\gamma$ satisfies the consistency requirement:

$$\gamma \dot{f}(\boldsymbol{s}, \boldsymbol{s}_{bk}, \alpha) = 0 \tag{2.28}$$

The conditions (2.27) and (2.28) are known as the *loading/unloading conditions* and the *consistency condition*, respectively. If the flow rule satisfies the condition $\dot{\boldsymbol{e}}_p = \left(\frac{\partial f}{\partial \boldsymbol{s}}\right)\gamma$, it is known as *associative*.

The normal $\boldsymbol{n}$ to the yield surface in Equation (2.26) can be expressed as:

$$\boldsymbol{n} = M_{pz}\frac{\partial \phi}{\partial \boldsymbol{s}}(\boldsymbol{s} - \boldsymbol{s}_{bk}) \tag{2.29}$$

where

$$\frac{\partial \phi}{\partial \boldsymbol{s}}(\boldsymbol{s} - \boldsymbol{s}_{bk}) = \begin{pmatrix} \sum_m a_m b_m \operatorname{sgn}(N - N_{bk}) \left|\frac{N - N_{bk}}{N_p}\right|^{b_m - 1} \left|\frac{M_z - M_{bk,z}}{M_{pz}}\right|^{c_m} \\ \sum_m a_m c_m \operatorname{sgn}(M_z - M_{bk,z}) \left|\frac{N - N_{bk}}{N_p}\right|^{b_m} \left|\frac{M_z - M_{bk,z}}{M_{pz}}\right|^{c_m - 1} \end{pmatrix} \tag{2.30}$$

and $\operatorname{sgn} : \mathbb{R} \to \mathbb{R}$ is the sign function defined as

$$\operatorname{sgn}(x) = \begin{cases} -1 \text{ if } x < 0 \\ 0 \text{ if } x = 0 \\ 1 \text{ if } x > 0 \end{cases} \tag{2.31}$$

The evolution of the back forces $\boldsymbol{s}_{bk}$ and of the isotropic variable $\alpha$ is governed by the following hardening rules:

$$\dot{\boldsymbol{s}}_{bk} = \mathbf{H}_k \dot{\boldsymbol{e}}_p = \mathbf{H}_k \boldsymbol{n} \gamma \tag{2.32}$$

$$\dot{\alpha} = -\left(\frac{\partial f}{\partial \left(H_i \alpha\right)}\right)\gamma = 2\gamma \tag{2.33}$$

where $\mathbf{H}_k$ is a 2x2 diagonal matrix referred to as the *kinematic hardening matrix* with the following components:

$$\mathbf{H}_k = \begin{bmatrix} H_{k,a} & 0 \\ 0 & H_{k,fz} \end{bmatrix} \tag{2.34}$$

and the subscripts $a$ and $fz$ stand for *axial* and *flexural about the z-axis*, respectively.

To facilitate the calibration of the hardening behavior, the kinematic hardening matrix $\mathbf{H}_k$ is expressed in terms of the dimensionless kinematic hardening ratio matrix $\mathbf{H}_{kr}$ through the elastic axial stiffness $EA$ and the elastic flexural stiffness $EI_z$ of the section:

$$\mathbf{H}_k = \begin{bmatrix} EA & 0 \\ 0 & EI_z \end{bmatrix} \mathbf{H}_{kr} \tag{2.35}$$

where $\mathbf{H}_{kr}$ takes the form:

$$\mathbf{H}_{kr} = \begin{bmatrix} H_{kr,a} & 0 \\ 0 & H_{kr,fz} \end{bmatrix} \tag{2.36}$$

Similarly, the isotropic hardening modulus $H_i$ is expressed in terms of the dimensionless isotropic hardening ratio $H_{ir}$ as follows

$$H_i = EI_z H_{ir} \tag{2.37}$$

Figure 2.4 shows the evolution of the yield envelope under kinematic and isotropic hardening.

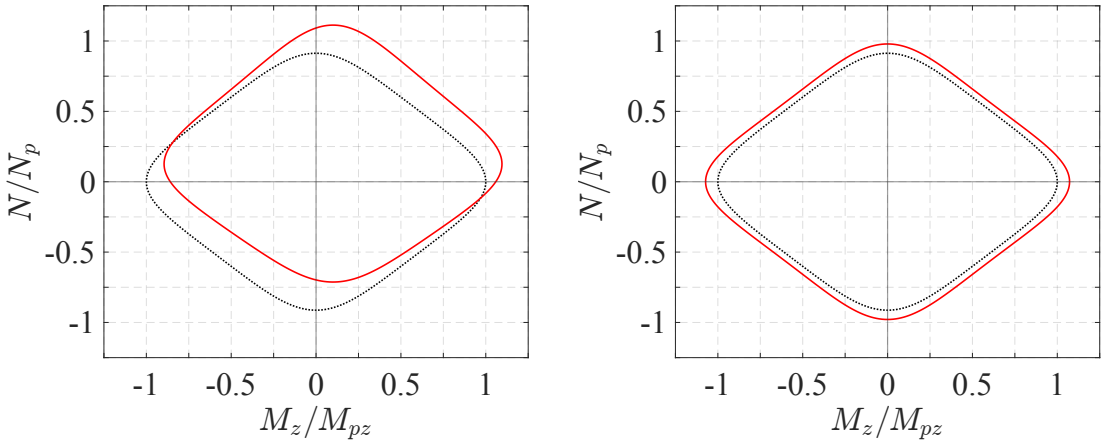


(a) Kinematic hardening (b) Isotropic hardening

Figure 2.4: Evolution of yield envelope for 2d resultant section model under kinematic and isotropic hardening

### 2.3.2 Stress resultant model for section under biaxial bending

The 2d resultant section model is extended to include the effect of biaxial bending. To this purpose, the following modifications are introduced. The 3d section model adopts three section deformations $\boldsymbol{e}$ and three section forces $\boldsymbol{s}$, as defined in Equations (2.1) and (2.2), repeated here for convenience:

$$\boldsymbol{e} = \begin{bmatrix} \varepsilon_a & \kappa_z & \kappa_y \end{bmatrix}^T \tag{2.38}$$

$$\boldsymbol{s} = \begin{bmatrix} N & M_z & M_y \end{bmatrix}^T \tag{2.39}$$

#### 2.3.2.1 Series model of section deformations

The section deformations are decomposed into the sum of an elastic deformation vector $\boldsymbol{e}_e$ and a plastic deformation vector $\boldsymbol{e}_p$ which now each have 3 components, that is:

$$\boldsymbol{e} = \boldsymbol{e}_e + \boldsymbol{e}_p \tag{2.40}$$

$$\boldsymbol{e}_e = \begin{bmatrix} \varepsilon_{a,e} & \kappa_{z,e} & \kappa_{y,e} \end{bmatrix}^T \tag{2.41}$$

$$\boldsymbol{e}_p = \begin{bmatrix} \varepsilon_{a,p} & \kappa_{z,p} & \kappa_{y,p} \end{bmatrix}^T \tag{2.42}$$

and the forces of the elastic and plastic components are equal at all times:

$$\boldsymbol{s} = \boldsymbol{s}_e = \boldsymbol{s}_p = \begin{bmatrix} N & M_z & M_y \end{bmatrix}^T \tag{2.43}$$

#### 2.3.2.2 Constitutive relation

Similarly to the uniaxial bending section model, the forces in the elastic spring are assumed to satisfy Hook's law with a stiffness equal to the elastic section stiffness $\mathbf{k}_{se}$, i.e.,

$$\boldsymbol{s} = \mathbf{k}_{se}\boldsymbol{e}_e = \mathbf{k}_{se}\left(\boldsymbol{e} - \boldsymbol{e}_p\right) \tag{2.44}$$

where $\mathbf{k}_{se}$ is the elastic section stiffness under biaxial bending conditions, which is given by

$$\mathbf{k}_{se} = \begin{bmatrix} EA & 0 & 0 \\ 0 & EI_z & 0 \\ 0 & 0 & EI_y \end{bmatrix} \tag{2.45}$$

$E$ is the Young's modulus of the material, $A$ is the cross-sectional area of the section and $I_z$ and $I_y$ are the moments of inertia about the z-axis and y-axis, respectively.

#### 2.3.2.3 Yield function

The function $\phi$ that characterizes the axial-flexure interaction surface is then modified to account for the interaction between the three stress resultants $N$, $M_z$ and $M_y$. The following unitless function is adopted:

$$\phi\left(\boldsymbol{s}\right) = \sum_m a_m \left|\frac{N}{N_p}\right|^{b_m} \left|\frac{M_z}{M_{pz}}\right|^{c_m} \left|\frac{M_y}{M_{py}}\right|^{d_m} \tag{2.46}$$

where a set of coefficients $d_m$ has been added. Singh [75] performed an extensive calibration study of the parameters of Equation (2.46) to match the biaxial behavior of a large range of wide-flange sections. This led to the following recommendation:

$$\begin{aligned} \phi\left(\boldsymbol{s}\right) = {} & 1.2\left|\frac{N}{N_p}\right|^2 + 1.0\left|\frac{M_z}{M_{pz}}\right|^2 + 1.0\left|\frac{M_y}{M_{py}}\right|^5 \\ & + 3.5\left|\frac{N}{N_p}\right|^2\left|\frac{M_z}{M_{pz}}\right|^2 + \frac{6A_f}{A_f + A_w}\left|\frac{N}{N_p}\right|^3\left|\frac{M_z}{M_{pz}}\right|^3 + 3.0\left|\frac{M_z}{M_{pz}}\right|^2\left|\frac{M_y}{M_{py}}\right|^2 \end{aligned} \tag{2.47}$$

where $A_f$ is the area of the two flanges and $A_w$ is the area of the web of the cross section. The present study adopts Equation (2.47) when modeling the biaxial bending behavior of wide-flange sections in subsequent examples, except where mentioned otherwise. Figure 2.5 shows the resulting polynomial approximation of the yield envelope when $\phi$ is defined in Equation (2.47)

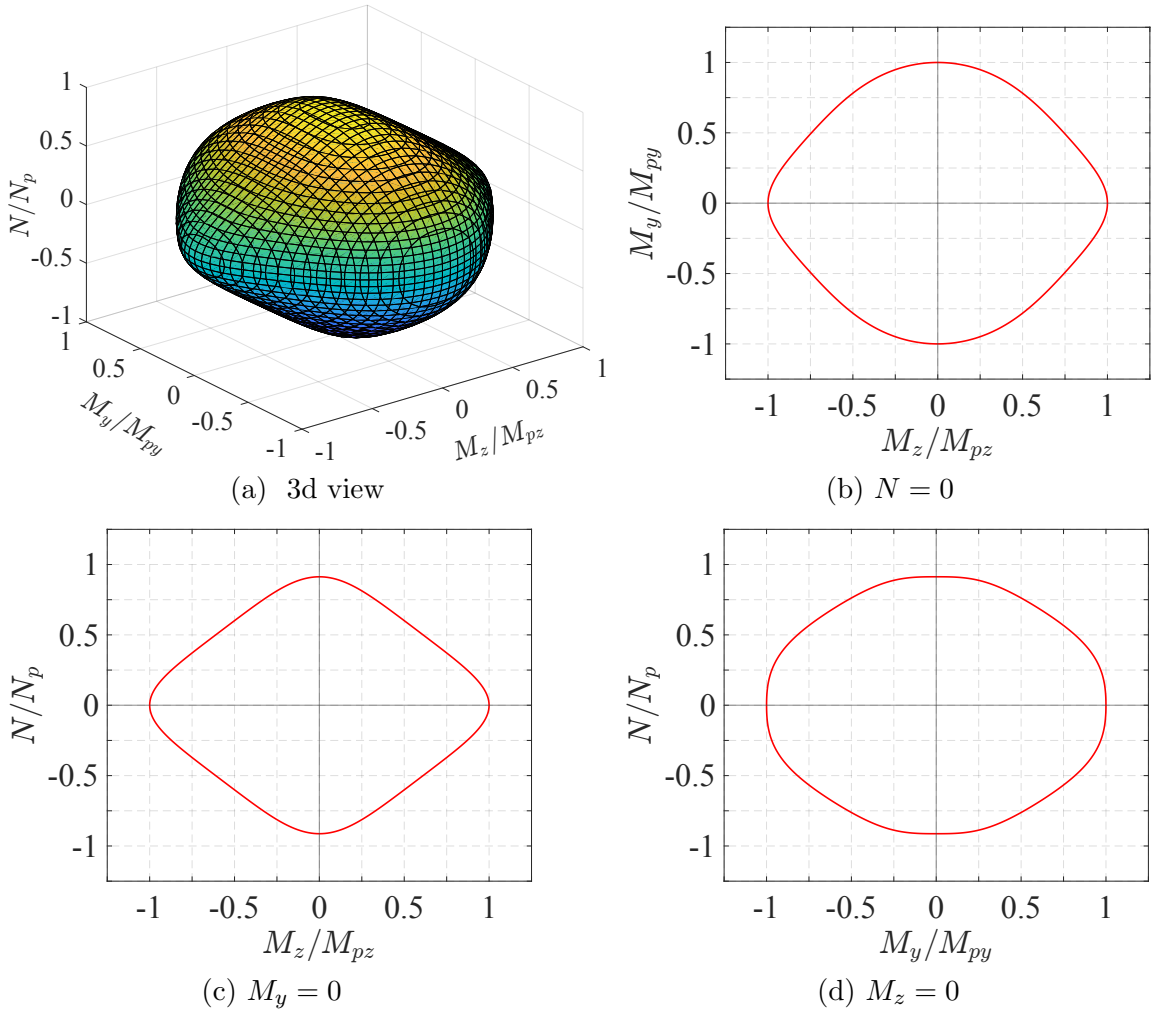


(a) 3d view (b) $N = 0$

(c) $M_y = 0$ (d) $M_z = 0$

Figure 2.5: Typical initial yield envelope for 3d resultant section model

The yield criterion is then defined as $f : \mathbb{R}^3 \times \mathbb{R}^3 \times \mathbb{R}^+ \to \mathbb{R}$:

$$f\left(\boldsymbol{s}, \boldsymbol{s}_{bk}, \alpha\right) = M_{pz}\phi\left(\boldsymbol{s} - \boldsymbol{s}_{bk}\right) - \left(M_{pz} + 2H_i\alpha\right) \tag{2.48}$$

where $\phi$ is given by Equation (2.46), $H_i \in \mathbb{R}$ is a given constant called *isotropic hardening modulus*, and

$$\boldsymbol{s}_{bk} = \begin{bmatrix} N_{bk} & M_{bk,z} & M_{bk,y} \end{bmatrix}^T \tag{2.49}$$

are the three section back forces. The set of admissible section forces becomes:

$$\mathbb{E}_{\boldsymbol{s}} = \{(\boldsymbol{s}, \boldsymbol{s}_{bk}, \alpha) \in \mathbb{R}^3 \times \mathbb{R}^3 \times \mathbb{R}^+ \mid f(\boldsymbol{s}, \boldsymbol{s}_{bk}, \alpha) \leq 0\} \tag{2.50}$$

Accordingly, the elastic domain takes the form:

$$\text{int}(\mathbb{E}_{\boldsymbol{s}}) = \{(\boldsymbol{s}, \boldsymbol{s}_{bk}, \alpha) \in \mathbb{R}^3 \times \mathbb{R}^3 \times \mathbb{R}^+ \mid f(\boldsymbol{s}, \boldsymbol{s}_{bk}, \alpha) < 0\} \tag{2.51}$$

whereas the yield surface is defined as:

$$\partial\mathbb{E}_{\boldsymbol{s}} = \{(\boldsymbol{s}, \boldsymbol{s}_{bk}, \alpha) \in \mathbb{R}^3 \times \mathbb{R}^3 \times \mathbb{R}^+ \mid f(\boldsymbol{s}, \boldsymbol{s}_{bk}, \alpha) = 0\} \tag{2.52}$$

#### 2.3.2.4 Evolutionary equations

The flow rule and the hardening laws are similar to the ones specified for the uniaxial bending section model, with the following prescribed evolutions:

$$\dot{\boldsymbol{e}}_p = \frac{\partial f}{\partial \boldsymbol{s}}\gamma = \boldsymbol{n}\gamma \tag{2.53}$$

$$\dot{\boldsymbol{s}}_{bk} = \mathbf{H}_k \dot{\boldsymbol{e}}_p = \mathbf{H}_k \boldsymbol{n}\gamma \tag{2.54}$$

$$\dot{\alpha} = -\frac{\partial f}{\partial\left(H_i \alpha\right)}\gamma = 2\gamma \tag{2.55}$$

where $\boldsymbol{n}$ is the normal to the yield function, which is defined as:

$$\boldsymbol{n} = \frac{\partial f}{\partial \boldsymbol{s}} = \begin{bmatrix} \dfrac{\partial f}{\partial N} & \dfrac{\partial f}{\partial M_z} & \dfrac{\partial f}{\partial M_y} \end{bmatrix}^T \tag{2.56}$$

and can be computed as:

$$\boldsymbol{n} = M_{pz}\frac{\partial \phi}{\partial \boldsymbol{s}}(\boldsymbol{s} - \boldsymbol{s}_{bk}) \tag{2.57}$$

$$\frac{\partial \phi}{\partial \boldsymbol{s}}(\boldsymbol{s} - \boldsymbol{s}_{bk}) = \begin{pmatrix} \displaystyle\sum_m a_m b_m \operatorname{sgn}(N - N_{bk}) \left|\frac{N - N_{bk}}{N_p}\right|^{b_m - 1} \left|\frac{M_z - M_{bk,z}}{M_{pz}}\right|^{c_m} \left|\frac{M_y - M_{bk,y}}{M_{py}}\right|^{d_m} \\ \displaystyle\sum_m a_m c_m \operatorname{sgn}(M_z - M_{bk,z}) \left|\frac{N - N_{bk}}{N_p}\right|^{b_m} \left|\frac{M_z - M_{bk,z}}{M_{pz}}\right|^{c_m - 1} \left|\frac{M_y - M_{bk,y}}{M_{py}}\right|^{d_m} \\ \displaystyle\sum_m a_m d_m \operatorname{sgn}(M_y - M_{bk,y}) \left|\frac{N - N_{bk}}{N_p}\right|^{b_m} \left|\frac{M_z - M_{bk,z}}{M_{pz}}\right|^{c_m} \left|\frac{M_y - M_{bk,y}}{M_{py}}\right|^{d_m - 1} \end{pmatrix} \tag{2.58}$$

$\mathbf{H}_k$ is a 3x3 kinematic hardening matrix with the following components:

$$\mathbf{H}_k = \begin{bmatrix} H_{k,a} & 0 & 0 \\ 0 & H_{k,fz} & 0 \\ 0 & 0 & H_{k,fy} \end{bmatrix} \tag{2.59}$$

where the subscripts $a$, $fz$ and $fy$ stand for *axial*, *flexural about z-axis* and *flexural about y-axis*, respectively.

The parameter $\gamma \in \mathbb{R}^+$ is a nonnegative function, called the *consistency parameter*, which is assumed to obey the same Kuhn-Tucker complementarity conditions as the 2d resultant section model, i.e.,

$$\begin{cases} \gamma \geq 0 \ , \ f(\boldsymbol{s}, \boldsymbol{s}_{bk}, \alpha) \leq 0, \\ \text{and} \\ \gamma f(\boldsymbol{s}, \boldsymbol{s}_{bk}, \alpha) = 0 \end{cases} \tag{2.60}$$

In addition to the conditions given by Equation (2.60), the parameter $\gamma$ satisfies the consistency requirement:

$$\gamma \dot{f}(\boldsymbol{s}, \boldsymbol{s}_{bk}, \alpha) = 0 \tag{2.61}$$

For calibration purposes, a 3x3 kinematic hardening ratio matrix $\mathbf{H}_{kr}$ as well as a scalar isotropic hardening ratio $H_{ir}$ are introduced in the following way:

$$\mathbf{H}_k = \begin{bmatrix} EA & 0 & 0 \\ 0 & EI_z & 0 \\ 0 & 0 & EI_y \end{bmatrix} \mathbf{H}_{kr} \tag{2.62}$$

$$\mathbf{H}_{kr} = \begin{bmatrix} H_{kr,a} & 0 & 0 \\ 0 & H_{kr,fz} & 0 \\ 0 & 0 & H_{kr,fy} \end{bmatrix} \tag{2.63}$$

$$H_i = EI_z H_{ir} \tag{2.64}$$

### 2.3.3 Summary of section formulation for stress resultants and generalized deformations

Table 2.1 summarizes the formulation of the 2d and 3d resultant plasticity section models.

Table 2.2 summarizes the dimensions of the various variables and parameters of the proposed 2d and 3d resultant plasticity section models.

1. **Elastic constitutive relation**

$$\boldsymbol{s} = \mathbf{k}_{se}\left(\boldsymbol{e} - \boldsymbol{e}_p\right)$$

where $\boldsymbol{e}$, $\boldsymbol{s}$, $\boldsymbol{e}_p$ and $\mathbf{k}_{se}$ are given by Equations (2.5), (2.6), (2.9) and (2.12) for the 2d model and (2.38), (2.39), (2.42) and (2.45) for the 3d model.

2. **Yield condition**

$$f\left(\boldsymbol{s}, \boldsymbol{s}_{bk}, \alpha\right) = M_{pz}\phi\left(\boldsymbol{s} - \boldsymbol{s}_{bk}\right) - \left(M_{pz} + 2H_i\alpha\right) \leq 0$$

where $\phi$ and $\boldsymbol{s}_{bk}$ are given by Equations (2.14) and (2.20) for the 2d model and (2.46) and (2.49) for the 3d model.

3. **Flow rule**

$$\dot{\boldsymbol{e}}_p = \frac{\partial f}{\partial \boldsymbol{s}}\gamma = \boldsymbol{n}\gamma$$

where $\boldsymbol{n}$ is given by Equations (2.26) and (2.56) for the 2d and 3d models, respectively.

4. **Kinematic and isotropic hardening laws**

$$\dot{\boldsymbol{s}}_{bk} = \mathbf{H}_k\dot{\boldsymbol{e}}_p = \mathbf{H}_k\boldsymbol{n}\gamma$$

$$\dot{\alpha} = -\frac{\partial f}{\partial\left(H_i\alpha\right)}\gamma = 2\gamma$$

where $\mathbf{H}_k$ is given by Equations (2.36) and (2.59) for the 2d and 3d models, respectively.

5. **Kuhn-Tucker complementarity conditions**

$$\gamma \geq 0\ ,\ f(\boldsymbol{s}, \boldsymbol{s}_{bk}, \alpha) \leq 0\ ,\ \gamma f(\boldsymbol{s}, \boldsymbol{s}_{bk}, \alpha) = 0$$

6. **Consistency condition**

$$\gamma\dot{f}(\boldsymbol{s}, \boldsymbol{s}_{bk}, \alpha) = 0 \quad (\text{if } f(\boldsymbol{s}, \boldsymbol{s}_{bk}, \alpha) = 0)$$

Table 2.1: 2d and 3d resultant plasticity section models formulation

| Variable/parameter | Dimension |
|---|---|
| $\varepsilon_a$, $\varepsilon_{a,e/p}$ | 1 |
| $\kappa_z$, $\kappa_{z,e/p}$, $\kappa_y$, $\kappa_{y,e/p}$ | 1 / length |
| $\alpha$, $\gamma$ | 1 / length |
| $N$, $N_{bk}$, $N_p$ | force |
| $M_z$, $M_{bk,z}$, $M_{pz}$ | force $\cdot$ length |
| $M_y$, $M_{bk,y}$, $M_{py}$ | force $\cdot$ length |
| $H_{ka}$ | force |
| $H_{k,fz}$, $H_{k,fy}$, $H_i$ | force $\cdot$ length$^2$ |
| $H_{kr,a}$, $H_{kr,fz}$, $H_{kr,fy}$, $H_{ir}$ | 1 |

Table 2.2: Dimensions of resultant plasticity section model variables and parameters

## 2.4 Implementation

### 2.4.1 State determination with return-mapping algorithm

The section state determination is the process of determining the section forces $\boldsymbol{s}$ under given section deformations $\boldsymbol{e}$ at a certain instant in time of the analysis.

First, the time or pseudo-time interval of interest is discretized into a finite number of smaller intervals $\bigcup_n [t_n, t_{n+1}]$. For a typical time step $[t_n, t_{n+1}]$, the problem can be posed as follows:

1. The state of the section at time $t_n$ characterized by the basic state variables
$$\{\boldsymbol{e}_n, \boldsymbol{e}_{p,n}, \boldsymbol{s}_{bk,n}, \alpha_n\} = \{\boldsymbol{e}(t_n), \boldsymbol{e}_p(t_n), \boldsymbol{s}_{bk}(t_n), \alpha(t_n)\} \tag{2.65}$$
is regarded as given and assumed to be equilibrated.

2. The section deformations increment
$$\Delta\boldsymbol{e}_{n+1} = \boldsymbol{e}_{n+1} - \boldsymbol{e}_n = \boldsymbol{e}(t_{n+1}) - \boldsymbol{e}(t_n) \tag{2.66}$$
is considered given.

3. The objective is to update the state variables to the values $\{\boldsymbol{e}_{n+1}, \boldsymbol{e}_{p,n+1}, \boldsymbol{s}_{bk,n+1}, \alpha_{n+1}\}$ at time $t_{n+1}$, so as to be able to calculate the corresponding section forces $\boldsymbol{s}_{n+1}$, in a way that is consistent with the resultant plasticity section formulation.

Note that knowing the basic state variables $\{\boldsymbol{e}_n, \boldsymbol{e}_{p,n}, \boldsymbol{s}_{bk,n}, \alpha_n\}$ at time $t_n$ fully determines the elastic section deformations $\boldsymbol{e}_{e,n}$ and the section forces $\boldsymbol{s}_n$ at that instant, with the following relations:
$$\boldsymbol{e}_{e,n} = \boldsymbol{e}_n - \boldsymbol{e}_{p,n} \tag{2.67}$$

$$\boldsymbol{s}_n = \mathbf{k}_{se}(\boldsymbol{e}_n - \boldsymbol{e}_{p,n}) = \mathbf{k}_{se}\boldsymbol{e}_{e,n} \tag{2.68}$$

For performing the section state determination at time $\boldsymbol{t}_{n+1}$, the discrete algorithmic counterparts of the flow rule and the hardening rules are obtained by applying the implicit backward Euler difference scheme. This numerical integration method produces an approximation for the solution of ordinary differential equations as follows. Let $y : \mathbb{R} \to \mathbb{R}$ be a smooth function and consider the following initial value problem:

$$\begin{cases} \dot{x}(t) = y(x(t)) \\ x(0) = x_0 \end{cases} \tag{2.69}$$

The backward Euler scheme produces a sequence $x_0, x_1, ...$ such that $x_n$ approximates $x(t_n)$. Specifically, assuming an approximation $x_n$ of the solution of (2.69) at time $t_n$ is known, the approximate solution at time $t_{n+1}$ is obtained by solving the following implicit equation for $x_{n+1}$:

$$x_{n+1} = x_n + \Delta t_{n+1} y(x_{n+1}) \tag{2.70}$$

where $\Delta t_{n+1} = t_{n+1} - t_n$.

Applying the backward Euler scheme (2.70) to Equations (2.53) - (2.55) gives:

$$\boldsymbol{e}_{p,n+1} = \boldsymbol{e}_{p,n} + \boldsymbol{n}_{n+1}\Delta\gamma \tag{2.71}$$

$$\boldsymbol{s}_{bk,n+1} = \boldsymbol{s}_{bk,n} + \mathbf{H}_k\boldsymbol{n}_{n+1}\Delta\gamma \tag{2.72}$$

$$\alpha_{n+1} = \alpha_n + 2\Delta\gamma \tag{2.73}$$

where $\Delta\gamma = \Delta t_{n+1}\gamma_{n+1} \geq 0$ is the algorithmic counterpart of the consistency parameter $\gamma$. The normal $\boldsymbol{n}_{n+1}$ is computed as

$$\boldsymbol{n}_{n+1} = \frac{\partial f}{\partial \boldsymbol{s}}(\boldsymbol{s}_{n+1}, \boldsymbol{s}_{bk,n+1}) \tag{2.74}$$

where

$$\boldsymbol{e}_{n+1} = \boldsymbol{e}_n + \Delta\boldsymbol{e}_{n+1} \tag{2.75}$$

$$\boldsymbol{s}_{n+1} = \mathbf{k}_{se}(\boldsymbol{e}_{n+1} - \boldsymbol{e}_{p,n+1}) \tag{2.76}$$

Additionally, the variables $(\boldsymbol{s}_{n+1}, \boldsymbol{s}_{bk,n+1}, \alpha_{n+1})$ are constrained by the following discrete version of the Kuhn-Tucker conditions:

$$\begin{cases} \Delta\gamma \geq 0 \ , \ f_{n+1} = f(\boldsymbol{s}_{n+1}, \boldsymbol{s}_{bk,n+1}, \alpha_{n+1}) \leq 0, \\ \text{and} \\ \Delta\gamma f_{n+1} = 0 \end{cases} \tag{2.77}$$

The problem described by Equations (2.71) - (2.77) is solved using a two step return-mapping algorithm that consists of:

1. an elastic *trial* predictor, followed by
2. a plastic corrector that performs the closest point projection of the trial state onto the yield surface.

#### 2.4.1.1 Elastic predictor

The following trial elastic state is introduced by freezing the plastic flow during the given time step, i.e. setting $\Delta\gamma = 0$ in Equations (2.71) - (2.73):

$$\boldsymbol{e}^{tr}_{p,n+1} = \boldsymbol{e}_{p,n} \tag{2.78}$$

$$\boldsymbol{s}^{tr}_{bk,n+1} = \boldsymbol{s}_{bk,n} \tag{2.79}$$

$$\alpha^{tr}_{n+1} = \alpha_n \tag{2.80}$$

This gives rise to the following trial elastic section forces:

$$\boldsymbol{s}^{tr}_{n+1} = \mathbf{k}_{se}\left(\boldsymbol{e}_{n+1} - \boldsymbol{e}_{p,n}\right) \tag{2.81}$$

and the corresponding trial normal to the yield function:

$$\boldsymbol{n}^{tr}_{n+1} = \frac{\partial f}{\partial \boldsymbol{s}}(\boldsymbol{s}^{tr}_{n+1}, \boldsymbol{s}^{tr}_{bk,n+1}) \tag{2.82}$$

Note that this trial state may not, and in general will not, correspond to any actual, physically admissible state unless the incremental process is actually elastic. The trial yield function is then evaluated as:

$$f^{tr}_{n+1} = f(\boldsymbol{s}^{tr}_{n+1}, \boldsymbol{s}^{tr}_{bk,n+1}, \alpha^{tr}_{n+1}) \tag{2.83}$$

If $f^{tr}_{n+1} \leq 0$, the trial state is admissible and the section response is elastic. Accordingly, the state variables are equal to their trial state values, i.e.,

$$\boldsymbol{e}_{p,n+1} = \boldsymbol{e}^{tr}_{p,n+1} \tag{2.84}$$

$$\boldsymbol{s}_{bk,n+1} = \boldsymbol{s}^{tr}_{bk,n+1} \tag{2.85}$$

$$\alpha_{n+1} = \alpha^{tr}_{n+1} \tag{2.86}$$

the section forces at the end of the time step $t_{n+1}$ are set to

$$\boldsymbol{s}_{n+1} = \boldsymbol{s}^{tr}_{n+1} \tag{2.87}$$

and the section tangent stiffness is computed according to Section 2.4.2, concluding the section state determination.

On the other hand, if $f^{tr}_{n+1} > 0$, the trial state is not admissible and a plastic correction is required.

#### 2.4.1.2 Plastic corrector

If $f_{n+1}^{tr} > 0$, an iterative solution is needed to enforce the Kuhn-Tucker conditions. Since the original assumption $\Delta\gamma = 0$ results in a non admissible trial state, it follows that the true plastic flow $\Delta\gamma$ must be nonzero. Combining this requirement with conditions (2.77) implies that

$$f_{n+1} = 0 \tag{2.88}$$

i.e. the corrected state at $t_{n+1}$ must lie on the yield surface.

Accordingly, the correction procedure adopts the Newton-Raphson method to compute the *closest point projection* from the trial state onto the yield surface [73]. Let

$$\Delta\boldsymbol{e}_{p,n+1} = \boldsymbol{e}_{p,n+1} - \boldsymbol{e}_{p,n+1}^{tr} = \boldsymbol{e}_{p,n+1} - \boldsymbol{e}_{p,n} \tag{2.89}$$

be the required correction for the plastic deformations. With the superscript $k$ indicating the iteration number, define the following residual equations for the plastic deformations, back forces, isotropic hardening variable and yield condition, respectively:

$$\begin{cases} \boldsymbol{R}_{ep}^{(k)} &= -\Delta\boldsymbol{e}_{p,n+1}^{(k)} + \boldsymbol{n}_{n+1}^{(k)}\Delta\gamma^{(k)} \\ \boldsymbol{R}_{bk}^{(k)} &= -\boldsymbol{s}_{bk,n+1}^{(k)} + \boldsymbol{s}_{bk,n} + \mathbf{H}_k\boldsymbol{n}_{n+1}^{(k)}\Delta\gamma^{(k)} \\ R_{\alpha}^{(k)} &= -\alpha_{n+1}^{(k)} + \alpha_n + 2\Delta\gamma^{(k)} \\ R_f^{(k)} &= f(\boldsymbol{s}_{n+1}^{(k)}, \boldsymbol{s}_{bk,n+1}^{(k)}, \alpha_{n+1}^{(k)}) \end{cases} \tag{2.90}$$

which are the counterparts of Equations (2.71) - (2.73) and (2.88). The vector of residuals $\boldsymbol{R}^{(k)}$ and the vector of unknowns $\boldsymbol{x}^{(k)}$ at iteration $k$ are:

$$\boldsymbol{R}^{(k)} = \begin{pmatrix} \boldsymbol{R}_{ep}^{(k)} \\ \boldsymbol{R}_{bk}^{(k)} \\ R_{\alpha}^{(k)} \\ R_f^{(k)} \end{pmatrix} \quad ; \quad \boldsymbol{x}^{(k)} = \begin{pmatrix} \boldsymbol{s}_{n+1}^{(k)} \\ \boldsymbol{s}_{bk,n+1}^{(k)} \\ \alpha_{n+1}^{(k)} \\ \Delta\gamma^{(k)} \end{pmatrix} \tag{2.91}$$

The Newton-Raphson iterations start by initializing the unknowns to the values of the trial state, i.e.,

$$\boldsymbol{x}^{(0)} = \begin{pmatrix} \boldsymbol{s}_{n+1}^{(0)} \\ \boldsymbol{s}_{bk,n+1}^{(0)} \\ \alpha_{n+1}^{(0)} \\ \Delta\gamma^{(0)} \end{pmatrix} = \begin{pmatrix} \boldsymbol{s}_{n+1}^{tr} \\ \boldsymbol{s}_{bk,n+1}^{tr} \\ \alpha_{n+1}^{tr} \\ 0 \end{pmatrix} \tag{2.92}$$

The state variables get updated at each iteration according to

$$\boldsymbol{x}^{(k+1)} = \boldsymbol{x}^{(k)} + \delta\boldsymbol{x}^{(k)} \tag{2.93}$$

where the correction is obtained as:

$$\delta \boldsymbol{x}^{(k)} = -\left[\mathbf{J}^{(k)}\right]^{-1} \boldsymbol{R}^{(k)} \tag{2.94}$$

and $\mathbf{J}^{(k)}$ is the Jacobian of the system of nonlinear equations (2.90) at the $k$-th iteration defined as

$$\mathbf{J}^{(k)} = \frac{\partial \boldsymbol{R}^{(k)}}{\partial \boldsymbol{x}^{(k)}} = \begin{bmatrix} \dfrac{\partial \boldsymbol{R}_{ep}^{(k)}}{\partial \boldsymbol{s}_{n+1}^{(k)}} & \dfrac{\partial \boldsymbol{R}_{ep}^{(k)}}{\partial \boldsymbol{s}_{bk,n+1}^{(k)}} & \dfrac{\partial \boldsymbol{R}_{ep}^{(k)}}{\partial \alpha_{n+1}^{(k)}} & \dfrac{\partial \boldsymbol{R}_{ep}^{(k)}}{\partial \Delta\gamma^{(k)}} \\ \dfrac{\partial \boldsymbol{R}_{bk}^{(k)}}{\partial \boldsymbol{s}_{n+1}^{(k)}} & \dfrac{\partial \boldsymbol{R}_{bk}^{(k)}}{\partial \boldsymbol{s}_{bk,n+1}^{(k)}} & \dfrac{\partial \boldsymbol{R}_{bk}^{(k)}}{\partial \alpha_{n+1}^{(k)}} & \dfrac{\partial \boldsymbol{R}_{bk}^{(k)}}{\partial \Delta\gamma^{(k)}} \\ \dfrac{\partial R_{\alpha}^{(k)}}{\partial \boldsymbol{s}_{n+1}^{(k)}} & \dfrac{\partial R_{\alpha}^{(k)}}{\partial \boldsymbol{s}_{bk,n+1}^{(k)}} & \dfrac{\partial R_{\alpha}^{(k)}}{\partial \alpha_{n+1}^{(k)}} & \dfrac{\partial R_{\alpha}^{(k)}}{\partial \Delta\gamma^{(k)}} \\ \dfrac{\partial R_{f}^{(k)}}{\partial \boldsymbol{s}_{n+1}^{(k)}} & \dfrac{\partial R_{f}^{(k)}}{\partial \boldsymbol{s}_{bk,n+1}^{(k)}} & \dfrac{\partial R_{f}^{(k)}}{\partial \alpha_{n+1}^{(k)}} & \dfrac{\partial R_{f}^{(k)}}{\partial \Delta\gamma^{(k)}} \end{bmatrix} \tag{2.95}$$

In order to evaluate $\boldsymbol{R}_{ep}^{(k+1)}$ at the next iteration, it is necessary to update the plastic section deformations increment in a way that is consistent with the correction $\delta \boldsymbol{x}^{(k)}$. The required correction is given by

$$\Delta \boldsymbol{e}_{p,n+1}^{(k+1)} = \Delta \boldsymbol{e}_{p,n+1}^{(k)} - \mathbf{f}_{se} \delta \boldsymbol{s}_{n+1}^{(k)} \tag{2.96}$$

where $\mathbf{f}_{se} = \mathbf{k}_{se}^{-1}$. It should be noted that the selection of residuals and vector of unknowns in Equation (2.91) can lead in certain cases to ill-conditioned Jacobian matrices in Equation (2.95). This is due to the large variability in the order of magnitude of the variables that represent different physical quantities and carry inconsistent units. A more robust implementation consists in normalizing the unknowns as well as the residuals with given reference quantities before setting up the Newton-Raphson iterations. This is taken into consideration in the current implementation of the model which uses normalized residuals and unknown variables to avoid convergence issues.

The iterations are terminated when the following convergence test is satisfied:

$$\left| \frac{\delta W^{(k)}}{\delta W^{(0)}} \right| \leq \text{tol} \tag{2.97}$$

where tol is a specified relative tolerance and $W^{(k)}$ represents the energy unbalance at iteration $k$ which is defined as follows:

$$\delta W^{(k)} = \left[\delta \boldsymbol{s}_{n+1}^{(k)}\right]^T \boldsymbol{R}_{ep}^{(k)} + \left[\boldsymbol{n}_{n+1}^{(k)} \delta \Delta\gamma^{(k)}\right]^T \boldsymbol{R}_{bk}^{(k)} + H_i \delta \alpha_{n+1}^{(k)} \cdot R_{\alpha}^{(k)} + \delta \Delta\gamma^{(k)} \cdot R_f^{(k)} \tag{2.98}$$

Upon convergence, the section plastic deformations are updated to

$$\boldsymbol{e}_{p,n+1} = \boldsymbol{e}_{p,n+1}^{tr} + \Delta \boldsymbol{e}_{p,n+1} \tag{2.99}$$

whereas the section tangent stiffness is computed according to Section 2.4.2.

### 2.4.2 Section tangent stiffness

If the step is elastic, i.e. if the trial state is admissible, the section tangent stiffness is set equal to the elastic stiffness:

$$\mathbf{k}_{s,n+1} = \frac{d\boldsymbol{s}_{n+1}}{d\boldsymbol{e}_{n+1}} = \mathbf{k}_{se} \tag{2.100}$$

If the trial state is not admissible, the section tangent stiffness is updated upon convergence of the Newton-Raphson iterations of the plastic correction procedure. Because it is calculated in a way that is consistent with the backward-Euler integration algorithm, it is referred to as the consistent (algorithmic) tangent stiffness. This characteristic is of crucial importance for maintaining the quadratic rate of convergence of the Newton-Raphson solution procedure [73].

Making use of Equations (2.68) and (2.76), one can rewrite the first equation of (2.90) after dropping the superscript $k$ as

$$\boldsymbol{R}_{ep} = -\boldsymbol{e}_{p,n+1} + \boldsymbol{e}_{p,n} + \boldsymbol{n}_{n+1}\Delta\gamma \tag{2.101}$$

$$= -\boldsymbol{e}_{n+1} + \boldsymbol{e}_n + \mathbf{f}_{se}\left(\boldsymbol{s}_{n+1} - \boldsymbol{s}_n\right) + \boldsymbol{n}_{n+1}\Delta\gamma \tag{2.102}$$

where $\mathbf{f}_{se} = \mathbf{k}_{se}^{-1}$.

After noting that $\boldsymbol{R} = 0$ upon convergence and making use of Equation (2.102), differentiating (2.90) under fixed variables at time $t_n$ gives the following equation:

$$d\boldsymbol{R} = \mathbf{0} = \frac{\partial \boldsymbol{R}}{\partial \boldsymbol{e}_{n+1}} d\boldsymbol{e}_{n+1} + \frac{\partial \boldsymbol{R}}{\partial \boldsymbol{x}} d\boldsymbol{x} \tag{2.103}$$

where

$$\frac{\partial \boldsymbol{R}}{\partial \boldsymbol{e}_{n+1}} = \begin{pmatrix} -\mathbf{I} \\ \mathbf{0} \\ \mathbf{0} \\ \mathbf{0} \end{pmatrix} \tag{2.104}$$

Rearranging the terms gives

$$\begin{pmatrix} d\boldsymbol{e}_{n+1} \\ \mathbf{0} \\ 0 \\ 0 \end{pmatrix} = \begin{bmatrix} \frac{\partial \boldsymbol{R}_{ep}}{\partial \boldsymbol{s}_{n+1}} & \frac{\partial \boldsymbol{R}_{ep}}{\partial \boldsymbol{s}_{bk,n+1}} & \frac{\partial \boldsymbol{R}_{ep}}{\partial \alpha_{n+1}} & \frac{\partial \boldsymbol{R}_{ep}}{\partial \Delta\gamma} \\ \frac{\partial \boldsymbol{R}_{bk}}{\partial \boldsymbol{s}_{n+1}} & \frac{\partial \boldsymbol{R}_{bk}}{\partial \boldsymbol{s}_{bk,n+1}} & \frac{\partial \boldsymbol{R}_{bk}}{\partial \alpha_{n+1}} & \frac{\partial \boldsymbol{R}_{bk}}{\partial \Delta\gamma} \\ \frac{\partial R_{\alpha}}{\partial \boldsymbol{s}_{n+1}} & \frac{\partial R_{\alpha}}{\partial \boldsymbol{s}_{bk,n+1}} & \frac{\partial R_{\alpha}}{\partial \alpha_{n+1}} & \frac{\partial R_{\alpha}}{\partial \Delta\gamma} \\ \frac{\partial R_f}{\partial \boldsymbol{s}_{n+1}} & \frac{\partial R_f}{\partial \boldsymbol{s}_{bk,n+1}} & \frac{\partial R_f}{\partial \alpha_{n+1}} & \frac{\partial R_f}{\partial \Delta\gamma} \end{bmatrix} \begin{pmatrix} d\boldsymbol{s}_{n+1} \\ d\boldsymbol{s}_{bk,n+1} \\ d\alpha_{n+1} \\ d\Delta\gamma \end{pmatrix} \tag{2.105}$$

With the definition of the block matrices

$$\mathbf{f}_{rr} = \left[\frac{\partial \boldsymbol{R}_{ep}}{\partial \boldsymbol{s}_{n+1}}\right] \quad ; \quad \mathbf{f}_{rc} = \left[\frac{\partial \boldsymbol{R}_{ep}}{\partial \boldsymbol{s}_{bk,n+1}} \quad \frac{\partial \boldsymbol{R}_{ep}}{\partial \alpha_{n+1}} \quad \frac{\partial \boldsymbol{R}_{ep}}{\partial \Delta\gamma}\right] \tag{2.106}$$

$$\mathbf{f}_{cr} = \begin{bmatrix} \dfrac{\partial \boldsymbol{R}_{bk}}{\partial \boldsymbol{s}_{n+1}} \\ \dfrac{\partial R_\alpha}{\partial \boldsymbol{s}_{n+1}} \\ \dfrac{\partial R_f}{\partial \boldsymbol{s}_{n+1}} \end{bmatrix} \quad ; \quad \mathbf{f}_{cc} = \begin{bmatrix} \dfrac{\partial \boldsymbol{R}_{bk}}{\partial \boldsymbol{s}_{bk,n+1}} & \dfrac{\partial \boldsymbol{R}_{bk}}{\partial \alpha_{n+1}} & \dfrac{\partial \boldsymbol{R}_{bk}}{\partial \Delta\gamma} \\ \dfrac{\partial R_\alpha}{\partial \boldsymbol{s}_{bk,n+1}} & \dfrac{\partial R_\alpha}{\partial \alpha_{n+1}} & \dfrac{\partial R_\alpha}{\partial \Delta\gamma} \\ \dfrac{\partial R_f}{\partial \boldsymbol{s}_{bk,n+1}} & \dfrac{\partial R_f}{\partial \alpha_{n+1}} & \dfrac{\partial R_f}{\partial \Delta\gamma} \end{bmatrix} \tag{2.107}$$

the stiffness condensation of Equation (2.105) gives the section flexibility matrix

$$\frac{d\boldsymbol{e}_{n+1}}{d\boldsymbol{s}_{n+1}} = \mathbf{f}_{rr} - \mathbf{f}_{rc}\mathbf{f}_{cc}^{-1}\mathbf{f}_{cr} \tag{2.108}$$

Inverting the flexibility as given by the expression in Equation (2.108) is one way of obtaining the section tangent stiffness matrix. However, this approach requires inverting $\mathbf{f}_{cc}$ which could be singular, which is the case in particular when $\mathbf{H}_k = \mathbf{0}$ and $H_i = 0$ [24]. An alternative solution is to use the Woodbury matrix identity:

$$(\mathbf{A} + \boldsymbol{U}\mathbf{C}\boldsymbol{V})^{-1} = \mathbf{A}^{-1} - \mathbf{A}^{-1}\boldsymbol{U}(\mathbf{C}^{-1} + \boldsymbol{V}\mathbf{A}^{-1}\boldsymbol{U})^{-1}\boldsymbol{V}\mathbf{A}^{-1} \tag{2.109}$$

Applying this identity to invert the right hand side of Equation (2.108) gives the following expression for the section tangent stiffness:

$$\mathbf{k}_{s,n+1} = \frac{d\boldsymbol{s}_{n+1}}{d\boldsymbol{e}_{n+1}} = \mathbf{f}_{rr}^{-1} + \mathbf{f}_{rr}^{-1}\mathbf{f}_{rc}(\mathbf{f}_{cc} - \mathbf{f}_{cr}\mathbf{f}_{rr}^{-1}\mathbf{f}_{rc})^{-1}\mathbf{f}_{cr}\mathbf{f}_{rr}^{-1} \tag{2.110}$$

The latter approach is adopted in the present formulation.

### 2.4.3 Summary of state determination algorithm

The state determination algorithm for the 2d and 3d resultant plasticity section models is summarized in Table 2.3.

## 2.5 Validation studies

### 2.5.1 Moment-curvature analyses of wide-flange sections

To characterize the performance of the resultant plasticity section model, an extensive set of moment-curvature analyses is conducted with uniaxial and biaxial bending under constant

**Objective:** Given $\boldsymbol{e}_n$, $\boldsymbol{e}_{p,n}$, $\boldsymbol{s}_{bk,n}$, $\alpha_n$ at time $t_n$ and $\boldsymbol{e}_{n+1}$ at time $t_{n+1}$, evaluate $\boldsymbol{e}_{p,n+1}$, $\boldsymbol{s}_{bk,n+1}$, $\alpha_{n+1}$, $\boldsymbol{s}_{n+1}$ and $\mathbf{k}_{s,n+1}$ at time $t_{n+1}$.

1. **Compute trial elastic state:**

   Evaluate $\boldsymbol{e}^{tr}_{p,n+1}$, $\boldsymbol{s}^{tr}_{bk,n+1}$, $\alpha^{tr}_{n+1}$ and $\boldsymbol{s}^{tr}_{n+1}$ in Equations (2.78)-(2.81)

2. **Check yield condition:**

   Evaluate $f^{tr}_{n+1} = f(\boldsymbol{s}^{tr}_{n+1}, \boldsymbol{s}^{tr}_{bk,n+1}, \alpha^{tr}_{n+1})$
   IF: $f^{tr}_{n+1} < 0$, THEN:

   a) Set $(\cdot)_{n+1} = (\cdot)^{tr}_{n+1}$

   b) Set $\mathbf{k}_{s,n+1} = \mathbf{k}_{se}$ and *EXIT*

   ELSE: Go to 3

3. **Perform plastic correction with closest point projection algorithm:**

   a) Initialize $k = 0$, set $(\cdot)^{(0)}_{n+1} = (\cdot)^{tr}_{n+1}$ and evaluate $\boldsymbol{x}^{(0)}$ in Equation (2.92)

   b) Evaluate residual vector $\boldsymbol{R}^{(k)}$ in Equations (2.90)-(2.91)

   c) Evaluate Jacobian of Newton-Raphson iterations $\mathbf{J}^{(k)}$ in Equation (2.95)

   d) Evaluate increment of state variables $\delta\boldsymbol{x}^{(k)} = -\left[\mathbf{J}^{(k)}\right]^{-1}\boldsymbol{R}^{(k)}$

   e) Update state variables $\boldsymbol{x}^{(k+1)} = \boldsymbol{x}^{(k)} + \delta\boldsymbol{x}^{(k)}$

   f) Update $\Delta\boldsymbol{e}^{(k+1)}_{p,n+1} = \Delta\boldsymbol{e}^{(k)}_{p,n+1} - \mathbf{f}_{se}\delta\boldsymbol{s}^{(k)}_{n+1}$ where $\mathbf{f}_{se} = \mathbf{k}^{-1}_{se}$

   g) Evaluate energy unbalance $\delta W^{(k)}$ in Equation (2.98)

   IF $\left|\dfrac{\delta W^{(k)}}{\delta W^{(0)}}\right| \leq$ tol, THEN:

   i. Set $(\cdot)_{n+1} = (\cdot)^{(k+1)}_{n+1}$

   ii. Set $\boldsymbol{e}_{p,n+1} = \boldsymbol{e}^{tr}_{p,n+1} + \Delta\boldsymbol{e}_{p,n+1}$

   iii. Evaluate $\mathbf{k}_{s,n+1}$ in Equations (2.106), (2.107) and (2.110) and *EXIT*

   ELSE: Set $k \leftarrow k + 1$ and Go to 3b

Table 2.3: Resultant plasticity section state determination algorithm

or variable axial force of multiple levels. Such analyses consist in imposing curvatures and axial force histories and solving for the resulting bending moments and reference axial strain. In other words, the histories of $\kappa_z$, $\kappa_y$ and $N$ are prescribed, and the unknowns are $M_z$, $M_y$ and $\varepsilon_a$. Two section sizes are investigated: a W14x730 and a W12x120 steel cross sections.

#### 2.5.1.1 Load and deformation histories

To evaluate the accuracy of the resultant section model under complex loading scenarios, seven different load patterns are investigated.

Four of these load patterns are representative of uniaxial bending about the strong axis of the section and identified with the letter "U". This type of loading is equivalent to what the base section of a cantilever column would undergo if a uniaxial displacement history in the y-direction was prescribed at the tip. The first load pattern, U0, consists in imposing a monotonically increasing curvature $\kappa_z$, while applying a constant axial force $N$ on the section. It is illustrated in Figure 2.6 (a). The second one, U1, consists in imposing four symmetric cycles of increasing magnitude for $\kappa_z$ while prescribing a constant value for $N$. The third one, U2, is similar to U1 but uses three non-symmetric curvature cycles. Lastly, the fourth load pattern UV1 is similar to U1, but imposes a cyclically variable axial force which magnitude increases with that of the curvature cycles. The letter "V", here, stands for variable axial force. Such variation of the axial force is representative of the overturning moment effect that is typically experienced by columns of multistory frames subjected to earthquake excitations. The curvature and axial load histories for load patterns U1, U2 and UV1 are shown in Figures 2.6 (b), (c) and (d).

Three biaxial load patterns are also investigated. The first one, B1 (where "B" now stands for biaxial), imposes four cycles of a circular tip displacement along with a constant axial force on the section. It is illustrated in Figure 2.6 (e). The second one, B2, describes four cycles of a clover-leaf tip displacement under constant axial force, as illustrated in Figure 2.6 (f). Lastly, BV1 describes a circular curvature history with variable axial force, and is illustrated in Figure 2.6 (g).

The curvature load factors depicted in Figure 2.6 are such that the imposed curvatures on the section are given by:

$$\kappa_z = \text{Curv. load factor} \cdot \kappa_{z,ref} \tag{2.111}$$

$$\kappa_y = \text{Curv. load factor} \cdot \kappa_{y,ref} \tag{2.112}$$

where $\kappa_{z,ref} = \kappa_{y,ref} = 5\kappa_{pz}$ and $\kappa_{pz} = M_{pz}/EI_z$.

For each load pattern, multiple axial force levels are investigated, as summarized in Table 2.4. These levels are measured with reference to the axial plastic capacity of the cross sections, $N_p$.

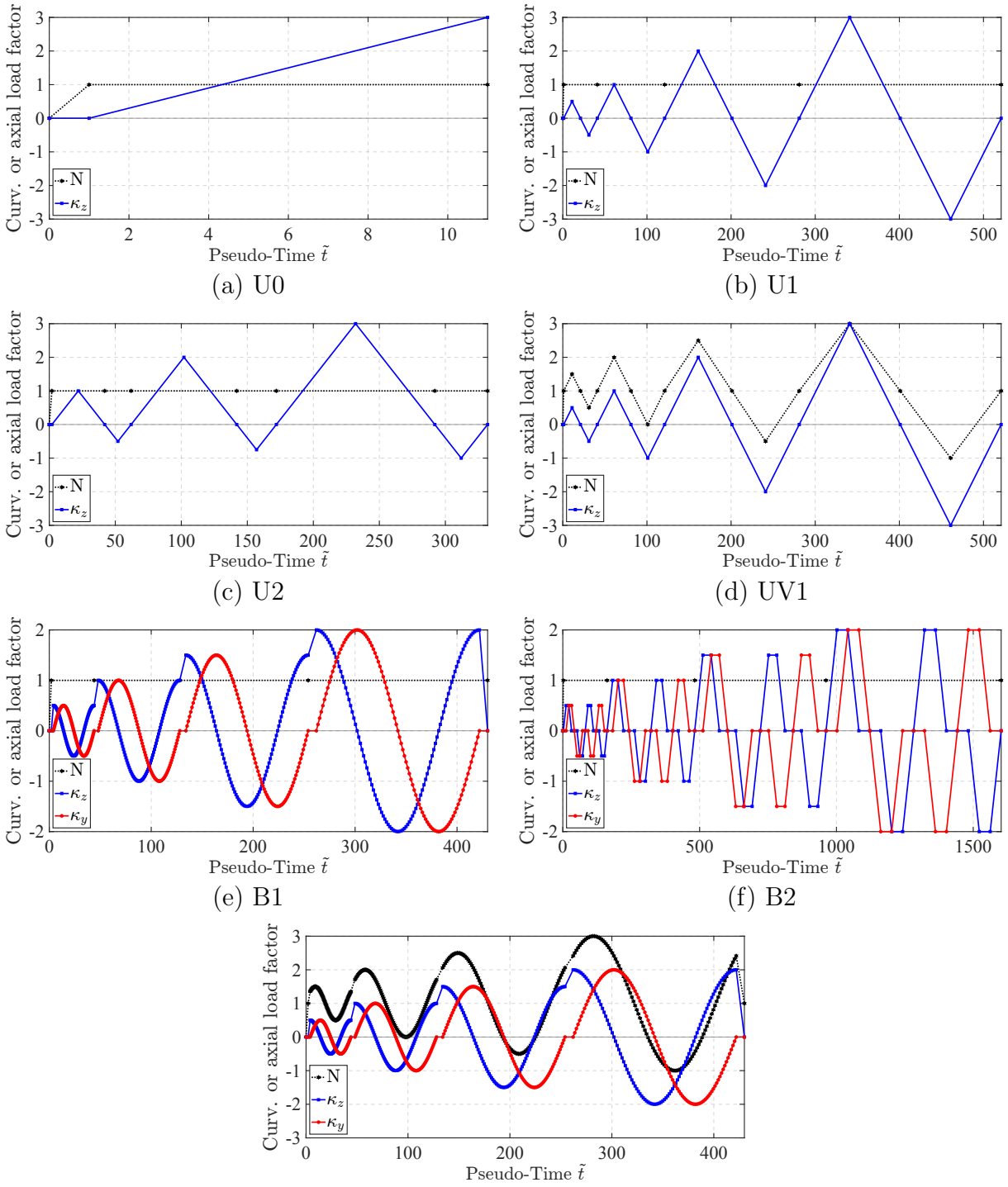


(a) U0 (b) U1

(c) U2 (d) UV1

(e) B1 (f) B2

(g) BV1

Figure 2.6: Curvature & axial force histories for moment-curvature analyses

| Name | Imposed Axial Force |
|---|---|
| U0 | $0, +10\%$, & $-25\%N_p$ |
| U1 | $0, -10\%$, & $-25\%N_p$ |
| U2 | $-25\%N_p$ |
| UV1 | $-10\%N_p \pm 20\%N_p$ & $-20\%N_p \pm 40\%N_p$ |
| B1 | $0, -10\%$, & $-25\%N_p$ |
| B2 | $0, -10\%$, & $-25\%N_p$ |
| BV1 | $-10\%N_p \pm 20\%N_p$ & $-20\%N_p \pm 40\%N_p$ |

Table 2.4: Summary of axial force levels for moment-curvature analyses

#### 2.5.1.2 Section models

The response of the resultant section model is compared with that of a reference fiber section model. For uniaxial bending load cases, the fiber section is discretized along the y-direction only with 3 layers evenly distributed in each flange, and 8 layers evenly distributed in the web, as illustrated in Figure 2.7 (a) and (b). For biaxial bending, the fiber section uses a mesh of 8x3 evenly distributed fibers in each flange, and 3x8 fibers evenly distributed in the web, as illustrated in Figure 2.7 (c) and (d).

In both cases, the steel fibers are assigned the Simo and Hughes inelastic linear-plastic 1d model with the return map algorithm [73]. The steel yield strength is taken as $f_y = 40$ ksi. The material model accommodates kinematic and isotropic hardening through the consideration of two modulii, $H_{k,m}$, and $H_{i,m}$, defined as:

$$H_{k,m} = H_{kr,m}E \tag{2.113}$$

$$H_{i,m} = H_{ir,m}E \tag{2.114}$$

where E is the Young modulus of the material, taken as $20,000$ ksi. To study the effect of these two types of hardening separately, four sets of parameters are investigated, as described in Table 2.5, giving rise to four fiber section models named from Fib1 to Fib4. Four equivalent resultant section models are then proposed, named from Res1 to Res4, with parameters described in Table 2.5.

The 2d resultant section model is used for uniaxial bending load cases, and the 3d model is used for biaxial bending cases. For the W14x730 section, this example adopts Equation (2.19) for the function $\phi$ that characterizes the axial-flexure interaction surface under uniaxial bending conditions and Equation (2.47) for biaxial bending conditions. For the W12x120 cross section, these coefficients are slightly modified to better match the exact $N$-$M$ interaction surface. The resulting $\phi$ functions are as follows:

$$\phi\left(\boldsymbol{s}\right) = 1.2\left|\frac{N}{N_p}\right|^2 + 1.0\left|\frac{M_z}{M_{pz}}\right|^2 + 4.0\left|\frac{N}{N_p}\right|^2\left|\frac{M_z}{M_{pz}}\right|^2 \tag{2.115}$$

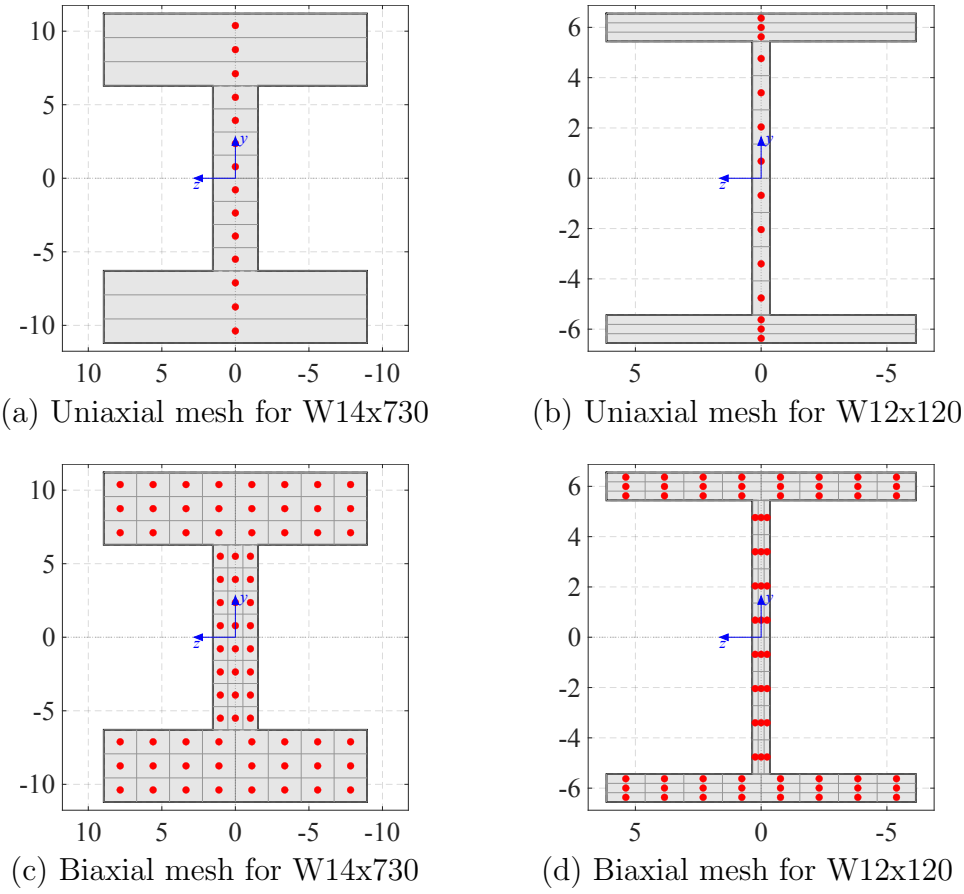

(a) Uniaxial mesh for W14x730

(b) Uniaxial mesh for W12x120

(c) Biaxial mesh for W14x730

(d) Biaxial mesh for W12x120

Figure 2.7: Section fiber discretization for moment-curvature analyses (dimensions in inches)

| **Section Model** | $H_{kr,m}$ (%) | $H_{ir,m}$ (‰) | **Section Model** | $H_{kr,a}$ (%) | $H_{kr,fz}$ (%) | $H_{kr,fy}$ (%) | $H_{ir}$ (‰) |
|---|---|---|---|---|---|---|---|
| **Fib1** | 0 | 0 | **Res1** | 0 | 0 | 0 | 0 |
| **Fib2** | 1 | 0 | **Res2** | 1 | 1 | 1 | 0 |
| **Fib3** | 0 | 1 | **Res3** | 0 | 0 | 0 | 1.25 |
| **Fib4** | 1 | 1 | **Res4** | 1 | 1 | 1 | 1.25 |

Table 2.5: Parameters for section analyses

for uniaxial bending, and

$$\begin{aligned}\phi(\boldsymbol{s}) = 1.2\left|\frac{N}{N_p}\right|^2 + 1.0\left|\frac{M_z}{M_{pz}}\right|^2 + 1.0\left|\frac{M_y}{M_{py}}\right|^5 \\ + 4.0\left|\frac{N}{N_p}\right|^2\left|\frac{M_z}{M_{pz}}\right|^2 + \frac{6A_f}{A_f + A_w}\left|\frac{N}{N_p}\right|^3\left|\frac{M_z}{M_{pz}}\right|^3 + 3.0\left|\frac{M_z}{M_{pz}}\right|^2\left|\frac{M_y}{M_{py}}\right|^2\end{aligned} \tag{2.116}$$

for biaxial bending.

Figure 2.8 shows the polynomial approximation of the initial yield surface under uniaxial bending conditions and compares it with the exact $N$-$M$ interaction surface for both investigated cross sections.

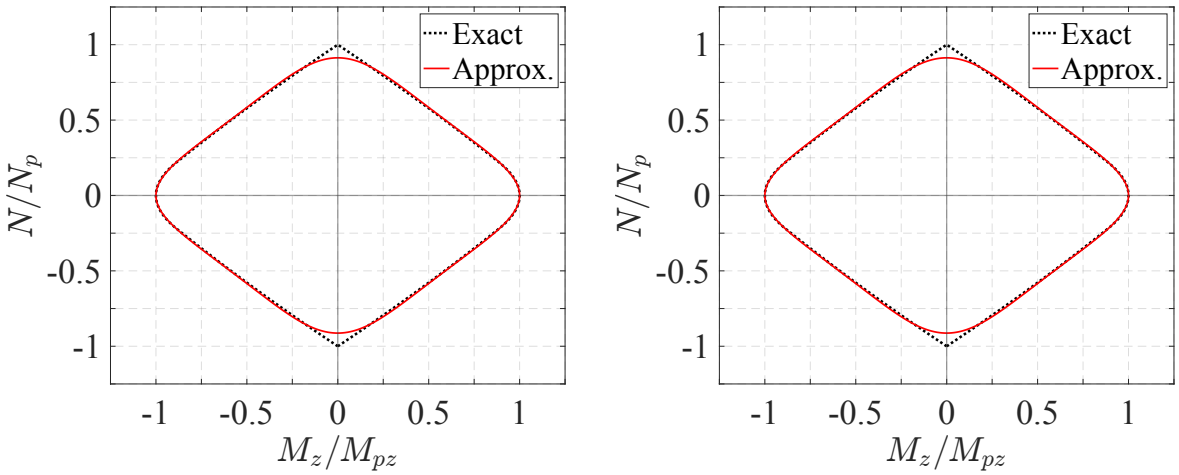


(a) W14x730 (b) W12x120

Figure 2.8: Polynomial approximation of initial yield surface for W14x730 and W12x120

Assuming a steel yield strength of $f_y = 40$ ksi, $N_p = 8,600$ kips, $M_{pz} = 66,400$ kip-in and $M_{py} = 32,640$ kip-in for the W14x730 profile; whereas $N_p = 1,408$ kips, $M_{pz} = 7,440$ kip-in and $M_{py} = 3,416$ kip-in for the W12x120 cross section.

#### 2.5.1.3 Results

First, the monotonic response of the two sections models without any type of hardening, Fib1 and Res1, is investigated. The results are shown in Figures 2.9 and 2.10 for the W14x730 and W12x120 sections, respectively. The calculated curvatures are normalized with respect to $\kappa_{pz} = M_{pz}/EI_z$. In absence of axial force, the moment-curvature response is linear elastic with the bending moment $M_z$ increasing until it reaches the plastic flexural capacity of the section $M_{pz}$, after which it can no longer increase due to the lack of hardening. When an axial force is added, whether it is in tension or in compression, the effective plastic flexural

capacity is reduced according to the approximate polynomial axial-flexure interaction surface depicted in grey in the axial force - bending moment response plots. The absence of hardening constrains the response to lie within the $N$-$M$ interaction surface, which does not move or expand. For both section sizes, and the three investigated levels of axial force, the response of the 2d resultant section almost perfectly matches that of the fiber section model, including for the axial strain response $\varepsilon_a$. For such short analyses, the computational times of the two models (indicated in the legend) are comparable.

Next, the monotonic response of the models with kinematic hardening only, Fib2 and Res2, is investigated. The results are shown in Figures 2.11 and 2.12 for the W14x730 and W12x120 sections, respectively. The plastic branch of the moment-curvature response is now inclined, with a slope equal to $H_{kr,fz} \cdot EI_z$. The response goes outside the original $N$-$M$ interaction surface because the surface shifts to the right as the plastic deformation increase under the consideration of kinematic hardening.

The cyclic response of these two models Fib2 and Res2 is then investigated under load pattern U1. The results are shown in Figures 2.13 and 2.14 for the W14x730 and W12x120 sections, respectively. Both the moment-curvature and the axial strain responses obtained with the 2d resultant section model impressively match the response of the fiber section model. For this load case that requires more time steps, the gain in computational time of about 50% with the resultant model becomes more evident.

The isotropic hardening behavior is then investigated with the cyclic response of the Fib3 and Res3 models. The results are shown in Figures 2.15 and 2.16 for the W14x730 and W12x120 sections, respectively. The isotropic hardening behavior is evident in the moment-curvature response, as well as in the axial force-bending moment response that goes out of the original $N$-$M$ interaction surface as the surface expands with the accumulation of plastic deformations. Additionally, the axial strain response is extremely well captured by the resultant section model, even under such a small hardening ratio.

Laslty, the combined effect of kinematic and isotropic hardening is investigated with the cyclic response of the Fib4 and Res4 models. The results for the load patterns U1, U2, and UV1 are shown in Figures 2.17 to 2.22. Even under non-symmetric loading conditions and under variable axial force, the quality of the response obtained with the 2d resultant section model very closely matches that of the fiber section, that takes 50% longer to run on average.

Next, the biaxial response of the Fib4 and Res4 models is investigated with the load patterns B1, B2 and BV1. The results are shown in Figures 2.23 to 2.30. The calculated curvatures are normalized with respect to $\kappa_{pz} = M_{pz}/EI_z$ and $\kappa_{py} = M_{py}/EI_y$. The accuracy of the 3d resultant section model under these complex loading scenarios is particularly impressive for the bending moment response about the strong-axis and the axial strain response, while the weak-axis bending moment response is sightly less accurate, with the resultant model tending to underestimate the value of $M_y$.

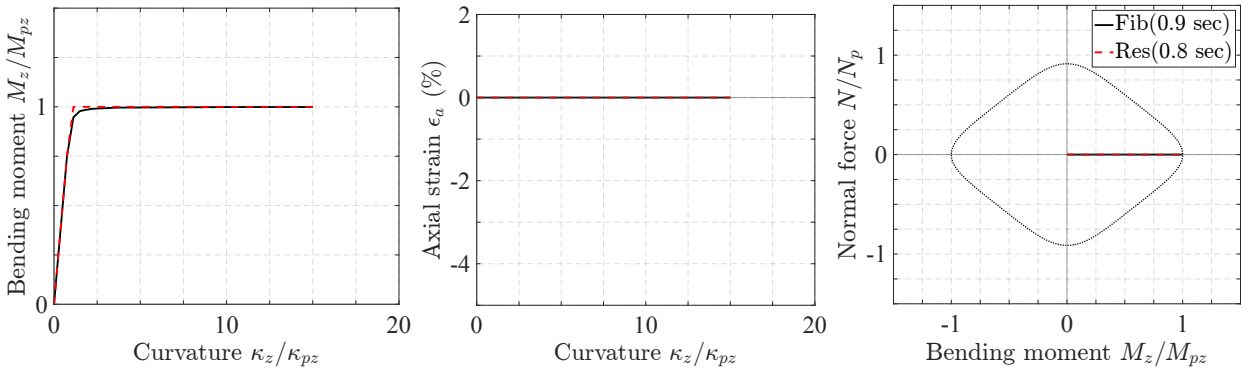


(a) $N = 0$

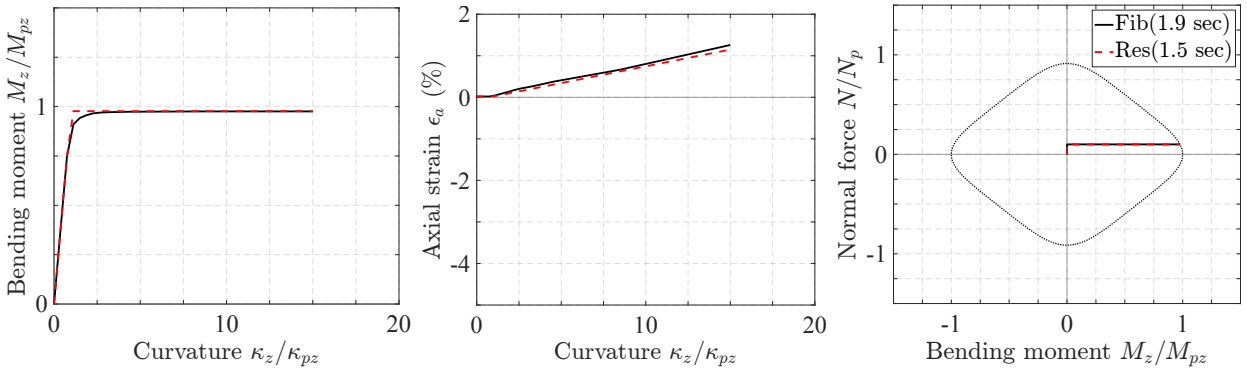


(b) $N = 10\%N_p$

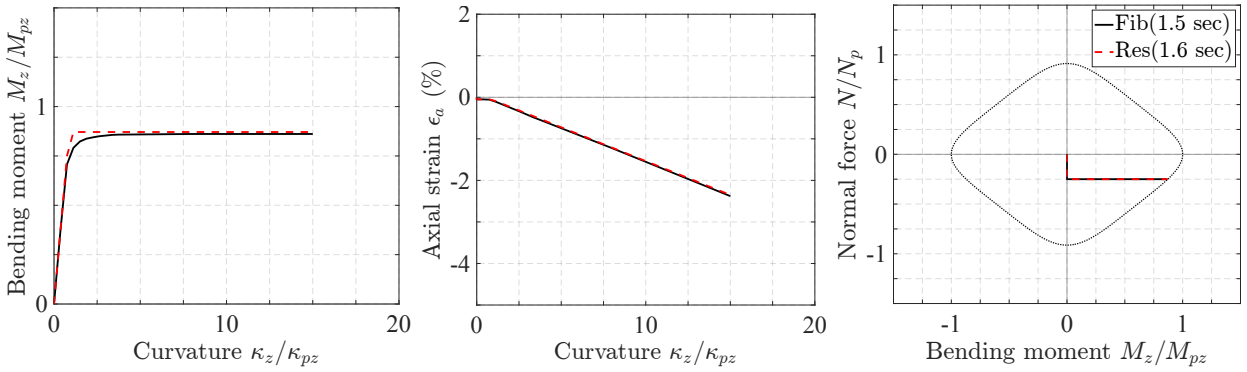


(c) $N = -25\%N_p$

Figure 2.9: Response of W14x730 section under U0 - Fib1 vs. Res1

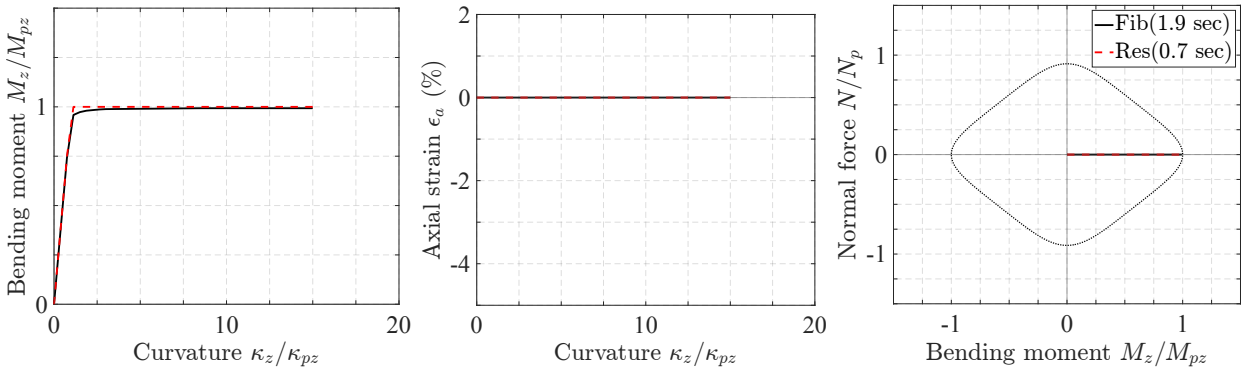


(a) $N = 0$

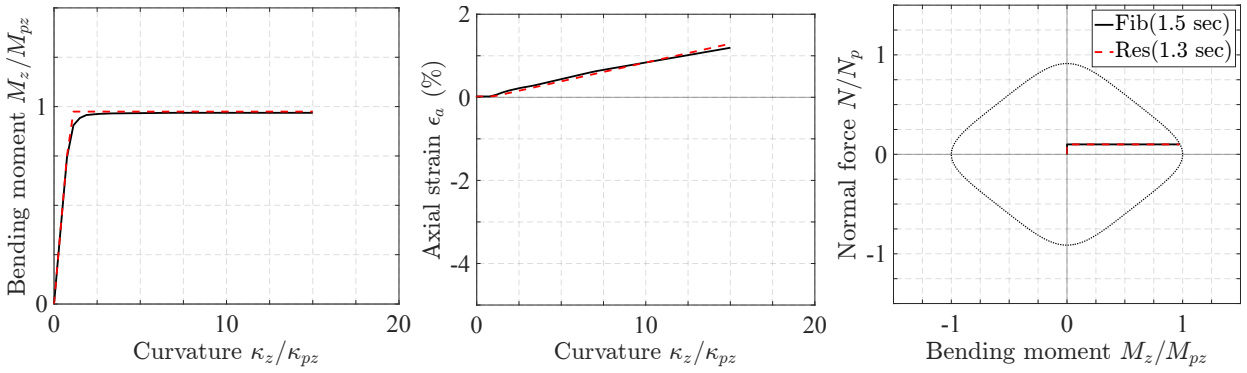


(b) $N = 10\%N_p$

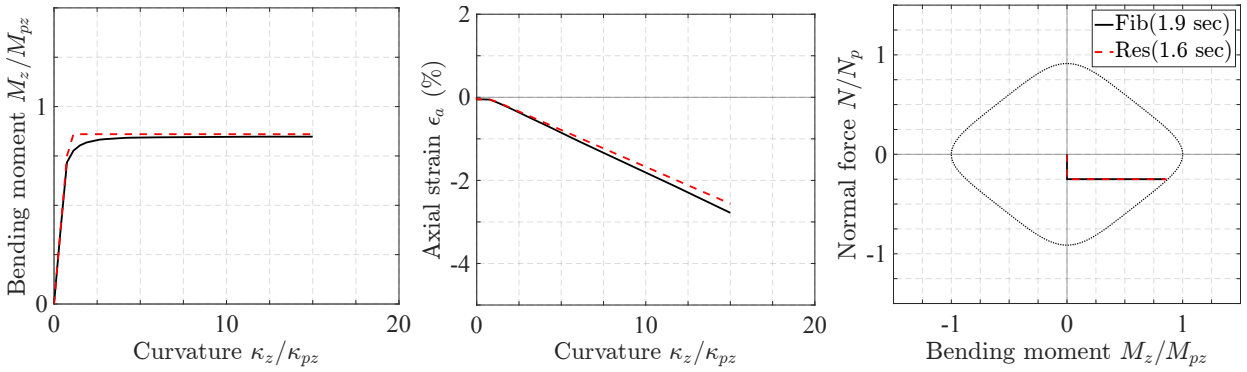


(c) $N = -25\%N_p$

Figure 2.10: Response of W12x120 section under U0 - Fib1 vs. Res1

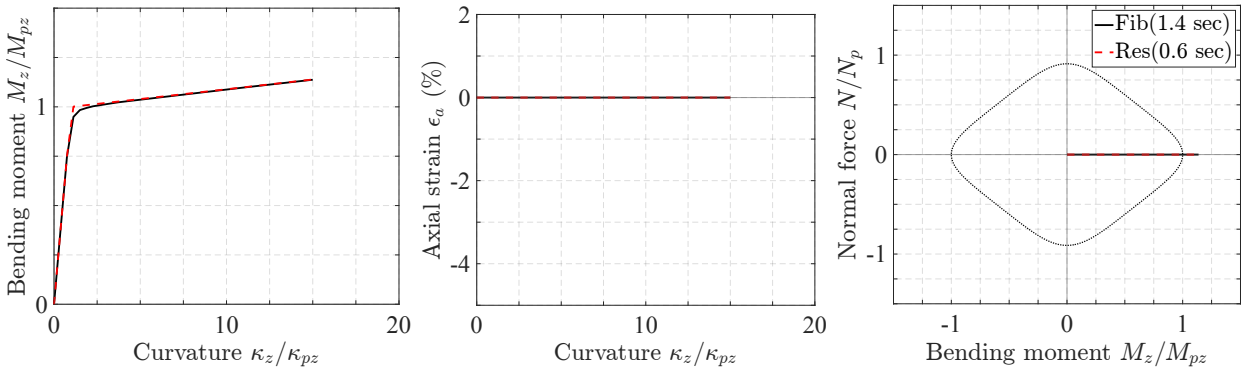


(a) $N = 0$

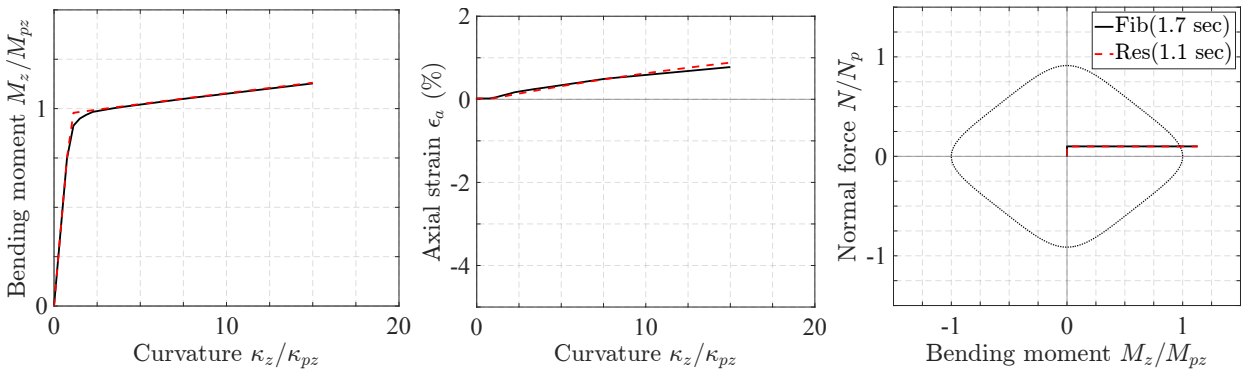


(b) $N = 10\%N_p$

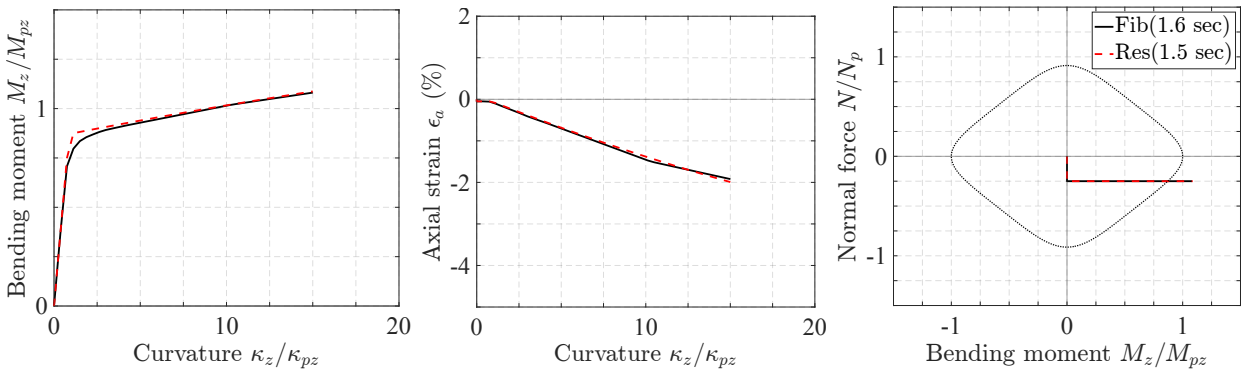


(c) $N = -25\%N_p$

Figure 2.11: Response of W14x730 section under U0 - Fib2 vs. Res2

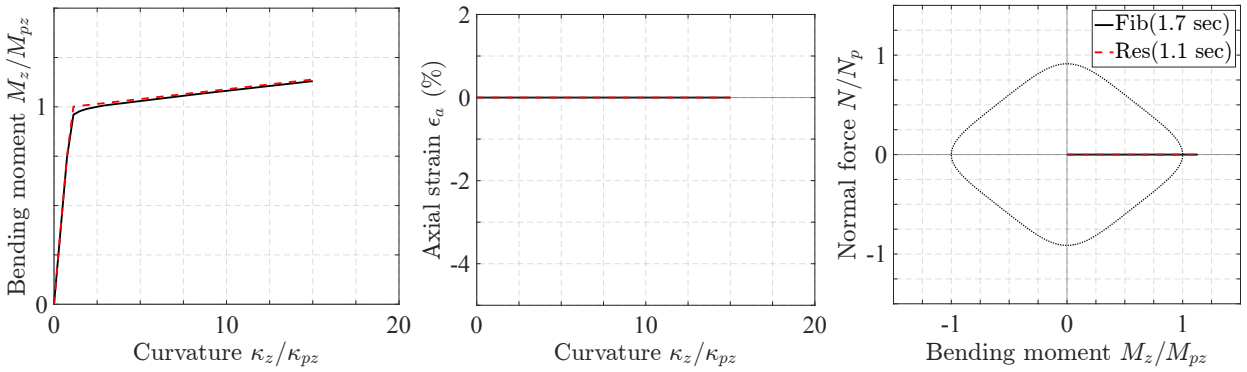


(a) $N = 0$

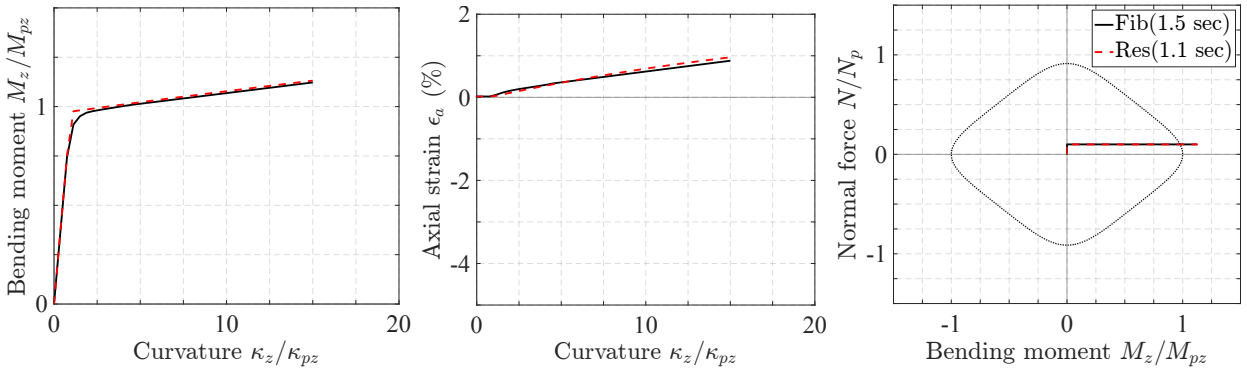


(b) $N = 10\%N_p$

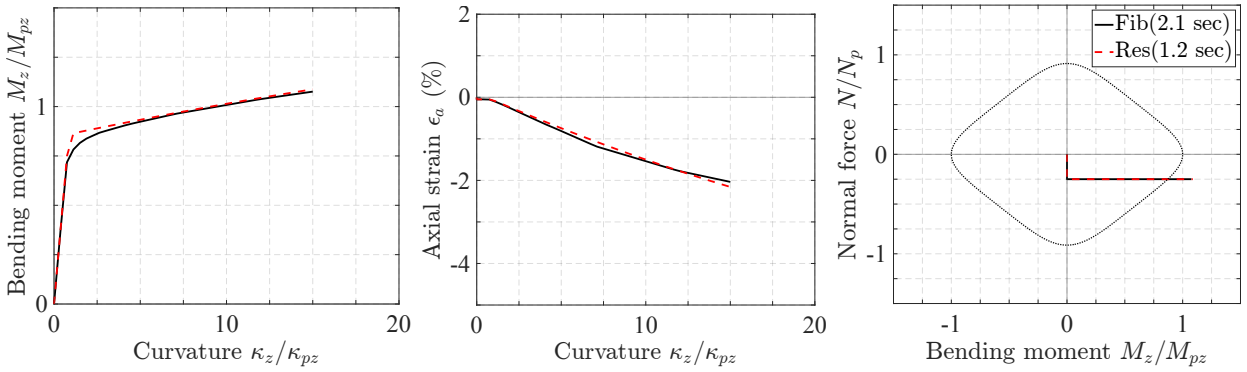


(c) $N = -25\%N_p$

Figure 2.12: Response of W12x120 section under U0 - Fib2 vs. Res2

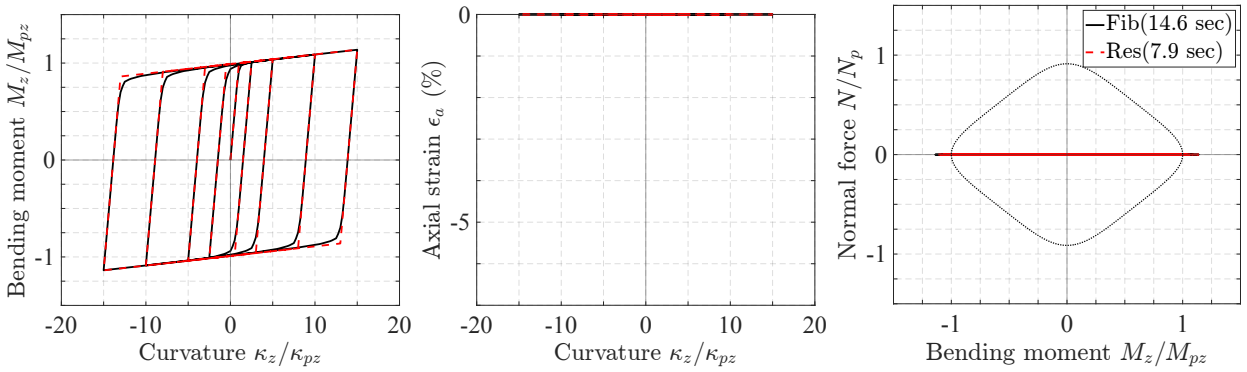


(a) $N = 0$

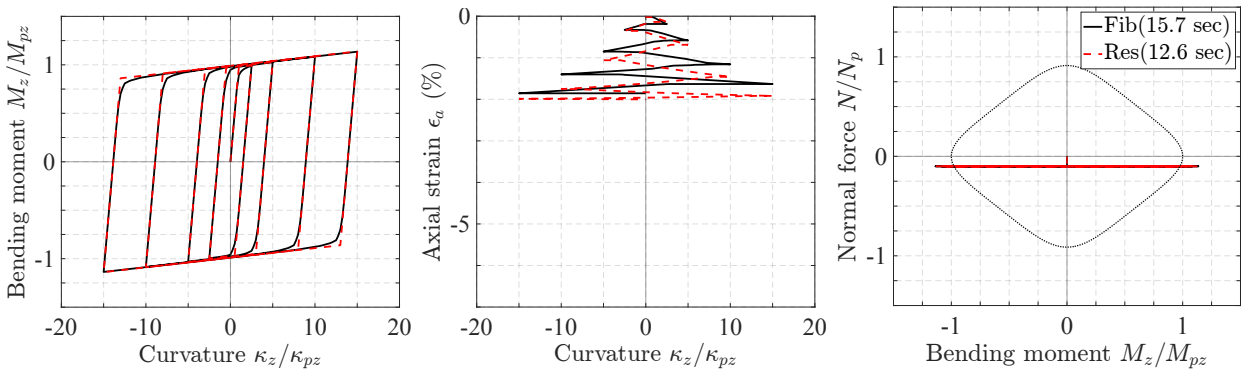


(b) $N = -10\%N_p$

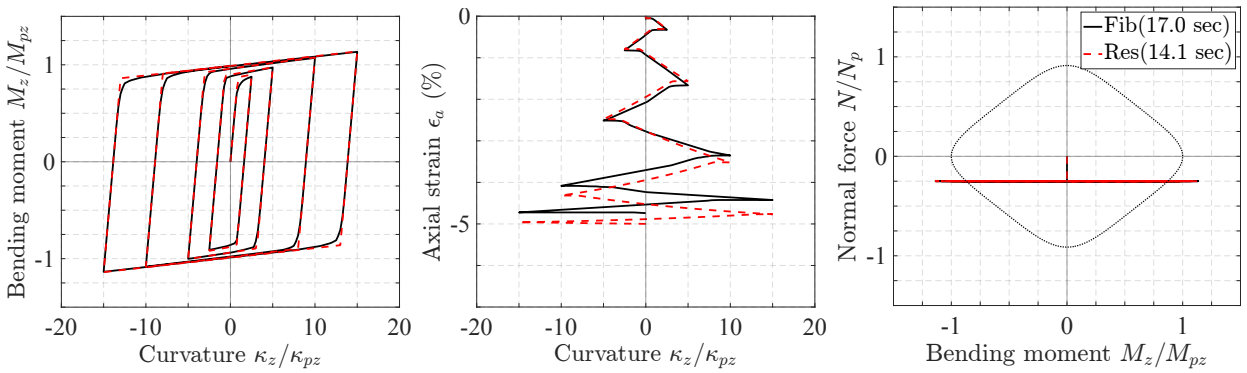


(c) $N = -25\%N_p$

Figure 2.13: Response of W14x730 section under U1 - Fib2 vs. Res2

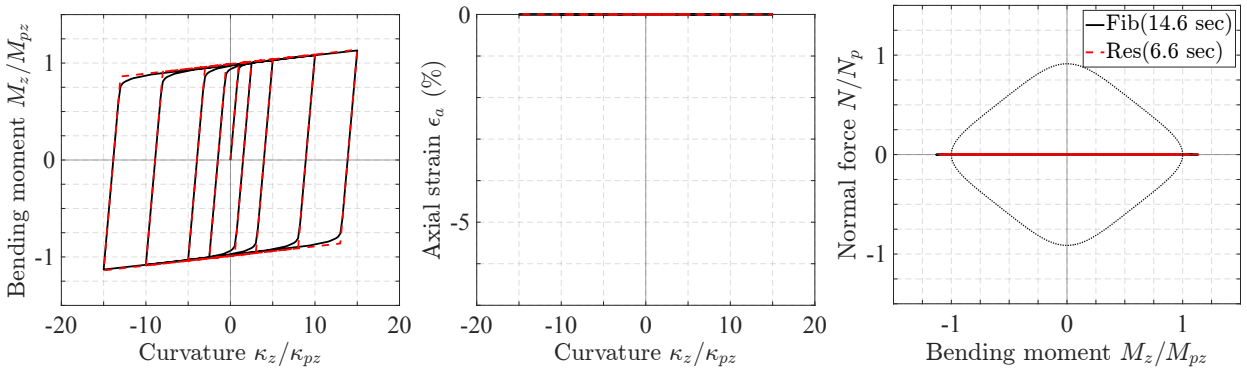


(a) $N = 0$

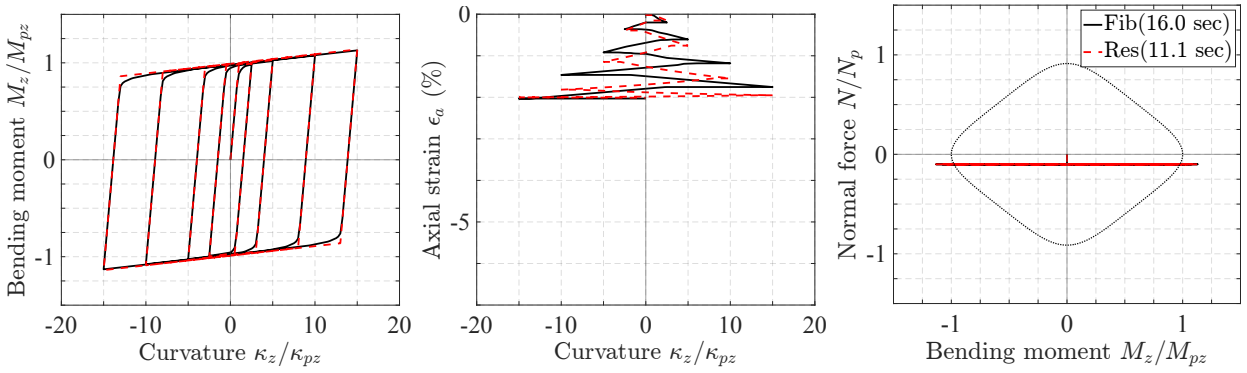


(b) $N = -10\%N_p$

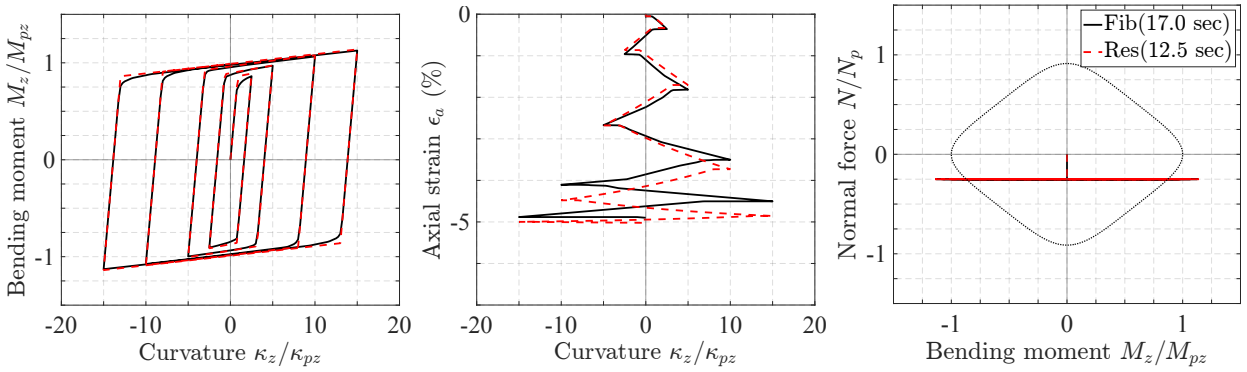


(c) $N = -25\%N_p$

Figure 2.14: Response of W12x120 section under U1 - Fib2 vs. Res2

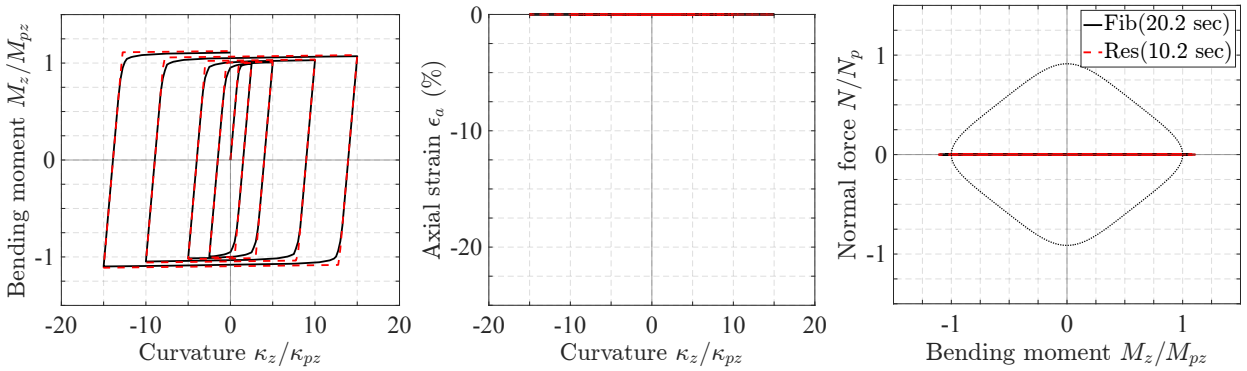


(a) $N = 0$

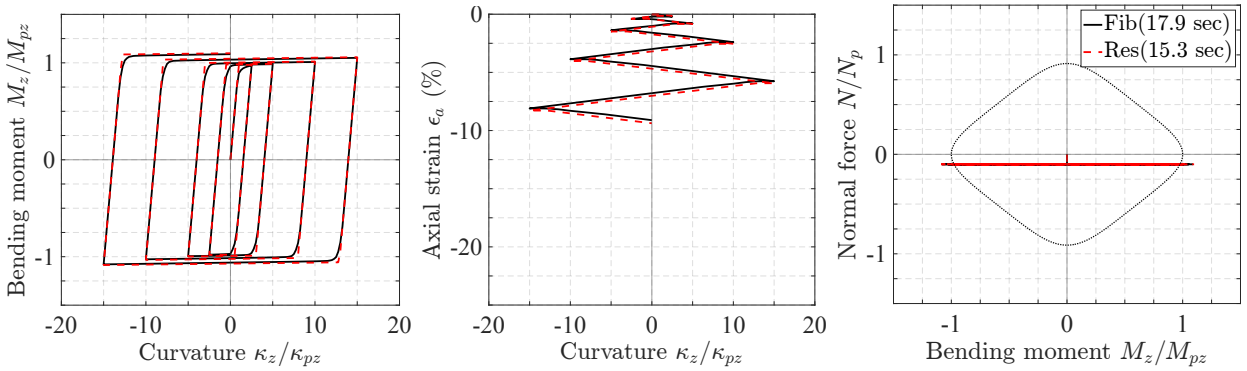


(b) $N = -10\%N_p$

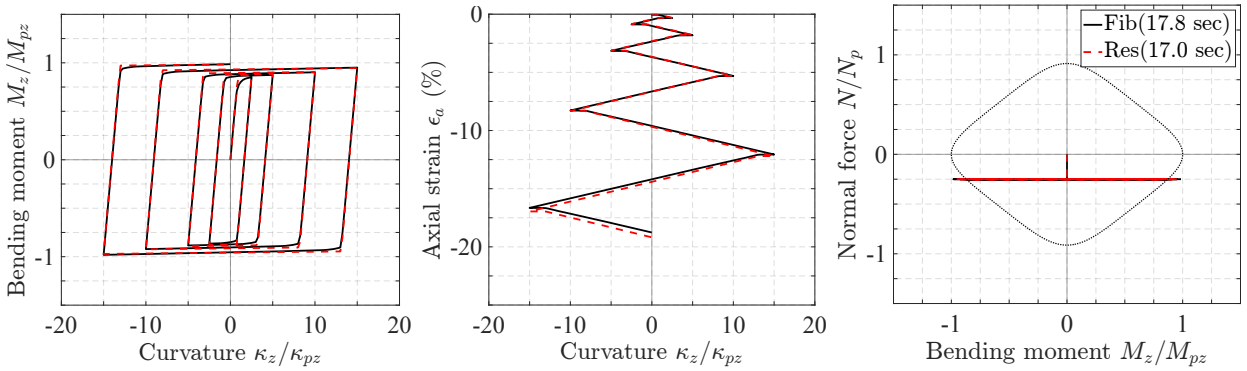


(c) $N = -25\%N_p$

Figure 2.15: Response of W14x730 section under U1 - Fib3 vs. Res3

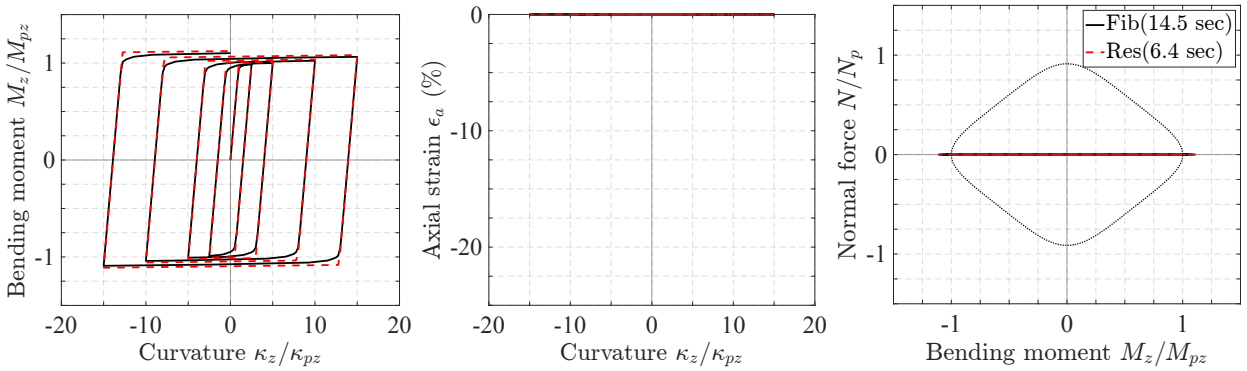


(a) $N = 0$

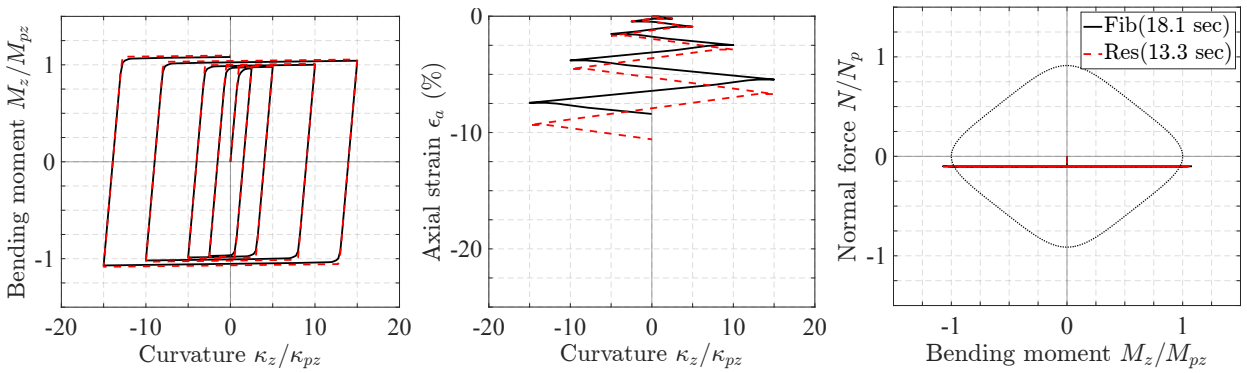


(b) $N = -10\%N_p$

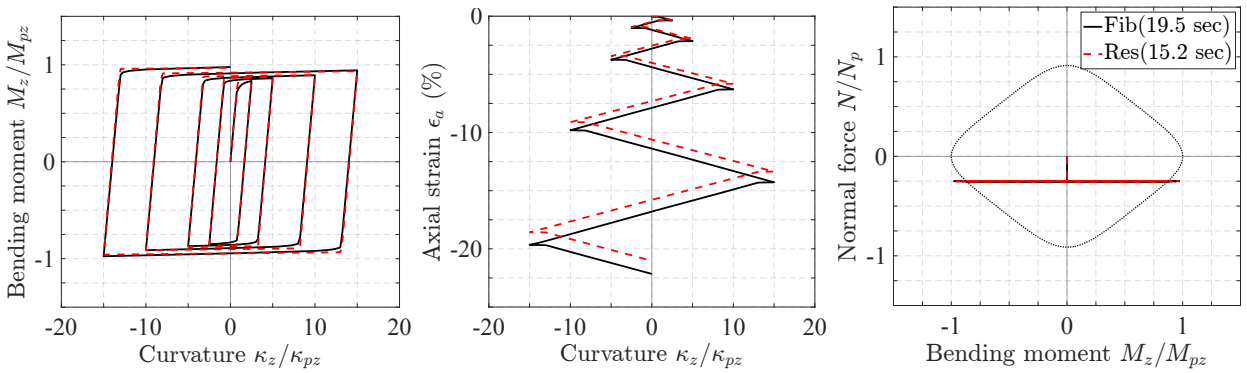


(c) $N = -25\%N_p$

Figure 2.16: Response of W12x120 section under U1 - Fib3 vs. Res3

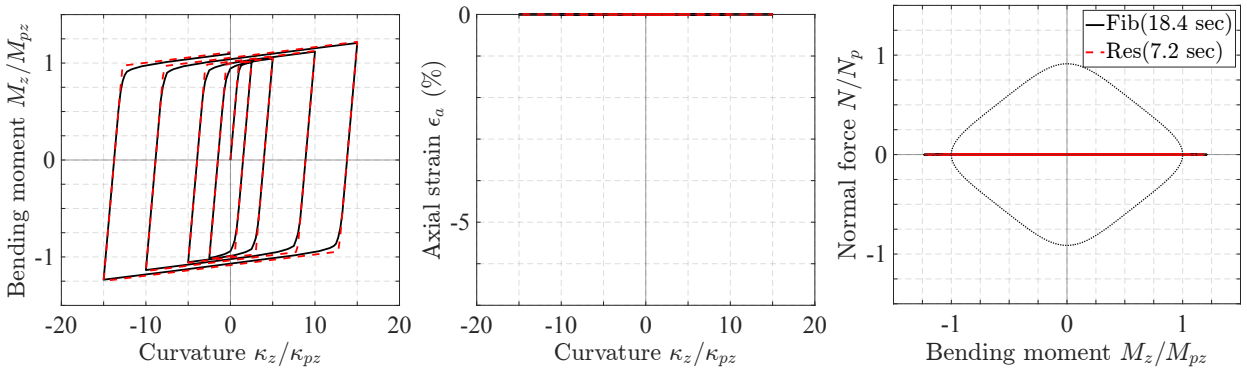


(a) $N = 0$

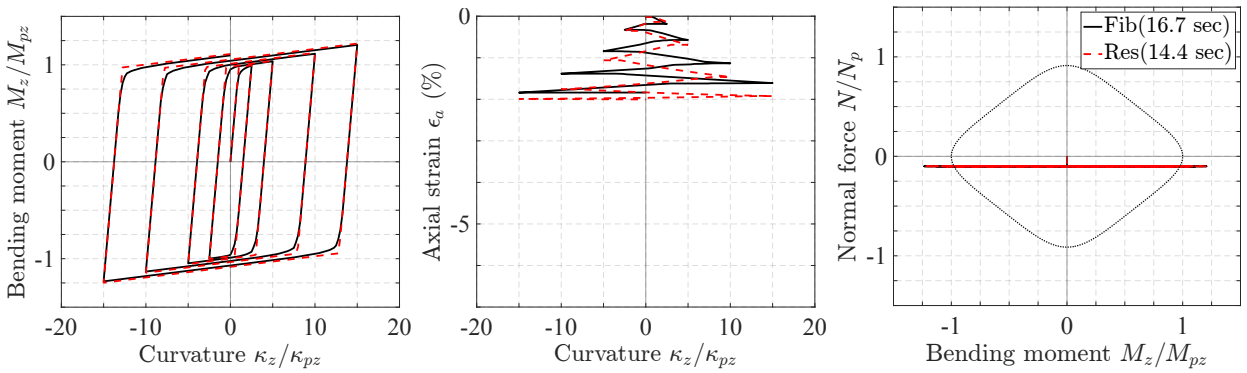


(b) $N = -10\%N_p$

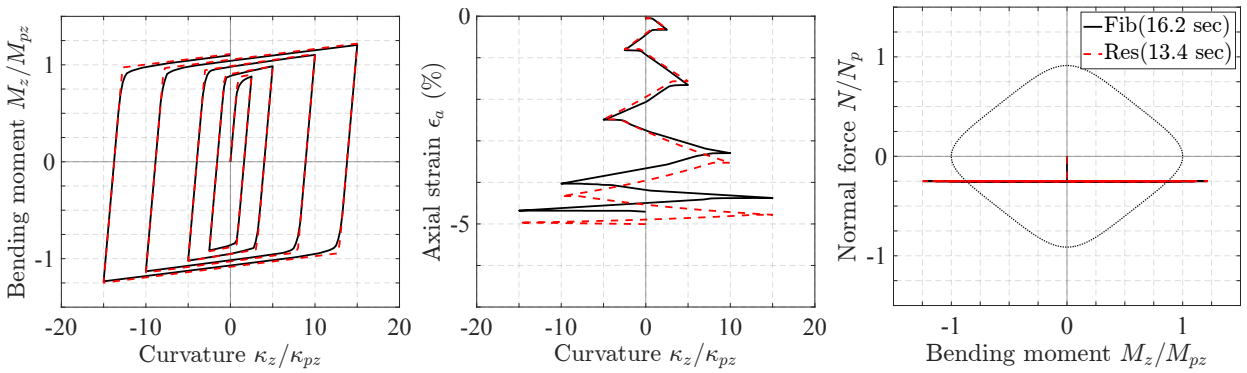


(c) $N = -25\%N_p$

Figure 2.17: Response of W14x730 section under U1 - Fib4 vs. Res4

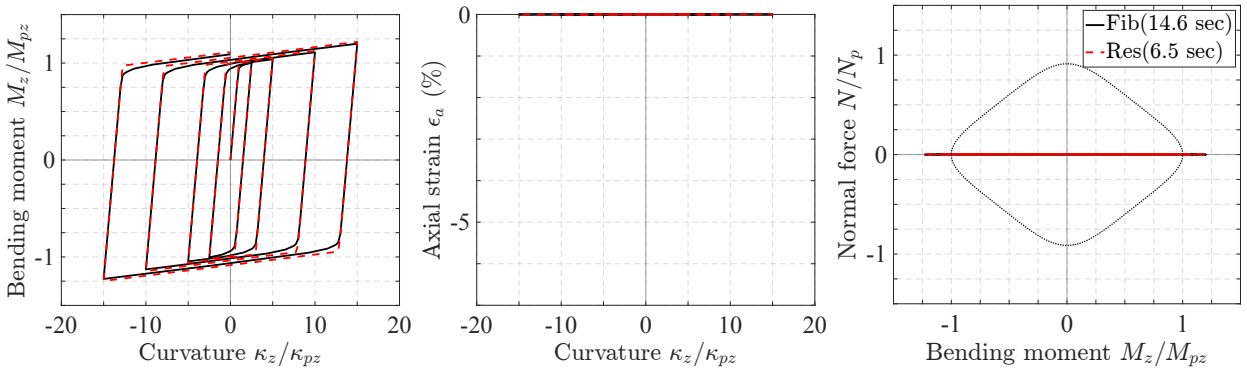


(a) $N = 0$

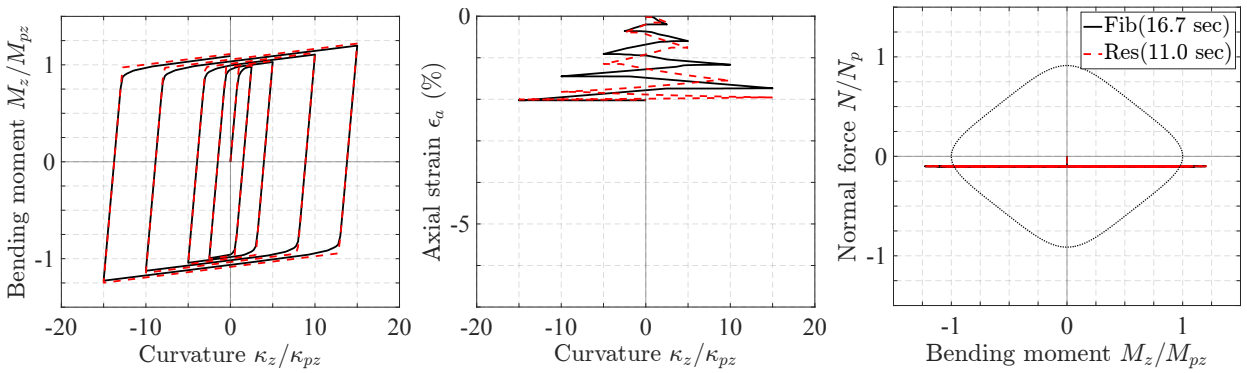


(b) $N = -10\%N_p$

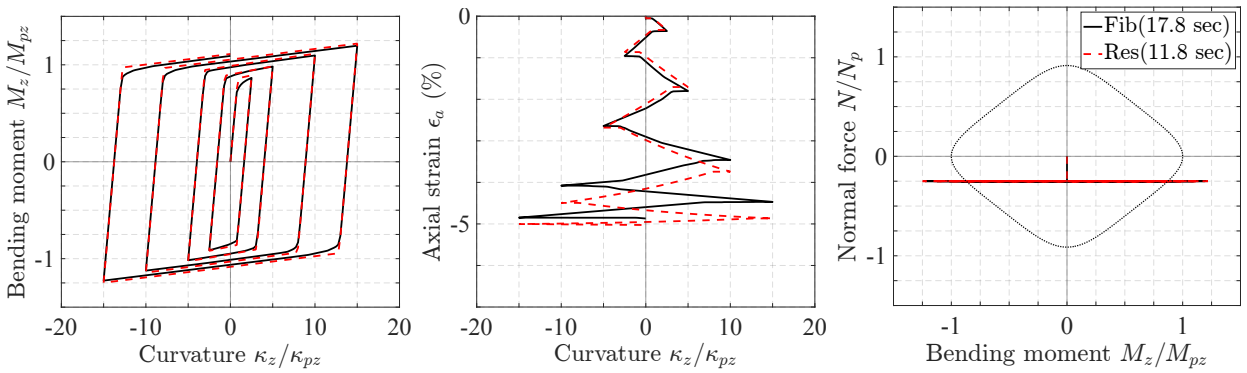


(c) $N = -25\%N_p$

Figure 2.18: Response of W12x120 section under U1 - Fib4 vs. Res4

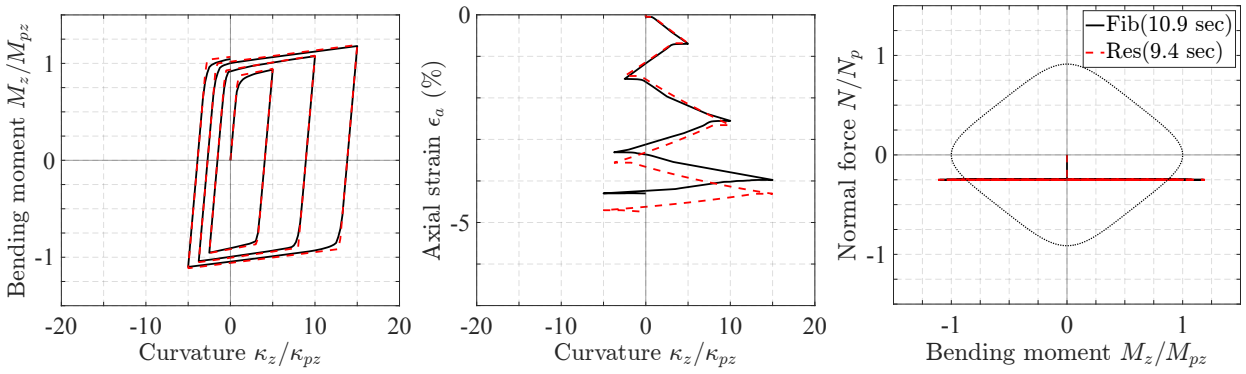


Figure 2.19: Response of W14x730 section under U2 with $N = -25\%N_p$ - Fib4 vs. Res4

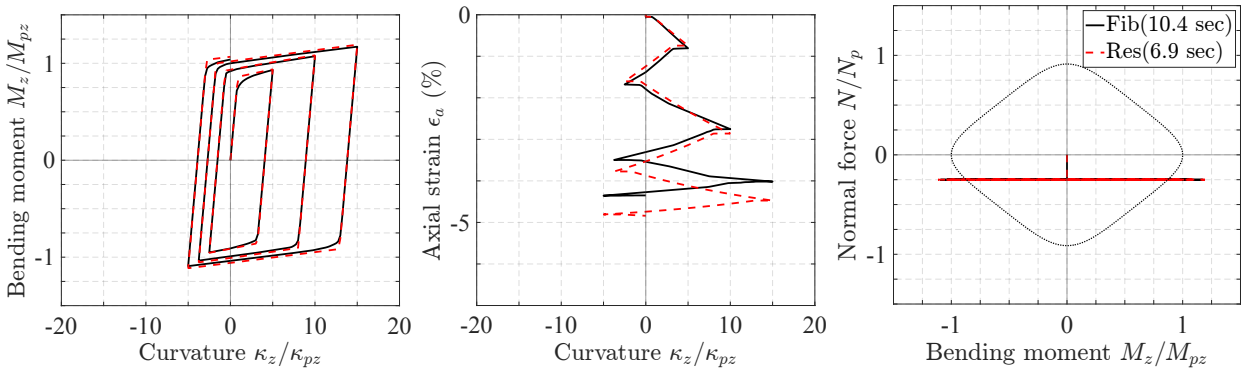


Figure 2.20: Response of W12x120 section under U2 with $N = -25\%N_p$ - Fib4 vs. Res4

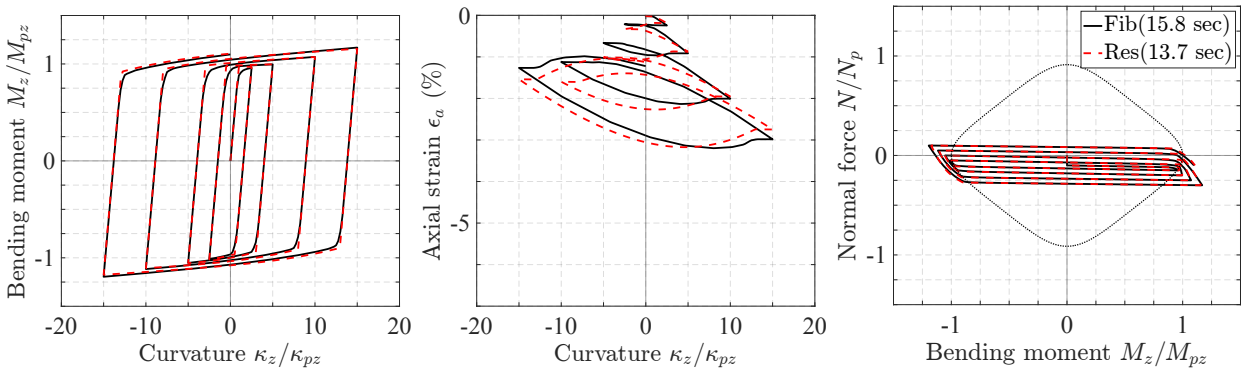


(a) $N = -10\%N_p \pm 20\%N_p$

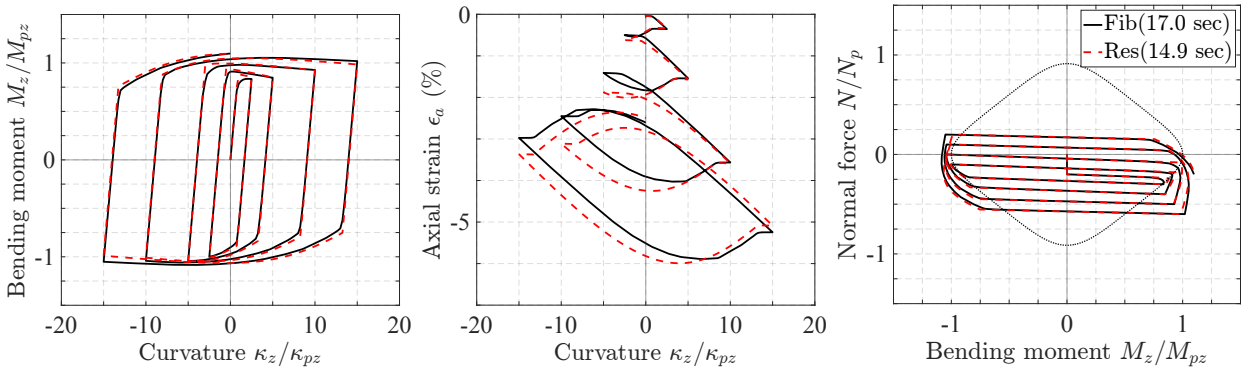


(b) $N = -20\%N_p \pm 40\%N_p$

Figure 2.21: Response of W14x730 section under UV1 - Fib4 vs. Res4

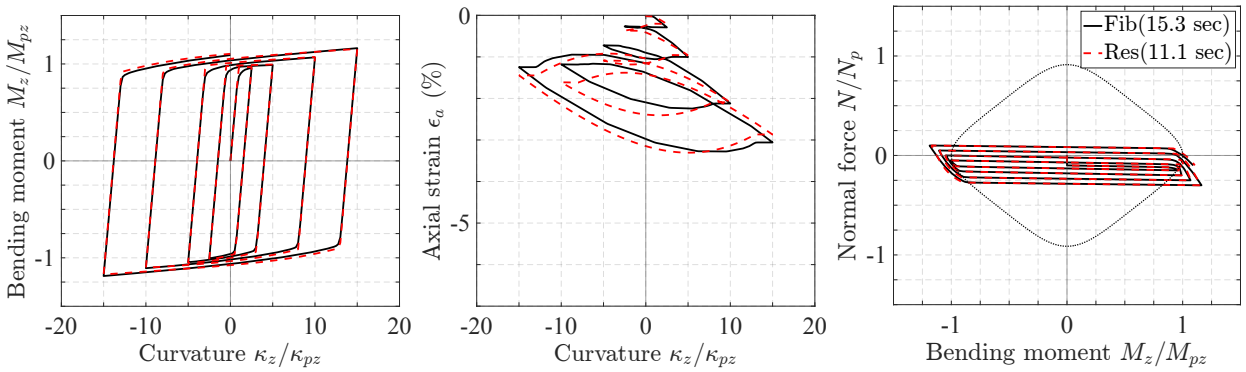


(a) $N = -10\%N_p \pm 20\%N_p$

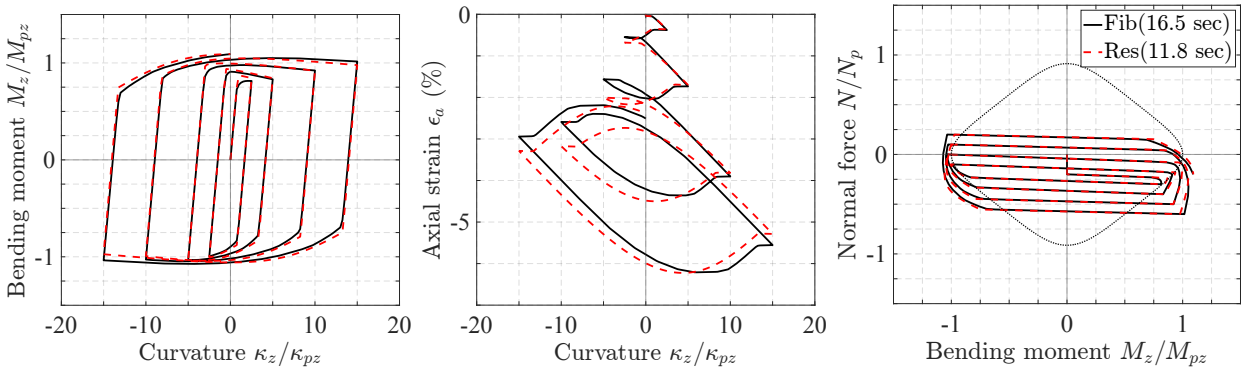


(b) $N = -20\%N_p \pm 40\%N_p$

Figure 2.22: Response of W12x120 section under UV1 - Fib4 vs. Res4

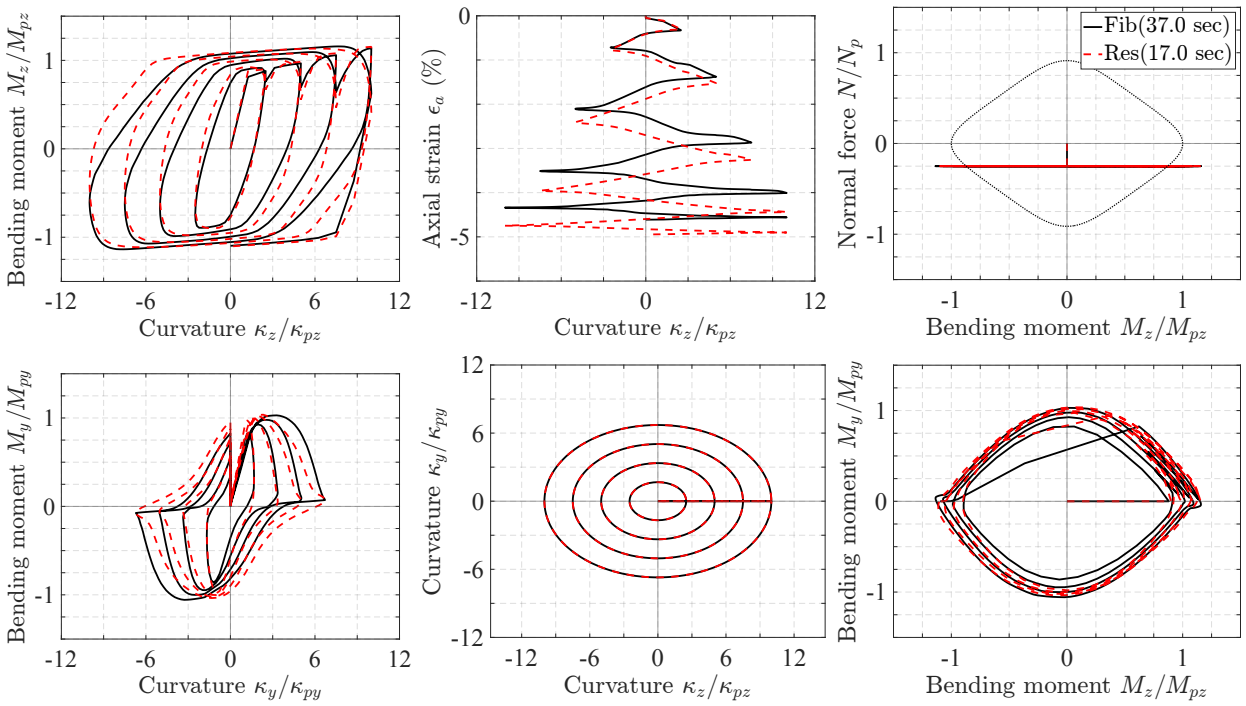


Figure 2.23: Response of W14x730 section under B1 with $N = -25\%N_p$ - Fib4 vs. Res4

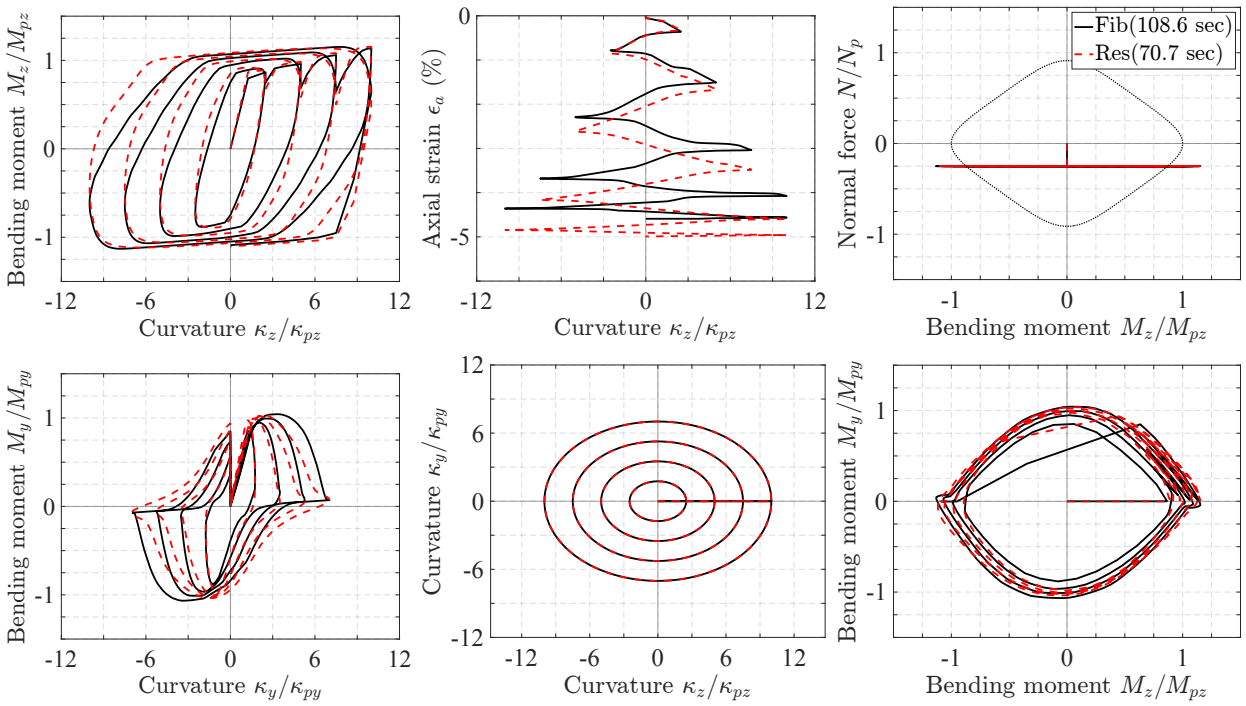


Figure 2.24: Response of W12x120 section under B1 with $N = -25\%N_p$ - Fib4 vs. Res4

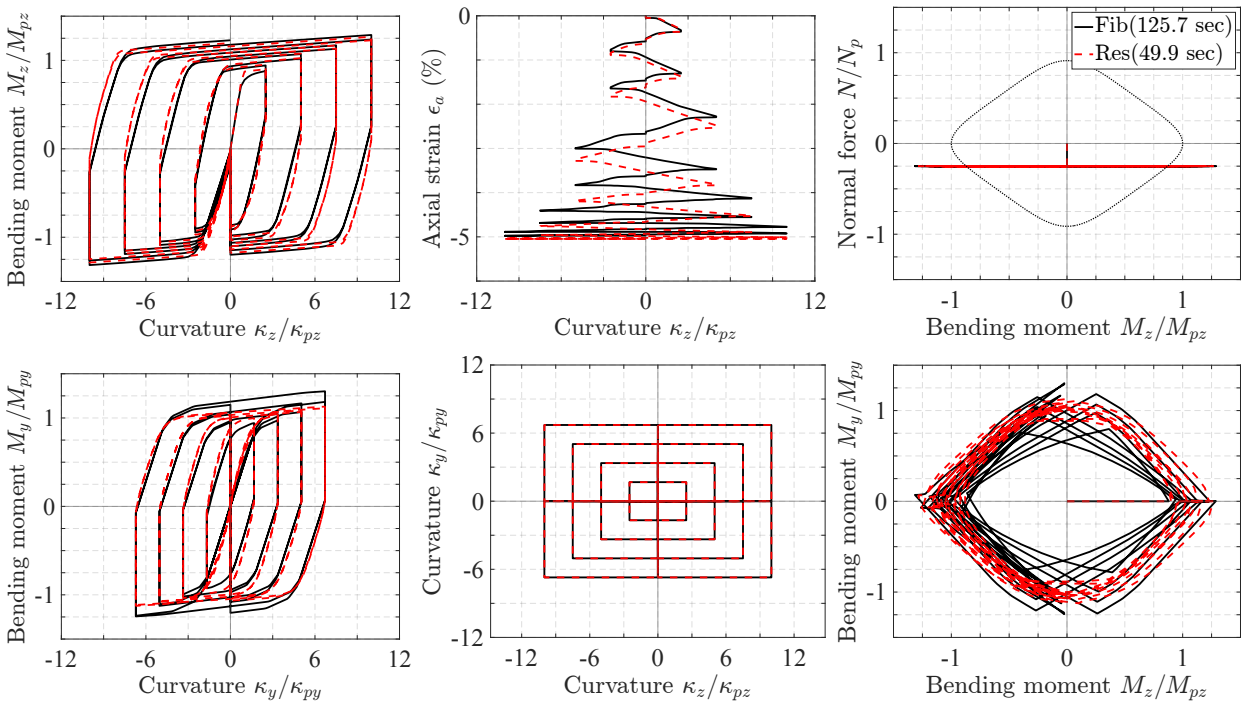


Figure 2.25: Response of W14x730 section under B2 with $N = -25\%N_p$ - Fib4 vs. Res4

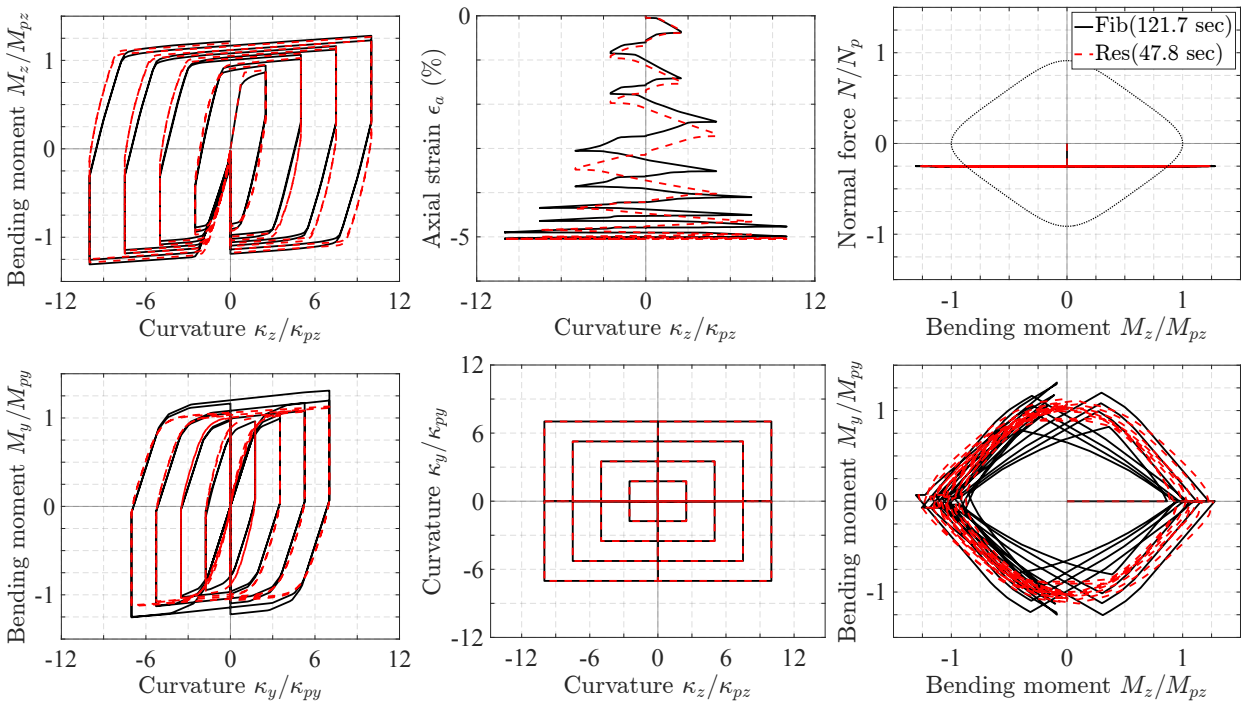


Figure 2.26: Response of W12x120 section under B2 with $N = -25\%N_p$ - Fib4 vs. Res4

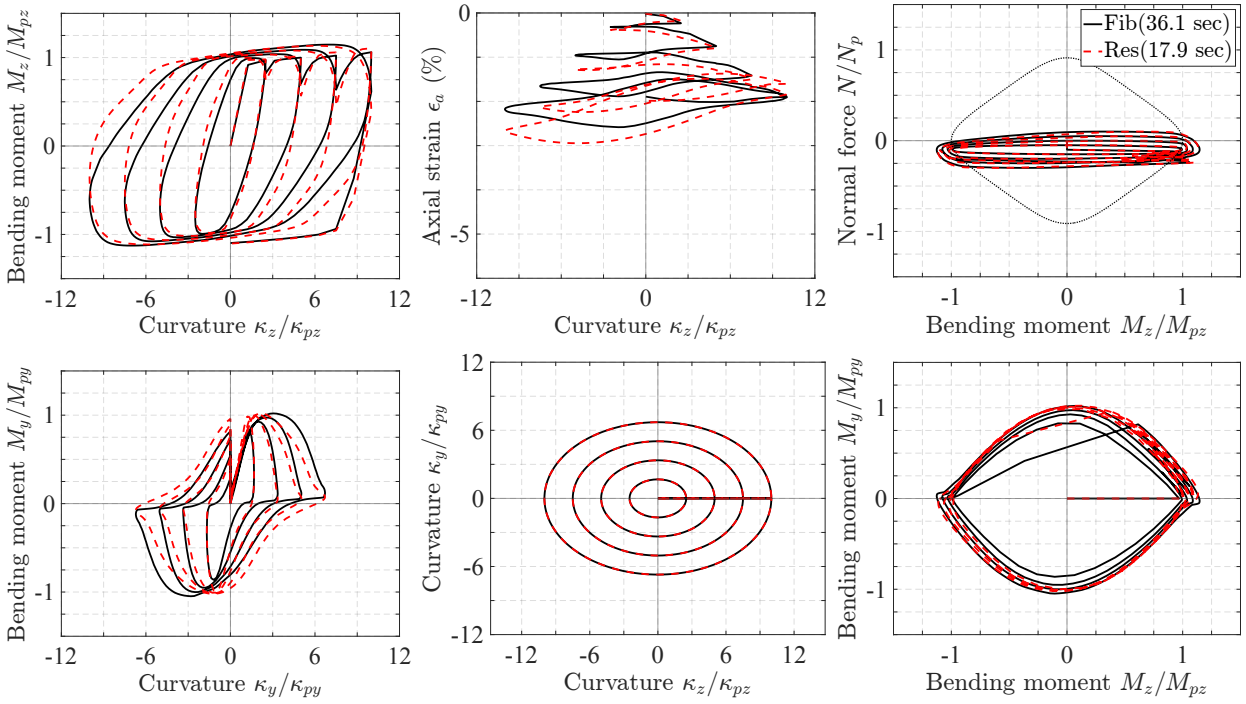


Figure 2.27: Response of W14x730 section under BV1 with $N = -10\%N_p \pm 20\%N_p$ - Fib4 vs. Res4

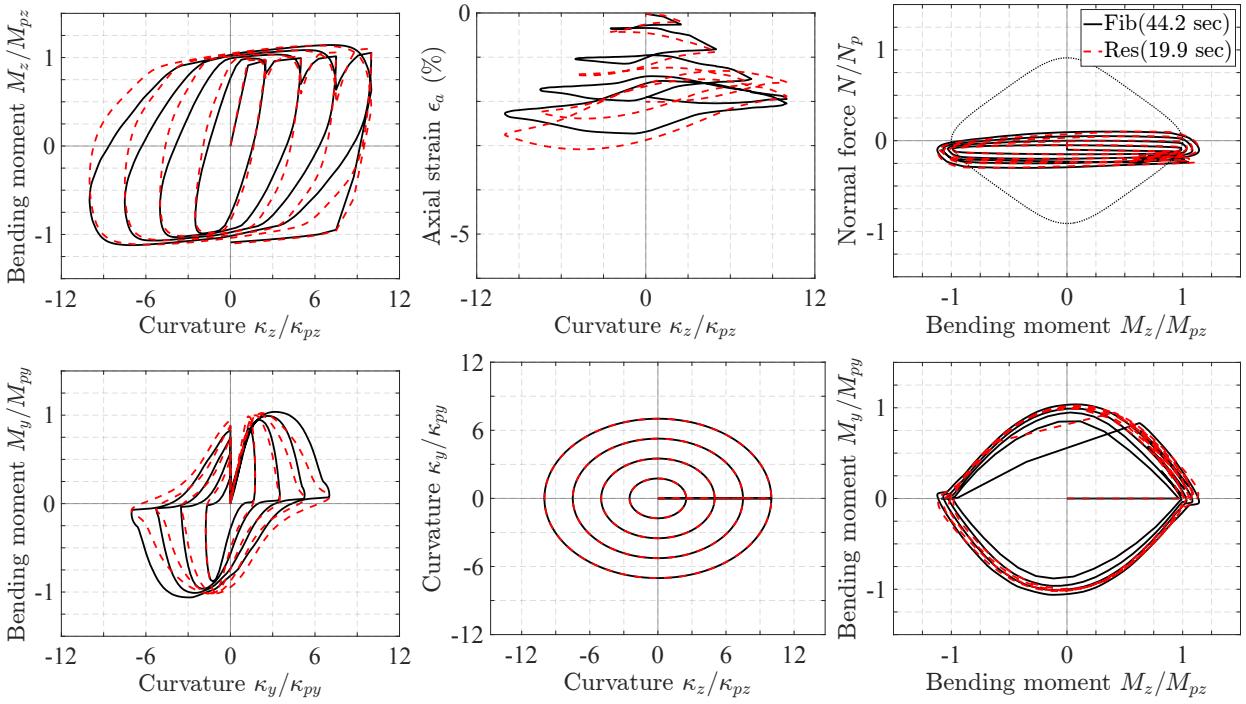


Figure 2.28: Response of W12x120 section under BV1 with $N = -10\%N_p \pm 20\%N_p$ - Fib4 vs. Res4

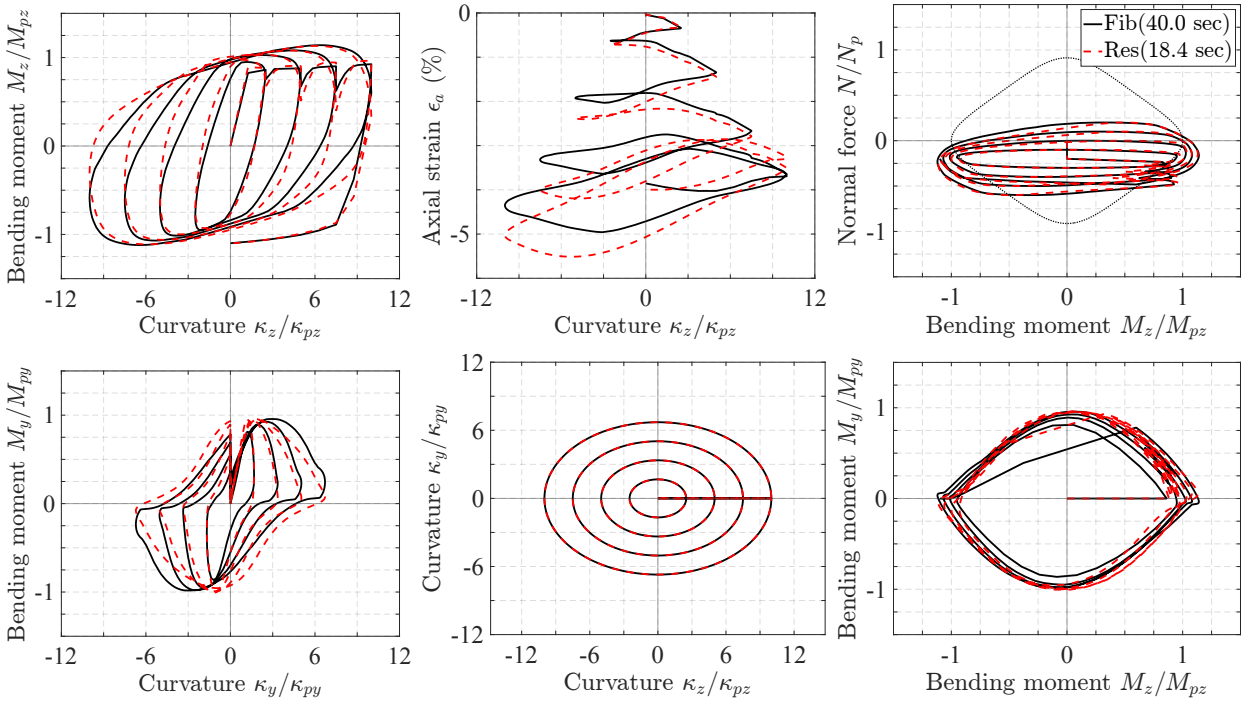


Figure 2.29: Response of W14x730 section under BV1 with $N = -20\%N_p \pm 40\%N_p$ - Fib4 vs. Res4

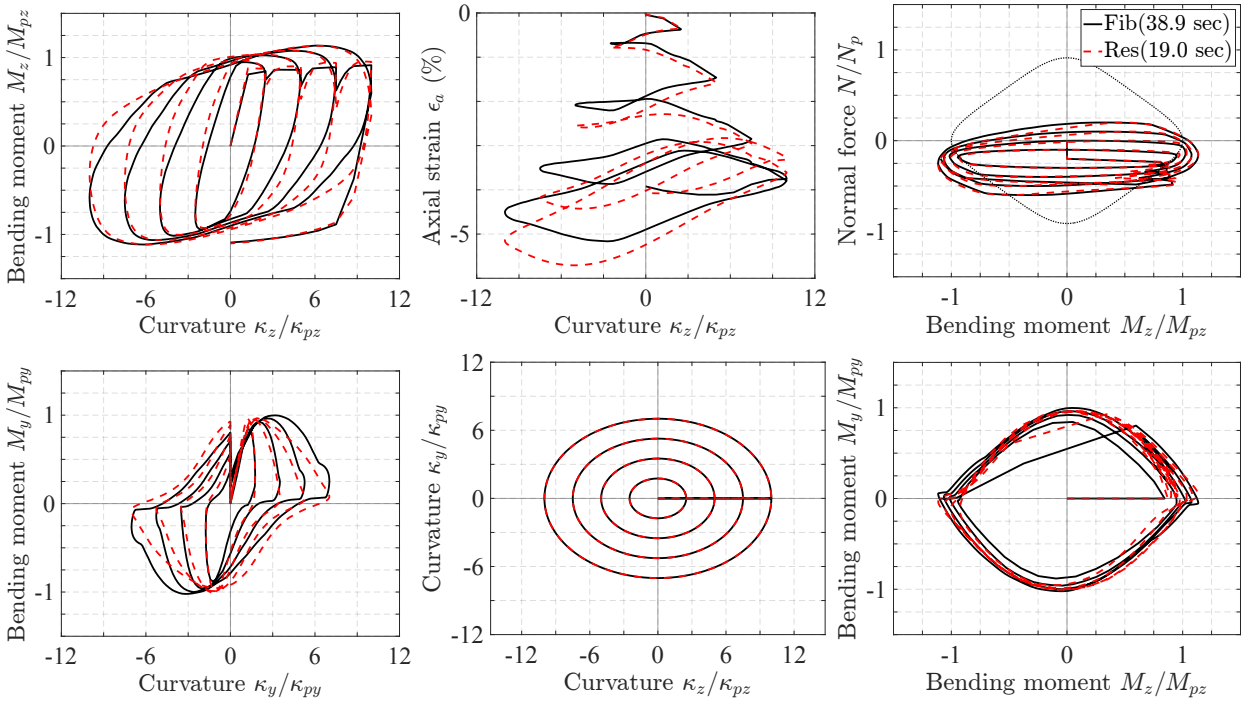


Figure 2.30: Response of W12x120 section under BV1 with $N = -20\%N_p \pm 40\%N_p$ - Fib4 vs. Res4

### 2.5.2 Analyses of cantilever columns with wide-flange sections

The resultant section and fiber section models for the W14x730 and W12x120 steel profiles are then inserted within a distributed plasticity beam-column element with force-formulation [86]. A 10 ft high cantilever column specimen with 7 Gauss-Lobatto integration points along its length is investigated, as illustrated in Figure 2.31. This number of integration points is sufficient to capture the spread of the plastic zone at the column base under hardening behavior. The objective here is not to optimize the number of integration points along the length of the element, but rather to assess the performance of the resultant section model within a distributed plasticity beam-column element, and compare it with that of a fiber section model, for a given element integration scheme. For element integration strategies under the consideration of hardening, the reader is referred to [71], [91].

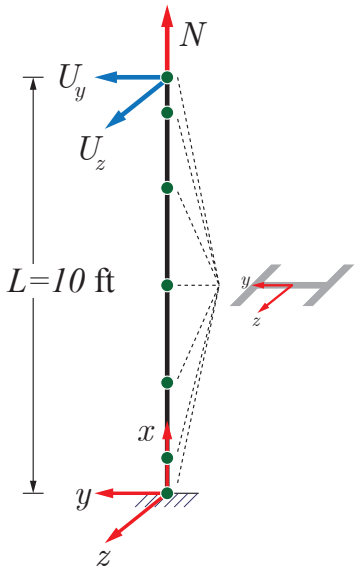


Figure 2.31: Cantilever column model with 7 Gauss-Lobatto integration points under imposed axial force and tip displacements

The monitoring sections are assigned either the Fib4 or Res4 section models introduced in Section 2.5.1.2 that account for kinematic and isotropic hardening. This gives rise to two column models: DP7Fib and DP7Res, where DP stands for Distributed Plasticity, the number 7 refers to the number of monitoring sections along the element length. The number 4 in the section names is dropped for brevity.

Uniaxial and biaxial displacements are imposed at the tip of the cantilever, along with an imposed axial force history. Six load patterns are investigated: U1, U2, UV1, B1, B2 and BV1, with a nomenclature consistent with Section 2.5.1.1, and the same levels of axial force are considered. The tip displacement and axial force histories are illustrated in Figure 2.32. The displacement load factors depicted in that figure are such that the imposed tip

displacements are given by:

$$U_y = \text{Disp. load factor} \cdot U_{y,ref} \tag{2.117}$$

$$U_z = \text{Disp. load factor} \cdot U_{z,ref} \tag{2.118}$$

where $U_{y,ref} = -U_{z,ref} = 2.5\%L$.

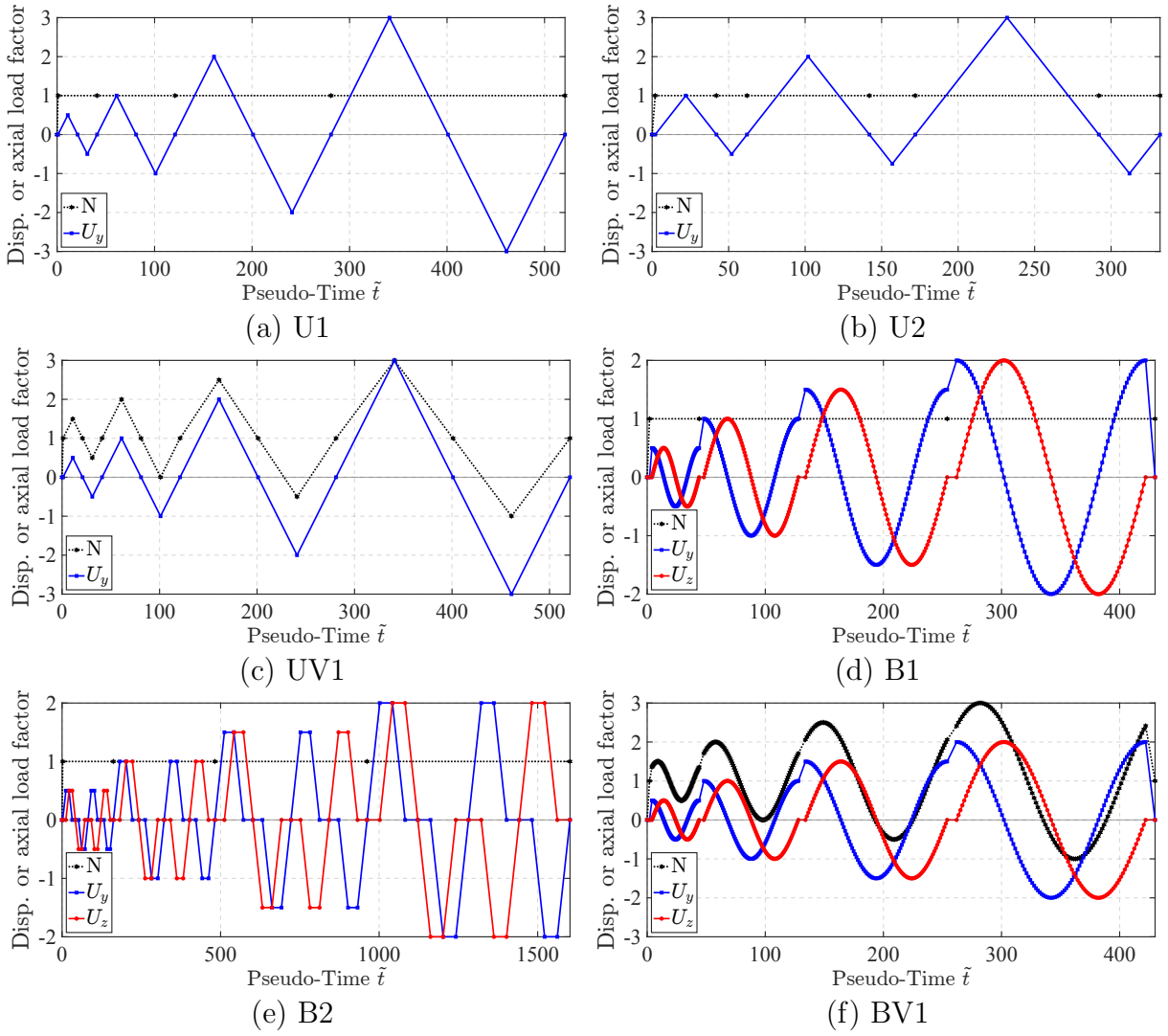


Figure 2.32: Displacement & axial force histories for cantilever column analyses

Figures 2.33 to 2.38 show the uniaxial response of the W14x730 and W12x120 columns. The agreement between the element with resultant section and the one with fiber section is excellent across all plots. A slight discrepancy is observed in the base curvature $\kappa_z$ response which appears to be exacerbated under variable axial force.

Figures 2.39 to 2.46 show the biaxial response of the W14x730 and W12x120 columns. The column model with resultant section captures the two bending moments, end plastic rotations, and axial deformation with impressive accuracy under these complex loading scenarios, including under extreme variations of the axial force. The base curvature responses $\kappa_z$ and $\kappa_y$ tend to be overestimated by the model with resultant section, especially for the curvature about the weak axis of the cross section.

Across the multiple loading cases, the computational time with the resultant section model instead of the fiber section model is reduced by a factor of 1.5 to 4.

To improve the quality of the base curvature response, another column model with 7 Gauss-Lobatto points is investigated. The column uses a resultant section model a higher value for the kinematic hardening ratio corresponding to the flexural bending about y-axis. The idea is that, with increased hardening, the same bending moment will result in a smaller curvature therefore reducing the overestimation effect. Figures 2.47 to 2.50 show the biaxial response of the W14x730 column with a resultant section with $H_{kr,fy} = 4\%$ instead of 1%. With no loss in accuracy in the bending moments, in the plastic rotations, and in the axial deformation responses, the base curvature $\kappa_y$ response is considerably more accurate.

### 2.5.3 Conclusions

From the moment curvature analyses and the cantilever column analyses of wide-flange cross sections, the following conclusions are drawn:

- The 2d and 3d resultant plasticity section models are able to represent the characteristic hysteretic behavior of steel cross sections, including the accumulation of plastic deformations and the kinematic and isotropic hardening under complex uniaxial and biaxial loading scenarios with axial force of multiple levels.

- Across the investigated loading cases for the nonlinear static analysis of a single steel column modeled with a typical distributed plasticity element, using the resultant plasticity section model rather than a fiber section model reduces the computation time by a factor of 1.5 to 4, while maintaining an excellent accuracy in the global and local response measures of the component. This gain in numerical efficiency is expected to scale up in large structural models with multiple beam-column elements.

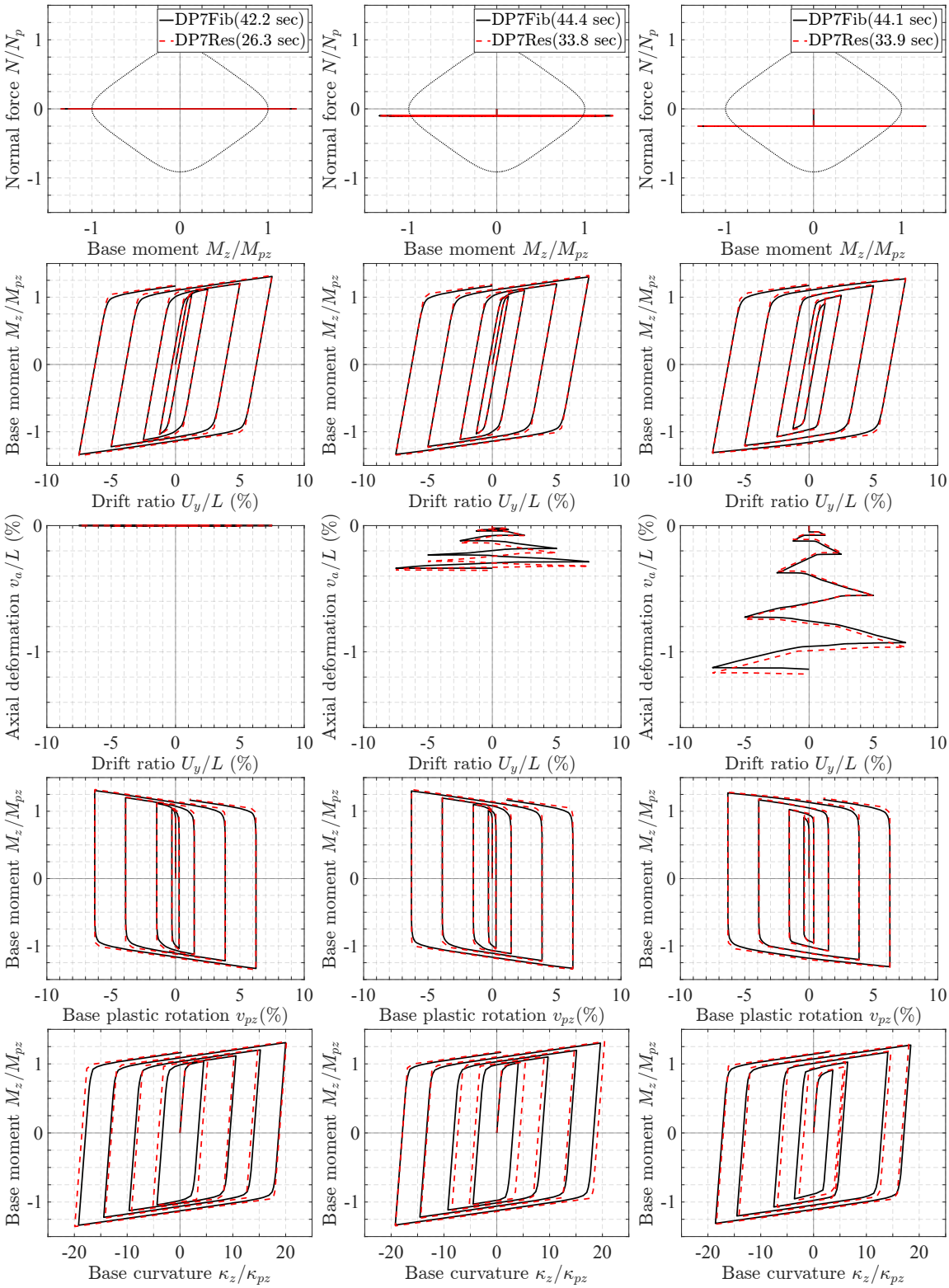


(a) $N = 0$ (b) $N = -10\%N_p$ (c) $N = -25\%N_p$

Figure 2.33: Response of W14x730 column under U1

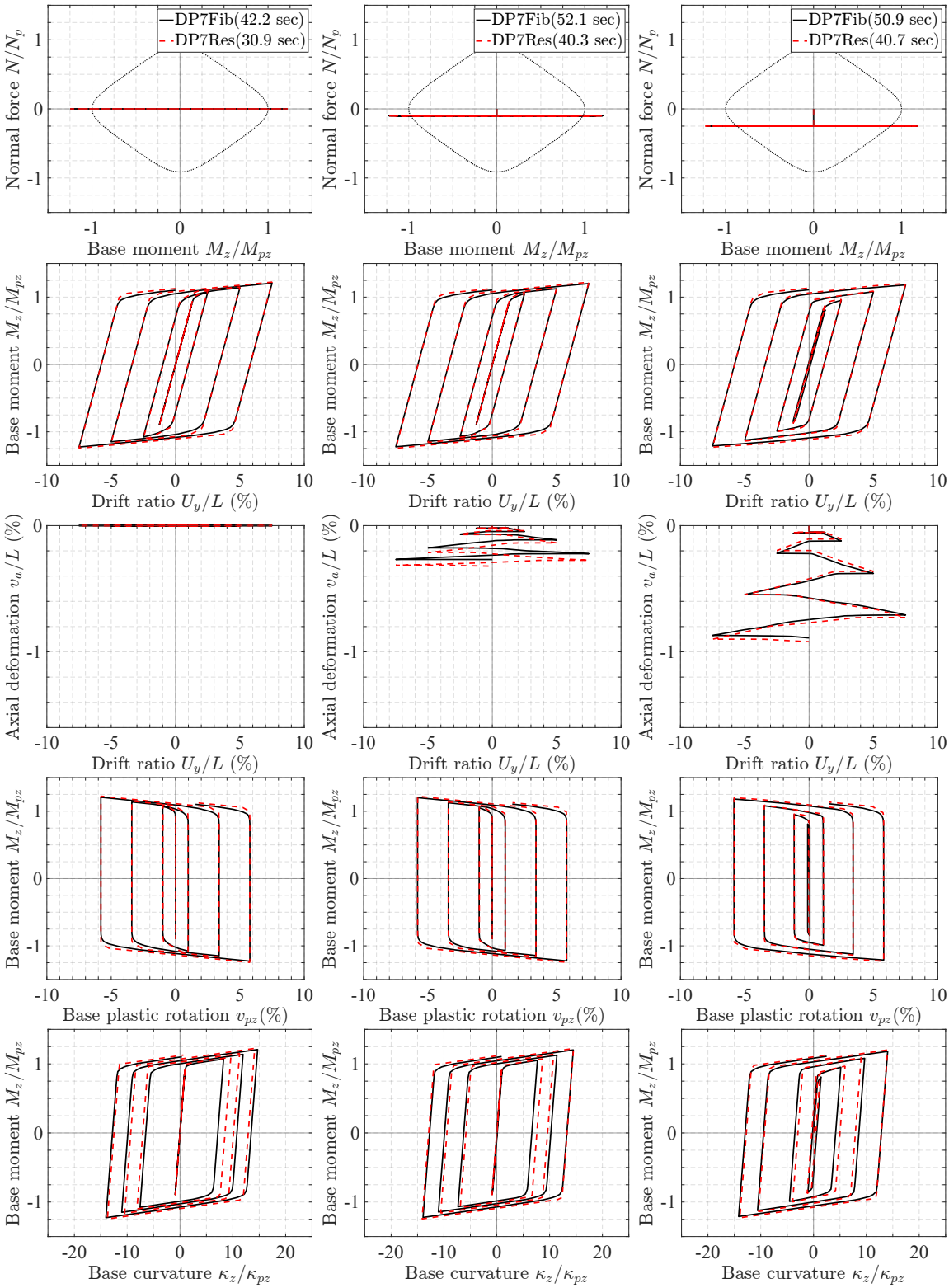


(a) $N = 0$ (b) $N = -10\%N_p$ (c) $N = -25\%N_p$

Figure 2.34: Response of W12x120 column under U1

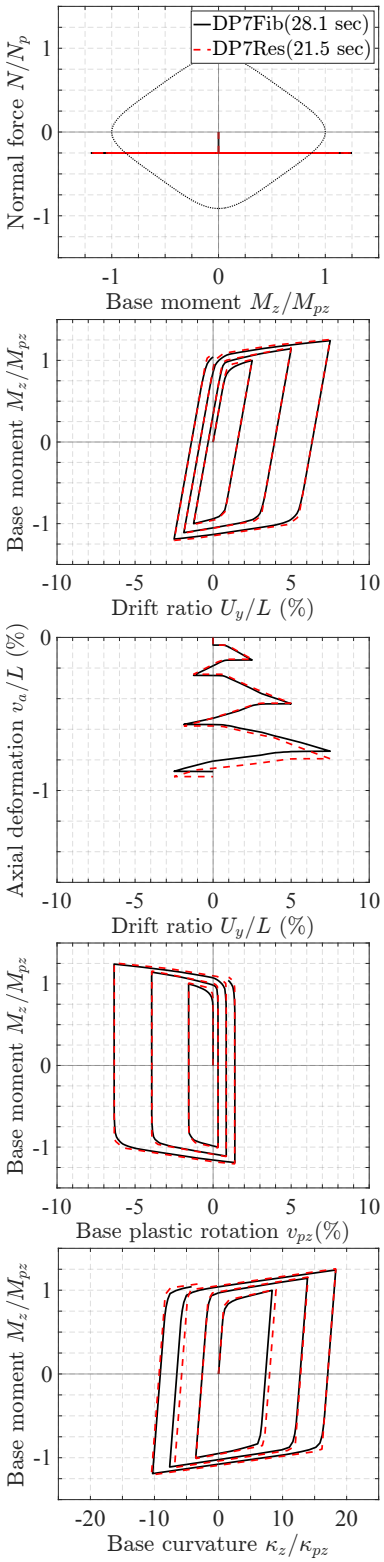


Figure 2.35: Response of W14x730 column under U2 with $N = -25\%N_p$

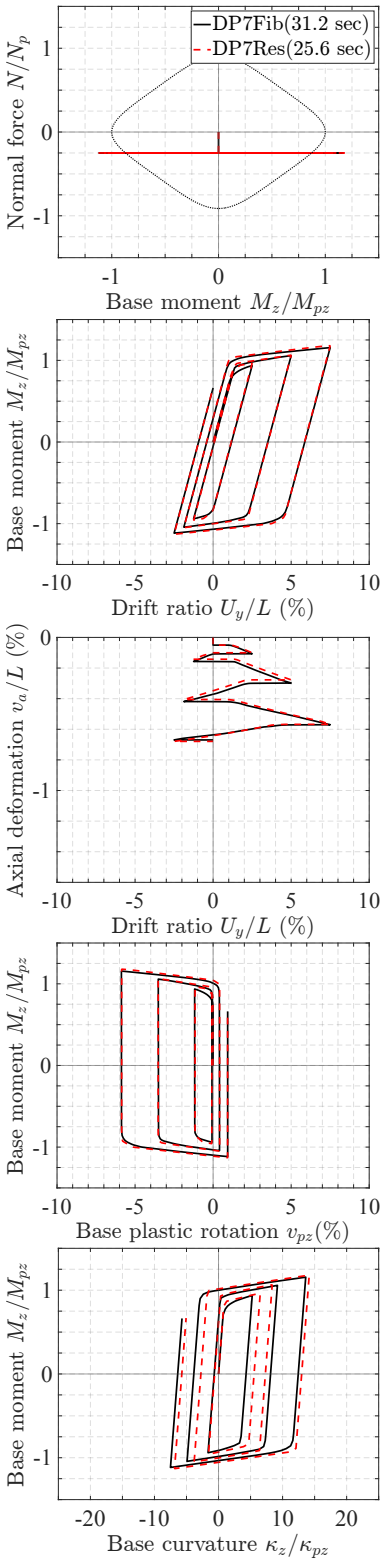


Figure 2.36: Response of W12x120 column under U2 with $N = -25\%N_p$

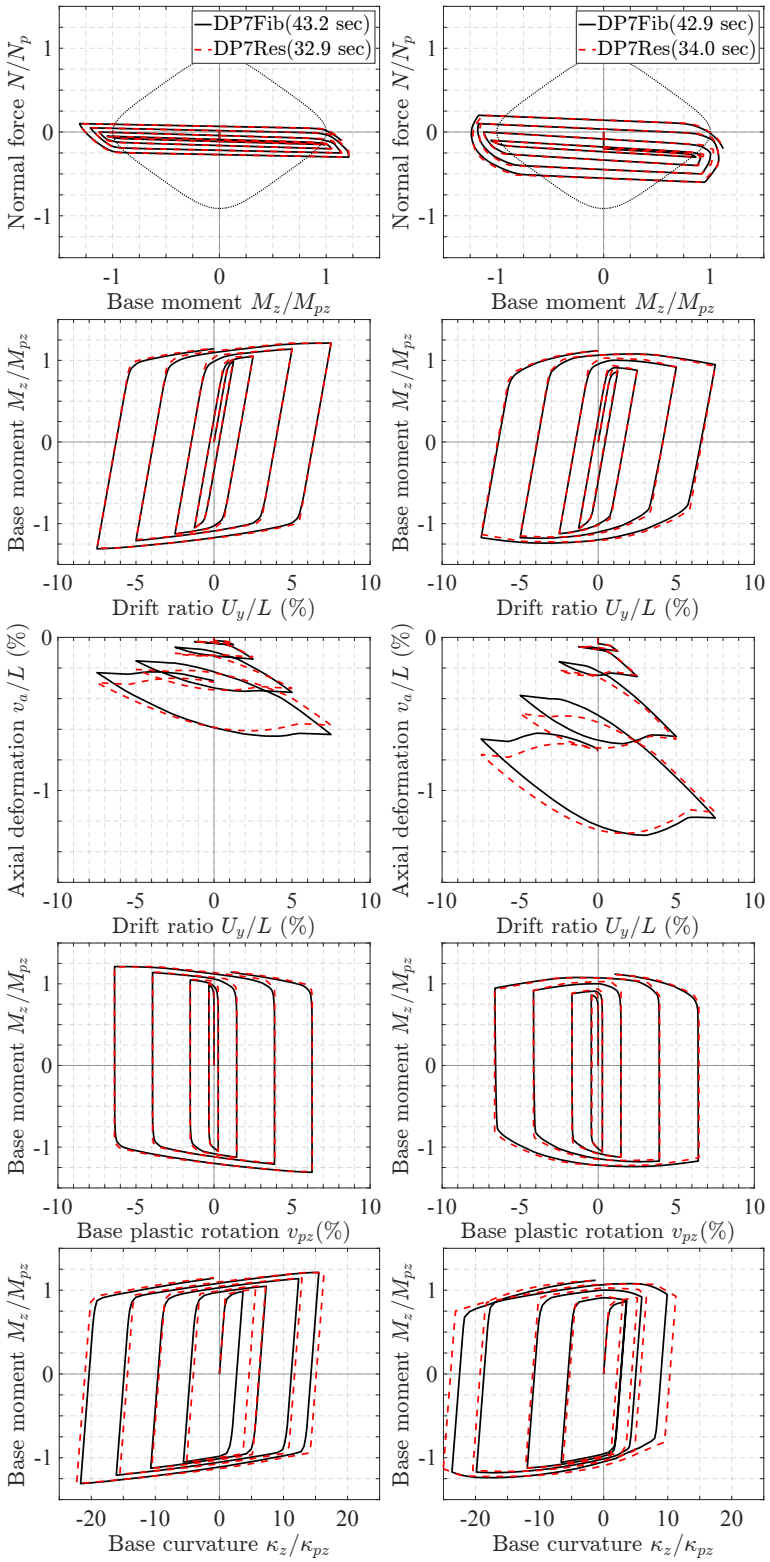


(a) $N = -10\%N_p \pm 20\%N_p$ (b) $N = -20\%N_p \pm 40\%N_p$

Figure 2.37: Response of W14x730 column under UV1

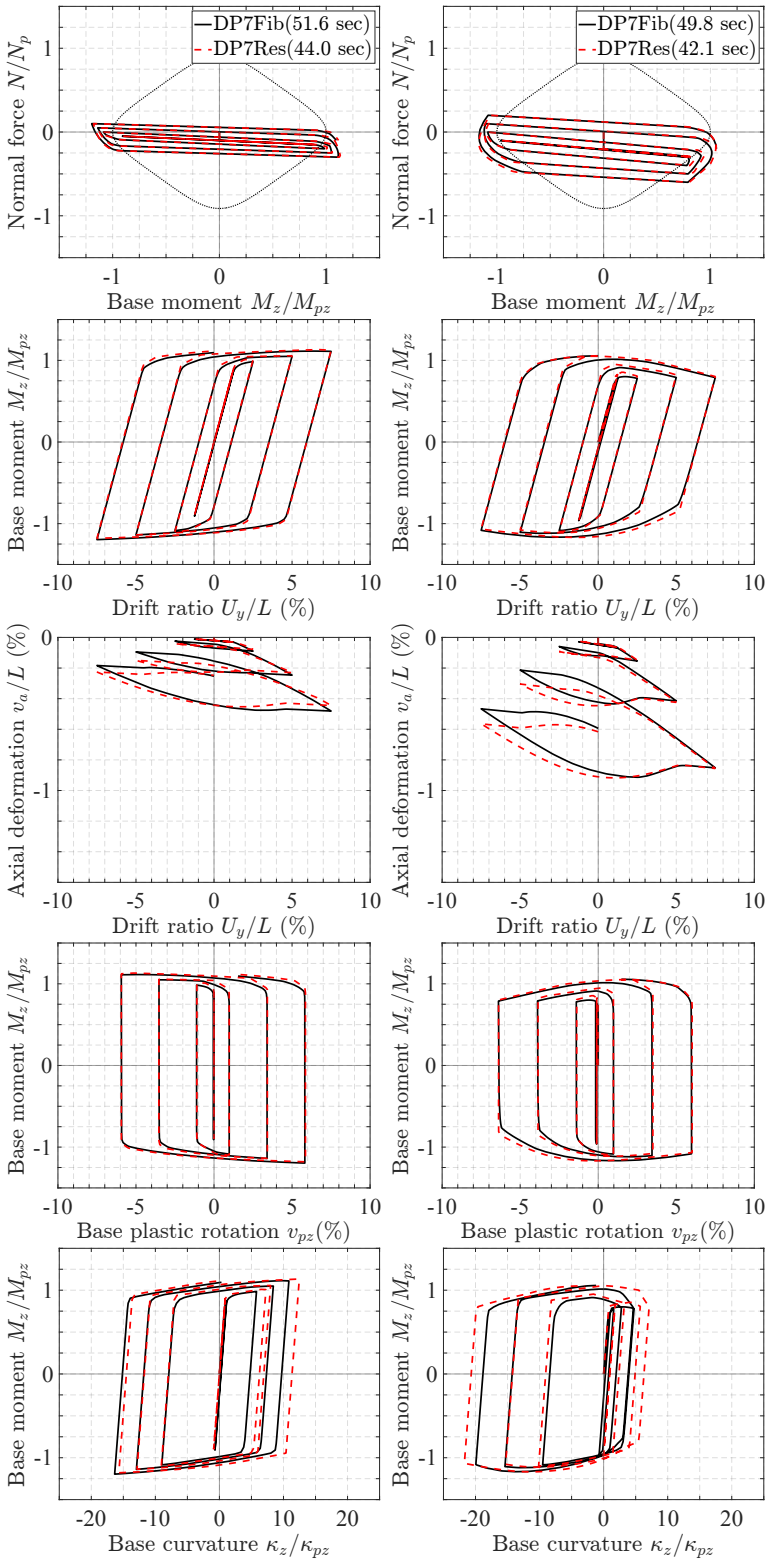


(a) $N = -10\%N_p \pm 20\%N_p$ (b) $N = -20\%N_p \pm 40\%N_p$

Figure 2.38: Response of W12x120 column under UV1

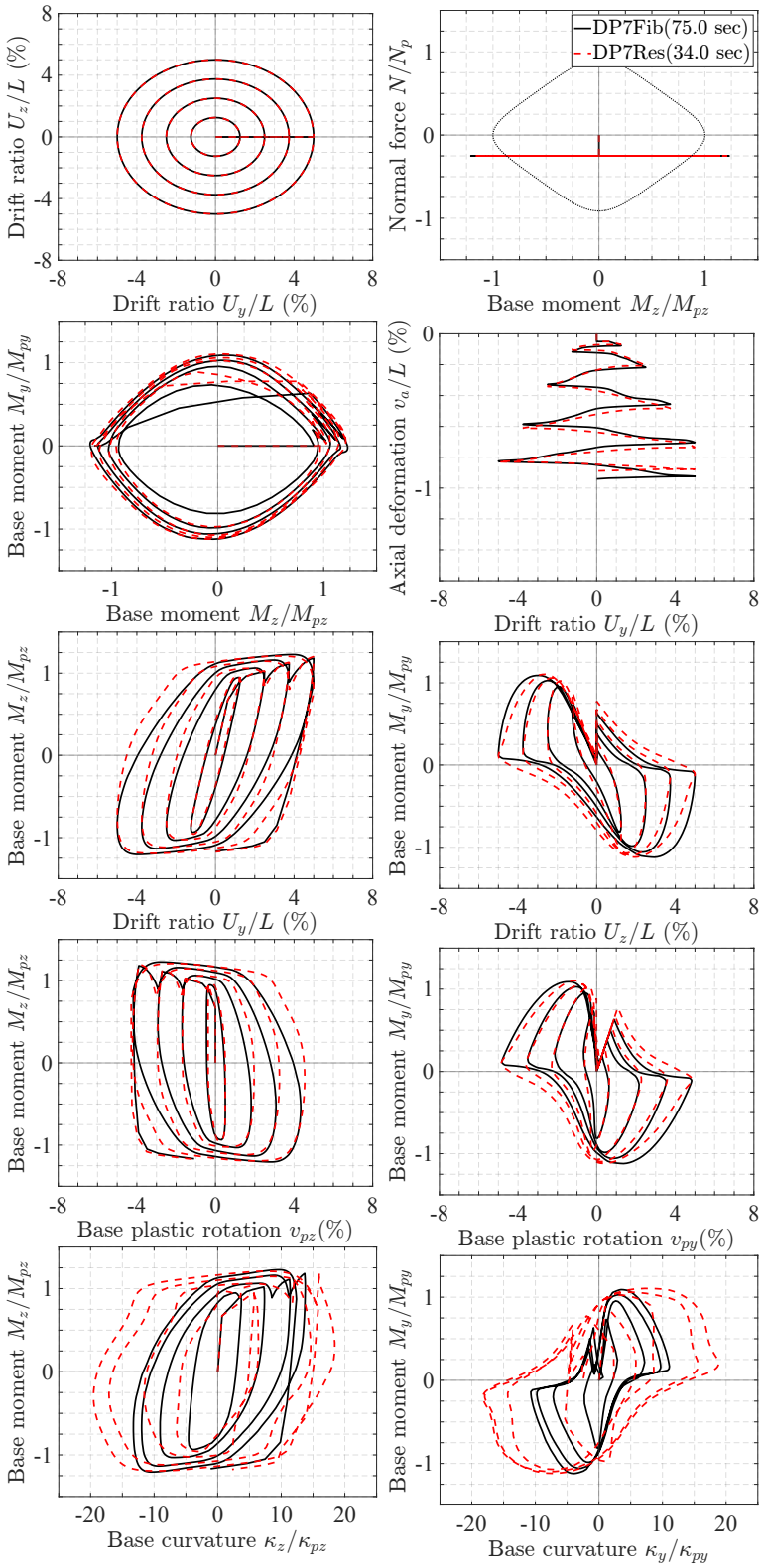


Figure 2.39: Response of W14x730 column under B1 with $N = -25\%N_p$

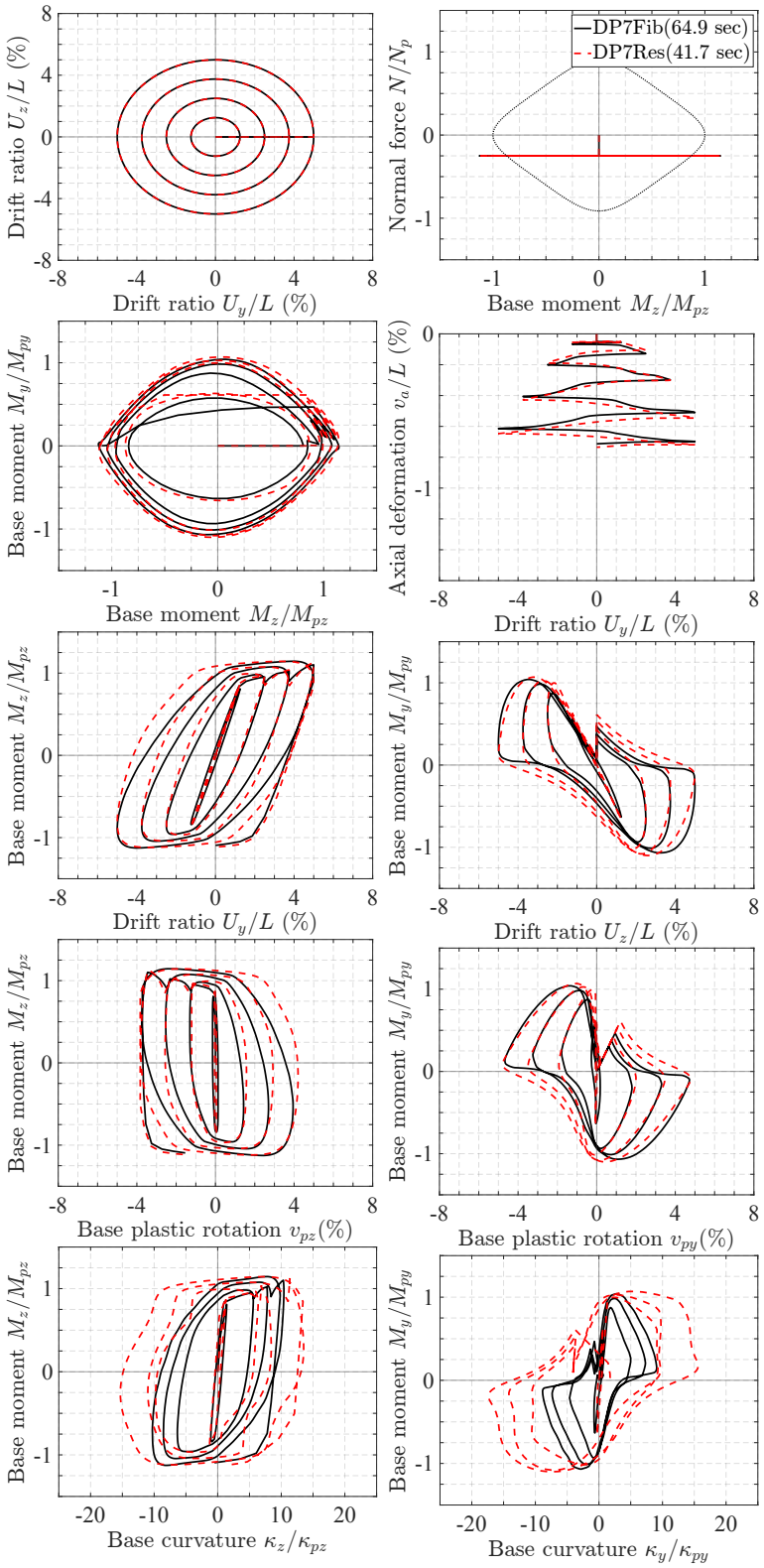


Figure 2.40: Response of W12x120 column under B1 with $N = -25\%N_p$

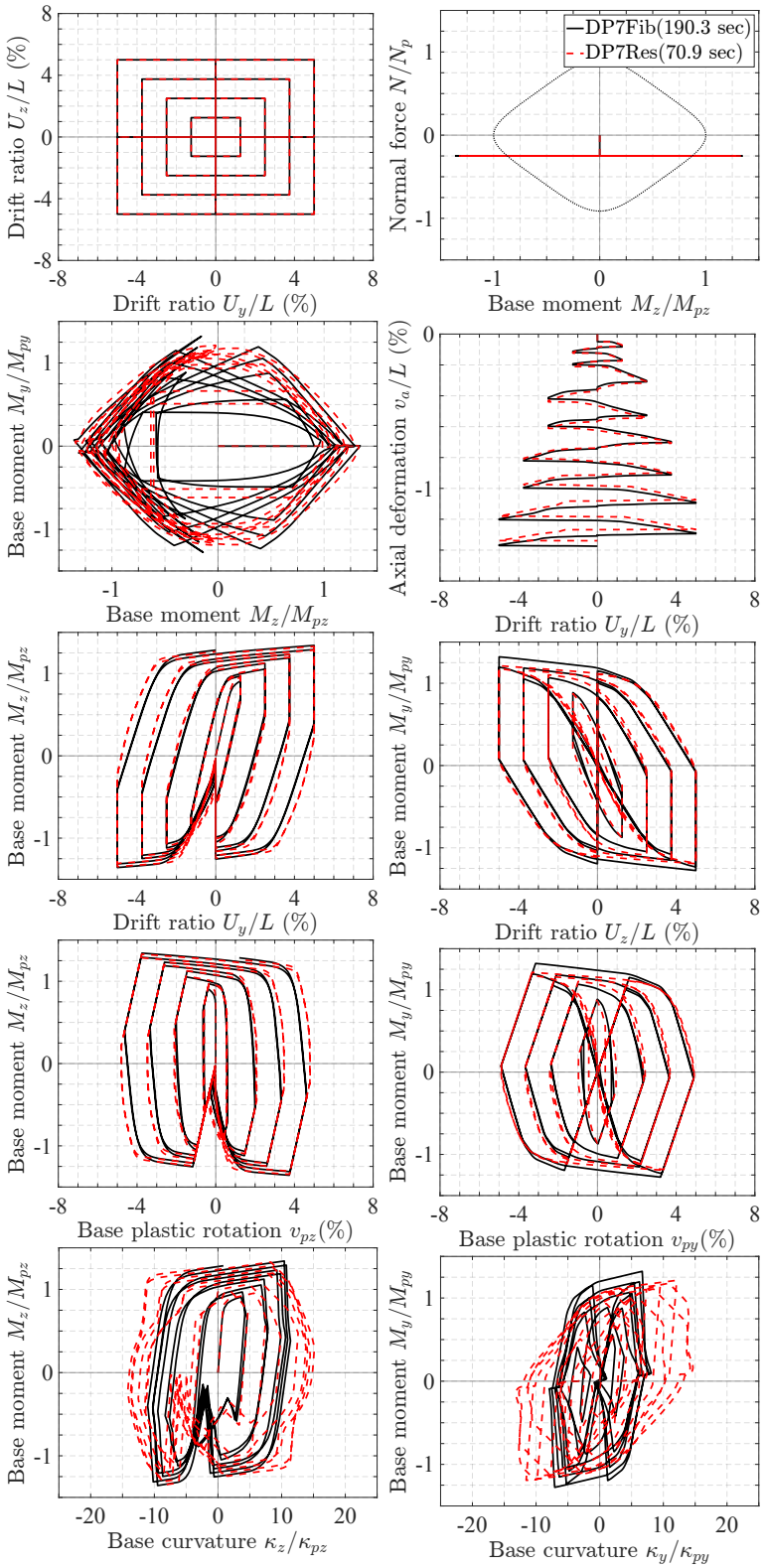


Figure 2.41: Response of W14x730 column under B2 with $N = -25\%N_p$

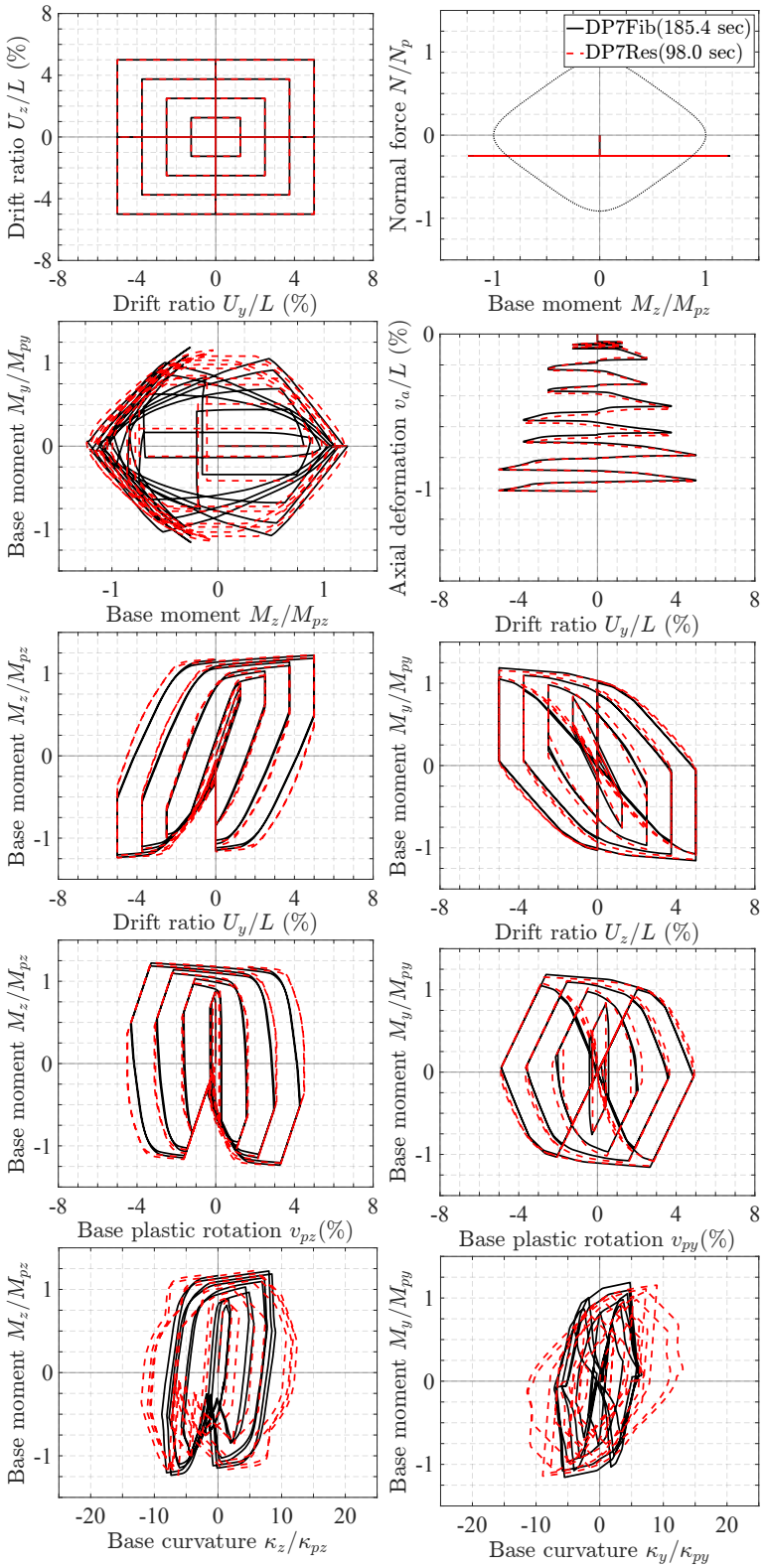


Figure 2.42: Response of W12x120 column under B2 with $N = -25\%N_p$

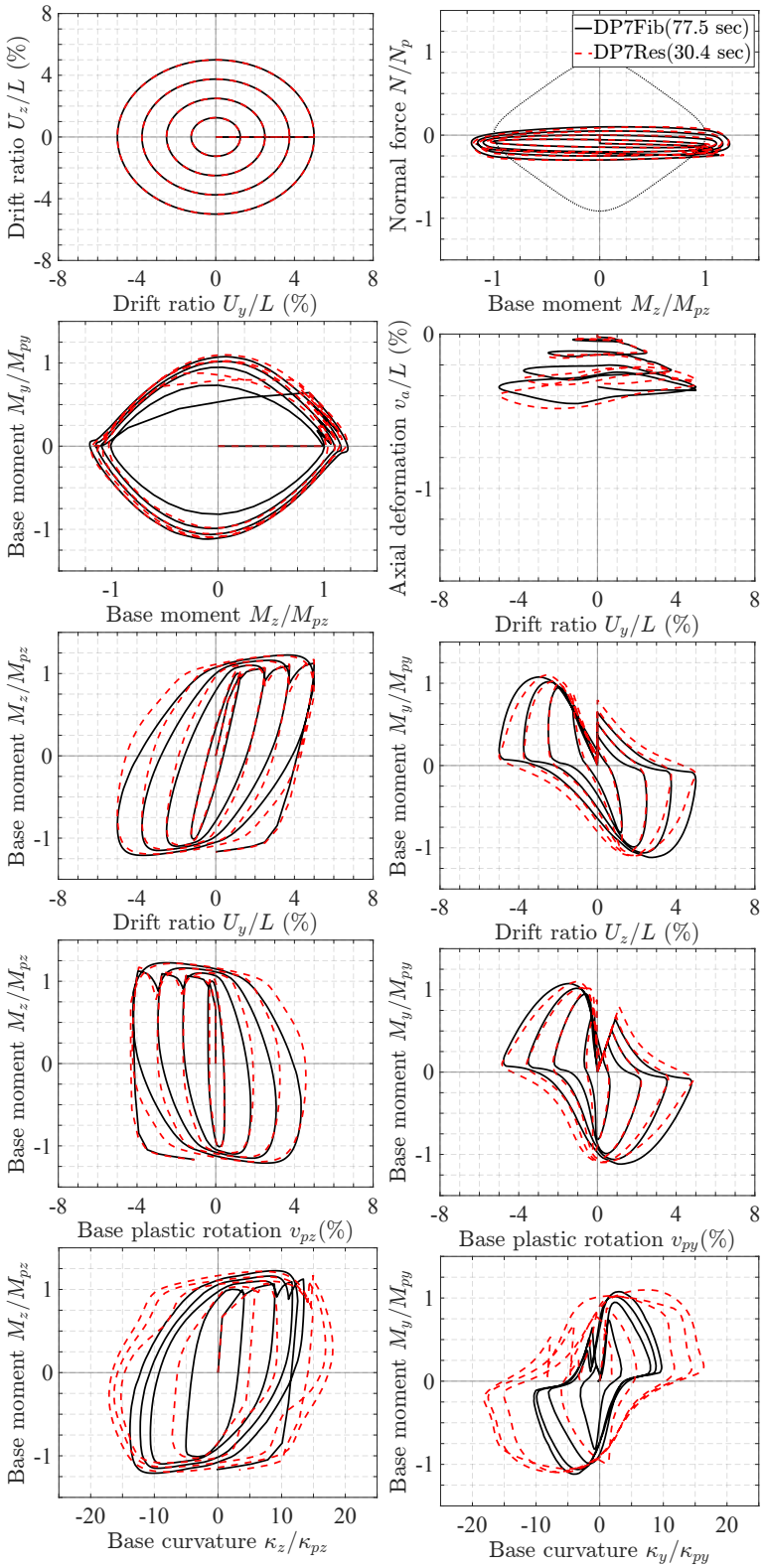


Figure 2.43: Response of W14x730 column under BV1 with $N = -10\%N_p \pm 20\%N_p$

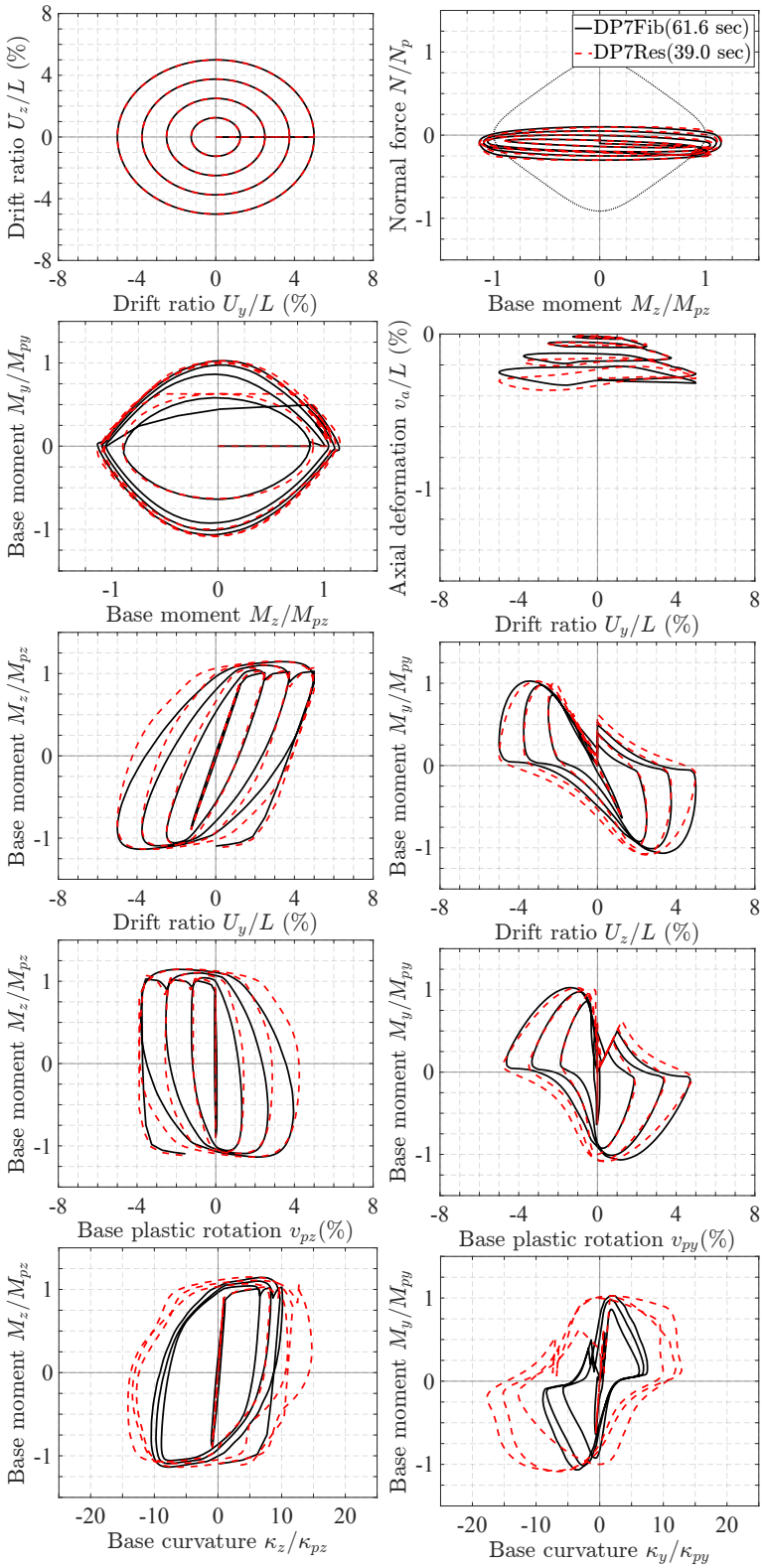


Figure 2.44: Response of W12x120 column under BV1 with $N = -10\%N_p \pm 20\%N_p$

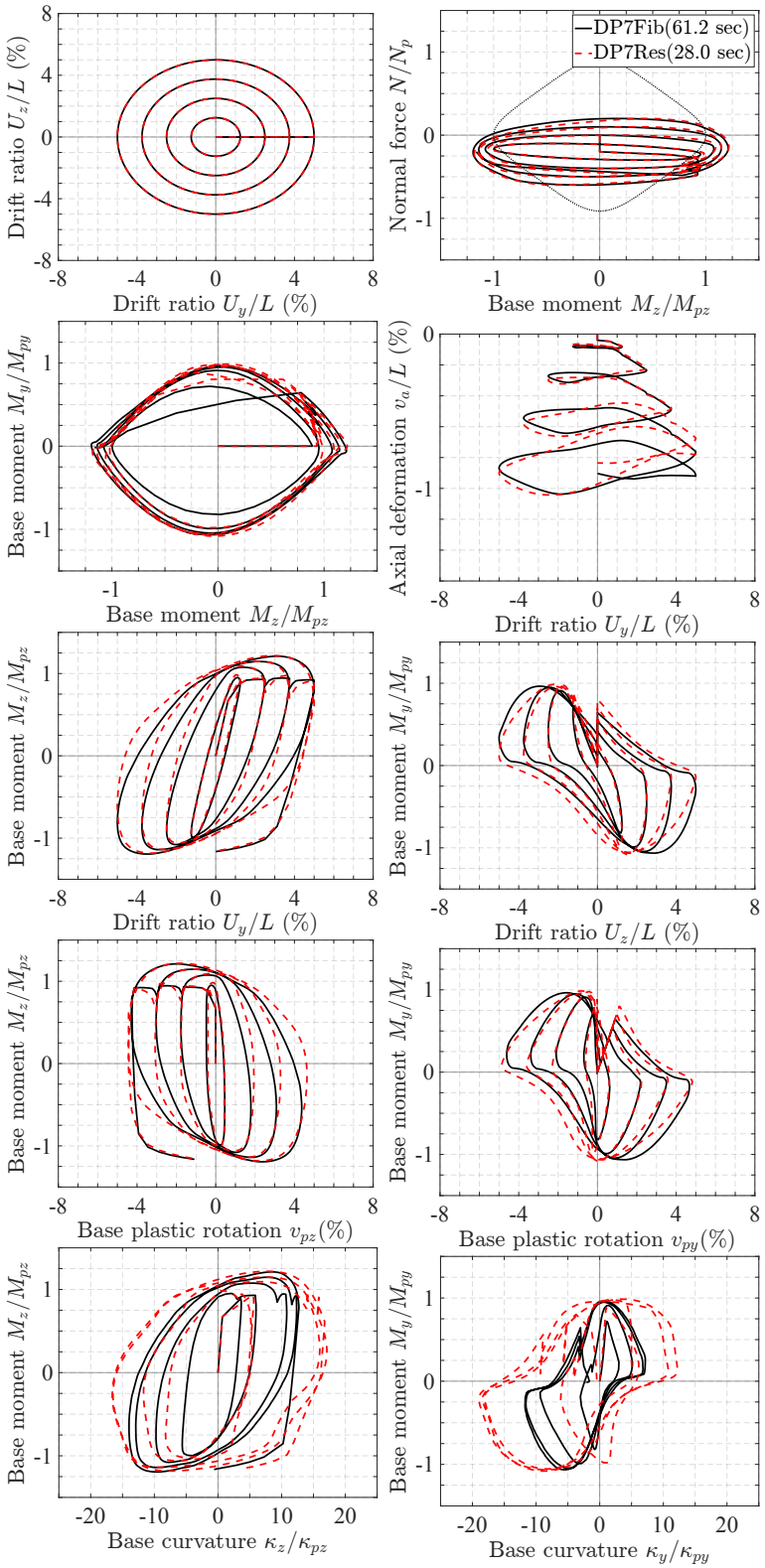


Figure 2.45: Response of W14x730 column under BV1 with $N = -20\%N_p \pm 40\%N_p$

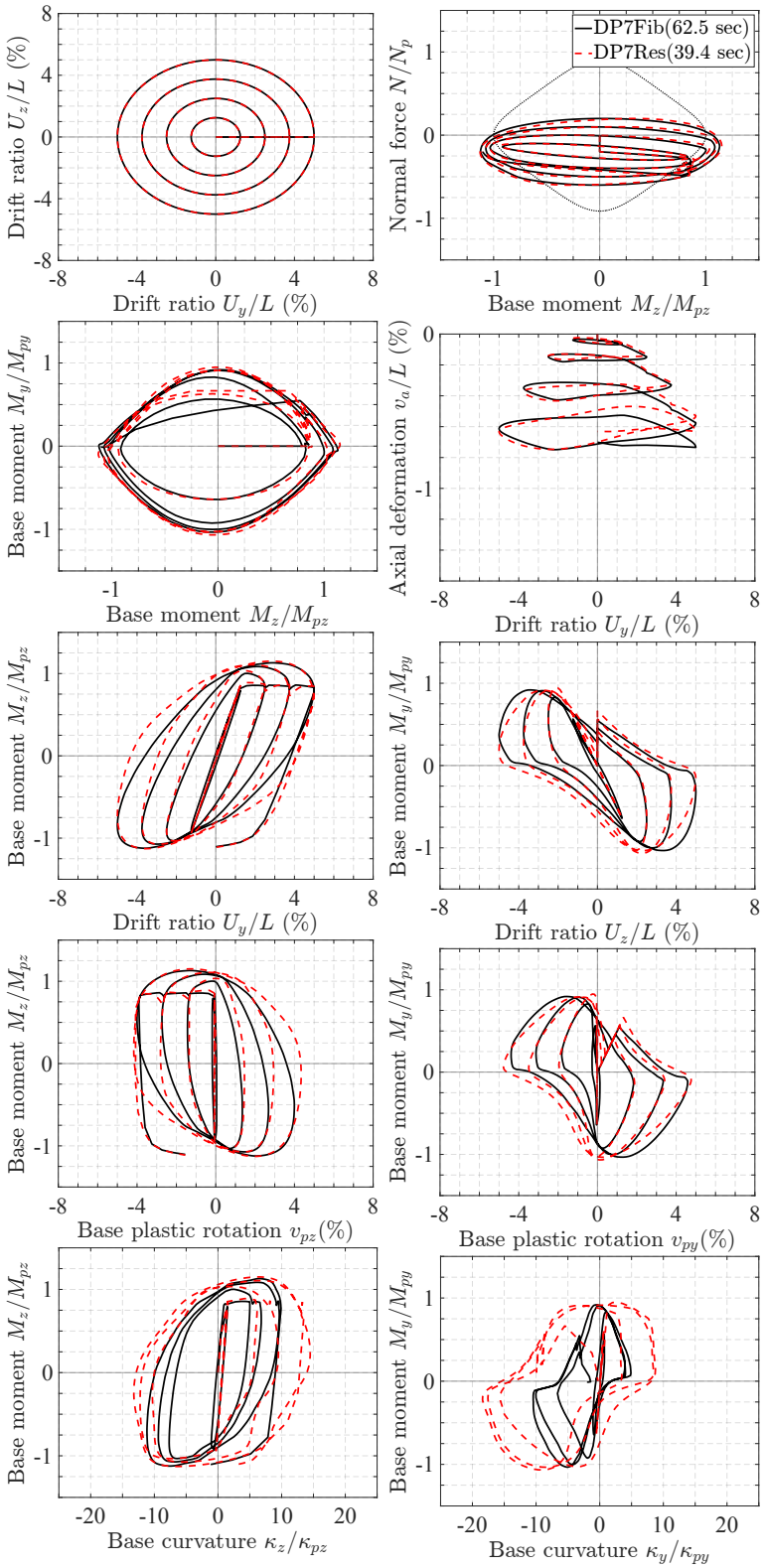


Figure 2.46: Response of W12x120 column under BV1 with $N = -20\%N_p \pm 40\%N_p$

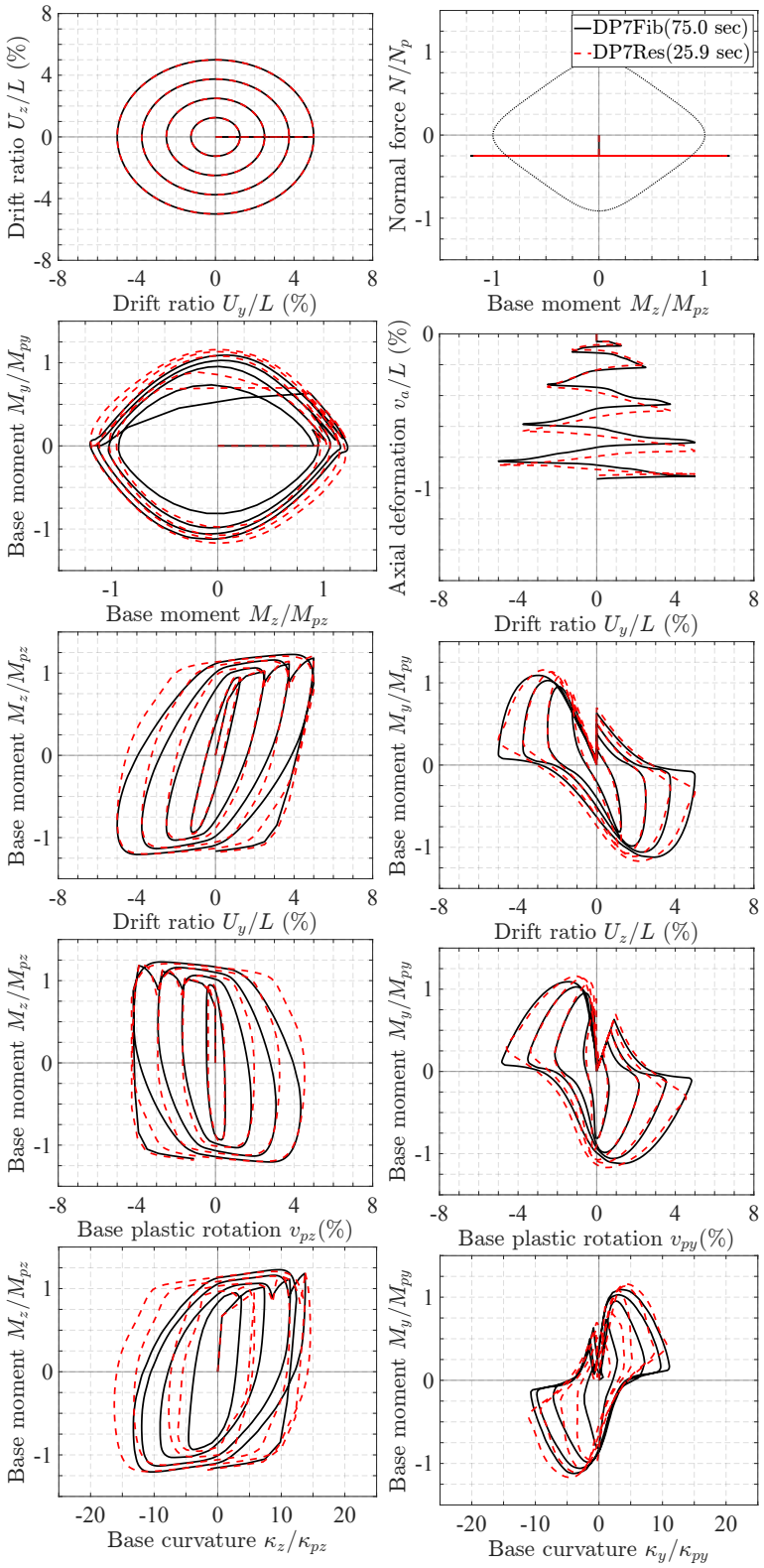


Figure 2.47: Response of W14x730 column under B1 with $N = -25\%N_p$ with $H_{kr,fy} = 4\%$

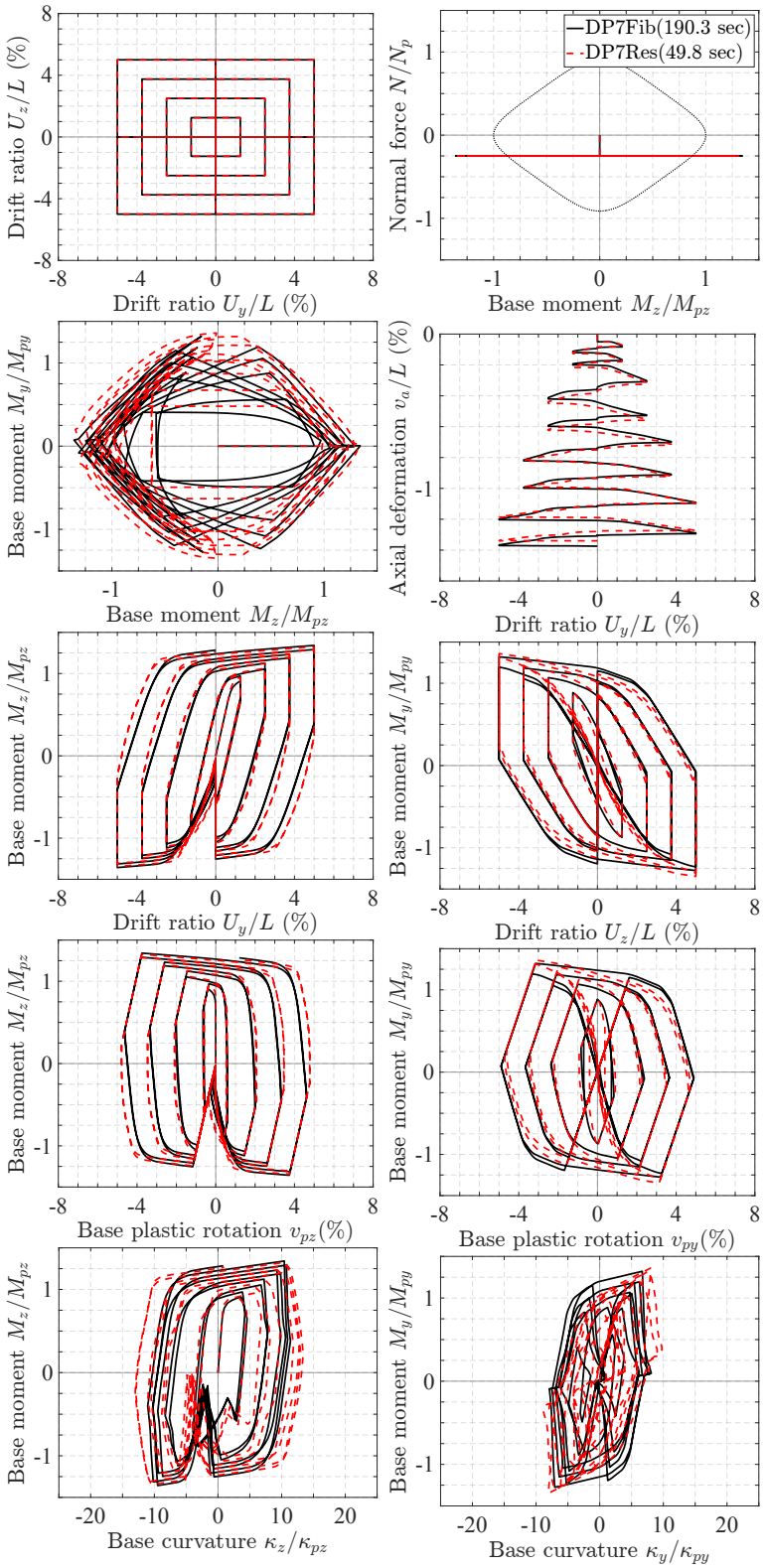


Figure 2.48: Response of W14x730 column under B2 with $N = -25\%N_p$ with $H_{kr,fy} = 4\%$

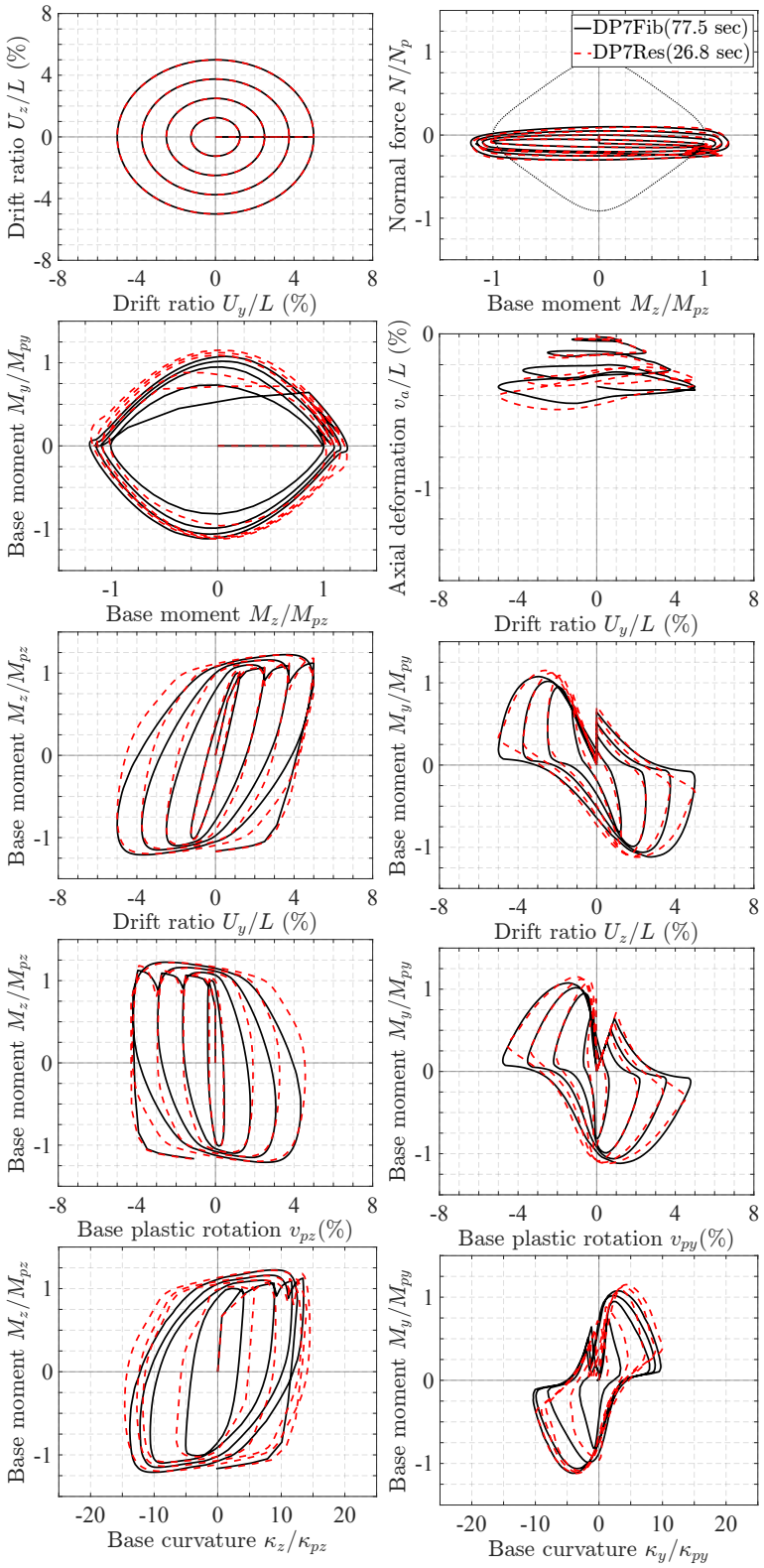


Figure 2.49: Response of W14x730 column under BV1 with $N = -10\%N_p \pm 20\%N_p$ with $H_{kr,fy} = 4\%$

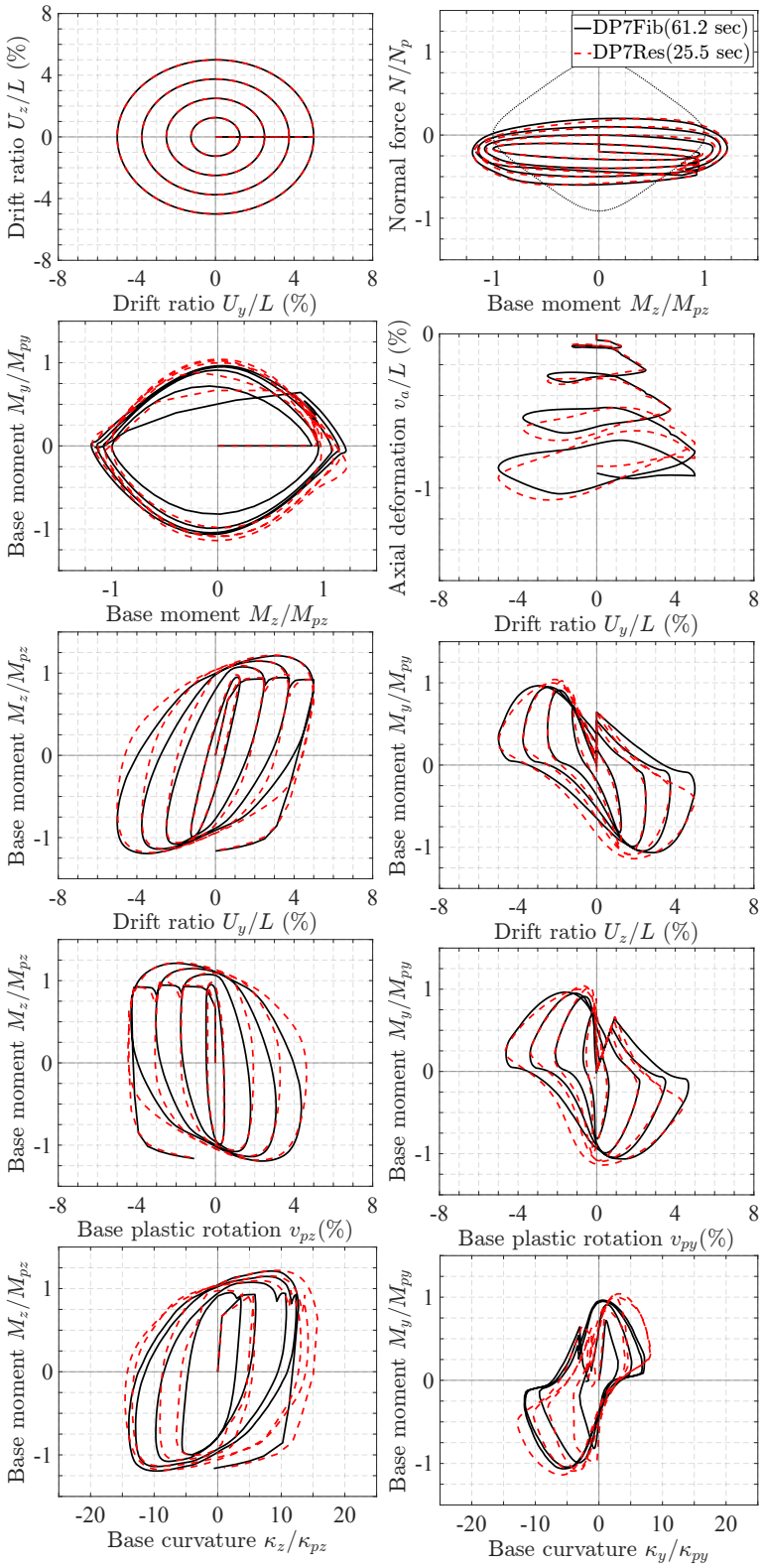


Figure 2.50: Response of W14x730 column under BV1 with $N = -20\%N_p \pm 40\%N_p$ with $H_{kr,fy} = 4\%$

# Chapter 3

# Beam element with concentrated resultant force plasticity

## 3.1 Overview

This chapter presents a frame element based on resultant plasticity theory suitable for the non-degrading uniaxial bending response of beam-column elements subjected to low axial forces. The model consists of a linear elastic element with two concentrated plastic hinges that can be offset from the element ends. The proposed beam formulation neglects the axial-flexure interaction and assumes a linear elastic axial response uncoupled from the flexural response. These assumptions are reasonable for beam members which experience only small axial forces. Another resultant plasticity frame element model that accounts for the effect of the axial force on the flexural yield strength and captures the axial inelastic response is proposed in Chapter 4. It is intended for modeling the behavior of column members subjected to higher axial forces and accommodates biaxial bending conditions.

## 3.2 Preliminaries

### 3.2.1 Local coordinate system for beam element

The behavior of a plane frame element subjected to uniaxial bending conditions can be characterized through the evaluation of three kinematic variables, also known as element deformations, and three element basic forces, also known as element resultant forces. These variables can be defined with reference to the local coordinate system x-y-z illustrated in Figure 3.1. The x-axis is longitudinal to the frame element and is oriented from end $i$ to end $j$, the z-axis points towards the viewer and the y-axis is such that x-y-z forms a right handed Cartesian coordinate system.

The three kinematic variables can be assembled into the element deformation vector $\boldsymbol{v}$

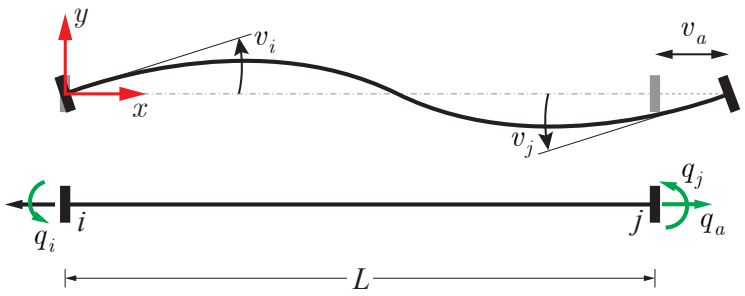


Figure 3.1: Kinematic variables and basic forces for plane frame element

defined as follows:

$$\boldsymbol{v} = \begin{bmatrix} v_a & v_i & v_j \end{bmatrix}^T \tag{3.1}$$

where $v_a$ is the axial deformation and $v_i$ and $v_j$ are the flexural deformations at end $i$ and end $j$ of the element, respectively. The axial deformation has units of length, whereas the flexural deformations are rotations with units of radians and their sign is defined as positive in the counterclockwise direction.

The three element basic forces or force resultants, can be assembled into the element basic force vector $\boldsymbol{q}$ which consists of the following components:

$$\boldsymbol{q} = \begin{bmatrix} q_a & q_i & q_j \end{bmatrix}^T \tag{3.2}$$

where $q_a$ is the axial force resultant and $q_i$ and $q_j$ are the flexural forces at end $i$ and $j$ of the element, respectively.

To be used in the context of numerical analysis, a frame element model needs to relate the element deformations $\boldsymbol{v}$ to the element forces $\boldsymbol{q}$ through a constitutive relation, a process referred to as element state determination.

### 3.2.2 Beam models with distributed vs. concentrated resultant force plasticity

One category of frame elements that is commonly used to capture the inelastic behavior of beam and column structural members are distributed plasticity models. These models monitor the element response at several integration points, also referred to as monitoring sections, distributed along the element length. The section state determination is performed at each integration point and the element response is obtained through numerical integration. The section response can either be determined from a resultant section model (such as the formulation proposed in Chapter 2) or a fiber section model.

Another type of model that captures the inelastic behavior of frame elements are resultant or concentrated plasticity models. Such models assume that the nonlinear behavior is concentrated at hinges that are typically located at the element ends. In particular, Do [24]

proposed a concentrated plasticity beam model suitable for describing the inelastic response of homogeneous steel beams under uniaxial bending conditions. The model consists of a linear elastic element in series with two rigid plastic springs that can accommodate kinematic and isotropic hardening. The plastic hinges can be offset from the element ends to account for the spread of inelasticity under hardening response and the size of the damage zones under softening response. This chapter proposes to improve the kinematic and isotropic hardening formulation of the beam element model of Do [24] and to develop a consistent calibration procedure for the associated hardening and hinge offset parameters.

## 3.3 Beam element with concentrated resultant force plasticity

### 3.3.1 Concentrated resultant force plasticity beam element for uniaxial flexure

Attention is put on developing a beam model for frame elements subjected to uniaxial bending conditions. The axis about which the flexural action is taking place can indifferently be the strong axis or the weak axis of the cross section. The beam resultant model adopts three element deformations $\boldsymbol{v}$ and three element basic forces $\boldsymbol{q}$, as defined in Equations (3.1) and (3.2).

The present formulation assumes that the axial response is linear elastic and uncoupled from the flexural response, a reasonable assumption for beams members. Consequently, for any given axial deformation $v_a$ and in the absence of initial deformation, the axial basic force $q_a$ can be computed from

$$q_a = \frac{EA}{L} v_a \tag{3.3}$$

The flexural response however is inelastic and the flexural basic forces $\boldsymbol{q}_f = \begin{bmatrix} q_i & q_j \end{bmatrix}^T$ are computed separately using the resultant plasticity model presented hereafter.

#### 3.3.1.1 Series model of element deformations

The proposed resultant plasticity beam model is based on plasticity theory [73] and uses an elastic component in series with a plastic component. Accordingly, the element end flexural deformations $\boldsymbol{v}_f = \begin{bmatrix} v_i & v_j \end{bmatrix}^T$ are decomposed into the sum of two contributions: the elastic flexural deformations $\boldsymbol{v}_e$ and the plastic flexural deformations $\boldsymbol{v}_p$ such that:

$$\boldsymbol{v}_f = \boldsymbol{v}_e + \boldsymbol{v}_p \tag{3.4}$$

with

$$\boldsymbol{v}_e = \begin{bmatrix} v_{i,e} & v_{j,e} \end{bmatrix}^T \tag{3.5}$$

$$\boldsymbol{v}_p = \begin{bmatrix} v_{i,p} & v_{j,p} \end{bmatrix}^T \tag{3.6}$$

where $v_{i,e}$ and $v_{j,e}$ are the elastic flexural deformations at end $i$ and end $j$, respectively, and $v_{i,p}$ and $v_{j,p}$ are the plastic flexural deformations at end $i$ and end $j$, respectively.

Consistent with the series model assumption of plasticity theory, the forces of the two components are equal at all times:

$$\boldsymbol{q}_f = \boldsymbol{q}_e = \boldsymbol{q}_p \tag{3.7}$$

$\boldsymbol{q}_e$ denotes the element flexural basic forces of the elastic component and $\boldsymbol{q}_p$ the flexural basic forces of the plastic component.

#### 3.3.1.2 Constitutive relation

It is postulated that the forces in the elastic component satisfy Hook's law with a stiffness equal to the elastic flexural element stiffness $\mathbf{k}_{fe}$, that is:

$$\boldsymbol{q}_f = \mathbf{k}_{fe}\boldsymbol{v}_e = \mathbf{k}_{fe}\left(\boldsymbol{v}_f - \boldsymbol{v}_p\right) \tag{3.8}$$

where $\mathbf{k}_{fe}$ is given by

$$\mathbf{k}_{fe} = \begin{bmatrix} \dfrac{4EI}{L} & \dfrac{2EI}{L} \\ \dfrac{2EI}{L} & \dfrac{4EI}{L} \end{bmatrix} \tag{3.9}$$

$E$ is the Young's modulus of the material, $A$ is the cross-sectional area of the section, $I$ is the moment of inertia about the bending axis, and $L$ is the length of the member.

To account for the spread of inelasticity at the element ends and model more accurately the post yield response, the two plastic hinges can be offset from the element ends, as illustrated in Figure 3.2. Denoting the offset ratios by $\chi_i$ and $\chi_j$, the hinges are located at a distance of $\chi_i L$ and $\chi_j L$ from end $i$ and end $j$, respectively.

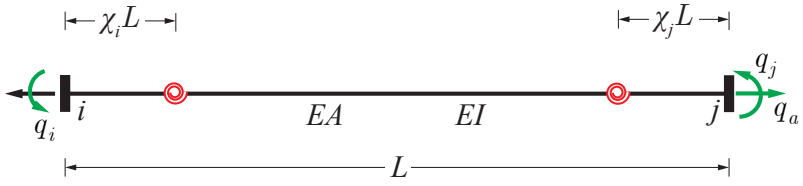


Figure 3.2: Resultant plasticity beam element with plastic hinge offsets

In the absence of element loading, the bending moment distribution is linear, as illustrated in Figure 3.3.

Accordingly, the bending moment at the plastic hinges can be determined from the basic flexural forces at the element ends $\boldsymbol{q}_f$ by linear interpolation

$$\boldsymbol{s}_h = \begin{pmatrix} M_{hi} \\ M_{hj} \end{pmatrix} = \mathbf{b}_h \boldsymbol{q}_f \tag{3.10}$$

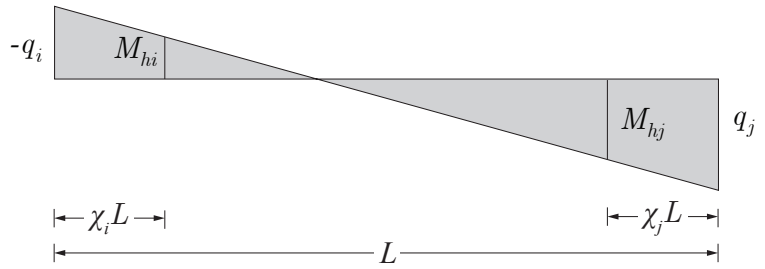


Figure 3.3: Bending moment interpolation at plastic hinge locations

where $M_{hi}$ and $M_{hj}$ are the bending moment values at the plastic hinge located near end $i$ and end $j$, respectively; $\boldsymbol{s}_h$ is the vector of hinge internal forces, and the interpolation matrix $\mathbf{b}_h$ is given by:

$$\mathbf{b}_h = \begin{pmatrix} \mathbf{b}_{hi} \\ \mathbf{b}_{hj} \end{pmatrix} = \begin{bmatrix} \chi_i - 1 & \chi_i \\ -\chi_j & 1 - \chi_j \end{bmatrix} \tag{3.11}$$

The vector of hinge deformations $\boldsymbol{e}_h$ that is work equivalent to $\boldsymbol{s}_h$ cannot be directly computed from the element deformations $\boldsymbol{v}_f$, but the principle of virtual work requires that

$$\boldsymbol{v}_f = \mathbf{b}_h^T \boldsymbol{e}_h \tag{3.12}$$

Similarly, introducing a vector of plastic hinge deformations $\boldsymbol{e}_{hp}$, these need to be related to the element plastic deformations $\boldsymbol{v}_p$ through

$$\boldsymbol{v}_p = \mathbf{b}_h^T \boldsymbol{e}_{hp} \tag{3.13}$$

Accordingly, $\boldsymbol{e}_h$ and $\boldsymbol{e}_{hp}$ each consist of two components:

$$\boldsymbol{e}_h = \begin{bmatrix} \theta_{h,i} & \theta_{h,j} \end{bmatrix}^T \tag{3.14}$$

$$\boldsymbol{e}_{hp} = \begin{bmatrix} \theta_{hp,i} & \theta_{hp,j} \end{bmatrix}^T \tag{3.15}$$

where $\theta$ denotes the rotations.

Combining Equations (3.8), (3.10), (3.12) and (3.13) gives a new constitutive relation between the forces $\boldsymbol{s}_h$ and the deformations $\boldsymbol{e}_h$ at the hinges. Accordingly,

$$\boldsymbol{s}_h = \mathbf{k}_{he} \left( \boldsymbol{e}_h - \boldsymbol{e}_{hp} \right) \tag{3.16}$$

where

$$\mathbf{k}_{he} = \mathbf{b}_h \mathbf{k}_{fe} \mathbf{b}_h^T \tag{3.17}$$

#### 3.3.1.3 Yield function

The yield criteria are defined based on the evolution of the internal forces at the two plastic hinges. Let $\mathbf{f} : \mathbb{R}^2 \times \mathbb{R}^2 \times (\mathbb{R}^+)^2 \to \mathbb{R}^2$:

$$\mathbf{f}\left(\boldsymbol{s}_h, \boldsymbol{s}_{bk}, \boldsymbol{\alpha}\right) := \begin{pmatrix} f_i\left(\boldsymbol{s}_h, \boldsymbol{s}_{bk}, \boldsymbol{\alpha}\right) \\ f_j\left(\boldsymbol{s}_h, \boldsymbol{s}_{bk}, \boldsymbol{\alpha}\right) \end{pmatrix} = \begin{pmatrix} |M_{hi} - M_{bk,i}| \\ |M_{hj} - M_{bk,j}| \end{pmatrix} - \left( \begin{pmatrix} M_{pi} \\ M_{pj} \end{pmatrix} + \mathbf{H}_{hi}\boldsymbol{\alpha} \right) \tag{3.18}$$

where $\boldsymbol{s}_{bk} = \begin{bmatrix} M_{bk,i} & M_{bk,j} \end{bmatrix}^T$ are the two flexural back forces at the hinges near end $i$ and $j$ of the element; $M_{pi}$ and $M_{pj}$ are the plastic flexural capacities at end $i$ and $j$ of the element; $\boldsymbol{\alpha} = \begin{bmatrix} \alpha_i & \alpha_j \end{bmatrix}^T$ are the internal isotropic hardening variables, and $\mathbf{H}_{hi}$ is 2x2 matrix defining the isotropic hardening properties of the hinges.

Let $\boldsymbol{M}_p = \begin{bmatrix} M_{pi} & M_{pj} \end{bmatrix}^T$. The yield criteria in Equation (3.18) can be rewritten more compactly as

$$\mathbf{f}\left(\boldsymbol{s}_h, \boldsymbol{s}_{bk}, \boldsymbol{\alpha}\right) = \boldsymbol{\phi}\left(\boldsymbol{s}_h - \boldsymbol{s}_{bk}\right) - \left(\boldsymbol{M}_p + \mathbf{H}_{hi}\boldsymbol{\alpha}\right) \tag{3.19}$$

where $\boldsymbol{\phi} : \mathbb{R}^2 \to (\mathbb{R}^+)^2$:

$$\boldsymbol{s} = \begin{pmatrix} M_i \\ M_j \end{pmatrix} \mapsto \boldsymbol{\phi}\left(\boldsymbol{s}\right) = \begin{pmatrix} |M_i| \\ |M_j| \end{pmatrix} \tag{3.20}$$

The corresponding set of admissible solutions is

$$\mathbb{E}_{\boldsymbol{s}_h} = \{(\boldsymbol{s}_h, \boldsymbol{s}_{bk}, \boldsymbol{\alpha}) \in \mathbb{R}^2 \times \mathbb{R}^2 \times (\mathbb{R}^+)^2 \mid \mathbf{f}(\boldsymbol{s}_h, \boldsymbol{s}_{bk}, \boldsymbol{\alpha}) \leq \mathbf{0}\} \tag{3.21}$$

Accordingly, the elastic domain takes the form:

$$\text{int}(\mathbb{E}_{\boldsymbol{s}_h}) = \{(\boldsymbol{s}_h, \boldsymbol{s}_{bk}, \boldsymbol{\alpha}) \in \mathbb{R}^2 \times \mathbb{R}^2 \times (\mathbb{R}^+)^2 \mid \mathbf{f}(\boldsymbol{s}_h, \boldsymbol{s}_{bk}, \boldsymbol{\alpha}) < \mathbf{0}\} \tag{3.22}$$

whereas the yield surface is defined as:

$$\begin{aligned} \partial\mathbb{E}_{\boldsymbol{s}_h} = \{(\boldsymbol{s}_h, \boldsymbol{s}_{bk}, \boldsymbol{\alpha}) \in \mathbb{R}^2 \times \mathbb{R}^2 \times (\mathbb{R}^+)^2 \mid & f_i(\boldsymbol{s}_h, \boldsymbol{s}_{bk}, \boldsymbol{\alpha}) = 0 \text{ or} \\ & f_j(\boldsymbol{s}_h, \boldsymbol{s}_{bk}, \boldsymbol{\alpha}) = 0\} \end{aligned} \tag{3.23}$$

States $(\boldsymbol{s}_h, \boldsymbol{s}_{bk}, \boldsymbol{\alpha})$ outside $\mathbb{E}_{\boldsymbol{s}_h}$ are non admissible and ruled out according to classical plasticity theory.

Before any hardening takes place, the yield envelope defined by Equation (3.23) consists of four lines $M_{hi} = \pm M_{pi}$ and $M_{hj} = \pm M_{pj}$, as illustrated in Figure 3.4. It is noteworthy that this yield surface is non-smooth with four singular points at the corners of the boundary of the elastic domain.

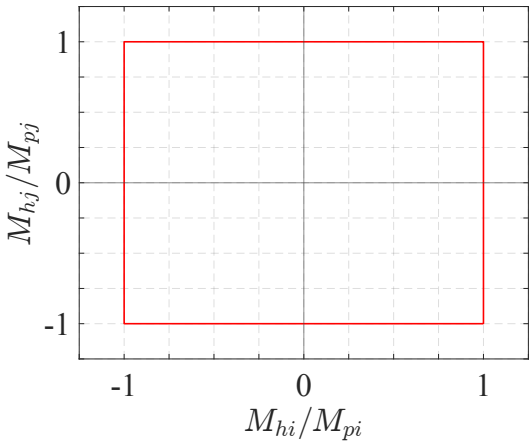


Figure 3.4: Initial yield envelope for resultant plasticity beam model

#### 3.3.1.4 Evolutionary equations

The associative flow rule and the hardening laws are prescribed as follows:

$$\dot{\boldsymbol{e}}_{hp} = \left(\frac{\partial \mathbf{f}}{\partial \boldsymbol{s}_h}\right)^T \boldsymbol{\gamma} = \boldsymbol{n}\boldsymbol{\gamma} \tag{3.24}$$

$$\dot{\boldsymbol{s}}_{bk} = \mathbf{H}_{hk}\dot{\boldsymbol{e}}_{hp} = \mathbf{H}_{hk}\boldsymbol{n}\boldsymbol{\gamma} \tag{3.25}$$

$$\dot{\boldsymbol{\alpha}} = -\frac{\partial \mathbf{f}}{\partial\left(\mathbf{H}_{hi}\boldsymbol{\alpha}\right)}\boldsymbol{\gamma} = \boldsymbol{\gamma} \tag{3.26}$$

where $\boldsymbol{n}$ is the normal to the yield envelope, which is defined as:

$$\boldsymbol{n} = \begin{bmatrix}\boldsymbol{n}_i & \boldsymbol{n}_j\end{bmatrix} = \left(\frac{\partial \mathbf{f}}{\partial \boldsymbol{s}_h}\right)^T = \begin{bmatrix}\dfrac{\partial f_i}{\partial M_{hi}} & \dfrac{\partial f_j}{\partial M_{hi}} \\ \dfrac{\partial f_i}{\partial M_{hj}} & \dfrac{\partial f_j}{\partial M_{hj}}\end{bmatrix} \tag{3.27}$$

$\boldsymbol{\gamma} = \begin{bmatrix}\gamma_i & \gamma_j\end{bmatrix}^T \in (\mathbb{R}^+)^2$ is the vector of consistency parameters, and $\mathbf{H}_{hk}$ is a 2x2 matrix that defines the kinematic hardening properties of the hinges.

The normal $\boldsymbol{n}$ can be computed as:

$$\boldsymbol{n} = \frac{\partial \boldsymbol{\phi}}{\partial \boldsymbol{s}_h}(\boldsymbol{s}_h - \boldsymbol{s}_{bk}) = \begin{bmatrix}\operatorname{sgn}(M_{hi} - M_{bk,i}) & 0 \\ 0 & \operatorname{sgn}(M_{hj} - M_{bk,j})\end{bmatrix} \tag{3.28}$$

The flow rule in Equation (3.24) accounts for the singularity of the yield envelope at the corners by specifying the rate of plastic deformation as a linear combination of the normals

$\boldsymbol{n}_i$ and $\boldsymbol{n}_j$ in accordance with Koiter's rule [43], i.e.,

$$\dot{\boldsymbol{e}_{hp}} = \gamma_i \boldsymbol{n}_i + \gamma_j \boldsymbol{n}_j \tag{3.29}$$

The vector of consistency parameters $\boldsymbol{\gamma}$ is assumed to obey the following Kuhn-Tucker conditions:

$$\begin{cases} \boldsymbol{\gamma} \geq \mathbf{0} \ , \ \mathbf{f}(\boldsymbol{s}_h, \boldsymbol{s}_{bk}, \boldsymbol{\alpha}) \leq \mathbf{0}, \\ \text{and} \\ \gamma_m f_m(\boldsymbol{s}_h, \boldsymbol{s}_{bk}, \boldsymbol{\alpha}) = 0 \ , \ m = i, j \end{cases} \tag{3.30}$$

In addition to the conditions given by Equation (3.30), $\boldsymbol{\gamma}$ satisfies the consistency requirement:

$$\gamma_m \dot{f}_m(\boldsymbol{s}_h, \boldsymbol{s}_{bk}, \boldsymbol{\alpha}) = 0 \ , \ m = i, j \tag{3.31}$$

#### 3.3.1.5 Kinematic and isotropic hardening

The kinematic and isotropic hardening properties of the plastic hinges are prescribed through the matrices $\mathbf{H}_{hk}$ and $\mathbf{H}_{hi}$ that are used in the yield function and the evolutionary equations. Because of the linear relations between $\boldsymbol{s}_h$ and $\boldsymbol{q}_f$ as well as between $\boldsymbol{e}_{hp}$ and $\boldsymbol{v}_p$, the presence of hardening at the hinges induces hardening in the element flexural end responses $q_i$ and $q_j$. The amount of hardening that is observed at the element ends is a function of the amount of hardening at the hinges but also of the location of the plastic hinges, i.e. of the hinge offset parameters $\chi_i$ and $\chi_j$ that appear in the interpolation matrix $\mathbf{b}_h$. To uncouple these two effects and obtain a consistent calibration of the hardening in the element end responses $q_i$ and $q_j$ regardless of the values of the hinge offset parameters, the matrices $\mathbf{H}_{hk}$ and $\mathbf{H}_{hi}$ can be derived from two other matrices, $\mathbf{H}_k$ and $\mathbf{H}_i$, that control directly the hardening behavior of the element ends.

Assume that the plastic modulus $\mathbf{k}_p$ that characterizes the hardening at the element ends takes the form:

$$\mathbf{k}_p := \frac{d\boldsymbol{q}_f}{d\boldsymbol{v}_p} = \mathbf{H}_k + \mathbf{H}_i \tag{3.32}$$

where

$$\frac{d\boldsymbol{q}_f}{d\boldsymbol{v}_p} = \begin{bmatrix} \dfrac{\partial q_i}{\partial v_{i,p}} & \dfrac{\partial q_i}{\partial v_{j,p}} \\ \dfrac{\partial q_j}{\partial v_{i,p}} & \dfrac{\partial q_j}{\partial v_{j,p}} \end{bmatrix} \quad ; \quad \mathbf{H}_k = \begin{bmatrix} H_{k,i} & 0 \\ 0 & H_{k,j} \end{bmatrix} \quad ; \quad \mathbf{H}_i = \begin{bmatrix} H_{i,i} & 0 \\ 0 & H_{i,j} \end{bmatrix} \tag{3.33}$$

Making use of the chain's rule and of Equations (3.10) and (3.13), the equivalent amount of hardening at the plastic hinge locations can be characterized by the hinge plastic modulus $\mathbf{k}_{ph}$ defined as:

$$\mathbf{k}_{ph} := \frac{d\boldsymbol{s}_h}{d\boldsymbol{e}_{hp}} = \mathbf{b}_h \frac{d\boldsymbol{q}_f}{d\boldsymbol{v}_p} \mathbf{b}_h^T = \mathbf{b}_h \mathbf{H}_k \mathbf{b}_h^T + \mathbf{b}_h \mathbf{H}_i \mathbf{b}_h^T \tag{3.34}$$

Considering the specific case where both plastic hinges are yielding and active i.e. when both $\gamma_i > 0$ and $\gamma_j > 0$, the consistency condition (3.31) requires that $\dot{\mathbf{f}} = \mathbf{0}$. Noticing that the yield function can be rewritten

$$\mathbf{f}(\boldsymbol{s}_h, \boldsymbol{s}_{bk}, \boldsymbol{\alpha}) = \boldsymbol{n}^T (\boldsymbol{s}_h - \boldsymbol{s}_{bk}) - (\boldsymbol{M}_p + \mathbf{H}_{hi}\boldsymbol{\alpha}) \tag{3.35}$$

and on account of Equations (3.16) and (3.24) - (3.26), one can show that:

$$\dot{\mathbf{f}} = \frac{\partial \mathbf{f}}{\partial \boldsymbol{s}_h}\dot{\boldsymbol{s}_h} + \frac{\partial \mathbf{f}}{\partial \boldsymbol{s}_{bk}}\dot{\boldsymbol{s}_{bk}} + \frac{\partial \mathbf{f}}{\partial \boldsymbol{\alpha}}\dot{\boldsymbol{\alpha}} \tag{3.36}$$

$$= \boldsymbol{n}^T \mathbf{k}_{he}\dot{\boldsymbol{e}_h} - \left[\boldsymbol{n}^T (\mathbf{k}_{he} + \mathbf{H}_{hk})\, \boldsymbol{n} + \mathbf{H}_{hi}\right] \boldsymbol{\gamma} \tag{3.37}$$

Therefore,

$$\dot{\mathbf{f}} = \mathbf{0} \quad \Rightarrow \quad \boldsymbol{\gamma} = \left[\boldsymbol{n}^T (\mathbf{k}_{he} + \mathbf{H}_{hk})\, \boldsymbol{n} + \mathbf{H}_{hi}\right]^{-1} \boldsymbol{n}^T \mathbf{k}_{he}\dot{\boldsymbol{e}_h} \tag{3.38}$$

Additionally, using Equations (3.16), (3.24) and (3.38) to conclude that

$$\dot{\boldsymbol{s}_h} = \mathbf{k}_{he} (\dot{\boldsymbol{e}_h} - \dot{\boldsymbol{e}_{hp}}) \tag{3.39}$$

$$= \left\{\mathbf{k}_{he} - \mathbf{k}_{he}\boldsymbol{n} \left[\boldsymbol{n}^T (\mathbf{k}_{he} + \mathbf{H}_{hk})\, \boldsymbol{n} + \mathbf{H}_{hi}\right]^{-1} \boldsymbol{n}^T \mathbf{k}_{he}\right\} \dot{\boldsymbol{e}_h} \tag{3.40}$$

the hinge elastoplastic tangent modulus can be identified as:

$$\mathbf{k}_h := \frac{d\boldsymbol{s}_h}{d\boldsymbol{e}_h} = \mathbf{k}_{he} - \mathbf{k}_{he}\boldsymbol{n} \left[\boldsymbol{n}^T (\mathbf{k}_{he} + \mathbf{H}_{hk})\, \boldsymbol{n} + \mathbf{H}_{hi}\right]^{-1} \boldsymbol{n}^T \mathbf{k}_{he} \tag{3.41}$$

Rearranging the terms in Equations (3.39) - (3.41), it is possible to rewrite $\dot{\boldsymbol{s}_h}$ as:

$$\dot{\boldsymbol{s}_h} = \mathbf{k}_{he} (\dot{\boldsymbol{e}_h} - \dot{\boldsymbol{e}_{hp}}) = \mathbf{k}_h \dot{\boldsymbol{e}_h} \quad \Rightarrow \quad \dot{\boldsymbol{e}_h} = (\mathbf{k}_{he} - \mathbf{k}_h)^{-1} \mathbf{k}_{he}\dot{\boldsymbol{e}_{hp}} \tag{3.42}$$

$$\Rightarrow \quad \dot{\boldsymbol{s}_h} = \left\{\mathbf{k}_{he} (\mathbf{k}_{he} - \mathbf{k}_h)^{-1} \mathbf{k}_{he} - \mathbf{k}_{he}\right\} \dot{\boldsymbol{e}_{hp}} \tag{3.43}$$

allowing to identify the hinge plastic modulus $\mathbf{k}_{ph}$ as:

$$\mathbf{k}_{ph} = \mathbf{k}_{he} (\mathbf{k}_{he} - \mathbf{k}_h)^{-1} \mathbf{k}_{he} - \mathbf{k}_{he} \tag{3.44}$$

Lastly, combining Equations (3.41) with (3.44) and noting that $\boldsymbol{n}$ is a 2x2 nonsingular matrix, the following expression is obtained for $\mathbf{k}_{ph}$:

$$\mathbf{k}_{ph} = \mathbf{k}_{he} \left(\mathbf{k}_{he}\boldsymbol{n} \left[\boldsymbol{n}^T (\mathbf{k}_{he} + \mathbf{H}_{hk})\, \boldsymbol{n} + \mathbf{H}_{hi}\right]^{-1} \boldsymbol{n}^T \mathbf{k}_{he}\right)^{-1} \mathbf{k}_{he} - \mathbf{k}_{he} \tag{3.45}$$

$$= \left(\boldsymbol{n} \left[\boldsymbol{n}^T (\mathbf{k}_{he} + \mathbf{H}_{hk})\, \boldsymbol{n} + \mathbf{H}_{hi}\right]^{-1} \boldsymbol{n}^T\right)^{-1} - \mathbf{k}_{he} \tag{3.46}$$

$$= \boldsymbol{n}^{-T} \left[\boldsymbol{n}^T (\mathbf{k}_{he} + \mathbf{H}_{hk})\, \boldsymbol{n} + \mathbf{H}_{hi}\right] \boldsymbol{n}^{-1} - \mathbf{k}_{he} \tag{3.47}$$

$$= \mathbf{H}_{hk} + \boldsymbol{n}^{-T}\mathbf{H}_{hi}\boldsymbol{n}^{-1} \tag{3.48}$$

Separating the effects of kinematic and isotropic hardening and equating the terms in Equations (3.34) and (3.48) one by one, the matrices $\mathbf{H}_{hk}$, $\mathbf{H}_{hi}$, $\mathbf{H}_k$ and $\mathbf{H}_i$ must satisfy the following relations:

$$\mathbf{H}_{hk} = \mathbf{b}_h \mathbf{H}_k \mathbf{b}_h^T \tag{3.49}$$

$$\boldsymbol{n}^{-T} \mathbf{H}_{hi} \boldsymbol{n}^{-1} = \mathbf{b}_h \mathbf{H}_i \mathbf{b}_h^T \tag{3.50}$$

Equation (3.49) explicitly expresses $\mathbf{H}_{hk}$ as a function of $\mathbf{H}_k$, offering a straightforward way to adjust the hinge kinematic hardening parameters to the desired element end kinematic hardening parameters. The same does not hold for the isotropic hardening behavior because of the presence of the normal $\boldsymbol{n}$ in Equation (3.50) that is not necessarily known in advance and is potentially changing throughout the analysis. However, given the simple expression of $\boldsymbol{n}$ in Equation (3.28), the normal can only take the following form:

- if $\text{sgn}(M_{hi} - M_{bk,i}) = \text{sgn}(M_{hj} - M_{bk,j})$, which is typically the case for single curvature bending, the normal $\boldsymbol{n}$ is equal to:

$$\boldsymbol{n} = \pm \boldsymbol{n}_{SC} \quad \text{where} \quad \boldsymbol{n}_{SC} = \mathbf{I} = \begin{bmatrix} 1 & 0 \\ 0 & 1 \end{bmatrix} \tag{3.51}$$

- if $\text{sgn}(M_{hi} - M_{bk,i}) = -\text{sgn}(M_{hj} - M_{bk,j})$, which is typically the case for double curvature bending, the normal $\boldsymbol{n}$ is equal to:

$$\boldsymbol{n} = \pm \boldsymbol{n}_{DC} \quad \text{where} \quad \boldsymbol{n}_{DC} = \begin{bmatrix} 1 & 0 \\ 0 & -1 \end{bmatrix} \tag{3.52}$$

Therefore, depending on the expected moment distribution, $\mathbf{H}_{hi}$ should be set equal to:

$$\mathbf{H}_{hi} = \begin{cases} \boldsymbol{n}_{SC}^T \mathbf{b}_h \mathbf{H}_i \mathbf{b}_h^T \boldsymbol{n}_{SC} & \text{for single curvature bending} \\ \boldsymbol{n}_{DC}^T \mathbf{b}_h \mathbf{H}_i \mathbf{b}_h^T \boldsymbol{n}_{DC} & \text{for double curvature bending} \end{cases} \tag{3.53}$$

When modeling beam elements as part of multistory frames, and in the absence of additional information, it is reasonable to assume that most beams will undergo double curvature bending and to therefore set $\mathbf{H}_{hi}$ to be equal to the second expression in Equation (3.53). This approach is chosen as the default here.

Lastly, for calibration purposes, the matrices $\mathbf{H}_k$ and $\mathbf{H}_i$ that characterize the hardening response at the element ends can be expressed as a function of hardening ratio matrices $\mathbf{H}_{kr}$ and $\mathbf{H}_{ir}$ which are introduced in the following way:

$$\mathbf{H}_k = \frac{6EI}{L} \mathbf{H}_{kr} \quad ; \quad \mathbf{H}_i = \frac{6EI}{L} \mathbf{H}_{ir} \tag{3.54}$$

$$\mathbf{H}_{kr} = \begin{bmatrix} H_{kr,i} & 0 \\ 0 & H_{kr,j} \end{bmatrix} \quad ; \quad \mathbf{H}_{ir} = \begin{bmatrix} H_{ir,i} & 0 \\ 0 & H_{ir,j} \end{bmatrix} \tag{3.55}$$

where $\dfrac{6EI}{L}$ is the linear elastic slope in the element end flexural response $q_i - v_i$ or $q_j - v_j$ for a frame element under antisymmetric bending, taken as a reference.

### 3.3.2 Summary of beam formulation with resultant force plasticity

Table 3.1 summarizes the formulation of the resultant plasticity beam model.

Table 3.2 summarizes the dimension of the various variables and parameters of the proposed resultant plasticity beam model.

## 3.4 Implementation

### 3.4.1 State determination with return-mapping algorithm

The beam element state determination is the process of determining the element basic forces $\boldsymbol{q}$ under given element deformations $\boldsymbol{v}$ at a certain instant in time of the analysis. Here, the focus is on determining the flexural forces $\boldsymbol{q}_f$ for given flexural deformations $\boldsymbol{v}_f$, as the axial response is determined separately according to Equation (3.3).

First, the time or pseudo-time interval of interest is discretized into a finite number of smaller intervals $\bigcup_n [t_n, t_{n+1}]$. For a typical time step $[t_n, t_{n+1}]$, the problem can be posed as follows:

1. The state of the element at time $t_n$ characterized by the basic state variables

$$\{\boldsymbol{v}_{f,n}, \boldsymbol{e}_{hp,n}, \boldsymbol{s}_{bk,n}, \boldsymbol{\alpha}_n\} = \{\boldsymbol{v}_f(t_n), \boldsymbol{e}_{hp}(t_n), \boldsymbol{s}_{bk}(t_n), \boldsymbol{\alpha}(t_n)\} \tag{3.56}$$

   is regarded as given and assumed to be equilibrated.

2. The element deformations increment

$$\Delta\boldsymbol{v}_{f,n+1} = \boldsymbol{v}_{f,n+1} - \boldsymbol{v}_{f,n} = \boldsymbol{v}_f(t_{n+1}) - \boldsymbol{v}_f(t_n) \tag{3.57}$$

   is considered given.

3. The objective is to update the state variables to the values $\{\boldsymbol{v}_{f,n+1}, \boldsymbol{e}_{hp,n+1}, \boldsymbol{s}_{bk,n+1}, \boldsymbol{\alpha}_{n+1}\}$ at time $t_{n+1}$, so as to be able to calculate the corresponding flexural basic forces $\boldsymbol{q}_{f,n+1}$, in a way that is consistent with the resultant plasticity beam formulation.

Note that knowing the basic state variables $\{\boldsymbol{v}_{f,n}, \boldsymbol{e}_{hp,n}, \boldsymbol{s}_{bk,n}, \boldsymbol{\alpha}_n\}$ at time $t_n$ fully determines the element plastic flexural deformtions $\boldsymbol{v}_{p,n}$, the element flexural basic forces $\boldsymbol{q}_{f,n}$ as well as the plastic hinge moments $\boldsymbol{s}_{h,n}$ at that instant, with the following relations:

$$\boldsymbol{v}_{p,n} = \mathbf{b}_h^T \boldsymbol{e}_{hp,n} \tag{3.58}$$

$$\boldsymbol{q}_{f,n} = \mathbf{k}_{fe}(\boldsymbol{v}_{f,n} - \boldsymbol{v}_{p,n}) \tag{3.59}$$

$$\boldsymbol{s}_{h,n} = \mathbf{b}_h \boldsymbol{q}_{f,n} \tag{3.60}$$

1. **Elastic constitutive relation**

$$\boldsymbol{s}_h = \mathbf{k}_{he}\left(\boldsymbol{e}_h - \boldsymbol{e}_{hp}\right)$$

where $\boldsymbol{s}_h$, $\boldsymbol{e}_h$, $\boldsymbol{e}_{hp}$ and $\mathbf{k}_{he}$ are given by Equations (3.10), (3.12), (3.13) and (3.17)

2. **Yield condition**

$$\mathbf{f}\left(\boldsymbol{s}_h, \boldsymbol{s}_{bk}, \boldsymbol{\alpha}\right) = \boldsymbol{\phi}\left(\boldsymbol{s}_h - \boldsymbol{s}_{bk}\right) - \left(\boldsymbol{M}_p + \mathbf{H}_{hi}\boldsymbol{\alpha}\right)$$

where $\boldsymbol{\phi}$ is given by Equation (3.20)

3. **Flow rule**

$$\dot{\boldsymbol{e}_{hp}} = \left(\frac{\partial \mathbf{f}}{\partial \boldsymbol{s}_h}\right)^T \boldsymbol{\gamma} = \boldsymbol{n}\boldsymbol{\gamma}$$

where $\boldsymbol{n}$ is given by Equation (3.28).

4. **Kinematic and isotropic hardening laws**

$$\dot{\boldsymbol{s}_{bk}} = \mathbf{H}_{hk}\dot{\boldsymbol{e}_{hp}} = \mathbf{H}_{hk}\boldsymbol{n}\boldsymbol{\gamma}$$

$$\dot{\boldsymbol{\alpha}} = -\frac{\partial \mathbf{f}}{\partial\left(\mathbf{H}_{hi}\boldsymbol{\alpha}\right)}\boldsymbol{\gamma} = \boldsymbol{\gamma}$$

5. **Kuhn-Tucker complementarity conditions**

$$\boldsymbol{\gamma} \geq \mathbf{0}\ ,\ \mathbf{f}(\boldsymbol{s}_h, \boldsymbol{s}_{bk}, \boldsymbol{\alpha}) \leq \mathbf{0}\ ,\ \gamma_m f_m(\boldsymbol{s}_h, \boldsymbol{s}_{bk}, \boldsymbol{\alpha}) = 0\ ,\ m = i, j$$

6. **Consistency conditions**

$$\gamma_m \dot{f}_m(\boldsymbol{s}_h, \boldsymbol{s}_{bk}, \boldsymbol{\alpha}) = 0 \quad (\text{if } f_m(\boldsymbol{s}_h, \boldsymbol{s}_{bk}, \boldsymbol{\alpha}) = 0)\ ,\ m = i, j$$

Table 3.1: Resultant plasticity beam model formulation

| Variable/parameter | Dimension |
|---|---|
| $v_a$ | length |
| $v_{i/j}$, $v_{i/j,e/p}$ | 1 (rotation) |
| $\theta_{h,i/j}$, $\theta_{hp,i/j}$ | 1 (rotation) |
| $\alpha_{i/j}$, $\gamma_{i/j}$ | 1 |
| $q_a$ | force |
| $q_{i/j}$ | force · length |
| $N_{hi/j}$, $N_{bk,i/j}$, $N_{pi/pj}$ | force |
| $M_{h,i/j}$, $M_{bk,i/j}$, $M_{pi/pj}$ | force · length |
| $H_{kr,i/j}$, $H_{ir,i/j}$ | 1 |

Table 3.2: Dimensions of resultant plasticity beam model variables and parameters

For performing the element state determination at time $\boldsymbol{t}_{n+1}$, the discrete algorithmic counterparts of the flow rule and the hardening rules are obtained by applying the implicit backward Euler difference scheme. This gives:

$$\boldsymbol{e}_{hp,n+1} = \boldsymbol{e}_{hp,n} + \boldsymbol{n}_{n+1}\Delta\boldsymbol{\gamma} \tag{3.61}$$

$$\boldsymbol{s}_{bk,n+1} = \boldsymbol{s}_{bk,n} + \mathbf{H}_{hk}\boldsymbol{n}_{n+1}\Delta\boldsymbol{\gamma} \tag{3.62}$$

$$\boldsymbol{\alpha}_{n+1} = \boldsymbol{\alpha}_n + \Delta\boldsymbol{\gamma} \tag{3.63}$$

where $\Delta\boldsymbol{\gamma} = \Delta t_{n+1}\boldsymbol{\gamma}_{n+1} \geq \mathbf{0}$ is the algorithmic counterpart of the vector of consistency parameters $\boldsymbol{\gamma}$. The normal $\boldsymbol{n}_{n+1}$ is computed as

$$\boldsymbol{n}_{n+1} = \left[\frac{\partial \mathbf{f}}{\partial \boldsymbol{s}_h}(\boldsymbol{s}_{h,n+1}, \boldsymbol{s}_{bk,n+1})\right]^T \tag{3.64}$$

where $\boldsymbol{s}_{h,n+1}$ is obtained as

$$\boldsymbol{v}_{f,n+1} = \boldsymbol{v}_{f,n} + \Delta\boldsymbol{v}_{f,n+1} \tag{3.65}$$

$$\boldsymbol{v}_{p,n+1} = \mathbf{b}_h^T\boldsymbol{e}_{hp,n+1} \tag{3.66}$$

$$\boldsymbol{q}_{f,n+1} = \mathbf{k}_{fe}(\boldsymbol{v}_{f,n+1} - \boldsymbol{v}_{p,n+1}) \tag{3.67}$$

$$\boldsymbol{s}_{h,n+1} = \mathbf{b}_h\boldsymbol{q}_{f,n+1} \tag{3.68}$$

Additionally, the variables $(\boldsymbol{s}_{h,n+1}, \boldsymbol{s}_{bk,n+1}, \boldsymbol{\alpha}_{n+1})$ are constrained by the following discrete version of the Kuhn-Tucker conditions:

$$\begin{cases} \Delta\boldsymbol{\gamma} \geq \mathbf{0}\ ,\ \mathbf{f}_{n+1} = \mathbf{f}(\boldsymbol{s}_{h,n+1}, \boldsymbol{s}_{bk,n+1}, \boldsymbol{\alpha}_{n+1}) \leq \mathbf{0}, \\ \text{and} \\ \Delta\gamma_m f_{m,n+1} = 0\ ,\ m = i, j \end{cases} \tag{3.69}$$

The problem described by Equations (3.61) - (3.69) is solved using a two step return-mapping algorithm that consists of:

1. an elastic *trial* predictor, followed by
2. a plastic corrector that performs the closest point projection of the trial state onto the yield surface.

#### 3.4.1.1 Elastic predictor

The following trial elastic state is introduced by freezing the plastic flow during the given time step, i.e. setting $\Delta\boldsymbol{\gamma} = \mathbf{0}$ in Equations (3.61) - (3.63):

$$\boldsymbol{e}^{tr}_{hp,n+1} = \boldsymbol{e}_{hp,n} \tag{3.70}$$

$$\boldsymbol{s}^{tr}_{bk,n+1} = \boldsymbol{s}_{bk,n} \tag{3.71}$$

$$\boldsymbol{\alpha}^{tr}_{n+1} = \boldsymbol{\alpha}_{n} \tag{3.72}$$

This gives rise to the following trial elastic element plastic deformations, basic forces and hinge internal forces:

$$\boldsymbol{v}^{tr}_{p,n+1} = \mathbf{b}_h^T \boldsymbol{e}^{tr}_{hp,n+1} = \boldsymbol{v}_{p,n} \tag{3.73}$$

$$\boldsymbol{q}^{tr}_{f,n+1} = \mathbf{k}_{fe}\left(\boldsymbol{v}_{f,n+1} - \boldsymbol{v}^{tr}_{p,n+1}\right) = \mathbf{k}_{fe}\left(\boldsymbol{v}_{f,n+1} - \boldsymbol{v}_{p,n}\right) \tag{3.74}$$

$$\boldsymbol{s}^{tr}_{h,n+1} = \mathbf{b}_h \boldsymbol{q}^{tr}_{f,n+1} = \mathbf{k}_{he}\left(\boldsymbol{e}_{h,n+1} - \boldsymbol{e}_{hp,n}\right) \tag{3.75}$$

and the corresponding trial normal to the yield function:

$$\boldsymbol{n}^{tr}_{n+1} = \left[\frac{\partial \mathbf{f}}{\partial \boldsymbol{s}_h}(\boldsymbol{s}^{tr}_{h,n+1}, \boldsymbol{s}^{tr}_{bk,n+1})\right]^T \tag{3.76}$$

Note that this trial state may not, and in general will not, correspond to any actual, physically admissible state unless the incremental process is actually elastic. The trial yield function is then evaluated as:

$$\mathbf{f}^{tr}_{n+1} = \mathbf{f}(\boldsymbol{s}^{tr}_{h,n+1}, \boldsymbol{s}^{tr}_{bk,n+1}, \boldsymbol{\alpha}^{tr}_{n+1}) \tag{3.77}$$

If $\mathbf{f}^{tr}_{n+1} \leq \mathbf{0}$, i.e if both $f^{tr}_{i,n+1} \leq 0$ and $f^{tr}_{j,n+1} \leq 0$, the trial state is admissible and the element response is elastic. Accordingly, the state variables are equal to their trial state values, i.e.,

$$\boldsymbol{e}_{hp,n+1} = \boldsymbol{e}^{tr}_{hp,n+1} \tag{3.78}$$

$$\boldsymbol{s}_{bk,n+1} = \boldsymbol{s}^{tr}_{bk,n+1} \tag{3.79}$$

$$\boldsymbol{\alpha}_{n+1} = \boldsymbol{\alpha}^{tr}_{n+1} \tag{3.80}$$

the flexural basic forces at the end of the time step $t_{n+1}$ are set to

$$\boldsymbol{q}_{f,n+1} = \boldsymbol{q}^{tr}_{f,n+1} \tag{3.81}$$

and the element tangent stiffness is computed according to Section 3.4.2, concluding the element state determination.

On the other hand, if $f^{tr}_{i,n+1} > 0$ or $f^{tr}_{j,n+1} > 0$, the trial state is not admissible and a plastic correction is required.

#### 3.4.1.2 Plastic corrector

If $f^{tr}_{i,n+1} > 0$ or $f^{tr}_{j,n+1} > 0$, a correction is needed to enforce the Kuhn-Tucker conditions. Since the original assumption $\Delta\boldsymbol{\gamma} = \mathbf{0}$ results in a non admissible trial state, it follows that the true plastic flow $\Delta\boldsymbol{\gamma}$ must be nonzero, i.e. $\Delta\gamma_i > 0$ and/or $\Delta\gamma_j > 0$. Combining this requirement with conditions (3.69) implies that

$$f_{i,n+1} = 0 \text{ and/or } f_{j,n+1} = 0 \tag{3.82}$$

i.e. the corrected state at $t_{n+1}$ must lie on the yield surface. When $\Delta\gamma_i > 0$, the yield surface near end $i$ is said to be *active*, whereas the yield surface near end $j$ is said to be active when $\Delta\gamma_j > 0$. To identify which of $i$ and $j$ yield surfaces is active, i.e. the algorithm uses a two-step process.

1. First, assume that both yield surfaces are active, i.e. $\Delta\gamma_i > 0$ and $\Delta\gamma_j > 0$. In that case, $f_{i,n+1} = 0$ and $f_{j,n+1} = 0$ i.e. $\mathbf{f}_{n+1} = \mathbf{0}$. After combining Equations (3.61) - (3.68) with Equations (3.70) - (3.75), one obtains:

$$\boldsymbol{s}_{h,n+1} = \boldsymbol{s}^{tr}_{h,n+1} - \mathbf{k}_{he}\boldsymbol{n}_{n+1}\Delta\boldsymbol{\gamma} \tag{3.83}$$

$$\boldsymbol{s}_{bk,n+1} = \boldsymbol{s}^{tr}_{bk,n+1} + \mathbf{H}_{hk}\boldsymbol{n}_{n+1}\Delta\boldsymbol{\gamma} \tag{3.84}$$

$$\boldsymbol{\alpha}_{n+1} = \boldsymbol{\alpha}^{tr}_{n+1} + \Delta\boldsymbol{\gamma} \tag{3.85}$$

   On account of Equations (3.35) and (3.83) - (3.85), one can then show that

$$\mathbf{f}_{n+1} = \mathbf{f}^{tr}_{n+1} - \left[\boldsymbol{n}^T_{n+1}\left(\mathbf{k}_{he} + \mathbf{H}_{hk}\right)\boldsymbol{n}_{n+1} + \mathbf{H}_{hi}\right]\Delta\boldsymbol{\gamma} \tag{3.86}$$

   Therefore, evaluate trial vector of consistency parameters $\Delta\boldsymbol{\gamma}^{tr}$ as:

$$\mathbf{f}_{n+1} = \mathbf{0} \quad \Rightarrow \quad \Delta\boldsymbol{\gamma}^{tr} = \left[\boldsymbol{n}^T_{n+1}\left(\mathbf{k}_{he} + \mathbf{H}_{hk}\right)\boldsymbol{n}_{n+1} + \mathbf{H}_{hi}\right]^{-1}\mathbf{f}^{tr}_{n+1} \tag{3.87}$$

2. Then, enforce the discrete Kuhn-Tucker conditions (3.69):

   - If both $\Delta\gamma^{tr}_i > 0$ and $\Delta\gamma^{tr}_j > 0$, remembering that $\mathbf{f}_{n+1} = \mathbf{0}$, the Kuhn-Tucker conditions are satisfied. The two yield surfaces are indeed active and the solution has been found. Set

$$\Delta\boldsymbol{\gamma} = \Delta\boldsymbol{\gamma}^{tr} \tag{3.88}$$

- Otherwise, only one yield surface is active, which can be identified by the index

$$\boldsymbol{J}_{act} = \{m \in \{i,j\} \mid \Delta\gamma_m^{tr} > 0\} \tag{3.89}$$

The consistency parameter corresponding to the inactive yield surface is set to 0, i.e.,

$$\Delta\gamma_m = 0, \quad m \in \{i,j\} \setminus \boldsymbol{J}_{act}, \tag{3.90}$$

whereas the active consistency parameter is obtained from the scalar condition:

$$f_{m,n+1} = 0, \quad m \in \boldsymbol{J}_{act} \tag{3.91}$$

Following the same reasoning as above and on account of Equation (3.90), this condition can be shown to be equivalent to:

$$f_{m,n+1} = f_{m,n+1}^{tr} - \left[\boldsymbol{n}_{a,n+1}^T \left(\mathbf{k}_{he} + \mathbf{H}_{hk}\right) \boldsymbol{n}_{a,n+1} + H_{hi,a}\right] \Delta\gamma_m = 0 \tag{3.92}$$

for $m \in \boldsymbol{J}_{act}$, where

$$\boldsymbol{n}_{a,n+1} = \boldsymbol{n}_{m,n+1}, \quad m \in \boldsymbol{J}_{act} \tag{3.93}$$

$$H_{hi,a} = \mathbf{H}_{hi}(m,m), \quad m \in \boldsymbol{J}_{act} \tag{3.94}$$

Therefore, set

$$\Delta\gamma_m = \left[\boldsymbol{n}_{a,n+1}^T \left(\mathbf{k}_{he} + \mathbf{H}_{hk}\right) \boldsymbol{n}_{a,n+1} + H_{hi,a}\right]^{-1} f_{m,n+1}^{tr}, \quad m \in \boldsymbol{J}_{act} \tag{3.95}$$

Following the determination of the vector of consistency parameters, the history variables can be corrected according to

$$\boldsymbol{e}_{hp,n+1} = \boldsymbol{e}_{hp,n+1}^{tr} + \boldsymbol{n}_{n+1}\Delta\boldsymbol{\gamma} \tag{3.96}$$

$$\boldsymbol{s}_{bk,n+1} = \boldsymbol{s}_{bk,n+1}^{tr} + \mathbf{H}_{hk}\boldsymbol{n}_{n+1}\Delta\boldsymbol{\gamma} \tag{3.97}$$

$$\boldsymbol{\alpha}_{n+1} = \boldsymbol{\alpha}_{n+1}^{tr} + \Delta\boldsymbol{\gamma} \tag{3.98}$$

The corresponding flexural basic forces at the end of the time step $t_{n+1}$ are set to

$$\boldsymbol{v}_{p,n+1} = \mathbf{b}_h^T \boldsymbol{e}_{hp,n+1} \tag{3.99}$$

$$\boldsymbol{q}_{f,n+1} = \mathbf{k}_{fe}(\boldsymbol{v}_{f,n+1} - \boldsymbol{v}_{p,n+1}) \tag{3.100}$$

and the element tangent stiffness is assembled according to Section 3.4.2, concluding the element state determination.

### 3.4.2 Element tangent stiffness

The element tangent stiffness at time $t_{n+1}$ is defined as

$$\mathbf{k}_{n+1} = \frac{d\boldsymbol{q}_{n+1}}{d\boldsymbol{v}_{n+1}} \tag{3.101}$$

Because of the assumption of linear elastic axial behavior that is uncoupled from the flexural behavior, and on account of

$$\boldsymbol{q} = \begin{pmatrix} q_a \\ \boldsymbol{q}_f \end{pmatrix} \quad \text{and} \quad \boldsymbol{v} = \begin{pmatrix} v_a \\ \boldsymbol{v}_f \end{pmatrix} \tag{3.102}$$

the tangent stiffness can be divided into two blocks

$$\mathbf{k}_{n+1} = \begin{bmatrix} k_a & \mathbf{0} \\ \mathbf{0} & \mathbf{k}_{f,n+1} \end{bmatrix} \tag{3.103}$$

where

$$k_a = \frac{dq_{a,n+1}}{dv_{a,n+1}} = \frac{EA}{L} \tag{3.104}$$

$$\mathbf{k}_{f,n+1} = \frac{d\boldsymbol{q}_{f,n+1}}{d\boldsymbol{v}_{f,n+1}} \tag{3.105}$$

The objective is to obtain $\mathbf{k}_{f,n+1}$ in a way that is consistent with the backward-Euler integration algorithm, also referred to as the consistent (algorithmic) tangent flexural stiffness.

If the step is elastic, i.e. if the trial state is admissible, the tangent flexural stiffness is set equal to the elastic flexural stiffness:

$$\mathbf{k}_{f,n+1} = \frac{d\boldsymbol{q}_{f,n+1}}{d\boldsymbol{v}_{f,n+1}} = \mathbf{k}_{fe} \tag{3.106}$$

If the trial state is not admissible, the element tangent stiffness is updated after the plastic correction procedure. Differentiating (3.100) gives the following equation:

$$d\boldsymbol{q}_{f,n+1} = \mathbf{k}_{fe}(d\boldsymbol{v}_{f,n+1} - d\boldsymbol{v}_{p,n+1}) \tag{3.107}$$

First, consider the case when both plastic hinges are active, i.e. when $\Delta\gamma_i > 0$ and $\Delta\gamma_j > 0$. In this case, $\Delta\boldsymbol{\gamma}$ is given by Equation (3.88). Differentiating the expression in Equation (3.87) under fixed variables at time $t_n$, one can show that

$$d\Delta\boldsymbol{\gamma} = \left[\boldsymbol{n}_{n+1}^T \left(\mathbf{k}_{he} + \mathbf{H}_{hk}\right) \boldsymbol{n}_{n+1} + \mathbf{H}_{hi}\right]^{-1} d\mathbf{f}_{n+1}^{tr} \tag{3.108}$$

with

$$d\mathbf{f}_{n+1}^{tr} = \boldsymbol{n}_{n+1}^T d\boldsymbol{s}_{h,n+1}^{tr} = \boldsymbol{n}_{n+1}^T \mathbf{b}_h \mathbf{k}_{fe} d\boldsymbol{v}_{f,n+1} \tag{3.109}$$

Additionally, differentiating Equations (3.96) and (3.99), one obtains:

$$d\boldsymbol{v}_{p,n+1} = \mathbf{b}_h^T \boldsymbol{n}_{n+1} d\Delta\boldsymbol{\gamma} \tag{3.110}$$

Combining Equations (3.107), (3.108), (3.109) and (3.110), the following expression is derived:

$$d\boldsymbol{q}_{f,n+1} = \left\{ \mathbf{k}_{fe} - \mathbf{k}_{fe}\mathbf{b}_h^T \boldsymbol{n}_{n+1} \left[ \boldsymbol{n}_{n+1}^T \left( \mathbf{k}_{he} + \mathbf{H}_{hk} \right) \boldsymbol{n}_{n+1} + \mathbf{H}_{hi} \right]^{-1} \boldsymbol{n}_{n+1}^T \mathbf{b}_h \mathbf{k}_{fe} \right\} d\boldsymbol{v}_{f,n+1} \tag{3.111}$$

allowing to identify the tangent flexural stiffness as

$$\mathbf{k}_{f,n+1} = \mathbf{k}_{fe} - \mathbf{k}_{fe}\mathbf{b}_h^T \boldsymbol{n}_{n+1} \left[ \boldsymbol{n}_{n+1}^T \left( \mathbf{k}_{he} + \mathbf{H}_{hk} \right) \boldsymbol{n}_{n+1} + \mathbf{H}_{hi} \right]^{-1} \boldsymbol{n}_{n+1}^T \mathbf{b}_h \mathbf{k}_{fe} \tag{3.112}$$

Considering now the case when only one plastic hinge is active. Following an almost identical procedure, one can show that the tangent flexural stiffness is given by:

$$\mathbf{k}_{f,n+1} = \mathbf{k}_{fe} - \mathbf{k}_{fe}\mathbf{b}_h^T \boldsymbol{n}_{a,n+1} \left[ \boldsymbol{n}_{a,n+1}^T \left( \mathbf{k}_{he} + \mathbf{H}_{hk} \right) \boldsymbol{n}_{a,n+1} + H_{hi,a} \right]^{-1} \boldsymbol{n}_{a,n+1}^T \mathbf{b}_h \mathbf{k}_{fe} \tag{3.113}$$

where $\boldsymbol{n}_{a,n+1}$ and $H_{hi,a}$ are given by Equations (3.93) and (3.94), respectively.

The complete element stiffness is assembled according to Equation (3.103) where $\mathbf{k}_{f,n+1}$ is given either by Equation (3.112) or (3.113).

### 3.4.3 Summary of state determination algorithm

The state determination algorithm for the resultant plasticity beam element model is summarized in Table 3.3.

## 3.5 Calibration of hardening and hinge offset parameters

The objective is to calibrate the hardening and hinge offset parameters of the resultant plasticity beam model under the assumption of linear material hardening behavior. The calibration is performed for the case of a simply supported homogeneous prismatic beam subjected to antisymmetric bending. Accordingly, the imposed flexural end deformations are such that $v_i = v_j$, as illustrated in Figure 3.5.

The reference model is taken as a distributed plasticity beam-column element with fiber section discretization. It is assumed to use a sufficient number of monitoring sections to capture the spread of plasticity during the hardening phase. The material fibers are assigned the Simo and Hughes inelastic linear-plastic 1d model with the return map algorithm [73]. The material model accounts for kinematic and isotropic hardening through the consideration of two modulii, $H_{k,m}$, and $H_{i,m}$, defined as:

$$H_{k,m} = H_{kr,m} E \tag{3.114}$$

$$H_{i,m} = H_{ir,m} E \tag{3.115}$$

**Objective:** Given $\boldsymbol{v}_n$, $\boldsymbol{e}_{hp,n}$, $\boldsymbol{s}_{bk,n}$, $\boldsymbol{\alpha}_n$ at time $t_n$ and $\boldsymbol{v}_{n+1}$ at time $t_{n+1}$, evaluate $\boldsymbol{e}_{hp,n+1}$, $\boldsymbol{s}_{bk,n+1}$, $\boldsymbol{\alpha}_{n+1}$, $\boldsymbol{q}_{n+1}$ and $\mathbf{k}_{n+1}$ at time $t_{n+1}$.

1. **Compute trial flexural elastic state:**

   Evaluate $\boldsymbol{e}^{tr}_{hp,n+1}$, $\boldsymbol{s}^{tr}_{bk,n+1}$, $\boldsymbol{\alpha}^{tr}_{n+1}$, $\boldsymbol{q}^{tr}_{f,n+1}$ and $\boldsymbol{s}^{tr}_{h,n+1}$ in Equations (3.70)-(3.75)

2. **Check yield condition:**

   Evaluate $\mathbf{f}^{tr}_{n+1} = \mathbf{f}(\boldsymbol{s}^{tr}_{h,n+1}, \boldsymbol{s}^{tr}_{bk,n+1}, \boldsymbol{\alpha}^{tr}_{n+1})$ where $\mathbf{f}$ is given by Equation (3.19)
   IF: $\mathbf{f}^{tr}_{n+1} < \mathbf{0}$, THEN:

   a) Set $(\cdot)_{n+1} = (\cdot)^{tr}_{n+1}$

   b) Set $\mathbf{k}_{f,n+1} = \mathbf{k}_{fe}$ and Go to 4

   ELSE: Go to 3

3. **Perform plastic correction with closest point projection algorithm:**

   a) Evaluate trial vector of consistency parameters $\Delta\boldsymbol{\gamma}^{tr}$ in Equation (3.87)
   IF: $\Delta\boldsymbol{\gamma}^{tr} \geq \mathbf{0}$, THEN:
   Set $\Delta\boldsymbol{\gamma} = \Delta\boldsymbol{\gamma}^{tr}$ and Go to 3b
   ELSE:
   i. Set $\boldsymbol{J}_{act} = \{m \in \{i, j\} \mid \Delta\gamma^{tr}_m > 0\}$
   ii. Evaluate $\Delta\boldsymbol{\gamma}$ according to Equations (3.90) and (3.95)

   b) Evaluate $\boldsymbol{e}_{hp,n+1}$, $\boldsymbol{s}_{bk,n+1}$, $\boldsymbol{\alpha}_{n+1}$ and $\boldsymbol{q}_{f,n+1}$ in Equations (3.96)-(3.100)

   c) Evaluate tangent flexural stiffness
   IF: $\Delta\boldsymbol{\gamma}^{tr} \geq \mathbf{0}$, THEN:
   Evaluate $\mathbf{k}_{f,n+1}$ in Equation (3.112)
   ELSE:
   Evaluate $\mathbf{k}_{f,n+1}$ in Equation (3.113)

4. **Assemble linear elastic axial response with flexural response:**

   a) Evaluate $q_{a,n+1} = \dfrac{EA}{L} v_{a,n+1}$ and $k_a = \dfrac{EA}{L}$

   b) Assemble $\boldsymbol{q}_{n+1} = \begin{pmatrix} q_{a,n+1} \\ \boldsymbol{q}_{f,n+1} \end{pmatrix}$ and $\mathbf{k}_{n+1} = \begin{bmatrix} k_a & \mathbf{0} \\ \mathbf{0} & \mathbf{k}_{f,n+1} \end{bmatrix}$

Table 3.3: Resultant plasticity beam element state determination algorithm

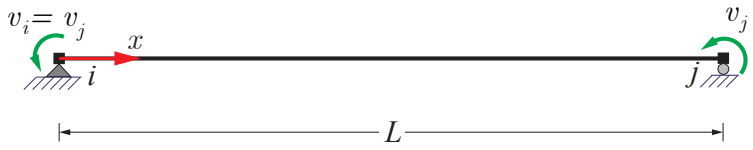


Figure 3.5: Simply supported beam under antisymmetric bending

where E is the Young modulus of the material. Accordingly, the elastoplastic tangent modulus for the hardening branch of the material stress-strain relation [73] is given by:

$$\frac{d\sigma}{d\varepsilon} = \frac{H_{r,m}}{1 + H_{r,m}} E \tag{3.116}$$

where

$$H_{r,m} = H_{kr,m} + H_{ir,m} \tag{3.117}$$

is the combined kinematic/isotropic hardening ratio of the material. The objective is to identify the components of the kinematic hardening ratio matrix $\mathbf{H}_{kr}$, of the isotropic hardening ratio matrix $\mathbf{H}_{ir}$, and the hinge offset parameters $\chi_i$ and $\chi_j$ to be used in a resultant plasticity beam model to satisfyingly match the response of the reference model.

The following quantities are assumed to be known: the Young's modulus of the material $E$, the material kinematic and isotropic hardening ratios $H_{kr,m}$ and $H_{ir,m}$, the moment of inertia of the beam about the bending axis $I$, the plastic flexural capacity $M_p = M_{pi} = M_{pj}$, and the length of the beam $L$. Because the calibration is performed under the assumption of antisymmetric bending, the following simplifications can be made:

1. The hinge offset parameters are symmetric, i.e.,

$$\chi_i = \chi_j = \chi \tag{3.118}$$

2. The hardening ratios at end $i$ and end $j$ are equal, i.e.,

$$H_{kr,i} = H_{kr,j} = H_{kr,CP} \tag{3.119}$$
$$H_{ir,i} = H_{ir,j} = H_{ir,CP} \tag{3.120}$$

where, $CP$ stands for concentrated plasticity.

Let $H_{r,CP}$ represent the combined kinematic/isotropic hardening ratio of the resultant plasticity beam model:

$$H_{r,CP} = H_{kr,CP} + H_{ir,CP} \tag{3.121}$$

Under the assumption of antisymmetric bending and in the absence of element loading, the bending moment distribution along the beam is linear with equal and opposite moments at the two ends, i.e. $M_i = -M_j$, as illustrated in Figure 3.6. Referring to this same figure,

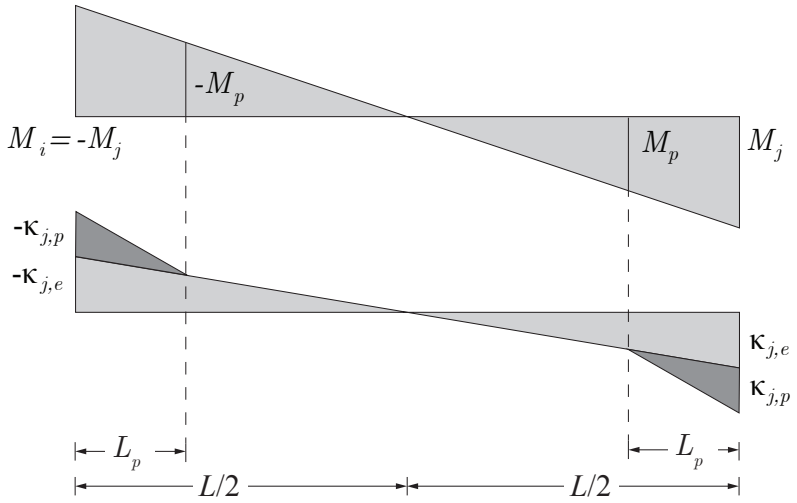


Figure 3.6: Bending moment and curvature distribution

the corresponding curvature distribution consists of an elastic and a plastic contributions. $L_p$ indicates the plastic hinge length, i.e. the portion at each end of the beam over which inelastic deformations take place, which is characterized by $|M| > M_p$ and $|\kappa_p| > 0$.

Consider a linear change of the moment distribution such that $M(x) \leftarrow M(x) + \Delta M(x)$ with

$$\Delta M(x) = \Delta M_j \left( \frac{2x}{L} - 1 \right) \quad , \quad x \in [0, L] \tag{3.122}$$

as illustrated in Figure 3.7.

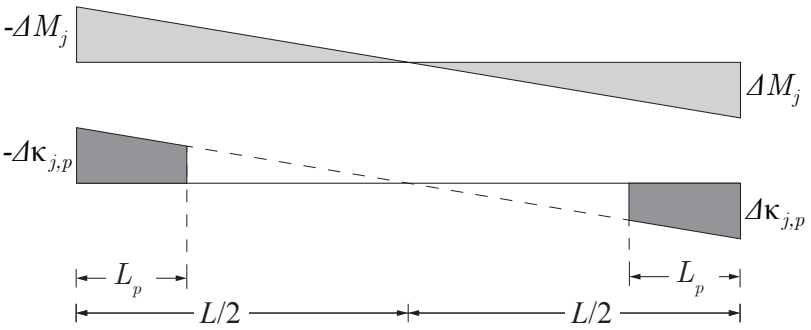


Figure 3.7: Change of bending moment and plastic curvature distribution

After integration of the material response over each cross section, it can be shown that

the change of plastic curvature distribution is given by:

$$\Delta\kappa_p(x) = \begin{cases} \Delta\kappa_{j,p}\left(\dfrac{2x}{L} - 1\right) & \text{if } x \in [0, L_p] \cup [L - L_p, L] \\ 0 & \text{otherwise} \end{cases} \tag{3.123}$$

where

$$\Delta\kappa_{j,p} = \frac{\Delta M_j}{H_{r,m} EI} \tag{3.124}$$

Integrating the plastic curvature field over the element length gives the corresponding plastic flexural deformation at end $j$ of the beam:

$$\Delta v_{j,p} = \int_0^L \left(\frac{x}{L}\right) \Delta\kappa_p(x)\, dx \tag{3.125}$$

$$= L_p \left(1 - \frac{2L_p}{L} + \frac{4L_p^2}{3L^2}\right) \frac{\Delta M_j}{H_{r,m} EI} \tag{3.126}$$

which can be rewritten as:

$$\Delta M_j = \frac{H_{r,m} EI}{L_p \left(1 - \dfrac{2L_p}{L} + \dfrac{4L_p^2}{3L^2}\right)} \Delta v_{j,p} \tag{3.127}$$

With the hardening parameters of the resultant plasticity model selected according to Section 3.3.1.5, the hardening branch of the $q_j$ - $v_{j,p}$ relation is linear with a slope equal to $H_{r,CP}\frac{6EI}{L}$, as illustrated in Figure 3.8. Consequently, the change of bending moment and change of plastic deformation at end $j$ satisfy the relation

$$\Delta M_j = \Delta q_j = (H_{k,j} + H_{i,j})\, \Delta v_{j,p} = H_{r,CP} \frac{6EI}{L} \Delta v_{j,p} \tag{3.128}$$

Combining Equations (3.127) and (3.128) and separating the effects of kinematic and isotropic hardening according to (3.117) and (3.121), the hardening ratios of the beam resultant model can be identified as:

$$H_{kr,CP} = \frac{1}{6\left(\dfrac{L_p}{L} - \dfrac{2L_p^2}{L^2} + \dfrac{4L_p^3}{3L^3}\right)} H_{kr,m} \tag{3.129}$$

$$H_{ir,CP} = \frac{1}{6\left(\dfrac{L_p}{L} - \dfrac{2L_p^2}{L^2} + \dfrac{4L_p^3}{3L^3}\right)} H_{ir,m} \tag{3.130}$$

There remains to identify the hinge offset parameter $\chi$ of the resultant plasticity beam model. For a given target deformation $v_j^\star$ at end $j$, the objective is to select $\chi$ such that

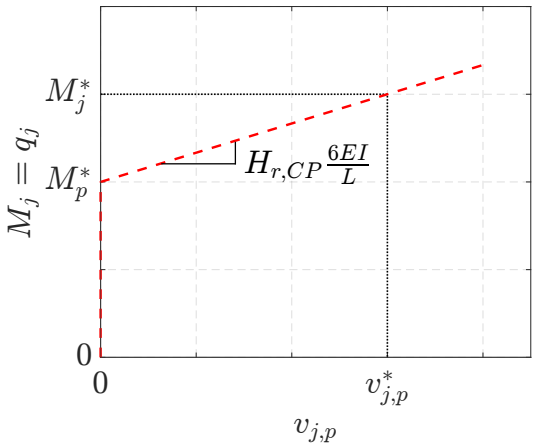


Figure 3.8: Relation between moment and plastic deformation at end $j$

the bending moment $M_j^\star$ at end $j$ associated with $v_j^\star$ matches the value expected from the reference model. Under antisymmetric bending conditions, one can introduce a target plastic deformation $v_{j,p}^\star$ corresponding to $v_j^\star$ that satisfies the following elasto-plastic relation:

$$M_j^\star = \frac{6EI}{L}\left(v_j^\star - v_{j,p}^\star\right) \quad \Rightarrow \quad v_{j,p}^\star = v_j^\star - \frac{L}{6EI}M_j^\star \tag{3.131}$$

Referring to Figure 3.8, the goal is to identify the bending moment value $M_p^\star$ such that $M_j = M_p^\star$ when $M_{hj} = M_p$, which corresponds to the instant the plastic hinge near end $j$ - as well as the one near end $i$ - gets activated. With the help of Figure 3.9, one can determine a corresponding hinge offset parameter $\chi$:

$$\chi = \frac{1}{2}\left(1 - \frac{M_p}{M_p^\star}\right) \tag{3.132}$$

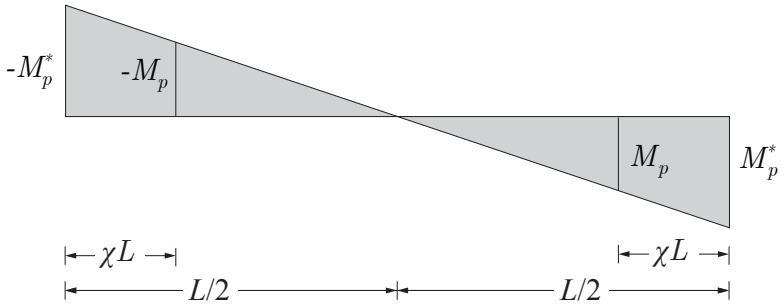


Figure 3.9: Identification of hinge offset parameter

As depicted in Figure 3.8, the relation between $M_j^\star$ and $M_p^\star$ for the resultant plasticity model is given by

$$M_j^\star = M_p^\star + H_{r,CP}\frac{6EI}{L}v_{j,p}^\star \tag{3.133}$$

Combining the previous equation with Equation (3.131), one can then show that

$$M_p^\star = (1 + H_{r,CP})\, M_j^\star - H_{r,CP}\frac{6EI}{L}v_j^\star \tag{3.134}$$

The target plastic deformation $v_{j,p}^\star$ results from the integration of a plastic curvature field $\kappa_p^\star(x)$ over the element length, as depicted in Figure 3.10. Accordingly, the relation between the target end curvature $\kappa_{j,p}^\star$ and $v_{j,p}^\star$ is

$$v_{j,p}^\star = \int_0^L \left(\frac{x}{L}\right)\kappa_p^\star(x)\, dx \tag{3.135}$$

$$= L_p\left(\frac{1}{2} - \frac{L_p}{3L}\right)\kappa_{j,p}^\star \tag{3.136}$$

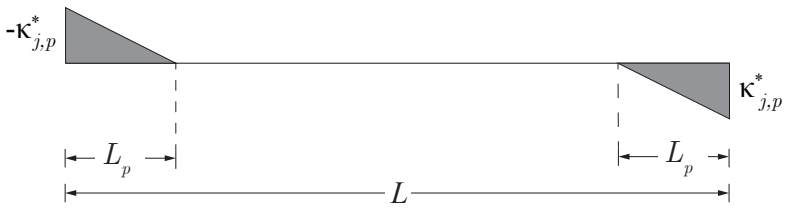


Figure 3.10: Target plastic curvature field

Considering now the hardening branch of the moment - plastic curvature response at end $j$ of the reference model, the target moment $M_j^\star$ is related to $\kappa_{j,p}^\star$ through the following linear relation

$$M_j^\star = M_p + H_{r,m}EI\kappa_{j,p}^\star \tag{3.137}$$

If the plastic hinge length $L_p$ is known or can be estimated from empirical equations, Equations (3.129) and (3.130) can be directly used to identify $H_{kr,CP}$ and $H_{ir,CP}$. Equation (3.121) can in turn be used to determinate $H_{r,CP}$. Combining Equations (3.131), (3.136) and (3.137), one can then solve for $M_j^\star$ as

$$M_j^\star = \frac{M_p\left(3L_pL - 2L_p^2\right) + 6H_{r,m}EILv_j^\star}{3L_pL - 2L_p^2 + H_{r,m}L^2} \tag{3.138}$$

This allows the determination of $M_p^\star$ and the corresponding hinge offset parameter $\chi$ according to Equations (3.134) and (3.132), respectively.

Alternatively, if the plastic hinge length $L_p$ is unknown, it can be estimated from the relation:

$$L_p = \frac{L}{2}\left(1 - \frac{M_p}{M_j^\star}\right) \tag{3.139}$$

Combining Equations (3.131), (3.136), (3.137) and (3.139), one can derive the following cubic equation for $M_j^\star$:

$$2\left(1 + H_{r,m}\right)\left(\frac{M_j^\star}{M_p}\right)^3 - \left(3 + \frac{12H_{r,m}EI}{M_pL}v_j^\star\right)\left(\frac{M_j^\star}{M_p}\right)^2 + 1 = 0 \tag{3.140}$$

The above cubic equation can be used to solve for the root $M_j^\star$ such that

$$\frac{M_j^\star}{M_p} \geq 1 \tag{3.141}$$

$L_p$ can then be evaluated from Equation (3.139), and Equations (3.129), (3.130) and (3.121) can be used to determine $H_{kr,CP}$, $H_{ir,CP}$ and $H_{r,CP}$. This in turn allows the determination of $M_p^\star$ and the corresponding hinge offset parameter $\chi$ according to Equations (3.134) and (3.132), respectively.

The calibration procedure of the hardening and hinge offset parameters of the resultant plasticity beam model under antisymmetric bending and linear material hardening is summarized in Table 3.4.

## 3.6 General bending of wide-flange girder

To characterize the performance of the resultant plasticity beam model and the validity of the proposed calibration procedure, a set of monotonic and cyclic analyses is conducted for a simply supported beam subjected to imposed flexural end deformations $v_i$ and $v_j$ and imposed axial force. The axial force is assumed to be null, such that $q_a = 0$. The beam specimens are tested under various bending conditions characterized by the fixed ratio of imposed deformations $\rho$ such that $v_i = \rho v_j$, as illustrated in Figure 3.11. $\rho = 1$ corresponds to purely antisymmetric double curvature bending conditions, whereas $\rho = -1$ corresponds to symmetric single curvature bending conditions. Three section sizes are investigated: a W30x173, a W18x143 and a W12x120 steel cross sections. All cross sections are assumed to be bending about their strong axis. The length of the beam is taken such that $L = 20d$ where $d$ is the depth of the cross section.

### 3.6.1 Load and deformation histories

Two load patterns are investigated, U0 and U1, with a nomenclature consistent with Section 2.5.1.1. The first load pattern, U0, consists in imposing monotonically increasing end deformations $v_i$ and $v_j$, while applying a constant axial force $N$ on the element. It is

**Objective:** Given $E$, $I$, $M_p$, $L$, $H_{kr,m}$, $H_{ir,m}$ and a target value of the end deformation $v_j^\star$, evaluate $H_{kr,CP}$, $H_{ir,CP}$ and $\chi$.

1. **Determination of $H_{kr,CP}$ and $H_{ir,CP}$ if the plastic hinge length $L_p$ is known:**
   a) Determine $H_{kr,CP}$, $H_{ir,CP}$ and $H_{r,CP}$ according to Equations (3.129), (3.130) and (3.121), respectively.
   b) Evaluate $M_j^\star$ in Equation (3.138)
   c) Go to 3
2. **Determination of $H_{kr,CP}$ and $H_{ir,CP}$ if the plastic hinge length $L_p$ is unknown:**
   a) Solve the cubic Equation (3.140) for the root $M_j^\star$ such that $\dfrac{M_j^\star}{M_p} \geq 1$
   b) Evaluate $L_p$ in Equation (3.139)
   c) Determine $H_{kr,CP}$, $H_{ir,CP}$ and $H_{r,CP}$ according to Equations (3.129), (3.130) and (3.121), respectively.
   d) Go to 3
3. **Determination of $\chi$**
   a) Evaluate $M_p^\star$ in Equation (3.134)
   b) Evaluate $\chi$ in Equation (3.132)

Table 3.4: Calibration procedure for hardening and hinge offset parameters of resultant plasticity beam model

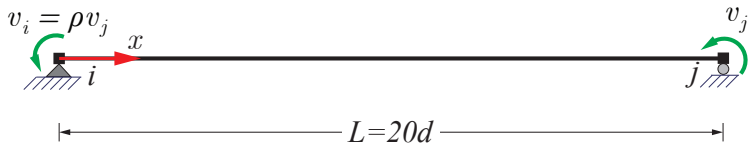


Figure 3.11: Simply supported beam under imposed end rotations with ratio $\rho$

illustrated in Figure 3.12 (a). The second one, U1, consists in imposing four symmetric cycles of increasing magnitude for $v_i$ and $v_j$ while prescribing a constant value for $N$. It is illustrated in Figure 3.12 (b). The deformation factors depicted in Figure 3.12 are such that the imposed end deformations are given by:

$$v_j = \text{Defo. load factor} \cdot v_{j,ref} \tag{3.142}$$

$$v_i = \text{Defo. load factor} \cdot v_{i,ref} \tag{3.143}$$

where $v_{j,ref} = 2.5\%$ and $v_{i,ref} = \rho v_{j,ref}$. The axial force is zero.

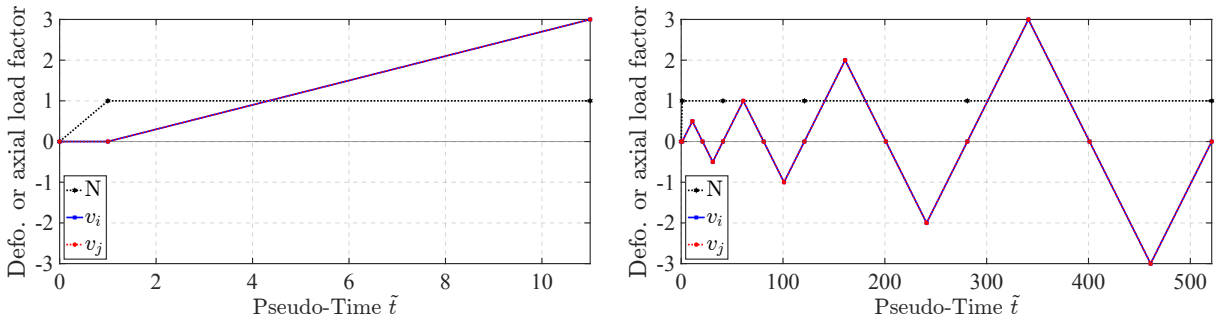


(a) U0 (b) U1

Figure 3.12: Deformation history for steel girder analyses (reference axial force is zero)

### 3.6.2 Beam models

The response of the resultant plasticity beam model is compared with that of a reference distributed plasticity beam-column element with fiber section discretization. The element response is integrated using the Gauss-Lobatto rule with 15 integration points distributed along the element length. The number of integration points is selected to accurately capture the spread of plasticity at the element ends during the hardening phase, but it should be noted that more efficient discretization schemes could have been equally used to produce a reference response. However, this is beyond the scope of this study. The 15 monitoring sections are each discretized along the y-direction with 3 layers evenly distributed in each flange, and 8 layers evenly distributed in the web, as illustrated in Figure 3.13.

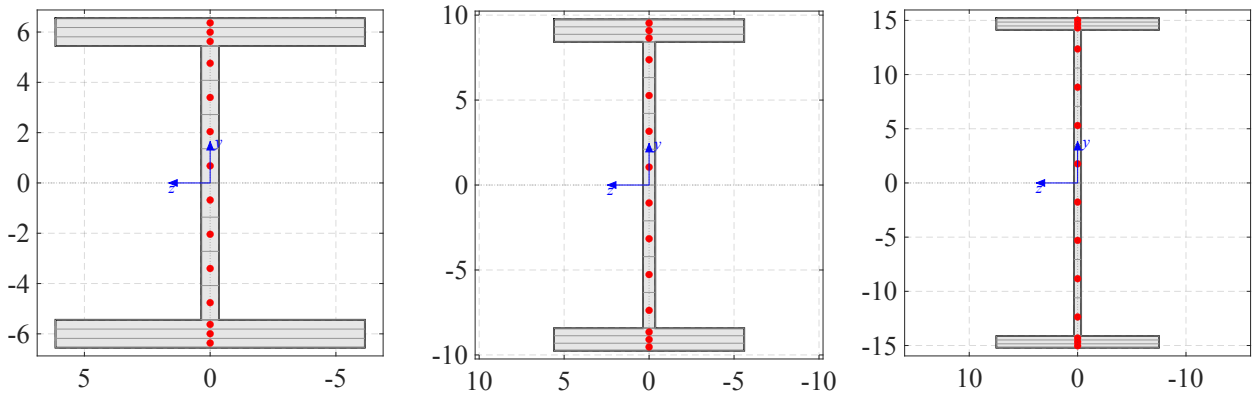

(a) Mesh for W12x120 (b) Mesh for W18x143 (c) Mesh for W30x173

Figure 3.13: Fiber discretization of section for steel girder analyses (dimensions in inches)

The steel stress-strain relation follows an inelastic linear-plastic 1d model with the return map algorithm [73]. The steel yield strength is taken as $f_y = 40$ ksi. The material model accommodates kinematic and isotropic hardening through the consideration of two modulii, $H_{k,m}$, and $H_{i,m}$, defined as:

$$H_{k,m} = H_{kr,m}E \tag{3.144}$$

$$H_{i,m} = H_{ir,m}E \tag{3.145}$$

where E is the Young modulus of the material, taken as $20,000$ ksi.

Several values of the material hardening ratios are investigated, ranging from 0.5% to 5%, giving rise to five distributed plasticity models named from DP15Fib1 to DP15Fib5, as detailed in Table 3.5. For each set of material hardening ratios and for each cross section, the calibration procedure presented in 3.5 is used to compute the corresponding hardening and hinge offset parameters of the resultant plasticity models with a target deformation $v_j^\star = 0.06$. These parameters are summarized in Table 3.5. The equivalent resultant plasticity models are named from CP1 to CP5.

Assuming a steel yield strength of $f_y = 40$ ksi, $M_{pz} = 7,440$ kip-in for the W12x120 profile; $M_{pz} = 12,880$ kip-in for the W18x143 profile, and $M_{pz} = 24,280$ kip-in for the W30x173 cross section.

## 3.6.3 Results

### 3.6.3.1 Monotonic response under antisymmetric bending

First, the antisymmetric bending monotonic response corresponding to U0 with $\rho = 1$ is investigated. The results for the models with kinematic hardening only, CP1 to CP4 is computed and compared with that of DP15Fib1 to DP15Fib4, as shown in Figures 3.14 to 3.17. The excellent agreement over the wide range of investigated material hardening

| **Cross Section** | **Beam Model** | $H_{kr,m}$ (%) | $H_{ir,m}$ (‰) | **Beam Model** | $H_{kr,CP}$ (%) | $H_{ir,CP}$ (‰) | $\chi$ (%) |
|---|---|---|---|---|---|---|---|
| W12x120 | **DP15Fib1** | 0.5 | 0.0 | **CP1** | 1.93 | 0.0 | 2.32 |
| | **DP15Fib2** | 1.0 | 0.0 | **CP2** | 2.92 | 0.0 | 3.18 |
| | **DP15Fib3** | 3.0 | 0.0 | **CP3** | 5.85 | 0.0 | 5.12 |
| | **DP15Fib4** | 5.0 | 0.0 | **CP4** | 8.31 | 0.0 | 6.27 |
| | **DP15Fib5** | 1.0 | 1.0 | **CP5** | 2.81 | 2.8 | 3.32 |
| W18x143 | **DP15Fib1** | 0.5 | 0.0 | **CP1** | 1.95 | 0.0 | 2.31 |
| | **DP15Fib2** | 1.0 | 0.0 | **CP2** | 2.93 | 0.0 | 3.18 |
| | **DP15Fib3** | 3.0 | 0.0 | **CP3** | 5.86 | 0.0 | 5.11 |
| | **DP15Fib4** | 5.0 | 0.0 | **CP4** | 8.32 | 0.0 | 6.26 |
| | **DP15Fib5** | 1.0 | 1.0 | **CP5** | 2.82 | 2.8 | 3.32 |
| W30x173 | **DP15Fib1** | 0.5 | 0.0 | **CP1** | 1.93 | 0.0 | 2.34 |
| | **DP15Fib2** | 1.0 | 0.0 | **CP2** | 2.90 | 0.0 | 3.21 |
| | **DP15Fib3** | 3.0 | 0.0 | **CP3** | 5.81 | 0.0 | 5.16 |
| | **DP15Fib4** | 5.0 | 0.0 | **CP4** | 8.26 | 0.0 | 6.32 |
| | **DP15Fib5** | 1.0 | 1.0 | **CP5** | 2.79 | 2.8 | 3.35 |

Table 3.5: Parameters for girder analyses

parameters and for all three cross sections confirms the validity of the calibration procedure of the resultant plasticity beam model parameters.

#### 3.6.3.2 Monotonic response under general bending

Next, the general bending monotonic response of the W18x143 girder is investigated under U0 with the following values for the ratio of imposed deformations: $\rho = 0.5$, $\rho = 0$, and $\rho = -0.5$. Figures 3.18 and 3.19 show the moment-rotation responses for the beam models with 1% and 5% material kinematic hardening parameters, respectively. Here again, the excellent agreement between the reference model and the resultant plasticity model response confirms the remarkable accuracy of the proposed beam model in capturing the moment-rotation response of the beam under spreading inelastic deformations, including when the bending conditions are not perfectly antisymmetric. The accuracy of the proposed beam element is slightly less satisfactory for single curvature bending conditions with $\rho = -0.5$. However, it should be noted that this last value of $\rho = -0.5$ is considered an extreme case as most girders of multistory frames subjected to gravity loads and high lateral forces are expected to undergo bending conditions equivalent to $0 < \rho < 1$.

#### 3.6.3.3 Cyclic response under general bending

Then, the general bending cyclic response of the W18x143 girder is investigated under U1 with the following values for the ratio of imposed deformations: $\rho = 1$, $\rho = 0.5$, and $\rho = 0$. Figures 3.20 to 3.21 show the moment-rotation responses for the beam models with 1% and 5% material kinematic hardening parameters, respectively. The proposed resultant plasticity beam model produce an excellent match with the reference models response.

Last, the general bending cyclic response under the consideration of combined kinematic and isotropic hardening for the W18x143 and W30x173 girders is investigated. The moment-rotation responses obtained with the DP15Fib5 and CP5 models are compared in Figures 3.22 and 3.23 for the W18x143 and W30x173 girders, respectively. Here again, the excellent agreement between the reference model and the resultant plasticity beam model response confirms the remarkable accuracy of the proposed model in capturing the general bending cyclic response of beam components under the consideration of combined kinematic and isotropic hardening.

#### 3.6.3.4 Evaluation of computational performance

To assess the computational performance of the proposed resultant plasticity beam model, its computational times are compared with that of a distributed plasticity beam column element with 5 Gauss-Lobatto integration points along its length and fiber section discretization. The latter element is broadly used to model moment resisting frame girders. It is identical to the reference model DP15Fib described in Section 3.6.2 except for the element discretization which uses 5 monitoring sections instead of 15. This new model is referred to a DP5Fib. The focus is on comparing the cyclic response for the models with combined isotropic/kinematic hardening. Figures 3.24 to 3.26 compare the antisymmetric bending responses of the CP5 and newly introduced DP5Fib5 models with that of the reference model DP15Fib5 for all three investigated cross sections. Figure 3.27 compares the single curvature bending responses under $\rho = -0.5$ of the CP5 and DP5Fib5 models with that of DP15Fib5. The run times for each model are indicated in the subcaptions.

The following conclusions are drawn:

- The results produced with the DP5Fib element are of lesser accuracy compared to those of the proposed resultant plasticity model under double curvature conditions. This is because the distributed plasticity model fails to capture the gradual spread of plastic deformations into the beam with 5 integrations points, as plastic deformations take place only at the end sections of the element and the effective plastic hinge length is not representative of the true plastic hinge length under double curvature conditions.

- The accuracy of the DP5Fib element is improved under single curvature conditions, since in this case several integration points might experience plastic deformations and the effective plastic hinge length is closer to the true plastic hinge length. For the extreme case of purely symmetric bending with $\rho = 1$, DP5Fib and DP15Fib are

expected to yield identical results. However, this type of bending distribution is rather unusual in girders of moment-resisting frames subjected high lateral loads.

- Across all three cross sections and investigated load cases, the computational time with the proposed resultant plasticity beam model instead of DP5Fib is reduced by a factor of 5 to 14.

Thus, for the simulation of moment resisting frame girders which typically undergo double curvature bending conditions, the proposed resultant plasticity beam model is expected to yield more accurate results than the DP5Fib model, in addition to being significantly more economical.

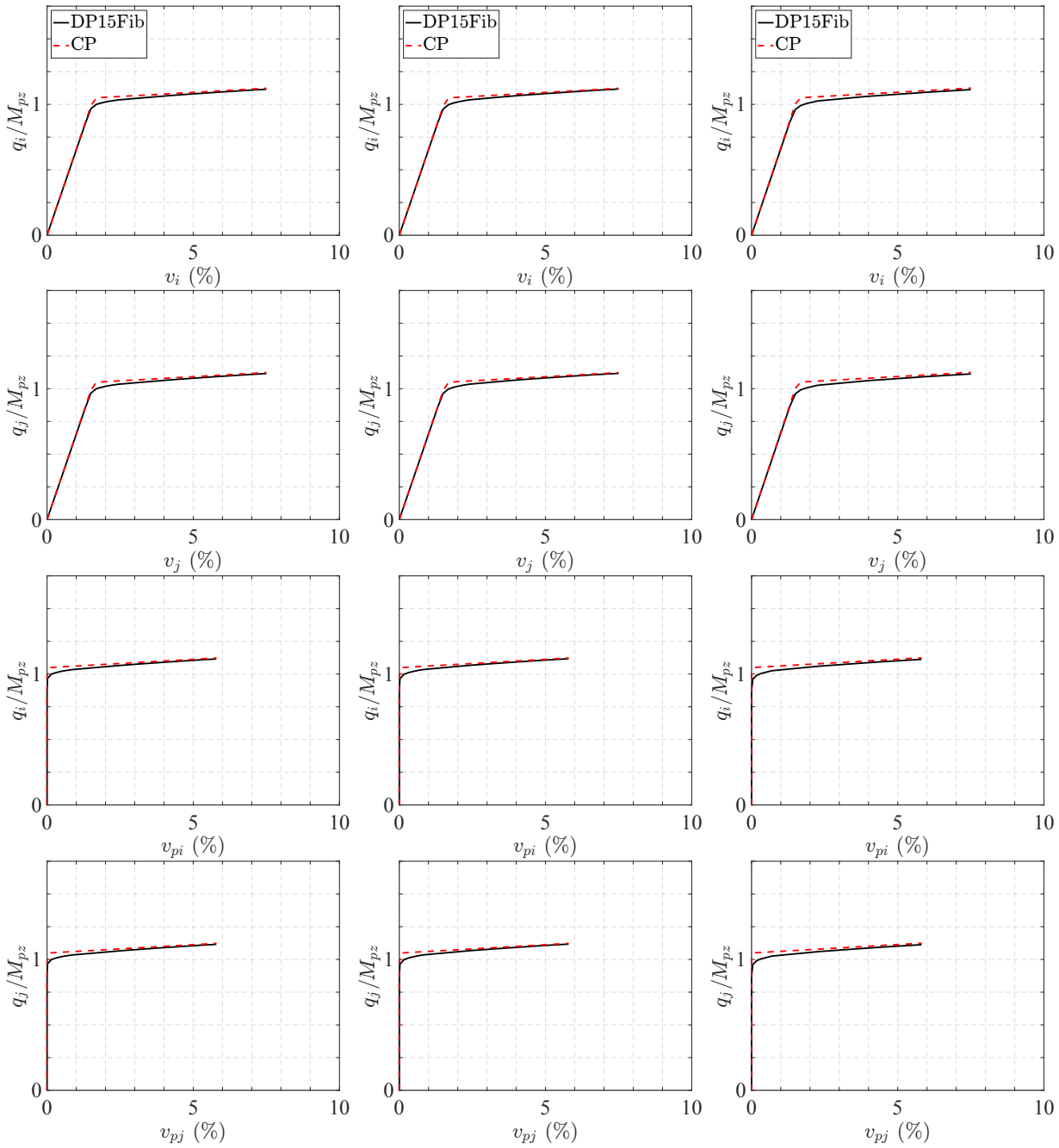


(a) W12x120 (b) W18x143 (c) W30x173

Figure 3.14: Antisymmetric bending monotonic response - DP15Fib1 vs. CP1

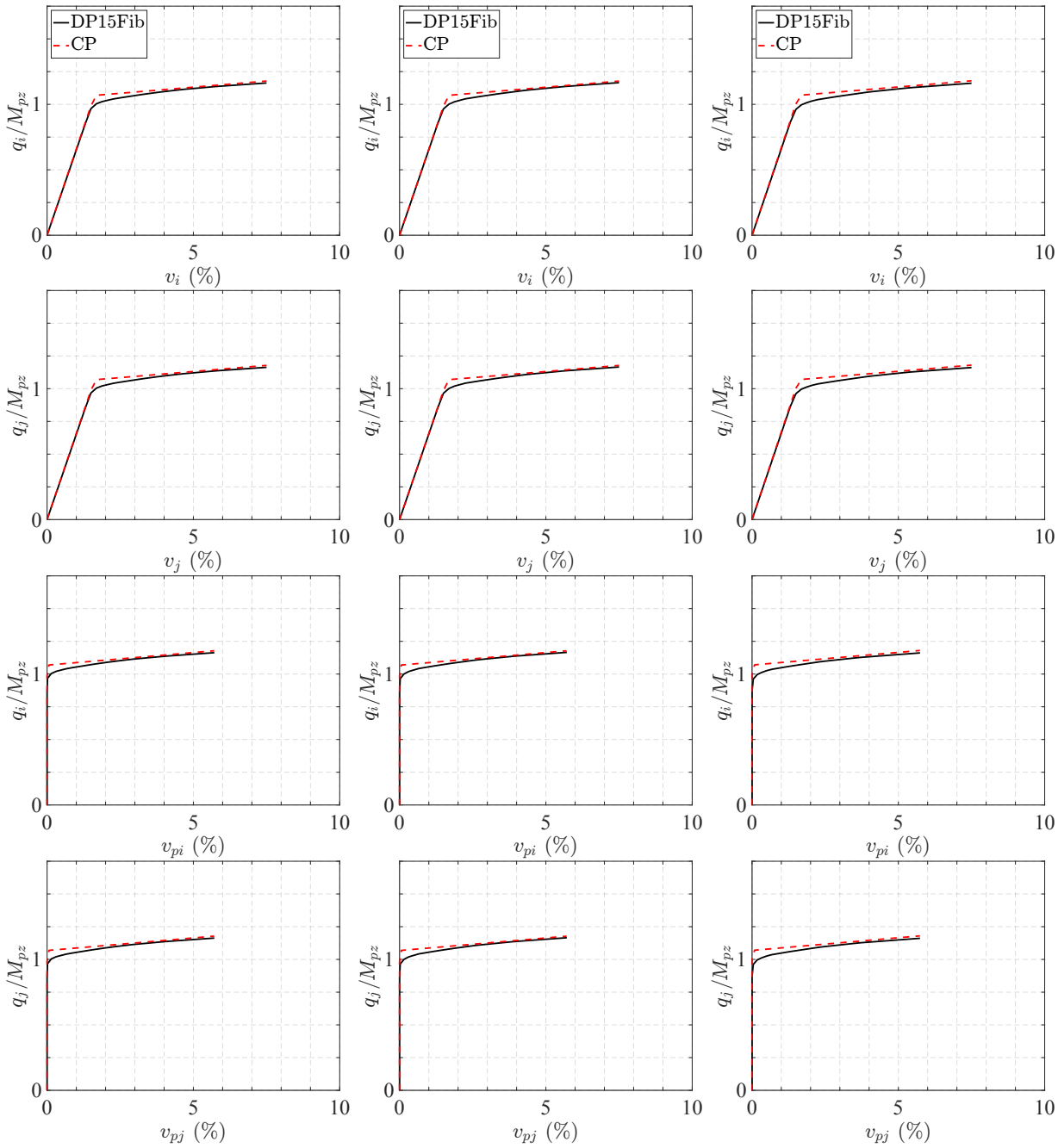


(a) W12x120 (b) W18x143 (c) W30x173

Figure 3.15: Antisymmetric bending monotonic response - DP15Fib2 vs. CP2

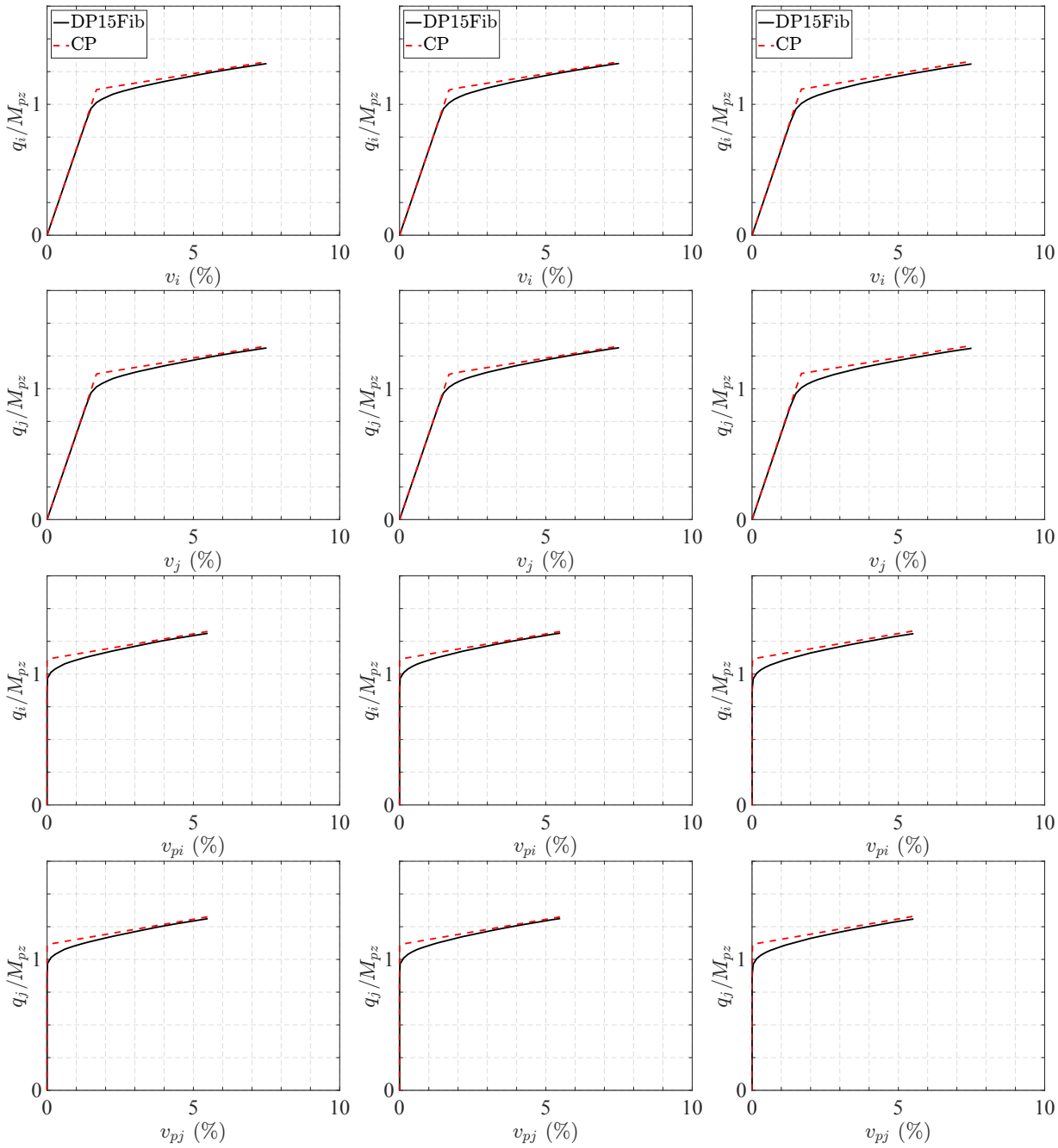


(a) W12x120 (b) W18x143 (c) W30x173

Figure 3.16: Antisymmetric bending monotonic response - DP15Fib3 vs. CP3

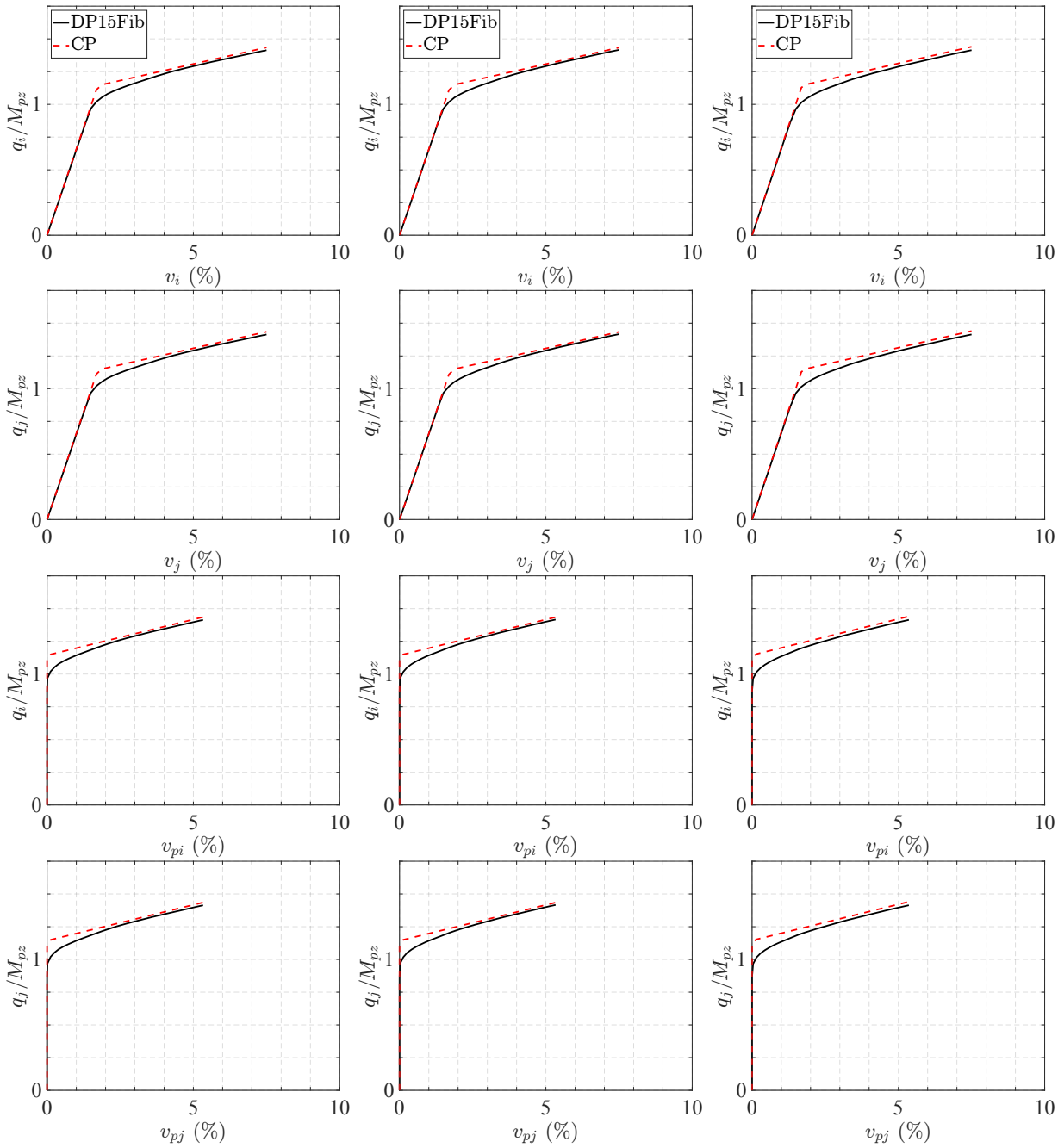


(a) W12x120 (b) W18x143 (c) W30x173

Figure 3.17: Antisymmetric bending monotonic response - DP15Fib4 vs. CP4

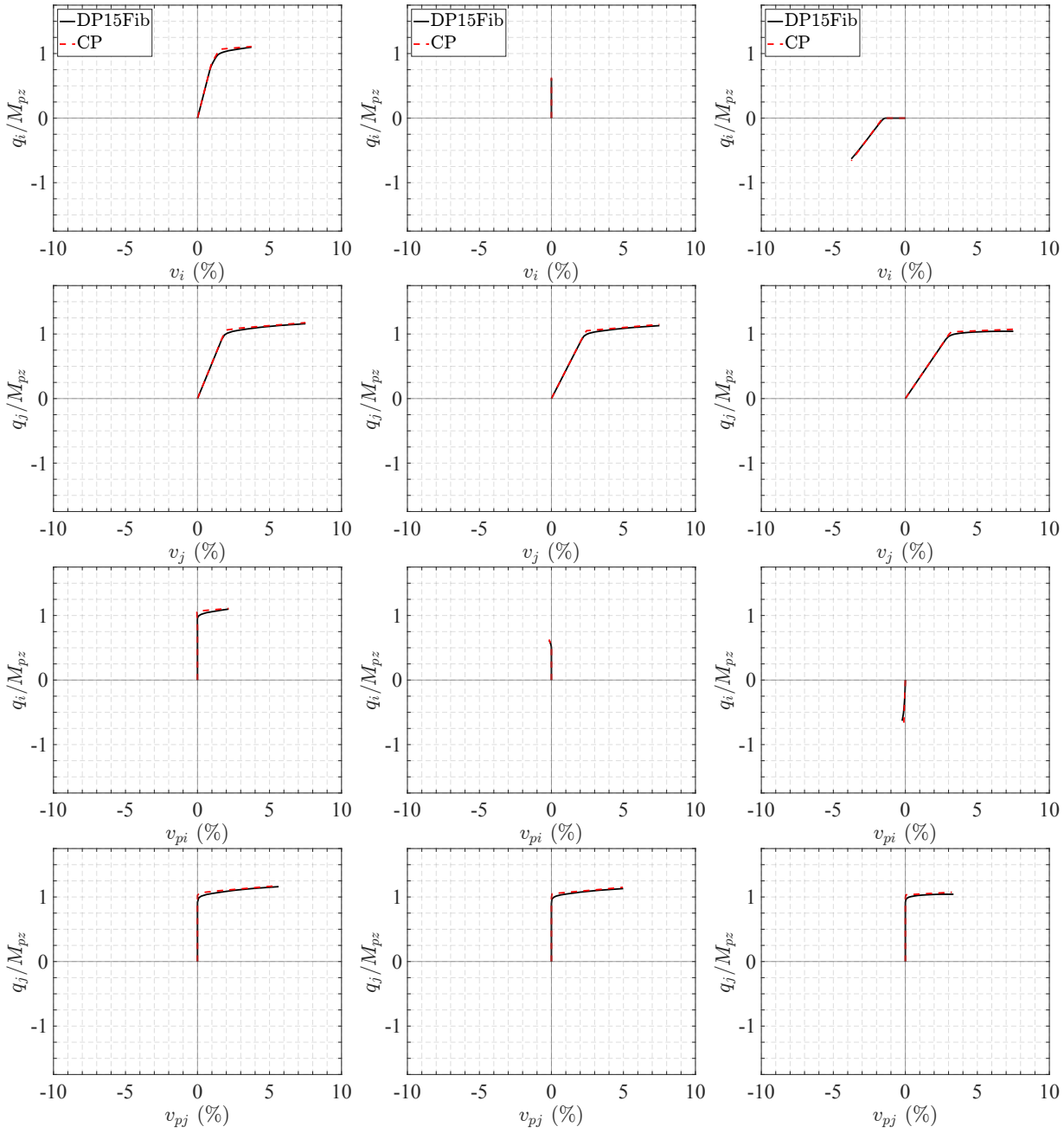


(a) $\rho = 0.5$ (b) $\rho = 0$ (c) $\rho = -0.5$

Figure 3.18: General bending monotonic response of W18x143 - DP15Fib2 vs. CP2

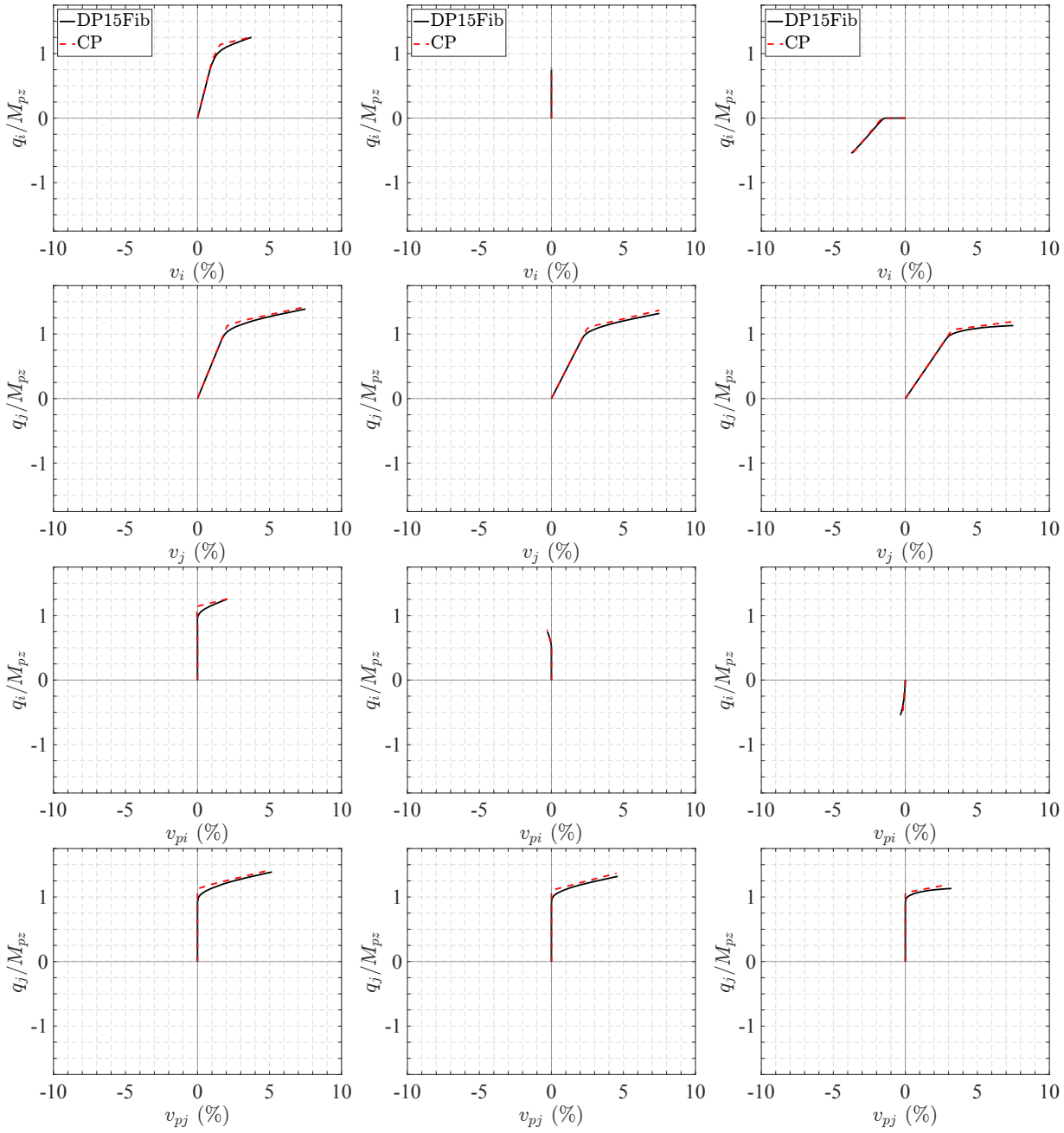


(a) $\rho = 0.5$ (b) $\rho = 0$ (c) $\rho = -0.5$

Figure 3.19: General bending monotonic response of W18x143 - DP15Fib4 vs. CP4

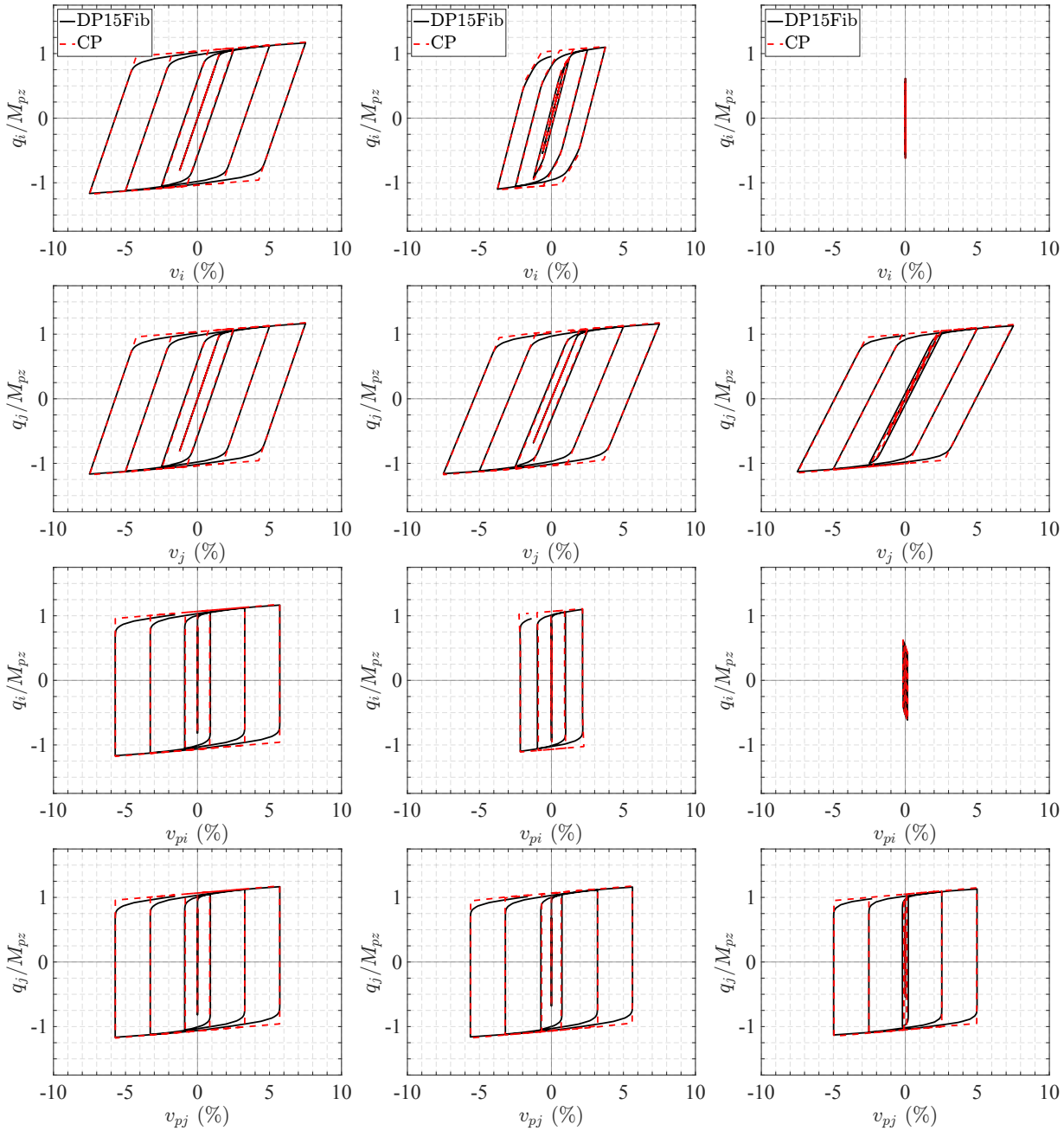


(a) $\rho = 1$ (b) $\rho = 0.5$ (c) $\rho = 0$

Figure 3.20: General bending cyclic response of W18x143 - DP15Fib2 vs. CP2

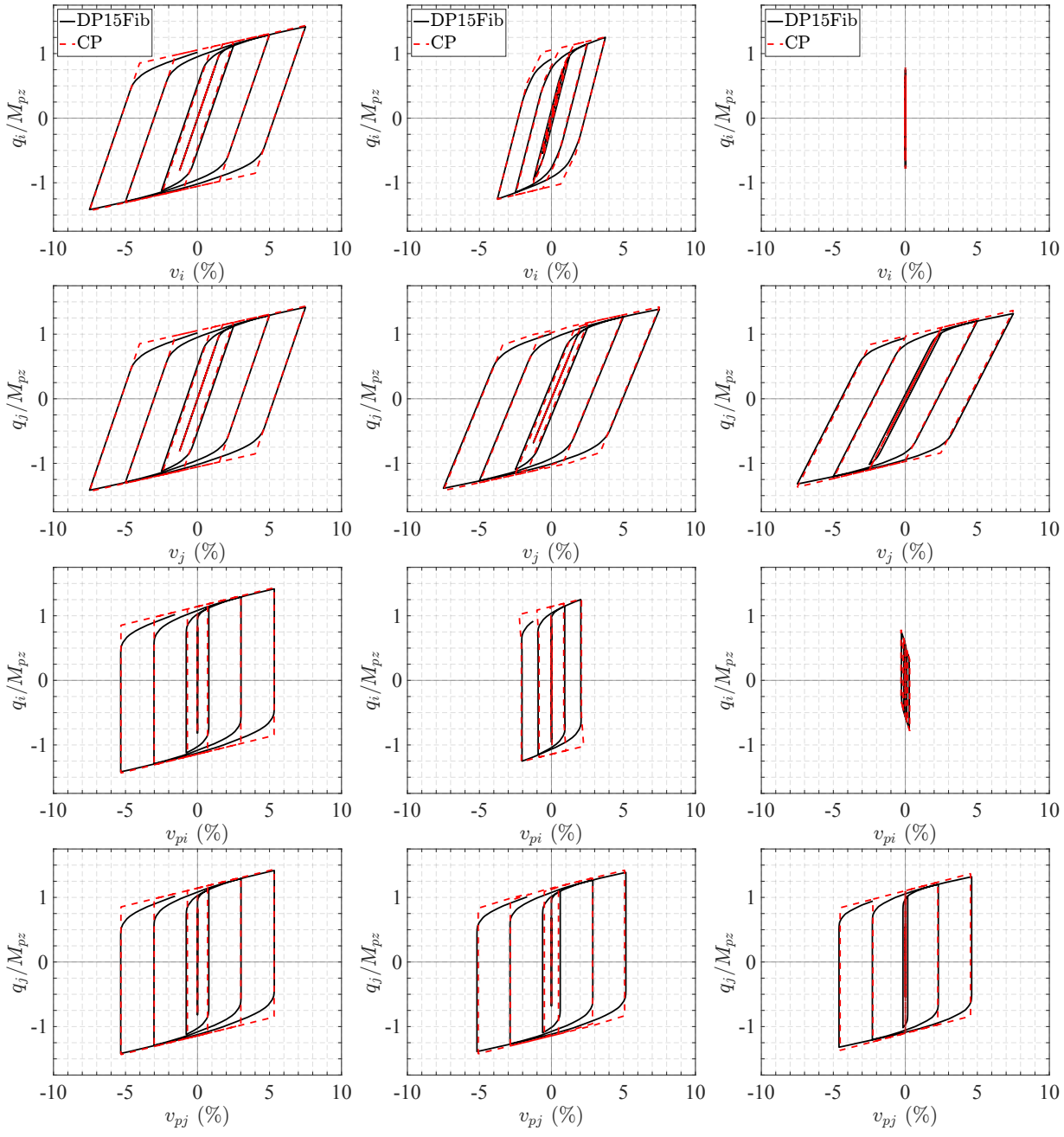


(a) $\rho = 1$ (b) $\rho = 0.5$ (c) $\rho = 0$

Figure 3.21: General bending cyclic response of W18x143 - DP15Fib4 vs. CP4

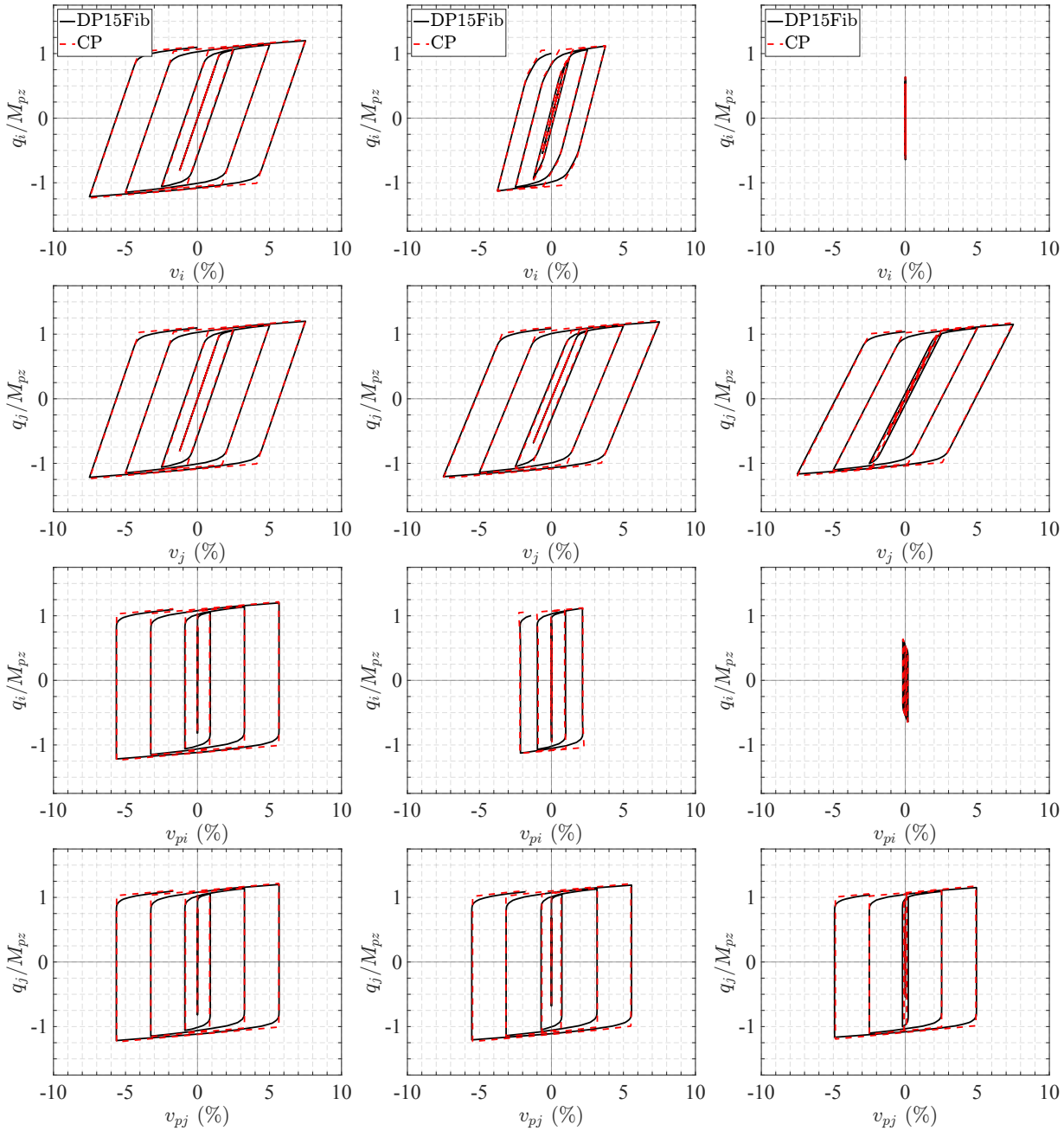


(a) $\rho = 1$ (b) $\rho = 0.5$ (c) $\rho = 0$

Figure 3.22: General bending cyclic response of W18x143 - DP15Fib5 vs. CP5

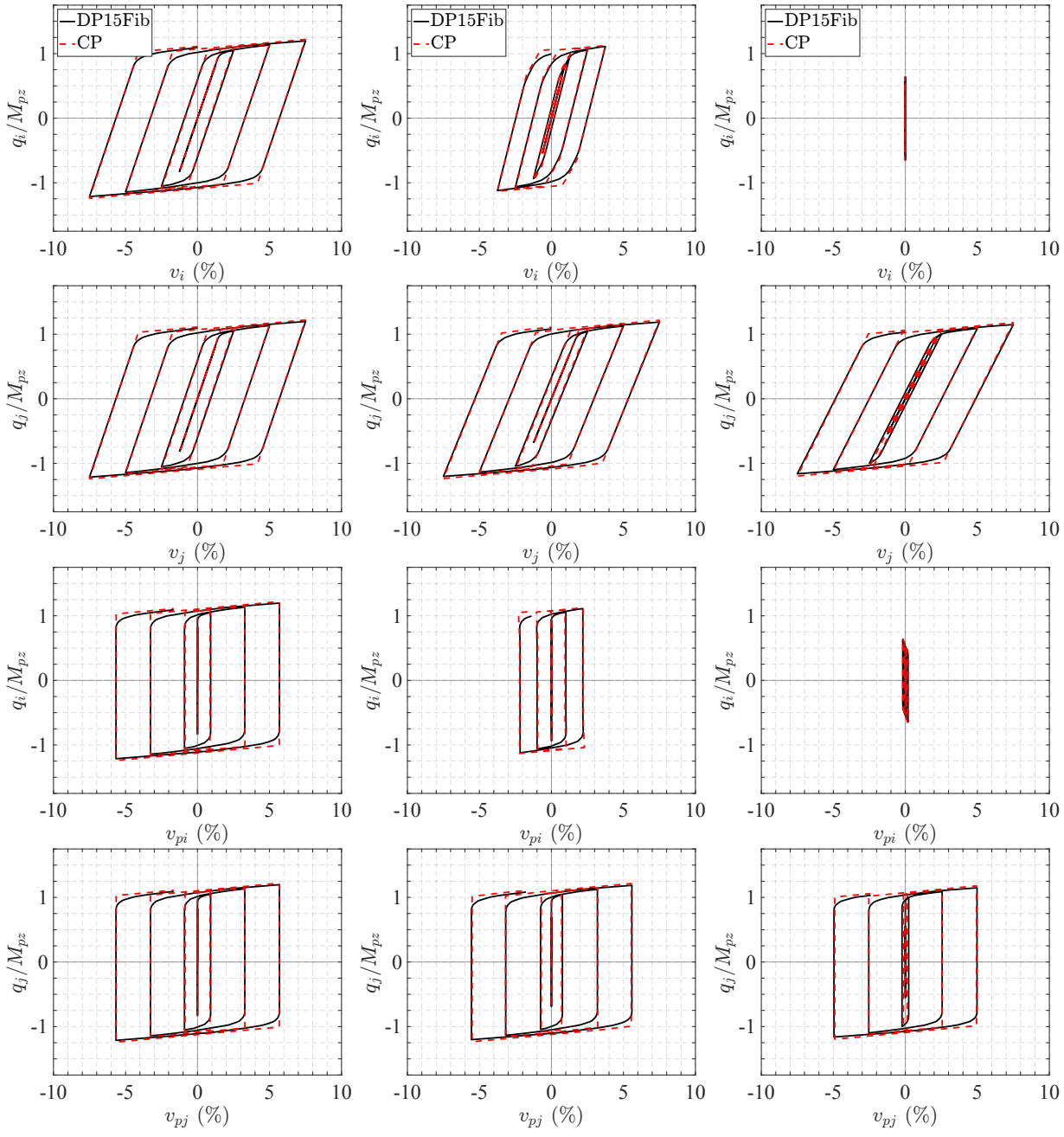


(a) $\rho = 1$ (b) $\rho = 0.5$ (c) $\rho = 0$

Figure 3.23: General bending cyclic response of W30x173 - DP15Fib5 vs. CP5

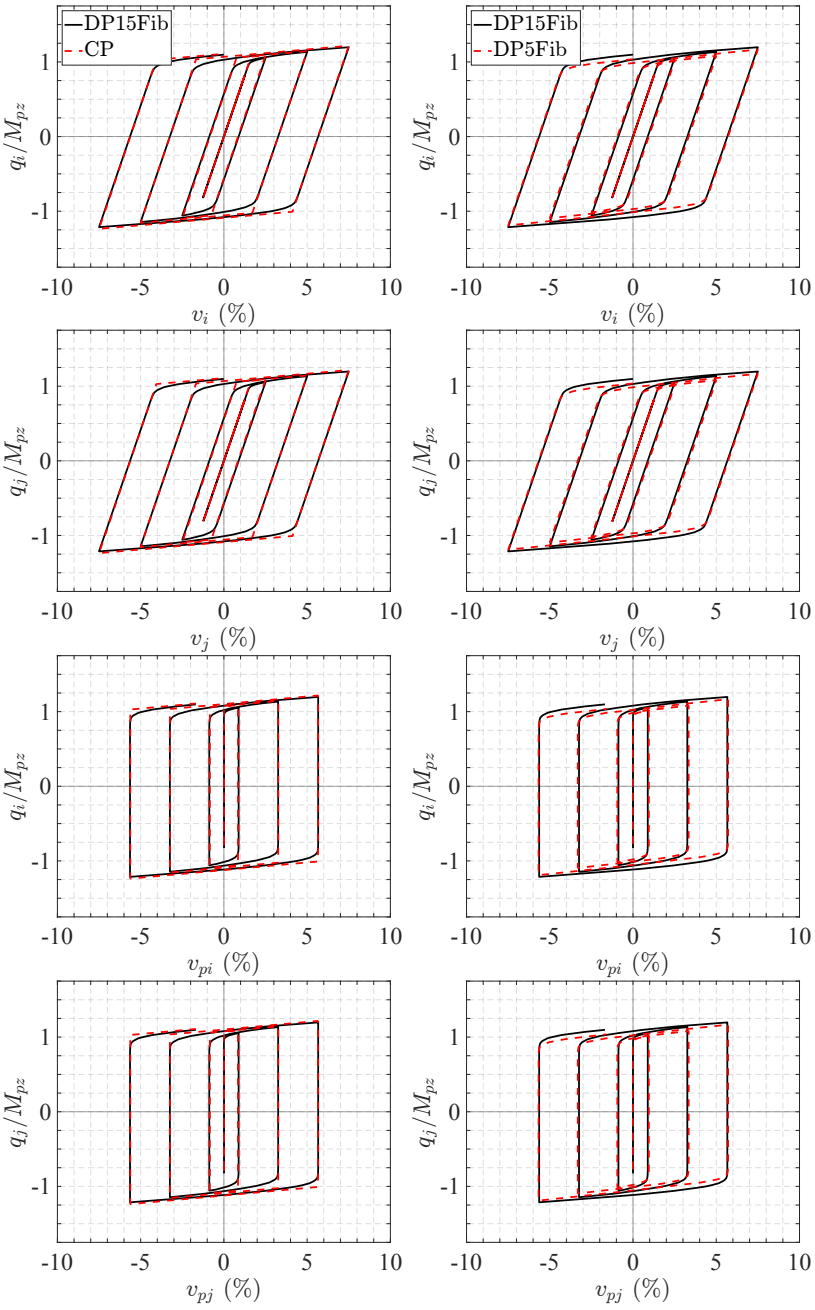


(a) CP (15.4 sec) (b) DP5Fib (104.2 sec)

Figure 3.24: Antisymmetric bending cyclic response of W12x120 - CP5 vs DP5Fib5

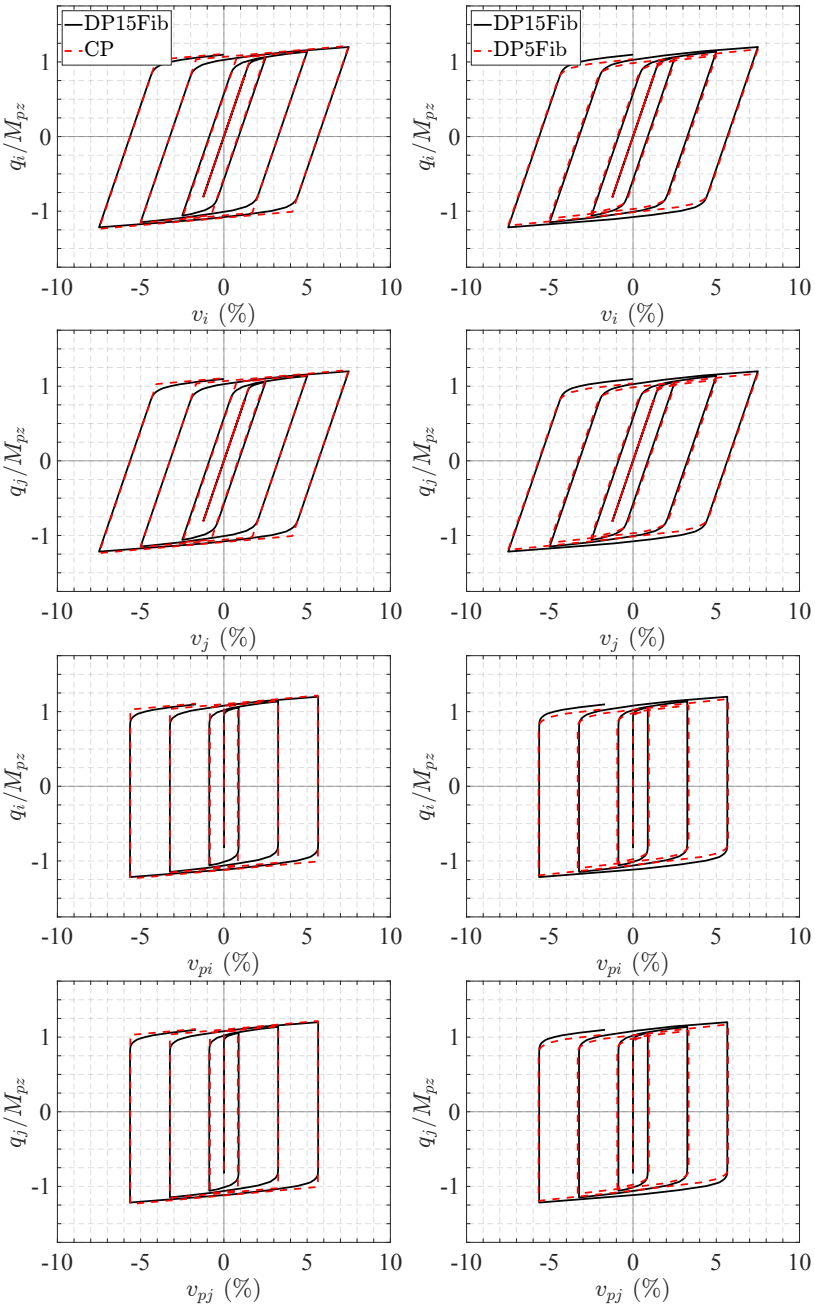


(a) CP (17.7 sec) (b) DP5Fib (113.7 sec)

Figure 3.25: Antisymmetric bending cyclic response of W18x143 - CP5 vs DP5Fib5

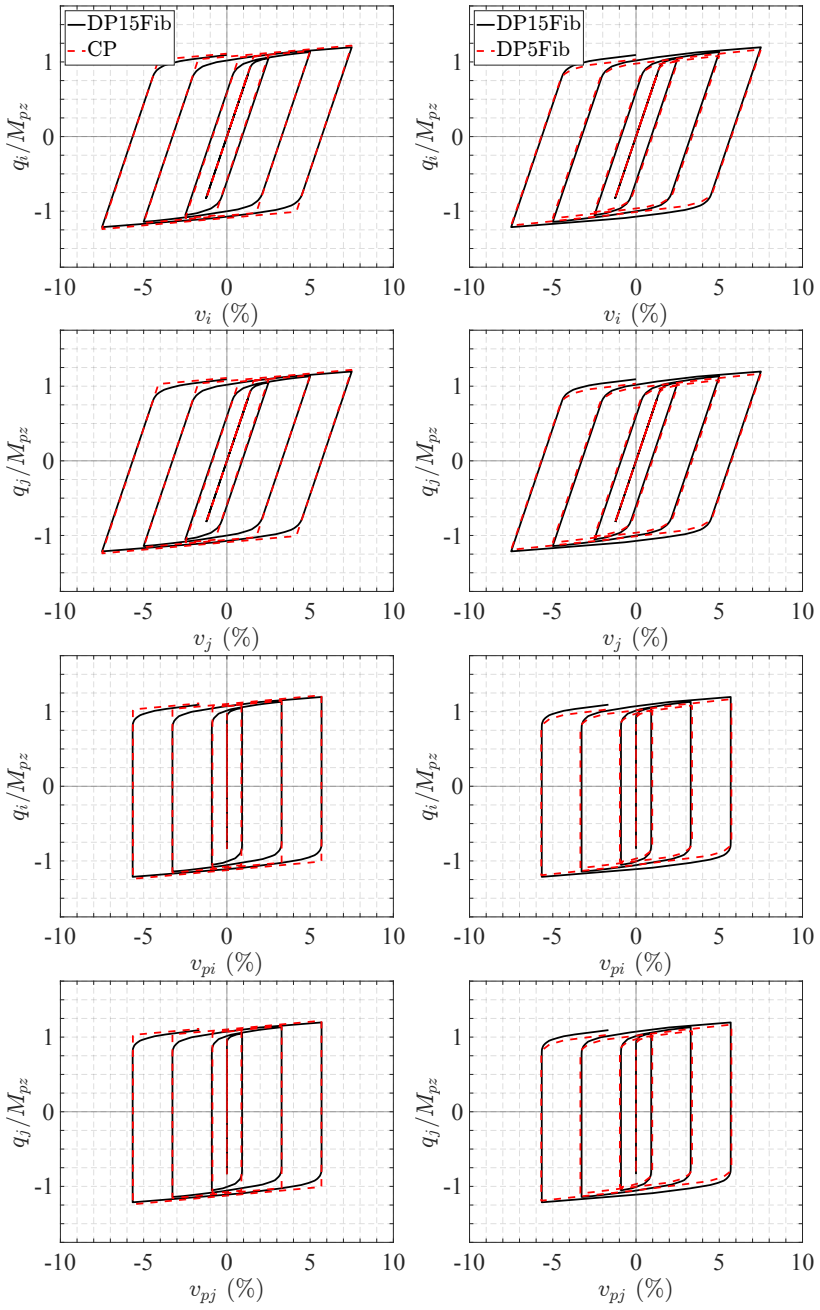


(a) CP (6.6 sec) (b) DP5Fib (93.3 sec)

Figure 3.26: Antisymmetric bending cyclic response of W30x173 - CP5 vs DP5Fib5

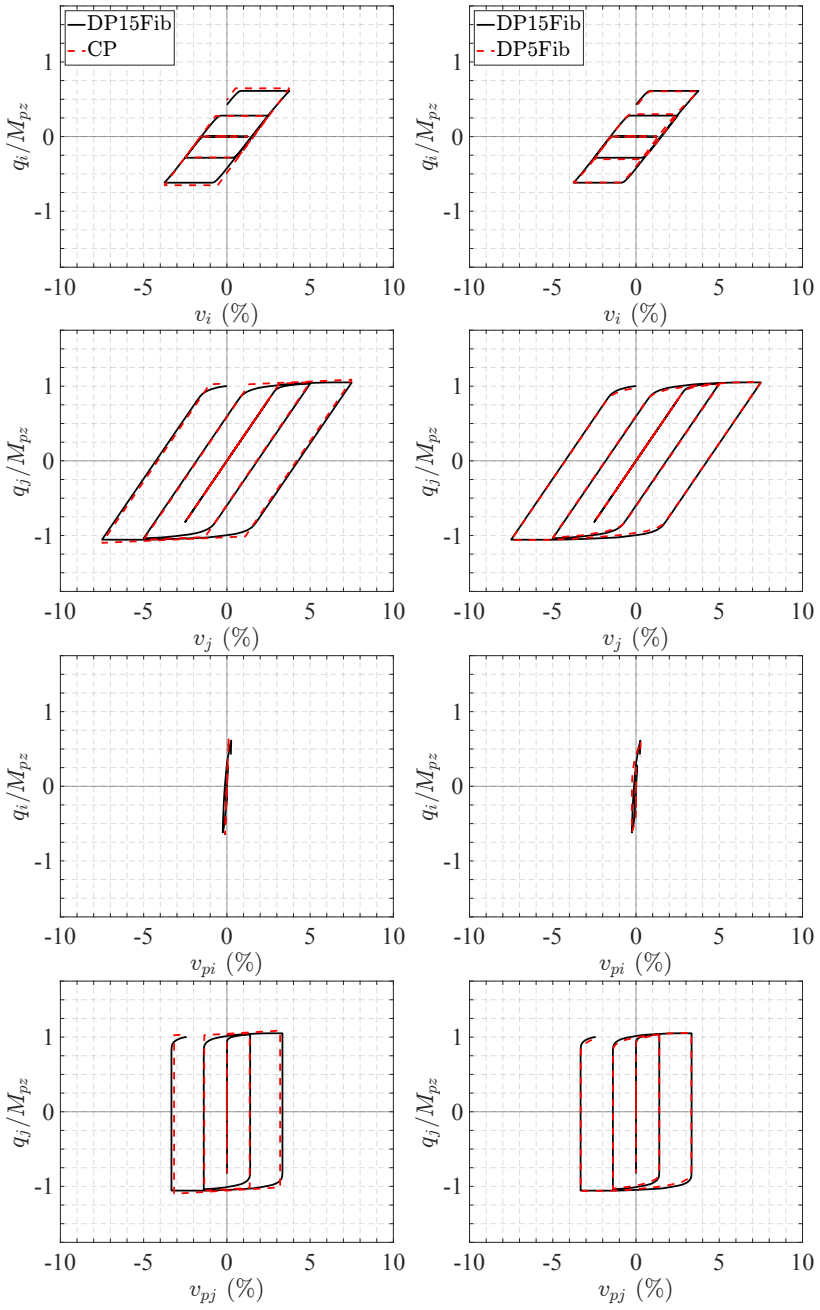


(a) CP (18.8 sec) (b) DP5Fib (92.3 sec)

Figure 3.27: Single curvature bending cyclic response of W18x143 - CP5 vs DP5Fib5

# Chapter 4

# Column element with concentrated resultant force plasticity

## 4.1 Overview

This chapter presents a beam-column element based on resultant plasticity theory suitable for the non-degrading uniaxial and biaxial bending response of frame elements. The model consists of a linear elastic element with two concentrated plastic hinges that can be offset from the element ends. The proposed column formulation accounts for the axial-flexure interaction through the consideration of a polynomial yield envelope which evolves with kinematic and isotropic hardening. The element state determination is based on the return-mapping algorithm, ensuring numerical robustness with quadratic convergence of the residual for the governing equations. Following the presentation of the model, correlation studies evaluate its suitability for the moment-curvature analysis of wide-flange sections under biaxial flexure with constant or variable axial force.

## 4.2 Column element with concentrated resultant force plasticity

### 4.2.1 Concentrated resultant force plasticity column element for uniaxial flexure and axial force

First, a column model for frame elements under uniaxial bending is described. The axis about which the flexural action is takes place can indifferently be the strong axis $z$ or the weak axis $y$ of the cross section, but the following derivations assume that the column bends about its strong axis. For uniaxial bending about the weak axis, all $z$ subscripts should be replaced by $y$ subscripts in the subsequent equations.

The 2d column resultant model adopts three kinematic variables and three stress resul-

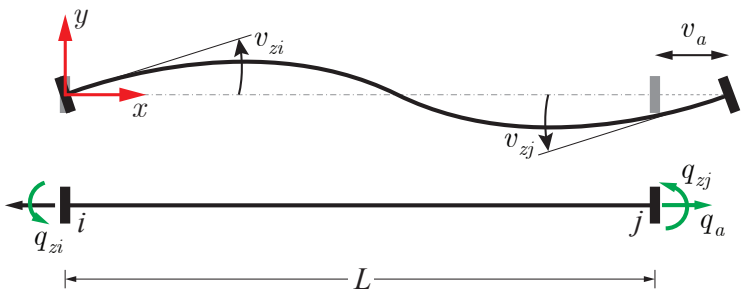


Figure 4.1: Kinematic variables and basic forces for 2d column element

tants, as illustrated in Figure 4.1. The three kinematic variables can be assembled into the element deformation vector $\boldsymbol{v}$ defined as:

$$\boldsymbol{v} = \begin{bmatrix} v_a & v_{zi} & v_{zj} \end{bmatrix}^T \tag{4.1}$$

where $v_a$ is the axial deformation and $v_{zi}$ and $v_{zj}$ are the flexural deformations about the $z$-axis at end $i$ and end $j$ of the element, respectively. The axial deformation has units of length, whereas the flexural deformations are rotations with units of radians and their sign is defined as positive in the counterclockwise direction. The three element basic forces or stress resultants, can be assembled into the element basic force vector $\boldsymbol{q}$ which consists of the following components:

$$\boldsymbol{q} = \begin{bmatrix} q_a & q_{zi} & q_{zj} \end{bmatrix}^T \tag{4.2}$$

$q_a$ is the axial force resultant and $q_{zi}$ and $q_{zj}$ are the flexural forces about the $z$-axis at end $i$ and $j$ of the element, respectively.

#### 4.2.1.1 Series model of element deformations

The proposed resultant plasticity column model is based on plasticity theory [73] and uses an elastic component in series with a plastic component. Accordingly, the element deformation vector $\boldsymbol{v}$ is decomposed into the sum of two contributions: an elastic deformation vector $\boldsymbol{v}_e$ and a plastic deformation vector $\boldsymbol{v}_p$ such that:

$$\boldsymbol{v} = \boldsymbol{v}_e + \boldsymbol{v}_p \tag{4.3}$$

with

$$\boldsymbol{v}_e = \begin{bmatrix} v_{a,e} & v_{zi,e} & v_{zj,e} \end{bmatrix}^T \tag{4.4}$$

$$\boldsymbol{v}_p = \begin{bmatrix} v_{a,p} & v_{zi,p} & v_{zj,p} \end{bmatrix}^T \tag{4.5}$$

$v_{a,e}$ is the elastic axial deformation, and $v_{zi,e}$ and $v_{zj,e}$ are the elastic flexural deformations about the $z$-axis at end $i$ and end $j$, respectively. $v_{a,p}$ is the plastic axial deformation, and

$v_{zi,p}$ and $v_{zj,p}$ are the plastic flexural deformations about the $z$-axis at end $i$ and end $j$, respectively.

Consistent with the series model assumption of plasticity theory, the forces of the two components are equal at all times:

$$\boldsymbol{q} = \boldsymbol{q}_e = \boldsymbol{q}_p \tag{4.6}$$

$\boldsymbol{q}_e$ denotes the element basic forces of the elastic component and $\boldsymbol{q}_p$ the basic forces of the plastic component.

#### 4.2.1.2 Constitutive relation

It is postulated that the forces in the elastic component satisfy Hook's law with a stiffness equal to the elastic frame element stiffness $\mathbf{k}_e$, that is:

$$\boldsymbol{q} = \mathbf{k}_e \boldsymbol{v}_e = \mathbf{k}_e \left(\boldsymbol{v} - \boldsymbol{v}_p\right) \tag{4.7}$$

where $\mathbf{k}_e$ is given by:

$$\mathbf{k}_e = \begin{bmatrix} \frac{EA}{L} & 0 & 0 \\ 0 & \frac{4EI_z}{L} & \frac{2EI_z}{L} \\ 0 & \frac{2EI_z}{L} & \frac{4EI_z}{L} \end{bmatrix} \tag{4.8}$$

Analogous to the resultant plasticity beam element formulation presented in Chapter 3, the two plastic hinges can be offset from the element ends to account for the spread of inelasticity at the element ends and model more accurately the post yield response. Denoting the offset ratios by $\chi_i$ and $\chi_j$, the hinges are located at a distance of $\chi_i L$ and $\chi_j L$ from end $i$ and end $j$, respectively, as depicted in Figure 4.2.

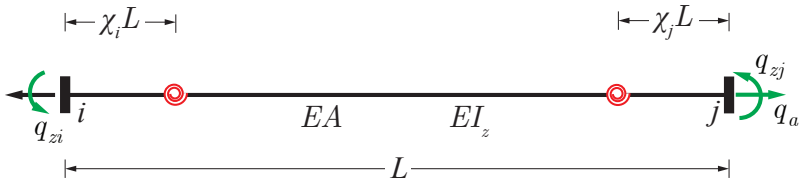


Figure 4.2: 2d resultant plasticity column element with plastic hinge offsets

In the absence of element loading, the axial force distribution along the element is constant and the bending moment distribution is linear, as illustrated in Figure 4.3.

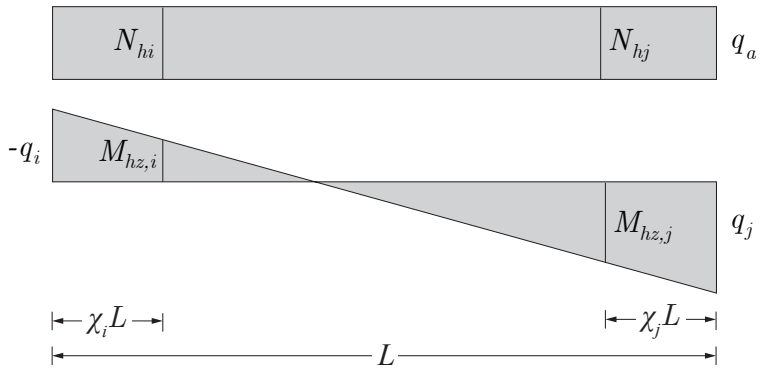


Figure 4.3: Axial force and bending moment interpolation at plastic hinge locations

Accordingly, the internal forces at the plastic hinge near end $i$ can be determined from the basic forces at the element ends $\boldsymbol{q}$ by linear interpolation

$$\boldsymbol{s}_{hi} = \begin{pmatrix} N_{hi} \\ M_{hz,i} \end{pmatrix} = \mathbf{b}_{hi}\boldsymbol{q} \tag{4.9}$$

where $N_{hi}$ and $M_{hz,i}$ are the axial force and bending moment values at the plastic hinge located near end $i$, respectively; $\boldsymbol{s}_{hi}$ is the vector of hinge internal forces near end $i$, and the interpolation matrix at $i$, $\mathbf{b}_{hi}$, is given by:

$$\mathbf{b}_{hi} = \begin{bmatrix} 1 & 0 & 0 \\ 0 & \chi_i - 1 & \chi_i \end{bmatrix} \tag{4.10}$$

Similarly, the internal forces at the hinge near end $j$ can be obtained as:

$$\boldsymbol{s}_{hj} = \begin{pmatrix} N_{hj} \\ M_{hz,j} \end{pmatrix} = \mathbf{b}_{hj}\boldsymbol{q} \tag{4.11}$$

with

$$\mathbf{b}_{hj} = \begin{bmatrix} 1 & 0 & 0 \\ 0 & -\chi_j & 1 - \chi_j \end{bmatrix} \tag{4.12}$$

In a more compact form, one can write:

$$\boldsymbol{s}_h = \begin{pmatrix} \boldsymbol{s}_{hi} \\ \boldsymbol{s}_{hj} \end{pmatrix} = \mathbf{b}_h\boldsymbol{q} \tag{4.13}$$

with

$$\mathbf{b}_h = \begin{bmatrix} \mathbf{b}_{hi} \\ \mathbf{b}_{hj} \end{bmatrix} \tag{4.14}$$

The vector of hinge deformations $\boldsymbol{e}_h$ that is work equivalent to $\boldsymbol{s}_h$ cannot be directly computed from the element deformations $\boldsymbol{v}$, but the principle of virtual work requires that

$$\boldsymbol{v} = \mathbf{b}_h^T \boldsymbol{e}_h \tag{4.15}$$

Similarly, introducing a vector of plastic hinge deformations $\boldsymbol{e}_{hp}$, these need to be related to the element plastic deformations $\boldsymbol{v}_p$ through

$$\boldsymbol{v}_p = \mathbf{b}_h^T \boldsymbol{e}_{hp} \tag{4.16}$$

As a result, $\boldsymbol{e}_h$ and $\boldsymbol{e}_{hp}$ can be seen as having the following components:

$$\boldsymbol{e}_h = \begin{pmatrix} \boldsymbol{e}_{hi} \\ \boldsymbol{e}_{hj} \end{pmatrix} \quad ; \quad \boldsymbol{e}_{hi} = \begin{bmatrix} \delta_{h,i} & \theta_{hz,i} \end{bmatrix}^T \quad ; \quad \boldsymbol{e}_{hj} = \begin{bmatrix} \delta_{h,j} & \theta_{hz,j} \end{bmatrix}^T \tag{4.17}$$

$$\boldsymbol{e}_{hp} = \begin{pmatrix} \boldsymbol{e}_{hpi} \\ \boldsymbol{e}_{hpj} \end{pmatrix} \quad ; \quad \boldsymbol{e}_{hpi} = \begin{bmatrix} \delta_{hp,i} & \theta_{hpz,i} \end{bmatrix}^T \quad ; \quad \boldsymbol{e}_{hpj} = \begin{bmatrix} \delta_{hp,j} & \theta_{hpz,j} \end{bmatrix}^T \tag{4.18}$$

where $\delta$ denotes the axial deformations and $\theta$ denotes rotations.

Combining Equations (4.7), (4.13), (4.15) and (4.16) gives a new constitutive relation for the force and deformations at the hinges. Accordingly,

$$\boldsymbol{s}_h = \mathbf{k}_{he} \left( \boldsymbol{e}_h - \boldsymbol{e}_{hp} \right) \tag{4.19}$$

where

$$\mathbf{k}_{he} = \mathbf{b}_h \mathbf{k}_e \mathbf{b}_h^T \tag{4.20}$$

#### 4.2.1.3 Yield function

The yield criteria are defined based on the evolution of the internal forces at the two plastic hinges. Let $\mathbf{f} : \mathbb{R}^4 \times \mathbb{R}^4 \times (\mathbb{R}^+)^2 \to \mathbb{R}^2$:

$$\mathbf{f}\left(\boldsymbol{s}_h, \boldsymbol{s}_{bk}, \boldsymbol{\alpha}\right) = \begin{pmatrix} f_i\left(\boldsymbol{s}_{hi}, \boldsymbol{s}_{bk,i}, \boldsymbol{\alpha}\right) \\ f_j\left(\boldsymbol{s}_{hj}, \boldsymbol{s}_{bk,j}, \boldsymbol{\alpha}\right) \end{pmatrix} = \begin{pmatrix} M_{pz,i}\phi_i\left(\boldsymbol{s}_{hi} - \boldsymbol{s}_{bk,i}\right) \\ M_{pz,j}\phi_j\left(\boldsymbol{s}_{hj} - \boldsymbol{s}_{bk,j}\right) \end{pmatrix} - \left(\boldsymbol{M}_{pz} + 2\mathbf{H}_{hi}\boldsymbol{\alpha}\right) \tag{4.21}$$

where:

- $\boldsymbol{s}_{bk,i} = \begin{bmatrix} N_{bk,i} & M_{bk,zi} \end{bmatrix}^T$ are the back forces at the hinge near end $i$;
- $\boldsymbol{s}_{bk,j} = \begin{bmatrix} N_{bk,j} & M_{bk,zj} \end{bmatrix}^T$ are the back forces at the hinge near end $j$;
- $\boldsymbol{M}_{pz} = \begin{bmatrix} M_{pz,i} & M_{pz,j} \end{bmatrix}^T$ are the plastic flexural capacities at end $i$ and end $j$;
- $\boldsymbol{\alpha} = \begin{bmatrix} \alpha_i & \alpha_j \end{bmatrix}^T$ are two internal isotropic hardening variables;
- $\mathbf{H}_{hi}$ is 2x2 matrix defining the isotropic hardening properties of the hinges;

- $\phi_i : \mathbb{R}^2 \to \mathbb{R}$ is a unitless polynomial function of the internal forces $\boldsymbol{s}_i$ defined by:

$$\boldsymbol{s}_i = \begin{pmatrix} N_i \\ M_{zi} \end{pmatrix} \mapsto \phi_i(\boldsymbol{s}_i) = \sum_m a_{i,m} \left| \frac{N_i}{N_{p,i}} \right|^{b_{i,m}} \left| \frac{M_{zi}}{M_{pz,i}} \right|^{c_{i,m}} \tag{4.22}$$

  where $a_{i,m}$, $b_{i,m}$, and $c_{i,m}$ are sets of user defined coefficients that characterize the polynomial approximation of the $N$-$M$ interaction diagram near end $i$, and $N_{p,i}$ is the plastic axial capacity at end $i$.

- $\phi_j : \mathbb{R}^2 \to \mathbb{R}$ is a unitless polynomial function of the internal forces $\boldsymbol{s}_j$ defined by:

$$\boldsymbol{s}_j = \begin{pmatrix} N_j \\ M_{zj} \end{pmatrix} \mapsto \phi_j(\boldsymbol{s}_j) = \sum_m a_{j,m} \left| \frac{N_j}{N_{p,j}} \right|^{b_{j,m}} \left| \frac{M_{zj}}{M_{pz,j}} \right|^{c_{j,m}} \tag{4.23}$$

  where $a_{j,m}$, $b_{j,m}$, and $c_{j,m}$ are sets of user defined coefficients that characterize the polynomial approximation of $N$-$M$ interaction diagram near end $j$, and $N_{p,j}$ is the plastic axial capacity at end $j$.

The yield criteria in Equation (4.21) can be rewritten more compactly as

$$\mathbf{f}(\boldsymbol{s}_h, \boldsymbol{s}_{bk}, \boldsymbol{\alpha}) = \text{diag}(\boldsymbol{M}_{pz})\boldsymbol{\phi}(\boldsymbol{s}_h - \boldsymbol{s}_{bk}) - (\boldsymbol{M}_{pz} + 2\mathbf{H}_{hi}\boldsymbol{\alpha}) \tag{4.24}$$

where

$$\text{diag}(\boldsymbol{M}_{pz}) = \begin{bmatrix} M_{pz,i} & 0 \\ 0 & M_{pz,j} \end{bmatrix} \tag{4.25}$$

and $\boldsymbol{\phi} : \mathbb{R}^4 \to (\mathbb{R}^+)^2$:

$$\boldsymbol{s} = \begin{pmatrix} \boldsymbol{s}_i \\ \boldsymbol{s}_j \end{pmatrix} \mapsto \boldsymbol{\phi}(\boldsymbol{s}) = \begin{pmatrix} \phi_i(\boldsymbol{s}_i) \\ \phi_j(\boldsymbol{s}_j) \end{pmatrix} \tag{4.26}$$

The corresponding set of admissible solutions is

$$\mathbb{E}_{\boldsymbol{s}_h} = \{(\boldsymbol{s}_h, \boldsymbol{s}_{bk}, \boldsymbol{\alpha}) \in \mathbb{R}^4 \times \mathbb{R}^4 \times (\mathbb{R}^+)^2 \mid \mathbf{f}(\boldsymbol{s}_h, \boldsymbol{s}_{bk}, \boldsymbol{\alpha}) \leq \mathbf{0}\} \tag{4.27}$$

Accordingly, the elastic domain takes the form:

$$\text{int}(\mathbb{E}_{\boldsymbol{s}_h}) = \{(\boldsymbol{s}_h, \boldsymbol{s}_{bk}, \boldsymbol{\alpha}) \in \mathbb{R}^4 \times \mathbb{R}^4 \times (\mathbb{R}^+)^2 \mid \mathbf{f}(\boldsymbol{s}_h, \boldsymbol{s}_{bk}, \boldsymbol{\alpha}) < \mathbf{0}\} \tag{4.28}$$

whereas the yield surface is defined as:

$$\begin{aligned} \partial\mathbb{E}_{\boldsymbol{s}_h} = \{(\boldsymbol{s}_h, \boldsymbol{s}_{bk}, \boldsymbol{\alpha}) \in \mathbb{R}^4 \times \mathbb{R}^4 \times (\mathbb{R}^+)^2 \mid & f_i(\boldsymbol{s}_{hi}, \boldsymbol{s}_{bk,i}, \boldsymbol{\alpha}) = 0 \text{ or} \\ & f_j(\boldsymbol{s}_{hj}, \boldsymbol{s}_{bk,j}, \boldsymbol{\alpha}) = 0\} \end{aligned} \tag{4.29}$$

In agreement with Chapter 2, a suitable approximation of the yield surface is given by the polynomial

$$\phi_i(\boldsymbol{s}_i) = 1.2 \left| \frac{N_i}{N_{p,i}} \right|^2 + 1.0 \left| \frac{M_{zi}}{M_{pz,i}} \right|^2 + 3.5 \left| \frac{N_i}{N_{p,i}} \right|^2 \left| \frac{M_{zi}}{M_{pz,i}} \right|^2 \tag{4.30}$$

$$\phi_j(\boldsymbol{s}_j) = 1.2 \left| \frac{N_j}{N_{p,j}} \right|^2 + 1.0 \left| \frac{M_{zj}}{M_{pz,j}} \right|^2 + 3.5 \left| \frac{N_j}{N_{p,j}} \right|^2 \left| \frac{M_{zj}}{M_{pz,j}} \right|^2 \tag{4.31}$$

This is a suitable choice for describing the behavior of many wide-flange sections [24], [75]. Before any hardening takes place, the yield surface defined by Equation (4.29) when $\phi_i$ and $\phi_j$ are defined in Equations (4.30) and (4.31) is illustrated in Figure 4.4. The yield envelope is depicted in the relative stress resultant space under the assumption that $N_{hi} = N_{hj} = N_h$ and $N_{p,i} = N_{p,j} = N_p$.

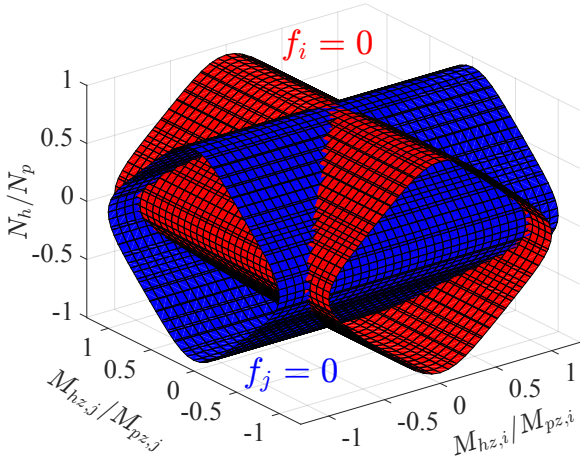


Figure 4.4: Typical initial yield envelope for 2d resultant plasticity column model

The set of admissible solutions $\mathbb{E}_{\boldsymbol{s}_h}$ is defined by the region inside the red and blue envelopes, with the red envelope describing $f_i = 0$ and the blue one describing $f_j = 0$. States outside $\mathbb{E}_{\boldsymbol{s}_h}$ are non admissible and ruled out, as prescribed by classical plasticity theory. It is noteworthy that the yield envelope $\partial\mathbb{E}_{\boldsymbol{s}_h}$ is non-smooth with singular points at the intersection between the blue and red surfaces.

The present study adopts Equations (4.30) and (4.31) when modeling the uniaxial bending behavior of wide-flange columns in subsequent examples, except where mentioned otherwise.

#### 4.2.1.4 Evolutionary equations

The associative flow rule and the hardening laws are prescribed as follows:

$$\dot{\boldsymbol{e}}_{hp} = \left(\frac{\partial \mathbf{f}}{\partial \boldsymbol{s}_h}\right)^T \dot{\boldsymbol{\gamma}} = \boldsymbol{n}\dot{\boldsymbol{\gamma}} \tag{4.32}$$

$$\dot{\boldsymbol{s}}_{bk} = \mathbf{H}_{hk}\dot{\boldsymbol{e}}_{hp} = \mathbf{H}_{hk}\boldsymbol{n}\dot{\boldsymbol{\gamma}} \tag{4.33}$$

$$\dot{\boldsymbol{\alpha}} = -\frac{\partial \mathbf{f}}{\partial\left(\mathbf{H}_{hi}\boldsymbol{\alpha}\right)}\dot{\boldsymbol{\gamma}} = 2\dot{\boldsymbol{\gamma}} \tag{4.34}$$

where $\boldsymbol{n}$ is the normal to the yield envelope, which is defined as:

$$\boldsymbol{n} = \begin{bmatrix} \boldsymbol{n}_i & \boldsymbol{n}_j \end{bmatrix} = \left( \frac{\partial \mathbf{f}}{\partial \boldsymbol{s}_h} \right)^T = \begin{bmatrix} \dfrac{\partial f_i}{\partial N_{hi}} & 0 \\ \dfrac{\partial f_i}{\partial M_{hz,i}} & 0 \\ 0 & \dfrac{\partial f_j}{\partial N_{hj}} \\ 0 & \dfrac{\partial f_j}{\partial M_{hz,j}} \end{bmatrix} \tag{4.35}$$

$\boldsymbol{\gamma} = \begin{bmatrix} \gamma_i & \gamma_j \end{bmatrix}^T \in (\mathbb{R}^+)^2$ is the vector of consistency parameters, and $\mathbf{H}_{hk}$ is a 4x4 matrix that defines the kinematic hardening properties of the hinges.

The components of the normal $\boldsymbol{n}$ can be computed as:

$$\begin{bmatrix} \dfrac{\partial f_i}{\partial N_{hi}} \\ \dfrac{\partial f_i}{\partial M_{hz,i}} \end{bmatrix} = M_{pz,i} \begin{bmatrix} \dfrac{\partial \phi_i}{\partial N_i}(\boldsymbol{s}_{hi} - \boldsymbol{s}_{bk,i}) \\ \dfrac{\partial \phi_i}{\partial M_{zi}}(\boldsymbol{s}_{hi} - \boldsymbol{s}_{bk,i}) \end{bmatrix} \quad ; \quad \begin{bmatrix} \dfrac{\partial f_j}{\partial N_{hj}} \\ \dfrac{\partial f_j}{\partial M_{hz,j}} \end{bmatrix} = M_{pz,j} \begin{bmatrix} \dfrac{\partial \phi_j}{\partial N_j}(\boldsymbol{s}_{hj} - \boldsymbol{s}_{bk,j}) \\ \dfrac{\partial \phi_j}{\partial M_{zj}}(\boldsymbol{s}_{hj} - \boldsymbol{s}_{bk,j}) \end{bmatrix} \tag{4.36}$$

The flow rule in Equation (4.32) accounts for the singularity of the yield envelope at the intersection between $f_i = 0$ and $f_j = 0$ by specifying the rate of plastic deformation as a linear combination of the normals $\boldsymbol{n}_i$ and $\boldsymbol{n}_j$ in accordance with Koiter's rule [43], i.e.,

$$\dot{\boldsymbol{e}_{hp}} = \gamma_i \boldsymbol{n}_i + \gamma_j \boldsymbol{n}_j \tag{4.37}$$

The vector of consistency parameters $\boldsymbol{\gamma}$ is assumed to obey the following Kuhn-Tucker conditions:

$$\begin{cases} \boldsymbol{\gamma} \geq \mathbf{0} \ , \ \mathbf{f}(\boldsymbol{s}_h, \boldsymbol{s}_{bk}, \boldsymbol{\alpha}) \leq \mathbf{0}, \\ \text{and} \\ \gamma_m f_m(\boldsymbol{s}_h, \boldsymbol{s}_{bk}, \boldsymbol{\alpha}) = 0 \ , \ m = i, j \end{cases} \tag{4.38}$$

In addition to the conditions given by Equation (4.38), $\boldsymbol{\gamma}$ satisfies the consistency requirement:

$$\gamma_m \dot{f}_m(\boldsymbol{s}_h, \boldsymbol{s}_{bk}, \boldsymbol{\alpha}) = 0 \ , \ m = i, j \tag{4.39}$$

#### 4.2.1.5 Kinematic and isotropic hardening parameters

Referring to Section 3.3.1.5 of Chapter 3, the matrices $\mathbf{H}_{hk}$ and $\mathbf{H}_{hi}$ that control the kinematic and isotropic hardening properties of the plastic hinges are expressed in terms of two other matrices, $\mathbf{H}_k$ and $\mathbf{H}_i$, that directly control the hardening behavior of the element ends. Accordingly, $\mathbf{H}_{hk}$ is set to:

$$\mathbf{H}_{hk} = \mathbf{b}_h \mathbf{H}_k \mathbf{b}_h^T \tag{4.40}$$

with

$$\mathbf{H}_k = \begin{bmatrix} \dfrac{EA}{L} & 0 & 0 \\ 0 & \dfrac{6EI_z}{L} & 0 \\ 0 & 0 & \dfrac{6EI_z}{L} \end{bmatrix} \mathbf{H}_{kr} \quad ; \quad \mathbf{H}_{kr} = \begin{bmatrix} H_{kr,a} & 0 & 0 \\ 0 & H_{kr,zi} & 0 \\ 0 & 0 & H_{kr,zj} \end{bmatrix} \tag{4.41}$$

Depending on the expected curvature profile of the column element, $\mathbf{H}_{hi}$ is set to one of the following expressions:

$$\mathbf{H}_{hi} = \begin{cases} \boldsymbol{n}_{SC}^T \mathbf{b}_h \mathbf{H}_i \mathbf{b}_h^T \boldsymbol{n}_{SC} & \text{for single curvature bending} \\ \boldsymbol{n}_{DC}^T \mathbf{b}_h \mathbf{H}_i \mathbf{b}_h^T \boldsymbol{n}_{DC} & \text{for double curvature bending} \end{cases} \tag{4.42}$$

in which

$$\boldsymbol{n}_{SC} = \begin{bmatrix} 0 & 0 \\ 1 & 0 \\ 0 & 0 \\ 0 & 1 \end{bmatrix} \quad ; \quad \boldsymbol{n}_{DC} = \begin{bmatrix} 0 & 0 \\ 1 & 0 \\ 0 & 0 \\ 0 & -1 \end{bmatrix} \tag{4.43}$$

$$\mathbf{H}_i = \frac{6EI_z}{L} \mathbf{H}_{ir} \quad ; \quad \mathbf{H}_{ir} = \begin{bmatrix} 0 & 0 & 0 \\ 0 & H_{ir,i} & 0 \\ 0 & 0 & H_{ir,j} \end{bmatrix} \tag{4.44}$$

### 4.2.2 Concentrated resultant force plasticity column element for biaxial flexure and axial force

The 2d column resultant plasticity model is extended to account for biaxial bending. To this end, the following modifications are introduced. The 3d column model uses six kinematic variables $\boldsymbol{v}$ with the following components:

$$\boldsymbol{v} = \begin{bmatrix} v_a & v_{zi} & v_{zj} & v_{yi} & v_{yj} & v_t \end{bmatrix}^T \tag{4.45}$$

$v_a$ is the axial deformation; $v_{zi}$ and $v_{zj}$ are the flexural deformations about the $z$-axis at end $i$ and end $j$ of the element, respectively; $v_{yi}$ and $v_{yj}$ are the flexural deformations about the $y$-axis at end $i$ and end $j$ of the element, respectively; and $v_t$ is the angle of twist about the $x$-axis. The axial deformation has units of length, whereas the remaining deformations are rotations with units of radians and with their sign defined with the right hand screw rule.

The corresponding element forces are grouped into the vector $\boldsymbol{q}$ with the following components:

$$\boldsymbol{q} = \begin{bmatrix} q_a & q_{zi} & q_{zj} & q_{yi} & q_{yj} & q_t \end{bmatrix}^T \tag{4.46}$$

as illustrated in Figure 4.5, where $q_a$ designates the axial force resultant; $q_{zi}$ and $q_{zj}$ are the flexural forces about the $z$-axis at end $i$ and $j$, respectively; $q_{yi}$ and $q_{yj}$ are the flexural

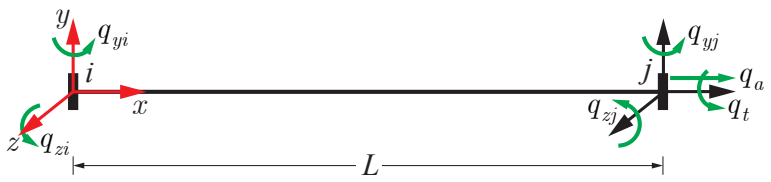


Figure 4.5: Kinematic variables and basic forces for 3d column element

forces about the $y$-axis at end $i$ and $j$, respectively; and $q_t$ is the torsional moment about the $x$-axis.

The present formulation assumes that the torsional response is linear elastic and uncoupled from the response of the remaining basic forces. Consequently, for any given angle of twist $v_t$ and in the absence of initial torsional deformation, the torsional basic force $q_t$ can be computed from

$$q_t = \frac{GJ_p}{L} v_t \tag{4.47}$$

where $G$ is the shear modulus of the material and $J_p$ is the polar moment of area of the cross-section. The response of the five remaining basic forces $\boldsymbol{q}_{in} = \begin{bmatrix} q_a & q_{zi} & q_{zj} & q_{yi} & q_{yj} \end{bmatrix}^T$ is however inelastic and computed separately using the resultant plasticity model presented hereafter.

#### 4.2.2.1 Series model of element deformations

The inelastic element deformations $\boldsymbol{v}_{in} = \begin{bmatrix} v_a & v_{zi} & v_{zj} & v_{yi} & v_{yj} \end{bmatrix}^T$ are decomposed into the sum of an elastic deformation vector $\boldsymbol{v}_e$ and a plastic deformation vector $\boldsymbol{v}_p$, such that:

$$\boldsymbol{v}_{in} = \boldsymbol{v}_e + \boldsymbol{v}_p \tag{4.48}$$

$$\boldsymbol{v}_e = \begin{bmatrix} v_{a,e} & v_{zi,e} & v_{zj,e} & v_{yi,e} & v_{yj,e} \end{bmatrix}^T \tag{4.49}$$

$$\boldsymbol{v}_p = \begin{bmatrix} v_{a,p} & v_{zi,p} & v_{zj,p} & v_{yi,p} & v_{yj,p} \end{bmatrix}^T \tag{4.50}$$

and the elastic and plastic components of the inelastic basic forces are equal:

$$\boldsymbol{q}_{in} = \boldsymbol{q}_e = \boldsymbol{q}_p \tag{4.51}$$

#### 4.2.2.2 Constitutive relation

It is postulated that the forces in the elastic component satisfy Hook's law with a stiffness equal to the elastic frame element stiffness corresponding to the inelastic degrees of freedom $\mathbf{k}_{in,e}$, that is:

$$\boldsymbol{q}_{in} = \mathbf{k}_{in,e} \boldsymbol{v}_e = \mathbf{k}_{in,e} \left( \boldsymbol{v}_{in} - \boldsymbol{v}_p \right) \tag{4.52}$$

where $\mathbf{k}_{in,e}$ is given by:

$$\mathbf{k}_{in,e} = \begin{bmatrix} \frac{EA}{L} & 0 & 0 & 0 & 0 \\ 0 & \frac{4EI_z}{L} & \frac{2EI_z}{L} & 0 & 0 \\ 0 & \frac{2EI_z}{L} & \frac{4EI_z}{L} & 0 & 0 \\ 0 & 0 & 0 & \frac{4EI_y}{L} & \frac{2EI_y}{L} \\ 0 & 0 & 0 & \frac{2EI_y}{L} & \frac{4EI_y}{L} \end{bmatrix} \tag{4.53}$$

Similarly to the 2d resultant plasticity column model, the two plastic hinges can be offset from the element ends to account for the spread of inelasticity at the element ends and model more accurately the post yield response. Denoting the offset ratios by $\chi_i$ and $\chi_j$, the hinges are located at a distance of $\chi_i L$ and $\chi_j L$ from end $i$ and end $j$, respectively, as depicted in Figure 4.6.

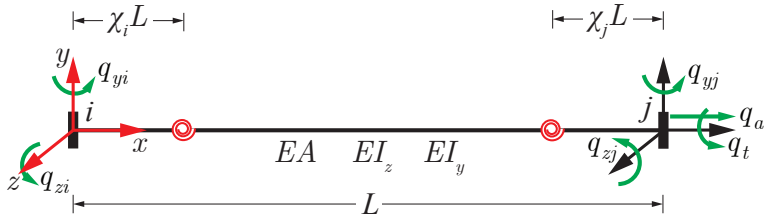


Figure 4.6: 3d resultant plasticity column element with plastic hinge offsets

The internal forces at the plastic hinge near end $i$ can be determined from the basic forces at the element ends $\boldsymbol{q}_{in}$ by linear interpolation

$$\boldsymbol{s}_{hi} = \begin{pmatrix} N_{hi} \\ M_{hz,i} \\ M_{hy,i} \end{pmatrix} = \mathbf{b}_{hi}\boldsymbol{q}_{in} \tag{4.54}$$

where $N_{hi}$, $M_{hz,i}$ and $M_{hy,i}$ are the axial force and bending moment values at the plastic hinge located near end $i$, respectively; $\boldsymbol{s}_{hi}$ is the vector of hinge internal forces near end $i$, and the interpolation matrix at $i$, $\mathbf{b}_{hi}$, is given by:

$$\mathbf{b}_{hi} = \begin{bmatrix} 1 & 0 & 0 & 0 & 0 \\ 0 & \chi_i - 1 & \chi_i & 0 & 0 \\ 0 & 0 & 0 & \chi_i - 1 & \chi_i \end{bmatrix} \tag{4.55}$$

Similarly, the internal forces at the hinge near end $j$ can be obtained as:

$$\boldsymbol{s}_{hj} = \begin{pmatrix} N_{hj} \\ M_{hz,j} \\ M_{hy,j} \end{pmatrix} = \mathbf{b}_{hj}\boldsymbol{q}_{in} \tag{4.56}$$

with

$$\mathbf{b}_{hj} = \begin{bmatrix} 1 & 0 & 0 & 0 & 0 \\ 0 & -\chi_j & 1-\chi_j & 0 & 0 \\ 0 & 0 & 0 & -\chi_j & 1-\chi_j \end{bmatrix} \tag{4.57}$$

In a more compact form, one can write:

$$\boldsymbol{s}_h = \begin{pmatrix} \boldsymbol{s}_{hi} \\ \boldsymbol{s}_{hj} \end{pmatrix} = \mathbf{b}_h\boldsymbol{q}_{in} \tag{4.58}$$

with

$$\mathbf{b}_h = \begin{bmatrix} \mathbf{b}_{hi} \\ \mathbf{b}_{hj} \end{bmatrix} \tag{4.59}$$

The vectors of hinge deformations $\boldsymbol{e}_h$ and plastic hinge deformations $\boldsymbol{e}_{hp}$ that are work equivalent to $\boldsymbol{s}_h$ satisfy the following relations:

$$\boldsymbol{v} = \mathbf{b}_h^T\boldsymbol{e}_h \tag{4.60}$$

$$\boldsymbol{v}_p = \mathbf{b}_h^T\boldsymbol{e}_{hp} \tag{4.61}$$

$\boldsymbol{e}_h$ and $\boldsymbol{e}_{hp}$ have the following components:

$$\boldsymbol{e}_h = \begin{pmatrix} \boldsymbol{e}_{hi} \\ \boldsymbol{e}_{hj} \end{pmatrix} \quad ; \quad \boldsymbol{e}_{hi} = \begin{bmatrix} \delta_{h,i} & \theta_{hz,i} & \theta_{hy,i} \end{bmatrix}^T \quad ; \quad \boldsymbol{e}_{hj} = \begin{bmatrix} \delta_{h,j} & \theta_{hz,j} & \theta_{hy,j} \end{bmatrix}^T \tag{4.62}$$

$$\boldsymbol{e}_{hp} = \begin{pmatrix} \boldsymbol{e}_{hpi} \\ \boldsymbol{e}_{hpj} \end{pmatrix} \quad ; \quad \boldsymbol{e}_{hpi} = \begin{bmatrix} \delta_{hp,i} & \theta_{hpz,i} & \theta_{hpy,i} \end{bmatrix}^T \quad ; \quad \boldsymbol{e}_{hpj} = \begin{bmatrix} \delta_{hp,j} & \theta_{hpz,j} & \theta_{hpy,j} \end{bmatrix}^T \tag{4.63}$$

where $\delta$ denotes the axial deformations and $\theta$ denotes the rotations.

Combining Equations (4.52), (4.58), (4.60) and (4.61), one can derive a new constitutive relation for the force and deformations at the hinges. Accordingly,

$$\boldsymbol{s}_h = \mathbf{k}_{he}\left(\boldsymbol{e}_h - \boldsymbol{e}_{hp}\right) \tag{4.64}$$

where

$$\mathbf{k}_{he} = \mathbf{b}_h\mathbf{k}_{in,e}\mathbf{b}_h^T \tag{4.65}$$

#### 4.2.2.3 Yield function

The yield criteria are defined based on the evolution of the internal forces at the two plastic hinges. Let $\mathbf{f} : \mathbb{R}^6 \times \mathbb{R}^6 \times (\mathbb{R}^+)^2 \to \mathbb{R}^2$:

$$\mathbf{f}\left(\boldsymbol{s}_h, \boldsymbol{s}_{bk}, \boldsymbol{\alpha}\right) = \begin{pmatrix} f_i\left(\boldsymbol{s}_{hi}, \boldsymbol{s}_{bk,i}, \boldsymbol{\alpha}\right) \\ f_j\left(\boldsymbol{s}_{hj}, \boldsymbol{s}_{bk,j}, \boldsymbol{\alpha}\right) \end{pmatrix} = \begin{pmatrix} M_{pz,i}\phi_i\left(\boldsymbol{s}_{hi} - \boldsymbol{s}_{bk,i}\right) \\ M_{pz,j}\phi_j\left(\boldsymbol{s}_{hj} - \boldsymbol{s}_{bk,j}\right) \end{pmatrix} - \left(\boldsymbol{M}_{pz} + 2\mathbf{H}_{hi}\boldsymbol{\alpha}\right) \tag{4.66}$$

where:

- $\boldsymbol{s}_{bk,i} = \begin{bmatrix} N_{bk,i} & M_{bk,zi} & M_{bk,yi} \end{bmatrix}^T$ are the back forces at the hinge near end $i$;
- $\boldsymbol{s}_{bk,j} = \begin{bmatrix} N_{bk,j} & M_{bk,zj} & M_{bk,yj} \end{bmatrix}^T$ are the back forces at the hinge near end $j$;
- $\boldsymbol{M}_{pz} = \begin{bmatrix} M_{pz,i} & M_{pz,j} \end{bmatrix}^T$ are the plastic flexural capacities about the z-axis at end $i$ and end $j$;
- $\boldsymbol{\alpha} = \begin{bmatrix} \alpha_i & \alpha_j \end{bmatrix}^T$ are two internal isotropic hardening variables;
- $\mathbf{H}_{hi}$ is 2x2 matrix defining the isotropic hardening properties of the hinges;
- $\phi_i : \mathbb{R}^3 \to \mathbb{R}$ is a unitless polynomial function of the internal forces $\boldsymbol{s}_i$ defined by:

$$\boldsymbol{s}_i = \begin{pmatrix} N_i \\ M_{zi} \\ M_{yi} \end{pmatrix} \mapsto \phi_i\left(\boldsymbol{s}_i\right) = \sum_m a_{i,m} \left|\frac{N_i}{N_{p,i}}\right|^{b_{i,m}} \left|\frac{M_{zi}}{M_{pz,i}}\right|^{c_{i,m}} \left|\frac{M_{yi}}{M_{py,i}}\right|^{d_{i,m}} \tag{4.67}$$

  where $a_{i,m}$, $b_{i,m}$, $c_{i,m}$ and $d_{i,m}$ are sets of user defined coefficients that determine the shape of the $N$-$M$ interaction diagram near end $i$; $N_{p,i}$ is the plastic axial capacity at end $i$; and $M_{py,i}$ is the plastic flexural capacity about the y-axis at end $i$.

- $\phi_j : \mathbb{R}^3 \to \mathbb{R}$ is a unitless polynomial function of the internal forces $\boldsymbol{s}_j$ defined by:

$$\boldsymbol{s}_j = \begin{pmatrix} N_j \\ M_{zj} \\ M_{yj} \end{pmatrix} \mapsto \phi_j\left(\boldsymbol{s}_j\right) = \sum_m a_{j,m} \left|\frac{N_j}{N_{p,j}}\right|^{b_{j,m}} \left|\frac{M_{zj}}{M_{pz,j}}\right|^{c_{j,m}} \left|\frac{M_{yj}}{M_{py,j}}\right|^{d_{j,m}} \tag{4.68}$$

  where $a_{j,m}$, $b_{j,m}$, $c_{j,m}$ and $d_{j,m}$ are sets of user defined coefficients that determine the shape of the $N$-$M$ interaction diagram near end $j$; $N_{p,j}$ is the plastic axial capacity at end $j$; and $M_{py,j}$ is the plastic flexural capacity about the y-axis at end $j$.

The yield criteria in Equation (4.66) can be rewritten more compactly as

$$\mathbf{f}\left(\boldsymbol{s}_h, \boldsymbol{s}_{bk}, \boldsymbol{\alpha}\right) = \mathrm{diag}(\boldsymbol{M}_{pz})\boldsymbol{\phi}\left(\boldsymbol{s}_h - \boldsymbol{s}_{bk}\right) - \left(\boldsymbol{M}_{pz} + 2\mathbf{H}_{hi}\boldsymbol{\alpha}\right) \tag{4.69}$$

with $\boldsymbol{\phi} : \mathbb{R}^6 \to (\mathbb{R}^+)^2$:

$$\boldsymbol{s} = \begin{pmatrix} \boldsymbol{s}_i \\ \boldsymbol{s}_j \end{pmatrix} \mapsto \boldsymbol{\phi}\left(\boldsymbol{s}\right) = \begin{pmatrix} \phi_i\left(\boldsymbol{s}_i\right) \\ \phi_j\left(\boldsymbol{s}_j\right) \end{pmatrix} \tag{4.70}$$

The corresponding set of admissible solutions is

$$\mathbb{E}_{\boldsymbol{s}_h} = \{(\boldsymbol{s}_h, \boldsymbol{s}_{bk}, \boldsymbol{\alpha}) \in \mathbb{R}^6 \times \mathbb{R}^6 \times (\mathbb{R}^+)^2 \mid \mathbf{f}(\boldsymbol{s}_h, \boldsymbol{s}_{bk}, \boldsymbol{\alpha}) \leq \mathbf{0}\} \tag{4.71}$$

Accordingly, the elastic domain takes the form:

$$\text{int}(\mathbb{E}_{\boldsymbol{s}_h}) = \{(\boldsymbol{s}_h, \boldsymbol{s}_{bk}, \boldsymbol{\alpha}) \in \mathbb{R}^6 \times \mathbb{R}^6 \times (\mathbb{R}^+)^2 \mid \mathbf{f}(\boldsymbol{s}_h, \boldsymbol{s}_{bk}, \boldsymbol{\alpha}) < \mathbf{0}\} \tag{4.72}$$

whereas the yield surface is defined as:

$$\begin{aligned}\partial\mathbb{E}_{\boldsymbol{s}_h} = \{(\boldsymbol{s}_h, \boldsymbol{s}_{bk}, \boldsymbol{\alpha}) \in \mathbb{R}^6 \times \mathbb{R}^6 \times (\mathbb{R}^+)^2 \mid & f_i(\boldsymbol{s}_{hi}, \boldsymbol{s}_{bk,i}, \boldsymbol{\alpha}) = 0 \text{ or} \\ & f_j(\boldsymbol{s}_{hj}, \boldsymbol{s}_{bk,j}, \boldsymbol{\alpha}) = 0\}\end{aligned} \tag{4.73}$$

States outside $\mathbb{E}_{\boldsymbol{s}_h}$ are non admissible and ruled out, as prescribed by classical plasticity theory.

In agreement with Chapter 2, a suitable approximation for the yield surface polynomial functions for wide-flange sections is given by the polynomial

$$\begin{aligned}\phi_i(\boldsymbol{s}_i) = {} & 1.2\left|\frac{N_i}{N_{p,i}}\right|^2 + 1.0\left|\frac{M_{zi}}{M_{pz,i}}\right|^2 + 1.0\left|\frac{M_{yi}}{M_{py,i}}\right|^5 \\ & + 3.5\left|\frac{N_i}{N_{p,i}}\right|^2\left|\frac{M_{zi}}{M_{pz,i}}\right|^2 + \frac{6A_f}{A_f + A_w}\left|\frac{N_i}{N_{p,i}}\right|^3\left|\frac{M_{zi}}{M_{pz,i}}\right|^3 + 3.0\left|\frac{M_{zi}}{M_{pz,i}}\right|^2\left|\frac{M_{yi}}{M_{py,i}}\right|^2\end{aligned} \tag{4.74}$$

$$\begin{aligned}\phi_j(\boldsymbol{s}_j) = {} & 1.2\left|\frac{N_j}{N_{p,j}}\right|^2 + 1.0\left|\frac{M_{zj}}{M_{pz,j}}\right|^2 + 1.0\left|\frac{M_{yj}}{M_{py,j}}\right|^5 \\ & + 3.5\left|\frac{N_j}{N_{p,j}}\right|^2\left|\frac{M_{zj}}{M_{pz,j}}\right|^2 + \frac{6A_f}{A_f + A_w}\left|\frac{N_j}{N_{p,j}}\right|^3\left|\frac{M_{zj}}{M_{pz,j}}\right|^3 + 3.0\left|\frac{M_{zj}}{M_{pz,j}}\right|^2\left|\frac{M_{yj}}{M_{py,j}}\right|^2\end{aligned} \tag{4.75}$$

where $A_f$ is the area of the two flanges and $A_w$ is the area of the web of the wide-flange cross section. The present study uses Equations (4.74) and (4.75) to represent the biaxial bending behavior of wide-flange columns in subsequent examples, except where mentioned otherwise.

#### 4.2.2.4 Evolutionary equations

The associative flow rule and the hardening laws are prescribed as follows:

$$\dot{\boldsymbol{e}}_{hp} = \left(\frac{\partial \mathbf{f}}{\partial \boldsymbol{s}_h}\right)^T \boldsymbol{\gamma} = \boldsymbol{n}\boldsymbol{\gamma} \tag{4.76}$$

$$\dot{\boldsymbol{s}}_{bk} = \mathbf{H}_{hk}\dot{\boldsymbol{e}}_{hp} = \mathbf{H}_{hk}\boldsymbol{n}\boldsymbol{\gamma} \tag{4.77}$$

$$\dot{\boldsymbol{\alpha}} = -\frac{\partial \mathbf{f}}{\partial\left(\mathbf{H}_{hi}\boldsymbol{\alpha}\right)}\boldsymbol{\gamma} = 2\boldsymbol{\gamma} \tag{4.78}$$

where $\boldsymbol{n}$ is the normal to the yield envelope, which is defined as:

$$\boldsymbol{n} = \begin{bmatrix} \boldsymbol{n}_i & \boldsymbol{n}_j \end{bmatrix} = \left( \frac{\partial \mathbf{f}}{\partial \boldsymbol{s}_h} \right)^T = \begin{bmatrix} \dfrac{\partial f_i}{\partial N_{hi}} & 0 \\ \dfrac{\partial f_i}{\partial M_{hz,i}} & 0 \\ \dfrac{\partial f_i}{\partial M_{hy,i}} & 0 \\ 0 & \dfrac{\partial f_j}{\partial N_{hj}} \\ 0 & \dfrac{\partial f_j}{\partial M_{hz,j}} \\ 0 & \dfrac{\partial f_j}{\partial M_{hy,j}} \end{bmatrix} \tag{4.79}$$

$\boldsymbol{\gamma} = \begin{bmatrix} \gamma_i & \gamma_j \end{bmatrix}^T \in (\mathbb{R}^+)^2$ is the vector of consistency parameters, and $\mathbf{H}_{hk}$ is a 6x6 matrix that defines the kinematic hardening properties of the hinges.

The components of the normal $\boldsymbol{n}$ can be computed as:

$$\begin{bmatrix} \dfrac{\partial f_i}{\partial N_{hi}} \\ \dfrac{\partial f_i}{\partial M_{hz,i}} \\ \dfrac{\partial f_i}{\partial M_{hy,i}} \end{bmatrix} = M_{pz,i} \begin{bmatrix} \dfrac{\partial \phi_i}{\partial N_i}(\boldsymbol{s}_{hi} - \boldsymbol{s}_{bk,i}) \\ \dfrac{\partial \phi_i}{\partial M_{zi}}(\boldsymbol{s}_{hi} - \boldsymbol{s}_{bk,i}) \\ \dfrac{\partial \phi_i}{\partial M_{yi}}(\boldsymbol{s}_{hi} - \boldsymbol{s}_{bk,i}) \end{bmatrix} \quad ; \quad \begin{bmatrix} \dfrac{\partial f_j}{\partial N_{hj}} \\ \dfrac{\partial f_j}{\partial M_{hz,j}} \\ \dfrac{\partial f_j}{\partial M_{hy,j}} \end{bmatrix} = M_{pz,j} \begin{bmatrix} \dfrac{\partial \phi_j}{\partial N_j}(\boldsymbol{s}_{hj} - \boldsymbol{s}_{bk,j}) \\ \dfrac{\partial \phi_j}{\partial M_{zj}}(\boldsymbol{s}_{hj} - \boldsymbol{s}_{bk,j}) \\ \dfrac{\partial \phi_j}{\partial M_{yj}}(\boldsymbol{s}_{hj} - \boldsymbol{s}_{bk,j}) \end{bmatrix} \tag{4.80}$$

The flow rule in Equation (4.76) accounts for the singularity of the yield envelope at the intersection between $f_i = 0$ and $f_j = 0$ by specifying the rate of plastic deformation as a linear combination of the normals $\boldsymbol{n}_i$ and $\boldsymbol{n}_j$ in accordance with Koiter's rule [43], i.e.,

$$\dot{\boldsymbol{e}_{hp}} = \gamma_i \boldsymbol{n}_i + \gamma_j \boldsymbol{n}_j \tag{4.81}$$

The vector of consistency parameters $\boldsymbol{\gamma}$ is assumed to obey the following Kuhn-Tucker conditions:

$$\begin{cases} \boldsymbol{\gamma} \geq \mathbf{0} \ , \ \mathbf{f}(\boldsymbol{s}_h, \boldsymbol{s}_{bk}, \boldsymbol{\alpha}) \leq \mathbf{0}, \\ \text{and} \\ \gamma_m f_m(\boldsymbol{s}_h, \boldsymbol{s}_{bk}, \boldsymbol{\alpha}) = 0 \ , \ m = i, j \end{cases} \tag{4.82}$$

In addition to the conditions given by Equation (4.82), $\boldsymbol{\gamma}$ satisfies the consistency requirement:

$$\gamma_m \dot{f}_m(\boldsymbol{s}_h, \boldsymbol{s}_{bk}, \boldsymbol{\alpha}) = 0 \ , \ m = i, j \tag{4.83}$$

#### 4.2.2.5 Kinematic and isotropic hardening parameters

Referring to Section 3.3.1.5 of Chapter 3, the matrices $\mathbf{H}_{hk}$ and $\mathbf{H}_{hi}$ that control the kinematic and isotropic hardening properties of the plastic hinges are expressed in terms of two other matrices, $\mathbf{H}_k$ and $\mathbf{H}_i$, that directly control the hardening behavior of the element ends. Accordingly, $\mathbf{H}_{hk}$ is set to:

$$\mathbf{H}_{hk} = \mathbf{b}_h \mathbf{H}_k \mathbf{b}_h^T \tag{4.84}$$

with

$$\mathbf{H}_k = \begin{bmatrix} \frac{EA}{L} & 0 & 0 & 0 & 0 \\ 0 & \frac{6EI_z}{L} & 0 & 0 & 0 \\ 0 & 0 & \frac{6EI_z}{L} & 0 & 0 \\ 0 & 0 & 0 & \frac{6EI_y}{L} & 0 \\ 0 & 0 & 0 & 0 & \frac{6EI_y}{L} \end{bmatrix} \mathbf{H}_{kr} \tag{4.85}$$

$$\mathbf{H}_{kr} = \begin{bmatrix} H_{kr,a} & 0 & 0 & 0 & 0 \\ 0 & H_{kr,zi} & 0 & 0 & 0 \\ 0 & 0 & H_{kr,zj} & 0 & 0 \\ 0 & 0 & 0 & H_{kr,yi} & 0 \\ 0 & 0 & 0 & 0 & H_{kr,yj} \end{bmatrix} \tag{4.86}$$

Depending on the expected curvature profile of the column element, $\mathbf{H}_{hi}$ is set to one of the following expressions:

$$\mathbf{H}_{hi} = \begin{cases} \boldsymbol{n}_{SC}^T \mathbf{b}_h \mathbf{H}_i \mathbf{b}_h^T \boldsymbol{n}_{SC} & \text{for single curvature bending about z-axis} \\ \boldsymbol{n}_{DC}^T \mathbf{b}_h \mathbf{H}_i \mathbf{b}_h^T \boldsymbol{n}_{DC} & \text{for double curvature bending about z-axis} \end{cases} \tag{4.87}$$

in which

$$\boldsymbol{n}_{SC} = \begin{bmatrix} 0 & 0 \\ 1 & 0 \\ 0 & 0 \\ 0 & 0 \\ 0 & 1 \\ 0 & 0 \end{bmatrix} \quad ; \quad \boldsymbol{n}_{DC} = \begin{bmatrix} 0 & 0 \\ 1 & 0 \\ 0 & 0 \\ 0 & 0 \\ 0 & -1 \\ 0 & 0 \end{bmatrix} \tag{4.88}$$

$$\mathbf{H}_i = \frac{6EI_z}{L} \mathbf{H}_{ir} \quad ; \quad \mathbf{H}_{ir} = \begin{bmatrix} 0 & 0 & 0 & 0 & 0 \\ 0 & H_{ir,i} & 0 & 0 & 0 \\ 0 & 0 & H_{ir,j} & 0 & 0 \\ 0 & 0 & 0 & 0 & 0 \\ 0 & 0 & 0 & 0 & 0 \end{bmatrix} \tag{4.89}$$

### 4.2.3 Summary of column formulation with resultant force plasticity

Table 4.1 summarizes the formulation of the 2d and 3d resultant plasticity column models.

Table 4.2 summarizes the dimension of the various variables and parameters of the proposed 2d and 3d resultant plasticity column models.

## 4.3 Implementation

### 4.3.1 State determination with return-mapping algorithm

The column element state determination is the process of determining the element basic forces $\boldsymbol{q}$ under given element deformations $\boldsymbol{v}$ at a certain instant in time of the analysis. For the 3d column element, the focus is on determining the inelastic basic forces $\boldsymbol{q}_{in}$ under given deformations $\boldsymbol{v}_{in}$ only, as the torsional basic force $q_t$ is determined separately according to Equation (4.47). While the following derivations use the notation $\boldsymbol{q}$ and $\boldsymbol{v}$ for the basic forces and element deformations, consistent with the 2d formulation, the 3d element state determination can be obtained by substituting $\boldsymbol{q}$, $\boldsymbol{v}$ and $\mathbf{k}_e$ with $\boldsymbol{q}_{in}$, $\boldsymbol{v}_{in}$ and $\mathbf{k}_{in,e}$ in the subsequent equations. In that case, the full vector of basic forces $\boldsymbol{q}$ can then be assembled according to

$$\boldsymbol{q} = \begin{pmatrix} \boldsymbol{q}_{in} \\ q_t \end{pmatrix} \tag{4.90}$$

First, the time or pseudo-time interval of interest is discretized into a finite number of smaller intervals $\bigcup_n [t_n, t_{n+1}]$. For a typical time step $[t_n, t_{n+1}]$, the problem can be posed as follows.

1. The state of the element at time $t_n$ characterized by the basic state variables

$$\{\boldsymbol{v}_n, \boldsymbol{e}_{hp,n}, \boldsymbol{s}_{bk,n}, \boldsymbol{\alpha}_n\} = \{\boldsymbol{v}(t_n), \boldsymbol{e}_{hp}(t_n), \boldsymbol{s}_{bk}(t_n), \boldsymbol{\alpha}(t_n)\} \tag{4.91}$$

   is regarded as given and assumed to be equilibrated.

2. The element deformations increment

$$\Delta\boldsymbol{v}_{n+1} = \boldsymbol{v}_{n+1} - \boldsymbol{v}_n = \boldsymbol{v}(t_{n+1}) - \boldsymbol{v}(t_n) \tag{4.92}$$

   is considered given.

3. The objective is to update the state variables to the values $\{\boldsymbol{v}_{n+1}, \boldsymbol{e}_{hp,n+1}, \boldsymbol{s}_{bk,n+1}, \boldsymbol{\alpha}_{n+1}\}$ at time $t_{n+1}$, so as to be able to calculate the corresponding basic forces $\boldsymbol{q}_{n+1}$, in a way that is consistent with the resultant plasticity column formulation.

1. **Elastic constitutive relation**

$$\boldsymbol{s}_h = \mathbf{k}_{he}\left(\boldsymbol{e}_h - \boldsymbol{e}_{hp}\right)$$

where $\boldsymbol{s}_h$, $\boldsymbol{e}_h$, $\boldsymbol{e}_{hp}$ and $\mathbf{k}_{he}$ are given by Equations (4.13), (4.15), (4.16) and (4.20) for the 2d model and by Equations (4.58), (4.60), (4.61) and (4.65) for the 3d model.

2. **Yield condition**

$$\mathbf{f}\left(\boldsymbol{s}_h, \boldsymbol{s}_{bk}, \boldsymbol{\alpha}\right) = \mathrm{diag}(\boldsymbol{M}_{pz})\boldsymbol{\phi}\left(\boldsymbol{s}_h - \boldsymbol{s}_{bk}\right) - \left(\boldsymbol{M}_{pz} + 2\mathbf{H}_{hi}\boldsymbol{\alpha}\right)$$

where

$$\boldsymbol{\phi}\left(\boldsymbol{s}\right) = \begin{pmatrix} \phi_i\left(\boldsymbol{s}_i\right) \\ \phi_j\left(\boldsymbol{s}_j\right) \end{pmatrix}$$

and $\phi_i$ and $\phi_j$ are given by Equations (4.22) and (4.23) for the 2d model and by Equations (4.67) and (4.68) for the 3d model.

3. **Flow rule**

$$\dot{\boldsymbol{e}_{hp}} = \left(\frac{\partial \mathbf{f}}{\partial \boldsymbol{s}_h}\right)^T \boldsymbol{\gamma} = \boldsymbol{n}\boldsymbol{\gamma}$$

where $\boldsymbol{n}$ is given by Equation (4.36) for the 2d model and by Equation (4.80) for the 3d model.

4. **Kinematic and isotropic hardening laws**

$$\dot{\boldsymbol{s}_{bk}} = \mathbf{H}_{hk}\dot{\boldsymbol{e}_{hp}} = \mathbf{H}_{hk}\boldsymbol{n}\boldsymbol{\gamma}$$

$$\dot{\boldsymbol{\alpha}} = -\frac{\partial \mathbf{f}}{\partial\left(\mathbf{H}_{hi}\boldsymbol{\alpha}\right)}\boldsymbol{\gamma} = \boldsymbol{\gamma}$$

5. **Kuhn-Tucker complementarity conditions**

$$\boldsymbol{\gamma} \geq \mathbf{0}\ ,\ \mathbf{f}(\boldsymbol{s}_h, \boldsymbol{s}_{bk}, \boldsymbol{\alpha}) \leq \mathbf{0}\ ,\ \gamma_m f_m(\boldsymbol{s}_h, \boldsymbol{s}_{bk}, \boldsymbol{\alpha}) = 0\ ,\ m = i, j$$

6. **Consistency conditions**

$$\gamma_m \dot{f}_m(\boldsymbol{s}_h, \boldsymbol{s}_{bk}, \boldsymbol{\alpha}) = 0 \quad (\text{if } f_m(\boldsymbol{s}_h, \boldsymbol{s}_{bk}, \boldsymbol{\alpha}) = 0)\ ,\ m = i, j$$

Table 4.1: Resultant plasticity column model formulation

| Variable/parameter | Dimension |
|---|---|
| $v_a$, $v_{a,e/p}$ | length |
| $v_{zi/zj}$, $v_{zi/zj,e/p}$ | 1 (rotation) |
| $v_{yi/yj}$, $v_{yi/yj,e/p}$, $v_t$ | 1 (rotation) |
| $\delta_{h,i/j}$, $\delta_{hp,i/j}$ | length |
| $\theta_{hz,i/j}$, $\theta_{hpz,i/j}$ | 1 (rotation) |
| $\theta_{hy,i/j}$, $\theta_{hpy,i/j}$ | 1 (rotation) |
| $\alpha_{i/j}$, $\gamma_{i/j}$ | 1 |
| $q_a$ | force |
| $q_{zi/zj}$, $q_{yi/yj}$, $q_t$, | force $\cdot$ length |
| $N_{hi/j}$, $N_{bk,i/j}$, $N_{pi/pj}$ | force |
| $M_{hz,i/j}$, $M_{bk,zi/zj}$, $M_{pz,i/j}$ | force $\cdot$ length |
| $M_{hy,i/j}$, $M_{bk,yi/yj}$, $M_{py,i/j}$ | force $\cdot$ length |
| $H_{kr,a}$, $H_{kr,zi/zj}$, $H_{kr,yi/yj}$, $H_{ir,i/j}$ | 1 |

Table 4.2: Dimensions of resultant plasticity column model variables and parameters

Note that knowing the basic state variables $\{\boldsymbol{v}_n, \boldsymbol{e}_{hp,n}, \boldsymbol{s}_{bk,n}, \boldsymbol{\alpha}_n\}$ at time $t_n$ fully determines the element plastic deformations $\boldsymbol{v}_{p,n}$, the element basic forces $\boldsymbol{q}_n$ as well as the plastic hinge internal forces $\boldsymbol{s}_{h,n}$ at that instant, with the following relations:

$$\boldsymbol{v}_{p,n} = \mathbf{b}_h^T \boldsymbol{e}_{hp,n} \tag{4.93}$$

$$\boldsymbol{q}_n = \mathbf{k}_e(\boldsymbol{v}_n - \boldsymbol{v}_{p,n}) \tag{4.94}$$

$$\boldsymbol{s}_{h,n} = \mathbf{b}_h \boldsymbol{q}_n \tag{4.95}$$

For performing the element state determination at time $\boldsymbol{t}_{n+1}$, the discrete algorithmic counterparts of the flow rule and the hardening rules are obtained by applying the implicit backward Euler difference scheme. This gives:

$$\boldsymbol{e}_{hp,n+1} = \boldsymbol{e}_{hp,n} + \boldsymbol{n}_{n+1} \Delta\boldsymbol{\gamma} \tag{4.96}$$

$$\boldsymbol{s}_{bk,n+1} = \boldsymbol{s}_{bk,n} + \mathbf{H}_{hk} \boldsymbol{n}_{n+1} \Delta\boldsymbol{\gamma} \tag{4.97}$$

$$\boldsymbol{\alpha}_{n+1} = \boldsymbol{\alpha}_n + 2\Delta\boldsymbol{\gamma} \tag{4.98}$$

where $\Delta\boldsymbol{\gamma} = \Delta t_{n+1} \boldsymbol{\gamma}_{n+1} \geq \mathbf{0}$ is the algorithmic counterpart of the vector of consistency parameters $\boldsymbol{\gamma}$. The normal $\boldsymbol{n}_{n+1}$ is computed as

$$\boldsymbol{n}_{n+1} = \left[ \frac{\partial \mathbf{f}}{\partial \boldsymbol{s}_h} (\boldsymbol{s}_{h,n+1}, \boldsymbol{s}_{bk,n+1}) \right]^T \tag{4.99}$$

where $\boldsymbol{s}_{h,n+1}$ is obtained as

$$\boldsymbol{v}_{n+1} = \boldsymbol{v}_n + \Delta\boldsymbol{v}_{n+1} \tag{4.100}$$

$$\boldsymbol{v}_{p,n+1} = \mathbf{b}_h^T \boldsymbol{e}_{hp,n+1} \tag{4.101}$$

$$\boldsymbol{q}_{n+1} = \mathbf{k}_e(\boldsymbol{v}_{n+1} - \boldsymbol{v}_{p,n+1}) \tag{4.102}$$

$$\boldsymbol{s}_{h,n+1} = \mathbf{b}_h \boldsymbol{q}_{n+1} \tag{4.103}$$

Additionally, the variables $(\boldsymbol{s}_{h,n+1}, \boldsymbol{s}_{bk,n+1}, \boldsymbol{\alpha}_{n+1})$ are constrained by the following discrete version of the Kuhn-Tucker conditions:

$$\begin{cases} \Delta\boldsymbol{\gamma} \geq \mathbf{0} \ , \ \mathbf{f}_{n+1} = \mathbf{f}(\boldsymbol{s}_{h,n+1}, \boldsymbol{s}_{bk,n+1}, \boldsymbol{\alpha}_{n+1}) \leq \mathbf{0}, \\ \text{and} \\ \Delta\gamma_m f_{m,n+1} = 0 \ , \ m = i, j \end{cases} \tag{4.104}$$

The problem described by Equations (4.96) - (4.104) is solved using a two step return-mapping algorithm that consists of:

1. an elastic *trial* predictor, followed by
2. a plastic corrector that performs the closest point projection of the trial state onto the yield surface.

#### 4.3.1.1 Elastic predictor

The following trial elastic state is introduced by freezing the plastic flow during the given time step, i.e. setting $\Delta\boldsymbol{\gamma} = \mathbf{0}$ in Equations (4.96) - (4.98):

$$\boldsymbol{e}_{hp,n+1}^{tr} = \boldsymbol{e}_{hp,n} \tag{4.105}$$

$$\boldsymbol{s}_{bk,n+1}^{tr} = \boldsymbol{s}_{bk,n} \tag{4.106}$$

$$\boldsymbol{\alpha}_{n+1}^{tr} = \boldsymbol{\alpha}_n \tag{4.107}$$

This gives rise to the following trial elastic element plastic deformations, basic forces and hinge internal forces:

$$\boldsymbol{v}_{p,n+1}^{tr} = \mathbf{b}_h^T \boldsymbol{e}_{hp,n+1}^{tr} = \boldsymbol{v}_{p,n} \tag{4.108}$$

$$\boldsymbol{q}_{n+1}^{tr} = \mathbf{k}_e \left(\boldsymbol{v}_{n+1} - \boldsymbol{v}_{p,n+1}^{tr}\right) = \mathbf{k}_e \left(\boldsymbol{v}_{n+1} - \boldsymbol{v}_{p,n}\right) \tag{4.109}$$

$$\boldsymbol{s}_{h,n+1}^{tr} = \mathbf{b}_h \boldsymbol{q}_{n+1}^{tr} = \mathbf{k}_{he} \left(\boldsymbol{e}_{h,n+1} - \boldsymbol{e}_{hp,n}\right) \tag{4.110}$$

and the corresponding trial normal to the yield function:

$$\boldsymbol{n}_{n+1}^{tr} = \left[\frac{\partial \mathbf{f}}{\partial \boldsymbol{s}_h}(\boldsymbol{s}_{h,n+1}^{tr}, \boldsymbol{s}_{bk,n+1}^{tr})\right]^T \tag{4.111}$$

Note that this trial state may not, and in general will not, correspond to any actual, physically admissible state unless the incremental process is actually elastic. The trial yield function is then evaluated as:

$$\mathbf{f}_{n+1}^{tr} = \mathbf{f}(\boldsymbol{s}_{h,n+1}^{tr}, \boldsymbol{s}_{bk,n+1}^{tr}, \boldsymbol{\alpha}_{n+1}^{tr}) \tag{4.112}$$

If $\mathbf{f}_{n+1}^{tr} \leq \mathbf{0}$, i.e if both $f_{i,n+1}^{tr} \leq 0$ and $f_{j,n+1}^{tr} \leq 0$, the trial state is admissible and the element response is elastic. Accordingly, the state variables are equal to their trial state values, i.e.,

$$\boldsymbol{e}_{hp,n+1} = \boldsymbol{e}_{hp,n+1}^{tr} \tag{4.113}$$

$$\boldsymbol{s}_{bk,n+1} = \boldsymbol{s}_{bk,n+1}^{tr} \tag{4.114}$$

$$\boldsymbol{\alpha}_{n+1} = \boldsymbol{\alpha}_{n+1}^{tr} \tag{4.115}$$

the basic forces at the end of the time step $t_{n+1}$ are set to

$$\boldsymbol{q}_{n+1} = \boldsymbol{q}_{n+1}^{tr} \tag{4.116}$$

and the element tangent stiffness is computed according to Section 4.3.2, concluding the element state determination.

On the other hand, if $f_{i,n+1}^{tr} > 0$ or $f_{j,n+1}^{tr} > 0$, the trial state is not admissible and a plastic correction is required.

#### 4.3.1.2 Plastic corrector

If $f_{i,n+1}^{tr} > 0$ or $f_{j,n+1}^{tr} > 0$, an iterative solution is needed to enforce the Kuhn-Tucker conditions. Since the original assumption $\Delta\boldsymbol{\gamma} = \mathbf{0}$ results in a non admissible trial state, it follows that the true plastic flow $\Delta\boldsymbol{\gamma}$ must be nonzero, i.e. $\Delta\gamma_i > 0$ and/or $\Delta\gamma_j > 0$. Combining this requirement with conditions (4.104) implies that

$$f_{i,n+1} = 0 \text{ and/or } f_{j,n+1} = 0 \tag{4.117}$$

i.e. the corrected state at $t_{n+1}$ must lie on the yield surface. When $\Delta\gamma_i > 0$, the yield surface near end $i$ is said to be *active*, whereas the yield surface near end $j$ is said to be active when $\Delta\gamma_j > 0$. To identify which of $i$ and $j$ yield surfaces is active and properly enforce the Kuhn-Tucker discrete conditions, the algorithm uses an initial set of trial active yield surfaces defined as:

$$\boldsymbol{J}_{act}^{(0)} = \{m \in \{i, j\} \mid f_m^{tr} > 0\} \tag{4.118}$$

that is subsequently updated at each Newton-Raphson iteration.

Let

$$\Delta\boldsymbol{e}_{hp,n+1} = \boldsymbol{e}_{hp,n+1} - \boldsymbol{e}_{hp,n+1}^{tr} = \boldsymbol{e}_{hp,n+1} - \boldsymbol{e}_{hp,n} \tag{4.119}$$

be the required correction for the plastic hinge deformations. With the superscript $k$ indicating the iteration number, define the following residual equations for the plastic hinge

deformations, internal back forces, isotropic hardening variables and yield condition, respectively:

$$\begin{cases} \boldsymbol{R}_{ehp}^{(k)} & = -\Delta \boldsymbol{e}_{hp,n+1}^{(k)} + \boldsymbol{n}_{n+1}^{(k)} \Delta\boldsymbol{\gamma}^{(k)} \\ \boldsymbol{R}_{bk}^{(k)} & = -\boldsymbol{s}_{bk,n+1}^{(k)} + \boldsymbol{s}_{bk,n} + \mathbf{H}_{hk} \boldsymbol{n}_{n+1}^{(k)} \Delta\boldsymbol{\gamma}^{(k)} \\ \boldsymbol{R}_{\alpha}^{(k)} & = -\boldsymbol{\alpha}_{n+1}^{(k)} + \boldsymbol{\alpha}_n + 2\Delta\boldsymbol{\gamma}^{(k)} \\ \boldsymbol{R}_{f}^{(k)} & = \mathbf{f}(\boldsymbol{s}_{n+1}^{(k)}, \boldsymbol{s}_{bk,n+1}^{(k)}, \boldsymbol{\alpha}_{n+1}^{(k)}) \end{cases} \tag{4.120}$$

which are the counterparts of Equations (4.96) - (4.98) and (4.117). The definition of the residuals in Equation (4.120) assume that both plastic hinges $i$ and $j$ are active, i.e., $\boldsymbol{J}_{act}^{(k)} = \{i, j\}$. If only one plastic hinge $m \in \{i, j\}$ is active, the following substitutions are required in Equation (4.120) as well as in the subsequent derivations:

- $\boldsymbol{n} \leftarrow \boldsymbol{n}_m$
- $\Delta\boldsymbol{\gamma} \leftarrow \Delta\gamma_m$
- $\boldsymbol{\alpha} \leftarrow \alpha_m$
- $\mathbf{f} \leftarrow f_m$

Accordingly, the dimension of $\boldsymbol{R}_{\alpha}^{(k)}$ and $\boldsymbol{R}_{f}^{(k)}$ varies with the number of active yield surfaces: each describes a scalar equation if only one plastic hinge is active and two scalar equations if both hinges are active.

The vector of residuals $\boldsymbol{R}^{(k)}$ and the vector of unknowns $\boldsymbol{x}^{(k)}$ at iteration $k$ are:

$$\boldsymbol{R}^{(k)} = \begin{pmatrix} \boldsymbol{R}_{ehp}^{(k)} \\ \boldsymbol{R}_{bk}^{(k)} \\ \boldsymbol{R}_{\alpha}^{(k)} \\ \boldsymbol{R}_{f}^{(k)} \end{pmatrix} \quad ; \quad \boldsymbol{x}^{(k)} = \begin{pmatrix} \boldsymbol{s}_{h,n+1}^{(k)} \\ \boldsymbol{s}_{bk,n+1}^{(k)} \\ \boldsymbol{\alpha}_{n+1}^{(k)} \\ \Delta\boldsymbol{\gamma}^{(k)} \end{pmatrix} \tag{4.121}$$

The Newton-Raphson iterations start by initializing the unknowns to the values of the trial state, i.e.,

$$\boldsymbol{x}^{(0)} = \begin{pmatrix} \boldsymbol{s}_{h,n+1}^{(0)} \\ \boldsymbol{s}_{bk,n+1}^{(0)} \\ \boldsymbol{\alpha}_{n+1}^{(0)} \\ \Delta\boldsymbol{\gamma}^{(0)} \end{pmatrix} = \begin{pmatrix} \boldsymbol{s}_{h,n+1}^{tr} \\ \boldsymbol{s}_{bk,n+1}^{tr} \\ \boldsymbol{\alpha}_{n+1}^{tr} \\ \mathbf{0} \end{pmatrix} \tag{4.122}$$

The state variables get updated at each iteration according to

$$\boldsymbol{x}^{(k+1)} = \boldsymbol{x}^{(k)} + \delta\boldsymbol{x}^{(k)} \tag{4.123}$$

where the correction is obtained as:

$$\delta \boldsymbol{x}^{(k)} = -\left[\mathbf{J}^{(k)}\right]^{-1} \boldsymbol{R}^{(k)} \tag{4.124}$$

and $\mathbf{J}^{(k)}$ is the Jacobian of the system of nonlinear equations (4.120) at the $k$-th iteration defined as

$$\mathbf{J}^{(k)} = \frac{\partial \boldsymbol{R}^{(k)}}{\partial \boldsymbol{x}^{(k)}} = \begin{bmatrix} \dfrac{\partial \boldsymbol{R}_{ehp}^{(k)}}{\partial \boldsymbol{s}_{h,n+1}^{(k)}} & \dfrac{\partial \boldsymbol{R}_{ehp}^{(k)}}{\partial \boldsymbol{s}_{bk,n+1}^{(k)}} & \dfrac{\partial \boldsymbol{R}_{ehp}^{(k)}}{\partial \boldsymbol{\alpha}_{n+1}^{(k)}} & \dfrac{\partial \boldsymbol{R}_{ehp}^{(k)}}{\partial \Delta\boldsymbol{\gamma}^{(k)}} \\ \dfrac{\partial \boldsymbol{R}_{bk}^{(k)}}{\partial \boldsymbol{s}_{h,n+1}^{(k)}} & \dfrac{\partial \boldsymbol{R}_{bk}^{(k)}}{\partial \boldsymbol{s}_{bk,n+1}^{(k)}} & \dfrac{\partial \boldsymbol{R}_{bk}^{(k)}}{\partial \boldsymbol{\alpha}_{n+1}^{(k)}} & \dfrac{\partial \boldsymbol{R}_{bk}^{(k)}}{\partial \Delta\boldsymbol{\gamma}^{(k)}} \\ \dfrac{\partial \boldsymbol{R}_{\alpha}^{(k)}}{\partial \boldsymbol{s}_{h,n+1}^{(k)}} & \dfrac{\partial \boldsymbol{R}_{\alpha}^{(k)}}{\partial \boldsymbol{s}_{bk,n+1}^{(k)}} & \dfrac{\partial \boldsymbol{R}_{\alpha}^{(k)}}{\partial \boldsymbol{\alpha}_{n+1}^{(k)}} & \dfrac{\partial \boldsymbol{R}_{\alpha}^{(k)}}{\partial \Delta\boldsymbol{\gamma}^{(k)}} \\ \dfrac{\partial \boldsymbol{R}_{f}^{(k)}}{\partial \boldsymbol{s}_{h,n+1}^{(k)}} & \dfrac{\partial \boldsymbol{R}_{f}^{(k)}}{\partial \boldsymbol{s}_{bk,n+1}^{(k)}} & \dfrac{\partial \boldsymbol{R}_{f}^{(k)}}{\partial \boldsymbol{\alpha}_{n+1}^{(k)}} & \dfrac{\partial \boldsymbol{R}_{f}^{(k)}}{\partial \Delta\boldsymbol{\gamma}^{(k)}} \end{bmatrix} \tag{4.125}$$

In order to evaluate $\boldsymbol{R}_{ehp}^{(k+1)}$ at the next iteration, it is necessary to update the plastic hinge deformations increment in a way that is consistent with the correction $\delta \boldsymbol{x}^{(k)}$. The required correction is given by

$$\Delta \boldsymbol{e}_{hp,n+1}^{(k+1)} = \Delta \boldsymbol{e}_{hp,n+1}^{(k)} - \mathbf{f}_{he} \delta \boldsymbol{s}_{h,n+1}^{(k)} \tag{4.126}$$

where $\mathbf{f}_{he} = \mathbf{k}_{he}^{-1}$.

The selection of residuals and unknowns in Equation (4.121) affects the rank of the Jacobian in Equation (4.125). The large difference in the magnitude of the physical quantities may lead to the ill-conditioning of the Jacobian. To resolve this, the variables are normalized with reference values, which minimizes numerical convergence problems, in addition to addressing the inconsistent units of the terms without normalization.

After each iteration, the discrete Kuhn-Tucker conditions are verified and the number of active plastic hinges is updated accordingly:

1. If there exists some index $m \in \boldsymbol{J}_{act}^{(k)}$ such that $\Delta\gamma_{m,n+1}^{(k+1)} < 0$, remove $m$ from the active set $\boldsymbol{J}_{act}^{(k)}$ and restart the iteration.

2. Evaluate $\mathbf{f}_{n+1}^{(k+1)} = \mathbf{f}(\boldsymbol{s}_{h,n+1}^{(k+1)}, \boldsymbol{s}_{bk,n+1}^{(k+1)}, \boldsymbol{\alpha}_{n+1}^{(k+1)})$. If there exists some index $m \in \{i, j\}$ that is not in $\boldsymbol{J}_{act}^{(k)}$ such that $\mathbf{f}_{m,n+1}^{(k+1)} > 0$, include $m$ in the active set $\boldsymbol{J}_{act}^{(k)}$ and restart the iteration.

The iterations are terminated when the following convergence test is satisfied:

$$\left| \frac{\delta W^{(k)}}{\delta W^{(0)}} \right| \leq \text{tol} \tag{4.127}$$

where tol is a specified relative tolerance and $W^{(k)}$ represents the energy unbalance at iteration $k$ which is defined as follows:

$$\delta W^{(k)} = \left[\delta \boldsymbol{s}_{h,n+1}^{(k)}\right]^T \boldsymbol{R}_{ehp}^{(k)} + \left[\boldsymbol{n}_{n+1}^{(k)} \delta \Delta\boldsymbol{\gamma}^{(k)}\right]^T \boldsymbol{R}_{bk}^{(k)} + \left[\mathbf{H}_{hi} \delta \boldsymbol{\alpha}_{n+1}^{(k)}\right]^T \boldsymbol{R}_{\alpha}^{(k)} + \left[\delta \Delta\boldsymbol{\gamma}^{(k)}\right]^T \boldsymbol{R}_{f}^{(k)} \tag{4.128}$$

Upon convergence, the plastic hinge deformations are updated to

$$\boldsymbol{e}_{hp,n+1} = \boldsymbol{e}_{hp,n+1}^{tr} + \Delta \boldsymbol{e}_{hp,n+1} \tag{4.129}$$

allowing the determination of the element basic forces as

$$\boldsymbol{v}_{p,n+1} = \mathbf{b}_h^T \boldsymbol{e}_{hp,n+1} \tag{4.130}$$

$$\boldsymbol{q}_{n+1} = \mathbf{k}_e (\boldsymbol{v}_{n+1} - \boldsymbol{v}_{p,n+1}) \tag{4.131}$$

whereas the element tangent stiffness is assembled according to Section 4.3.2, which concludes the element state determination.

### 4.3.2 Element tangent stiffness

The following derivations use the notation $\boldsymbol{q}$ and $\boldsymbol{v}$ for the basic forces and element deformations, consistent with the 2d formulation. The tangent stiffness for the 3d column element can be obtained by substituting $\boldsymbol{q}$, $\boldsymbol{v}$ and $\mathbf{k}_e$ with $\boldsymbol{q}_{in}$, $\boldsymbol{v}_{in}$ and $\mathbf{k}_{in,e}$ in the subsequent equations. In that case, the full stiffness matrix $\mathbf{k}$ can then be assembled at the end of the time step as

$$\mathbf{k} = \begin{bmatrix} \mathbf{k}_{in} & \mathbf{0} \\ \mathbf{0} & k_t \end{bmatrix} \tag{4.132}$$

where $k_t = \dfrac{GJ_p}{L}$.

If the step is elastic, i.e. if the trial state is admissible, the element tangent stiffness at time $t_{n+1}$ is set equal to the elastic stiffness:

$$\mathbf{k}_{n+1} = \frac{d\boldsymbol{q}_{n+1}}{d\boldsymbol{v}_{n+1}} = \mathbf{k}_e \tag{4.133}$$

If the trial state is not admissible, the element tangent stiffness is updated upon convergence of the Newton-Raphson iterations of the plastic correction procedure. Because it is calculated in a way that is consistent with the backward-Euler integration algorithm, it is referred to as the consistent (algorithmic) tangent stiffness. This characteristic is of crucial importance for maintaining the quadratic rate of convergence of the Newton-Raphson solution procedure [73].

Making use of Equation (4.20), one can rewrite the first equation of (4.120) after dropping the superscript $k$ as

$$\boldsymbol{R}_{ehp} = -\boldsymbol{e}_{hp,n+1} + \boldsymbol{e}_{hp,n} + \boldsymbol{n}_{n+1} \Delta\boldsymbol{\gamma} \tag{4.134}$$

$$= -\boldsymbol{e}_{h,n+1} + \boldsymbol{e}_{h,n} + \mathbf{f}_{he} \left(\boldsymbol{s}_{h,n+1} - \boldsymbol{s}_{h,n}\right) + \boldsymbol{n}_{n+1} \Delta\boldsymbol{\gamma} \tag{4.135}$$

where $\mathbf{f}_{he} = \mathbf{k}_{he}^{-1} = (\mathbf{b}_h \mathbf{k}_e \mathbf{b}_h^T)^{-1}$.

After noting that $\boldsymbol{R} = 0$ upon convergence and making use of Equation (4.135), differentiating (4.120) under fixed variables at time $t_n$ gives the following equation:

$$d\boldsymbol{R} = \mathbf{0} = \frac{\partial \boldsymbol{R}}{\partial \boldsymbol{e}_{h,n+1}} d\boldsymbol{e}_{h,n+1} + \frac{\partial \boldsymbol{R}}{\partial \boldsymbol{x}} d\boldsymbol{x} \tag{4.136}$$

where

$$\frac{\partial \boldsymbol{R}}{\partial \boldsymbol{e}_{h,n+1}} = \begin{pmatrix} -\mathbf{I} \\ \mathbf{0} \\ \mathbf{0} \\ \mathbf{0} \end{pmatrix} \tag{4.137}$$

Rearranging the terms gives

$$\begin{pmatrix} d\boldsymbol{e}_{h,n+1} \\ \mathbf{0} \\ \mathbf{0} \\ \mathbf{0} \end{pmatrix} = \begin{bmatrix} \frac{\partial \boldsymbol{R}_{ehp}}{\partial \boldsymbol{s}_{n+1}} & \frac{\partial \boldsymbol{R}_{ehp}}{\partial \boldsymbol{s}_{bk,n+1}} & \frac{\partial \boldsymbol{R}_{ehp}}{\partial \boldsymbol{\alpha}_{n+1}} & \frac{\partial \boldsymbol{R}_{ehp}}{\partial \Delta\boldsymbol{\gamma}} \\ \frac{\partial \boldsymbol{R}_{bk}}{\partial \boldsymbol{s}_{n+1}} & \frac{\partial \boldsymbol{R}_{bk}}{\partial \boldsymbol{s}_{bk,n+1}} & \frac{\partial \boldsymbol{R}_{bk}}{\partial \boldsymbol{\alpha}_{n+1}} & \frac{\partial \boldsymbol{R}_{bk}}{\partial \Delta\boldsymbol{\gamma}} \\ \frac{\partial \boldsymbol{R}_{\alpha}}{\partial \boldsymbol{s}_{n+1}} & \frac{\partial \boldsymbol{R}_{\alpha}}{\partial \boldsymbol{s}_{bk,n+1}} & \frac{\partial \boldsymbol{R}_{\alpha}}{\partial \boldsymbol{\alpha}_{n+1}} & \frac{\partial \boldsymbol{R}_{\alpha}}{\partial \Delta\boldsymbol{\gamma}} \\ \frac{\partial \boldsymbol{R}_{f}}{\partial \boldsymbol{s}_{n+1}} & \frac{\partial \boldsymbol{R}_{f}}{\partial \boldsymbol{s}_{bk,n+1}} & \frac{\partial \boldsymbol{R}_{f}}{\partial \boldsymbol{\alpha}_{n+1}} & \frac{\partial \boldsymbol{R}_{f}}{\partial \Delta\boldsymbol{\gamma}} \end{bmatrix} \begin{pmatrix} d\boldsymbol{s}_{h,n+1} \\ d\boldsymbol{s}_{bk,n+1} \\ d\boldsymbol{\alpha}_{n+1} \\ d\Delta\boldsymbol{\gamma} \end{pmatrix} \tag{4.138}$$

With the definition of the block matrices

$$\mathbf{f}_{rr} = \left[ \frac{\partial \boldsymbol{R}_{ehp}}{\partial \boldsymbol{s}_{h,n+1}} \right] \quad ; \quad \mathbf{f}_{rc} = \begin{bmatrix} \frac{\partial \boldsymbol{R}_{ehp}}{\partial \boldsymbol{s}_{bk,n+1}} & \frac{\partial \boldsymbol{R}_{ehp}}{\partial \boldsymbol{\alpha}_{n+1}} & \frac{\partial \boldsymbol{R}_{ehp}}{\partial \Delta\boldsymbol{\gamma}} \end{bmatrix} \tag{4.139}$$

$$\mathbf{f}_{cr} = \begin{bmatrix} \frac{\partial \boldsymbol{R}_{bk}}{\partial \boldsymbol{s}_{h,n+1}} \\ \frac{\partial \boldsymbol{R}_{\boldsymbol{\alpha}}}{\partial \boldsymbol{s}_{h,n+1}} \\ \frac{\partial \boldsymbol{R}_{f}}{\partial \boldsymbol{s}_{h,n+1}} \end{bmatrix} \quad ; \quad \mathbf{f}_{cc} = \begin{bmatrix} \frac{\partial \boldsymbol{R}_{bk}}{\partial \boldsymbol{s}_{bk,n+1}} & \frac{\partial \boldsymbol{R}_{bk}}{\partial \boldsymbol{\alpha}_{n+1}} & \frac{\partial \boldsymbol{R}_{bk}}{\partial \Delta\boldsymbol{\gamma}} \\ \frac{\partial \boldsymbol{R}_{\alpha}}{\partial \boldsymbol{s}_{bk,n+1}} & \frac{\partial \boldsymbol{R}_{\alpha}}{\partial \boldsymbol{\alpha}_{n+1}} & \frac{\partial \boldsymbol{R}_{\alpha}}{\partial \Delta\boldsymbol{\gamma}} \\ \frac{\partial \boldsymbol{R}_{f}}{\partial \boldsymbol{s}_{bk,n+1}} & \frac{\partial \boldsymbol{R}_{f}}{\partial \boldsymbol{\alpha}_{n+1}} & \frac{\partial \boldsymbol{R}_{f}}{\partial \Delta\boldsymbol{\gamma}} \end{bmatrix} \tag{4.140}$$

$$\tag{4.141}$$

the stiffness condensation of Equation (4.138) gives the hinge flexibility matrix

$$\frac{d\boldsymbol{e}_{h,n+1}}{d\boldsymbol{s}_{h,n+1}} = \mathbf{f}_{rr} - \mathbf{f}_{rc} \mathbf{f}_{cc}^{-1} \mathbf{f}_{cr} \tag{4.142}$$

The element flexibility matrix can then be obtained with the chain rule as

$$\frac{d\boldsymbol{v}_{n+1}}{d\boldsymbol{q}_{n+1}} = \mathbf{b}_h^T \frac{d\boldsymbol{e}_{h,n+1}}{d\boldsymbol{s}_{h,n+1}} \mathbf{b}_h = \mathbf{b}_h^T \mathbf{f}_{rr} \mathbf{b}_h - \mathbf{b}_h^T \mathbf{f}_{rc} \mathbf{f}_{cc}^{-1} \mathbf{f}_{cr} \mathbf{b}_h \tag{4.143}$$

Introducing the matrices

$$\mathbf{F}_{rr} = \mathbf{b}_h^T \mathbf{f}_{rr} \mathbf{b}_h \quad ; \quad \mathbf{F}_{rc} = \mathbf{b}_h^T \mathbf{f}_{rc} \quad ; \quad \mathbf{F}_{cc} = \mathbf{f}_{cc} \quad ; \quad \mathbf{F}_{cr} = \mathbf{f}_{cr} \mathbf{b}_h \tag{4.144}$$

Equation (4.143) can be rewritten as

$$\frac{d\boldsymbol{v}_{n+1}}{d\boldsymbol{q}_{n+1}} = \mathbf{F}_{rr} - \mathbf{F}_{rc} \mathbf{F}_{cc}^{-1} \mathbf{F}_{cr} \tag{4.145}$$

Inverting the flexibility as given by the expression in Equation (4.145) is one way of obtaining the element tangent stiffness matrix. However, this approach requires inverting $\mathbf{F}_{cc}$ which could be singular, which is the case in particular when $\mathbf{H}_{hk} = \mathbf{0}$ and $\mathbf{H}_{hi} = \mathbf{0}$ [24]. In agreement with Chapter 2, an alternative solution is to use the Woodbury matrix identity:

$$(\mathbf{A} + \boldsymbol{U}\mathbf{C}\boldsymbol{V})^{-1} = \mathbf{A}^{-1} - \mathbf{A}^{-1}\boldsymbol{U}(\mathbf{C}^{-1} + \boldsymbol{V}\mathbf{A}^{-1}\boldsymbol{U})^{-1}\boldsymbol{V}\mathbf{A}^{-1} \tag{4.146}$$

Applying this identity to invert the right hand side of Equation (4.145) gives the following expression for the element tangent stiffness:

$$\mathbf{k}_{n+1} = \frac{d\boldsymbol{q}_{n+1}}{d\boldsymbol{v}_{n+1}} = \mathbf{F}_{rr}^{-1} + \mathbf{F}_{rr}^{-1} \mathbf{F}_{rc} (\mathbf{F}_{cc} - \mathbf{F}_{cr} \mathbf{F}_{rr}^{-1} \mathbf{F}_{rc})^{-1} \mathbf{F}_{cr} \mathbf{F}_{rr}^{-1} \tag{4.147}$$

The latter approach is adopted in the present formulation.

### 4.3.3 Summary of state determination algorithm

The state determination algorithm for the 2d and 3d resultant plasticity column element model is summarized in Tables 4.3 and 4.4.

## 4.4 Analyses of cantilever columns with wide-flange sections

To assess the performance of the 2d and 3d resultant plasticity column formulation, the analyses of the W14x730 and W12x120 cantilever columns in Section 2.5.2 are repeated with the proposed models. The selected cantilever specimens are subjected to a set of monotonic and cyclic uniaxial and biaxial bending conditions. The response produced with the resultant plasticity column models is compared with that of the reference distributed plasticity model with 7 Gauss-Lobatto integration points and fiber section discretization DP7Fib, as described in Section 2.5.2.

**Objective:** Given $\boldsymbol{v}_n$, $\boldsymbol{e}_{hp,n}$, $\boldsymbol{s}_{bk,n}$, $\boldsymbol{\alpha}_n$ at time $t_n$ and $\boldsymbol{v}_{n+1}$ at time $t_{n+1}$, evaluate $\boldsymbol{e}_{hp,n+1}$, $\boldsymbol{s}_{bk,n+1}$, $\boldsymbol{\alpha}_{n+1}$, $\boldsymbol{q}_{n+1}$ and $\mathbf{k}_{n+1}$ at time $t_{n+1}$.

1. **Compute trial elastic state:**

   Evaluate $\boldsymbol{e}^{tr}_{hp,n+1}$, $\boldsymbol{s}^{tr}_{bk,n+1}$, $\boldsymbol{\alpha}^{tr}_{n+1}$, $\boldsymbol{q}^{tr}_{n+1}$ and $\boldsymbol{s}^{tr}_{h,n+1}$ in Equations (4.105)-(4.110)

2. **Check yield condition:**

   Evaluate $\mathbf{f}^{tr}_{n+1} = \mathbf{f}(\boldsymbol{s}^{tr}_{h,n+1}, \boldsymbol{s}^{tr}_{bk,n+1}, \boldsymbol{\alpha}^{tr}_{n+1})$ where $\mathbf{f}$ is given by Equation (4.24)
   IF: $\mathbf{f}^{tr}_{n+1} < \mathbf{0}$, THEN:

   a) Set $(\cdot)_{n+1} = (\cdot)^{tr}_{n+1}$

   b) Set $\mathbf{k}_{n+1} = \mathbf{k}_e$ and EXIT

   ELSE: Go to 3

3. **Perform plastic correction with closest point projection algorithm:**

   Perform plastic correction algorithm in Table 4.5

Table 4.3: 2d resultant plasticity column element state determination algorithm

**Objective:** Given $\boldsymbol{v}_n$, $\boldsymbol{e}_{hp,n}$, $\boldsymbol{s}_{bk,n}$, $\boldsymbol{\alpha}_n$ at time $t_n$ and $\boldsymbol{v}_{n+1}$ at time $t_{n+1}$, evaluate $\boldsymbol{e}_{hp,n+1}$, $\boldsymbol{s}_{bk,n+1}$, $\boldsymbol{\alpha}_{n+1}$, $\boldsymbol{q}_{n+1}$ and $\mathbf{k}_{n+1}$ at time $t_{n+1}$.

1. **Compute trial elastic state:**

   Evaluate $\boldsymbol{e}^{tr}_{hp,n+1}$, $\boldsymbol{s}^{tr}_{bk,n+1}$, $\boldsymbol{\alpha}^{tr}_{n+1}$, $\boldsymbol{q}^{tr}_{in,n+1}$ and $\boldsymbol{s}^{tr}_{h,n+1}$ in Equations (4.105)-(4.110)

2. **Check yield condition:**

   Evaluate $\mathbf{f}^{tr}_{n+1} = \mathbf{f}(\boldsymbol{s}^{tr}_{h,n+1}, \boldsymbol{s}^{tr}_{bk,n+1}, \boldsymbol{\alpha}^{tr}_{n+1})$ where $\mathbf{f}$ is given by Equation (4.69)
   IF: $\mathbf{f}^{tr}_{n+1} < \mathbf{0}$, THEN:

   a) Set $(\cdot)_{n+1} = (\cdot)^{tr}_{n+1}$

   b) Set $\mathbf{k}_{in,n+1} = \mathbf{k}_{in,e}$ and Go to 4

   ELSE: Go to 3

3. **Perform plastic correction with closest point projection algorithm:**

   Perform plastic correction algorithm in Table 4.5 and Go to 4

4. **Assemble inelastic response with linear elastic torsional response:**

   a) Evaluate $q_{t,n+1} = \dfrac{GJ_p}{L} v_{t,n+1}$ and $k_t = \dfrac{GJ_p}{L}$

   b) Assemble $\boldsymbol{q}_{n+1} = \begin{pmatrix} \boldsymbol{q}_{in,n+1} \\ q_{t,n+1} \end{pmatrix}$ and $\mathbf{k}_{n+1} = \begin{bmatrix} \mathbf{k}_{in,n+1} & \mathbf{0} \\ \mathbf{0} & k_t \end{bmatrix}$

Table 4.4: 3d resultant plasticity column element state determination algorithm

**Objective:** Evaluate $\boldsymbol{q}_{n+1}$ and $\mathbf{k}_{n+1}$ for 2d model or $\boldsymbol{q}_{in,n+1}$ and $\mathbf{k}_{in,n+1}$ for 3d model at time $t_{n+1}$ after plastic correction.

1. Initialize $k = 0$, set $(\cdot)_{n+1}^{(0)} = (\cdot)_{n+1}^{tr}$, set $\boldsymbol{J}_{act}^{(0)} = \{m \in \{i, j\} \mid f_{m,n+1}^{tr} > 0\}$ and evaluate $\boldsymbol{x}^{(0)}$ in Equation (4.122)
2. Evaluate residual vector $\boldsymbol{R}^{(k)}$ in Equations (4.120)-(4.121)
3. Evaluate Jacobian of Newton-Raphson iterations $\mathbf{J}^{(k)}$ in Equation (4.125)
4. Evaluate increment of state variables $\delta\boldsymbol{x}^{(k)} = -\left[\mathbf{J}^{(k)}\right]^{-1}\boldsymbol{R}^{(k)}$
5. Update state variables $\boldsymbol{x}^{(k+1)} = \boldsymbol{x}^{(k)} + \delta\boldsymbol{x}^{(k)}$
6. Update $\Delta\boldsymbol{e}_{hp,n+1}^{(k+1)} = \Delta\boldsymbol{e}_{hp,n+1}^{(k)} - \mathbf{f}_{he}\delta\boldsymbol{s}_{h,n+1}^{(k)}$ where $\mathbf{f}_{he} = \mathbf{k}_{he}^{-1}$
7. IF $\exists m \in \boldsymbol{J}_{act}^{(k)} \mid \Delta\gamma_{m,n+1}^{(k+1)} < 0$, THEN:

   Update $\boldsymbol{J}_{act}^{(k)} = \{m \in \{i, j\} \mid \Delta\gamma_{m,n+1}^{(k+1)} \geq 0\}$ and Go to 2

   ELSE Go to 8
8. Evaluate $\mathbf{f}_{n+1}^{(k+1)} = \mathbf{f}(\boldsymbol{s}_{h,n+1}^{(k+1)}, \boldsymbol{s}_{bk,n+1}^{(k+1)}, \boldsymbol{\alpha}_{n+1}^{(k+1)})$

   IF $\exists m \in \{i, j\} \mid m \notin \boldsymbol{J}_{act}^{(k)}$ and $f_{m,n+1}^{(k+1)} > 0$, THEN:

   Update $\boldsymbol{J}_{act}^{(k)} = \boldsymbol{J}_{act}^{(k)} \cup \{m \in \{i, j\} \mid f_{m,n+1}^{(k+1)} > 0\}$ and Go to 2

   ELSE Go to 9
9. Evaluate energy unbalance $\delta W^{(k)}$ in Equation (4.128)

   IF $\left|\dfrac{\delta W^{(k)}}{\delta W^{(0)}}\right| \leq$ tol, THEN:

   a) Set $(\cdot)_{n+1} = (\cdot)_{n+1}^{(k+1)}$

   b) Evaluate $\boldsymbol{q}_{n+1}$ for 2d model and $\boldsymbol{q}_{in,n+1}$ for 3d model in Equations (4.129) - (4.131)

   c) Evaluate $\mathbf{k}_{n+1}$ for 2d model or $\mathbf{k}_{in,n+1}$ for 3d model in Equations (4.139), (4.141), (4.144) and (4.147) and EXIT

   ELSE: Set $k \leftarrow k + 1$ and Go to 2

Table 4.5: Plastic correction algorithm for resultant plasticity column model

For the uniaxial bending load patterns U0, U1, U2, and UV1, the column is modeled with the 2d resultant plasticity model, whereas the 3d resultant formulation is used for the biaxial bending load patterns B1, B2 and BV1.

The resultant plasticity models, referred to as CP, take advantage of the hinge offset capability and use the hardening parameters described in Table 4.6. Only one hinge offset is specified at the base of the column since no plastic hinge is expected to form at the top. For the approximation of the $N$-$M$ interaction surface, the 2d and 3d CP models use coefficients that are identical to those used for the resultant plasticity section models in Section 2.5.1.2, with corresponding yield surfaces illustrated in Figure 2.8. The DP7Fib and CP models are illustrated in Figure 4.7.

| **Column Model** | $H_{kr,a}$ (%) | $H_{kr,fz,i}$ (%) | $H_{kr,fz,j}$ (%) | $H_{kr,fy,i}$ (%) | $H_{kr,fy,j}$ (%) | $H_{ir,i}$ (‰) | $H_{ir,j}$ (‰) | $\chi_i$ (%) | $\chi_j$ (%) |
|---|---|---|---|---|---|---|---|---|---|
| **CP** | 6.5 | 1.0 | 1.0 | 1.0 | 1.0 | 1.63 | 1.63 | 6.5 | 0 |

Table 4.6: Parameters for column analyses

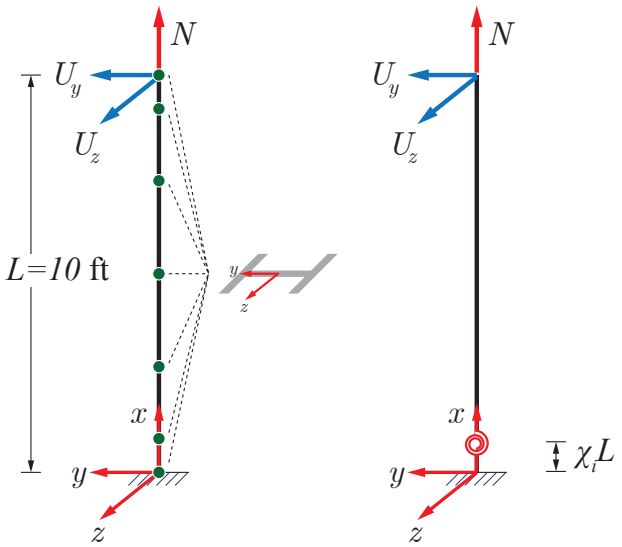


Figure 4.7: Cantilever column models: DP7Fib (left) and CP (right)

Figures 4.8 and 4.9 show the monotonic uniaxial response of the W14x730 and W12x120 columns, respectively. The agreement between the resultant plasticity model CP and the distributed plasticity model DP7Fib is excellent across all levels of axial force. The resultant plasticity model captures the reduction in flexural strength under increasing axial force

with remarkable accuracy through the use of the polynomial approximation of the $N$-$M$ interaction surface. The initial approximation of the yield surface is depicted in grey in the top plots. The axial force - bending moment response goes beyond that grey line because the yield surface shifts and expands under the effect of kinematic and isotropic hardening as the plastic deformations accumulate. The bending moment response at the base $M_z := -q_{zi}$, the axial deformation $v_a$ and the plastic deformation at the base $v_{pz} := v_{pz,i}$ are all captured with a very satisfying accuracy by the 2d CP model.

Figures 4.10 to 4.15 show the cyclic uniaxial response of the W14x730 and W12x120 columns under load patterns U1, U2 and UV1. Complementing the earlier observations, these plots demonstrate the ability of the CP element to capture the isotropic hardening under various levels of axial force. They also show that the measure of axial force deformation produced by the CP model is extremely accurate for axial shortening less than 0.8%. As the axial deformation increases beyond this value under higher levels of axial force, the CP model slightly underestimates the axial shortening, but the discrepancy does not exceed 0.2%.

Lastly, Figures 4.16 to 4.23 show the cyclic biaxial response of the two cross sections under load patterns B1, B2 and BV1. The 3d resultant plasticity column model captures the two bending moments, the end plastic rotations, and the axial deformation with impressive accuracy under these complex loading scenarios, including under extreme variations of the axial force.

Overall, the recommended values for the hinge offset and the hardening parameters in Table 4.6 gives results of excellent accuracy across all levels of axial force for both cross sections while reducing the computational time by a factor of 2 to 4 compared to the model DP7Fib.

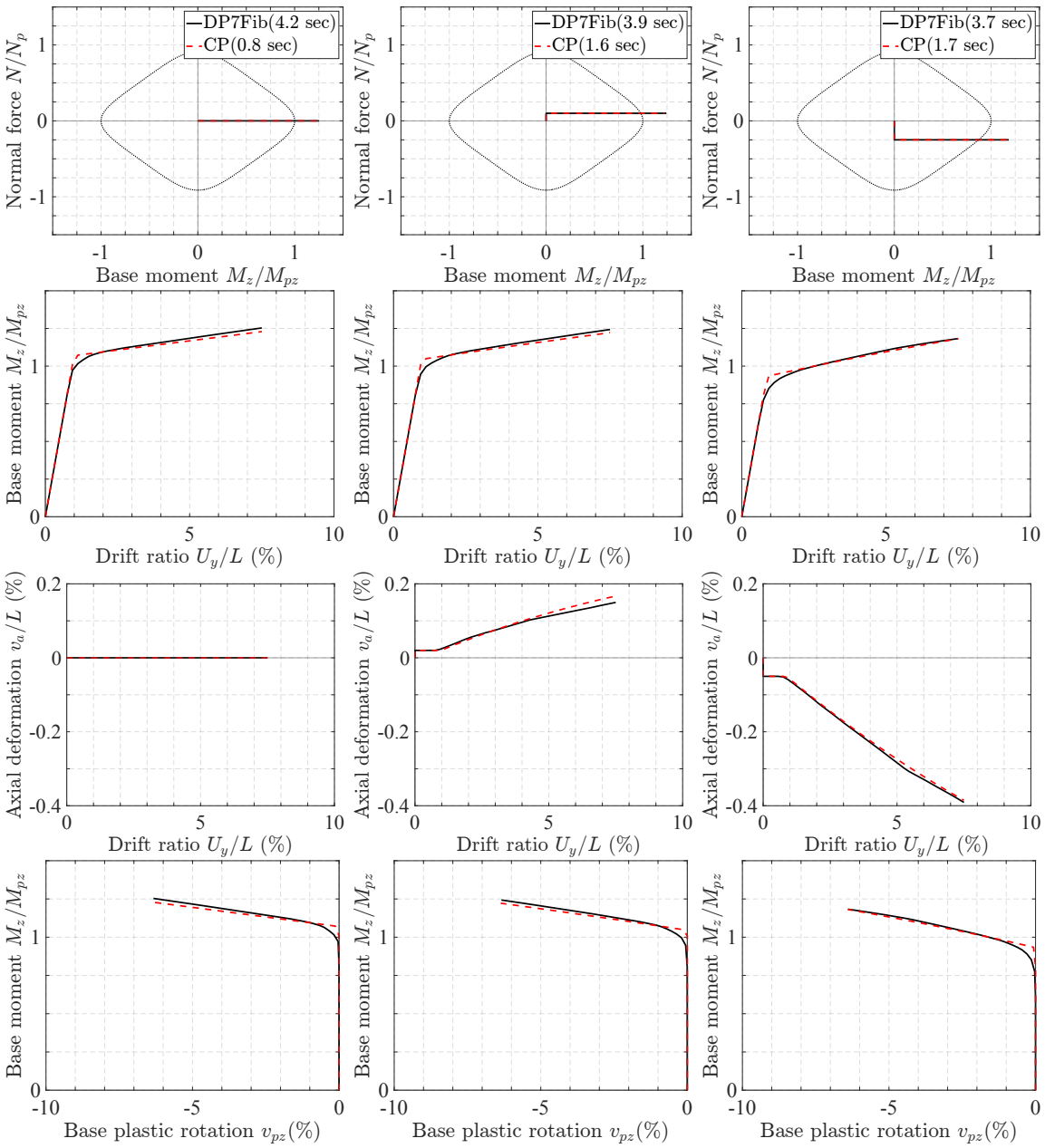


(a) $N = 0$ (b) $N = 10\%N_p$ (c) $N = -25\%N_p$

Figure 4.8: Response of W14x730 column under U0

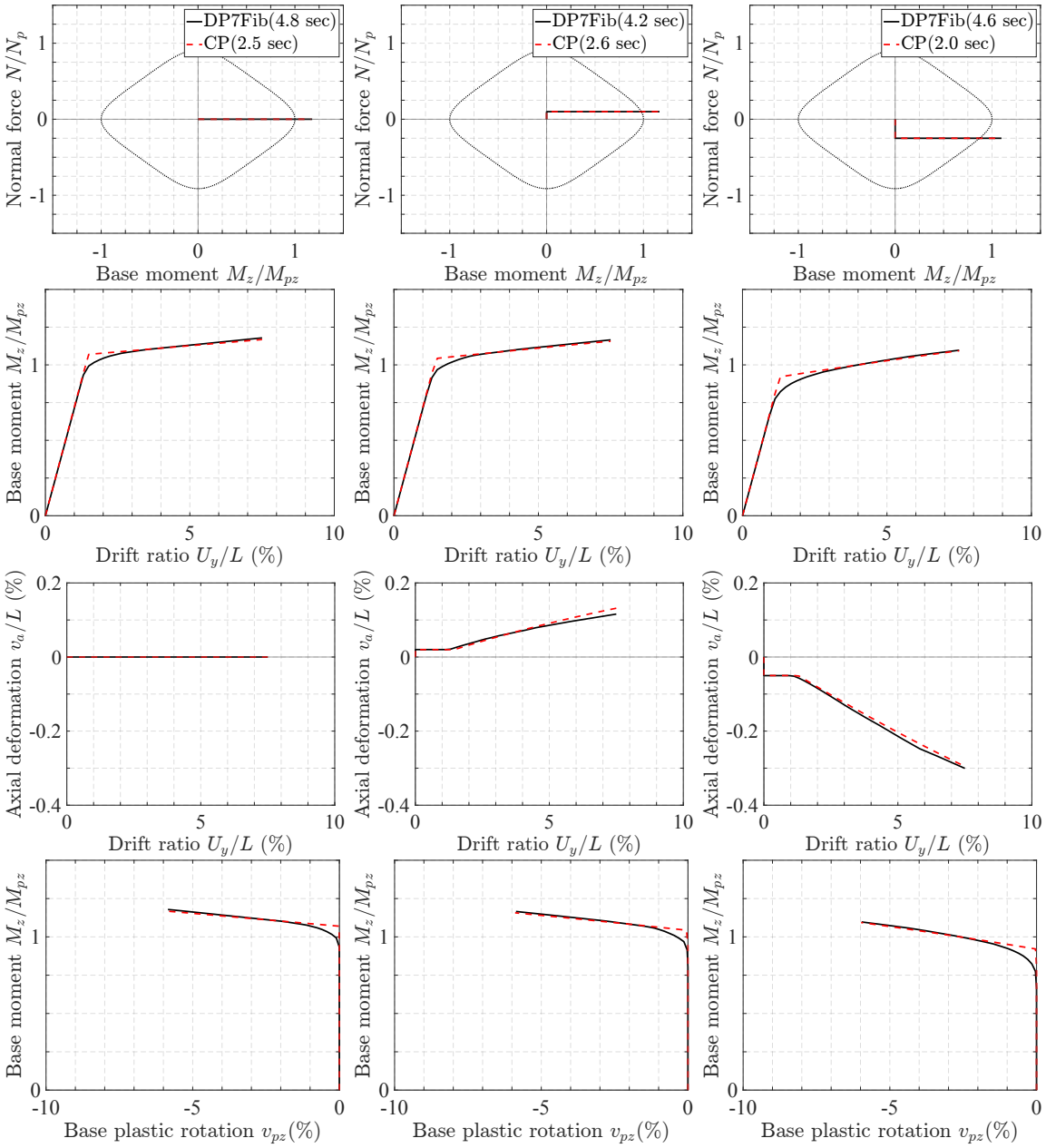


(a) $N = 0$ (b) $N = 10\%N_p$ (c) $N = -25\%N_p$

Figure 4.9: Response of W12x120 column under U0

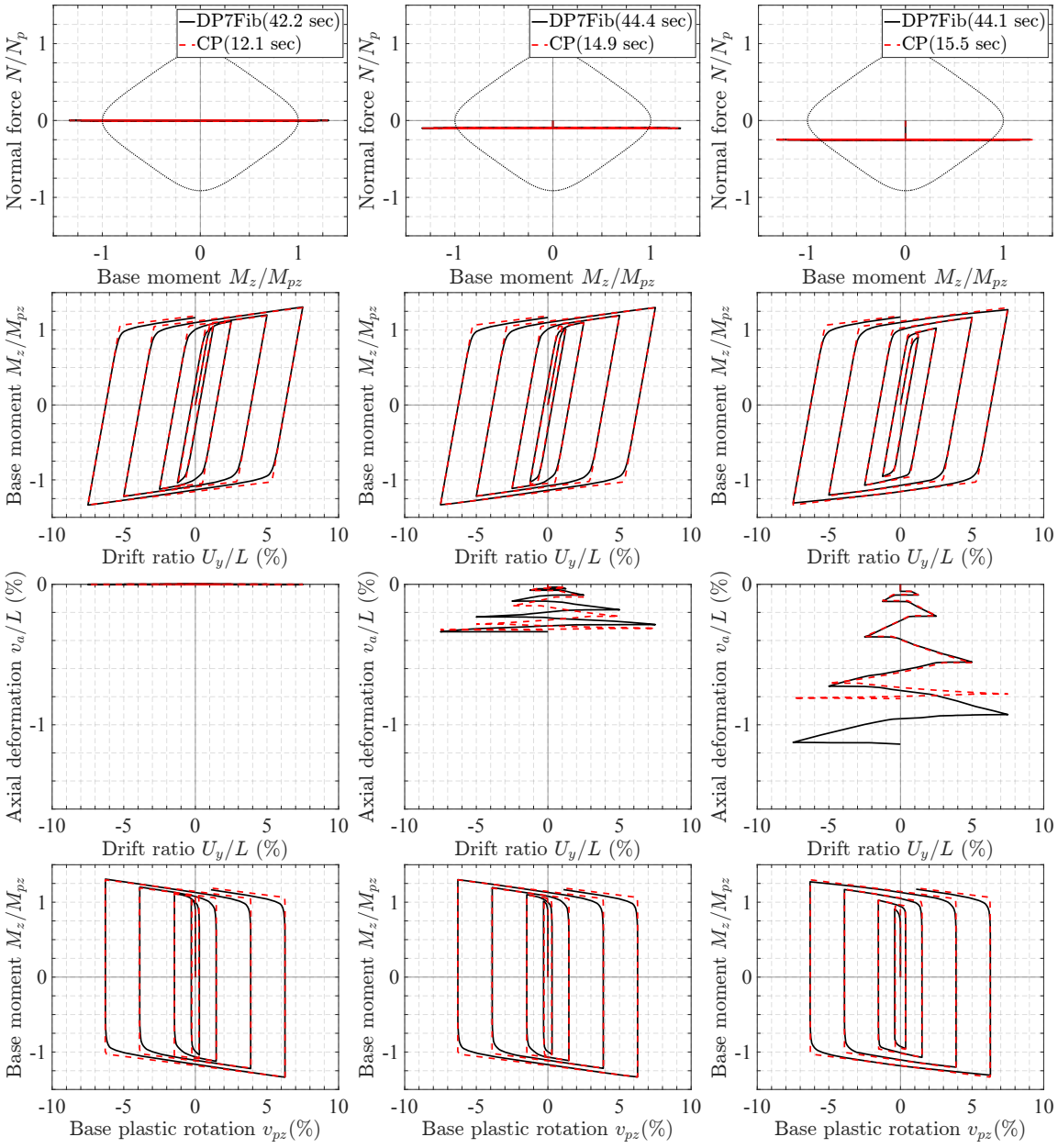


(a) $N = 0$ (b) $N = -10\%N_p$ (c) $N = -25\%N_p$

Figure 4.10: Response of W14x730 column under U1

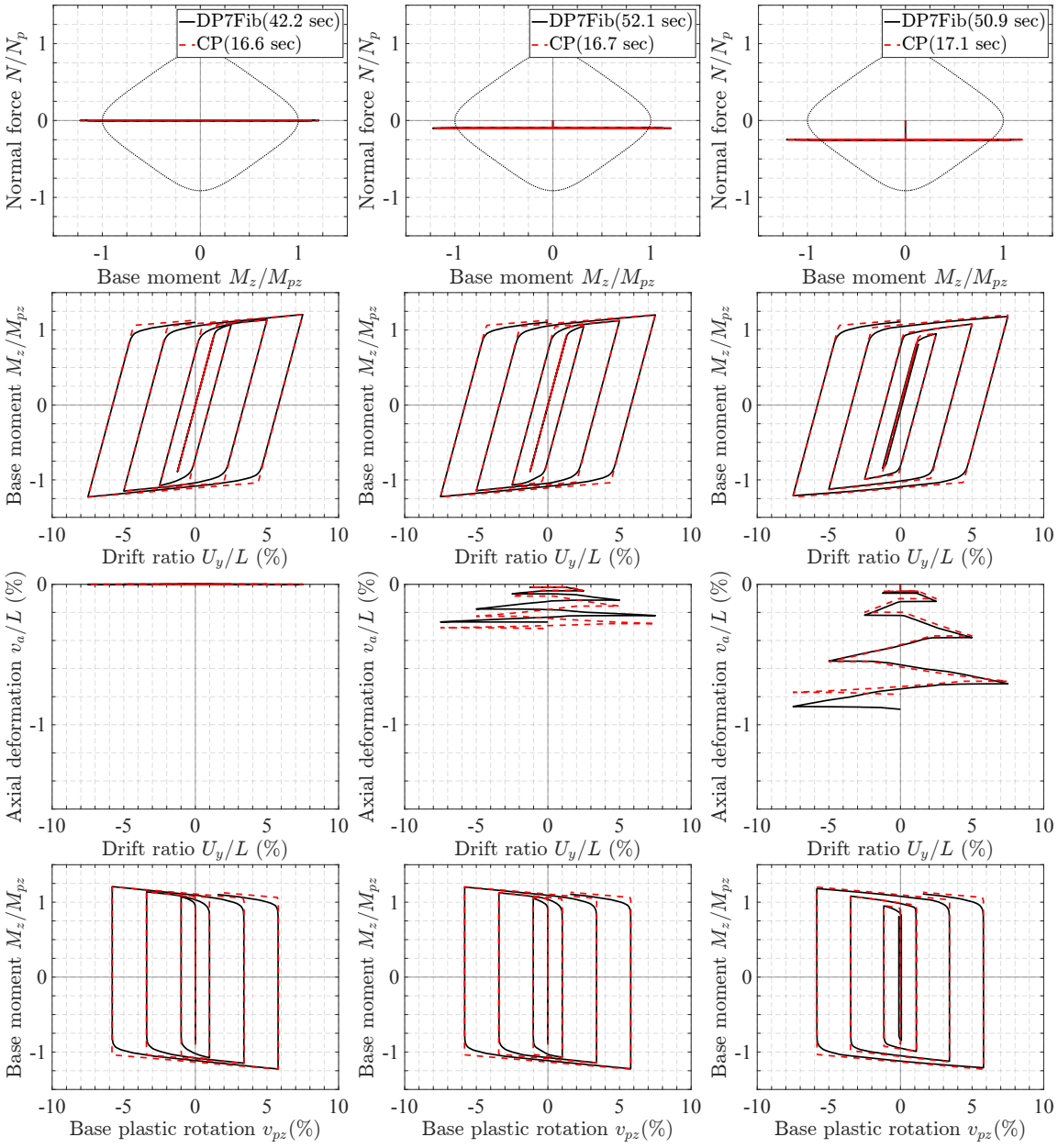


(a) $N = 0$ (b) $N = -10\%N_p$ (c) $N = -25\%N_p$

Figure 4.11: Response of W12x120 column under U1

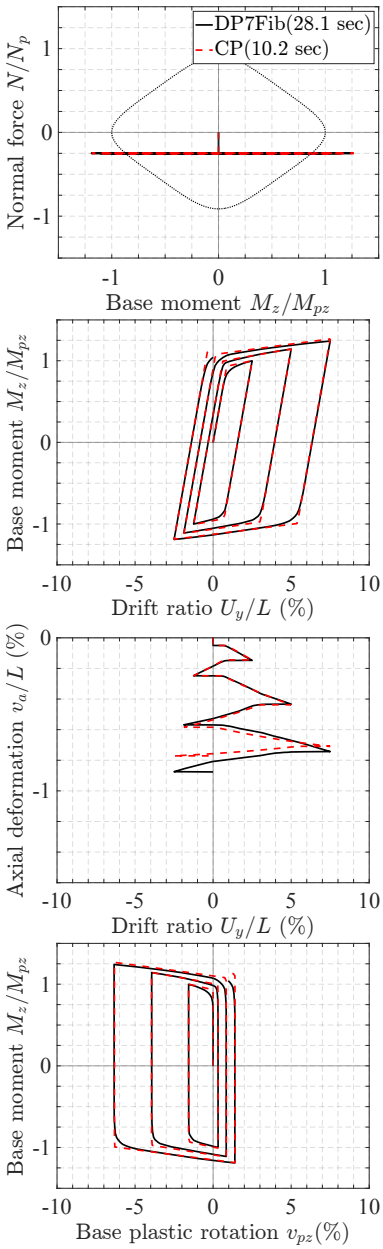


Figure 4.12: Response of W14x730 column under U2 with $N = -25\%N_p$

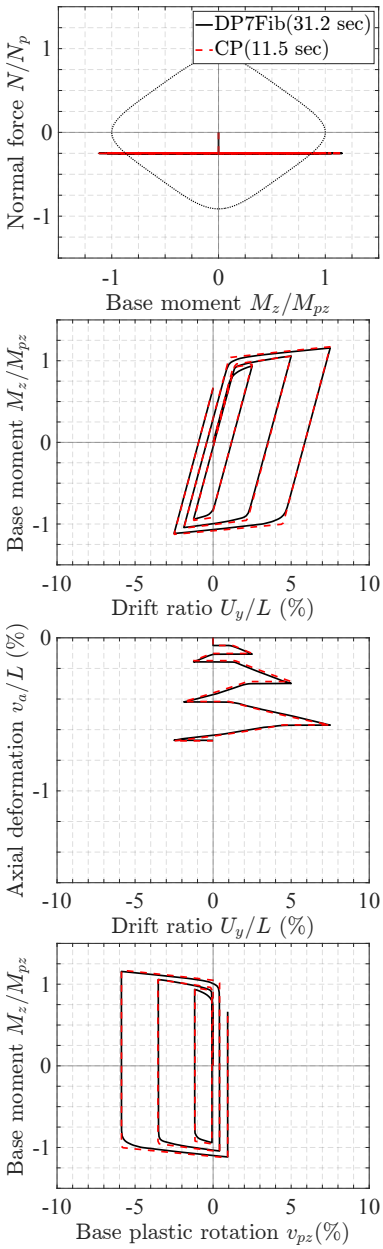


Figure 4.13: Response of W12x120 column under U2 with $N = -25\%N_p$

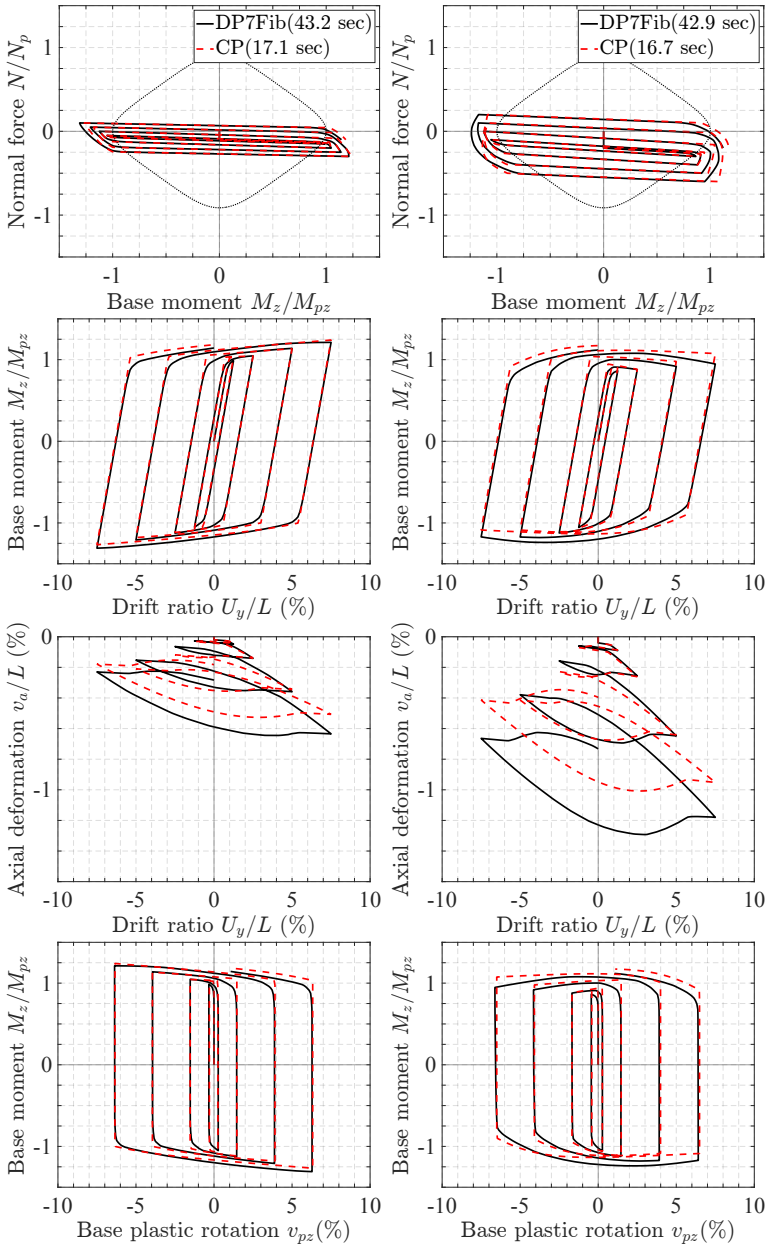


(a) $N = -10\%N_p \pm 20\%N_p$ (b) $N = -20\%N_p \pm 40\%N_p$

Figure 4.14: Response of W14x730 column under UV1

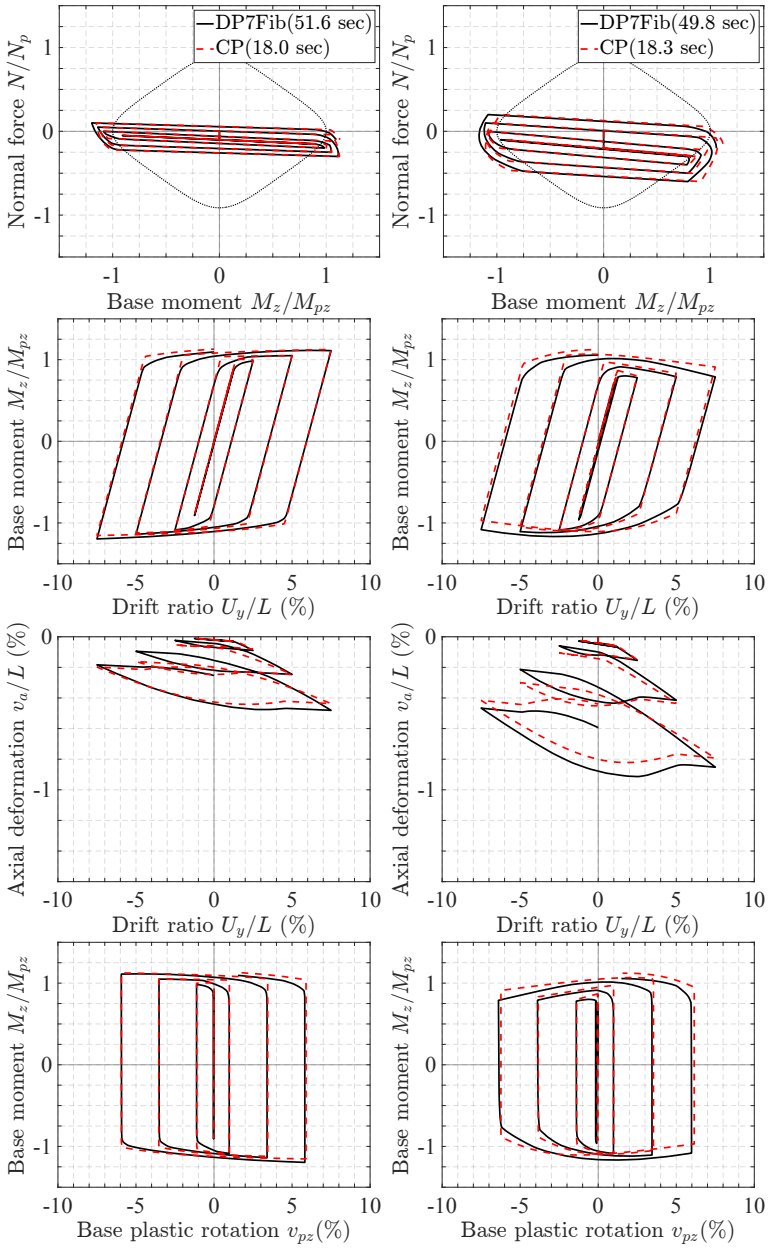


(a) $N = -10\%N_p \pm 20\%N_p$ (b) $N = -20\%N_p \pm 40\%N_p$

Figure 4.15: Response of W12x120 column under UV1

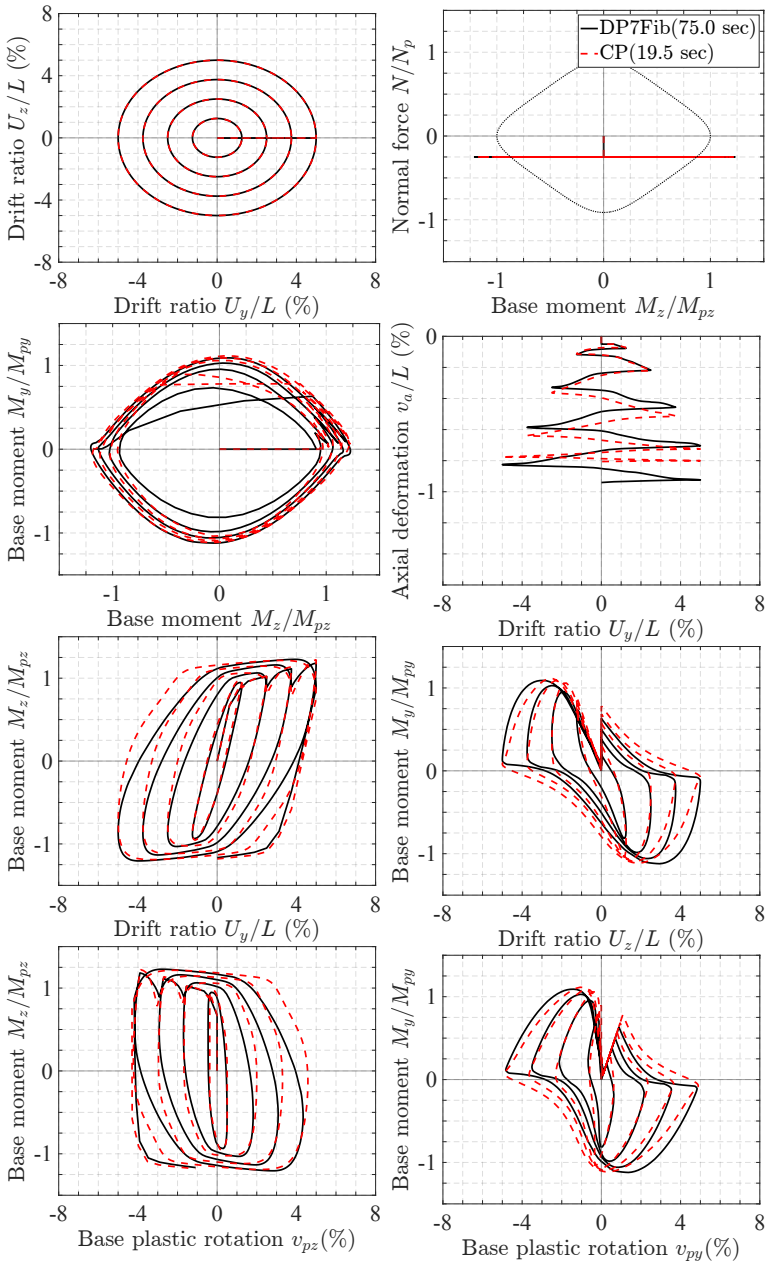


Figure 4.16: Response of W14x730 column under B1 with $N = -25\%N_p$

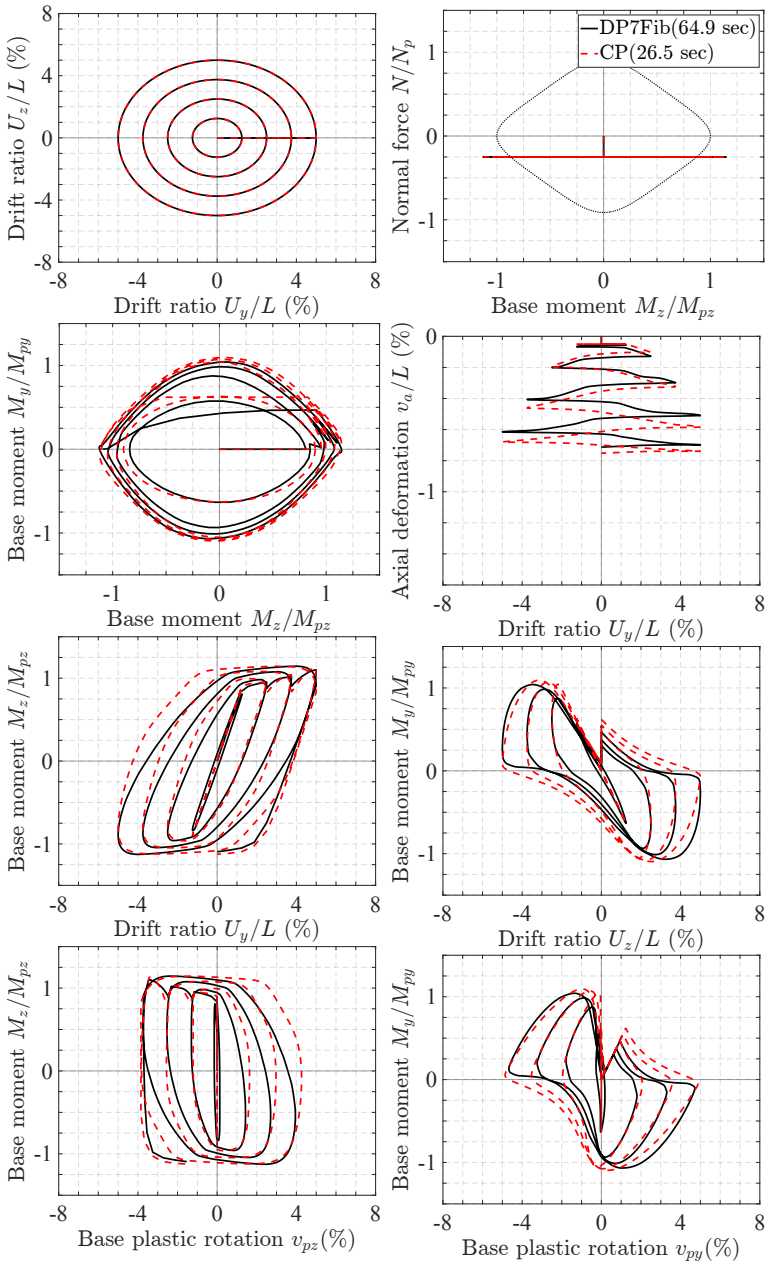


Figure 4.17: Response of W12x120 column under B1 with $N = -25\%N_p$

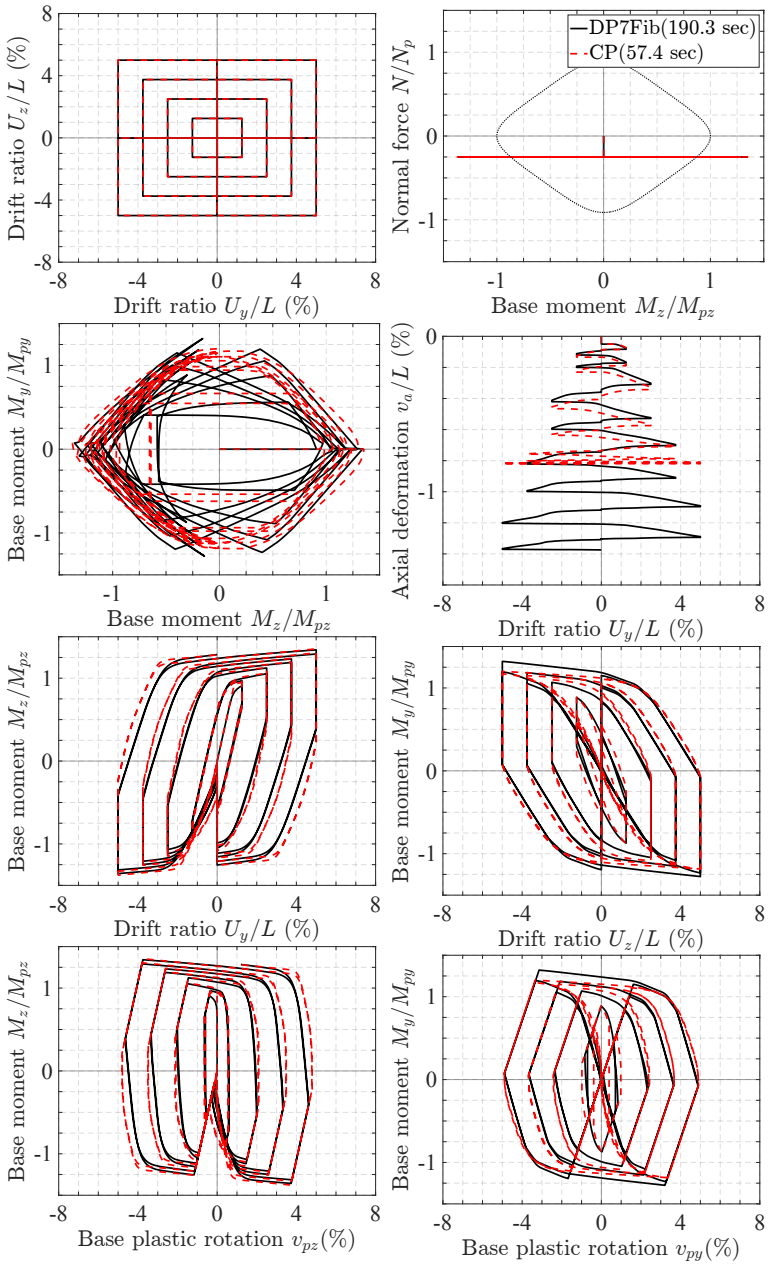


Figure 4.18: Response of W14x730 column under B2 with $N = -25\%N_p$

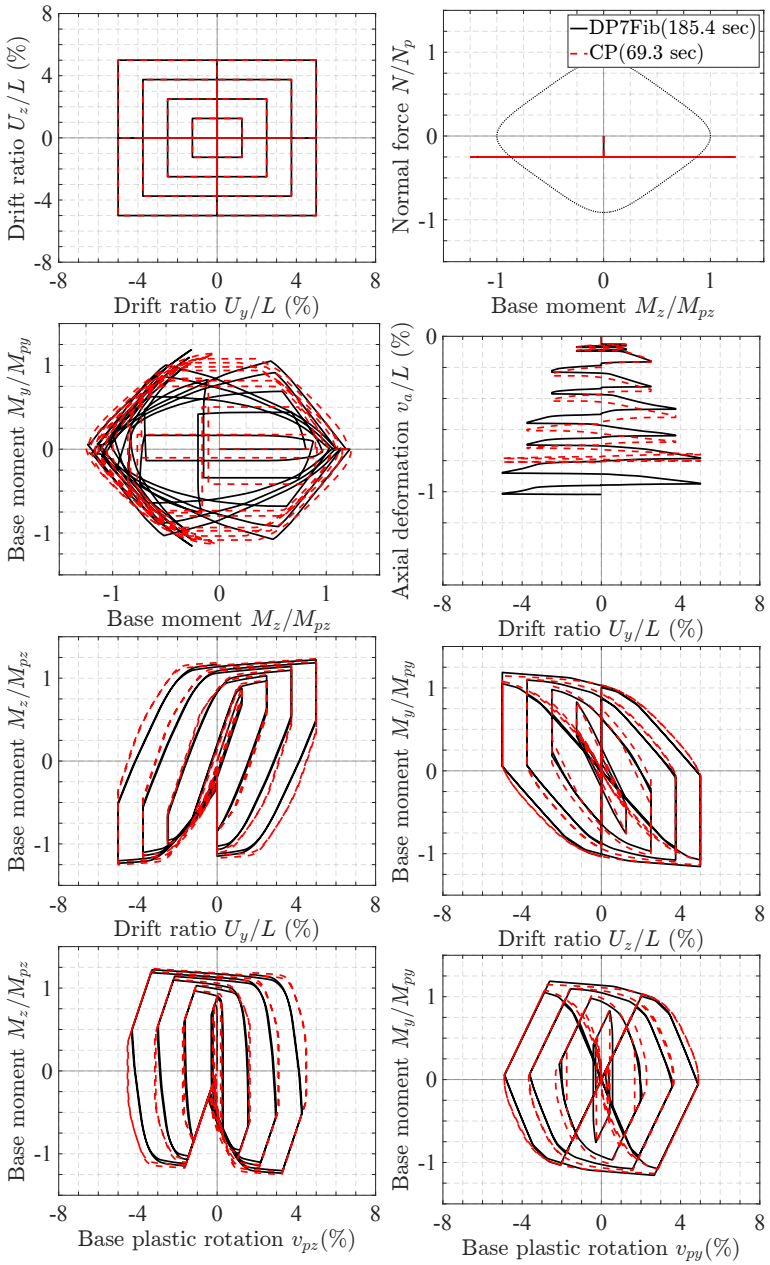


Figure 4.19: Response of W12x120 column under B2 with $N = -25\%N_p$

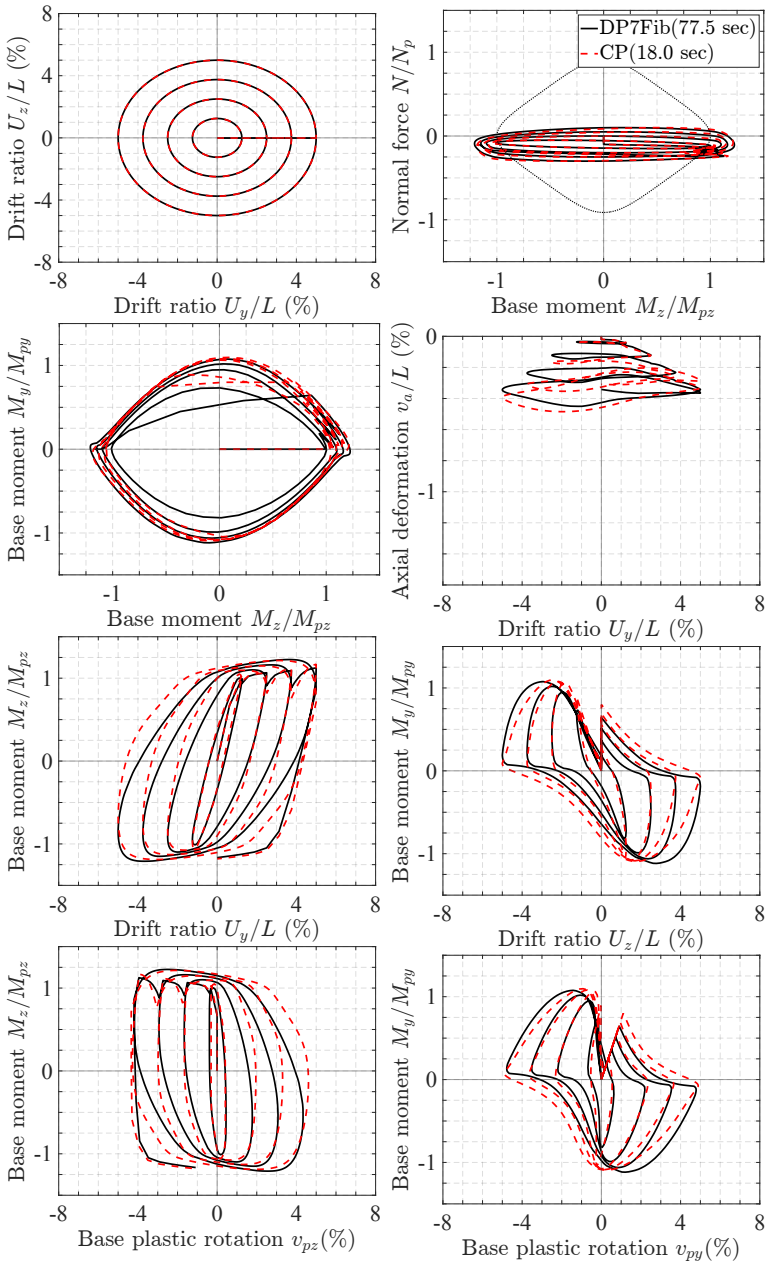


Figure 4.20: Response of W14x730 column under BV1 with $N = -10\%N_p \pm 20\%N_p$

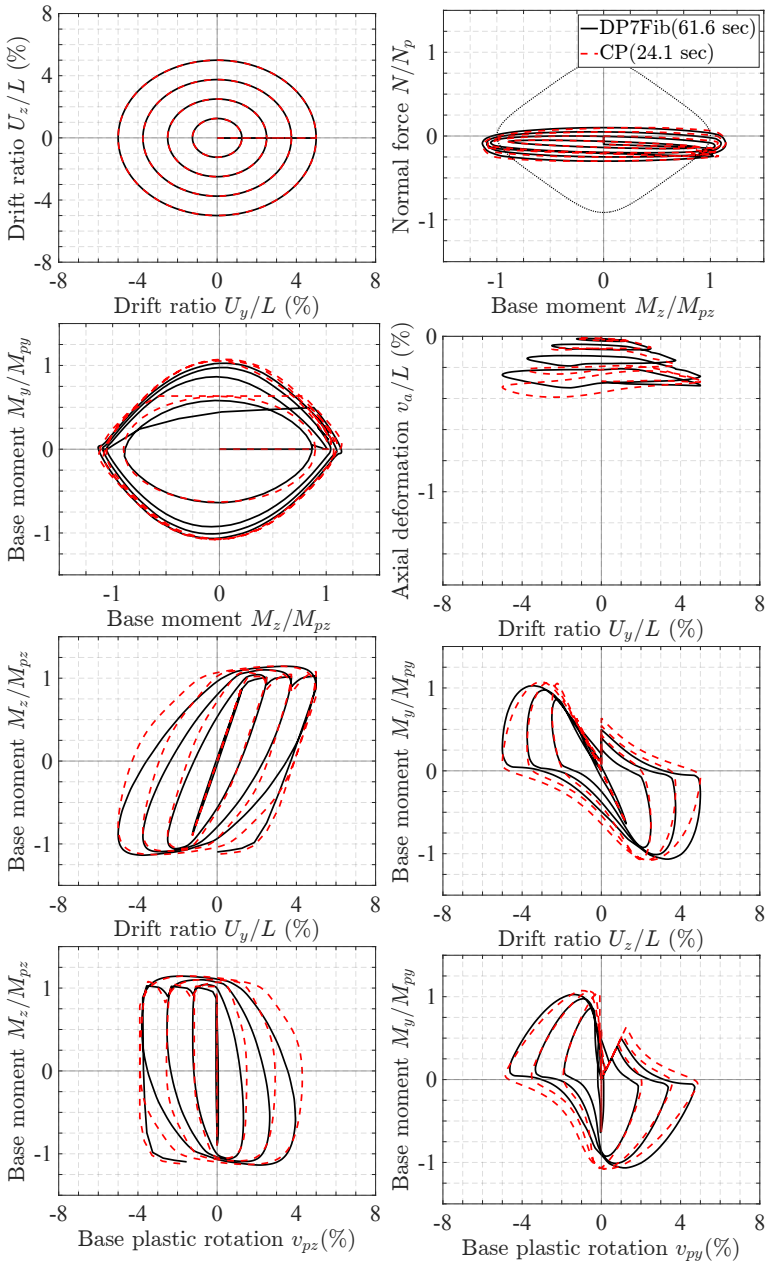


Figure 4.21: Response of W12x120 column under BV1 with $N = -10\%N_p \pm 20\%N_p$

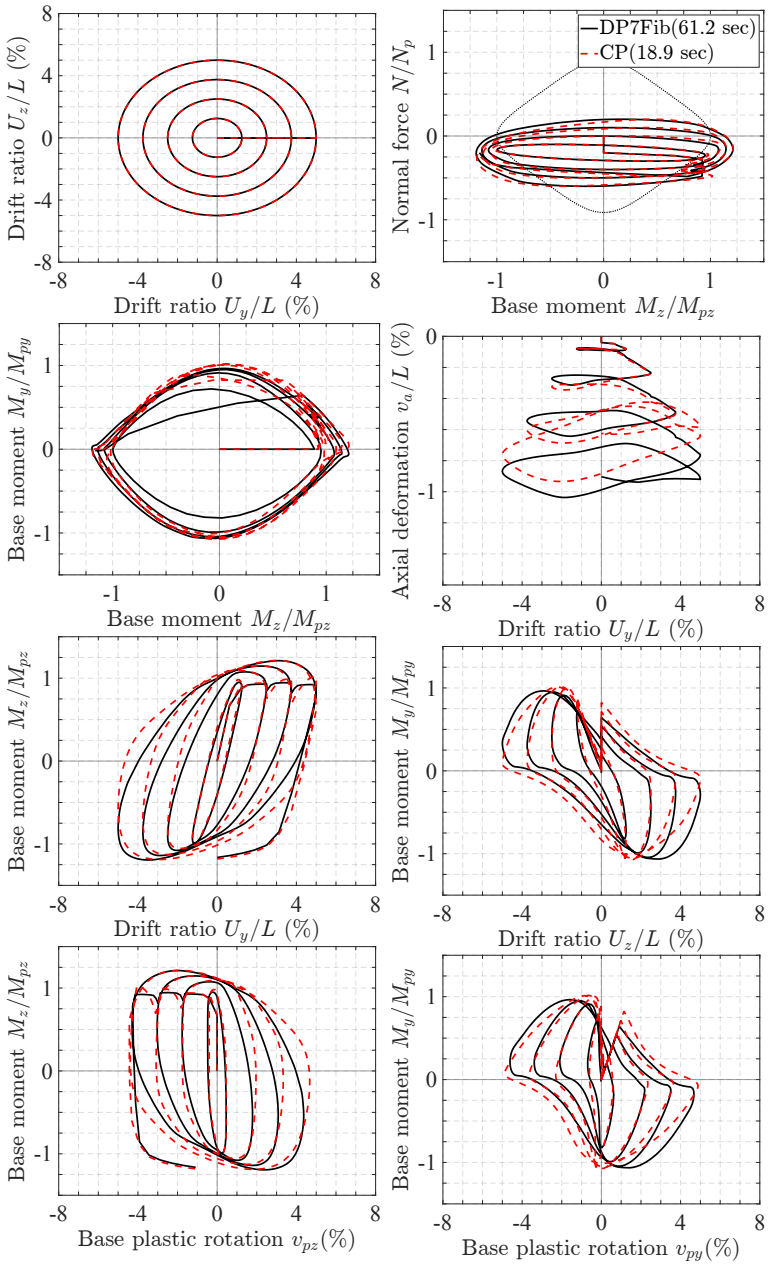


Figure 4.22: Response of W14x730 column under BV1 with $N = -20\%N_p \pm 40\%N_p$

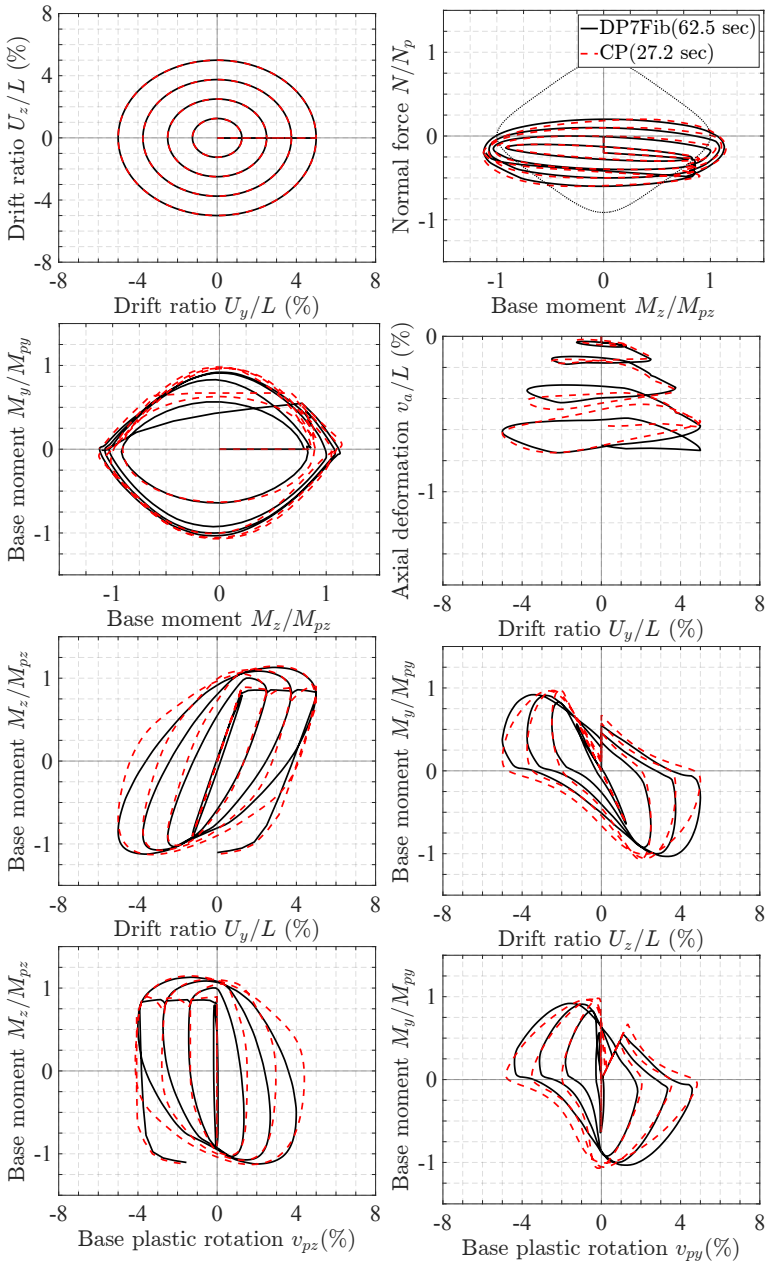


Figure 4.23: Response of W12x120 column under BV1 with $N = -20\%N_p \pm 40\%N_p$

# Chapter 5

# A damage model for N stress resultants

## 5.1 Overview

This chapter extends an existing damage model for describing the strength and stiffness deterioration under cyclic deformations of structural components. The model takes an existing constitutive relation between any two sets of work-conjugate variables and computes a corresponding degraded multivariate response with consistent tangent stiffness. The formulation is based on concepts of continuum damage mechanics and uses multiple damage variables that continuously evolve with the hysteretic energy dissipation and extreme deformation values. Examples of relations that can be degraded with the proposed formulation include material constitutive relations, section force-deformation relations, or frame element force-deformation relations, as illustrated in Chapter 6.

## 5.2 Generalized damage model formulation

The damage model in this study extends the damage model by Do [24], [25], [26], which allows to degrade the hysteretic relation between a pair of work-conjugate variables. The model is extended to accommodate any number N of stress resultants and the corresponding deformations, and new damage loading functions are introduced.

### 5.2.1 Effective space vs. true space

The proposed damage model builds on the concept of *effective stress* introduced by Kachanov [40] and the hypothesis of *strain equivalence* by Lemaitre and Chaboche [13],[51],[74]. These concepts are extended to stress resultant and corresponding deformations, which has been shown to be thermodynamically consistent with the theory of continuum damage mechanics and experimental results [18],[31],[28]. Consequently, the present model is formulated

for the general case of $N$ stresses or stress resultants, referred to as *generalized forces*, which are related to a corresponding set of $N$ strains or deformations, referred to as *generalized deformations*, through a constitutive relation. The generalized forces and generalized deformations are grouped in the vectors $\boldsymbol{s}$ and $\boldsymbol{e}$, respectively,

$$\boldsymbol{s} = \begin{bmatrix} s_1 & ... & s_N \end{bmatrix}^T \tag{5.1}$$

$$\boldsymbol{e} = \begin{bmatrix} e_1 & ... & e_N \end{bmatrix}^T \tag{5.2}$$

It is assumed that a constitutive relation exists between $\boldsymbol{s}$ and $\boldsymbol{e}$, such that for any deformations, it is possible to compute the corresponding forces as well as the tangent stiffness matrix

$$\mathbf{k} = \frac{d\boldsymbol{s}}{d\boldsymbol{e}} \tag{5.3}$$

Furthermore, the existence of $N$ damage parameters $d = \begin{bmatrix} d_1 & ... & d_N \end{bmatrix}^T$ is postulated to characterize the damage state of each generalized force. These damage variables can take values between zero (absence of damage) and one (complete loss of strength), consistent with models in continuum damage mechanics. The concept of *effective generalized force* is then introduced by analogy with the concept of effective stress in the form

$$\bar{\boldsymbol{s}} = \begin{bmatrix} \bar{s}_1 & ... & \bar{s}_N \end{bmatrix}^T = \begin{bmatrix} \dfrac{s_1}{1-d_1} & ... & \dfrac{s_N}{1-d_N} \end{bmatrix}^T \tag{5.4}$$

where $\bar{\boldsymbol{s}}$ is the vector of effective generalized forces. By analogy with the hypothesis of strain equivalence, the principle of *deformation equivalence* states that the effective deformations are equal to the true deformations, so that

$$\bar{\boldsymbol{e}} = \boldsymbol{e} \tag{5.5}$$

and that the damaged state law of the structural member can be obtained by substituting the generalized forces $\boldsymbol{s}$ with the effective generalized forces $\bar{\boldsymbol{s}}$ in the given member constitutive relation. This constitutive relation gives the effective forces $\bar{\boldsymbol{s}}$ for any given deformations $\boldsymbol{e}$ as well as the effective tangent stiffness

$$\bar{\mathbf{k}} = \frac{d\bar{\boldsymbol{s}}}{d\boldsymbol{e}} \tag{5.6}$$

which fully characterizes the response in the effective (undamaged) space.

The force-deformation relation in the effective space defines an upper bound for the true (damaged) response under positive force components and a lower bound for the true response under negative force components. Figure 5.1 illustrates the relation between effective response and true response for the $m$-th generalized force component.

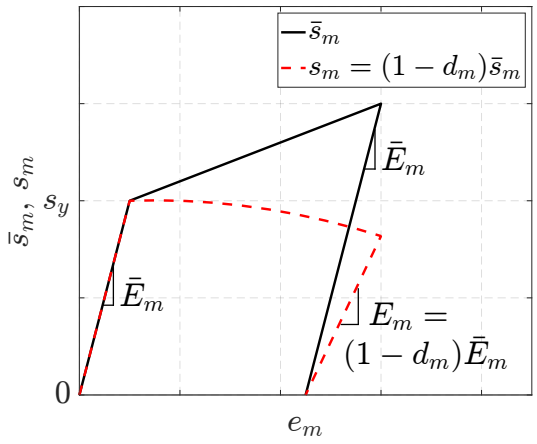


Figure 5.1: Relation between effective response $\bar{s}_m$ and true response $s_m$

### 5.2.2 Positive/negative damage variables

Because structural components may exhibit different damage evolution under a positive force than under a negative force, it is important that the evolution of the damage parameters distinguish between positive effective force states and negative effective force states. Therefore, two separate sets of damage parameters are introduced:

$$\boldsymbol{d}^+ = \begin{bmatrix} d_1^+ & \dots & d_N^+ \end{bmatrix}^T \tag{5.7}$$

$$\boldsymbol{d}^- = \begin{bmatrix} d_1^- & \dots & d_N^- \end{bmatrix}^T \tag{5.8}$$

such that for the $m$-th component $\bar{s}_m$ of the effective force vector, $m \in [\![1, N]\!]$, the corresponding true (degraded) force $s_m$ is equal to

$$s_m = \begin{cases} (1 - d_m^+)\bar{s}_m & \text{if } \bar{s}_m \geq 0 \\ (1 - d_m^-)\bar{s}_m & \text{if } \bar{s}_m < 0 \end{cases} \tag{5.9}$$

This can be rewritten more compactly as:

$$s_m = (1 - d_m^+)\bar{s}_m^+ + (1 - d_m^-)\bar{s}_m^- \tag{5.10}$$

where

$$\bar{s}_m^+ = \frac{\bar{s}_m + |\bar{s}_m|}{2} \quad ; \quad \bar{s}_m^- = \frac{\bar{s}_m - |\bar{s}_m|}{2} \tag{5.11}$$

### 5.2.3 Damage loading function

The damage loading functions provide the criteria for damage growth. Two types of criteria are proposed and are defined either in terms of the total energy dissipation or the

plastic energy dissipation. In both cases, the energy terms are calculated in the effective force space, which is shown to be thermodynamically consistent [24].

Let $m \in [\![1, N]\!]$ represent the index of a particular generalized force or deformation component. A positive and negative damage loading function $g_m^+$ and $g_m^-$, respectively, are introduced to characterize the damage growth as follows:

- If $g_m^+ > 0$, positive damage occurs at $s_m$ and $d_m^+$ increases.
- If $g_m^- > 0$, negative damage occurs at $s_m$ and $d_m^-$ increases.

In order to express the damage loading criteria in terms of either the total or plastic energy dissipation, an auxiliary variable $\tilde{\boldsymbol{e}}$ is introduced:

$$\tilde{\boldsymbol{e}} = \begin{cases} \boldsymbol{e} & \text{for total dissipated energy} \\ \boldsymbol{e}_p = \boldsymbol{e} - \bar{\mathbf{f}}_e \bar{\boldsymbol{s}} & \text{for plastic dissipated energy} \end{cases} \tag{5.12}$$

In the first expression, $\tilde{\boldsymbol{e}}$ is simply equal to the generalized deformation vector $\boldsymbol{e}$. In the second expression, $\tilde{\boldsymbol{e}}$ represents the plastic components of the generalized deformations. These can either be provided directly by effective force-deformation relations, or can be computed explicitly with Equation (5.12), where $\bar{\mathbf{f}}_e$ is elastic compliance of the constitutive relation in the effective space.

With the auxiliary variable $\tilde{\boldsymbol{e}}$, the following integrals describe the scaled energy dissipation under positive effective forces $\varphi_m^+$ and negative effective forces $\varphi_m^-$, respectively.

$$\varphi_m^+(t) = \int_{t_0}^{t} C_{wc,m}^+(\tilde{e}_m)\bar{s}_m(e_m)\dot{\tilde{e}}_m(\tau)d\tau \tag{5.13}$$

$$\varphi_m^-(t) = \int_{t_0}^{t} C_{wc,m}^-(\tilde{e}_m)\bar{s}_m(e_m)\dot{\tilde{e}}_m(\tau)d\tau \tag{5.14}$$

In these integrals, $\dot{\tilde{e}}_m$ denotes the derivative with respect to real time or pseudo-time $\tau$, $t_0$ is the time or pseudo-time at the start of loading, and $t$ is the time or pseudo-time at the current state. $C_{wc,m}^+$ and $C_{wc,m}^-$ are weight functions for the deformations $\tilde{e}_m$ to differentiate between the effects of *primary half-cycles* and *follower half-cycles*. This distinction was first introduced by Konig and Ötes [44] and further explored by Krätzig et al. [46]. Primary half-cycles are characterized by deformation amplitudes that exceed the previous extreme deformations, whereas follower half-cycles have deformation amplitudes that do not exceed the previous extreme deformation values. A feature of the proposed formulation is that the energy dissipation variables $\varphi_m^+$ and $\varphi_m^-$ are continuously updated during the analysis, instead of the discreet updating at the end of each half-cycle in many earlier models [46], [54].

With $\tilde{e}_{m,\min}$ and $\tilde{e}_{m,\max}$ denoting the minimum and maximum previous deformations, i.e.,

$$\tilde{e}_{m,\min} = \min_{t_0 \le \tau \le t} (\tilde{e}_m(\tau)) \tag{5.15}$$

$$\tilde{e}_{m,\max} = \max_{t_0 \le \tau \le t} (\tilde{e}_m(\tau)) \tag{5.16}$$

the weight functions are defined as follows: $C^{+}_{wc,m} : \mathbb{R} \to [0,1]$:

$$C^{+}_{wc,m}(\tilde{e}_m) = \begin{cases} w^{+}_m & \text{if } \tilde{e}_{m,\min} \leq \tilde{e}_m \leq \tilde{e}_{m,\max} \\ 1 & \text{otherwise} \end{cases} \tag{5.17}$$

and $C^{-}_{wc,m} : \mathbb{R} \to [0,1]$:

$$C^{-}_{wc,m}(\tilde{e}_m) = \begin{cases} w^{-}_m & \text{if } \tilde{e}_{m,\min} \leq \tilde{e}_m \leq \tilde{e}_{m,\max} \\ 1 & \text{otherwise} \end{cases} \tag{5.18}$$

where $w^{+}_m \in [0,1]$ and $w^{-}_m \in [0,1]$ are model parameters for the effect of follower half-cycles. Figure 5.2 illustrates the weight functions. Selecting $w^{+}_m = 0$ (or $w^{-}_m = 0$) leads to a formulation in which positive (or negative) follower half-cycles have no effect on the damage growth, while selecting $w^{+}_m = 1$ (or $w^{-}_m = 1$) erases the distinction between positive (or negative) primary and follower half-cycles.

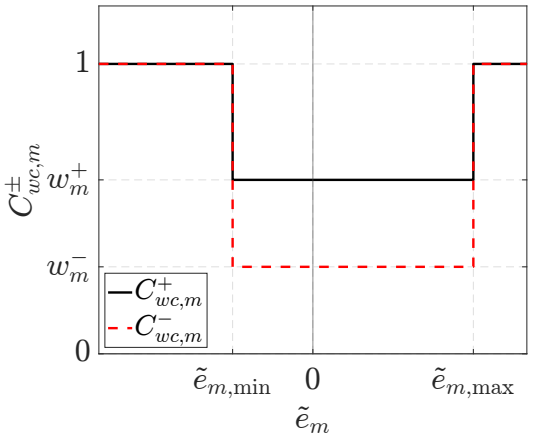


Figure 5.2: Positive and negative weight functions for follower half-cycle effect

A third damage growth criterion is also possible with the following definition for $\varphi^{+}_m$ and $\varphi^{-}_m$

$$\varphi^{+}_m(t) = \int_{t_0}^{t} C^{+}_{wc,m}(\tilde{e}_m)\dot{\tilde{e}}_m(\tau)d\tau \tag{5.19}$$

$$\varphi^{-}_m(t) = \int_{t_0}^{t} C^{-}_{wc,m}(\tilde{e}_m)\dot{\tilde{e}}_m(\tau)d\tau \tag{5.20}$$

This criterion is based on cumulative plastic deformations but this formulation is not further pursued here.

To account for the coupling effect of the positive energy dissipation $\varphi_m^+$ on the negative damage variable $d_m^-$ or, vice versa, the effect of the negative energy dissipation $\varphi_m^-$ on the positive damage variable $d_m^+$, two coupling parameters $C_{cd,m}^+ \geq 0$ and $C_{cd,m}^- \geq 0$ are introduced along with two energy variables $\psi_m^+$ and $\psi_m^-$ as linear combinations of $\varphi_m^+$ and $\varphi_m^-$:

$$\psi_m^+ = \varphi_m^+ + C_{cd,m}^+ \varphi_m^- \quad ; \quad \psi_m^- = \varphi_m^- + C_{cd,m}^- \varphi_m^+ \tag{5.21}$$

Lastly, to account for the effect of $\varphi_l^+$ and $\varphi_l^-$, with $l \in [\![1, N]\!]$ and $l \neq m$ on the evolutions of $d_m^+$ and $d_m^-$, four sets of interaction coefficients $C_{i,m,l}^{++}$, $C_{i,m,l}^{-+}$,$C_{i,m,l}^{--}$ and $C_{i,m,l}^{+-}$ are introduced; and the energy variables $\psi_m^+$ and $\psi_m^-$ are modified as follows:

$$\psi_m^+ = \varphi_m^+ + C_{cd,m}^+ \varphi_m^- + C_{wc,m}^+(e_m) \sum_{\substack{l=1 \\ l \neq m}}^{N} \left[ C_{i,m,l}^{++} \varphi_l^+ + C_{i,m,l}^{-+} \varphi_l^- \right] \tag{5.22}$$

$$\psi_m^- = \varphi_m^- + C_{cd,m}^- \varphi_m^+ + C_{wc,m}^-(e_m) \sum_{\substack{l=1 \\ l \neq m}}^{N} \left[ C_{i,m,l}^{--} \varphi_l^- + C_{i,m,l}^{+-} \varphi_l^+ \right] \tag{5.23}$$

The interaction coefficients take positive values and play the following role

- $C_{i,m,l}^{++}$ controls the effect of $\varphi_l^+$ on $d_m^+$
- $C_{i,m,l}^{-+}$ controls the effect of $\varphi_l^-$ on $d_m^+$
- $C_{i,m,l}^{--}$ controls the effect of $\varphi_l^-$ on $d_m^-$
- $C_{i,m,l}^{+-}$ controls the effect of $\varphi_l^+$ on $d_m^-$

The positive and negative damage loading functions $g_m^+$ and $g_m^-$ are defined with the help of the positive and negative energy thresholds $\psi_{m,\max}^+$ and $\psi_{m,\max}^-$ in the following way:

$$g_m^+ = \psi_m^+ - \psi_{m,\max}^+ \quad ; \quad g_m^- = \psi_m^- - \psi_{m,\max}^- \tag{5.24}$$

where

$$\psi_{m,\max}^+ = \max_{t_0 \leq \tau \leq t} (\psi_m^+(\tau)) \quad ; \quad \psi_{m,\max}^- = \max_{t_0 \leq \tau \leq t} (\psi_m^-(\tau)) \tag{5.25}$$

In other words, the damage variables $d_m^+$ and $d_m^-$ increase when $\psi_m^+$ and $\psi_m^-$ exceed their previous maximum values, respectively.

### 5.2.4 Damage evolution function

The damage evolution function provides the relation between the energy dissipation variables $\psi_m^+$ and $\psi_m^-$ and the damage variables $d_m^+$ and $d_m^-$. The energy dissipation variables are first normalized in the range 0 to 1 according to:

$$\hat{\psi}_m^+ = \frac{\psi_m^+ - \psi_{d0,m}^+}{\psi_{d1,m}^+ - \psi_{d0,m}^+} \quad ; \quad \hat{\psi}_m^- = \frac{\psi_m^- - \psi_{d0,m}^-}{\psi_{d1,m}^- - \psi_{d0,m}^-} \tag{5.26}$$

$\psi_{d0,m}^+$ and $\psi_{d0,m}^-$ are the threshold energy values for the positive and negative damage initiation, respectively. Specifically, positive damage starts accumulating when $\psi_m^+$ reaches $\psi_{d0,m}^+$, and negative damage initiates when $\psi_m^-$ reaches $\psi_{d0,m}^-$. $\psi_{d1,m}^+$ and $\psi_{d1,m}^-$ represent the limit (ultimate) values of the positive and negative energy variables before complete loss of strength. Accordingly, $\psi_m^+ = \psi_{d1,m}^+$ corresponds to $d_m^+ = 1$, while $\psi_m^- = \psi_{d1,m}^-$ corresponds to $d_m^- = 1$.

To facilitate the calibration of the damage parameters, the threshold and limit energy values can be expressed by factoring the corresponding dissipated energy at yield initiation $\psi_{y,m}^+$ and $\psi_{y,m}^-$ with the positive coefficients $C_{d0,m}^+$, $C_{d0,m}^-$, $C_{d1,m}^+$ and $C_{d1,m}^-$:

$$\psi_{d0,m}^+ = C_{d0,m}^+ \psi_{y,m}^+ \quad ; \quad \psi_{d0,m}^- = C_{d0,m}^- \psi_{y,m}^- \tag{5.27}$$

$$\psi_{d1,m}^+ = C_{d1,m}^+ \psi_{y,m}^+ \quad ; \quad \psi_{d1,m}^- = C_{d1,m}^- \psi_{y,m}^- \tag{5.28}$$

The effect of $C_{d0,m}^+$ and $C_{d0,m}^-$ on the damage initiation differs slightly whether the damage loading function is based on total or plastic dissipated energy. If the criteria is based on the total energy dissipation, $C_{d0,m}^+ = 0$ implies that the positive damage evolution starts with the virgin material, while $C_{d0,m}^+ = 1$ implies that the positive damage initiation coincides with the yield point of the effective force-deformation relation between $e_m$ and $\bar{s}_m$. A value $C_{d0,m}^+ > 1$ delays the positive damage initiation after yielding. If however the damage loading function is based on the plastic energy dissipation, the positive damage initiation coincides with the yield point of the effective force-deformation relation when $C_{d0,m}^+ = 0$, while $C_{d0,m}^+ > 0$ leads to a positive damage that initiate after yielding. Such criteria based on the plastic energy does not allow to capture a degradation of the response that would initiate with the virgin material. Analogous statements hold for the negative damage initiation. The remaining two coefficients $C_{d1,m}^+$ and $C_{d1,m}^-$ characterize the total or plastic deformation ductility at the complete loss of strength of the positive and negative force components. Higher values of these coefficients correspond to increased ductility values i.e. a delayed complete loss of strength.

Adopting the proposition of Do [24] and noting that the damage variables $d_m^+$ and $d_m^-$ range from 0 to 1, the current damage formulation uses the beta cumulative probability distribution function $F_B$ for the damage evolution functions. The normalized energy variables $\hat{\psi}_m^+$ and $\hat{\psi}_m^-$ take the place of the random variable and the damage variable $d_m^+$ and $d_m^-$ the place of the cumulative probability, such that:

$$d_m^+ = F_B\left(\hat{\psi}_m^+, \beta_{1,m}^+, \beta_{2,m}^+\right) \quad ; \quad d_m^- = F_B\left(\hat{\psi}_m^-, \beta_{1,m}^-, \beta_{2,m}^-\right) \tag{5.29}$$

where $\beta^+_{1,m}$ and $\beta^+_{2,m}$ are the parameters of the beta cumulative distribution function for the positive damage and $\beta^-_{1,m}$ and $\beta^-_{2,m}$ are the parameters of the beta cumulative distribution function for the negative damage. For better identification of the effect of the parameters $\beta^\pm_{1,m}$ and $\beta^\pm_{2,m}$ on the damage evolution, Do [24] introduced the following alternative parametrization of the beta cumulative distribution function:

$$d^+_{p1,m} = \frac{\beta^+_{2,m}}{\beta^+_{1,m}} \quad ; \quad d^-_{p1,m} = \frac{\beta^-_{2,m}}{\beta^-_{1,m}} \tag{5.30}$$

$$d^+_{p2,m} = \min\left(\beta^+_{1,m}, \beta^+_{2,m}\right) \quad ; \quad d^-_{p2,m} = \min\left(\beta^-_{1,m}, \beta^-_{2,m}\right) \tag{5.31}$$

Figure 5.3 shows the resulting damage evolution function for different values of the parameters $d^\pm_{p1,m}$ and $d^\pm_{p2,m}$. The figure shows that the selection of $d^\pm_{p1,m} > 1$ tends to bias the damage rate accumulation toward the early stages of the energy dissipation, while the selection of $d^\pm_{p1,m} < 1$ biases it toward the later stages. On the other hand, the selection of $d^\pm_{p2,m} > 1$ concentrates the damage accumulation in the middle range of energy dissipation, whereas the selection of $d^\pm_{p2,m} < 1$ concentrates it in the early and the late stage of the response. More information about the effect of the damage model parameters in the context of a 1d constitutive relation can be found in [25].

## 5.3 Implementation

The following description of the implementation of the multivariate damage model presented hereafter does not take advantage of vector notation, so that the explicit nature of the resulting equations facilitate the understanding. However, for the purpose of implementing the damage model into a specific structural analysis software, considerable gain in efficiency can be achieved with the vectorization of the algorithm. The current implementation of the model uses a successfully vectorized version of the algorithm below.

### 5.3.1 State determination algorithm

The state determination is the process of determining the damaged generalized forces $\boldsymbol{s}$ under given generalized deformations $\boldsymbol{e}$ at a certain instant of the response history. First, the time or pseudo-time interval of interest is discretized into a finite number of smaller intervals $\bigcup_n [t_n, t_{n+1}]$. For a typical time step $[t_n, t_{n+1}]$, the effective states at time $t_n$ and $t_{n+1}$ as characterized by the state variables

$$\left\{\boldsymbol{e}_n, \bar{\boldsymbol{s}}_n, \bar{\mathbf{k}}_n\right\} = \left\{\boldsymbol{e}(t_n), \bar{\boldsymbol{s}}(t_n), \bar{\mathbf{k}}(t_n)\right\} \tag{5.32}$$

$$\left\{\boldsymbol{e}_{n+1}, \bar{\boldsymbol{s}}_{n+1}, \bar{\mathbf{k}}_{n+1}\right\} = \left\{\boldsymbol{e}(t_{n+1}), \bar{\boldsymbol{s}}(t_{n+1}), \bar{\mathbf{k}}(t_{n+1})\right\} \tag{5.33}$$

are given from a given constitutive relation between $\bar{\boldsymbol{s}}$ and $\boldsymbol{e}$. The objective is to compute the corresponding damaged generalized forces $\boldsymbol{s}_{n+1}$ and damaged tangent stiffness matrix

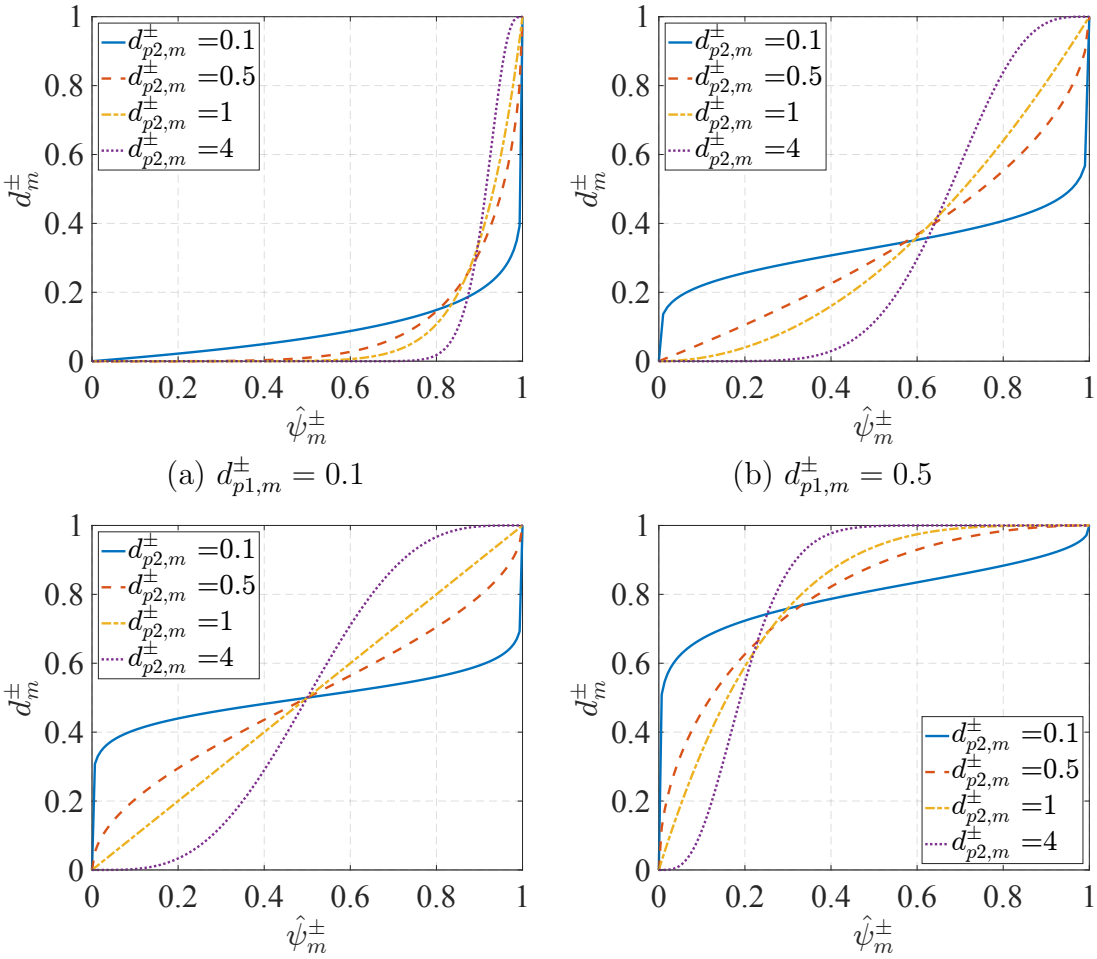


(a) $d^{\pm}_{p1,m} = 0.1$ (b) $d^{\pm}_{p1,m} = 0.5$

(c) $d^{\pm}_{p1,m} = 1$ (d) $d^{\pm}_{p1,m} = 4$

Figure 5.3: Effect of parameters $d^{\pm}_{p1,m}$ and $d^{\pm}_{p2,m}$ on damage evolution function

$\mathbf{k}_{n+1}$ at time $t_{n+1}$, in a way that is consistent with the proposed multivariate damage model. The implementation of the state determination algorithm involves the following steps.

1. Compute the deformation vectors $\tilde{\boldsymbol{e}}_n$ and $\tilde{\boldsymbol{e}}_{n+1}$ at time $t_n$ and $t_{n+1}$:

$$\tilde{\boldsymbol{e}}_n = \begin{cases} \boldsymbol{e}_n & \text{for total dissipated energy} \\ \boldsymbol{e}_{p,n} = \boldsymbol{e}_n - \bar{\mathbf{f}}_e \bar{\boldsymbol{s}}_n & \text{for plastic dissipated energy} \end{cases} \tag{5.34}$$

$$\tilde{\boldsymbol{e}}_{n+1} = \begin{cases} \boldsymbol{e}_{n+1} & \text{for total dissipated energy} \\ \boldsymbol{e}_{p,n+1} = \boldsymbol{e}_{n+1} - \bar{\mathbf{f}}_e \bar{\boldsymbol{s}}_{n+1} & \text{for plastic dissipated energy} \end{cases} \tag{5.35}$$

2. FOR $m = 1$ to $N$:

a) Compute the effective positive and negative forces at time $t_n$ and $t_{n+1}$:

$$\bar{s}^+_{m,n} = \frac{\bar{s}_{m,n} + |\bar{s}_{m,n}|}{2} \quad ; \quad \bar{s}^-_{m,n} = \frac{\bar{s}_{m,n} - |\bar{s}_{m,n}|}{2} \tag{5.36}$$

$$\bar{s}^+_{m,n+1} = \frac{\bar{s}_{m,n+1} + |\bar{s}_{m,n+1}|}{2} \quad ; \quad \bar{s}^-_{m,n+1} = \frac{\bar{s}_{m,n+1} - |\bar{s}_{m,n+1}|}{2} \tag{5.37}$$

b) Compute the scaled positive and negative deformation increments:

$$\Delta^+\tilde{e}_{m,n+1} = \begin{cases} w^+_m \left(\tilde{e}_{m,n+1} - \tilde{e}_{m,n}\right) & \text{if } \tilde{e}_{m,n+1} \leq \tilde{e}_{m,\max} \\ \left(\tilde{e}_{m,n+1} - \tilde{e}_{m,\max}\right) + w^+_m \left(\tilde{e}_{m,\max} - \tilde{e}_{m,n}\right) & \text{otherwise} \end{cases} \tag{5.38}$$

$$\Delta^-\tilde{e}_{m,n+1} = \begin{cases} w^-_m \left(\tilde{e}_{m,n+1} - \tilde{e}_{m,n}\right) & \text{if } \tilde{e}_{m,n+1} \geq \tilde{e}_{m,\min} \\ \left(\tilde{e}_{m,n+1} - \tilde{e}_{m,\min}\right) + w^-_m \left(\tilde{e}_{m,\min} - \tilde{e}_{m,n}\right) & \text{otherwise} \end{cases} \tag{5.39}$$

c) Compute positive and negative scaled dissipated energy variables with the trapezoidal integration rule:

$$\varphi^+_{m,n+1} = \varphi^+_{m,n} + \frac{\bar{s}^+_{m,n+1} + \bar{s}^+_{m,n}}{2} \cdot \Delta^+\tilde{e}_{m,n+1} \tag{5.40}$$

$$\varphi^-_{m,n+1} = \varphi^-_{m,n} + \frac{\bar{s}^-_{m,n+1} + \bar{s}^-_{m,n}}{2} \cdot \Delta^-\tilde{e}_{m,n+1} \tag{5.41}$$

d) Set the positive and negative primary/follower half-cycle coefficients:

$$C^+_{wc,m} = C^+_{wc,m}\left(\tilde{e}_{m,n+1}\right) \quad ; \quad C^-_{wc,m} = C^-_{wc,m}\left(\tilde{e}_{m,n+1}\right) \tag{5.42}$$

e) Update the maximum and minimum deformations:

- IF $\tilde{e}_{m,n+1} > \tilde{e}_{m,\max}$, set $\tilde{e}_{m,\max} = \tilde{e}_{m,n+1}$
- IF $\tilde{e}_{m,n+1} < \tilde{e}_{m,\min}$, set $\tilde{e}_{m,\min} = \tilde{e}_{m,n+1}$

3. FOR $m = 1$ to $N$:

a) Account for the positive/negative energy coupling and inter-component interaction in the determination of $\psi^+_{m,n+1}$ and $\psi^-_{m,n+1}$:

$$\psi^+_{m,n+1} = \varphi^+_{m,n+1} + C^+_{cd,m}\varphi^-_{m,n+1} + C^+_{wc,m}\sum_{\substack{l=1 \\ l\neq m}}^{N}\left[C^{++}_{i,m,l}\varphi^+_{l,n+1} + C^{-+}_{i,m,l}\varphi^-_{l,n+1}\right] \tag{5.43}$$

$$\psi^-_{m,n+1} = \varphi^-_{m,n+1} + C^-_{cd,m}\varphi^+_{m,n+1} + C^-_{wc,m}\sum_{\substack{l=1 \\ l\neq m}}^{N}\left[C^{--}_{i,m,l}\varphi^-_{l,n+1} + C^{+-}_{i,m,l}\varphi^+_{l,n+1}\right] \tag{5.44}$$

b) Evaluate the positive and negative damage loading functions:

$$g^+_{m,n+1} = \psi^+_{m,n+1} - \psi^+_{m,\max} \quad ; \quad g^-_{m,n+1} = \psi^-_{m,n+1} - \psi^-_{m,\max} \tag{5.45}$$

c) FOR $* = +, -$:
IF $g^*_{m,n+1} \leq 0$, implying no damage growth, set $d^*_{m,n+1} = d^*_{m,n}$.
ELSE, damage accumulates:

- Update the energy threshold:

$$\psi^*_{m,\max} = \psi^*_{m,n+1} \tag{5.46}$$

- Compute the normalized dissipated energy:

$$\hat{\psi}^*_{m,n+1} = \frac{\psi^*_{m,n+1} - \psi^*_{d0,m}}{\psi^*_{d1,m} - \psi^*_{d0,m}} \tag{5.47}$$

- Compute the corresponding damage variable:

$$d^*_{m,n+1} = F_B\left(\hat{\psi}^*_{m,n+1}, \beta^*_{1,m}, \beta^*_{2,m}\right) \tag{5.48}$$

d) Evaluate $m$-th component of the damaged generalized forces:

$$s_{m,n+1} = (1 - d^+_{m,n+1})\bar{s}^+_{m,n+1} + (1 - d^-_{m,n+1})\bar{s}^-_{m,n+1} \tag{5.49}$$

4. Evaluate degraded tangent stiffness $\mathbf{k}_{n+1}$ according to Section 5.3.2

### 5.3.2 Degraded consistent tangent stiffness

The degraded consistent tangent stiffness $\mathbf{k}_{n+1}$ at time $t_{n+1}$ is evaluated one row at a time with the determination of

$$\frac{ds_{m,n+1}}{d\boldsymbol{e}_{n+1}} = \left[\frac{ds_{m,n+1}}{de_{1,n+1}} \quad \cdots \quad \frac{ds_{m,n+1}}{de_{N,n+1}}\right] \tag{5.50}$$

for all $m \in [\![1, N]\!]$, followed by the assembly of the full stiffness matrix as:

$$\mathbf{k}_{n+1} = \frac{d\boldsymbol{s}_{n+1}}{d\boldsymbol{e}_{n+1}} = \begin{bmatrix} \dfrac{ds_{1,n+1}}{d\boldsymbol{e}_{n+1}} \\ \vdots \\ \dfrac{ds_{N,n+1}}{d\boldsymbol{e}_{n+1}} \end{bmatrix} \tag{5.51}$$

The steps described below focus on the determination of the $m$-th row of the stiffness matrix, and should be repeated for all values of $m \in [\![1, N]\!]$. The expression for the $m$-th row of the stiffness matrix can be split into three contributions:

$$\frac{ds_{m,n+1}}{d\boldsymbol{e}_{n+1}} = \left[\frac{ds_{m,n+1}}{d\boldsymbol{e}_{n+1}}\right]_A + \left[\frac{ds_{m,n+1}}{d\boldsymbol{e}_{n+1}}\right]_B + \left[\frac{ds_{m,n+1}}{d\boldsymbol{e}_{n+1}}\right]_C \tag{5.52}$$

$$\left[\frac{ds_{m,n+1}}{d\boldsymbol{e}_{n+1}}\right]_A = (1-d^+_{m,n+1})\frac{1+\mathrm{sgn}(\bar{s}_{m,n+1})}{2}\frac{d\bar{s}_{m,n+1}}{d\boldsymbol{e}_{n+1}} \tag{5.53}$$

$$\left[\frac{ds_{m,n+1}}{d\boldsymbol{e}_{n+1}}\right]_B = (1-d^-_{m,n+1})\frac{1-\mathrm{sgn}(\bar{s}_{m,n+1})}{2}\frac{d\bar{s}_{m,n+1}}{d\boldsymbol{e}_{n+1}} \tag{5.54}$$

$$\left[\frac{ds_{m,n+1}}{d\boldsymbol{e}_{n+1}}\right]_C = -\bar{s}^+_{m,n+1}\frac{dd^+_{m,n+1}}{d\boldsymbol{e}_{n+1}} - \bar{s}^-_{m,n+1}\frac{dd^-_{m,n+1}}{d\boldsymbol{e}_{n+1}} \tag{5.55}$$

The first two contributions $[\cdot]_A$ and $[\cdot]_B$ can be directly evaluated following the effective state determination process, after noting that

$$\frac{d\bar{s}_{m,n+1}}{d\boldsymbol{e}_{n+1}} \tag{5.56}$$

is the $m$-th row of $\bar{\mathbf{k}}_{n+1}$, which is assumed to be known. The third contribution $[\cdot]_C$ requires the determination of

$$\frac{dd^+_{m,n+1}}{d\boldsymbol{e}_{n+1}} = \frac{dd^+_{m,n+1}}{d\hat{\psi}^+_{m,n+1}}\frac{d\hat{\psi}^+_{m,n+1}}{d\psi^+_{m,n+1}}\frac{d\psi^+_{m,n+1}}{d\boldsymbol{e}_{n+1}} \quad \text{and} \quad \frac{dd^-_{m,n+1}}{d\boldsymbol{e}_{n+1}} = \frac{dd^-_{m,n+1}}{d\hat{\psi}^-_{m,n+1}}\frac{d\hat{\psi}^-_{m,n+1}}{d\psi^-_{m,n+1}}\frac{d\psi^-_{m,n+1}}{d\boldsymbol{e}_{n+1}} \tag{5.57}$$

which each consists of the product of three terms. These three terms can be evaluated as follows:

$$\frac{dd^+_{m,n+1}}{d\hat{\psi}^+_{m,n+1}} = f_B\left(\hat{\psi}^+_{m,n+1}, \beta^+_{1,m}, \beta^+_{2,m}\right) \quad ; \quad \frac{dd^-_{m,n+1}}{d\hat{\psi}^-_{m,n+1}} = f_B\left(\hat{\psi}^-_{m,n+1}, \beta^-_{1,m}, \beta^-_{2,m}\right) \tag{5.58}$$

$$\frac{d\hat{\psi}^+_{m,n+1}}{d\psi^+_{m,n+1}} = \frac{1}{\psi^+_{d1}-\psi^+_{d0}} \quad ; \quad \frac{d\hat{\psi}^-_{m,n+1}}{d\psi^-_{m,n+1}} = \frac{1}{\psi^-_{d1}-\psi^-_{d0}} \tag{5.59}$$

$$\frac{d\psi^+_{m,n+1}}{d\boldsymbol{e}_{n+1}} = \frac{d\varphi^+_{m,n+1}}{d\boldsymbol{e}_{n+1}} + C^+_{cd,m}\frac{d\varphi^-_{m,n+1}}{d\boldsymbol{e}_{n+1}} + C^+_{wc,m}\sum_{\substack{l=1\\l\neq m}}^{N}\left[C^{++}_{i,m,l}\frac{d\varphi^+_{l,n+1}}{d\boldsymbol{e}_{n+1}} + C^{-+}_{i,m,l}\frac{d\varphi^-_{l,n+1}}{d\boldsymbol{e}_{n+1}}\right] \tag{5.60}$$

$$\frac{d\psi^-_{m,n+1}}{d\boldsymbol{e}_{n+1}} = \frac{d\varphi^-_{m,n+1}}{d\boldsymbol{e}_{n+1}} + C^-_{cd,m}\frac{d\varphi^+_{m,n+1}}{d\boldsymbol{e}_{n+1}} + C^-_{wc,m}\sum_{\substack{l=1\\l\neq m}}^{N}\left[C^{--}_{i,m,l}\frac{d\varphi^-_{l,n+1}}{d\boldsymbol{e}_{n+1}} + C^{+-}_{i,m,l}\frac{d\varphi^+_{l,n+1}}{d\boldsymbol{e}_{n+1}}\right] \tag{5.61}$$

where $f_B$ is the beta probability density function; $\dfrac{d\varphi^+_{m,n+1}}{d\boldsymbol{e}_{n+1}}$ and $\dfrac{d\varphi^-_{m,n+1}}{d\boldsymbol{e}_{n+1}}$ are evaluated as:

$$\frac{d\varphi^+_{m,n+1}}{d\boldsymbol{e}_{n+1}} = C^+_{wc,m}\frac{\bar{s}^+_{m,n+1}+\bar{s}^+_{m,n}}{2}\frac{d\tilde{e}_{m,n+1}}{d\boldsymbol{e}_{n+1}} + \Delta^+\tilde{e}_{m,n+1}\frac{1+\mathrm{sgn}(\bar{s}_{m,n+1})}{2}\frac{1}{2}\frac{d\bar{s}_{m,n+1}}{d\boldsymbol{e}_{n+1}} \tag{5.62}$$

$$\frac{d\varphi^-_{m,n+1}}{d\boldsymbol{e}_{n+1}} = C^-_{wc,m}\frac{\bar{s}^-_{m,n+1}+\bar{s}^-_{m,n}}{2}\frac{d\tilde{e}_{m,n+1}}{d\boldsymbol{e}_{n+1}} + \Delta^-\tilde{e}_{m,n+1}\frac{1-\mathrm{sgn}(\bar{s}_{m,n+1})}{2}\frac{1}{2}\frac{d\bar{s}_{m,n+1}}{d\boldsymbol{e}_{n+1}} \tag{5.63}$$

with analogous expressions for $\dfrac{d\varphi^{+}_{l,n+1}}{d\boldsymbol{e}_{n+1}}$ and $\dfrac{d\varphi^{-}_{l,n+1}}{d\boldsymbol{e}_{n+1}}$; and $\dfrac{d\tilde{e}_{m,n+1}}{d\boldsymbol{e}_{n+1}}$ is the $m$-th row of

$$\frac{d\tilde{\boldsymbol{e}}_{n+1}}{d\boldsymbol{e}_{n+1}} = \begin{cases} \boldsymbol{I} & \text{if } \tilde{\boldsymbol{e}} = \boldsymbol{e} \text{ (total dissipated energy)} \\ \boldsymbol{I} - \bar{\mathbf{f}}_e \bar{\mathbf{k}}_{n+1} & \text{if } \tilde{\boldsymbol{e}} = \boldsymbol{e}_p \text{ (plastic dissipated energy)} \end{cases} \tag{5.64}$$

# Chapter 6

# A family of damage-plasticity frame elements with axial-flexure interaction

## 6.1 Overview

This chapter presents a family of damage-plasticity frame elements with axial-flexure interaction. The proposed models are based on stress resultant plasticity or distributed plasticity formulations with an independent damage wrapper that is inserted within the element state determination. The family allows the representation of the strength and stiffness deterioration in the material response, section response, or overall element response. The detailed state determination algorithm is presented for several elements of interest, followed by the calibration and validation of the models against available experimental data.

## 6.2 Concept

The multivariate damage model of Chapter 5 is deployed for the degradation of the inelastic response of frame elements. A first option consists of wrapping the damage model around the entire frame element state determination to degrade the relation between the element basic forces $\boldsymbol{q}$ and the element deformations $\boldsymbol{v}$. This approach has the advantage that it can be used with any type of frame element, thus offering great flexibility. In particular, the damage model can be combined with the resultant plasticity beam-column elements of this study to generate damage resultant plasticity frame elements. A second option for element formulations with several nested levels of state determination, consists of wrapping the damage model around a particular level of state determination. Specifically, for the case of a distributed plasticity beam-column element with fiber section discretization with three nested levels of state determination, the damage model can be wrapped around the element basic state variables $\boldsymbol{q}$ and $\boldsymbol{v}$, the section state variables $\boldsymbol{s}$ and $\boldsymbol{e}$ or the material state variables $\boldsymbol{\sigma}$ and $\boldsymbol{\varepsilon}$. A benefit of this approach is that it can be used with 3d material models to account for shear deformations, or with phenomenological material models for metals

that account for the Bauschinger effect. For distributed plasticity beam-column elements with stress-resultant section, the element formulation involves two nested levels of state determination and the damage model can be wrapped either around the element basic state variables $\boldsymbol{q}$ and $\boldsymbol{v}$ or the section state variables $\boldsymbol{s}$ and $\boldsymbol{e}$. Table 6.1 summarizes these model alternatives, with CP referring to concentrated or resultant plasticity element formulations and DP referring to distributed plasticity formulations.

| **Element Model** | **Section Model** | **Damage Wrapper** |
|---|---|---|
| CP | - | Element |
| DP | Resultant | Element |
| DP | Resultant | Section |
| DP | Fiber | Element |
| DP | Fiber | Section |
| DP | Fiber | Material |

Table 6.1: Different frame element models with damage

The elements in Table 6.1 are listed in order of increasing complexity and computational effort. These elements offer significant flexibility for iterative refinement strategies in the simulation of large structural models. Specifically, the proposed elements can be used to gradually refine specific elements within a large scale model, so as to achieve a target level of accuracy at critical locations while optimizing the computational effort of the analysis. An example of such strategy is described below:

- Start with the simplest element for the entire structure (e.g. resultant plasticity beam-column elements with damage), and assess the effect of deterioration on the global response;
- Identify the locations of major damage and replace the corresponding elements with more sophisticated ones that offer more accurate of the local response at the critical locations.

The following discussion assesses and validates four elements from Table 6.1 against experimental data:

- The resultant plasticity frame element with damage wrapped at the element level;
- The distributed plasticity frame element with a resultant section model and damage wrapped at the section level;

- The distributed plasticity frame element with a fiber section model and damage wrapped at the section level;
- The distributed plasticity frame element with a fiber section model and damage wrapped at the material level.

## 6.3 Concentrated resultant force plasticity frame elements with damage

This section describes the formulation of a concentrated resultant force plasticity beam element with damage, followed by the formulation of a concentrated resultant force plasticity column element with damage that accounts for the axial-flexure interaction.

### 6.3.1 Concentrated resultant force plasticity beam element with damage

#### 6.3.1.1 Formulation and implementation

The resultant plasticity beam element with damage combines the damage model of Chapter 5 with the uniaxial bending beam element of Chapter 3. The formulation assumes that the axial response is linear elastic and uncoupled from the flexural response. The damage is wrapped around the relation between the flexural basic forces $\boldsymbol{q}_f = \begin{bmatrix} q_i & q_j \end{bmatrix}^T$ and the flexural deformations $\boldsymbol{v}_f = \begin{bmatrix} v_i & v_j \end{bmatrix}^T$, while the axial response does not include damage. The state determination of the combined element involves the following steps:

1. Perform the resultant plasticity beam element state determination in Table 3.3 up to Step 4a. This results in the axial force $q_a$ and the axial stiffness $k_a$, which are final, and the effective (undamaged) flexural forces $\bar{\boldsymbol{q}}_f$ and effective flexural stiffness $\bar{\mathbf{k}}_f$, which will be degraded.
2. Determine the damaged flexural forces $\boldsymbol{q}_f$ and damaged flexural stiffness $\mathbf{k}_f$ with the algorithm of Section 5.3.1.
3. Aggregate the axial and flexural responses according to Step 4b of Table 3.3.

The process is summarized in Figure 6.1, in which $\boldsymbol{H}_{v,e}$ refers to the history variables of the element effective state determination and $\boldsymbol{H}_{v,d}$ refers to the history variables of the damage state determination algorithm.

The damage evolution functions require the flexural energy dissipation at yield initiation associated with the flexural response at each beam end for the determination of the damage threshold and the limit energy values. These are defined as:

$$\psi_{y,1}^{\pm} = \frac{L}{6EI} M_{pi}^2 \quad ; \quad \psi_{y,2}^{\pm} = \frac{L}{6EI} M_{pj}^2 \tag{6.1}$$

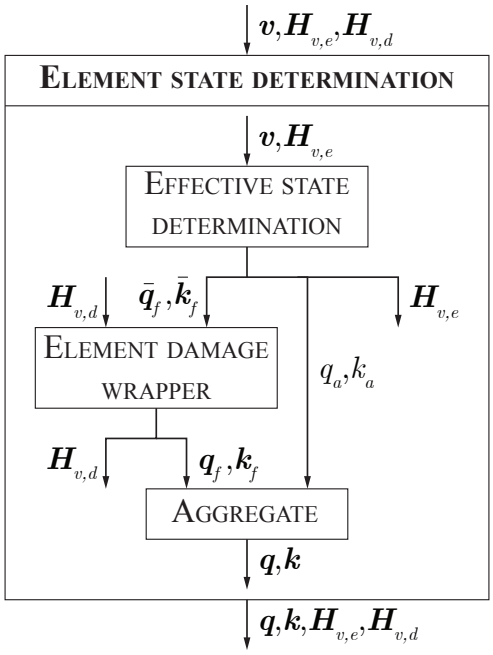


Figure 6.1: State determination for resultant plasticity beam element with damage

which corresponds to the flexural yield energy under an antisymmetric curvature distribution. Additionally, when using the damage evolution criteria based on the plastic energy dissipation, the damage model requires the specification of the elastic flexural flexibility of the beam element which is given by $\bar{\mathbf{f}}_e = \mathbf{k}_{fe}^{-1}$, where $\mathbf{k}_{fe}$ is the elastic flexural stiffness in Equation (3.9).

## 6.3.2 Concentrated resultant force plasticity column element with damage

### 6.3.2.1 2d element formulation and implementation

The 2d resultant plasticity column element with damage combines the damage model of Chapter 5 with the 2d column element model of Chapter 4. The axial response is no longer linear elastic and is coupled with the flexural response under uniaxial bending. The damage is wrapped around the relation between the element basic forces $\boldsymbol{q} = \begin{bmatrix} q_a & q_i & q_j \end{bmatrix}^T$ and the element deformations $\boldsymbol{v} = \begin{bmatrix} v_a & v_i & v_j \end{bmatrix}^T$. The state determination of the combined element involves the following steps:

1. Perform the resultant plasticity column element state determination in Tables 4.3. This results in the effective (undamaged) basic forces $\bar{\boldsymbol{q}}$ and the effective stiffness $\bar{\mathbf{k}}$, which will be degraded.

2. Determine the damaged basic forces $\boldsymbol{q}$ and the damaged flexural stiffness $\mathbf{k}$ with the algorithm of Section 5.3.1.

The process is summarized in Figure 6.2, in which $\boldsymbol{H}_{v,e}$ refers to the history variables of the element effective state determination and $\boldsymbol{H}_{v,d}$ refers to the history variables of the damage state determination algorithm.

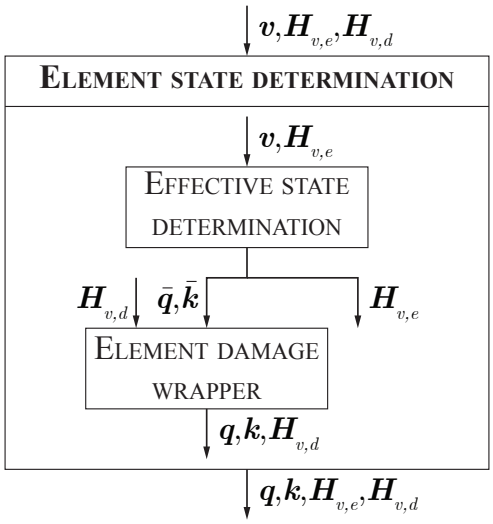


Figure 6.2: State determination for 2d resultant plasticity column with damage

The damage evolution functions require the energy dissipation at yield initiation associated with each basic force for the determination of the damage threshold and the limit energy values. These are defined as:

$$\psi^{\pm}_{y,1} = \frac{L}{2EA} N_p^2 \quad ; \quad \psi^{\pm}_{y,2} = \frac{L}{6EI} M_{pi}^2 \quad ; \quad \psi^{\pm}_{y,3} = \frac{L}{6EI} M_{pj}^2 \tag{6.2}$$

Additionally, when using the damage evolution criteria based on the plastic energy dissipation, the damage model requires the specification of the elastic flexibility of the frame element which is given by $\bar{\mathbf{f}}_e = \mathbf{k}_e^{-1}$, where $\mathbf{k}_e$ is the elastic stiffness in Equation (4.8).

#### 6.3.2.2 3d element formulation and implementation

The 3d resultant plasticity column element with damage combines the damage model of Chapter 5 with the 3d column element model of Chapter 4. It is an extension of the 2d damage resultant plasticity column model that accommodates biaxial bending. The torsional behavior is assumed to be linear elastic and uncoupled from the axial and the flexural responses. The damage is wrapped around the relation between the inelastic basic forces $\boldsymbol{q}_{in} = \begin{bmatrix} q_a & q_{zi} & q_{zj} & q_{yi} & q_{yj} \end{bmatrix}^T$ and the corresponding inelastic deformations $\boldsymbol{v}_{in} =$

$\begin{bmatrix} v_a & v_{zi} & v_{zj} & v_{yi} & v_{yj} \end{bmatrix}^T$, while the torsional response does not include damage. The state determination of the combined element involves the following steps:

1. Perform the resultant plasticity beam element state determination in Table 4.4 up to Step 4a. This results in the torsional force $q_t$ and the torsional stiffness $k_t$ which are final, and the effective (undamaged) inelastic forces $\bar{\boldsymbol{q}}_{in}$ and the effective inelastic stiffness $\bar{\mathbf{k}}_{in}$, which will be degraded.

2. Determine the damaged inelastic basic forces $\boldsymbol{q}_{in}$ and damaged inelastic stiffness $\mathbf{k}_{in}$ with the algorithm of Section 5.3.1.

3. Aggregate the elastic torsional and inelastic responses according to Step 4b of Table 4.4.

The process is summarized in Figure 6.3, in which $\boldsymbol{H}_{v,e}$ refers to the history variables of the element effective state determination and $\boldsymbol{H}_{v,d}$ refers to the history variables of the damage state determination algorithm.

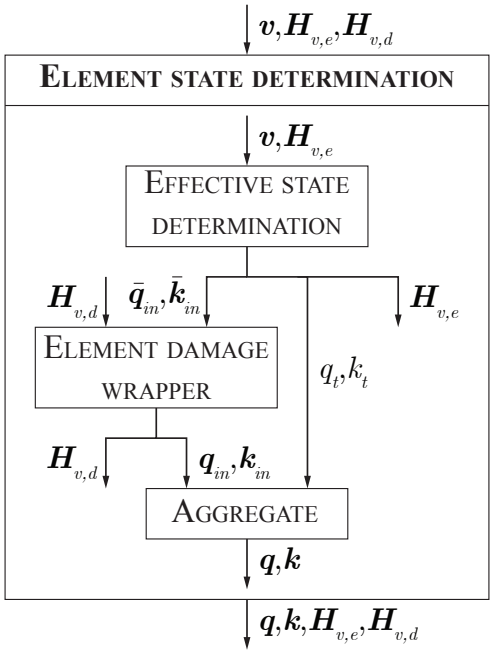


Figure 6.3: State determination for 3d resultant plasticity column element with damage

The damage evolution functions require the energy dissipation at yield initiation associated with each inelastic basic force for the determination of the damage threshold and the limit energy values. These are defined as:

$$\psi^{\pm}_{y,1} = \frac{L}{2EA} N_p^2 \quad ; \quad \psi^{\pm}_{y,2} = \frac{L}{6EI_z} M^2_{pz,i} \quad ; \quad \psi^{\pm}_{y,3} = \frac{L}{6EI_z} M^2_{pz,j} \tag{6.3}$$

$$\psi^{\pm}_{y,4} = \frac{L}{6EI_y} M_{py,i} \quad ; \quad \psi^{\pm}_{y,5} = \frac{L}{6EI_y} M^2_{py,j} \tag{6.4}$$

Additionally, when using the damage evolution criteria based on the plastic energy dissipation, the damage model requires the specification of the elastic flexibility associated with the inelastic basic forces which is given by $\bar{\mathbf{f}}_e = \mathbf{k}^{-1}_{in,e}$, where $\mathbf{k}_{in,e}$ is the elastic stiffness in Equation (4.53).

#### 6.3.2.3 Validation studies with experimental data

The proposed frame elements with damage are assessed with available experimental data for the cyclic strength and stiffness deterioration of steel column specimens. The column specimens were tested under different boundary conditions and were subjected to uniaxial and biaxial bending conditions with constant or variable axial force. The correlation studies of the proposed frame elements with damage do not strive for exhaustive accuracy but hope to demonstrate the potential of the element to capture the hysteretic response of multiple steel members up to failure with a consistent set of damage parameters.

**Columns by Cravero et al. [23]** Cravero et al. [23] investigated the experimental behavior of 12 wide-flange steel cantilever columns under prescribed axial load and lateral drift demands. Three cross sections were selected: W14x61 (specimens A1-A4), W16x89 (specimens B1-B4) and W14x82 (specimens C1-C4). These are representative of first-story columns of mid-rise moment resisting frames (4 to 8 stories) at a two-third scale [23]. The specimens were all tested in a cantilever configuration with fixed-pinned boundary conditions and were subjected to prescribed displacements at the top of the column inducing strong-axis bending. The specimens were supported so as to prevent out-of-plane deformations. First, the monotonic backbone curves are obtained for each selected cross section under two levels of constant compressive axial loads: $N = -30\%N_p$ and $N = -50\%N_p$, where $N_p$ is the plastic axial capacity of the cross section. These tests are referred to as A1-A2, B1-B2 and C1-C2, as summarized in Table 6.2. The specimens are then tested under two types of cyclic protocols:

- A modified version of the standard AISC symmetric cyclic load protocol [72] [19], in which the number of elastic cycles has been reduced to focus on the response under large deformations. This protocol is composed of consecutive cycles with increasing magnitudes and is representative of seismic demands under a design-basis earthquake.
- A collapse-consistent lateral loading protocol [83] representative of seismic demands under a ground motion with low-probability of occurrence. This motion is characterized by a lateral motion leading to ratcheting effect, that results in dynamic instability.

The lateral drift protocols are combined with a constant or variable axial load, with levels ranging from $N = -75\%N_p$ (compression) to $N = +15\%N_p$ (tension). These tests are

| **Specimen** | Section Size | Lateral protocol | $N/N_p$ |
|---|---|---|---|
| **A1** | W14x61 | Monotonic | $-30\%$ |
| **A2** | W14x61 | Monotonic | $-50\%$ |
| **B1** | W16x89 | Monotonic | $-30\%$ |
| **B2** | W16x89 | Monotonic | $-50\%$ |
| **C1** | W14x82 | Monotonic | $-30\%$ |
| **C2** | W14x82 | Monotonic | $-50\%$ |

Table 6.2: Summary of monotonic tests conducted by Cravero et al. [23]

| **Specimen** | Section Size | Lateral protocol | $N/N_p$ |
|---|---|---|---|
| **A3** | W14x61 | Collapse-consistent | $-50\%$ |
| **A4** | W14x61 | Symmetric | $-30\% \pm 45\%$ |
| **B3** | W16x89 | Symmetric | $-50\%$ |
| **B4** | W16x89 | Symmetric | $-50\% \pm 25\%$ |
| **C3** | W14x82 | Symmetric | $-50\%$ |
| **C4** | W14x82 | Symmetric | $-75\%$ |

Table 6.3: Summary of cyclic tests conducted by Cravero et al. [23]

referred to as A3-A4, B3-B4 and C3-C4, as summarized in Table 6.3. More details about the loading protocols can be found in [23].

The 2d resultant plasticity column element with damage is used to replicate the behavior of the tested specimens. The columns are modeled with a single element of length $L = 1,825$ mm $= 5.99$ ft, as illustrated in Figure 6.4. The three degrees of freedom at the base of the column are restrained (fixed) and the top of the column is free except for the horizontal degree of freedom which is subjected to the imposed lateral drift protocol. The imposed axial force is applied at the column tip. The effect of nonlinear geometry is accounted for with the P-$\Delta$ formulation.

The coefficients for the polynomial approximation of the yield surface are selected to match the exact yield surface of each cross section. The following polynomial is used for the W14x61 and W14x82 cross sections of the specimens A1-A4 and C1-C4:

$$\phi\left(\boldsymbol{s}\right) = 1.2\left|\frac{N}{N_p}\right|^2 + 1.0\left|\frac{M_z}{M_{pz}}\right|^2 + 4.0\left|\frac{N}{N_p}\right|^2\left|\frac{M_z}{M_{pz}}\right|^2 \tag{6.5}$$

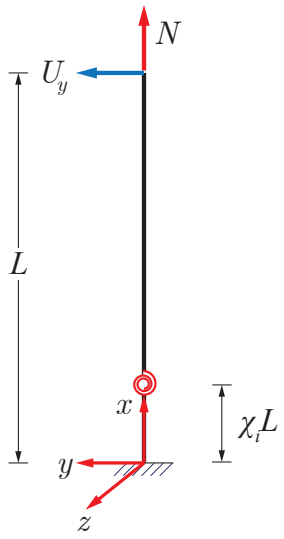


Figure 6.4: Resultant plasticity cantilever column model for Cravero et al. specimens [23]

and the following polynomial is used for the W16x89 cross section of the specimens B1-B4:

$$\phi(\boldsymbol{s}) = 1.2\left|\frac{N}{N_p}\right|^2 + 1.0\left|\frac{M_z}{M_{pz}}\right|^2 + 3.5\left|\frac{N}{N_p}\right|^2\left|\frac{M_z}{M_{pz}}\right|^2 \tag{6.6}$$

Figure 6.5 shows the quality of the approximation of the initial yield surface for each cross section.

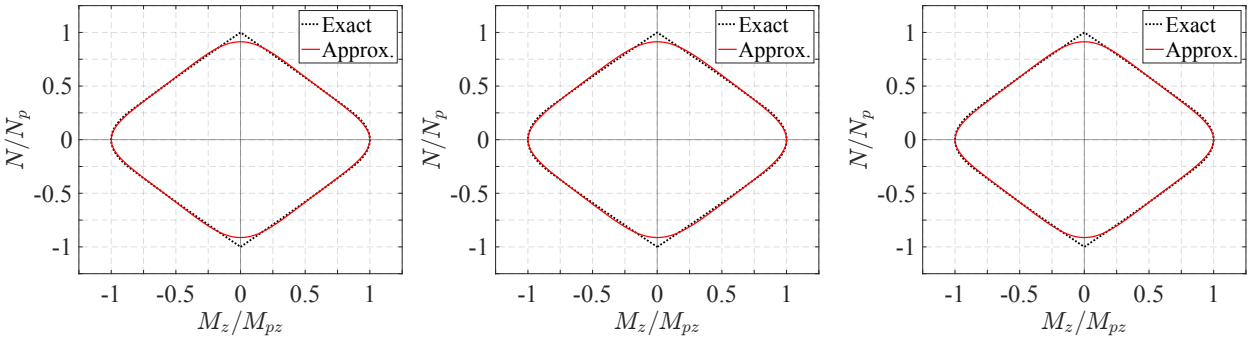


(a) A1-A4 (W14x61) (b) B1-B4 (W16x89) (c) C1-C4 (W14x82)

Figure 6.5: Polynomial approximation of initial yield surface for Cravero et al. specimens [23]

The plastic axial and flexural capacities of the specimens are defined as $N_p = Af_y$ and $M_{pz} = Z_z f_y$ where $f_y$ is the expected yield stress of steel, $A$ is the area of the cross section,

and $Z_z$ is the plastic modulus of the cross section with respect to its strong axis. The values used for $f_y$, as well as for the Young Modulus of steel $E$, are based on the average results of the uniaxial tensile coupon tests reported in [23]. These values are summarized in Table 6.4, and the resulting plastic capacities are listed in Table 6.5. The numerical model make use of kinematic and isotropic hardening as well as the hinge offset capabilities of the resultant plasticity column element, with parameter values in Table 6.6. The beam-column element also includes the elastic shear deformations, as recommended in [23]. These are uncoupled from the plastic axial-flexure response.

| **Column Specimen** | $f_y$ (ksi) | $E$ (ksi) |
|---|---|---|
| **A1-A4** | 53.1 | 29,343 |
| **B1-B4** | 54.5 | 28,921 |
| **C1-C4** | 57.6 | 28,989 |

Table 6.4: Material parameters for Cravero et al. specimens [23]

| **Column Specimen** | $N_p$ (kips) | $M_{pz}$ (kip-in) |
|---|---|---|
| **A1-A4** | 950.20 | 5,414.5 |
| **B1-B4** | 1,426.9 | 9,530.8 |
| **C1-C4** | 1,381.9 | 8,003.6 |

Table 6.5: Plastic axial and flexural capacities for Cravero et al. specimens [23]

| **Column Specimen** | $H_{kr,a}$ (%) | $H_{kr,fz,i}$ (%) | $H_{kr,fz,j}$ (%) | $H_{ir,i}$ (‰) | $H_{ir,j}$ (‰) | $\chi_i$ (%) | $\chi_j$ (%) |
|---|---|---|---|---|---|---|---|
| **A1-A4** | 0.4 | 0.4 | 0.4 | 0.5 | 0.5 | 0 | 0 |
| **B1-B4** | 0.4 | 0.4 | 0.4 | 0.5 | 0.5 | 20 | 0 |
| **C1-C4** | 1.0 | 1.0 | 1.0 | 0.5 | 0.5 | 23 | 0 |

Table 6.6: Resultant plasticity column parameters for Cravero et al. specimens [23]

The damage model is wrapped around the three element basic forces $\boldsymbol{q}$ and the three element deformations $\boldsymbol{v}$. The following discussion addresses the selection of suitable damage model parameters for the simulation of the column specimens.

- The coefficients $C^{\pm}_{d0,m}$, $m \in [\![1,3]\!]$, control the positive/negative damage initiation for the $m$-th basic force. These are set to:

$$C^{\pm}_{d0,1} = C_{d0,a} \quad ; \quad C^{\pm}_{d0,2} = C^{\pm}_{d0,3} = C_{d0,f} \tag{6.7}$$

with the values for $C_{d0,a}$ and $C_{d0,f}$ in Table 6.7. The subscript $a$ refers to the axial response, whereas the subscript $f$ refers to the flexural response at both ends of the element. No distinction is made between the deterioration under positive and negative effective basic forces. The choice of $C_{d0,a} = 200$ for all specimens delays the onset of axial damage sufficiently to avoid triggering this damage mechanism during the analyses. This is motivated by the fact that damaging the axial force of a member under a prescribed load history can lead to numerical issues if not done carefully, especially under high axial load values. Indeed, under a prescribed axial force $N$, equilibrium requires that the true (damaged) axial basic force be $q_a = N$, which implies an effective axial force of $\bar{q}_a = N/(1-d^{\pm}_a)$. For high values of $N$ or values of $d^{\pm}_a$ close to 1, the effective axial force will exceed the plastic axial capacity $N_p$ which is difficult to accommodate in a plasticity formulation. When including axial damage in a resultant plasticity element, it is recommended to cap the axial damage index $d^{\pm}_a$ to:

$$\frac{|N|}{1-d^{\pm}_a} \leq N_p \Longleftrightarrow d^{\pm}_a \leq 1 - \frac{|N|}{N_p} \tag{6.8}$$

Modeling the axial strength and stiffness deterioration may be of particular importance for components subjected to variable axial loads because it is expected to affect the multiple axial reloading branches. This may be particularly relevant for exterior columns in moment resisting frames which may experience variable axial forces under dynamic overturning moments. The following results show that this was not necessary for the specimens of this study. The coefficient $C_{d0,f}$ is set to values between 12 and 42, representative of the different delays in the onset of local buckling for the three sections. The value $C_{d0,f} = 12$ used for the A specimens is representative of higher local slenderness ratios (flange slenderness ratio $b_f/(2t_f) = 7.8$, web slenderness ratio $h/t_w = 30.4$) which lead to an earlier onset of local buckling, relative to specimens B and C. These last two specimens have identical flange slenderness ratios ($b_f/(2t_f) = 5.9$) but different web slenderness ratio ($h/t_w = 25.9$ for B specimens and $h/t_w = 22.4$ for C specimens), so that the C specimens are the stockiest. Additionally, the latter are made of a different steel material with higher hardening [23], which further delays the onset of local buckling. This motivates the selection of a higher value $C_{d0,f} = 42$ for the specimens C than for specimens B, which use a coefficient $C_{d0,f} = 30$.

- The coefficients $C^{\pm}_{d1,m}$, $m \in [\![1,3]\!]$, control the positive/negative damage ductility for the $m$-th basic force. These are set to:

$$C^{\pm}_{d1,1} = C_{d1,a} \quad ; \quad C^{\pm}_{d1,2} = C^{\pm}_{d1,3} = C_{d1,f} \tag{6.9}$$

with the values for $C_{d1,a}$ and $C_{d1,f}$ in Table 6.7. The choice of $C_{d1,a} = 200$ for all the specimens has no effect on the results since axial damage is not triggered over the analyses. The coefficient $C_{d1,f}$ is set to values between 150 and 320, representative of the different damage limit values for the three specimens. The value $C_{d1,f} = 150$ used for the A specimens is representative of higher local slenderness ratios which result in an accelerated rate of strength and stiffness deterioration, relative to specimens B and C. The selection of a lower value $C_{d1,f} = 240$ for the specimens C than for specimens B, which use $C_{d1,f} = 320$ is representative of the more gradual post-capping slope exhibited by the latter which result in increased damaged ductility.

- The primary/follower half-cycle parameter $w^{\pm}_m$ and the positive/negative coupling parameters $C^{\pm}_{cd,m}$ associated with the $m$-th basic force are set to:

$$w^{\pm}_1 = w^{\pm}_2 = w^{\pm}_3 = w \tag{6.10}$$

$$C^{\pm}_{cd,1} = C^{\pm}_{cd,2} = C^{\pm}_{cd,3} = C_{cd} \tag{6.11}$$

where $w = 0.35$ and $C_{cd} = 0.2$, as listed in Table 6.7. The value for $w$ indicates a moderate but not negligible effect of follower half-cycles on the damage accumulation. The value for $C_{cd}$ indicates the presence of minor coupling between the positive and the negative response: the strength deterioration in the positive direction slightly affects the behavior in the negative direction and vice-versa.

- The stress-resultant interaction coefficients $C^{\pm\pm}_{i,m,l}$ are used to model the effect of a negative axial force on the flexural strength and stiffness deterioration. This is achieved by prescribing

$$C^{-+}_{i,m,l} = \begin{cases} C_i & \text{if } (m,l) = (2,1) \text{ or } (m,l) = (3,1) \\ 0 & \text{otherwise} \end{cases} \tag{6.12}$$

$$C^{--}_{i,m,l} = \begin{cases} C_i & \text{if } (m,l) = (2,1) \text{ or } (m,l) = (3,1) \\ 0 & \text{otherwise} \end{cases} \tag{6.13}$$

$$C^{++}_{i,m,l} = C^{+-}_{i,m,l} = 0 \quad \forall (m,l) \in [\![1,3]\!] \times [\![1,3]\!] \tag{6.14}$$

with $C_i$ in Table 6.7. The value $C_i = 2$ gives satisfactory results for all specimens, except for A4 which required the smaller value of $C_i = 0.5$ for the interaction coefficient.

| **Column Specimen** | $C_{d0,a}$ | $C_{d1,a}$ | $C_{d0,f}$ | $C_{d1,f}$ | $w$ | $C_{cd}$ | $C_i$ |
|---|---|---|---|---|---|---|---|
| **A1-A4** | 200 | 200 | 12 | 150 | 0.35 | 0.20 | 2.0 (0.5 for A4) |
| **B1-B4** | 200 | 200 | 30 | 320 | 0.35 | 0.20 | 2.0 |
| **C1-C4** | 200 | 200 | 42 | 240 | 0.35 | 0.20 | 2.0 |

Table 6.7: Column damage parameters for Cravero et al. specimens [23]

- The damage evolution law uses the beta cumulative distribution function with a criterion based on the plastic energy dissipation. The beta distribution function parameters are set as $\beta^{\pm}_{1,m} = 1$ and $\beta^{\pm}_{2,m} = 4$, or equivalently, $d^{\pm}_{p1,m} = 4$, $d^{\pm}_{p2,m} = 1$, $\forall m \in [\![1, 3]\!]$.

Figures 6.6 and 6.7 show the base moment rotation response and the axial deformation response for the specimens under monotonic loading protocols. The following observations are made:

- For a given section size, increasing the axial load reduces the flexural strength capacity as well as the yield rotation capacity of the column. This is well captured by the polynomial approximation of the axial-flexure interaction surface.
- The material hardening behavior and the spread of plasticity are well represented with the specification of kinematic and isotropic hardening along with the hinge offset parameter of the resultant plasticity column model. Some discrepancy in the transition from the elastic to the plastic range is observed, which is a typical limitation of the linear hardening assumption.
- The increase of the hinge offset from specimens A to specimens C, where A have the most slender cross section and C have the stockiest cross section, agrees with the finding of Cravero et al. [23] that the extent of plastic hinge length decreases with increasing slenderness of the cross section.
- Regardless of the applied axial compressive force, the most compact column (C specimens) experiences a delayed onset of local buckling, compared with the other two types of specimens. This is captured with the use of a coefficient $C_{d0,f}$ that decreases with increasing slenderness of the cross section.
- For a given section size, increasing the axial load accelerates the onset of local buckling which occurs at smaller rotation levels. This is captured by the interaction coefficient $C_i$ which includes part of the plastic axial energy dissipation into the flexural energy dissipation. Under increasing levels of axial force, that axial energy terms grow faster which triggers the flexural damage at smaller levels of drift ratio.

Figures 6.8 and 6.9 show the base moment rotation response and the axial deformation response for the specimens under cyclic loading protocols. The following observations are made:

- For identical axial load ratios and cross section size, local buckling occurs at a smaller chord rotation values under cyclic loading rather than monotonic loading. This is well captured by the damage loading function that grows with the hysteretic (plastic) dissipated energy. Under reversed cyclic loading, this energy accumulates continuously and the energy threshold required to trigger the damage initiation is reached at smaller levels of drift ratio than under monotonic loading.

- The rate of cyclic flexural strength deterioration increases with increasing values of the axial load. This is captured by the interaction coefficient $C_i$.

- The stockiest specimen (C) develops a larger flexural strength and experiences strength deterioration at greater chord rotation values. Additionally, the rate of cyclic strength deterioration is faster for the more slender cross sections. This is captured with the use of different coefficients $C_{d0,f}$ and $C_{d1,f}$ for each cross section.

- The strength and stiffness deterioration is slower over the course of a follower half-cycle (i.e. when the deformation stays within the range of the previous extreme deformations) than under a primary half-cycle (when the deformation goes beyond previous extreme deformations). This is captured by the use of a coefficient $w = 0.35 < 1$.

- The amount of axial deformation increases with the axial load level and with the web slenderness ratio. This is because the web becomes more susceptible to local buckling-induced softening [23].

- The amount of axial deformation is higher under cyclic lateral loading than under monotonic loading due to a higher level of cumulative inelastic rotation.

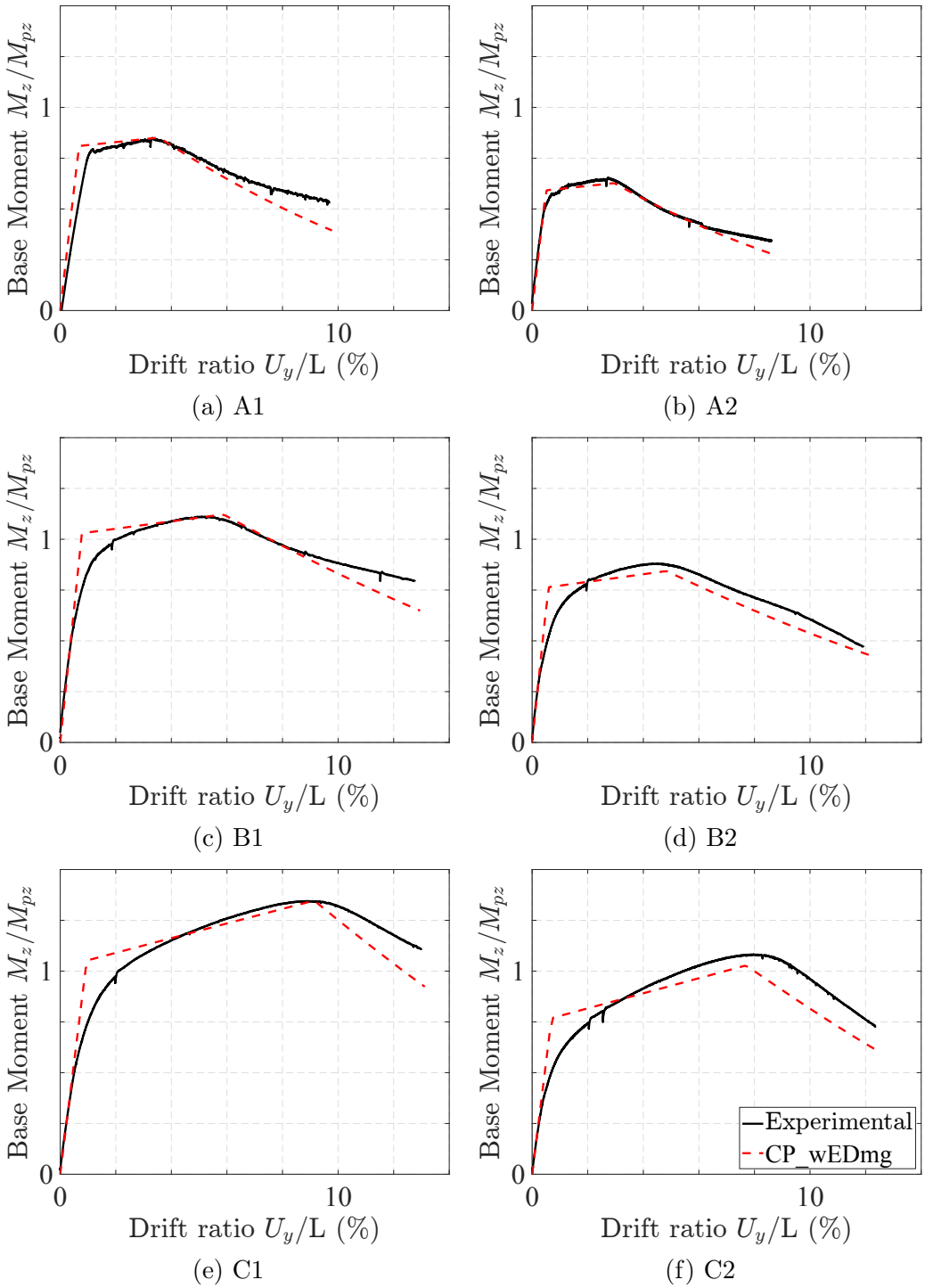


Figure 6.6: Monotonic flexural response - Cravero et al. specimens [23]

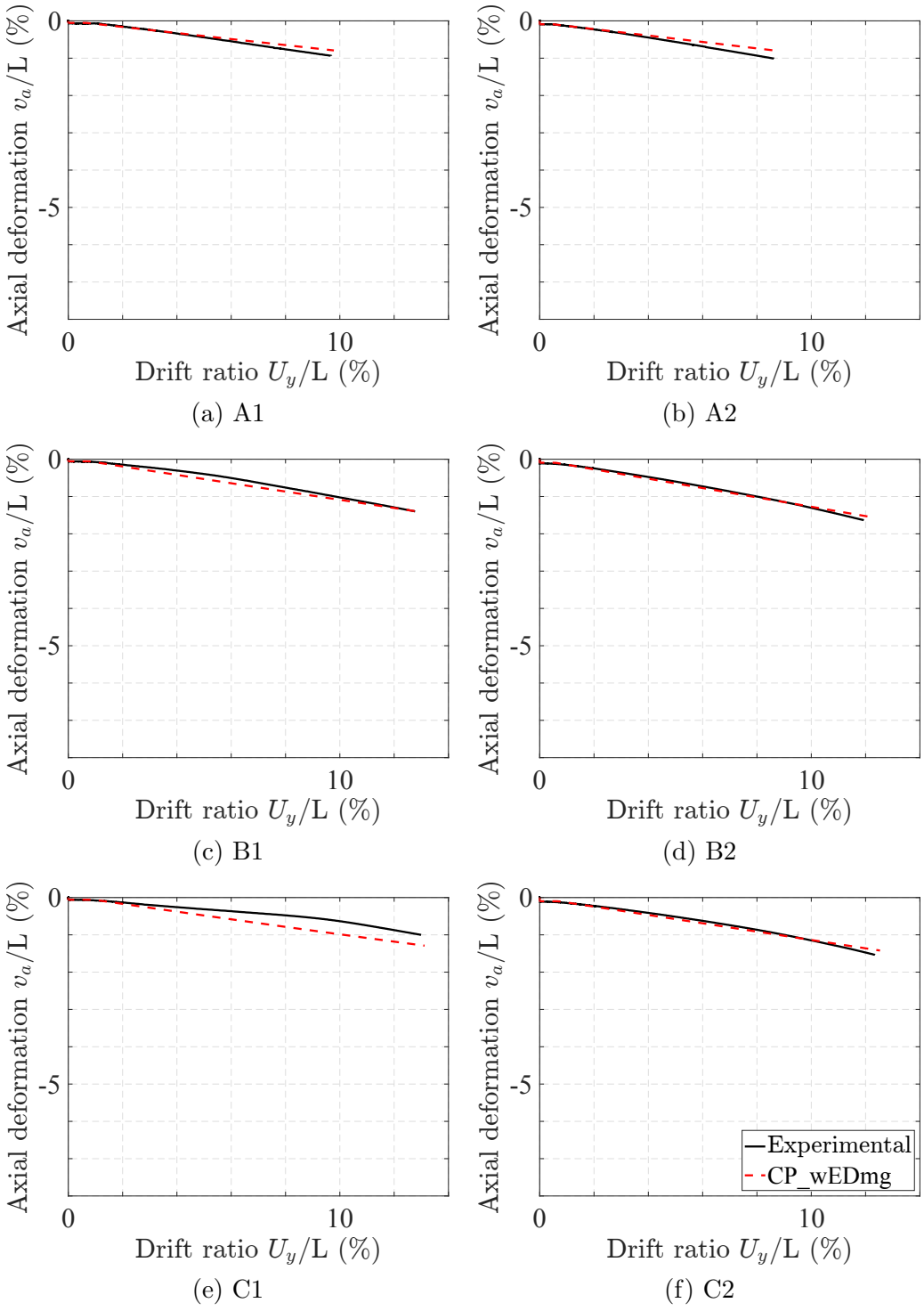


Figure 6.7: Monotonic axial response - Cravero et al. specimens [23]

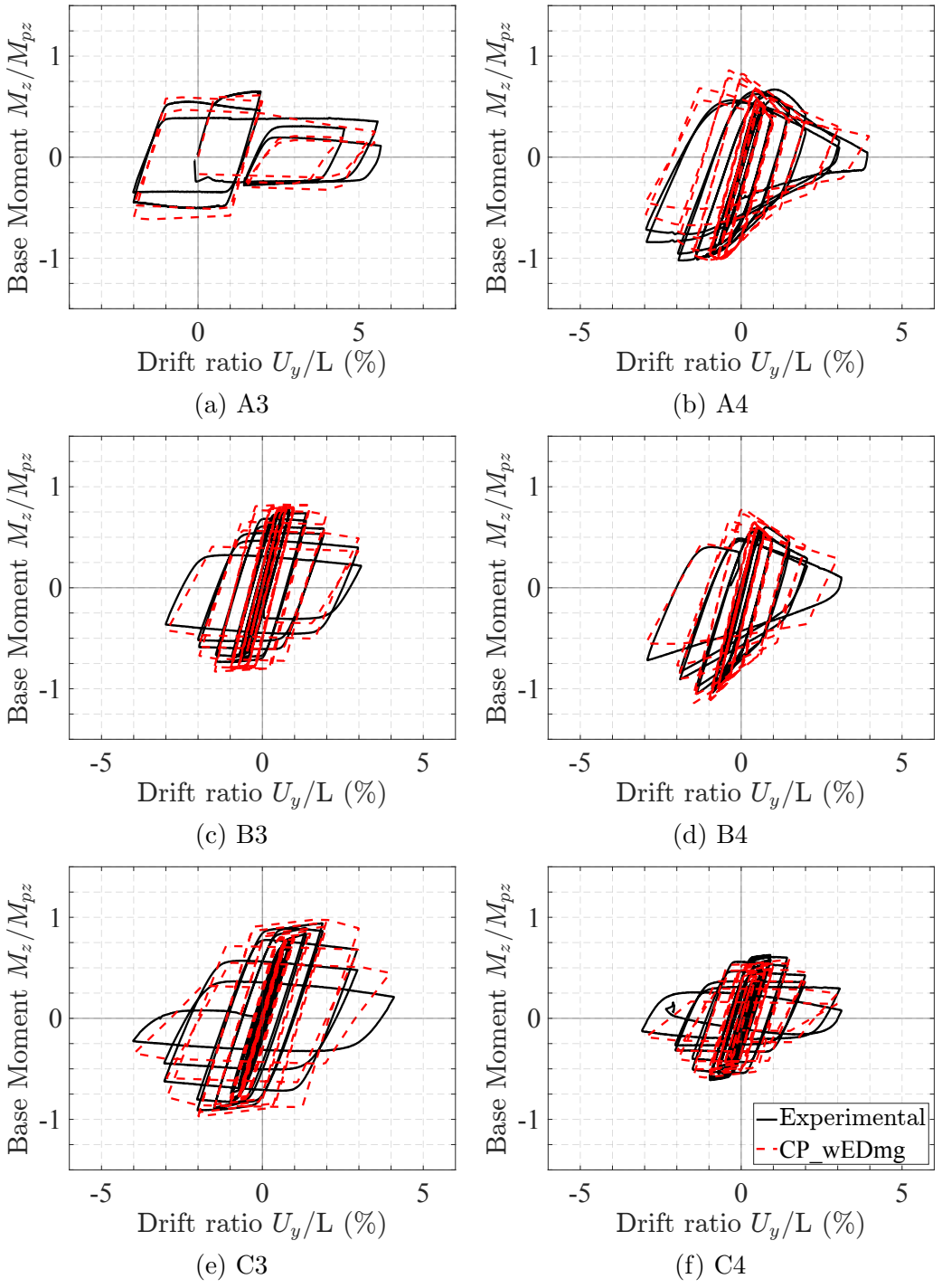


Figure 6.8: Cyclic flexural response - Cravero et al. specimens [23]

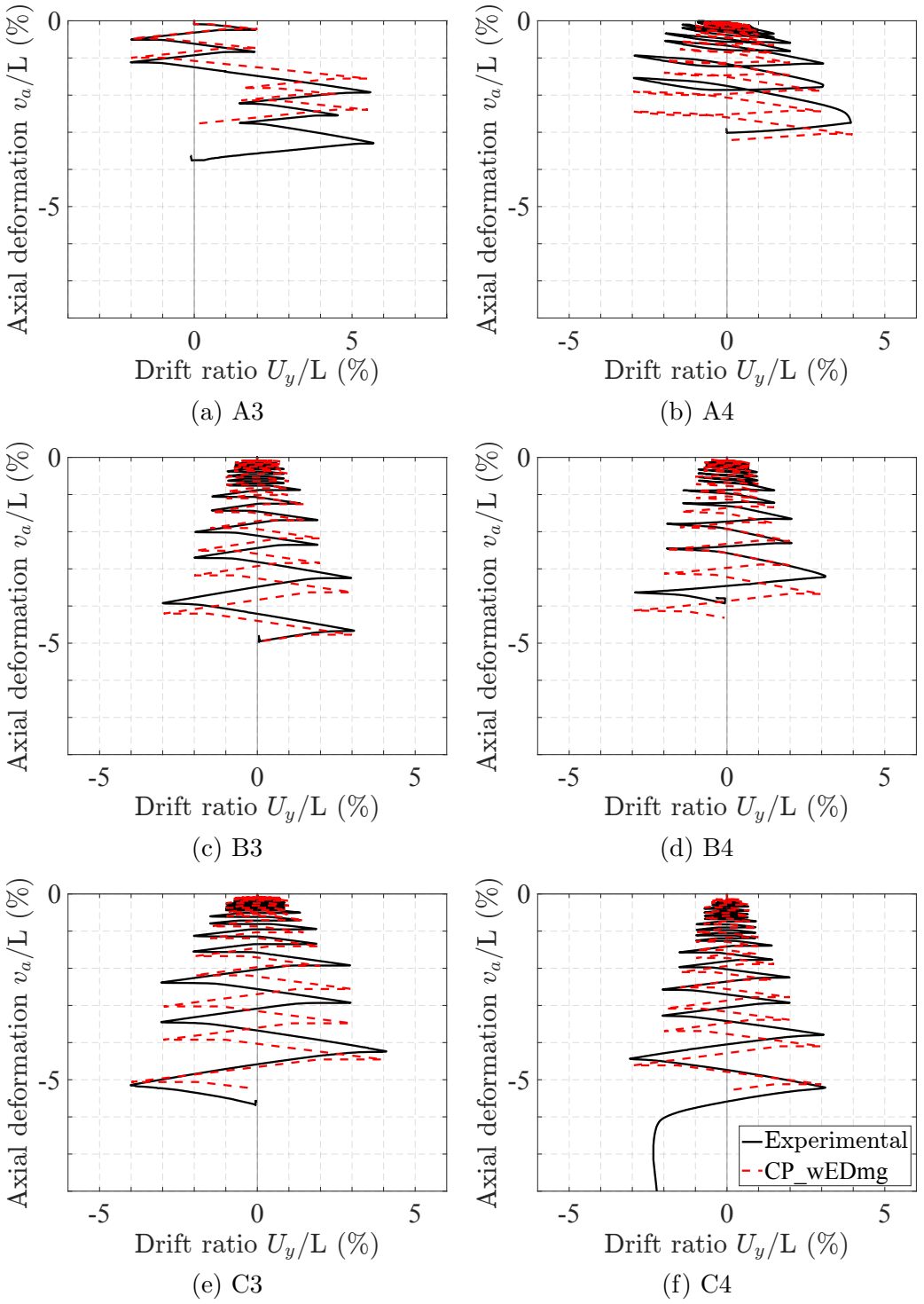


Figure 6.9: Cyclic axial response - Cravero et al. specimens [23]

**Columns by Elkady and Lignos [27]** Elkady and Lignos [27] investigated the behavior of 10 full-scale deep wide-flange steel columns under prescribed axial load and lateral drift demands. Two cross sections were used for the specimens: W24x146 (specimens C1-C6) and W24x84 (specimens C7-C10). These are representative of first story columns in modern low- to mid-rise moment resisting steel frames [27]. The specimens were tested under constant axial load and prescribed displacements at the top of the column.

First, the unidirectional bending behavior of the selected cross sections with fixed-fixed or fixed-flexible boundary conditions was investigated. The fixed-flexible conditions was achieved by prescribing the rotation history at the top of the column. As for the specimens of Cravero et al specimens [23], the columns were tested under two types of cyclic protocol: a symmetric cyclic and a collapse-consistent lateral loading protocol. These were combined with constant levels of axial load of either $N = -20\%N_p$ or $N = -50\%N_p$, where $N_p$ is the plastic axial capacity of the cross section. These tests are referred to as C1-C5 and C7-C8, as summarized in Table 6.8. The results of C4 were discarded by the authors because of a control error [27]. More details about the loading protocols can be found in [27].

| **Specimen** | Section Size | Boundary conditions | Lateral protocol | $N/N_p$ |
|---|---|---|---|---|
| **C1** | W24x146 | Fixed-fixed | Symmetric | $-20\%$ |
| **C2** | W24x146 | Fixed-fixed | Symmetric | $-50\%$ |
| **C3** | W24x146 | Fixed-flexible | Symmetric | $-20\%$ |
| **C5** | W24x146 | Fixed-flexible | Collapse-consistent | $-20\%$ |
| **C7** | W24x84 | Fixed-flexible | Symmetric | $-20\%$ |
| **C8** | W24x84 | Fixed-flexible | Collapse-consistent | $-20\%$ |

Table 6.8: Summary of unidirectional loading tests conducted by Elkady and Lignos [27]

The specimens were then tested under bidirectional cyclic loading with fixed-flexible boundary conditions and a constant axial load of $N = -20\%N_p$. These tests are referred to as C6 and C9-C10, as summarized in Table 6.9.

| **Specimen** | Section Size | Boundary conditions | Lateral protocol | $N/N_p$ |
|---|---|---|---|---|
| **C6** | W24x146 | Fixed-flexible | Symmetric | $-20\%$ |
| **C9** | W24x84 | Fixed-flexible | Symmetric | $-20\%$ |
| **C10** | W24x84 | Fixed-flexible | Collapse-consistent | $-20\%$ |

Table 6.9: Summary of bidirectional loading tests conducted by Elkady and Lignos [27]

The 2d resultant plasticity column element with damage is used to simulate the behavior of the specimens under unidirectional loading, while the 3d element is used for the specimens under bidirectional loading. The columns are modeled with a single element of length $L = 3,900$ mm $= 12.8$ ft, as illustrated in Figure 6.10. The degrees of freedom at the base and at the top of the column are fully restrained. The horizontal degree(s) of freedom at the top of the specimens are subjected to the imposed lateral drift protocol, along with the applied axial force. For the specimens with fixed-flexible conditions, an additional rotation about the strong axis of the section is prescribed at the top of the column. The effect of nonlinear geometry is accounted for with the P-$\Delta$ formulation.

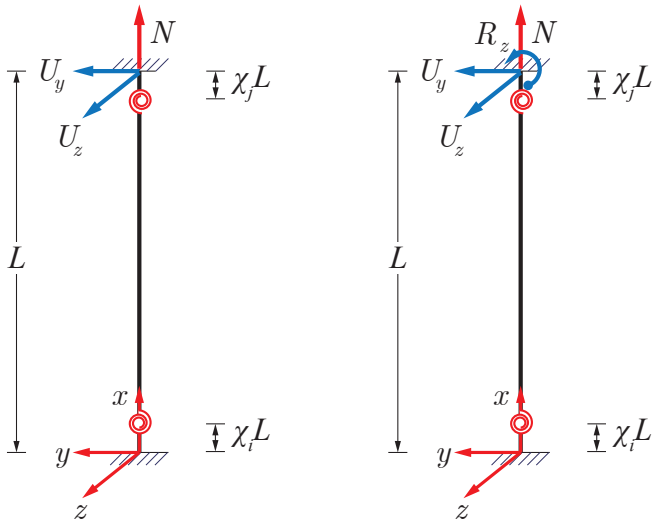


Figure 6.10: Resultant plasticity cantilever model for specimens by Elkady et al. [27] under fixed-fixed conditions (left) and fixed-flexible conditions (right)

For the specimens under unidirectional lateral loading protocols, the coefficients of the polynomial approximation of the yield surface of the 2d resultant plasticity model are selected to match the exact yield surface of each cross sections. The following polynomial is used for the W24x146 cross section of the C1-C5 specimens:

$$\phi(\boldsymbol{s}) = 1.2\left|\frac{N}{N_p}\right|^2 + 1.0\left|\frac{M_z}{M_{pz}}\right|^2 + 3.0\left|\frac{N}{N_p}\right|^2\left|\frac{M_z}{M_{pz}}\right|^2 \tag{6.15}$$

and the following polynomial is used for the W24x84 cross section of the C7-C8 specimens:

$$\phi(\boldsymbol{s}) = 1.2\left|\frac{N}{N_p}\right|^2 + 1.0\left|\frac{M_z}{M_{pz}}\right|^2 + 2.5\left|\frac{N}{N_p}\right|^2\left|\frac{M_z}{M_{pz}}\right|^2 \tag{6.16}$$

Figure 6.11 shows the resulting polynomial approximation of the initial yield surface for the two cross sections.

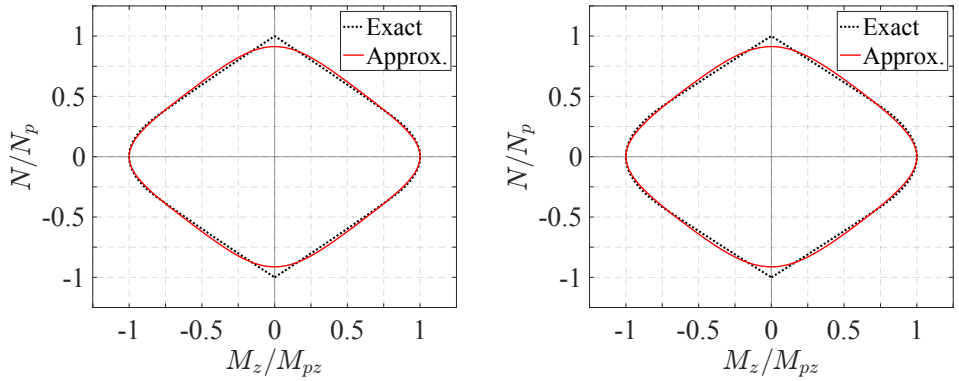


(a) C1-C5 (W24x146) (b) C7 (W24x84)

Figure 6.11: Polynomial approximation of initial yield surface for Elkady and Lignos specimens [27]

For the specimens under bidirectional lateral loading protocols, the following polynomial is used for the 3d yield surface of the W24x146 cross section i.e., C6 specimen:

$$\begin{aligned}\phi(\boldsymbol{s}) = 1.2\left|\frac{N}{N_p}\right|^2 + 1.0\left|\frac{M_z}{M_{pz}}\right|^2 + 1.0\left|\frac{M_y}{M_{py}}\right|^5 \\ + 3.0\left|\frac{N}{N_p}\right|^2\left|\frac{M_z}{M_{pz}}\right|^2 + \frac{6A_f}{A_f+A_w}\left|\frac{N}{N_p}\right|^3\left|\frac{M_z}{M_{pz}}\right|^3 + 3.0\left|\frac{M_z}{M_{pz}}\right|^2\left|\frac{M_y}{M_{py}}\right|^2\end{aligned} \tag{6.17}$$

and the following polynomial is used for the W24x84 cross section i.e., C9-C10 specimens:

$$\begin{aligned}\phi(\boldsymbol{s}) = 1.2\left|\frac{N}{N_p}\right|^2 + 1.0\left|\frac{M_z}{M_{pz}}\right|^2 + 1.0\left|\frac{M_y}{M_{py}}\right|^5 \\ + 2.5\left|\frac{N}{N_p}\right|^2\left|\frac{M_z}{M_{pz}}\right|^2 + \frac{6A_f}{A_f+A_w}\left|\frac{N}{N_p}\right|^3\left|\frac{M_z}{M_{pz}}\right|^3 + 3.0\left|\frac{M_z}{M_{pz}}\right|^2\left|\frac{M_y}{M_{py}}\right|^2\end{aligned} \tag{6.18}$$

In the above equations, $A_f$ is the area of the two flanges and $A_w$ is the area of the web for the wide-flange cross section.

The plastic axial and flexural capacities of the specimens are defined as $N_p = Af_y$, $M_{pz} = Z_z f_y$ and $M_{py} = Z_y f_y$, where $f_y$ is the expected yield stress of steel, $A$ is the area of the cross section, and $Z_z$ and $Z_y$ are the plastic modulii of the cross section with respect to its strong axis and weak axis, respectively. The value used for $f_y$, as well as for the Young Modulus of steel $E$, are based on the average results of the uniaxial tensile coupon tests reported in [27]. These values are summarized in Table 6.10, and the resulting plastic capacities are listed in Table 6.11. The numerical model includes the kinematic and isotropic

hardening as well as hinge offset capabilities of the resultant plasticity column element, with parameter values listed in Table 6.12. The beam-column element also includes the elastic shear deformations, as recommended in [23]. These are uncoupled from the plastic axial-flexure response.

| **Column Specimen** | $f_y$ (ksi) | $E$ (ksi) |
|---|---|---|
| **C1-C3** | 60.1 | 27,627 |
| **C5-C6** | 54.1 | 29,648 |
| **C7-C10** | 49.9 | 28,312 |

Table 6.10: Material parameters for Elkady and Lignos specimens [27]

For the 2d resultant plasticity column element, the damage model is wrapped around the three element basic forces $\boldsymbol{q}$ and the three work-conjugate element deformations $\boldsymbol{v}$. The damage parameters are specified as follows:

- The coefficients $C^{\pm}_{d0,m}$, $m \in [\![1,3]\!]$ are set equal to:

$$C^{\pm}_{d0,1} = C_{d0,a} \quad ; \quad C^{\pm}_{d0,2} = C^{\pm}_{d0,3} = C_{d0,f} \tag{6.19}$$

  with the values for $C_{d0,a}$ and $C_{d0,f}$ in Table 6.13. The subscript $a$ refers to the axial behavior and the subscript $f$ refers to the flexural behavior at both ends of the element.

- The coefficients $C^{\pm}_{d1,m}$, $m \in [\![1,3]\!]$ are set equal to:

$$C^{\pm}_{d1,1} = C_{d1,a} \quad ; \quad C^{\pm}_{d1,2} = C^{\pm}_{d1,3} = C_{d1,f} \tag{6.20}$$

  with the values for $C_{d1,a}$ and $C_{d1,f}$ in Table 6.13.

- The primary/follower half-cycle parameter $w^{\pm}_m$ and the positive/negative coupling parameters $C^{\pm}_{cd,m}$ for the $m$-th basic force are set equal to:

$$w^{\pm}_1 = w^{\pm}_2 = w^{\pm}_3 = w \tag{6.21}$$

$$C^{\pm}_{cd,1} = C^{\pm}_{cd,2} = C^{\pm}_{cd,3} = C_{cd} \tag{6.22}$$

  where $w = 0.35$ and $C_{cd} = 0.2$, as listed in Table 6.13.

- The inter-component interaction coefficients $C^{\pm\pm}_{i,m,l}$ account for the effect of a negative axial force on the flexural strength and stiffness deterioration. These are specified as follows

$$C^{-+}_{i,m,l} = \begin{cases} C_i & \text{if } (m,l) = (2,1) \text{ or } (m,l) = (3,1) \\ 0 & \text{otherwise} \end{cases} \tag{6.23}$$

| **Column Specimen** | $N_p$ (kips) | $M_{pz}$ (kip-in) | $M_{py}$ (kip-in) |
|---|---|---|---|
| **C1-C3** | 2,585.1 | 25,129 | - |
| **C5-C6** | 2,326.3 | 22,613 | 5,042.0 |
| **C7-C10** | 1,212.7 | 10,997 | 1,600.5 |

Table 6.11: Plastic axial and flexural capacities for Elkady and Lignos specimens [27]

| **Column Specimen** | $H_{kr,a}$ (%) | $H_{kr,fz,i}$ (%) | $H_{kr,fz,j}$ (%) | $H_{kr,fy,i}$ (%) | $H_{kr,fy,j}$ (%) | $H_{ir,i}$ (‰) | $H_{ir,j}$ (‰) | $\chi_i$ (%) | $\chi_j$ (%) |
|---|---|---|---|---|---|---|---|---|---|
| **C1-C3** | 0.4 | 0.4 | 0.4 | - | - | 0.5 | 0.5 | 3.0 | 3.0 |
| **C5-C6** | 0.4 | 0.4 | 0.4 | 0.4 | 0.4 | 0.5 | 0.5 | 6.0 | 6.0 |
| **C7-C8** | 0.4 | 0.4 | 0.4 | - | - | 0.5 | 0.5 | 6.0 | 6.0 |
| **C9-C10** | 0.4 | 0.4 | 0.4 | 0.4 | 0.4 | 0.5 | 0.5 | 6.0 | 6.0 |

Table 6.12: Resultant plasticity column parameters for Elkady and Lignos specimens [27]

$$C^{--}_{i,m,l} = \begin{cases} C_i & \text{if } (m,l) = (2,1) \text{ or } (m,l) = (3,1) \\ 0 & \text{otherwise} \end{cases} \tag{6.24}$$

$$C^{++}_{i,m,l} = C^{+-}_{i,m,l} = 0 \quad \forall (m,l) \in [\![1,3]\!] \times [\![1,3]\!] \tag{6.25}$$

with $C_i$ in Table 6.13.

- The damage law is based on the plastic energy dissipation and uses the modified beta cumulative distribution function for the damage evolution. The parameters for the beta distribution function are $\beta^{\pm}_{1,m} = 1$ and $\beta^{\pm}_{2,m} = 4$, or equivalently, $d^{\pm}_{p1,m} = 4$, $d^{\pm}_{p2,m} = 1$, $\forall m \in [\![1,3]\!]$ for the modified version of the beta distribution.

For the 3d resultant plasticity column element, the damage model is wrapped around the five element basic forces $\boldsymbol{q}_{in}$ and the five work-conjugate element deformations $\boldsymbol{v}_{in}$. The damage parameters are specified as follows:

- The coefficients $C^{\pm}_{d0,m}$, $m \in [\![1,5]\!]$ are set equal to:

$$C^{\pm}_{d0,1} = C_{d0,a} \quad ; \quad C^{\pm}_{d0,2} = C^{\pm}_{d0,3} = C^{\pm}_{d0,4} = C^{\pm}_{d0,5} = C_{d0,f} \tag{6.26}$$

  with the values for $C_{d0,a}$ and $C_{d0,f}$ in Table 6.13. The subscript $a$ refers to the axial behavior and the subscript $f$ refers to the flexural behavior at both ends of the element.

- The coefficients $C^{\pm}_{d1,m}$, $m \in [\![1,5]\!]$ are set equal to:

$$C^{\pm}_{d1,1} = C_{d1,a} \quad ; \quad C^{\pm}_{d1,2} = C^{\pm}_{d1,3} = C^{\pm}_{d1,4} = C^{\pm}_{d1,5} = C_{d1,f} \tag{6.27}$$

  with the values for $C_{d1,a}$ and $C_{d1,f}$ in Table 6.13.

- The primary/follower half-cycle parameter $w^{\pm}_m$ and the positive/negative coupling parameters $C^{\pm}_{cd,m}$ for the $m$-th basic force are set equal to:

$$w^{\pm}_1 = w^{\pm}_2 = w^{\pm}_3 = w^{\pm}_4 = w^{\pm}_5 = w \tag{6.28}$$

$$C^{\pm}_{cd,1} = C^{\pm}_{cd,2} = C^{\pm}_{cd,3} = C^{\pm}_{cd,4} = C^{\pm}_{cd,5} = C_{cd} \tag{6.29}$$

  where $w = 0.35$ and $C_{cd} = 0.2$, as listed in Table 6.13.

- The inter-component interaction coefficients $C^{\pm\pm}_{i,m,l}$ account for the effect of a negative axial force on the flexural strength and stiffness deterioration. These are specified as follows

$$C^{-+}_{i,m,l} = \begin{cases} C_i & \text{if } m \in [\![2,5]\!] \text{ and } l = 1 \\ 0 & \text{otherwise} \end{cases} \tag{6.30}$$

$$C^{--}_{i,m,l} = \begin{cases} C_i & \text{if } m \in [\![2,5]\!] \text{ and } l = 1 \\ 0 & \text{otherwise} \end{cases} \tag{6.31}$$

$$C^{++}_{i,m,l} = C^{+-}_{i,m,l} = 0 \quad \forall (m,l) \in [\![1,5]\!] \times [\![1,5]\!] \tag{6.32}$$

  where $C_i = 2$, as listed in Table 6.13.

- The damage law is based on the plastic energy dissipation and uses the modified beta cumulative distribution function for the damage evolution. The parameters for the beta distribution function are $\beta^{\pm}_{1,m} = 1$ and $\beta^{\pm}_{2,m} = 4$, or equivalently, $d^{\pm}_{p1,m} = 4$, $d^{\pm}_{p2,m} = 1$, $\forall m \in [\![1,5]\!]$ for the modified version of the beta distribution.

| **Column Specimen** | $C_{d0,a}$ | $C_{d1,a}$ | $C_{d0,f}$ | $C_{d1,f}$ | $w$ | $C_{cd}$ | $C_i$ |
|---|---|---|---|---|---|---|---|
| **C1-C6** | 200 | 200 | 10 | 180 | 0.35 | 0.20 | 2.0 |
| **C7-C10** | 200 | 200 | 8 | 170 | 0.35 | 0.20 | 2.0 |

Table 6.13: Column damage parameters for Elkady and Lignos specimens [27]

As for the specimens of Cravero et al. [23], the coefficient $C_{d0,a}$ for the specimens by Elkady/Lignos is set to a high value so as not to trigger any strength deterioration for the axial force. The values for the flexural damage $C_{d0,f} = 8$ and $C_{d1,f} = 170$ are slightly lower for the slender cross section W24x84 of specimens C7-C10, compared with the values $C_{d0,f} = 10$ and $C_{d1,f} = 180$ for the slightly more compact cross section W24x146 of specimens C1-C6. The range of values for these two coefficients is lower than for the specimens of Cravero et al. This is motivated by two observations:

- The web slenderness $h/t_w$ of the specimens by Elkady/Lignos is $\approx 40$ and thus significantly larger than the web slenderness $h/t_w$ of the Cravero et al. specimens, which is $\approx 25$). This causes an earlier onset of local buckling in the web.
- The column slenderness $L_b/r_y$ of the Elkady/Lignos specimens is $\approx 65$) and, thus, more than two times the column slenderness of the specimens of Cravero et al. which is ($\approx 30$). This renders the specimens by Elkady/Lignos susceptible to an earlier onset of member instability.

The values for the coefficients $w = 0.35$, $C_{cd} = 0.2$ and $C_i = 2$ are the same with those for the specimens by Cravero et al..

Figure 6.12 shows the base moment rotation response and the axial deformation response for the specimens of Elkady/Lignos under the unidirectional loading protocols. Figure 6.13 shows the base moment rotation response about both axes of bending and the axial deformation response for the specimens of Elkady/Lignos under the bidirectional loading protocols. The following observations result:

- The specimens with the less-compact cross section W24x84 experience faster strength deterioration than the W24x146 specimens. This is captured by a lower value of $C_{d1,f}$ for specimens C7-C10 than for specimens C1-C6.
- The rate of cyclic and in-cycle flexural strength deterioration increases considerably under a higher compressive axial load. This is captured by the interaction coefficient $C_i$.

- For drift ratios larger than 2%, the specimens which are subjected to a lateral load history with equal positive and negative drift reversals exhibit a faster flexural strength deterioration that those subjected to a collapse-consistent loading history. This is captured well by the damage loading function that grows with the plastic energy dissipation leading to faster damage accumulation under the large number of inelastic cycles for the symmetric cyclic loading histories.

- The resultant plasticity column element with damage tends to overestimate the bending moment about the weak axis of the cross section for specimens subjected to bidirectional loading. Nonetheless, it captures the following two experimentally observed phenomena:

  - For drifts ratio up to 2% in the strong-axis direction, the hysteretic behavior of specimen C6 is fairly stable without any observed weak-axis flexural strength deterioration.
  - On the contrary, specimen C10 (with higher cross section slenderness) exhibits appreciable cyclic flexural strength deterioration in the weak-axis bending direction. This is due to the larger inelastic cycles (up to 3% drift ratio) experienced by the specimen in the strong axis direction.

- The resultant plasticity column element with damage captures the axial deformation response with sufficient accuracy for axial shortening values up to $3\%L$, after which the axial deformation appears to saturate. Nonetheless, it captures the following three important aspects of the axial deformation response:

  - Under identical axial load ratio and boundary conditions, the W24x84 columns undergo more axial shortening than the W24x146 columns, regardless of the loading direction. This is attributed to the pronounced local buckling of the web experienced by the more slender cross section.
  - Under identical lateral drift and axial load protocols, the axial shortening of specimen C1 with both ends fixed is nearly twice as large as the shortening for specimen C3 with one end fixed and the other end partially restrained against rotation. This is attributed to the onset of local buckling at both ends of the column specimen with both ends fixed, which results in the simultaneous loss of its torsional and warping resistance at both ends.
  - Regardless of the cross section, the amount of column axial shortening is not affected by the bidirectional loading.

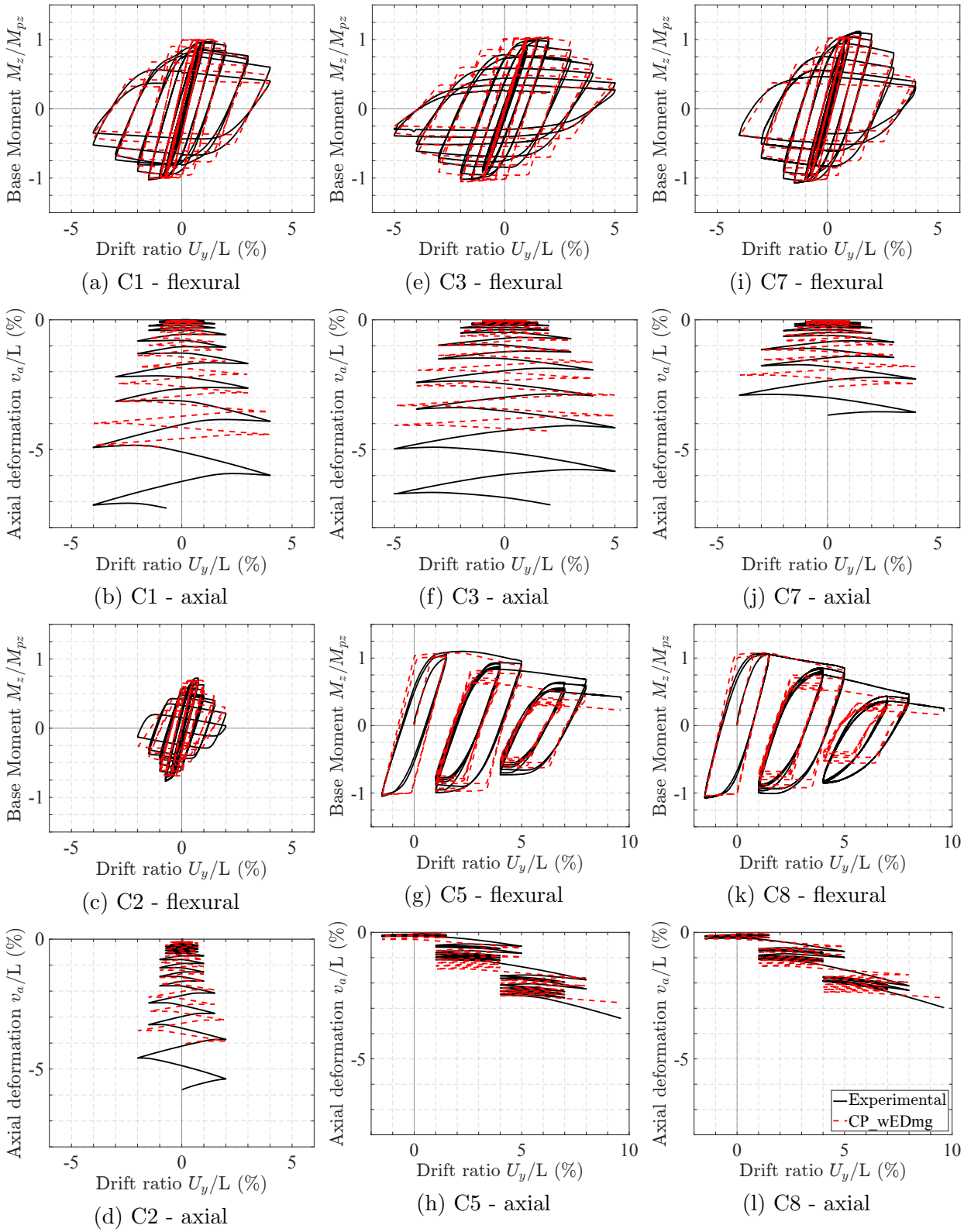


(a) C1 - flexural (e) C3 - flexural (i) C7 - flexural

(b) C1 - axial (f) C3 - axial (j) C7 - axial

(c) C2 - flexural (g) C5 - flexural (k) C8 - flexural

(d) C2 - axial (h) C5 - axial (l) C8 - axial

Figure 6.12: Unidirectional bending cyclic response - Elkady and Lignos specimens [27]

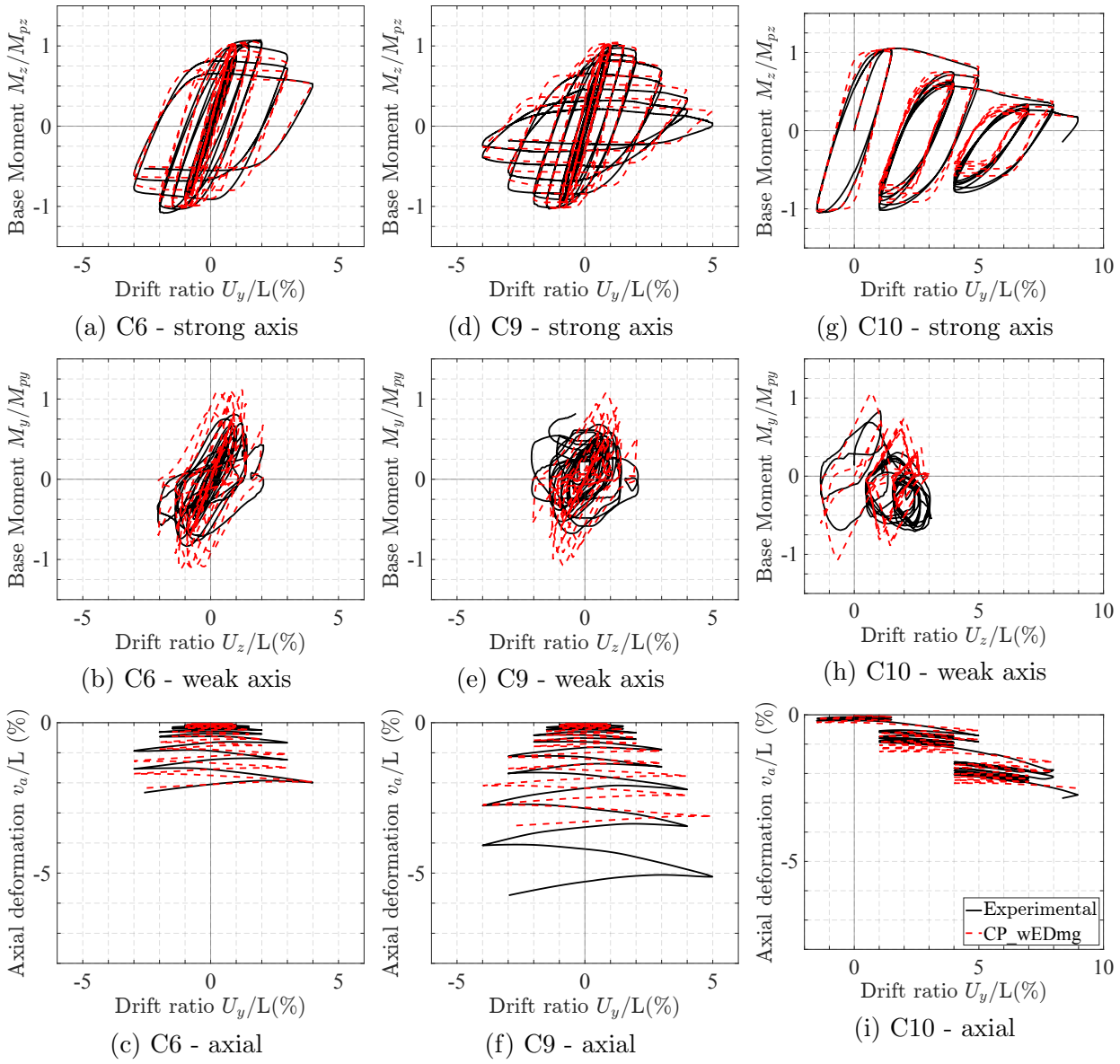


Figure 6.13: Bidirectional bending cyclic response - Elkady and Lignos specimens [27]

## 6.4 Distributed plasticity frame element with damage

The distributed plasticity frame element with damage results from wrapping the damage model of Chapter 5 around the element or the section or the material state determination of the nested element formulation. While wrapping the damage around the element response offers benefits regarding the description of the hysteretic response of an element with a fiber discretization of the cross section, the option of wrapping the damage model around the section or the material offer modeling alternatives that are not available with the resultant-plasticity frame element.

The element with a damage wrapper for the section response with stress-resultants is able to capture the gradual spread of plasticity better than is possible with the concentrated plasticity element with offset plastic hinges. Further flexibility is provided by the same element with a fiber section model based on the integration of the material stress-strain relation over the cross section area. In this case, uniaxial material models that include the Bauschinger effect of steel can be deployed.

Finally, the most flexibility for the damage modeling of steel frame elements is offered by a distributed plasticity frame element with a section model that integrates the material stress-strain relation over the cross section area. By wrapping the damage model around this material it is possible to account for the gradual strength loss under low cycle fatigue and the sudden strength loss under fracture.

The following sections describe briefly the parameters for a distributed plasticity frame element with the damage model wrapped at the section level and for a frame element with damage at the material level.

### 6.4.1 Distributed plasticity frame element with section damage

#### 6.4.1.1 Formulation and implementation

The distributed plasticity frame elements with section damage results from the introduction of the damage model as wrapper around the section state determination algorithm. The flexible analysis framework for this study allows for a force-based or a displacement based formulation and for a section model that is based on stress-resultants or on the integration of the material stress-relation over the cross section area.

Figure 6.14 summarizes the element state determination process. The symbols $\boldsymbol{H}_{v,e}$, $\boldsymbol{H}_{v,s}$ and $\boldsymbol{H}_{v,d}$ refer to the history variables associated with the element, the section, and the damage, respectively. These are encapsulated in the corresponding state determination algorithms.

The damage evolution function requires the specification of the energy dissipation at yield initiation for each section stress resultant, because it is used to establish the damage threshold and the limit damage value. For a 2d section model with uniaxial bending about

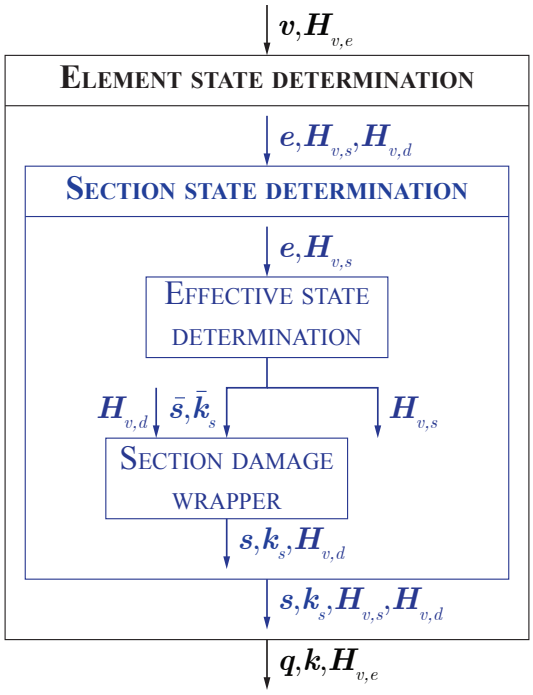


Figure 6.14: State determination for distributed plasticity element with section damage

the strong axis, the energy dissipation at yield initiation for the section stress resultants is:

$$\psi_{y,1}^{\pm} = \frac{N_p^2}{2EA} \quad ; \quad \psi_{y,2}^{\pm} = \frac{M_{pz}^2}{2EI_z} \tag{6.33}$$

For a 3d section model that accounts for biaxial bending, the energy dissipation at yield initiation for the section stress resultants is:

$$\psi_{y,1}^{\pm} = \frac{N_p^2}{2EA} \quad ; \quad \psi_{y,2}^{\pm} = \frac{M_{pz}^2}{2EI_z} \quad ; \quad \psi_{y,3}^{\pm} = \frac{M_{py}^2}{2EI_y} \tag{6.34}$$

When the damage evolution criterion is based on the plastic energy dissipation, the damage model requires the effective elastic section flexibility $\bar{\mathbf{f}}_e$. $\bar{\mathbf{f}}_e$ is the inverse of the effective section stiffness $\mathbf{k}_{se}$ given by Equation (2.12) for a 2d section model and Equation (2.45) for a 3d section model.

#### 6.4.1.2 Validation studies with experimental data

The distributed plasticity frame element with section damage is validated against the experimental data used for the resultant plasticity frame elements. The specimens B3 and B4 from the experimental campaign by Cravero et al. [23] are selected for the purpose.

Each column specimen is modeled with a single distributed plasticity frame element with force formulation [86] with damage wrapped around the section state determination. The analysis uses the P-$\Delta$ approximation for the nonlinear geometry effect. To avoid the mesh dependence for strain-softening section response, the element uses a regularized integration scheme that follows the work of Scott and Hamutcuoglu [71], Addessi and Ciampi [1], and Yadav [91]. Accordingly, the element is subdivided into two sub-regions: one near the base of the column where curvatures and damage are expected to localize, and one in the remaining part of the element which is expected to respond elastically. The weight associated with the integration point closest to the column base corresponds to the extent of the localization zone. This length is set equal to the plastic hinge length, which is assumed equal to the cross section depth $d = 16.8$ in for a W16x89 column. Two Gauss points with weight $0.2338L$ are used in the base sub-region and two Gauss points with weight $0.2662L$ are used in the elastic sub-region, resulting in the integration scheme in Figure 6.15. The monitoring sections use either the 2d resultant plasticity model of Chapter 2, or a fiber section model. The former section model is referred to as DPRes_wSDmg, and the latter as DPFib_wSDmg, where wSDmg denotes a section with damage.

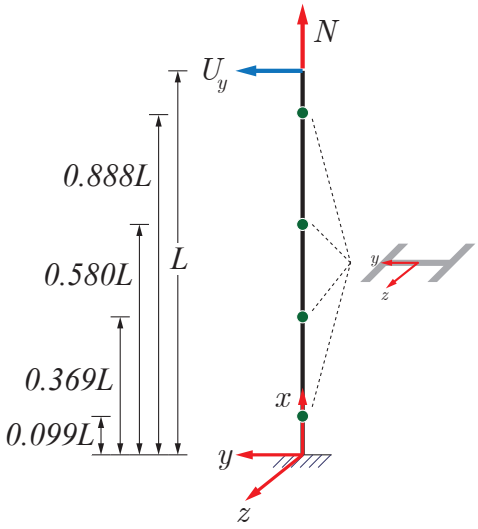


Figure 6.15: Distributed plasticity cantilever column model with 4 integration points for Cravero et al. specimens [23]

The 2d resultant plasticity section model uses the hardening parameters in Table 6.14, which are consistent with the parameters used in the resultant plasticity column element in Section 6.3.2.3. The plastic axial and flexural capacities of the cross section correspond to the values in Table 6.5. The coefficients for the polynomial approximation of the yield surface are given by Equation (6.6), as for the resultant plasticity column model.

The fiber section model divides each flange into 3 layers, and the web into 8 layers of

uniform thickess, as Figure 6.16 shows. The steel stress-strain relation follows the uniaxial Giuffrè-Menegotto-Pinto (GMP) model with isotropic hardening [55], [30] with the parameters in Table 6.15.

| **Column Specimen** | $H_{kr,a}$ (%) | $H_{kr,fz}$ (%) | $H_{ir}$ (‰) |
|---|---|---|---|
| **B3-B4** | 0.4 | 0.4 | 0.5 |

Table 6.14: Resultant plasticity section parameters for specimens of Cravero et al. [23]

| **Column Specimen** | $f_y$ (ksi) | $E$ (ksi) | $b$ (%) | $a_1$ (‰) | $a_2$ | $a_3$ (‰) | $a_4$ | $R_0$ | $C_{R1}$ | $C_{R2}$ |
|---|---|---|---|---|---|---|---|---|---|---|
| **B3-B4** | 54.5 | 28,921 | 4.0 | 1.0 | 0 | 1.0 | 0 | 20 | 0.925 | 0.150 |

Table 6.15: GMP material model parameters for specimens B3 and B4 of Cravero et al. [23]

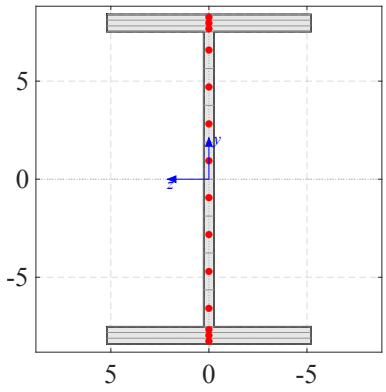


Figure 6.16: Fiber mesh for W16x89 section of specimens B3 and B4 by Cravero et al. [23] (dimensions in inches)

The damage model is wrapped around the two section forces $\boldsymbol{s}$ and the two work-conjugate section deformations $\boldsymbol{e}$. The damage parameters are specified as follows:

- The coefficients $C^{\pm}_{d0,m}$, $m \in [\![1,2]\!]$ are equal to

$$C^{\pm}_{d0,1} = C_{d0,a} \quad ; \quad C^{\pm}_{d0,2} = C_{d0,f} \tag{6.35}$$

  with the values for $C_{d0,a}$ and $C_{d0,f}$ in Table 6.16. The subscript $a$ refers to the axial response and the subscript $f$ refers to the flexural response of the section.

- The coefficients $C^{\pm}_{d1,m}$, $m \in [\![1,2]\!]$ are set equal to:

$$C^{\pm}_{d1,1} = C_{d1,a} \quad ; \quad C^{\pm}_{d1,2} = C_{d1,f} \tag{6.36}$$

  with the values for $C_{d1,a}$ and $C_{d1,f}$ in Table 6.16.

- The primary/follower half-cycle parameter $w^{\pm}_m$ and the positive/negative coupling parameters $C^{\pm}_{cd,m}$ for the $m$-th section force are set equal to:

$$w^{\pm}_1 = w^{\pm}_2 = w \tag{6.37}$$

$$C^{\pm}_{cd,1} = C^{\pm}_{cd,2} = C_{cd} \tag{6.38}$$

  where $w = 0.35$ and $C_{cd} = 0.2$, as listed in Table 6.16.

- The inter-component interaction coefficients $C^{\pm\pm}_{i,m,l}$ account for the effect of a negative axial force on the flexural strength and stiffness deterioration. These are specified as follows

$$C^{-+}_{i,m,l} = \begin{cases} C_i & \text{if } (m,l) = (2,1) \\ 0 & \text{otherwise} \end{cases} \tag{6.39}$$

$$C^{--}_{i,m,l} = \begin{cases} C_i & \text{if } (m,l) = (2,1) \\ 0 & \text{otherwise} \end{cases} \tag{6.40}$$

$$C^{++}_{i,m,l} = C^{+-}_{i,m,l} = 0 \quad \forall (m,l) \in [\![1,2]\!] \times [\![1,2]\!] \tag{6.41}$$

  with $C_i$ in Table 6.13.

- The damage law is based on the plastic energy dissipation and uses the modified beta cumulative distribution function for the damage evolution. The parameters for the beta distribution function are $\beta^{\pm}_{1,m} = 1$ and $\beta^{\pm}_{2,m} = 4$, or equivalently, $d^{\pm}_{p1,m} = 4$, $d^{\pm}_{p2,m} = 1$, $\forall m \in [\![1,2]\!]$ for the modified version of the beta distribution.

| Section Model | $C_{d0,a}$ | $C_{d1,a}$ | $C_{d0,f}$ | $C_{d1,f}$ | $w$ | $C_{cd}$ | $C_i$ |
|---|---|---|---|---|---|---|---|
| **Resultant** | 200 | 200 | 30 | 380 | 0.35 | 0.20 | 2.0 |
| **Fiber** | 60 | 380 | 30 | 380 | 0.35 | 0.20 | 2.0 |

Table 6.16: Section damage parameters for B3-B4 Cravero et al. specimens [23]

Figures 6.17 and 6.18 show the base moment rotation response and the axial deformation response for the specimens B3 and B4 with the DPRes_wSDmg and DPFib_wSDmg models. The figures also include the correlation studies for the concentrated plasticity model with damage from Section 6.3.2.3. The latter model is referred to as CP_wEDmg, where wEDmg denotes a model with element damage. The computational times for each model are included in the legend next to the model name. The following observations are possible:

- In Figures 6.17 (a), (c) and (e), the DPRes_wSDmg and DPFib_wSDmg models capture the strength and stiffness deterioration of the flexural response for specimen B3 slightly better than the CP_wEDmg model. The two distributed plasticity models with section damage also describe better the onset of damage and the rate of deterioration.

- In Figures 6.17 (b) and (d), the DPRes_wSDmg overestimates the rate of strength and stiffness deterioration of the flexural response for specimen B4, especially under negative bending moments. The agreement with the experimental response is better for the CP_wEDmg and DPFib_wSDmg models.

- For both specimens, the DPFib_wSDmg model captures two features of the response that are not captured by the two resultant plasticity models: (1) the gradual transition between the elastic and the plastic range, and (2) the Bauschinger effect of the steel material.

- In Figure 6.18, both DPRes_wSDmg and CP_wEDmg models give equally accurate axial deformation responses for specimens B3 and B4. DPFib_wSDmg underestimates the amount of axial shortening, especially in the last loading cycles.

- From the results for these two specimens, the computational time for the distributed plasticity model with the section model of stress-resultants is 1.6 times less than for the fiber section model. This time is further reduced by a factor of 1.7 with the use of the concentrated plasticity model with the basic forces serving as stress-resultants.

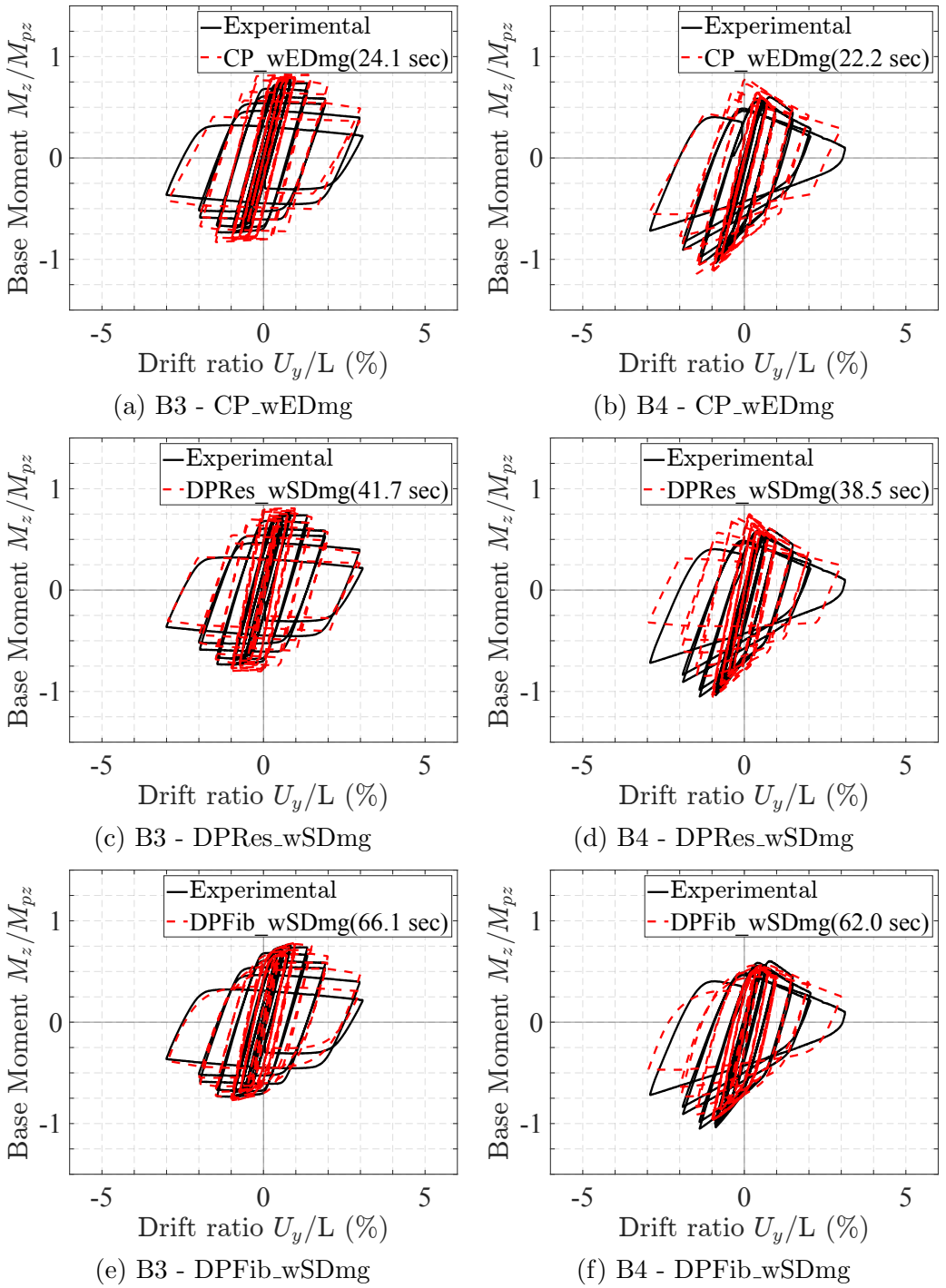


Figure 6.17: Element damage vs. section damage - B3-B4 specimens [23] - flexural response

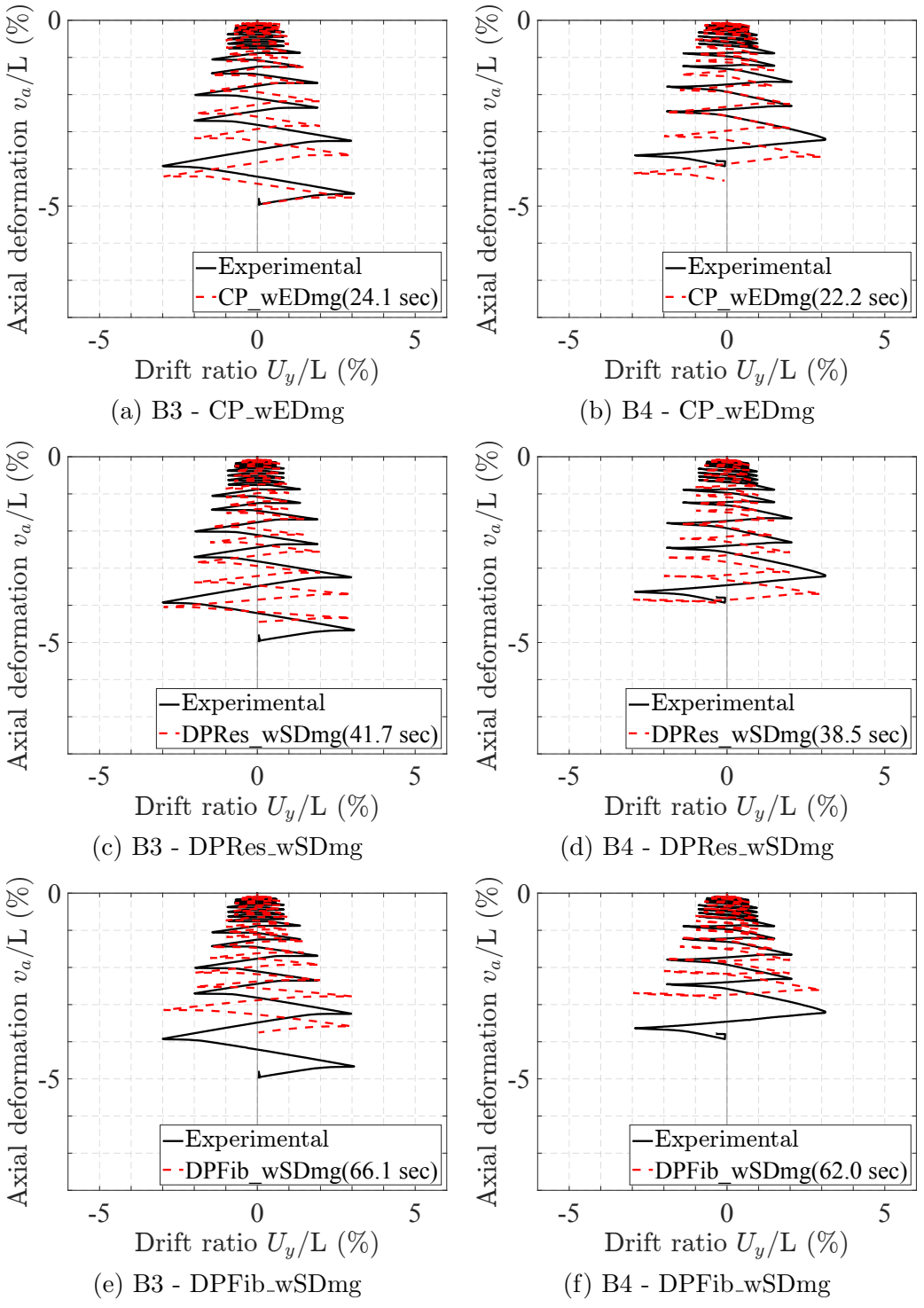


(a) B3 - CP_wEDmg (b) B4 - CP_wEDmg

(c) B3 - DPRes_wSDmg (d) B4 - DPRes_wSDmg

(e) B3 - DPFib_wSDmg (f) B4 - DPFib_wSDmg

Figure 6.18: Element damage vs. section damage - B3-B4 specimens [23] - axial response

## 6.4.2 Distributed plasticity frame element with material damage

### 6.4.2.1 Formulation and implementation

The distributed plasticity frame element with material damage results from the introduction of the damage wrapper around the material state determination. The flexible analysis framework for this study allows for a force-based or a displacement based formulation for the frame element with a fiber section model that integrates the true stress-strain relation over the cross section area. The latter results from the effective stress-strain relation following damage mechanics concepts.

Figure 6.19 summarizes the element state determination process. The symbols $\boldsymbol{H}_{v,e}$, $\boldsymbol{H}_{v,s}$, $\boldsymbol{H}_{v,m}$, and $\boldsymbol{H}_{v,d}$ refer to the history variables associated with the element, the section, the material, and the damage, respectively. These are encapsulated in the corresponding state determination algorithms.

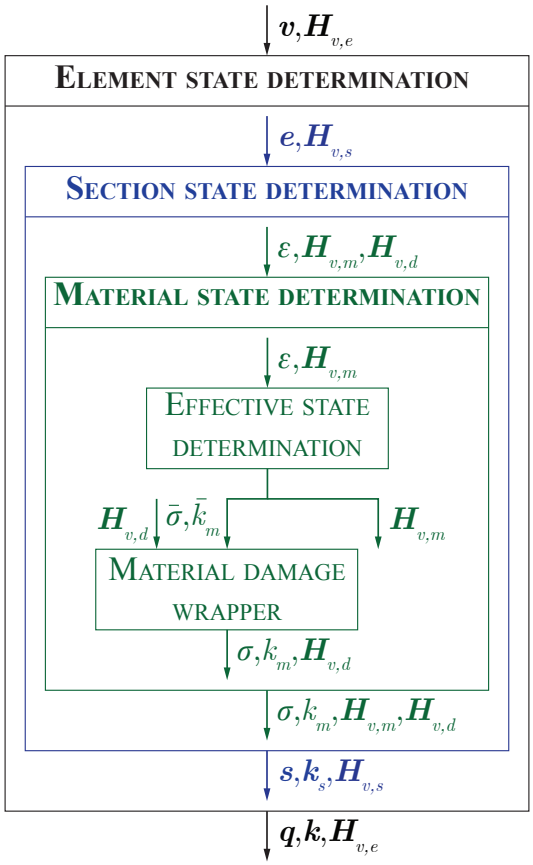


Figure 6.19: State determination for distributed plasticity element with material damage

The damage evolution function requires the specification of the energy dissipation at yield initiation of the material, because it is used to establish the damage threshold and the

limit damage value. For a 1d material model, this is defined as:

$$\psi_{y,1}^{\pm} = \frac{f_y^2}{2E} \tag{6.42}$$

When the damage evolution criterion is based on the plastic energy dissipation, the damage model requires the effective elastic flexibility $\bar{\mathbf{f}}_e$ of the material which is equal to the material compliance $\bar{\mathbf{f}}_e = \dfrac{1}{E}$, where $E$ is the Young modulus of the material.

#### 6.4.2.2 Validation studies with experimental data

The distributed plasticity frame element with material damage is validated against the experimental data used for the correlation studies of the other damage-based elements. The specimens B3 and B4 from the experimental campaign by Cravero et al. [23] are selected. The columns are modeled with a single distributed plasticity frame element with force formulation. The element is identical with the DPFib_wSDmg model described in 6.4.1.2, except that the damage is now wrapped around the material state determination rather than the section state determination. This model is referred to as DPFib_wMDmg, where wMDmg denotes an element with material damage.

The damage model is wrapped around the stress $\sigma$ and the strain $\varepsilon$ of the material integration points (fibers). The damage parameters are specified as follows:

- The coefficient $C_{d0,1}^{\pm}$ is set equal to:

$$C_{d0,1}^{\pm} = C_{d0,GMP} \tag{6.43}$$

  where $C_{d0,GMP} = 50$, as listed in Table 6.17. The subscript $GMP$ refers to the GMP material model.

- The coefficient $C_{d1,1}^{\pm}$ is set equal to:

$$C_{d1,1}^{\pm} = C_{d1,GMP} \tag{6.44}$$

  where $C_{d1,GMP} = 1,000$, as listed in Table 6.17.

- The primary/follower half-cycle parameter $w_1^{\pm}$ and the positive/negative coupling parameter $C_{cd,1}^{\pm}$ are set equal to:

$$w_1^{\pm} = w \tag{6.45}$$

$$C_{cd,1}^{\pm} = C_{cd} \tag{6.46}$$

  where $w = 0.15$ and $C_{cd} = 0.2$, as listed in Table 6.17.

- The damage law is based on the plastic energy dissipation and uses the modified beta cumulative distribution function for the damage evolution. The parameters for the beta distribution function are $\beta_{1,m}^{\pm} = 1$ and $\beta_{2,m}^{\pm} = 3$, or equivalently, $d_{p1,m}^{\pm} = 3$, $d_{p2,m}^{\pm} = 1$for the modified version of the beta distribution.

| **Material model** | $C_{d0,GMP}$ | $C_{d1,GMP}$ | $w$ | $C_{cd}$ |
|---|---|---|---|---|
| **GMP** | 50 | 1000 | 0.15 | 0.20 |

Table 6.17: Material damage parameters for B3-B4 Cravero et al. specimens [23]

Figures 6.20 and 6.21 show the base moment rotation response and the axial deformation response for specimens B3 and B4 with the DPFib_wMDmg model. The figures also include the correlation study for the concentrated plasticity model with damage from Section 6.3.2.3. The computational times for each model are included in the legend next to the model name. The following observations are possible:

- In Figure 6.20, the DPFib_wMDmg model captures the degrading flexural response of specimens B3 and B4 with impressive accuracy. The model also captures the gradual transition between the elastic and the plastic range, and the Bauschinger effect of the steel material that the CP_wEDmg model is unable to capture.
- In Figure 6.18, both DPFib_wMDmg and CP_wEDmg models give equally accurate axial deformation responses for specimens B3 and B4.
- From the results for these two specimens, the computational time with the distributed plasticity model with fiber section and material damage DPFib_wMDmg is 5 times larger than for the concentrated plasticity model CP_wEDmg with damage wrapped around the basic element forces.

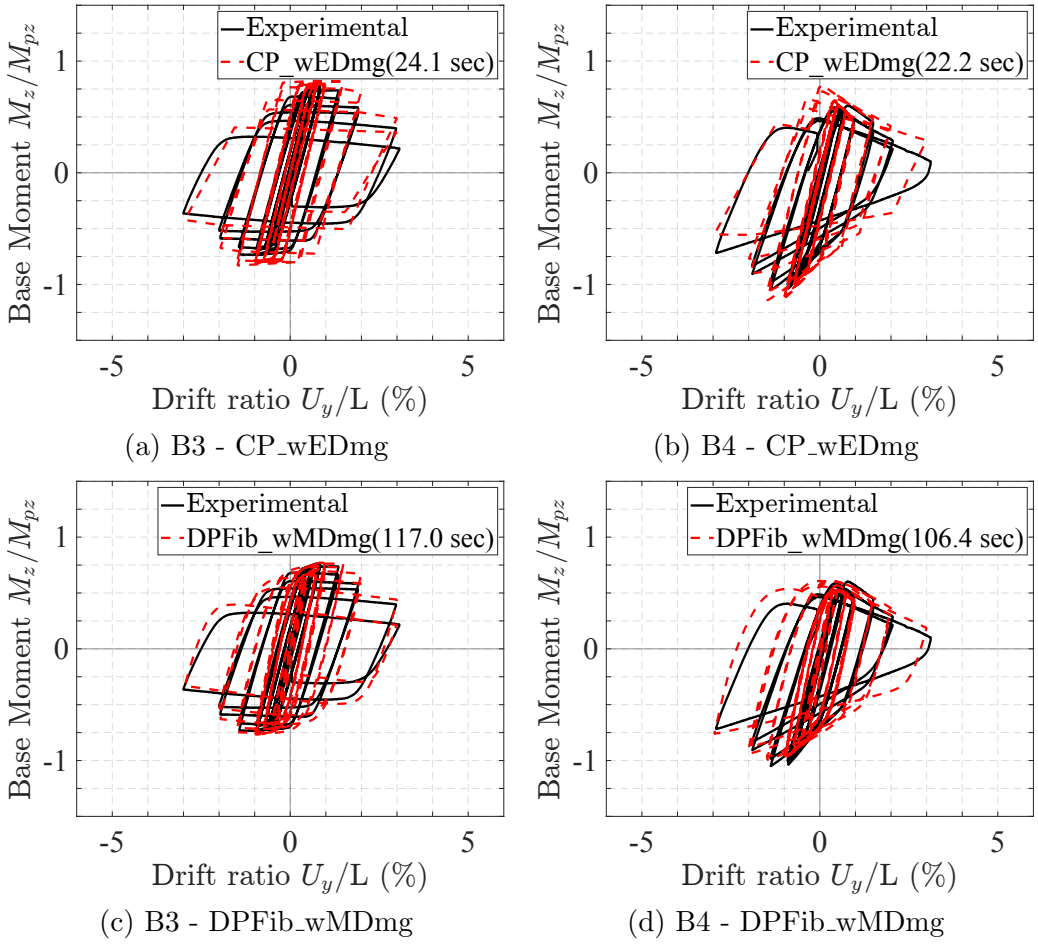


(a) B3 - CP_wEDmg (b) B4 - CP_wEDmg

(c) B3 - DPFib_wMDmg (d) B4 - DPFib_wMDmg

Figure 6.20: Element damage vs. material damage - B3-B4 specimens [23] - flexural response

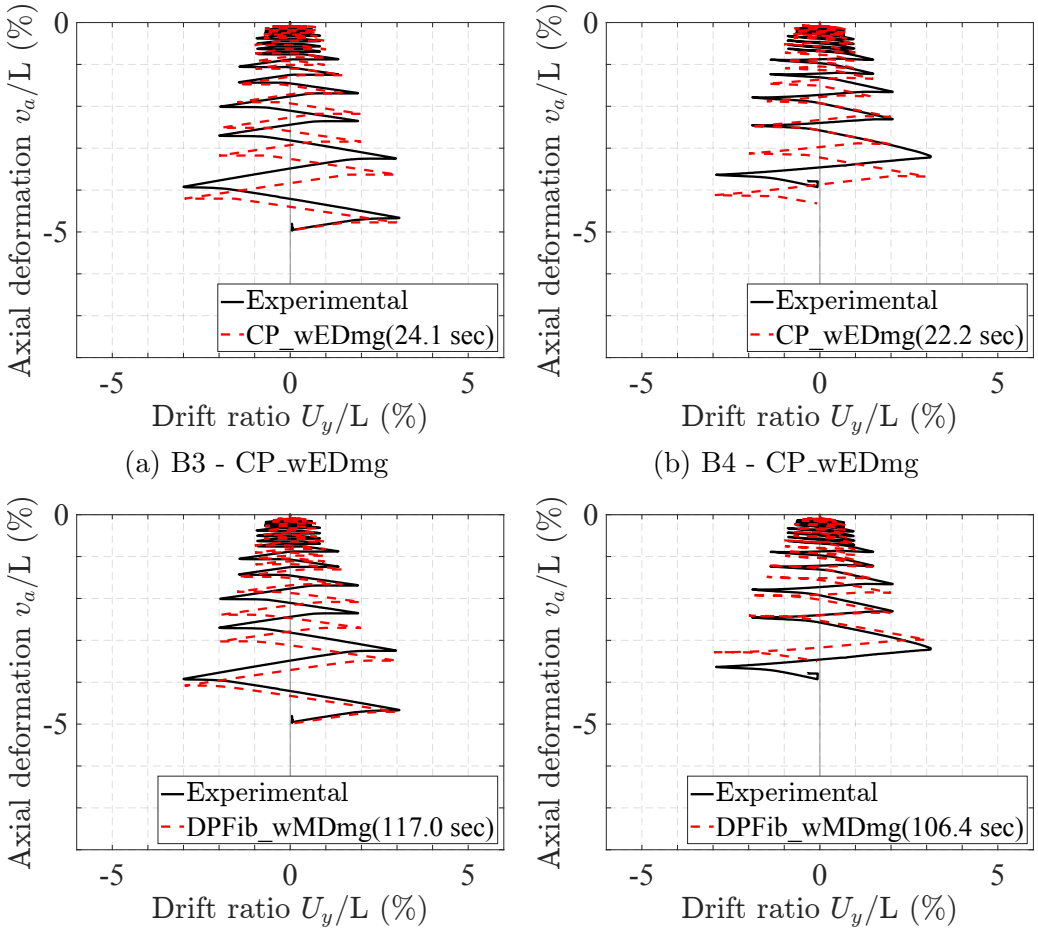


(a) B3 - CP_wEDmg (b) B4 - CP_wEDmg

(c) B3 - DPFib_wMDmg (d) B4 - DPFib_wMDmg

Figure 6.21: Element damage vs. material damage - B3-B4 specimens [23] - axial response

# Chapter 7

# Nonlinear response history analysis of irregular six-story steel frame

## 7.1 Overview

This chapter uses the 3d resultant plasticity frame element with damage of Chapter 6 for the collapse assessment of an irregular six-story frame under biaxial earthquake excitation. The study investigates the effect of nonlinear element geometry, material nonlinearity, element strength and stiffness deterioration, and ground motion intensity level, on the global structural and local element responses.

## 7.2 Structural model

The irregular six-story frame geometry stems from earlier studies by several researchers [61], [14]. The original structure underwent a significant re-design to meet the current seismic design requirements of Eurocode 8 for a medium ductility class [45]. Figures 7.1 and 7.2 show the geometry of the frame, the member sizes as well as the column section orientations. The steel material has yield strength $f_y = 250$ MPa $= 36.26$ ksi and Young modulus $E = 206.85$ GPa $= 30,001$ ksi.

### 7.2.1 Frame elements

Each column and girder element is modeled with a single 3d resultant plasticity frame element with damage, as introduced in Section 6.3.2.2. The frame elements use the following

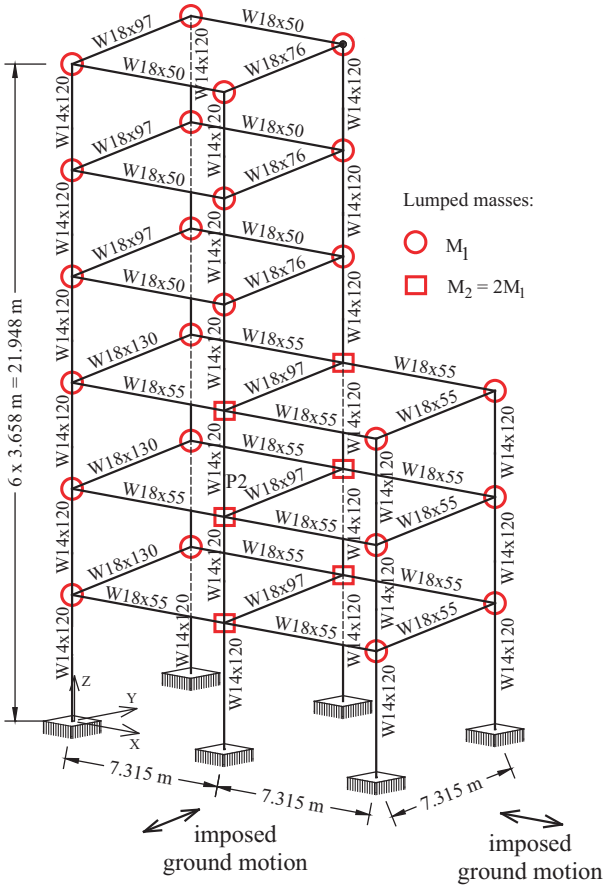


Figure 7.1: Geometry, member sizes and mass distribution for 6-story steel frame [45]

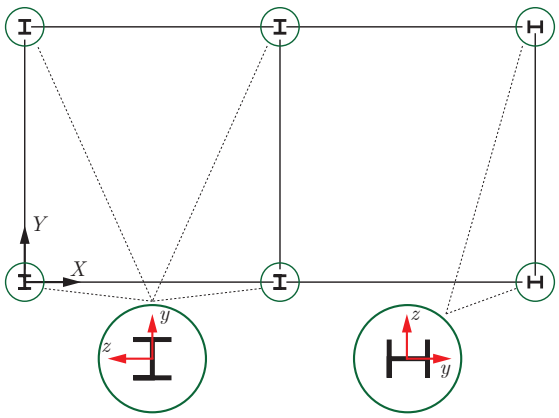


Figure 7.2: Column orientation for 6-story steel frame

polynomial for the three-dimensional axial-flexure interaction surface:

$$\begin{aligned}\phi(\boldsymbol{s}) = 1.2\left|\frac{N}{N_p}\right|^2 + 1.0\left|\frac{M_z}{M_{pz}}\right|^2 + 1.0\left|\frac{M_y}{M_{py}}\right|^5 \\ + 3.5\left|\frac{N}{N_p}\right|^2\left|\frac{M_z}{M_{pz}}\right|^2 + 5\left|\frac{N}{N_p}\right|^3\left|\frac{M_z}{M_{pz}}\right|^3 + 3.0\left|\frac{M_z}{M_{pz}}\right|^2\left|\frac{M_y}{M_{py}}\right|^2\end{aligned} \tag{7.1}$$

Table 7.1 lists the hardening and hinge offset parameters of the frame elements. Table 7.2 lists the damage parameters which are consistent with specimen C6 of the study by Elkady and Lignos [27] in Section 6.3.2.3.

The frame element and node numbering is shown in Figure 7.3.

| $H_{kr,a}$ (%) | $H_{kr,fz,i}$ (%) | $H_{kr,fz,j}$ (%) | $H_{kr,fy,i}$ (%) | $H_{kr,fy,j}$ (%) | $H_{ir,i}$ (‰) | $H_{ir,j}$ (‰) | $\chi_i$ (%) | $\chi_j$ (%) |
|---|---|---|---|---|---|---|---|---|
| 0.4 | 0.4 | 0.4 | 0.4 | 0.4 | 0.5 | 0.5 | 6.0 | 6.0 |

Table 7.1: Resultant plasticity frame element parameters for 6-story frame

| $C_{d0,a}$ | $C_{d1,a}$ | $C_{d0,f}$ | $C_{d1,f}$ | $w$ | $C_{cd}$ | $C_i$ |
|---|---|---|---|---|---|---|
| 200 | 200 | 10 | 180 | 0.35 | 0.20 | 2.0 |

Table 7.2: Damage parameters for the elements of the 6-story steel frame

Four node linear elastic planar quadrilateral elements with high in-plane stiffness are used to constrain the motion of each floor to a translation in X, a translation in Y and a rotation about the Z-axis. The quadrilateral elements do not affect the translation in Z and the out-of-plane rotations at the nodes, which are thus independent.

### 7.2.2 Gravity loads, mass distribution and damping

The model assumes a uniform gravity load of 6 kPa = 0.87 psi on each floor, which is applied in the form of equivalent concentrated vertical nodal forces with the following values: 80.26 kN = 18.04 kips at each corner column and 160.53 kN = 36.09 kips at each interior column. A lumped mass is assumed with $M_1 = 8,185$ kg at the nodes of the corner columns, and $M_2 = 2M_1$ at the nodes of the interior columns, as illustrated in Figure 7.1

Damping is specified with the Wilson/Penzien modal damping model [15] with 2% damping in the first three modes of vibration.

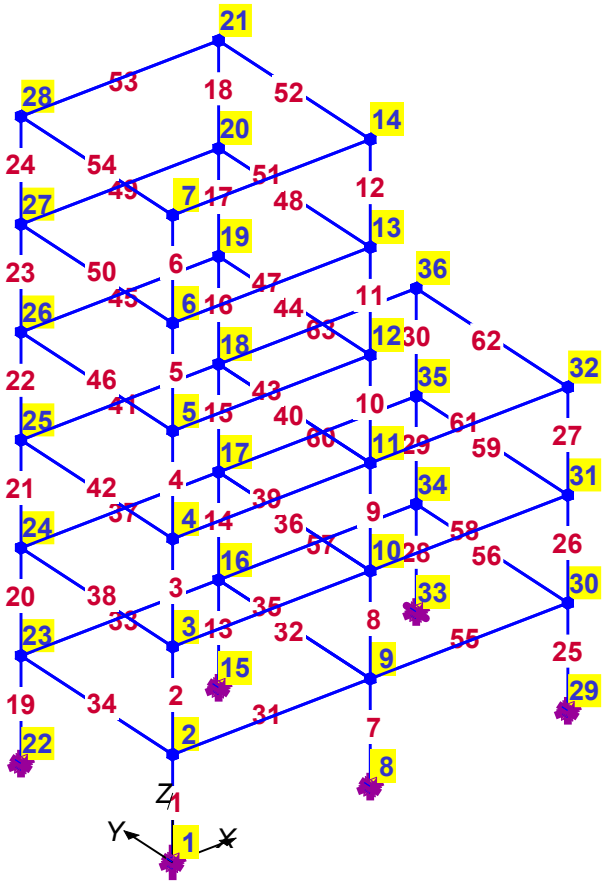


Figure 7.3: Node and element numbering for the model of the 6-story steel frame

### 7.2.3 Natural vibration periods and modes

The eigenvalue analysis of the structural model gives the periods and shapes for the lowest three natural modes of vibration in Figure 7.4. The first mode of vibration corresponds to a translation of the structure in the X-direction, the second mode corresponds to a translation in the Y-direction (with minor torsion), and the third mode corresponds to a torsional motion about the Z-axis.

## 7.3 Static pushover analysis

Two pushover analyses are conducted under the gravity loads and monotonically increasing lateral forces in the X- and Y-direction. The former are distributed proportional to the first mode, and the latter proportional to the second mode. The former analysis is identified with pushover analysis in X, and the latter with pushover analysis in Y. The corotational formulation is used to account for the nonlinear geometry effect.

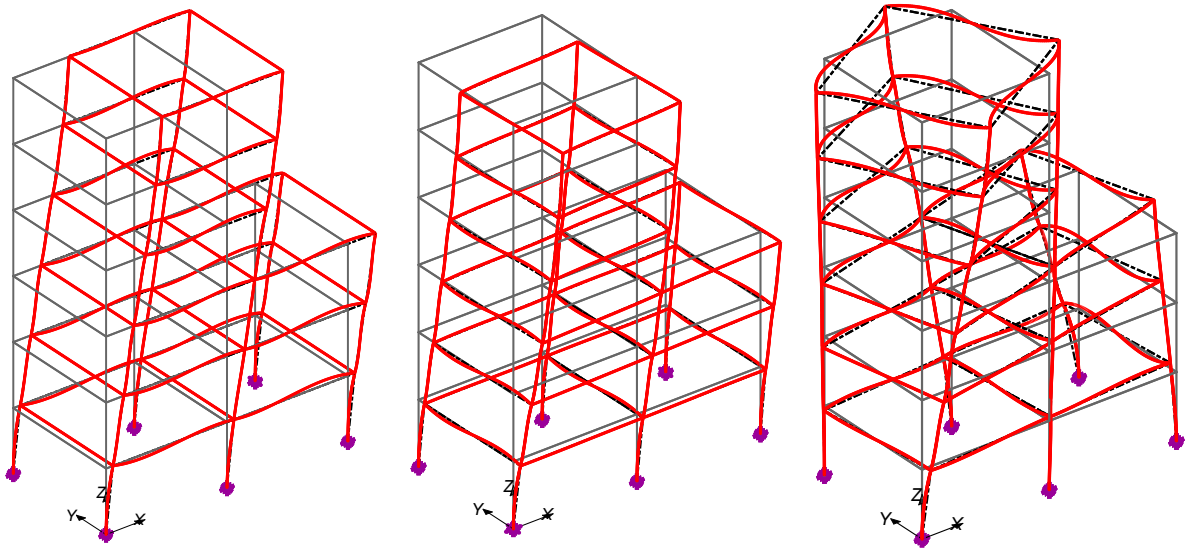

(a) Mode 1: $T_1 = 1.0282$ sec (b) Mode 2: $T_2 = 0.8074$ sec (c) Mode 3: $T_3 = 0.7939$ sec

Figure 7.4: Three lowest natural periods and modes of vibration for 6-story steel frame

### 7.3.1 Pushover analysis in X-direction

Figure 7.5 reports the horizontal load factor as a function of the average roof drift ratio and as a function of the average story drift ratios in both X- and Y-directions for the pushover analysis in X. The average roof drift ratios are reported at the four nodes on the roof, i.e., nodes 7, 14, 21 and 28, and are calculated as:

$$\text{Roof drift ratio in X at node N} = \frac{\text{(X-disp. at node N)}}{\text{total height of building}}$$

$$\text{Roof drift ratio in Y at node N} = \frac{\text{(Y-disp. at node N)}}{\text{total height of building}}$$

The average story drift ratios are calculated as:

$$\text{Story drift ratio in X} = \frac{\text{(avg. nodal X-disp. at floor } i+1\text{) - (avg. nodal X-disp. at floor } i\text{)}}{\text{height of story } i}$$

$$\text{Story drift ratio in Y} = \frac{\text{(avg. nodal Y-disp. at floor } i+1\text{) - (avg. nodal Y-disp. at floor } i\text{)}}{\text{height of story } i}$$

It is worth noting that the story drift measure cancels the effect of any torsional motion by averaging the nodal displacements of each floor in a given direction. However, the presence of torsional deformations is sufficiently captured by the roof drift measure which is reported at all four nodes.

Referring to Figure 7.5(a), the roof nodes exhibit pure translations in the X-direction, consistent with the first natural mode of vibration. Referring to Figure 7.5(b), the drift is uniformly distributed over the first three stories, with story drift values of $6 - 7\%$ at the end of the analysis, and decreases gradually in the upper stories. These observations are consistent with the deformed shape at the end of the pushover analysis in Figure 7.6 with a magnification factor of 3. The inclusion of the nonlinear geometry effect through the corotational formulation leads to a slowly descending post-yield branch in Figure 7.5, which is followed by a steeper descending branch when the element damage gets triggered at about 4.2% roof drift in the X-direction.

Figure 7.7 shows the plastic hinge distribution and the damage index distribution at the end of the pushover analysis. The larger rectangles indicate larger values of plastic deformations/damage index. For the damage distribution, the size of the rectangles is based on the average of the positive and the negative flexural damage index at a given location. Rectangles depicted in orange indicate the presence of a plastic axial deformation/axial damage index in combination with the flexural plastic hinge/flexural damage index; whereas those depicted in red indicate pure flexural hinges or pure flexural damage.

Referring to Figure 7.7(a), flexural plastic hinges associated with bending about the global Y-axis form in both end regions of all girders in the X-directions. Combined axial-flexural hinges form preferentially in the interior columns which are subjected to larger axial forces under the effect of gravity loads than the corner columns. Under increasing lateral load, plastic hinges eventually form at the top and bottom ends of all the first-story columns and the structure forms a soft-story collapse mechanism.

As the damage distribution in Figure 7.7(b) shows, flexural damage accumulates preferentially in the interior columns which are subjected to large plastic flexural deformations combined with higher axial loads than the corner columns. Additionally, the flexural damage index gets triggered at the bottom of the corner columns of the three-story portion of the structure (columns 25 and 28) as the compressive axial load demands increase under the overturning moments.

### 7.3.2 Pushover analysis in Y-direction

Figure 7.8 reports the horizontal load factor as a function of the average roof drift ratio and as a function of the average story drift ratios in both X- and Y-directions for the pushover analysis in Y.

Referring to Figure 7.8(a), the roof nodes exhibit translations in the Y-direction, accompanied by a minor torsional motion about the Z-axis, consistent with the second natural mode of vibration. Referring to Figure 7.8(b), the Y-drift is larger in the first two stories with story drift values of $5 - 6\%$ at the end of the analysis, and decreases gradually in the upper stories with the sixth story only exhibiting a drift of 1%. These observations are consistent with the deformed shape at the end of the pushover analysis in Figure 7.9 with a magnification factor of 3.

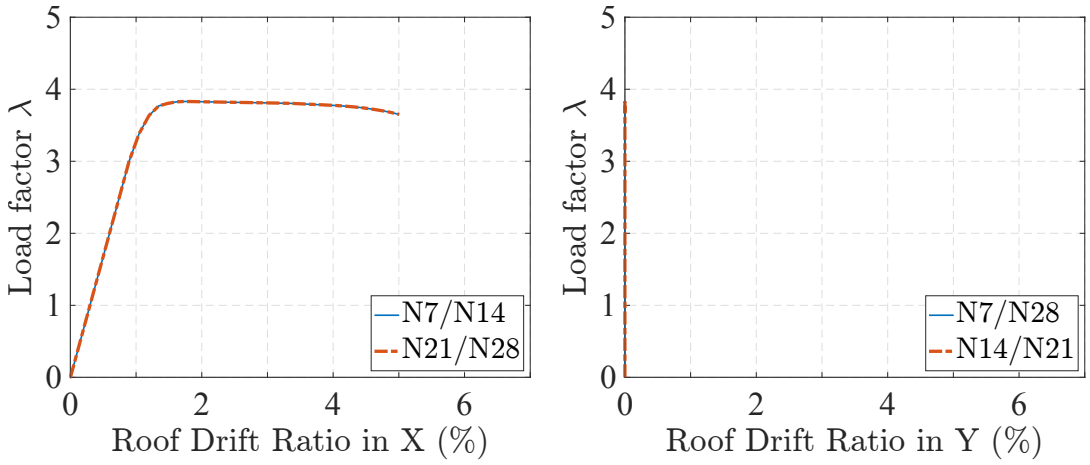


(a) Average roof drift ratio

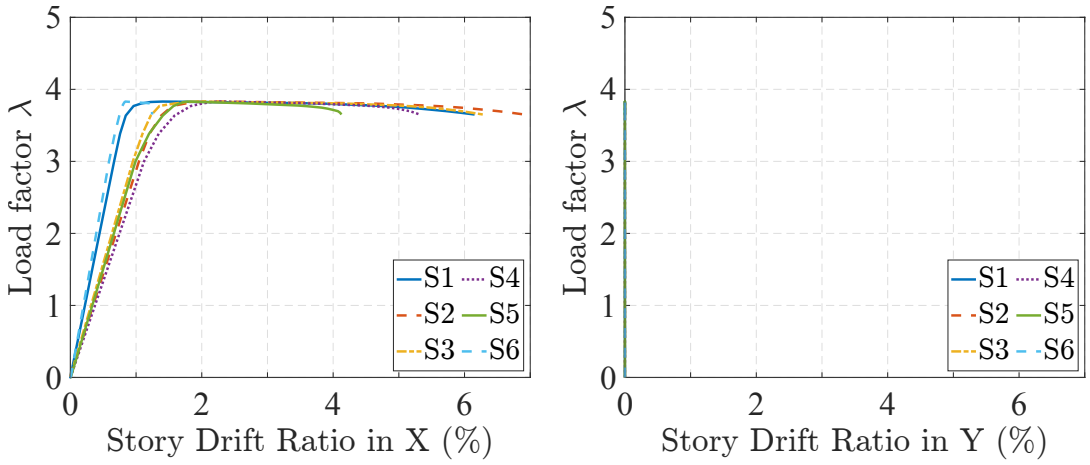


(b) Average story drift ratio

Figure 7.5: Lateral load factor vs. relative drift ratios for the pushover analysis in X

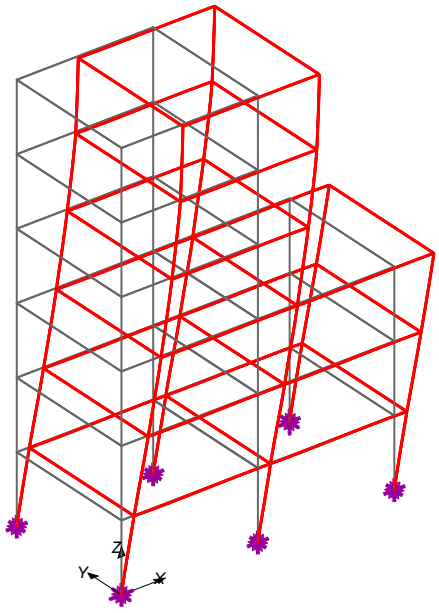


(a) 3d view

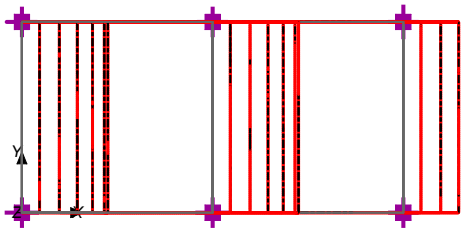


(b) X-Y plane

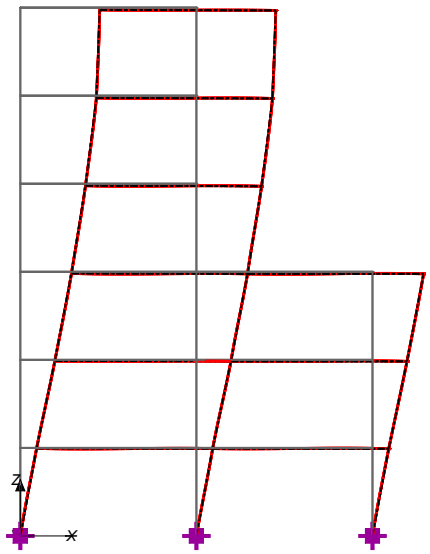


(c) X-Z plane

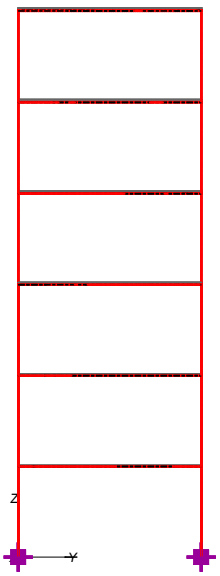


(d) Y-Z plane

Figure 7.6: Deformed shape at the end of the pushover analysis in X

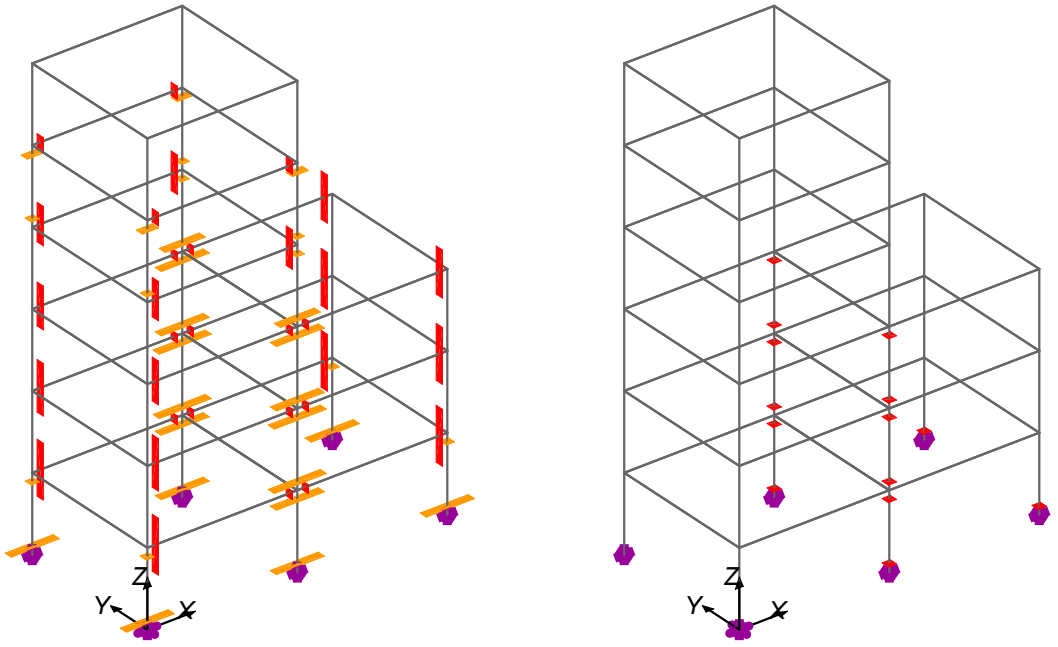


(a) Plastic hinges (b) Damage index

Figure 7.7: Plastic hinges and damage indices at the end of the pushover analysis in X

Figure 7.10 shows the plastic hinge distribution and the damage index distribution at the end of the pushover analysis.

Referring to Figure 7.10(a), flexural plastic hinges associated with bending about the global X-axis form in both end regions of most of the girders in the Y-direction, except in the upper two floors. Combined axial-flexural hinges form at the top and bottom of the first and second story columns, forming a two-story collapse mechanism. The corner columns below the six-story portion of the structure (columns 1 and 19) exhibit higher flexural plastic rotations as they are subjected to higher drifts values under the torsional motion.

The damage distribution in Figure 7.10(b) reflects the large plastic flexural deformations in the first story columns below the six-story portion and in the girder element 34. The flexural damage index gets triggered in both bending directions at the bottom of the corner column 19 under the effect of the torsional motion. Besides, the damage index is higher at that location than in the remaining columns because it is subjected to higher axial load demands under the overturning moments.

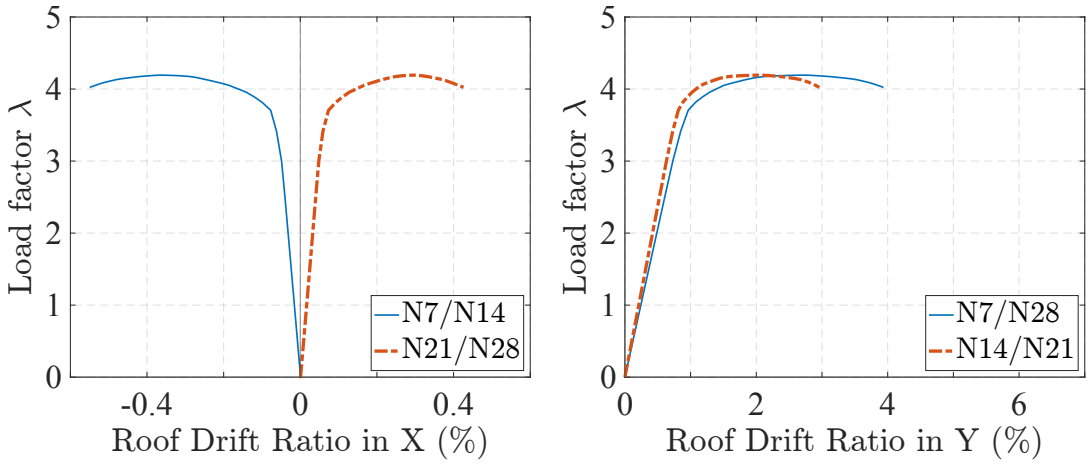


(a) Average roof drift ratio

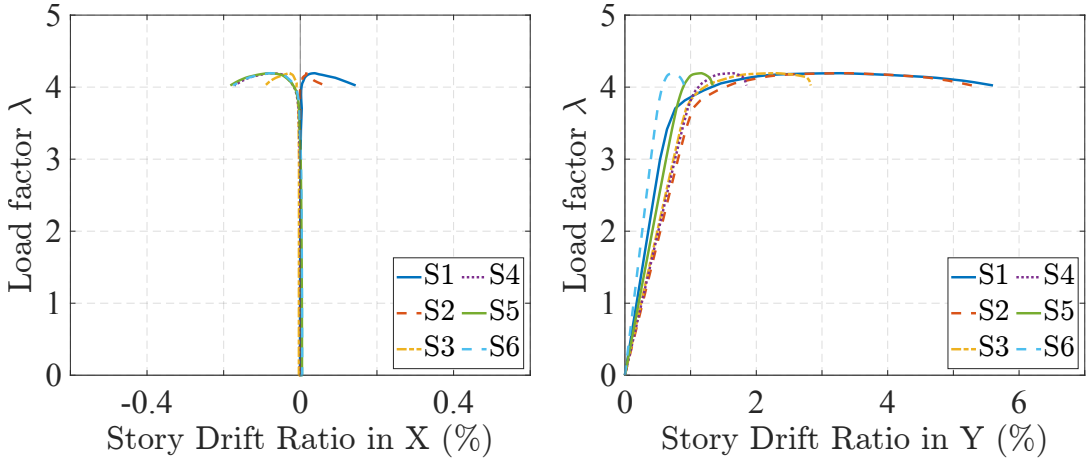


(b) Average story drift ratio

Figure 7.8: Relative drift ratios for the pushover analysis in Y

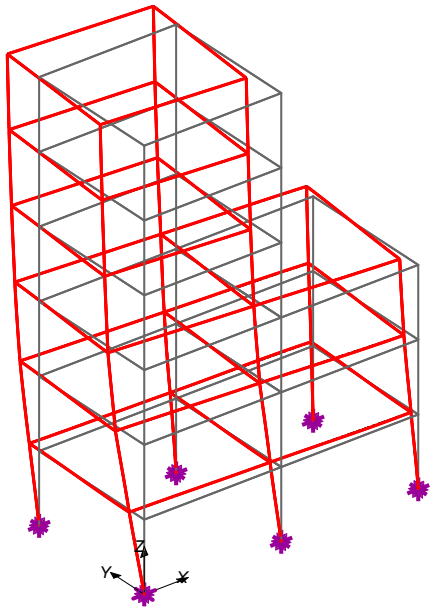

(a) 3d view

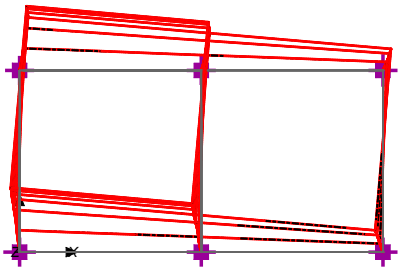

(b) X-Y plane

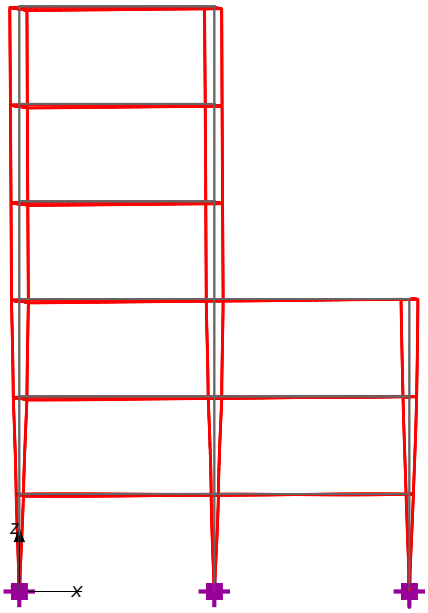

(c) X-Z plane

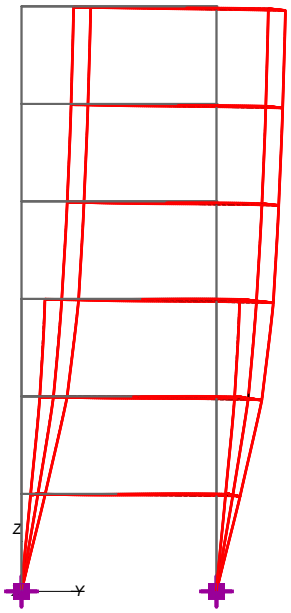

(d) Y-Z plane

Figure 7.9: Deformed shape at the end of the pushover analysis in Y

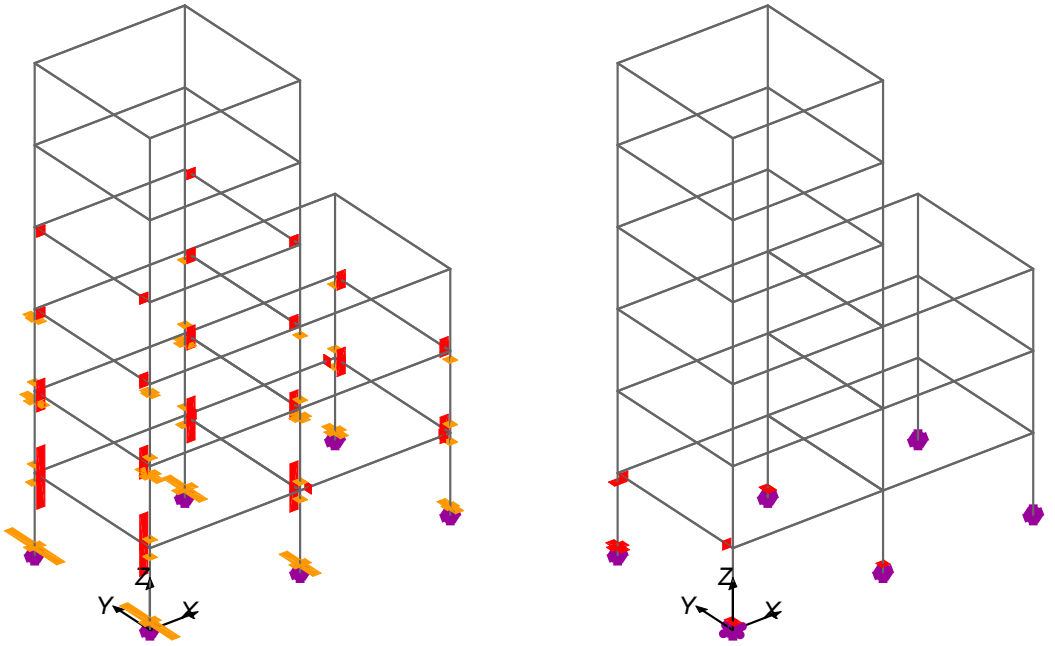


(a) Plastic hinges (b) Damage index

Figure 7.10: Plastic hinges and damage indices at the end of the pushover analysis in Y

### 7.3.3 Effect of nonlinear geometry

To investigate the effect of nonlinear geometry, the two pushover analyses are repeated under the following assumptions: (1) linear geometry and (2) P-$\Delta$ geometry. Figure 7.11 compares the resulting roof drift ratio at Node 28 with the response under the corotational geometry assumption.

The following observations are made:

1. The inclusion of nonlinear geometry is important for capturing the degrading strength of the model under increasing rotations and high axial force demands due to overturning moments.

2. The P-$\Delta$ approximation of the nonlinear element geometry yields almost identical results with the corotational geometry for both pushover analyses.

### 7.3.4 Effect of damage

To investigate the effect of the strength and stiffness deterioration of the frame elements on the global response, the pushover analyses are repeated with the 3d resultant plasticity element without damage. This model is referred to as CP. The resultant plasticity element parameters are the same as those for the analyses of Section 7.2.1. The nonlinear geometry effect is accounted for with the corotational formulation. Figure 7.12 compares the resulting roof drift ratio history at Node 28 with that for the 3d degrading resultant plasticity element (CP_wEDmg).

The following observations are made:

1. The roof drift value of the two models is identical until the onset of damage, after which the model with degrading elements exhibits a faster rate of strength deterioration under increasing plastic deformations and increasing axial force levels in the columns due to overturning.

2. For the pushover analysis in the X-direction, the effect of damage on the global structural response becomes noticeable at a roof drift value of about 4.5%. For the pushover analysis in the Y-direction, this occurs sooner, at a roof drift value of about 3%.

In conclusion, the inclusion of damage in the frame element models is important for accurately capturing the global loss of strength of the structural model.

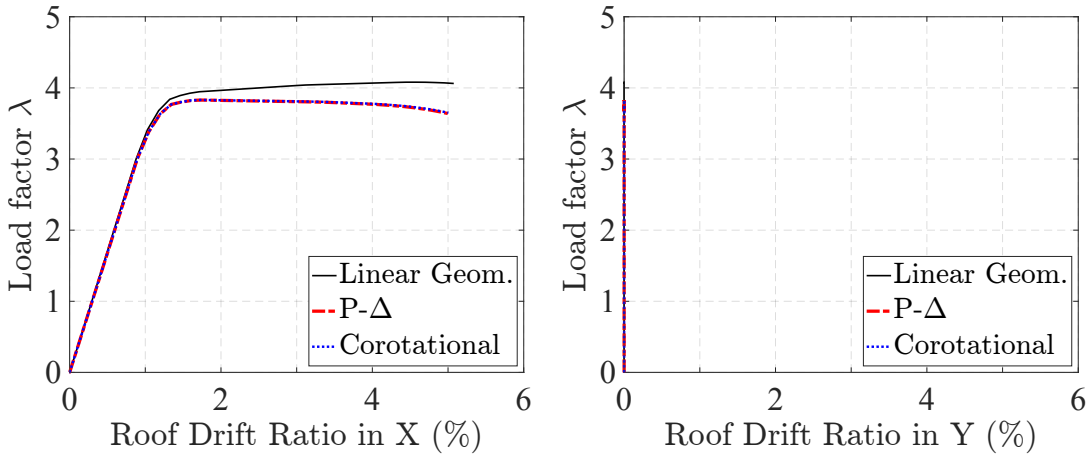


(a) Pushover analysis in X

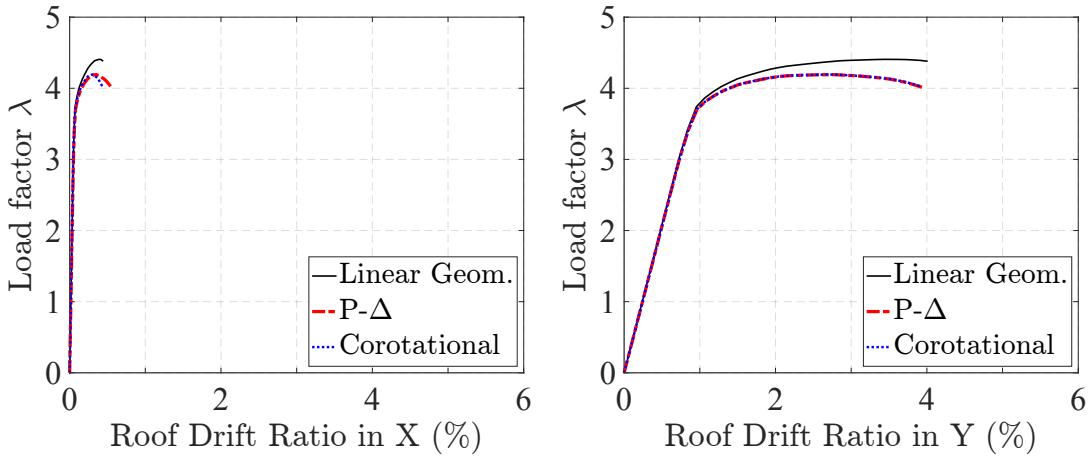


(b) Pushover analysis in Y

Figure 7.11: Effect of nonlinear geometry on average roof drift ratio at Node 28

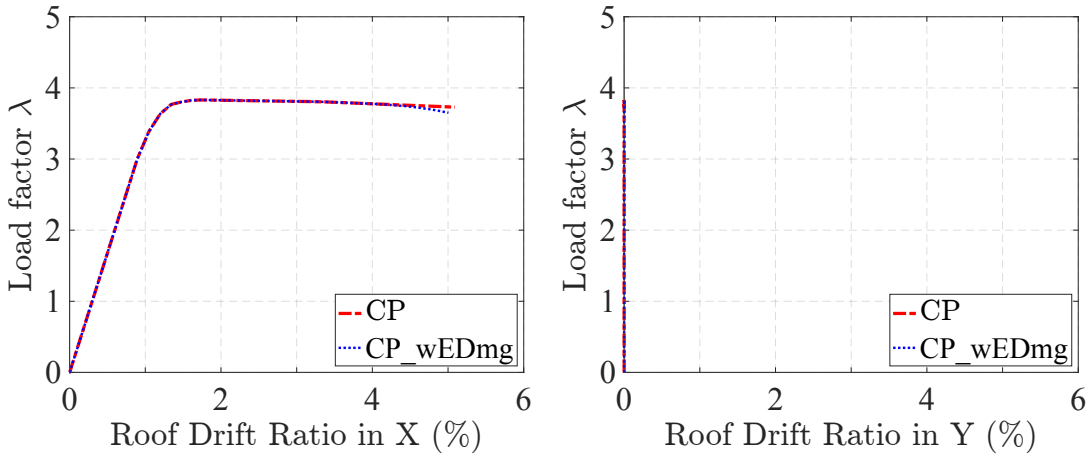


(a) Pushover analysis in X

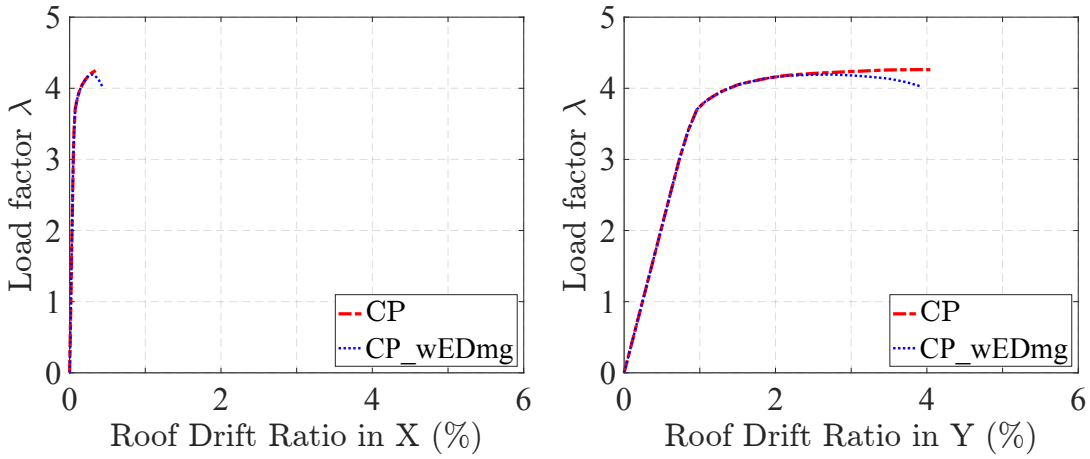


(b) Pushover analysis in Y

Figure 7.12: Effect of damage on average roof drift ratio at Node 28

## 7.4 Dynamic response under bidirectional ground acceleration

### 7.4.1 Ground motion record

The structural model is then subjected to a bidirectional ground motion. The Takatori station recording (Component 0) of the 1995 Kobe earthquake is selected for this study. The recording is obtained from the NGA-West2 PEER Ground Motion Database [64]. The selected ground motion has a peak ground acceleration of 0.62 g. The horizontal ground acceleration history is shown in Figure 7.13 along with the corresponding elastic response spectra.

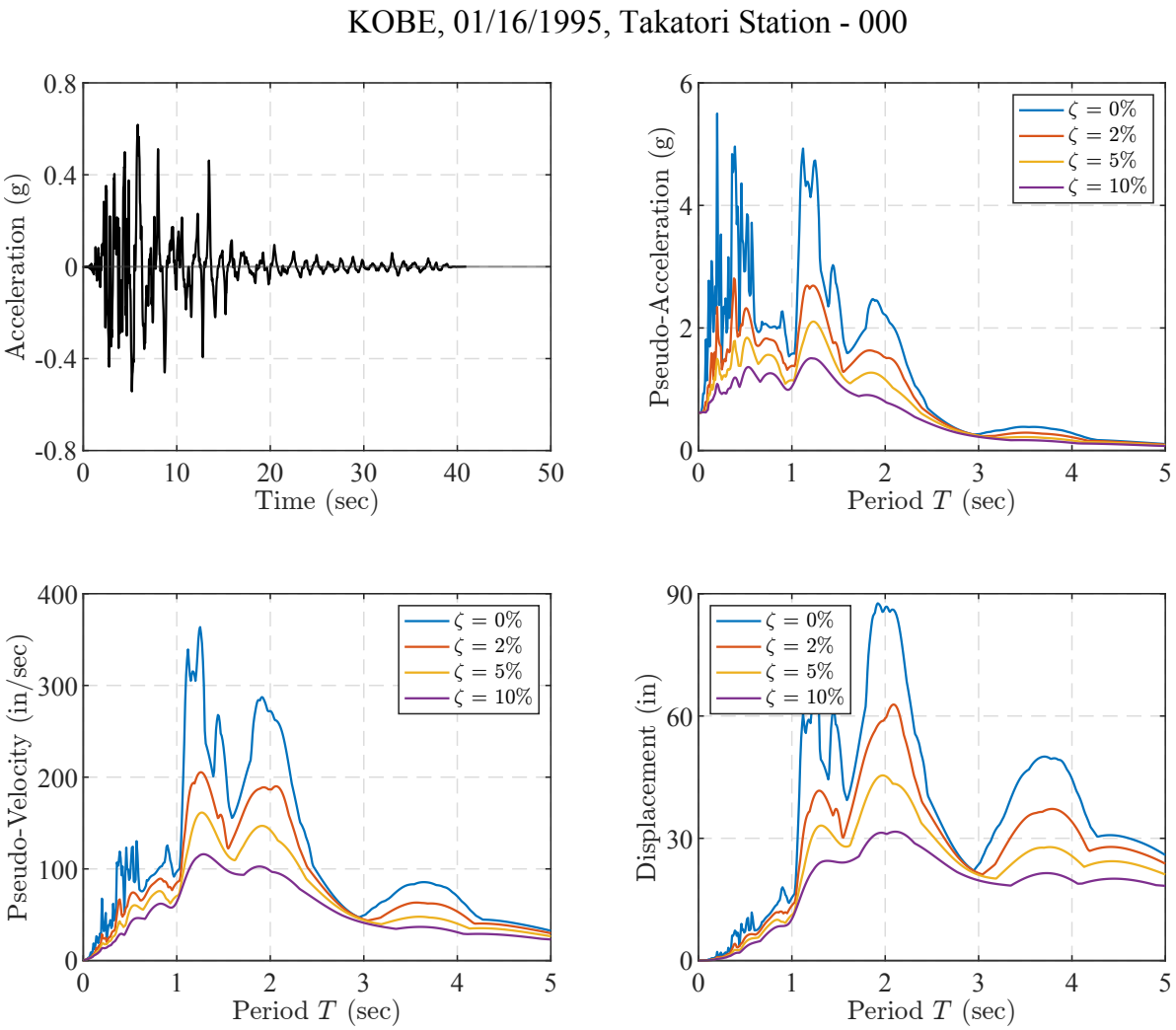


Figure 7.13: Elastic response spectra for Takatori record of Kobe 1995 earthquake

### 7.4.2 Degrading response with corotational geometry

The 6-story frame is subjected to the ground acceleration record described in Section 7.4.1 with a scale factor of 1 in both horizontal X- and Y- directions simultaneously. The element nonlinear geometry is accounted for with the corotational formulation. The analysis stops after 17.65 sec as the frame collapses under excessive levels of deformation.

Figure 7.14 shows the average roof drift ratio and average story drift ratio histories in the X- and Y-direction. As Figure 7.14(a) shows, the frame starts drifting away from its original position at around $t = 6$ sec, as irreversible plastic deformations take place in the beam-column elements. It then oscillates about this new position at a relative roof drift value of 2% in the X- and Y-direction until $t = 14$ sec, after which the deformations grow exponentially as the damage accumulates in the frame elements, leading to the collapse of the structure. Referring the Figure 7.14(b), the deformations accumulate primarily in the first story, which experiences a relative drift of up to 80% in the X-direction and up to 20% drift levels in the Y-direction, while the remaining stories experience smaller values of relative drift. The frame collapses in a first-story mechanism characterized by a translational motion in the negative X- and Y-directions and a slight twisting motion about the Z-axis, as illustrated in Figure 7.15 which uses a magnification factor of 1 for the deformed shape.

Figure 7.16 shows the plastic hinge distribution and the damage index distribution at the end of the analysis at $t = 17.65$ sec. Referring to Figure 7.16(a), significant plastic deformations take place in the first story columns under the combined effect of axial force and biaxial flexure. The plastic deformations form mostly about the Y-axis under translations in the X-direction, but the corner columns of the three-story portion (Elements 25 and 28) experience also large plastic deformations about the X-axis because they are subjected to large Y-drift values under the twisting motion (see Figure 7.15(b)). As Figure 7.16(b) shows, the damage index distribution closely reflects the plastic hinge distribution. The damage mostly concentrates in the first story columns as large axial and biaxial flexure plastic deformations take place and plastic energy dissipation increases under reversed cyclic loading.

The local response of the first story columns is critical for understanding what triggers the collapse of the structure. Figure 7.17 shows the damage index evolution for the flexural response about the global X-axis under translations in the Y-direction of the first-story column elements 1, 7, 13, 19, 25 and 28, and Figure 7.18 shows the damage index evolution for the flexural response about the global Y-axis under translations in the X-direction of the same column elements. The layout of the plots reflects the location of the six columns in a plan view of the first-story rotated at 90°, for easier understanding. The first letter in the subscript of the damage index denotes the local bending axis with z for strong-axis flexure and y for weak-axis flexure; the second letter indicates the end of the element where the flexure is taking place with $i$ for the bottom end and $j$ for the top end of the column; and the superscript indicates whether the damage index is associated with the positive (+) or negative (-) flexural response. For example, index $d_{zi}^{+}$ represents the positive damage index for the flexural response about the strong local z-axis of the section at the bottom of the

column. Figure 7.19 shows the axial force-bending moment history at the bottom of the first-story columns. Figure 7.20 shows the drift history for the nodes at the top of the first story columns. The markers in Figure 7.20 correspond to each second of the analysis, with labels in red corresponding to $t = 5$ sec, $t = 10$ sec and $t = 15$ sec. Lastly, Figure 7.21 shows the history of the node displacement magnitude at the top of the same columns defined as $\sqrt{U_X^2 + U_Y^2}$ and normalized by the story height $H$. The layout of the last two figures follows the same arrangement as Figures 7.17 - 7.19. For example, Node 2 is located at the top of Element 1, and Node 23 is located at the top of Element 19.

Consistent with previous observations, a first pulse at $t = 6$ sec displaces the first story diagonally in the negative X- and Y-directions. The accumulation of plastic flexural deformations is accompanied by plastic flexural energy dissipation which triggers the flexural damage indices in most of the first story columns. As the building drifts in the negative Y-direction and X-direction, the damage index for the flexural response about the X-axis and Y-axis grows, respectively, with the largest increase in the corner column element 1 which undergoes the highest compressive axial force under the overturning moment. The second largest increase of the flexural damage index arises in the interior column element 7 which carries larger gravity loads than the corner columns as well as an additional compressive axial force due to the overturning moment. The strength deterioration at the bottom of elements 25 and 28 is also appreciable. As a given positive damage index grows, the corresponding negative damage index grows in parallel at a slower rate because of the positive/negative damage coupling coefficient of 0.2.

At time $t = 14$ sec, a second pulse displaces the structure further in the X-direction, causing bending about the Y-axis and increasing the damage of most first story columns. This additional loss of strength initiates a twisting motion of the frame which accelerates the damage accumulation and initiates the collapse of the building. Figure 7.22 shows the deformed shape of the first-story in plan view (X-Y) at key instants of the analysis: at $t = 6$ sec (blue line), at $t = 14$ sec (red line) and at the end of the analysis at $t = 17.65$ sec (black line).

Figure 7.19 confirms that Element 1 is subjected to the largest variation of axial force with axial force levels between $-45\%N_p$ (compression) and $+25\%N_p$ (tension). Elements 13 and 19 also undergo large variations of axial force between $-35\%N_p$ (compression) and $+15\%N_p$ (tension). Elements 25 and 28 of the three-story portion carry smaller gravity loads and thus exhibit the smallest change of axial force with Element 28 slightly higher than Element 25 because of the overturning moment.

Additionally, Figure 7.20 shows that Nodes 2, 9 and 30, at the top of Elements 1, 7 and 25, respectively, exhibit larger displacements in X than the other three nodes of the same floor. This leads to higher damage for the flexural response about the Y-axis of these three columns (see Figure 7.18). Nodes 30 and 34 at the top of Elements 25 and 28 also exhibit larger Y-displacements than the other nodes, but this is does not cause higher damage for the flexural response abut the X-axis because of the lower level of axial compression in these two columns.

Lastly, Figure 7.21 confirms that $t = 6$ sec corresponds to a large increase in rotation

demand of the first-story columns, causing large plastic rotations and triggering the damage onset, and that $t = 14$ sec causes the second wave of damage accumulation. Past this instant, the first-story columns loose significant strength and the deformations grow exponentially leading to the collapse.

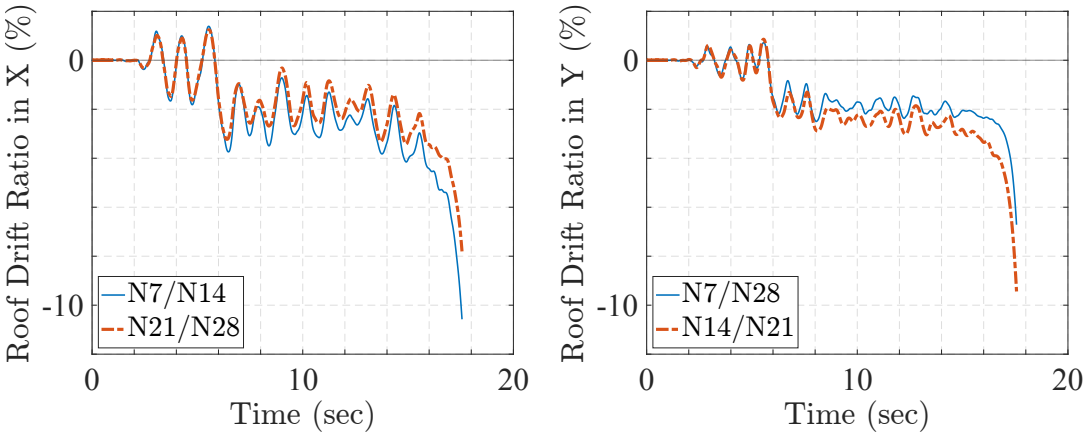


(a) Average roof drift ratio

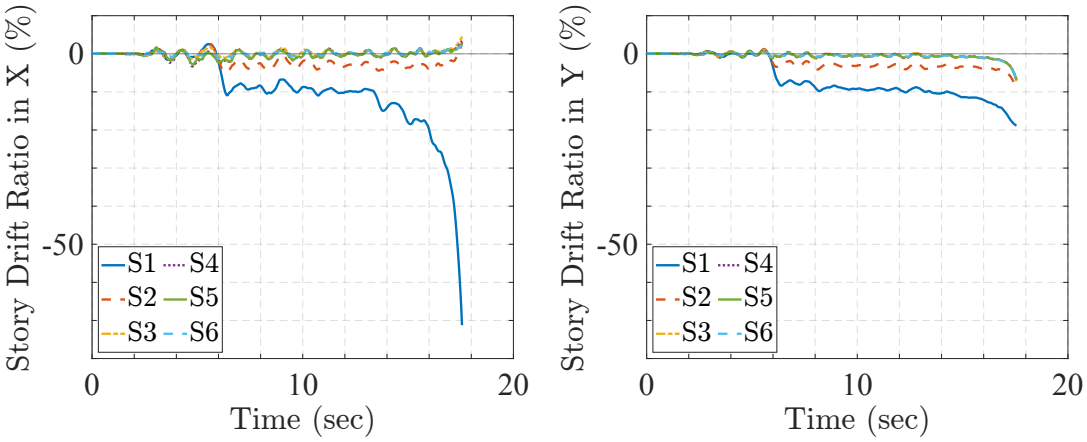


(b) Average story drift ratio

Figure 7.14: Relative drift ratio histories under biaxial ground acceleration

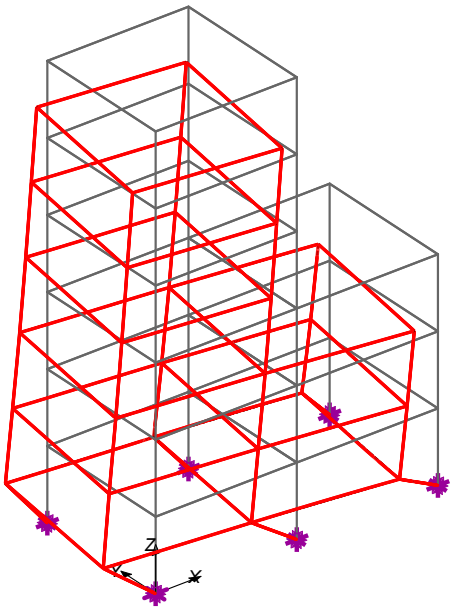

(a) 3d view

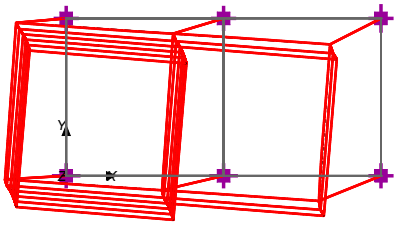

(b) X-Y plane

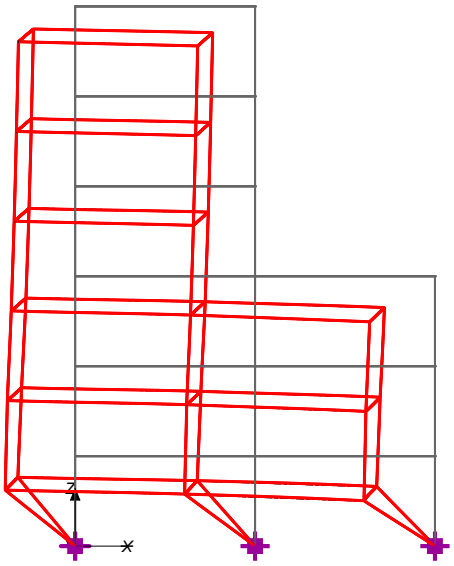

(c) X-Z plane

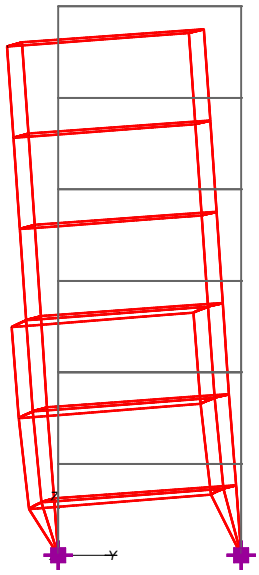

(d) Y-Z plane

Figure 7.15: Deformed shape at $t = 17.65$ sec under biaxial ground acceleration

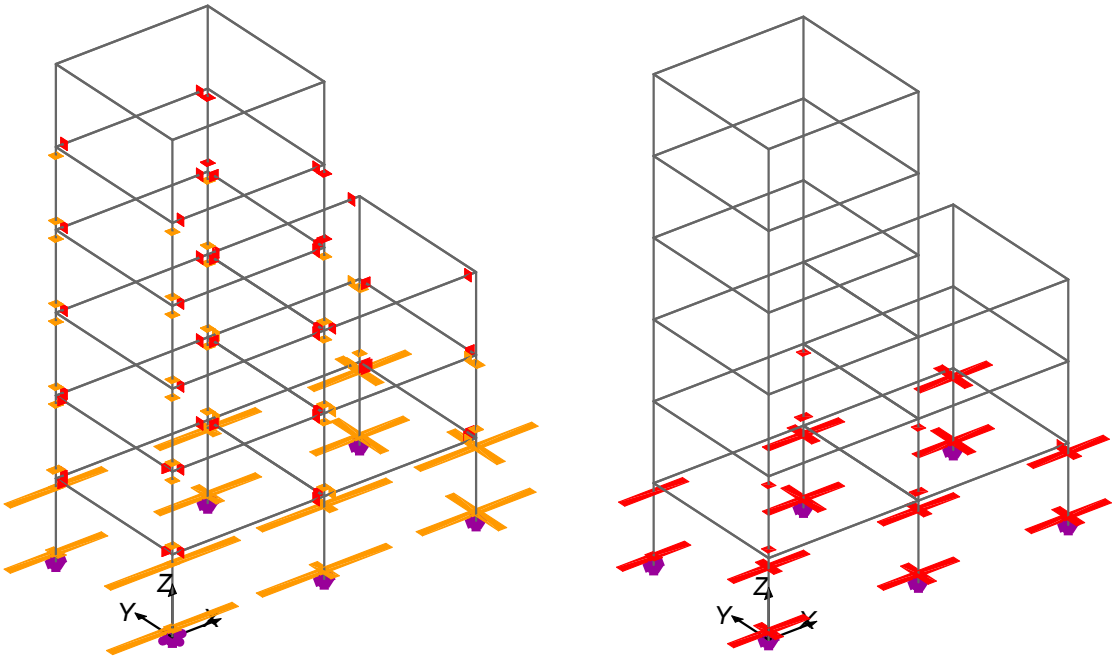


(a) Plastic hinges (b) Damage index

Figure 7.16: Plastic hinges and damage indices at $t = 17.65$ sec under biaxial ground acceleration

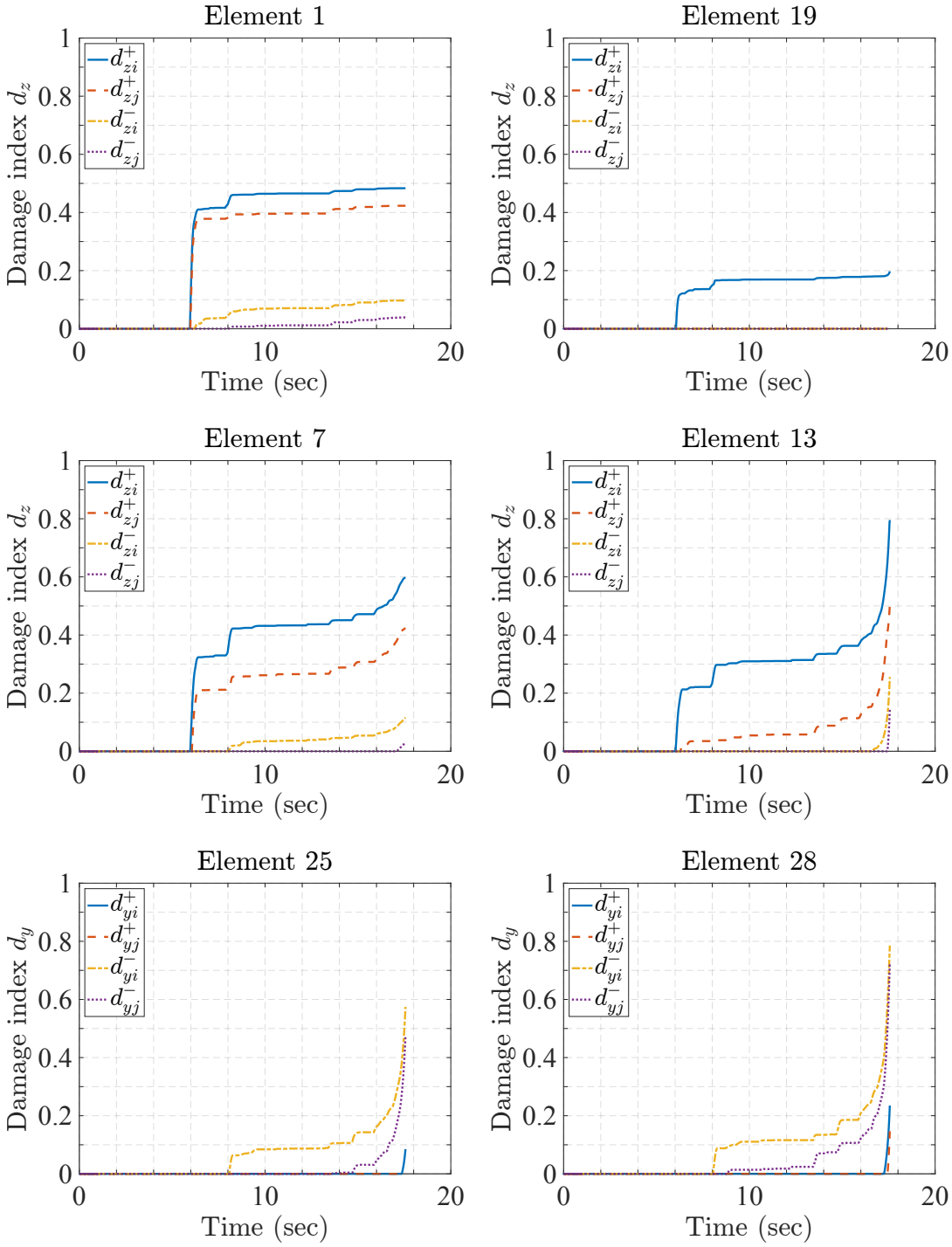


Figure 7.17: Damage index evolution for flexural response of first-story columns about global X-axis

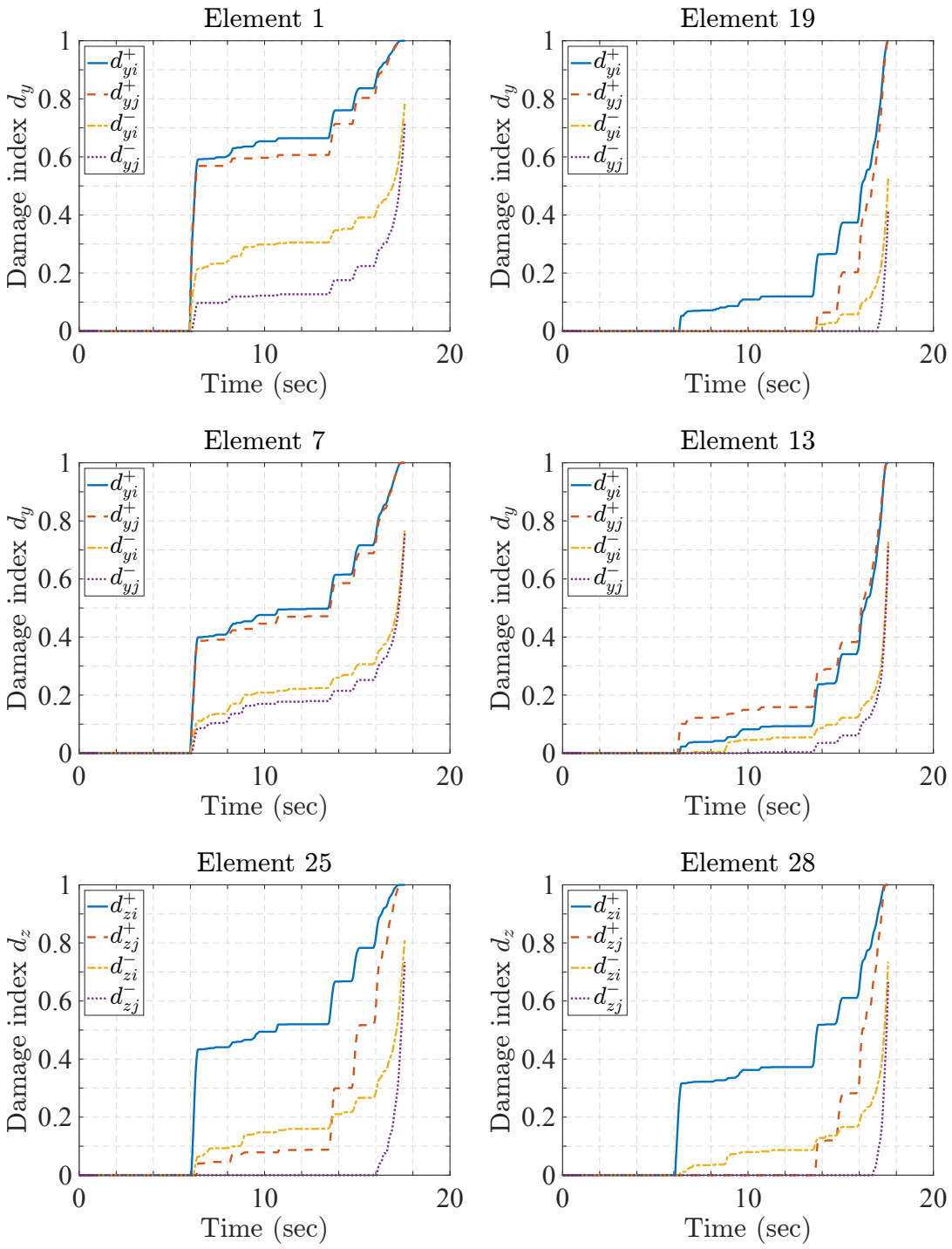


Figure 7.18: Damage index evolution of first-story columns for flexure about global Y-axis

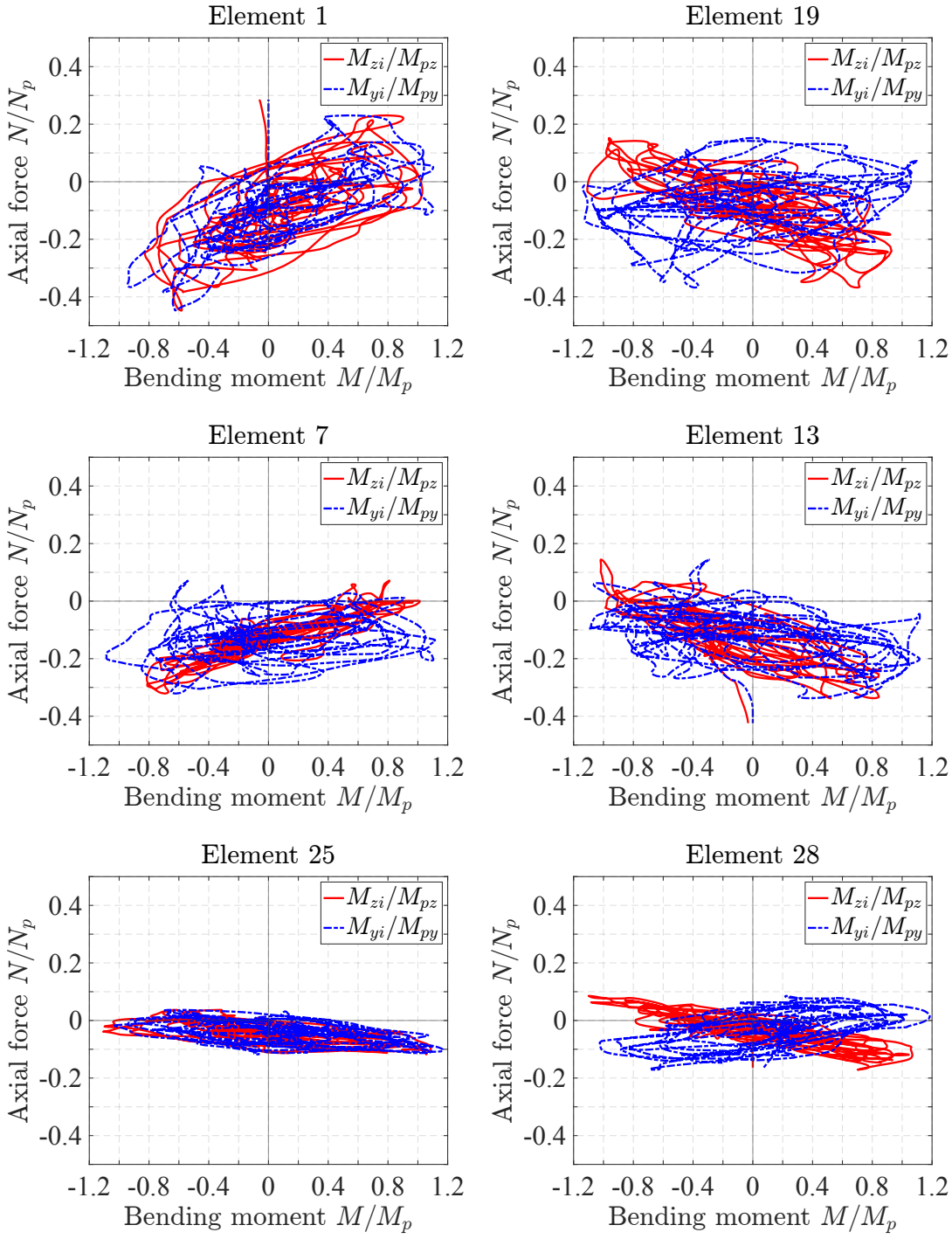


Figure 7.19: Axial force-bending moment history at the bottom of first-story columns

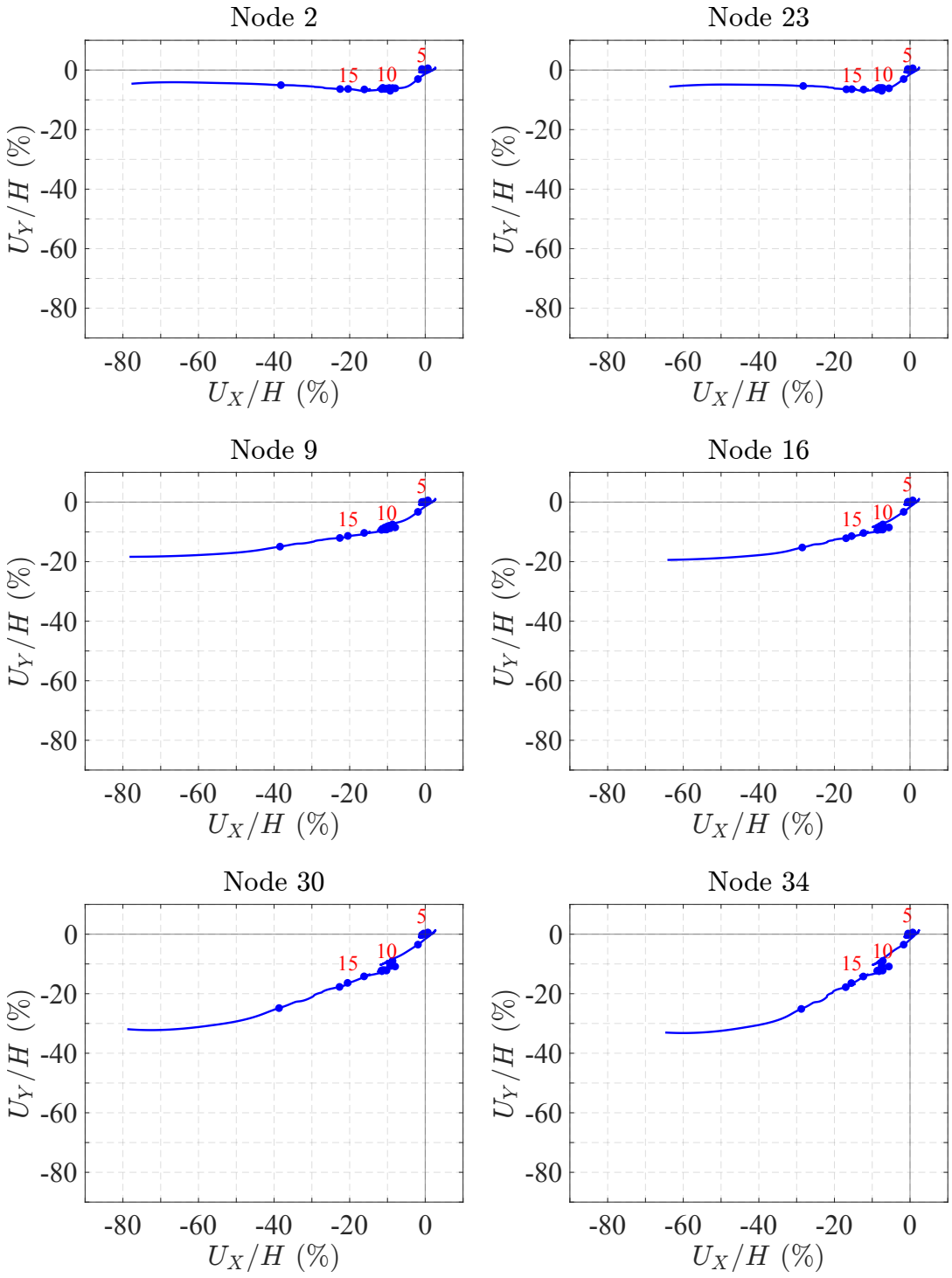


Figure 7.20: Node displacement path at the top of first-story columns

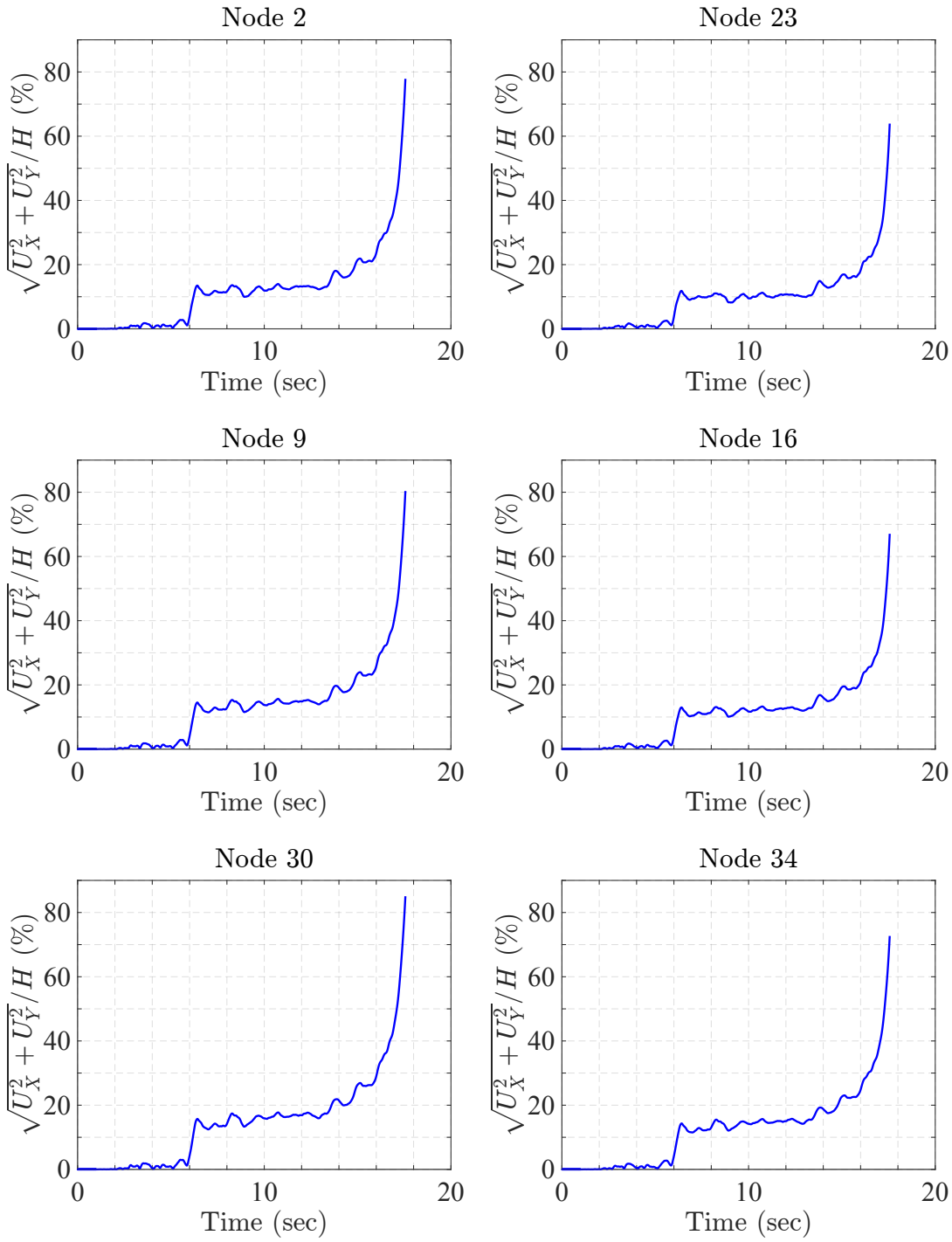


Figure 7.21: Node displacement history at the top of first-story columns

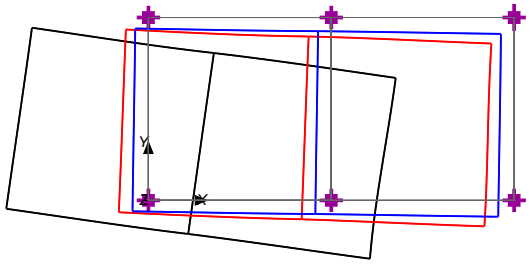

Figure 7.22: Plan view of the first floor slab at $t = 6$ sec (blue), $t = 14$ sec (red) and $t = 17.65$ sec (black) of the dynamic response history with a magnification factor of 2

### 7.4.3 Effect of nonlinear geometry

To investigate the effect of nonlinear geometry, the dynamic response history analysis is repeated under the following assumptions: (1) linear geometry and (2) P-$\Delta$ geometry. Figure 7.23(a) compares the resulting roof drift ratio history at Node 28 with that under corotational geometry. Figures 7.23(b) and 7.23(c) present similar plots for the average first-story drift ratio and for the displacement history of Node 30.

The following observations are made:

1. Under linear geometry, the dynamic analysis runs successfully until the end of the strong motion and the multistory frame does not collapse. On the other hand, the structure collapses after 14 sec when considering the geometric nonlinearity with the corotational formulation or the P-$\Delta$ approximation.

2. The response history for P-$\Delta$ geometry and corotational geometry are almost identical results until the incipient collapse at about $t = 14$ sec.

3. In the early stage of the dynamic response history under relative story drift ratios not exceeding 5%, all three geometry assumptions give identical results. For story drift ratios in excess of 5%, the approximate or exact consideration of nonlinear geometry with the P-$\Delta$ or corotational formulation yield first-story drift values that are 50% higher than under linear geometry. This discrepancy in the rotation responses results in significantly different global structural response. With the former assumption, the system accumulates plastic deformations and is left with a permanent residual roof drift of about 2%, i.e., a residual first-story drift of about 5%, but it does not collapse. With the inclusion of nonlinear geometry, the system undergoes displacements that are sufficiently larger relative to the linear geometry formulation to create significantly more damage, which weakens the first-story columns and leads to the collapse of the structure.

It is concluded that the inclusion of nonlinear geometry is critical for capturing the strength and stiffness deterioration of structural systems under earthquake excitations, especially if the structural model experiences story drifts ratios in excess of 5%.

### 7.4.4 Effect of damage

To investigate the effect of strength and stiffness deterioration of the frame elements on the global response, the dynamic analysis is repeated with the 3d resultant plasticity beam-column element without damage. This model is referred to as CP. For the CP model, the resultant plasticity element parameters are identical with those in Section 7.2.1. The nonlinear geometry effect is captured through the corotational formulation. Figure 7.24(a) compares the resulting roof drift ratio history at Node 28 with that for the 3d degrading resultant plasticity element (CP_wEDmg). The response history with 3d linear elastic (LE) frame elements is also shown for reference. Figures 7.24(b) and 7.24(c) present similar plots for the average first-story drift ratio and for the displacement history at Node 30.

The following observations are made:

1. With the consideration of plasticity through the CP model, the structure drifts away from its initial position and a 2% residual roof drift persists at the end of the shaking. The structure does not collapse.

2. With the additional consideration of strength and stiffness deterioration in model CP_wEDmg, the accumulated plastic rotations under reversed cyclic loading are accompanied by plastic dissipated energy and a corresponding accumulation of damage in the first-story columns. As these columns loose a considerable amount of strength, the building is not able to sustain the shaking and it collapses after $t = 14$ sec.

It is concluded that the consideration of damage in the frame element models is particularly important for accurately capturing the global loss of strength of the structural model under dynamic analysis, especially if the structure experiences story drift ratios in excess 10%.

### 7.4.5 Effect of peak ground acceleration

Lastly, the effect of the peak ground acceleration of the Takatori ground motion on the dynamic response of the frame is investigated. The frame is subjected to the same bidirectional ground acceleration record, but the motion is scaled down by the factor $SF = 0.98$. The response history for the scaled down record is compared with the original record in Figure 7.25. The small reduction of the peak ground acceleration gives slightly smaller plastic deformations than for the original ground motion, but this slight reduction is sufficient to prevent the collapse of the multistory frame. As Figure 7.25(c) shows, the irreversible growth of lateral deformations appears to take place at a first story drift ratio in Y of about 10%, consistent with previous observations.

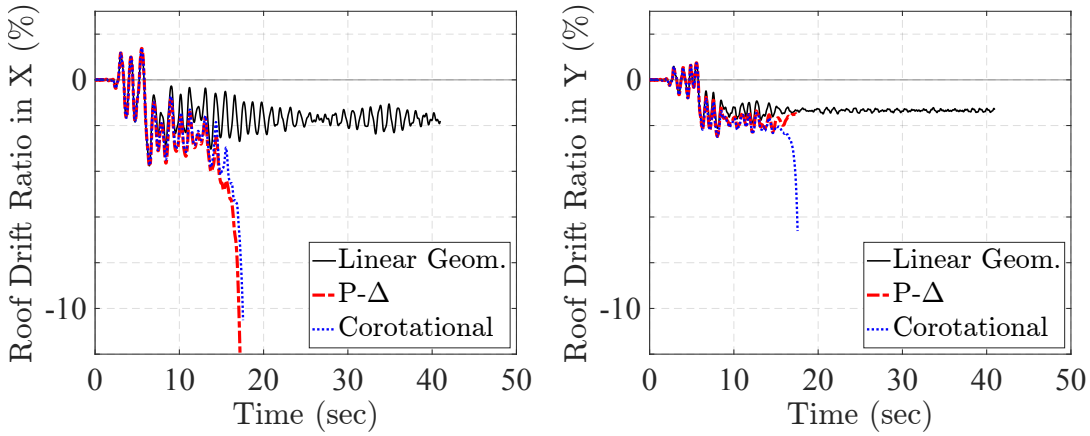


(a) Average roof drift ratio at Node 28

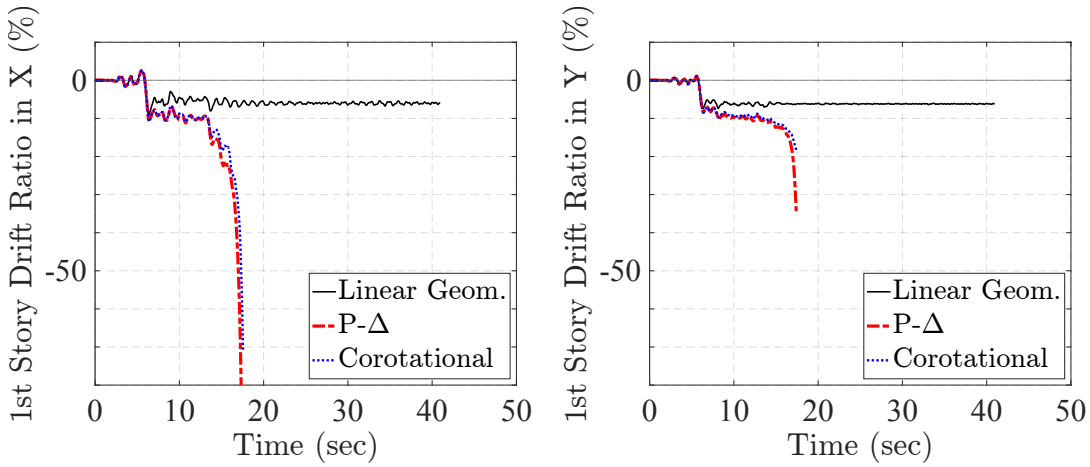


(b) Average first-story drift ratio

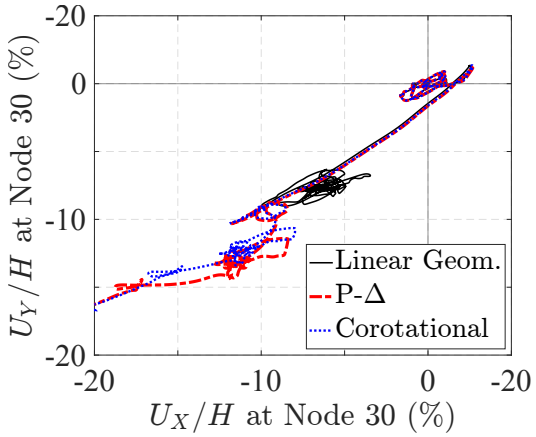


(c) Rotation demand at the top of Element 25

Figure 7.23: Effect of nonlinear geometry on nonlinear response history

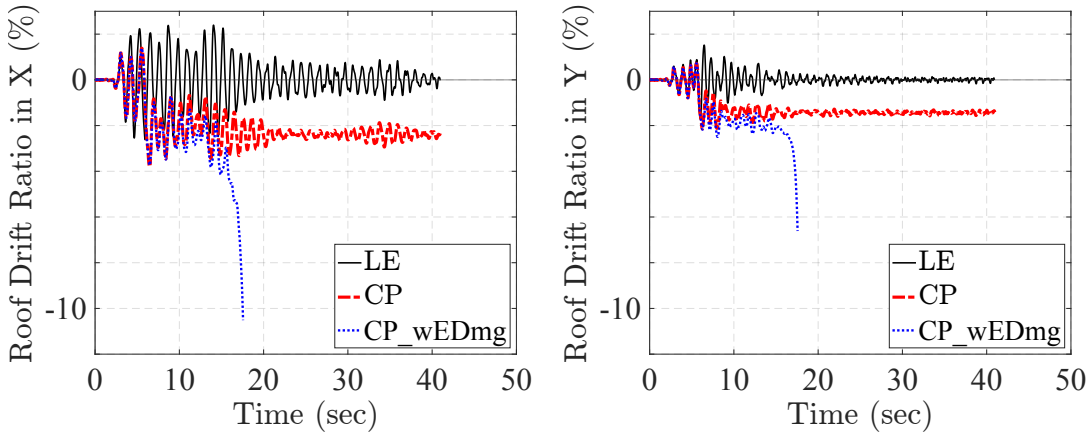


(a) Average roof drift ratio at Node 28

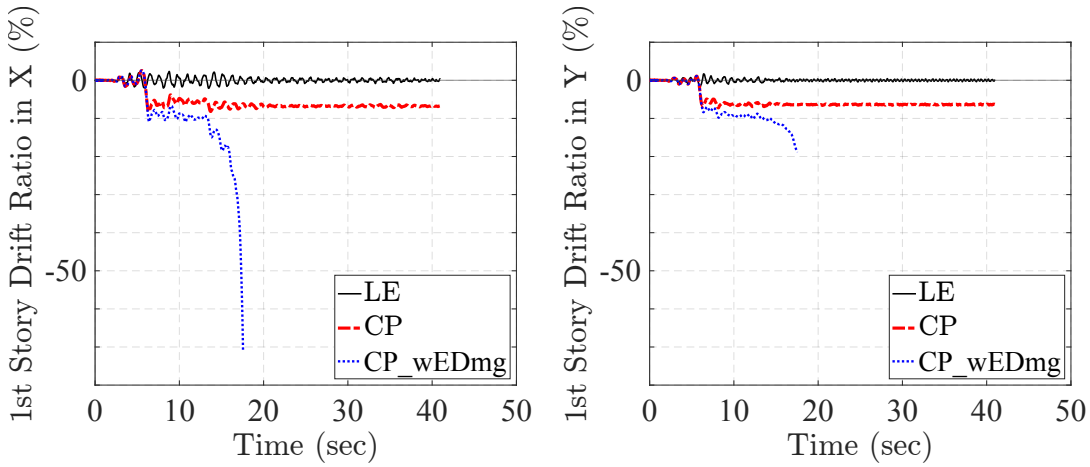


(b) Average first-story drift ratio

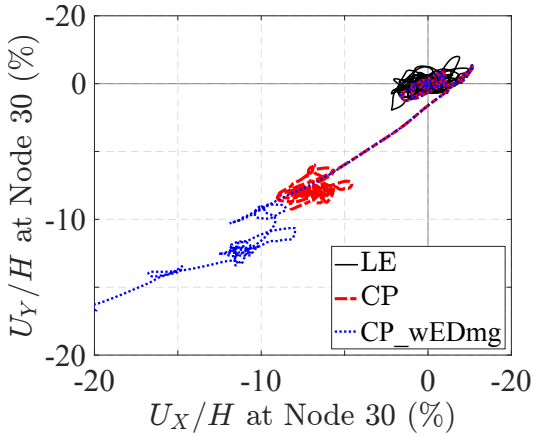


(c) Rotation demand at the top of Element 25

Figure 7.24: Effect of damage on nonlinear response history

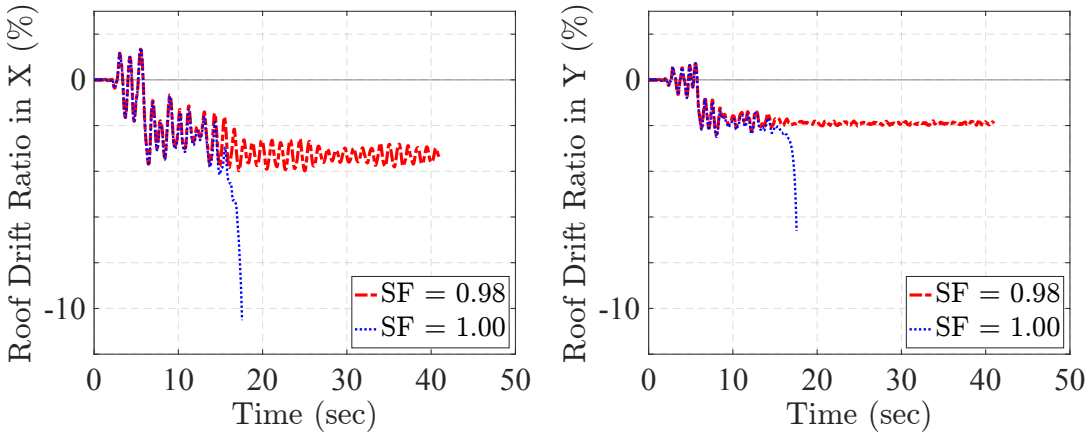


(a) Average roof drift ratio at Node 28

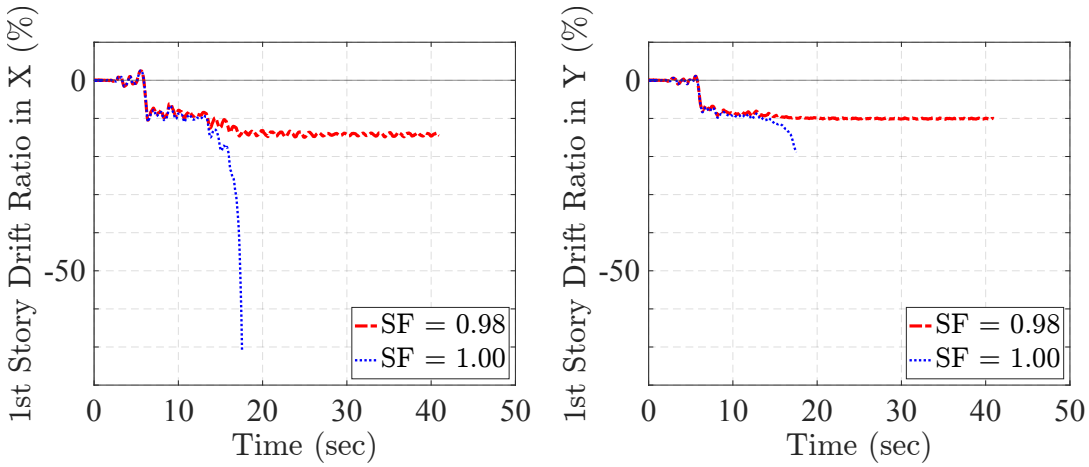


(b) Average first-story drift ratio

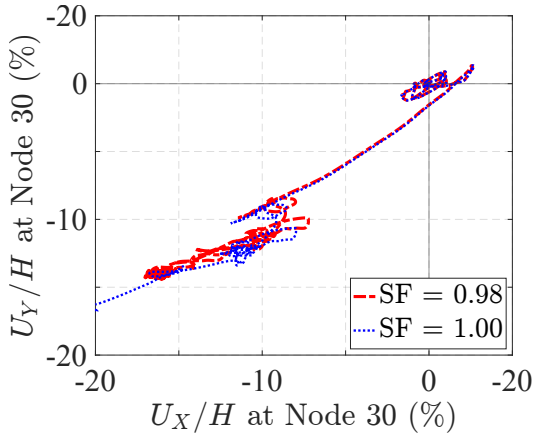


(c) Rotation demand at the top of Element 25

Figure 7.25: Effect of peak ground acceleration on nonlinear response history

# Chapter 8

# Summary and conclusions

## 8.1 Summary

The objective of this study is the development of analytical capabilities for the simulation of the inelastic response of structures under the strength and stiffness deterioration they experience when subjected to extreme events. The study addresses the development of such an analytical capability for steel frames. To this end, a family of 2d and 3d frame element models is proposed based on damage-plasticity. The strength and stiffness of these models degrade continuously as a function of one or more damage indices making them suitable for the damage assessment of steel frames up to incipient collapse.

The study extends an existing damage model to cover the damage evolution of the constitutive relation of the frame element under multiple, interacting stresses or stress resultants. The formulation uses several damage indices that evolve continuously with the weighted sum of the plastic energy dissipation of the stress resultants with the work-conjugate deformation variables. The damage evolution function accounts for low-cycle fatigue and the different rate of damage accumulation in primary and follower deformation cycles. The function also accounts for the fact that the behavior in one loading direction may be affected by the damage accumulated in the opposite direction.

The damage model operates as an independent wrapper of the effective force-deformation relation of the element, section or material and returns the true forces or stress resultants and the true tangent stiffness of the force-deformation relation under damage. With this modular formulation it is possible to use the damage wrapper with a material stress-strain relation, with a section force-deformation relation, or with the constitutive relation between the element basic forces and the work-conjugate deformations. Consequently, the study investigates the following three modeling alternatives for steel frame members without damage: a plasticity-based frame element with the basic forces and the work-conjugate deformations in the role of stress resultants and generalized strains, and a frame element that integrates the section force-deformation relation over the element length, with the section model based on plasticity theory for stress-resultants and generalized strains, or on the integration of

the material stress-strain relation over the cross-section, a model commonly referred to as fiber section model. With the introduction of the damage wrapper at the element, or at the section, or at the material level, six modeling alternatives for steel frame members under damage result.

Before embarking on the evaluation of the damage plasticity formulations, this study assesses the accuracy of the section model for stress-resultants by comparing its response with the response of the section model that integrates the material stress-strain relation over the cross section. To this end, an existing formulation is extended to accommodate the kinematic and isotropic hardening of the stress-resultants and the numerical implementation is enhanced with the scaling of the state determination variables to minimize the risk for an ill-conditioning of the Jacobian for the return-mapping algorithm of the section state determination.

The same process is repeated for two existing stress-resultant frame elements: a 2d beam element with linear elastic axial response, and a 3d beam-column element with axial force-biaxial flexure interaction and linear elastic torsional response. The former is suitable for steel girders experiencing small to negligible axial forces, while the latter is suitable for steel columns under any level of axial force, including variable axial forces due to the overturning effect of steel frames under lateral loads. The existing elements are extended to accommodate the kinematic and isotropic hardening of the stress-resultants and the numerical implementation is again enhanced with the scaling of the state determination variables to minimize the risk for an ill-conditioning of the Jacobian for the return-mapping algorithm of the element state determination. To account for the spread of inelasticity at the ends of steel beams and columns under strain hardening, both elements allow for the plastic hinges to be offset from the element ends. This feature requires the careful determination of the equivalent kinematic and isotropic hardening ratio for the element to match the moment-rotation relation of steel members under symmetric or anti-symmetric flexure. The study derives the necessary analytical expressions for this calibration, which are exact for beams and approximate for columns under axial force-flexure interaction. Correlation studies are conducted to assess the quality of the approximation for typical load-deformation scenarios of a steel member.

After completing the evaluation of the resultant plasticity formulations, the study compares the response of four alternatives for a frame element under damage against available experimental data from the hysteretic uniaxial and biaxial bending response of steel columns under constant and variable axial force. These comparisons lead to recommendations on a consistent set of damage parameter values for typical steel members.

The study concludes with the seismic response analysis of an irregular six-story steel frame under a strong ground acceleration in both principal directions at the base. The inelastic response history evaluates the effect of the damage evolution on the collapse risk of the frame and assesses the effect of nonlinear geometry and ground motion intensity on its global and local response.

## 8.2 Conclusions

The conclusions of the present study are:

- The plasticity based section model for stress resultants and corresponding generalized strains is quite accurate for steel sections even in the presence of kinematic and isotropic hardening. The evaluation studies confirm the ability of the model to describe the strength of the section and its plastic deformations very well. Especially, noteworthy is the quality of the plastic axial strain estimation under constant or variable axial load for imposed uniaxial or biaxial curvature histories.

- The computational savings of the plasticity based section model for stress resultants relative to the fiber section model that integrates the material stress-strain relation over the cross section ranges from 33% to 75%, even for relatively coarse fiber meshes, with the larger savings corresponding to biaxial response. The storage savings for the history variables are even more impressive, and can increase the computational efficiency significantly for large structural models.

- The 2d beam element with the flexural basic forces as stress-resultants and linear elastic axial response matches very well the response of steel members and is able to account for the spread of inelastic deformations at the element ends under hardening by offsetting the location of the plastic hinges from the element ends. The reference solution is based on a frame element with force interpolation functions that integrates the material stress-strain relation first over each control section (integration point) and then over the element length. With the proposed analytical expressions for calibrating the kinematic and isotropic hardening parameters to match a given end-moment rotation of the steel girder under general flexure conditions, the element gives very accurate estimates of rotation ductility and energy dissipation for any loading condition of the steel member. The offset of the plastic hinges from the element ends also accounts for the coupling of the plastic deformations at the offset hinges.

- The 2d/3d beam-column element with the basic forces as stress-resultants and the work-conjugate deformations as generalized strains matches very well the response of steel members under the interaction of axial force and biaxial flexure. The reference solution is based on a frame element with force interpolation functions that integrates the material stress-strain relation first over each control section (integration point) and then over the element length. The 2d/3d beam-column with resultant plasticity describes very well the spread of inelastic deformations at the ends of the steel column under hardening by offsetting the location of the plastic hinges from the ends. The computational effort of this element is 4 to 5 times smaller than the reference solution, especially under biaxial response. Moreover, the factor is several times larger for very fine section mesh subdivisions of the cross section for the reference solution. With the proposed calibration of the kinematic and isotropic hardening parameters, the element

gives accurate estimates of rotation ductility and energy dissipation for any loading condition of the steel column. The offset of the plastic hinges from the element ends also accounts for the coupling of the plastic deformations at the offset hinges.

- The plasticity based formulation of the 2d beam element and the 2d/3d beam-column element with the basic forces and work-conjugate deformations serving in the role of stress-resultants and generalized strains does not suffer from the limitations of existing frame element models which are formulated as springs in series. These models assign a very high pre-yield stiffness to the plastic spring with a corresponding reduction of the stiffness of the elastic component. This approach is prone to numerical problems under cyclic loading conditions. Instead, the plasticity formulation treats the plastic hinge as a friction-slip component and uses the return-mapping algorithm for the element state determination algorithm. This results in an accurate and numerically robust element for *elastic-plastic* response.

- Following concepts of damage mechanics, the proposed damage model for multiple, interacting stresses or stress resultants and the work-conjugate strains or generalized strains operates independently of the effective constitutive relation. It can, therefore, be used at the material level, at the section level, or at the element level of the frame element formulation. The modular architecture of the analysis framework for the simulations of this study furnishes a family of six frame elements that account for the damage-based strength and stiffness deterioration.

- The inclusion of damage in the frame element formulation with stress-resultants removes some of the limitations of classical plasticity regarding the description of the hysteretic behavior for steel frame members.

- The correlation studies of the damage-based frame element models with available experimental data of the hysteretic response of steel columns under uniaxial or biaxial flexure with constant or variable axial force demonstrate the ability of the proposed models to describe the strength and stiffness deterioration of the specimens with very satisfactory accuracy. It is important that this quality of agreement is achieved with a consistent set of damage parameters for the entire set of specimens under different load regimes and histories. In particular, the frame element models with damage describe well the low-cycle fatigue behavior, the gradual strength and stiffness deterioration with the onset of local buckling, and the damage evolution under different load histories of the steel column specimens.

- While the number of parameters is smaller for the damage model at the material level, the available experimental data under large cyclic inelastic excursions may not be suitable for the parameter estimation, because the damage at a material point of the steel member depends on the three dimensional stress state, while available steel coupon tests refer to uniaxial stress conditions.

- The number of parameters increases for the damage model at the section level, because of the introduction of interaction parameters for the effect of the plastic energy dissipation of one stress-resultant-deformation pair on the damage of another. With three force-deformation pairs for a section under axial force and biaxial flexure the increase in the number of parameters is appreciable. It is even larger for the 5 force-deformation pairs of the 3d beam-column element with one axial and 4 flexural basic forces as stress-resultants. Despite this increase in the number of parameters, most available experimental data for the hysteretic response of steel specimens is in the form of lateral force-deformation or moment-rotation relations. This fact facilitates the parameter selection for the damage model, as demonstrated for the specimens used in the correlation studies.

- The axial plastic energy dissipation plays an important role in the damage evolution of the flexural strength and stiffness of the steel specimens. The good agreement between the frame element with damage and the experimental data confirms that it is possible to describe this influence with confidence, if a well thought experimental campaign with several specimens serves as the basis for the estimation of the interaction parameter.

- The numerical implementation of the damage-based frame elements is efficient to have a small impact on the computational effort of a particular type of element relative to the element without damage. This is rather encouraging for the large scale deployment of the proposed damage-based frame elements.

- The inclusion of damage in the nonlinear response history analysis of an irregular six-story steel frame under a strong ground acceleration in the two principal directions of its base led to the collapse of the structure under the gradual strength and stiffness deterioration of its critical elements. In contrast, the same excitation only produced a significant residual drift for the model with frame elements without damage.

- The computational effort for the nonlinear response history analysis with a fiber beam-column element with damage was 10 times larger than the effort for the stress-resultant beam-column element with damage-based strength and stiffness deterioration.

## 8.3 Recommendations for future research

Possible areas for further study are:

- Exploring the benefits and limitations of accounting for damage at the material, at the section, or at the element level of steel frames.

- Exploring the automatic determination of the damage model parameters with parameter identification methods.

- Assessing the effect of damage on the nonlinear response history analysis under a suite of ground motions to quantify its importance in the presence of multiple, inelastic excursions during one seismic event or a sequence of seismic events.
- Correlating the damage indices of the proposed model to repair costs so as to assess the recovery costs of steel frame structures under different earthquake scenarios.
- Developing adaptive modeling strategies for steel frame structures with damage-based elements.
- Including the effect of shear and torsion on the flexural strength and stiffness deterioration of the frame element with a suitable extension of the proposed damage model.
- Extending the damage formulation to reinforced concrete frame elements.

# Bibliography


[1] D. Addessi and V. Ciampi. "A regularized force-based beam element with a damage–plastic section constitutive law". In: *International Journal for Numerical Methods in Engineering* 70.5 (2007), pp. 610–629. DOI: https://doi.org/10.1002/nme.1911.

[2] S. A. Anagnostopoulos. "Inelastic Beams for Seismic Analyses of Structures". In: *Journal of the Structural Division* 107.7 (1981), pp. 1297–1311. DOI: 10.1061/JSDEAG.0005733.

[3] M. R. Attalla, G. G. Deierlein, and W. McGuire. "Spread of Plasticity: Quasi-Plastic-Hinge Approach". In: *Journal of Structural Engineering-ASCE* 120.8 (1994), pp. 2451–2473. DOI: 10.1061/(ASCE)0733-9445(1994)120:8(2451).

[4] M. R. Azadi Kakavand and E. Taciroglu. "An enhanced damage plasticity model for predicting the cyclic behavior of plain concrete under multiaxial loading conditions". In: *Frontiers of Structural and Civil Engineering* 14 (2020), pp. 1531–1544. DOI: 10.1007/s11709-020-0675-7.

[5] T. Baber and M. Noori. "Random Vibration of Degrading, Pinching Systems". In: *Journal of Engineering Mechanics-ASCE* 111.8 (1985), pp. 1010–1026. DOI: 10.1061/(ASCE)0733-9399(1985)111:8(1010).

[6] T. Baber and Y.-K. Wen. "Random Vibration of Hysteretic, Degrading Systems". In: *Journal of the Engineering Mechanics Division* 107.6 (1981), pp. 1069–1087. DOI: 10.1061/JMCEA3.0002768.

[7] J.M. Bairan and A.R. Mari. "Multiaxial-coupled analysis of RC cross-sections subjected to combined forces". In: *Engineering Structures* 29.8 (2007), pp. 1722–1738. ISSN: 0141-0296. DOI: https://doi.org/10.1016/j.engstruct.2006.09.007.

[8] G. Ballio and C. Castiglioni. "Seismic behavior of steel sections". In: *Journal of Constructional Steel Research* 29 (Dec. 1994), pp. 21–54. DOI: 10.1016/0143-974X(94)90055-8.

[9] K. J. Bathe. "Finite Element Procedures for Solids and Structures LinearAnalysis". In: *Finite Element Procedures* (1982), pp. 148–214.

[10] R. Bouc. "Forced Vibration of Mechanical Systems with Hysteresis". In: Proceedings of 4th Conference Nonlinear Oscillation. Prague, 1967.

[11] Y. Bozorgnia and V. Bertero. "Damage Spectra: Characteristics and Applications to Seismic Risk Reduction". In: *Journal of Structural Engineering-ASCE* 129 (Oct. 2003). DOI: 10.1061/(ASCE)0733-9445(2003)129:10(1330).

[12] F. Casciati. "Stochastic dynamics of hysteretic media". In: *Structural Safety* 6.2 (1989), pp. 259–269. ISSN: 0167-4730. DOI: https://doi.org/10.1016/0167-4730(89)90026-X.

[13] J. L. Chaboche. "Sur l'utilisation des variables d'état interne pour la description de la viscoplasticité cyclique avec endommagement". In: *Problèmes Non Linéaires de Mécanique, Symposium Franco-Polonais de Rhéologie et Mécanique, Cracovie, 1977*. 1977, pp. 137–159.

[14] C. G. Chiorean. "A computer method for nonlinear inelastic analysis of 3D semi-rigid steel frameworks". In: *Engineering Structures* 31.12 (2009), pp. 3016–3033. ISSN: 0141-0296. DOI: https://doi.org/10.1016/j.engstruct.2009.08.003.

[15] A. K. Chopra. *Dynamics of Structures: Theory and Applications to Earthquake Engineering*. Civil Engineering and Engineering Mechanics Series. Prentice Hall, 2012. ISBN: 9780132858038.

[16] A. K. Chopra and F. McKenna. "Modeling viscous damping in nonlinear response history analysis of buildings for earthquake excitation". In: *Earthquake Engineering & Structural Dynamics* 45.2 (2016), pp. 193–211. DOI: https://doi.org/10.1002/eqe.2622.

[17] V. Ciampi and L. Carlesimo. "A nonlinear beam element for seismic analysis of structures". In: *8th European Conference on Earthquake Engineering*. Vol. 3. Laboratorio Nacional de Engenharia Civil. Lisbon, 1986, pp. 6.3/73–6.3/80.

[18] A. Cipollina, A. López-Inojosa, and J. Flórez-López. "A simplified damage mechanics approach to nonlinear analysis of frames". In: *Computers & Structures* 54.6 (1995), pp. 1113–1126. ISSN: 0045-7949. DOI: https://doi.org/10.1016/0045-7949(94)00394-I.

[19] P. Clark et al. *Protocol for fabrication, inspection, testing and documentation of beam-colum connection tests and other experimental specimens*. Tech. rep. SAC/BD-97/02. SAC Joint Venture, Oct. 1997.

[20] R. W. Clough, K. L. Benuska, and E. L. Wilson. "Inelastic earthquake response of tall buildings". In: *Proceedings, Third World Conference on Earthquake Engineering*. Vol. II. Auckland, New Zealand, 1965, pp. 68–89.

[21] R.W. Clough, Structural Engineers Association of California, and Berkeley. Department of Civil Engineering University of California. *Effect of Stiffness Degradation on Earthquake Ductility Requirements*. Tech. rep. UCB/SESM-1966/16. Department of Civil Engineering, University of California, Berkeley, 1966.

[22] J. Coleman and E. Spacone. "Localization issues in force-based frame elements". In: *Journal of Structural Engineering* 127.11 (2001), pp. 1257–1265.

[23] J. Cravero, A. Elkady, and D. Lignos. "Experimental Evaluation and Numerical Modeling of Wide-Flange Steel Columns Subjected to Constant and Variable Axial Load Coupled with Lateral Drift Demands". In: *Journal of Structural Engineering-ASCE* 146.3 (2020), p. 04019222. DOI: 10.1061/(ASCE)ST.1943-541X.0002499.

[24] T. N. Do. "Damage Assessment and Collapse Simulations of Structures under Extreme Loading Conditions". PhD thesis. University of California, Berkeley, 2017. ISBN: 978-0-355-03488-2.

[25] T. N. Do and F. C. Filippou. "A damage model for structures with degrading response". In: *Earthquake Engineering & Structural Dynamics* 47.2 (2018), pp. 311–332. DOI: https://doi.org/10.1002/eqe.2952.

[26] Thanh N. Do and Filip C. Filippou. "A Damage Model for the Simulation and Assessment of Structures with Degrading Element Behavior". In: *Structures Congress 2017*. 2017, pp. 315–327. DOI: 10.1061/9780784480427.027.

[27] A. Elkady and D. Lignos. "Full-Scale Testing of Deep Wide-Flange Steel Columns under Multiaxis Cyclic Loading: Loading Sequence, Boundary Effects, and Lateral Stability Bracing Force Demands". In: *Journal of Structural Engineering-ASCE* 144 (Nov. 2017), p. 04017189. DOI: 10.1061/(ASCE)ST.1943-541X.0001937.

[28] J. Faleiro, S. Oller, and A. Barbat. "Plastic-damage analysis of reinforced concrete frames". In: *Engineering Computations* 27 (2010), pp. 57–83.

[29] F. C. Filippou and A. Issa. *Nonlinear analysis of reinforced concrete frames under cyclic load reversals*. Tech. rep. UCB/EERC–88/12. University of California, Berkeley: Earthquake Engineering Research Center, 1988.

[30] F. C. Filippou, E. P. Popov, and V. V. Bertero. *Effects of Bond Deterioration on Hysteretic Behavior of Reinforced Concrete Joints*. Tech. rep. 1983.

[31] J. Flórez-López. "Frame analysis and continuum damage mechanics". In: *European Journal of Mechanics - A/Solids* 17.2 (1998), pp. 269–283. ISSN: 0997-7538. DOI: https://doi.org/10.1016/S0997-7538(98)80086-7.

[32] M. F. Giberson. "The response of nonlinear multi-story structures subjected to earthquake excitation". PhD thesis. California Institute of Technology, Pasadena, 1967.

[33] J. F. Hajjar and B. C. Gourley. "A cyclic nonlinear model for concrete-filled tubes. I: Formulation". In: *Journal of Structural Engineering-ASCE* 123.6 (1997), pp. 736–744.

[34] S. I. Hilmy and J. F. Abel. "Material and geometric nonlinear dynamic analysis of steel frames using computer graphics". In: *Computers & Structures* 21.4 (1985), pp. 825–840. ISSN: 0045-7949. DOI: https://doi.org/10.1016/0045-7949(85)90159-2.

[35] K. Hjelmstad and E. Taciroglu. "Mixed methods and flexibility approaches for nonlinear frame analysis". In: *Journal of Constructional Steel Research* 58.5-8 (2002), pp. 967–993. DOI: 10.1016/S0143-974X(01)00100-6.

[36] Y. Huang and S. A. Mahin. "Simulating the Inelastic Seismic Behavior of Steel Braced Frames Including the Effects of Low-Cycle Fatigue". PhD thesis. University of California, Berkeley, 2009.

[37] L. Ibarra, R. Medina, and H. Krawinkler. "Hysteretic Models that Incorporate Strength and Stiffness Deterioration". In: *Earthquake Engineering & Structural Dynamics* 34 (Oct. 2005), pp. 1489–1511. DOI: 10.1002/eqe.495.

[38] P. Inglessis et al. "Model of damage for steel frame members". In: *Engineering Structures* 21.10 (1999), pp. 954–964. ISSN: 0141-0296. DOI: https://doi.org/10.1016/S0141-0296(98)00038-8.

[39] J. Jin and S. El-Tawil. "Inelastic cyclic model for steel braces". In: *Journal of Engineering Mechanics-ASCE* 129.5 (2003), pp. 548–557.

[40] L. M. Kachanov. "Time of the Rupture Process under Creep Conditions". In: *Izvestia Akademi Nauk U.S.S.R. Otd Tech Nauk, Moskwa* 8 (1958), pp. 26–31.

[41] G. Kaewkulchai and E. B. Williamson. "Beam element formulation and solution procedure for dynamic progressive collapse analysis". In: *Computers & Structures* 82.7 (2004), pp. 639–651. ISSN: 0045-7949. DOI: https://doi.org/10.1016/j.compstruc.2003.12.001.

[42] K. Kasai, T. T. Nam, and B. F. Maison. "Structural collapse correlative analysis using phenomenological fiber hinge elements to simulate two-directional column deteriorations". In: *Earthquake Engineering & Structural Dynamics* 45.10 (2016), pp. 1581–1601. DOI: https://doi.org/10.1002/eqe.2742.

[43] W. T. Koiter. *General Theorems for Elastic-Plastic Solids*. North-Holland, 1960.

[44] G. Konig and A. Ötes. "Modelling of stiffness and damping change in reinforced concrete structures under seismic actions". In: *Transactions of the 8th International Conference on Structural Mechanics in Reactor Technology*. 1985, pp. 401–406. ISBN: 9780444869647.

[45] S. M. Kostic and F. C. Filippou. "An Adaptive Section Discretization Scheme for the Nonlinear Dynamic Analysis of Steel Frames". In: *Journal of Structural Engineering-ASCE* (2023). (accepted for publication).

[46] W. B. Krätzig, I. F. Meyer, and K. Meskouris. "Damage Evolution in Reinforced Concrete Members Under Cyclic Loading". In: *Structural Safety and Reliability: Proceedings of ICOSSAR '89, the 5th International Conference on Structural Safety and Reliability, San Francisco, August 7-11, 1989*. Vol. I. ASCE, New York, 1989, pp. 795–804. ISBN: 0872627438.

[47] H. Krawinkler and M. Zohrei. "Cumulative damage in steel structures subjected to earthquake ground motions". In: *Computers & Structures* 16.1 (1983), pp. 531–541. ISSN: 0045-7949. DOI: https://doi.org/10.1016/0045-7949(83)90193-1.

[48] V. Le Corvec. "Nonlinear 3d frame element with multi-axial coupling under consideration of local effects". PhD thesis. University of California, Berkeley, 2012.

[49] C.-L. Lee. "Hu-Washizu 3d Frame Formulations Including Bond-Slip and Singular Section Response". PhD thesis. University of California, Berkeley, Dec. 2008.

[50] C.-L. Lee and F. C. Filippou. "Efficient Beam-Column Element with Variable Inelastic End Zones". In: *Journal of Structural Engineering-ASCE* 135.11 (2009), pp. 1310–1319. DOI: 10.1061/(ASCE)ST.1943-541X.0000064.

[51] J. Lemaitre and J. L. Chaboche. "Aspect phénoménologique de la rupture par endommagement". In: *Jounal de Mécanique Appliquée* 2.3 (1978), pp. 317–365.

[52] S. A. Mahin and V. V. Bertero. "Problems in establishing and predicting ductility in aseismic design". In: *Proceedings, International Symposium on Earthquake Structural Engineering*. Saint Louis, Missouri, 1976, pp. 613–628.

[53] J. Mazars and G. Pijaudier-Cabot. "Continuum Damage Theory - Application to Concrete". In: *Journal of Engineering Mechanics-ASCE* 115 (1989), pp. 345–365.

[54] S. S. F. Mehanny. "Damage Assessment and Collapse Simulations of Structures under Extreme Loading Conditions". PhD thesis. Stanford University, 1999.

[55] M. L. Menegotto and P. E. Pinto. "Method of analysis for cyclically loaded R.C. plane frames including changes in geometry and non-elastic behaviour of elements under combined normal force and bending". ger ; eng. In: *Rapports des commissions de travail AIPC = IVBH Berichte der Arbeitskommissionen = IABSE reports of the working commissions* 13 (1973), pp. 15–22. ISSN: 0074-1442.

[56] C. Meyer, M. S. L. Roufaiel, and S. G Arzoumanidis. "Analysis of damaged concrete frames for cyclic loads". In: *Earthquake Engineering & Structural Dynamics* 11.2 (1983), pp. 207–228.

[57] A. Neuenhofer and F. C. Filippou. "Evaluation of nonlinear frame finite-element models". In: *Journal of Structural Engineering-ASCE* 123.7 (1997), pp. 958–966.

[58] N. C. Nigam. "Yielding in framed structures under dynamic loads". In: *Journal of the Engineering Mechanics Division* 96.5 (1970), pp. 687–709.

[59] P. K. V. V. Nukala and D. W. White. "A mixed finite element for three-dimensional nonlinear analysis of steel frames". In: *Computer Methods in Applied Mechanics and Engineering* 193.23-26 (2004), pp. 2507–2545.

[60] *OpenSees*. URL: https://opensees.berkeley.edu.

[61] J. G. Orbison, W. McGuire, and J. F. Abel. "Yield surface applications in nonlinear steel frame analysis". In: *Computer Methods in Applied Mechanics and Engineering* 33.1 (1982), pp. 557–573. ISSN: 0045-7825. DOI: https://doi.org/10.1016/0045-7825(82)90122-0.

[62] Y. J. Park and A. H.-S. Ang. "Mechanistic seismic damage model for reinforced concrete". In: *Journal of Structural Engineering-ASCE* 111.4 (1985), pp. 722–739.

[63] Y. J. Park, A. M. Reinhorn, and S. K. Kunnath. *IDARC: Inelastic Damage Analysis of Reinforced Concrete Frames*. Tech. rep. NCEER-87-0008. State University of New York at Buffalo, Buffalo, NY: National Center for Earthquake Engineering Research, 1987.

[64] *PEER Ground Motion Database*. URL: https://ngawest2.berkeley.edu.

[65] *Perform3d*. URL: https://www.csiamerica.com/products/perform3d.

[66] M. Petrangeli and V. Ciampi. "Equilibrium based iterative solutions for the non-linear beam problem". In: *International Journal for Numerical Methods in Engineering* 40.3 (1997), pp. 423–437.

[67] G. H. Powell and P. F. S. Chen. "3D beam-column element with generalized plastic hinges". In: *Journal of Engineering Mechanics-ASCE* 112.7 (1986), pp. 627–641.

[68] P. S. Rao et al. "Damage model for reinforced concrete elements under cyclic loading". In: *Materials Journal* 95.6 (1998), pp. 682–690.

[69] A. Reinhorn et al. *Modeling of Masonry Infill Panels for Structural Analysis*. Tech. rep. NCEER-95-0018. State University of New York at Buffalo, Buffalo, NY: National Center for Earthquake Engineering Research, 1995.

[70] M. H. Scott and G. L. Fenves. "Plastic hinge integration methods for force-based beam-column elements". In: *Journal of Structural Engineering* 132.2 (2006), pp. 244–252.

[71] M. H. Scott and O. M. Hamutcuoglu. "Numerically consistent regularization of force-based frame elements". In: *International Journal for Numerical Methods in Engineering* 76.10 (2008), pp. 1612–1631. DOI: https://doi.org/10.1002/nme.2386.

[72] *Seismic Provisions for Structural Steel Buildings, ANSI/AISC 341-10*. AISC. AISC, 2016.

[73] J. C. Simo and T. J. R. Hughes. *Computational Inelasticity*. Interdisciplinary applied mathematics. Springer, 1998. ISBN: 9783540975205.

[74] J. C. Simo and J. W. Ju. "Strain- and stress-based continuum damage models—I. Formulation". In: *International Journal of Solids and Structures* 23.7 (1987), pp. 821–840. ISSN: 0020-7683. DOI: https://doi.org/10.1016/0020-7683(87)90083-7.

[75] A. Singh. "Performance Based Analysis of Steel Structures using Concentrated Plasticity Frame Element". MA thesis. University of California, Berkeley, 2020.

[76] M. Sivaselvan and A. Reinhorn. *Hysteretic Models for Cyclic Behavior of Deteriorating Inelastic Structures*. Tech. rep. MCEER-99-0018. State University of New York at Buffalo, Buffalo, NY: Multidisciplinary Center for Earthquake Engeenering Research, 1999.

[77] D. Soleimani, E. P. Popov, and V. V. Bertero. "Nonlinear beam model for R/C frame analysis". In: *Seventh Conference on Electronic Computation*. ASCE. 1979, pp. 483–509.

[78] J. K. Song and J. A. Pincheira. "Spectral Displacement Demands of Stiffness- and Strength-Degrading Systems". In: *Earthquake Spectra* 16.4 (2000), pp. 817–851. DOI: 10.1193/1.1586141.

[79] R. M. de Souza. "Force-based finite element for large displacement inelastic analysis of frames". PhD thesis. University of California, Berkeley, 2000. ISBN: 978-0-493-10466-9.

[80] E. Spacone, V. Ciampi, and Filippou F. C. "Mixed formulation of nonlinear beam finite element". In: *Computers & Structures* 58.1 (1996), pp. 71–83. ISSN: 0045-7949. DOI: https://doi.org/10.1016/0045-7949(95)00103-N.

[81] E. Spacone, F. C. Filippou, and F. F. Taucer. "Fibre beam-column model for non-linear analysis of R/C frames: Part I. Formulation". In: *Earthquake Engineering & Structural Dynamics* 25.7 (1996), pp. 711–725.

[82] E. Spacone, F. C. Filippou, and F. F. Taucer. "Fibre beam-column model for non-linear analysis of R/C frames: Part II. Applications". In: *Earthquake Engineering & Structural Dynamics* 25.7 (1996), pp. 727–742.

[83] Y. Suzuki and D. Lignos. "Development of loading protocols for experimental testing of steel columns subjected to combined high axial load and lateral drift demands near collapse". In: *NCEE 2014 - 10th U.S. National Conference on Earthquake Engineering: Frontiers of Earthquake Engineering* (Jan. 2014). DOI: 10.4231/D3M32N99R.

[84] T. Takeda, M. A. Sozen, and N. N. Nielsen. "Reinforced Concrete Response to Simulated Earthquakes". In: *Journal of the Structural Division* 96.12 (1970), pp. 2557–2573. DOI: 10.1061/JSDEAG.0002765.

[85] H. Takizawa and H. Aoyama. "Biaxial effects in modelling earthquake response of R/C structures". In: *Earthquake Engineering & Structural Dynamics* 4.6 (1976), pp. 523–552. DOI: https://doi.org/10.1002/eqe.4290040602.

[86] F. Taucer, E. Spacone, and F. C. Filippou. *A fiber beam-column element for seismic response analysis of reinforced concrete structures*. Berkeley, Calif.: Earthquake Engineering Research Center, College of Engineering, University of California, 1991.

[87] S. El-Tawil and G. G. Deierlein. "Stress-resultant plasticity for frame structures". In: *Journal of Engineering Mechanics-ASCE* 124.12 (1998), pp. 1360–1370.

[88] R. L. Taylor et al. "A mixed element method for beam and frame problems". In: *Computational Mechanics* 31.1-2 (2003), pp. 192–203. DOI: 10.1007/s00466-003-0410-y.

[89] Y.-K. Wen. "Method for Random Vibration of Hysteretic Systems". In: *Journal of the Engineering Mechanics Division* 102.2 (1976), pp. 249–263. DOI: 10.1061/JMCEA3.0002106.

[90] J. Y. Wu, J. Li, and R. Faria. "An energy release rate-based plastic-damage model for concrete". In: *International Journal of Solids and Structures* 43.3 (2006), pp. 583–612. ISSN: 0020-7683. DOI: https://doi.org/10.1016/j.ijsolstr.2005.05.038.

[91] U. Yadav. "A Beam Element with Efficient Inelastic Zone Integration". MA thesis. University of California, Berkeley, 2021.

[92] O. C. Zienkiewicz and R. L. Taylor. *The finite element method for solid and structural mechanics*. Elsevier, 2005.

[93] O. C. Zienkiewicz, R. L. Taylor, and J. Z. Zhu. *The Finite Element Method: Its Basis and Fundamentals*. Elsevier Science, 2005. ISBN: 9780080472775.